CASE HISTORY - BASED ANALYSIS OF LIQUEFACTION IN SLOPING GROUND

BY

KASHIF MUHAMMAD

DISSERTATION

Submitted in partial fulfillment of the requirements
for the degree of Doctor of Philosophy in Civil Engineering
in the Graduate College of the
University of Illinois at Urbana-Champaign, 2012

Urbana, Illinois

Doctoral Committee:

Associate Professor Scott M. Olson, Director of Research
Professor Gholamreza Mesri
Professor James H. Long
Professor Erol Tutumluer

ABSTRACT

Liquefaction is one of the most interesting and controversial phenomenon in geotechnical engineering. This phenomenon has caused numerous slope failures in saturated deposits of fine, loose sands and other cohesionless soils. Because of the catastrophic nature of the failures and their impact on the built environment, liquefaction problems have received a great deal of attention among the geotechnical community and many efforts have been made to clarify basic mechanisms and various aspects of the problems associated with liquefaction. Although liquefaction can occur in both level and sloping ground, this research focuses on sloping ground liquefaction.

The analysis of liquefaction in sloping ground is divided into three steps: (1) liquefaction susceptibility; (2) liquefaction triggering; and (3) post-triggering stability analysis. Existing procedures to evaluate liquefaction susceptibility, triggering, and post-triggering stability in sloping ground include: (1) methods based on laboratory soil testing; (2) methods based on empirical relationships back-calculated from case histories; (3) finite element methods involving constitutive models of sandy soils; and (4) combination laboratory testing and back-analysis of case histories or laboratory testing and finite element modeling. This study investigates approach (2) because it does not require expensive and time-consuming laboratory testing, it is simple for engineers to apply in practice, and it do not require input parameters that are hard to determine and may have little or no physical meaning. Specifically in this study, the author documented and analyzed 31 reasonably well-documented case histories and combined those with 33 case histories analyzed by Olson (2001).

Liquefaction susceptibility analysis evaluates whether a particular soil is susceptible to liquefaction, i.e., is the soil contractive or dilative during shear? The combined case history database was used to evaluate: (1) empirical and semi-empirical contractive-dilative boundaries; (2) the role of fines content on liquefaction susceptibility in sloping ground conditions; and (3) the viability of an extended cone penetration test “compressibility” correction factor for susceptibility analysis.

If a soil deposit is susceptible to liquefaction, a liquefaction triggering analysis is performed. This step involves evaluating whether a particular combination of static and dynamic/seismic loads are sufficient to trigger liquefaction. The author used the combined case history database to evaluate: (1) available empirical and semi-empirical relationships for yield shear strength ratios, $s_u(\text{yield})/\sigma'_{vo}$; and (2)

the effect of the mode of shear on yield shear strengths mobilized in flow failure case histories.

If liquefaction is triggered in a soil deposit, a post-triggering stability (flow failure) analysis is performed. This step evaluates whether the geo-structure is stable when the shear resistance includes the liquefied shear strength, $s_u(liq)$. The author used the combined case history database to evaluate: (1) available empirical and semi-empirical relationships for liquefied shear strength ratios, $s_u(liq)/s'_{vo}$; (2) the effect of the mode of shear on yield shear strengths mobilized in flow failure case histories; and (3) the relation between brittleness index and $s_u(liq)$.

Finally, three case histories subjected to six separate earthquakes were used to evaluate the proposed liquefaction evaluation procedure. These cases were analyzed for susceptibility, triggering and post triggering to predict the field behavior, and illustrated that the proposed procedure is able to capture the severity of failure experienced at the individual sites during earthquake shaking.

TO MY PARENTS AND FAMILY

ACKNOWLEDGMENTS

First of all I am thankful to Almighty Allah (SWT) for giving me the strengths and blessing in completing this thesis.

Secondly my deep gratitude goes to my advisor, Professor Scott M. Olson, who helped me throughout my doctoral program. I highly appreciate his guidance, support, and encouragement. His commitment to me and my research was far exceeding my expectations of an advisor - graduate student relationship. I am fortunate to have worked with him.

I also would like to express my sincere appreciation to the members of my doctoral defense committee members: Professors Gholamreza Mesri, Professor James H. Long, and Professor Erol Tutumluer for their constructive criticism and input. In particular Professor Gholamreza Mesri who I benefited from his great wisdom, vision, and experience throughout my entire study and research. I would also like to thank Professor Timothy D. Stark who time to time helped my in my research.

I extend my thanks to all former and current geotechnical engineering graduate students for their friendship and thoughtful discussions which contributed greatly to my education, especially Dr. Nejan Huvaj, Dr. Abouzar Sadrekarimi, Dr. Manzoor Hussain, Dr. Abdul Qudoos Khan, Dr. Kamran Akhtar, Mr. Mark Muszynski, Mr. Jason Funk, Mr. David Groholski, and Mrs. Randa Al Asmar.

I would like to acknowledge the support of the Government of Pakistan (Ministry of Defense), not only for providing the funding which allowed me to undertake this research, but also for the health insurance of my family and books expenditure so that I can focus on my studies. Without their support I would not be able to come to USA and pursue my PhD.

I owe the most to my parents, whose value to me only grows with age. And finally, I acknowledge my wife, Laila and my kids Fatima, Mujtaba, Fizza and Maryam who blessed me with a life of joy and support in the hours when my office lights were off.

TABLE OF CONTENTS

CHAPTER ONE:

INTRODUCTION

1.1 Introduction to the Problem

Liquefaction is one of the most interesting and controversial phenomenon in geotechnical engineering. The term “liquefied” was first used by Hazen (1918, 1920) to describe the sandy soils involved in the failure of Calaveras Dam, and later Terzaghi and Peck (1948) used the term “spontaneous liquefaction” to describe the behavior of metastable, very loose sands. This phenomenon was considered to be the main cause of numerous slope failures in saturated deposits of fine, loose sands. The devastating earthquakes of Prince William Sound, Alaska, and Niigata, Japan, in 1964 are considered milestones in the study of liquefaction as the occurrence of liquefaction and its consequences were well-documented and publicized following these events. Because of its engineering importance and the catastrophic nature of the failures, liquefaction problems have received a great deal of attention among the geotechnical community and many efforts have been made to clarify basic mechanisms and various aspects of the problems associated with liquefaction.

Liquefaction can occur in both level and sloping ground. This research focuses on sloping ground liquefaction. Existing procedures to evaluate liquefaction susceptibility, triggering, and post-triggering stability in sloping ground include: (1) methods based on laboratory soil testing (e.g., Poulos 1985; Ishihara 1993); (2) methods based on empirical relationships back-calculated from case histories (e.g., Seed 1987; Seed and Harder 1990; Stark and Mesri 1992; Baziar and Dobry 1995; Olson and Stark 2002, 2003; Olson et al. 2006; Idriss and Boulanger 2006, 2007; Mesri 2009; Olson 2009; Robertson 2010); (3) finite element methods involving constitutive models of sandy soils (e.g., Prevost 1985, Finn et al. 1986; Byrne 1991; Popescu and Prevost 1992; Byrne et al. 1992; Byrne and Beaty 1997; Finn 1999; Beaty 2001; Prevost 2002; Byrne et al. 2004; Byrne 2008); and

(4) combination laboratory testing and back-analysis of case histories or laboratory testing and finite element modeling (Ishihara 1993; Byrne et al. 2004; Robertson 2004; Jefferies and Been 2006; and Beaty and Byrne 2008).

These approaches all suffer from one or more shortcomings. For example Approach (1) requires expensive laboratory testing on specimens that are difficult to obtain; Approach (2) is hampered by a lack of adequate number of case histories, and in some cases, requires significant correction factors that exhibit large scatter; Approach (3) involves stress-strain constitutive models that require numerous (uncertain) input parameters; and Approach (4) suffers from problems associated with both Approaches (2) and (3). This study investigates Approach (2) because it does not require expensive and time-consuming sampling and laboratory testing, it is simple for engineers to apply in practice, and it does not require input parameters that are hard to determine and may have little or no physical meaning.

The analysis of liquefaction in sloping ground can be divided into three steps as defined by Olson (2001): (1) liquefaction susceptibility; (2) liquefaction triggering; and (3) post-triggering/flow failure stability. Despite the considerable work that has been done by many investigators to characterize these steps, there are few case histories available to validate any one approach. Additional work, particularly in terms of increasing the number of case histories, could reduce the uncertainties associated with analyzing liquefaction flow failures. The following paragraphs briefly discuss each step in the procedure and indicate the issues associated with them.

Liquefaction susceptibility was first described about 40 years ago by Tsuchida (1970). This study simply separated soils that did or did not liquefy during past earthquakes based on grain size distribution. However, this approach chiefly involves sites of level-ground liquefaction, and more importantly, it does not quantitatively evaluate the contractive or dilative nature of the soil, i.e., its susceptibility to strain-softening response, or flow liquefaction. Later, Sladen and Hewitt (1989), Robertson et al. (1992), Ishihara (1993), Baziar and Dobry (1995), Fear and Robertson (1995), Olson

(2001, 2003, 2009), and Robertson (2004, 2009, 2010) suggested various procedures to evaluate whether soils were in a contractive state (i.e., susceptible to flow liquefaction) based on penetration resistance and effective vertical stress. These investigators proposed various "susceptibility boundaries" to identify contractive soils. However, these susceptibility boundaries are hampered by a lack of case histories and a poor understanding of the effect of nonplastic fines content (FC, percent of soil by weight smaller than 0.075mm) on liquefaction susceptibility. Recently, Olson (2009) indicated the importance of soil compressibility on the liquefaction susceptibility boundary and suggested that fines content only may not be adequate to capture the influence of compressibility. Therefore, more case histories are needed to evaluate available liquefaction susceptibility boundaries. Further investigation of the role of compressibility on liquefaction susceptibility is needed.

Among the three steps that are used to analyze liquefaction in ground subjected to static shear stress (i.e., sloping ground), few procedures are available to evaluate the triggering of liquefaction (Olson 2001). While procedures to evaluate the triggering of liquefaction in level ground were proposed in the early 1970s (Seed and Idriss 1971; Whitman 1971), the role of sloping ground on liquefaction was not investigated in detail until later. Four more widely-used methods to evaluate the triggering of liquefaction in sloping ground are: (1) Poulos et al. (1985) and Castro et al. (1989), largely based on laboratory tests; Seed (1979), Seed (1983), Rollins and Seed (1990) and Seed and Harder (1990) (termed the K_α-approach), also largely based on laboratory tests; (3) Olson (2001) and Olson and Stark (2003) (termed the yield strength ratio approach), based on empirical correlations from liquefaction flow failure case histories; and (4) Byrne (1991) and Byrne et al. (1992), based largely on numerical simulations. The current study is focused on case histories and empirical correlation; therefore, the K_α and yield strength ratio approaches are discussed here.

During the last two decades, the K_α approach has been revised and updated by Seed and Harder (1990), Harder and Boulanger (1997), Boulanger (2003), Idriss and Boulanger (2004), and Idriss and Boulanger (2006). Based on the concept proposed by

Terzaghi et al. (1996), Olson (2001) and Olson and Stark (2003) proposed the yield strength ratio approach, which was later updated by Olson et al. (2006), Mesri (2007), Olson (2009), and Olson and Zitny (2012). Both the K_α and yield strength ratio approaches can be applied to evaluate liquefaction of sloping ground. The K_α approach uses correction factors, termed K_α and K_σ, to adjust level-ground liquefaction resistance relationships to accommodate static shear stress on the horizontal plane greater than zero and vertical effective stresses different than atmospheric pressure (approximately 100 kPa), respectively. Despite numerous updates, these factors exhibit large scatter. Similarly, the yield strength ratio approaches by Olson et al. (2006) and Mesri (2007) are hampered by a lack of an adequate number of case histories to validate the method.

Numerous investigators have proposed procedures and/or correlations to estimate the liquefied shear strength used for post-triggering or flow failure stability analysis (e.g., Poulos et al. 1985; Seed 1987, Seed and Harder 1990; Jefferies et al. 1990; Stark and Mesri 1992; Ishihara 1993; Konrad and Watts 1995; Fear and Robertson 1995; Olson 2001, Olson and Stark 2002; Jefferies and Been 2005; Mesri 2007; Idriss and Boulanger 2008; and Robertson 2010). Again, because of the difficulties associated with retrieving samples of sandy soils, the case history-based empirical correlations to estimate the liquefied shear strength proposed by Seed and Harder (1990) and by Olson and Stark (2002) are most widely used. The primary difference between the two approaches is that the former correlation yields the liquefied (or residual) shear strength, while the latter correlation yields the liquefied shear strength *ratio*. Furthermore, the Seed and Harder (1990) correlation involves both flow failures and lateral spreads, while the Olson and Stark (2002) correlation is based solely on flow failures. The correlations from Mesri (2007) and Idriss and Boulanger (2008) largely use the data compiled by Olson (2001) and are quite similar to the Olson and Stark (2002) correlation. These uncertainties include: (1) combining liquefaction flow failures and lateral spreads; (2) selecting "representative" values of penetration resistance; and (3) many of the back-analyses are not well-documented, and the more recent back-analyses performed by Olson (2001) yielded liquefied shear strengths that, in many cases, differed fairly significantly.

Olson (2001) and Olson and Stark (2002) proposed a correlation between the liquefied shear strength ratio and “representative” penetration resistance. While this correlation still involves uncertainties related to selecting a “representative” penetration resistance, the correlation is based on nearly twice as many case histories as previous correlations. Olson (2001) and Olson and Stark (2002) analyzed 33 reasonably-documented case histories to estimate the liquefied shear strength and liquefied shear strength ratios, but increasing the number of reasonably-documented cases will reduce uncertainties involved in the correlation.

Mesri (2007) suggested a possible relationship between the liquefied shear strength ratio and the static shear stress ratio. Additional case histories would be valuable in assessing this concept.

Idriss and Boulanger (2008) suggest separate correlations for liquefied shear strength and liquefied shear strength ratio that differ depending on whether the liquefied soil experiences drainage or void redistribution during failure. However, these differences are not supported quantitatively by any available liquefaction flow failure case histories. Therefore, additional case histories would be valuable in assessing this concept.

In addition to the issues discussed above, liquefaction assessment methods for sloping ground have not been adequately verified using case histories where flow liquefaction has occurred (because few flow failures are well-documented; all well-documented cases have been used for developing correlations) and where flow failure has not occurred after strong shaking. Therefore, this study uses a limited number of case histories, including a site that experienced multiple shaking events, to initially validate the liquefaction analysis procedure proposed by Olson (2001)/Olson and Stark (2003).

1.2 Objectives of the Study

The objectives of this study are to improve available procedures to evaluate the liquefaction of sloping ground, primarily by increasing the number of documented liquefaction flow failure case histories. Specifically, this study addresses the following issues.

1. Increase substantially the number of documented liquefaction flow failure case histories for use in evaluating liquefaction susceptibility, yield shear strength ratio, and liquefied shear strength ratio.
2. Evaluate liquefaction susceptibility relationships based on cone penetration test (CPT) and standard penetration test (SPT) results from Fear and Robertson (1995), Olson (2001), and Olson (2009). In this evaluation, this study focuses on the role of fines content and compressibility on liquefaction susceptibility.
3. Evaluate correlations for yield shear strength ratio and the liquefaction triggering procedure proposed by Olson (2001) and Olson et al. (2006). Evaluate correlations for liquefied shear strength ratio proposed by Seed and Harder (1990), Olson and Stark (2002), Mesri (2007), and Idriss and Boulanger (2008).
4. Validate the proposed or adopted liquefaction evaluation procedure using case histories of slopes or embankments that experienced and did not experience liquefaction flow failure during earthquakes.

In order to evaluate the existing relationships from Olson (2001) and Olson et al. (2006), the author collected more than 100 liquefaction flow failure case histories from all over the world. However, most of the case histories were discarded because key parameters, e.g., pre-failure geometry or penetration resistance were missing. The author then selected 31 reasonably documented case histories, in which most of the information was available or could be reasonably estimated for further analysis. These flow failure case histories were back-analyzed to evaluate the yield shear strength and yield shear

strength ratio mobilized at the triggering of liquefaction. In addition, the flow failure case histories also were back-analyzed to evaluate the liquefied shear strength and liquefied strength ratio mobilized at large displacements. For cases with sufficient information, the post-triggering stability back-analysis incorporated the kinetics of failure (i.e., momentum).

1.3 Scope and Outline of Current Study

The chapters in this thesis are organized as follows. Chapter 1 explores the problems in available liquefaction evaluation procedures for sloping ground. Chapter 2 briefly describes basic concepts related to liquefaction, liquefaction mechanisms, and important terms and definitions that are frequently used throughout this dissertation. Chapter 3 is devoted to review of previous research in published literature. Chapter 4 focuses on SPT- and CPT-based liquefaction susceptibility relationships, including the role of compressibility and fines content on liquefaction susceptibility. SPT- and CPT-based liquefaction triggering relationships are evaluated in Chapter 5. Chapter 6 deals with SPT- and CPT-based liquefied shear strengths. Chapter 7 describes case histories used to validate the proposed liquefaction evaluation procedure. Chapter 8 summarizes the results of the study and presents conclusions. A detailed analysis of each case history is given in Appendix A.

1.4 References

Baziar, M.H. and Dobry, R. (1995). Residual strength and large-deformation potential of loose silty snads. *Journal of Geotechnical Engineering,* ASCE, vol. 121, iss. 12, p. 896 – 906.

Beaty, M.H., and Byrne, P.M. (2008). Liquefaction and deformation analysis using a total stress approach. *Journal of Geotechnical and Geoenvironmental Engineering,* vol. 134, iss. 8, p. 1059 – 1072.

Boulanger, R.W. (2003). High overburden stress effects in liquefaction analyses. *Journal of Geotechnical and Geoenvironmental Engineering,* ASCE, vol. 129, iss. 12, p. 1071 – 1082.

Byrne, P.M. (1991). A model for predicting liquefaction induced displacements. *Proceedings of the Second International Conference on Recent Advances in Geotechnical Earthquake Engineering and Soil Dynamics,* St. Louis, vol. 2, p. 1027 – 1035.

Byrne, P.M., Salgado, F., and Jinto, H. (1992). Earthquake induced displacement of soil structure systems. *Proceedings of the Tenth World Conference on Earthquake Engineering,* Madrid, Spain, vol. 3, p. 1407 – 1412.

Byrne, P.M., and Beaty, M.H. (1997). Post-liquefaction shear strength of granular soils: theoretical/conceptual issues. *In proceedings, Workshop on Post-Liquefaction Shear Strength of Granular Soils,* Urbana-Champaign, Illinois, April 17-18, 1997, p. 16 – 45.

Byrne, P.M., Park, S., Beaty, M., Sharp, M., Gonzalez, L., and Abdoun T. (2004). Numerical modeling of liquefaction and comparison with centrifuge tests. *Canadian Geotechnical Journal,* vol. 41, p. 193 – 211.

Castro, G., Keller, T.O., and Boynton, S.S. (1989). Re-evaluation of the Lower San Fernando Dam: Report 1, an investigation of the February 9, 1971 slide. *U.S. Army Corps of Engineers Contract Report GL-89-2,* vols. 1 and 2, U.S. Army Corps of Engineers Waterways Experiment Station, Vicksburg, Mississippi.

Fear, C.E. and Robertson, P.K. (1995). Estimating the undrained strength of sand: a theoretical framework. *Canadian Geotechnical Journal,* vol. 32, iss. 4, p. 859 – 870.

Finn, W.D.L., Yogendrakumar, M. and Yoshida, N. (1986). Response of 2D embankment systems to seismic loading – program TARA-3. *Soil Mechanics Series,* University of British Columbia, Canada.

Finn, W.D. Liam. (1998). Seismic safety of embankment dams development in research and practice 1988 – 1998. *Geotechnical Special Publication No. 75,* Proceedings of a Specialty Conference on Geotechnical Earthquake Engineering and Soil Dynamics III, p. 812 – 853.

Harder, L.F., Jr., and Boulanger, R. (1997). Application of K and K correction factors. *In Proceedings of the National Center for Earthquake Engineering Research (NCEER) Workshop on Evaluation of Liquefaction Resistance of Soils.* Salt Lake City, Utah, 5 – 6 January 1996. NCEER, State University of New York at Buffalo, N.Y. Edited by T.L. Youd and I.M. Idriss, NCEER-97-0022. p. 167 – 190.

Hazen, A. (1918). A study of the slip in the Calaveras Dam. *Engineering News-Record,* vol. 81, iss. 26, p. 1158 – 1164.

Hazen, A. (1920). Hydraulic-fill dams. *Transactions of the American Society of Civil Engineers,* Paper No. 1458, p. 1713 – 1821 (including discussions).

Idriss, I.M. and Boulanger, R.W. (2006). Semi-empirical procedures for evaluating liquefaction potential during earthquakes. *Soil Dynamics and Earthquake Engineering,* vol. 26, p. 115 – 130.

Idriss, I.M. and Ross W. Boulanger (2007). SPT – and – CPT – based relationships for the residual shear strength of liquefied soils, *Proceedings, 27th USSD Annual Meeting and Conference, Modernization and Optimization of Existing Dams and Reservoirs,* United States Society on Dams, Philadelphia, Pennsylvania, March 5 – 9, 2007.

Ishihara, K. (1993). Liquefaction and flow failure during earthquakes. *Geotechnique,* vol. 43, iss. 3, p. 351 – 415.

Jefferies, M., and Been, K. (2006). Soil liquefaction: a critical state approach. *Taylor and Francis,* p. 512.

Konrad, J.M. and Watts, B.D. (1995). Undrained shear strength for liquefaction flow failure analysis. *Canadian Geotechnical Journal,* vol. 32, p. 783 – 794.

Mesri G. (2007). Yield strength and critical strength of liquefiable sands in sloping ground, *Geotechnique,* vol. 57, issue 3, p. 309 – 311.

Olson, S. M. (2001). Liquefaction analysis of level and sloping ground using field case histories and penetration resistance, *Ph.D. Thesis,* University of Illinois at Urbana-Champaign, Urbana, Illinois.

Olson, S.M. and Stark, T.D. (2002). Liquefied strength ratio from liquefied flow failure case histories, *Canadian Geotechnical Journal,* vol. 39, p. 629 – 647.

Olson, S.M. and Stark, T.D. (2003). Use of laboratory data to confirm yield and liquefied strength ratio concepts, *Canadian Geotechnical Journal,* vol. 40, p. 1164 – 1184.

Olson S.M. (2003). Strength ratio-based liquefaction analysis of sloping ground. *Proceedings of the 12th Panamerican Conference on Soil Mechanics and Geotechnical Engineering,* June 23 – 26, Boston, MA, Paper No. 271.

Olson, S. M., Sacks, A. L., Mattson, B. B., and Servigna, D. A. (2006). Role of static shear stress in liquefaction analysis of sloping ground, *Proceedings of the 8th US National Conference on Earthquake Engineering*

Olson, S. M. (2009). Strength ratio approach for liquefaction analysis of tailings dams, *University of Missouri Conference*.

Popescue, R., and Prevost, J.H. (1993). Centrifuge validation of a numerical model for dynamic soil liquefaction. *Soil Dynamics and Earthquake Engineering,* vol. 12, iss. 2, p. 73 – 90.

Poulos, S.J., Castro, G. and France, W. (1985). Liquefaction evaluation procedure. *Journal of Geotechnical Engineering, ASCE,* vol. 111, iss. 6, p. 772 – 792.

Prevost, J.H. (1985). A simple plasticity theory for frictional cohesionless soils. *Soil Dynamics and Earthquake Engineering,* vol. 4, iss. 1, p. 9 – 17.

Prevost, J.H. (2002). Dynaflow – A nonlinear transient finite element analysis program, version 02. *Tech Report,* Department of Civil and Environmental Engineering Princeton University, Princeton, NJ (http://www.princeton.edu/~dynaflow/).

Robertson, P.K., Woeller, D.J., and Finn, W.D.L. (1992). Seismic cone penetration test for evaluating liquefaction potential under cyclic loading. *Canadian Geotechnical Journal,* Ottawa, Canada, vol. 29, p. 686 – 695.

Robertson, P.K. (2004). Evaluating soil liquefaction and post-earthquake deformations using the CPT location. *Proceedings ISC-2 on Geotechnical and Geophysical Site Characterizations,* p. 233 – 249.

Robertson, P.K. (2009). Performance based earthquake design using the CPT. *Proceedings of IS Tokyo Conference,* Tokyo, June 2009.

Robertson, P.K. (2010). Evaluation of flow liquefaction and liquefied strength using the cone penetration test, *Journal of Geotechnical and Geoenvironmental Engineering,* vol. 136, iss. 6, p. 842 – 853.

Rollins, K.M. and Seed, H.B. (1990). Influence of buildings on potential liquefaction damage, *Journal of Geotechnical Engineering,* ASCE, vol. 116, iss. 2, p. 165 – 195.

Seed, H.B., and Idriss, I.M. (1971). Simplified procedure for evaluating soil liquefaction potential. *Journal of the Soil Mechanics and Foundation Division,* ASCE, New York, NY, vol. 97, SM9, p. 1249 – 1273.

Seed, H.B. (1979). Considerations in the earthquake-resistant design of earth and rockfill dams. *Geotechnique,* vol. 29, iss. 3, p. 215 – 263.

Seed, H.B., Idriss, I.M. and Arango, I. (1983). Evaluation of liquefaction potential using field performance data. *Journal of Geotechnical Engineering Division,* ASCE, vol. 109, iss. 3, p. 458 – 482.

Seed, H.B. (1987). Design problems in soil liquefaction. *Journal of Geotechnical Engineering Division,* ASCE, vol. 113, iss. 8, p. 827 – 845.

Seed, R.B. and Harder, L.F. Jr. (1990). SPT – based analysis of cyclic pore pressure generation and undrained residual strength. *Proceedings of H. Bolton Seed Memorial Symposium,* Bi-Tech Publishing Ltd., vol. 2, p. 351 – 376.

Sladen, J.A. and Hewitt, K.J. (1989). Influence of placement method on the in situ density of hydraulic sand fills. *Canadian Geotechnical Journal*, vol. 26, p. 453 – 466.

Stark, T.D. and Mesri, G. (1992). Undrained shear strength of liquefied sands for stability analysis. *Journal of Geotechnical Engineering,* ASCE, vol. 118, iss. 11, p. 1727 – 1747.

Terzaghi, K., and Ralph B. Peck (1948). *Soil Mechanics in Engineering Practice,* John Wiley and Sons, New York.

Tsuchida, H. (1970). Prediction and countermeans against the liquefaction in sand deposits. *Abstract of the Seminar in the Port and Harbor Research Institute,* Yokohama, Japan, p. 3.1 – 3.33.

Whitman, R.V. (1971). Resistance of soil to liquefaction and settlement. *Soils and Foundations,* vol. 11, iss. 4, p. 59 – 68.

CHAPTER TWO:

BASIC CONCEPTS AND DEFINITIONS

2.1 Introduction

Failures related to liquefaction can produce substantial human, environmental and financial consequences with observable ground manifestation ranging from limited sand boils to disastrous flow slides. The failure observed in the field depends on the type and extent of liquefaction that occurs. The following sections provide basic definition of liquefaction phenomena along with definitions of yield and liquefied shear strength and yield and liquefied shear strength ratios.

2.2 Definitions and Concepts of Shearing Behavior of Sands during Liquefaction

2.2.1 Liquefaction

The term “liquefaction” is defined as the sudden drop of shear strength of a loose (contractive), saturated, cohesionless soil, from the peak (or yield) strength to a much smaller liquefied (or critical) shear strength as a result of excess pore water pressure generation during undrained shearing (e.g., Castro 1969; Casagrande 1976; Poulos 1981; Terzaghi et al. 1996). Liquefaction phenomenon described above can be divided into two main types (Kramer 1996): (1) flow liquefaction; and (2) cyclic mobility.

2.2.1.1 Flow Liquefaction

Flow liquefaction can result in catastrophic failures in dam embankments and landslides under static or dynamic loading. In sloping ground, static shear stresses are present on horizontal planes. If static equilibrium is disturbed by additional static or

dynamic loading, a flow failure may occur. As shown schematically in Figure 2.1, flow liquefaction is the process of strain softening of contractive, saturated, cohesionless soils during undrained shear. As a prerequisite of flow liquefaction, the static shear stress carried by the sloping ground must be greater than the liquefied (or critical state) shear strength represented by point C in Figure 2.1 (Poulos et al. 1985a). Static undrained loads that can trigger flow liquefaction include rapid fill placement, rising water levels resulting from reservoir filling or rainwater infiltration, among others. Dynamic undrained loads that can trigger flow liquefaction include earthquakes, blasting, pile driving, among others. Often, flow liquefaction is identified in the field by very large slope displacements. The large displacements produced by flow liquefaction are driven by static shear stresses that exceed the cumulative shear resistance, including the liquefied shear strength.

2.2.1.2 Cyclic Mobility

Cyclic mobility is a phenomenon in which cyclic stresses, produced by harmonic or seismic loading, cause excess porewater pressure generation and concurrent degradation of shear stiffness. Unlike flow liquefaction, cyclic mobility may result or reversal of sign of imposed shear stress when the static shear stress is smaller than the liquefied (or critical state) shear strength of the soil. Cyclic mobility can occur in both contractive and dilative soils. Displacements produced by cyclic mobility develop incrementally during earthquake shaking as the combined static and dynamic shear stresses exceed the shear resistance. Thus, once the loading ceases, the displacements also stop. The manifestations of cyclic mobility in mildly-sloping ground are designated *lateral spreading*.

A special case of cyclic mobility is *level-ground liquefaction* in which the static shear stress on horizontal planes in soil is zero. In the absence of static shear stress, transient and occasional permanent displacements develop as a result of dynamic loading only. the soil moves under the influence of cyclic loading only. In this case, the direction

of the shear stress changes so that each cycle include both compressional and extensional loading. As a result, excess porewater pressure generally increases rapidly (compared to cases without stress reversal), and the soil mass may undergo large chaotic movements known as *surface oscillations*.

2.2.2 Yield and Liquefied Shear Strengths and Strength Ratios

Figure 2.1 schematically presents the behavior of saturated, loose (contractive), sandy soil during undrained loading. Consider a soil element in a slope that carries a static shear stress (τ_{static}) due to its location within the slope and is subjected to an effective confining pressure. The soil element is represented as Point A in Figure 2.1(a). The stress conditions at Point A can be achieved either by drained, undrained, or partially drained loading conditions during embankment construction (or other loading). If the element at Point A is loaded monotonically under undrained (i.e., constant volume) conditions (e.g., by placing another fill lift), the porewater pressure increases and the effective stress decreases as the initially loose soil has a tendency to contract during shearing. It is assumed that a temporary undrained condition prevailed during this construction stage and excess pore water pressure generated as a result of fill placement does not have time to dissipate. During this process, the shearing resistance reaches a peak at Point B. The peak shear strength mobilized at Point B is termed the *yield shear strength, s_u(yield),* and represents the triggering condition for static liquefaction. Liquefaction is triggered once the stress in soil element attempts to exceed the yield strength envelope (further described below) as a result of monotonic loading under undrained conditions.

Once s_u(yield) is mobilized and the yield envelope is exceeded, the soil structure collapses and strain softening occurs causing excess pore water pressure to increase at a greater rate. A rapid drop in shear strength occurs and the element moves from Point B to Point C. At this stage (Point C), the soil deforms with a constant volume, constant shear stress, and constant effective stress. The shearing resistance mobilized at this condition is

termed the *critical state shear strength, s_u(critical)*, under controlled laboratory conditions and termed the *liquefied shear strength, s_u(liq)*, under field conditions. As stated above, the soil element under discussion is located in a slope that would have experienced a flow failure at this stage. The soil mass will continue to move downslope, thereby reducing the driving shear stress, until the driving shear stress drops below s_u(liq), allowing the failure mass to decelerate and the velocity of the failure mass to reach zero. The liquefied shear strength differs from the laboratory-measured critical state shear strength in that the liquefied shear strength estimated from flow liquefaction failures in the field and implicitly includes any potential effects of void redistribution, drainage, water layer formation, soil mixing, hydroplaning, etc.

Consider two other soil elements (Points A' and A" in Figure 2.1a) that are located in other parts of the slope, and have the same relative density as the element at Point A. The stress conditions represented by Points A' and A" can be achieved either by drained, undrained, or partially drained loading conditions during embankment construction (or other loading). When sheared monotonically, Points A' and A" reach their yield shear strengths at Points B' and B", respectively. Although Points A, A', and A" follow similar contractive stress paths, elements initially subjected to a higher static shear stress will exhibit a higher yield shear strength. The line in stress path space connecting the yield shear strengths is termed the yield strength envelope. The friction angle mobilized at yield is termed ϕ'_{yield}. Similar to other friction angles, the yield friction angle increases with increasing relative density. If soils at different static shear stresses exhibit the same initial relative density, the liquefied shear strength (Point C in Figure 2.1) will be independent of the static shear stress. However, if the application of shear stresses occurs under drained (or partially drained) conditions, Point A will have a higher relative density than Point A' and will exhibit a larger liquefied shear strength. Line connecting origin and liquefied shear strength (Point C) represents the failure envelope of the soil at constant volume and the friction angle mobilize at failure is termed the critical state friction angle, ϕ'_{cs}, or the constant volume friction angle, ϕ'_{cv}. It should be noted that friction angle mobilized at failure is larger than the friction angle mobilized at yield, i.e., $\phi'_{cs} > \phi'_{yield}$.

Consider another case in which soil element has same stress condition as previously represented by Point A'. However, instead of loading the soil element monotonically, seismic load is applied. Assume that the intensity and duration of the applied seismic loading are sufficient to cause excess pore water pressure buildup that moves the element from Point A' to Point D (i.e., to the yield strength envelope). At this stage, liquefaction is triggered, and the element moves from Point D to Point C. As shown in Figure 2.1a, the shear stress represented by Point A' is less than the yield shear strength (Point B'). Therefore, the mobilized shear stress calculated from a limit-equilibrium analysis of the pre-failure geometry (i.e., Point A') in such cases may be less then the yield shear strength (i.e., Point B'). This concept is discussed further in Chapter 4.

The yield and liquefied shear strengths have been normalized using the consolidation stress, such as mean ($\sigma'_{c,mean}$), normal (σ'_{nc}), or vertical (σ'_{vc}) (Terzaghi et al. 1996). The initial (or prefailure) effective vertical stress is used in this study for several reasons. First, the effective vertical stress can be readily computed. In addition, in normally consolidated, young, uncemented sandy soils, the effective vertical stress and mean effective stress are directly related via the coefficient of earth pressure at rest, Ko. Strength ratios are useful in assessing the variation of yield and liquefied shear strength with depth (i.e., consolidation stress). At larger depths, the increase in initial effective vertical stress will result in a decrease in void ratio and a corresponding increase in both yield and liquefied shear strengths. Also, while considering liquefaction mitigation techniques (e.g., stabilizing berms or soil densification), strength ratios can be used for assessing strengths in the remedial design (Olson and Stark 2002).

2.2.3 Critical Density, Critical Void Ratio, Critical State Line

Casagrande (1936) performed drained, strain-controlled triaxial compression tests on initially loose and initially dense sand specimens. The results showed that all specimens tested at the same effective confining pressure approached the same density when sheared to large strains. At large strains, all specimens continued to shear with a

constant void ratio and constant shearing resistance. This density was termed the *critical density*, the void ratio corresponding to critical density was termed the *critical void ratio* (CVR), and the locus of critical void ratios versus effective confining stress was termed the *critical void ratio line* by Taylor (1948). The equipment needed to measure pore pressure was not available at the time, but Casagrande (1936) speculated that strain-controlled undrained testing would produce positive excess pore pressure (due to the tendency for contraction) in loose specimens, and negative excess pore water pressure (due to the tendency for dilation) in dense specimens until the critical void ratio line was reached. Figure 2.2 shows the Casagrande (1936) concept of critical void ratio in terms of effective vertical stress. In undrained shear, loose soil specimens tend to contract, producing positive excess pore pressures and concurrent decreases in effective stress. On the other hand, dense specimen tends to dilate during undrained shear, producing negative excess pore pressures and concurrent increases in effective stress. The effective stress continues to change in both loose and dense specimens until the critical void ratio line is approached. In drained shear, specimens move toward the critical void ratio line by changes in volume (see Figure 2.2).

The Casagrande hypothesis was subsequently verified experimentally when Roscoe et al. (1958) defined the critical void ratio state. This is a state during shearing at which any further increment of shear deformation does not result in any void ratio change in a drained test or does not result in any change in effective stress and shear resistance in an undrained test. The critical void ratio state later was termed the critical state, and the CVR line was termed the *critical state line* (CSL). These terms will be used in this study. The CSL thus defines the boundary between contractive and dilative response to shear. If a soil in its initial state (its stress and density characteristics) plots above its CSL, it generally exhibits contractive response while a soil that plots below its CSL exhibits dilative response.

2.2.4 State Parameter

As inferred from Figure 2.2, the shear behavior of a saturated, cohesionless soil is a function of its initial void ratio and effective confining pressure (i.e., state) with respect to the CSL at the start of shear (Schofield and Wroth 1968). To describe the soil state, Been and Jefferies (1985) suggested a *state parameter,ψ,* based on void ratio and confining pressure. The state parameter is defined as (see Figure 2.3):

$$\psi = e - e_c \qquad \textbf{Eq.2.1}$$

where e is the in situ void ratio and e_c is the void ratio at the critical state at the same effective confining pressure. When the state parameter is positive, the soil exhibits contractive behavior and may be susceptible to flow liquefaction. When it is negative, dilative behavior will be observed and the soil is not susceptible to flow liquefaction. However, Jefferies and Been (2006) suggested that contractive response may occur in soils with ψ as low as -0.05.

2.2.5 Parallelism of Normal Compression Line and Critical State Line

The yield and liquefied strength ratios [$s_u(yield)/\sigma'_{vo}$ and $s_u(liq)/\sigma'_{vo}$ respectively] allow designers to incorporate the variations of $s_u(yield)$ and $s_u(liq)$ with consolidation stress into an analyses instead of using a single value. However, for strength ratios to be correct, the CSL and yield state line (YSL; i.e., the locus of void ratios and effective confining stresses that correspond to mobilizing the yield shear strength) should be parallel to the normal compression line (NCL) for the range of effective stresses applicable to civil engineering structures. For most clays, it is reasonable to assume that the NCL and CSL are roughly parallel (Rutledge 1947). As a result, a given normally consolidated clay deposit exhibits a constant ψ and s_u/σ'_{vo} is independent of σ'_{vo} (Terzaghi et al. 1996). However, sand can be deposited in more varied geologic environments than clays, and the method of deposition and depositional energy affects both the initial

density and initial compressibility, i.e., the NCL slope. Olson and Stark (2002) hypothesized that for sands loose enough to be susceptible to flow liquefaction, the NCL is likely to be parallel to the CSL, particularly for silty sands with fines contents of 12% or more. And as discussed below, this hypothesis was supported by additional data collected by Sadrekarimi (2009).

Figure 2.4 to Figure 2.8 illustrate laboratory tests conducted by Castro and Poulos (1977), Poulos et al. (1985b), and Ishihara (1993) on various clean and silty sands that exhibit parallel CSLs and NCLs in the compression range. Figure 2.9 summarizes data collected by Olson (2001) and Sadrekarimi (2009) on the CSL slope (λ) and NCL slope (C_c) for sands prepared at very loose states. These data generally suggest that for many sandy soils (with a large range of fines contents, grain sizes and shapes, and CSL slopes) the slopes of the CSL and consolidation behavior are roughly parallel.

2.2.6 Effect of Increased Density at the same Confining Stress

The results of undrained triaxial compression test conducted by Ishihara (2008) on samples with post consolidation void ratios 0.804, 0.837, 0.847, and 0.871 are presented in Figure 2.10. These void ratios correspond to relative densities (D_R) of 66%, 61%, 59%, and 55% respectively. In Figure 2.10 the deviator stress ($q = \sigma_1 - \sigma_3$) is plotted versus the effective mean confining stress defined as $p' = (\sigma'_1 + 2\sigma'_3)/3$. The saturated samples were consolidated with a vertical stress of σ'_{1c} = 98kPa and a lateral stress of σ'_{3c} = 49kPa producing an initial state of $K_o = 0.5$. Figure 2.10 illustrates that dilatant behavior is exhibited when the void ratio after consolidation less than about 0.83 (D_R = 62%). At higher void ratios after consolidation, contractive behavior is observed.

The initial states of the specimens with respect to the CSL are illustrated in Figure 2.11. Relative densities of 55%, 59%, and 61% correspond to state parameters of 0.037, 0.013, and 0.003, respectively. These state parameters correspond to highly contractive response to a response that is mildly contractive at intermediate strains and mildly dilative at larger

strains. Castro (1969) termed this stress-strain behavior “limited liquefaction.” Ishihara (1993) called the minimum shear resistance that is reached while the soil is contracting the “quasi-steady state” shear strength. This quasi-steady state shear strength is reached during intermediate strains prior to strain-hardening to the critical state shear strength. An even more pronounced change in stress-strain behavior is observed in Figure 2.11 for the specimen with D_R = 66% (state parameter of -0.03). This specimen exhibited highly dilative behavior during shearing.

2.3 References

Been, K., and Jefferies, M.G. (1985). A state parameter for sands. *Geotechnique,* vol. 35, iss. 2, p. 99 – 112.

Casagrande, A. (1936). Characteristics of chohesionless soils affecting the stability of slopes and earth fills. *Journal of the Boston Society of Civil Engineers.* January: reprinted in *Contributions to Soil Mechanics* 1925 – 1940, BSCE, p. 25 J – 276.

Casagrande, A. (1976). Liquefaction and cyclic deformation of sands: a critical review. *Harvard Soil Mechanics Series No. 88,* Harvard University Cambridge, MA.

Castro, G. (1969). Liquefaction of Sands. *Ph.D. Thesis,* Harvard University, Cabridge, Massachusetts.

Ishihara, K. (1993). Liquefaction and flow failure during earthquakes. *Geotechnique,* vol. 43, iss. 3, p. 351 – 415.

Jefferies, M., and Been, K. (2006). Soil liquefaction: a critical state approach. *Taylor and Francis,* p. 512.

Kramer, S.L. (1996). *Geotechnical Earthquake Engineering.* Prentice Hall, New Jersey, 653 p.

Olson, S. M. (2001). Liquefaction analysis of level and sloping ground using field case histories and penetration resistance, *Ph.D. Thesis,* University of Illinois at Urbana-Champaign, Urbana, Illinois.

Olson, S.M. and Stark, T.D. (2002). Liquefied strength ratio from liquefied flow failure case histories, *Canadian Geotechnical Journal,* vol. 39, p. 629 – 647.

Poulos, S.J. (1981). The steady state of deformation. *Journal of Geotechnical Engineering Division, ASCE,* 17 (GT5), 553-562.

Poulos, S.J., Castro, G. and France, W. (1985a). Liquefaction evaluation procedure. *Journal of Geotechnical Engineering, ASCE,* vol. 111, iss. 6, p. 772 – 792.

Poulos, S.J., Robinsky, E.I., and Keller, T.O. (1985b). Liquefaction resistance of thickened tailings. *Journal of Geotechnical Engineering, ASCE,* vol. 111, iss. 12, p. 1380 – 1394.

Rutledge, P.C. (1947). Cooperative triaxial shear research program. *Progress Report on Soil Mechanics Fact Finding Survey,* U.S. Army Corps of Engineers, Waterways Experiment Station, Vicksburg, Miss.

Sadrekarimi, A. (2009). Development of a new ring shear apparatus for investigating the critical state of sands, *PhD Thesis,* University of Illinois Urbana Champaign, p. 451.

Schfield, A.N. and Wroth, C.P. (1968). *Critical state soil mechanics,* McGraw – Hill, London.

Taylor, D. (1948). *Fundamentals of Soil Mechanics.* New York: Wiley.

Terzaghi, K., Peack, R.B., and Mesri, G. (1996). *Soil Mechanics in Engineering Practice, Third Edition.* John Wiley & Sons, Inc., New York, 549 p.

2.4 Figures

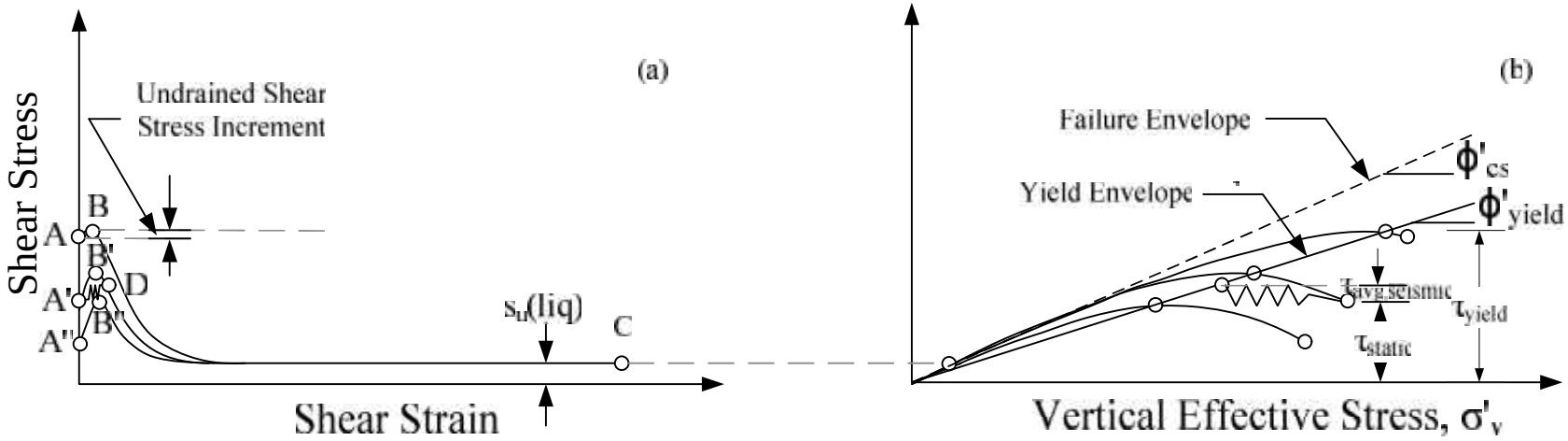

Figure 2.1 Schematic undrained response of a saturated, contractive sandy soil (modified from Olson 2001 and Terzaghi et al. 1996)

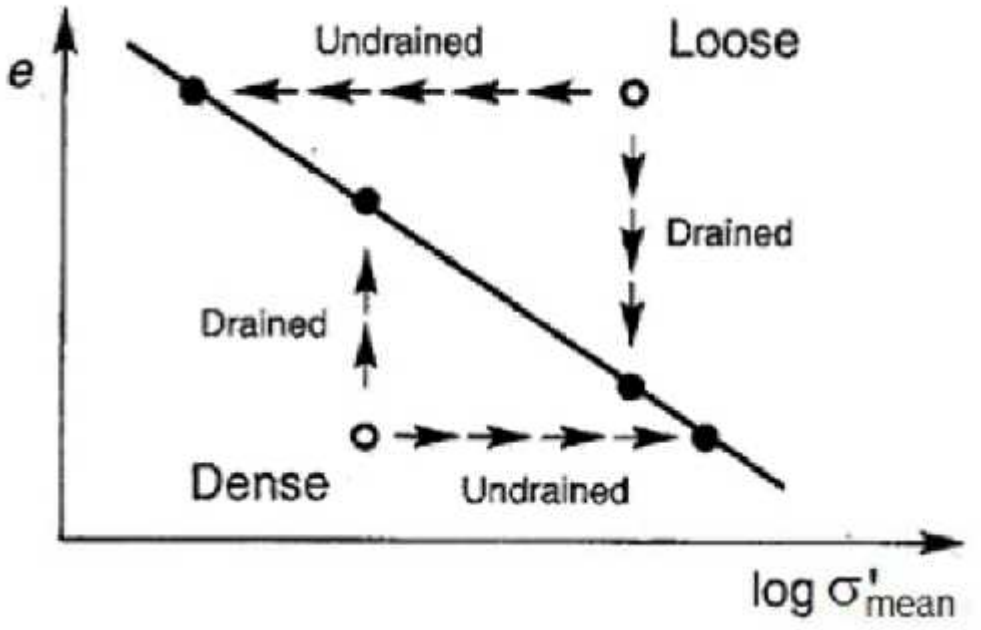

Figure 2.2 Behavior of loose and dense sands under drained and undrained conditions (from Kramer 1996)

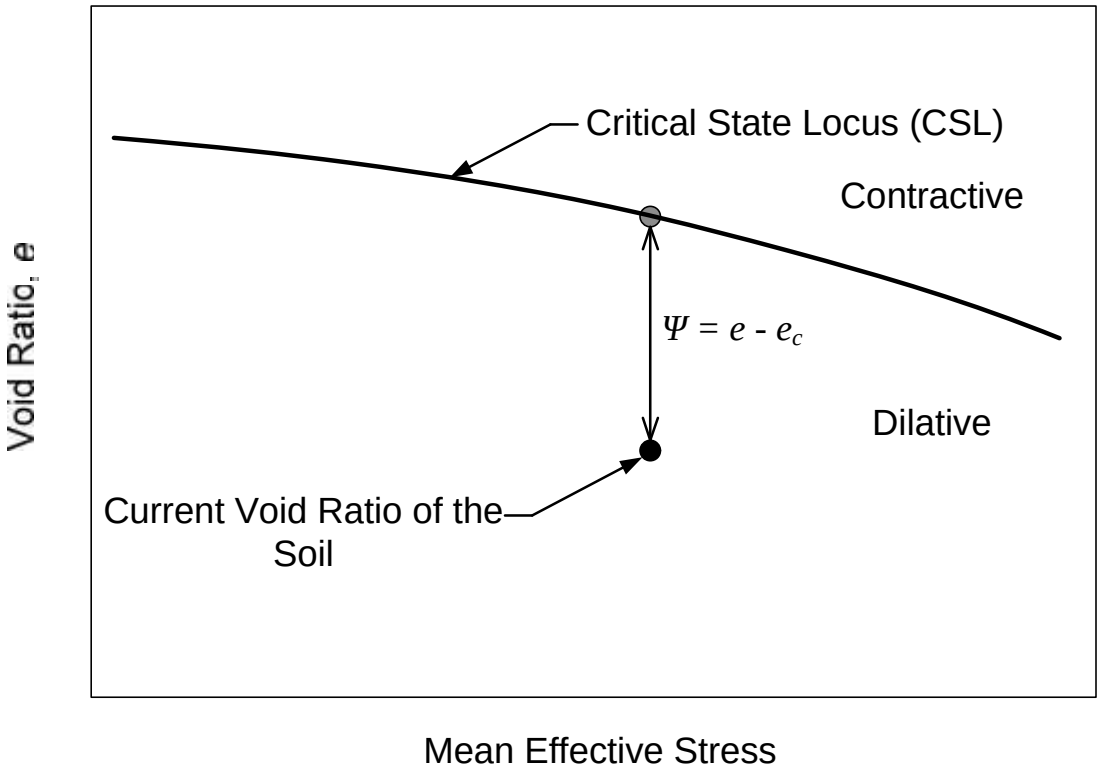

Figure 2.3 Definition of state parameter ψ

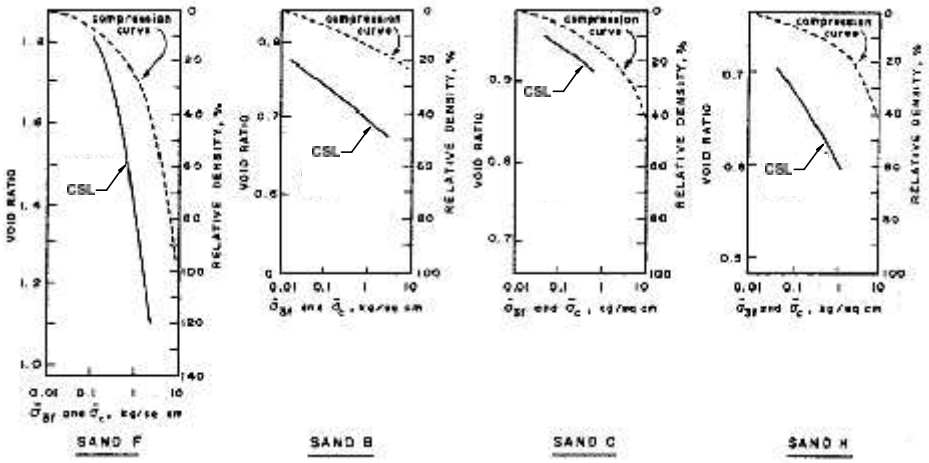

Figure 2.4 Comparison of consolidation behavior and CSL for four sandy soils (modified from Castro and Poulos 1977)

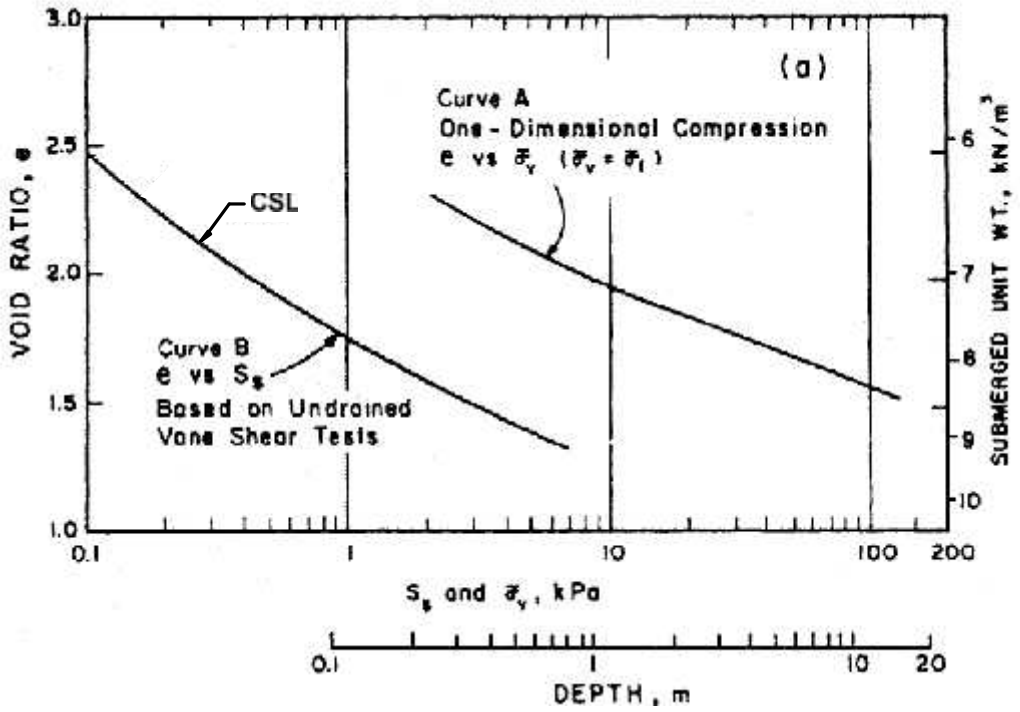

Figure 2.5 Comparison of consolidation behavior and CSL slope of Alcan tailings sand (modified from Poulos et al. 1985b)

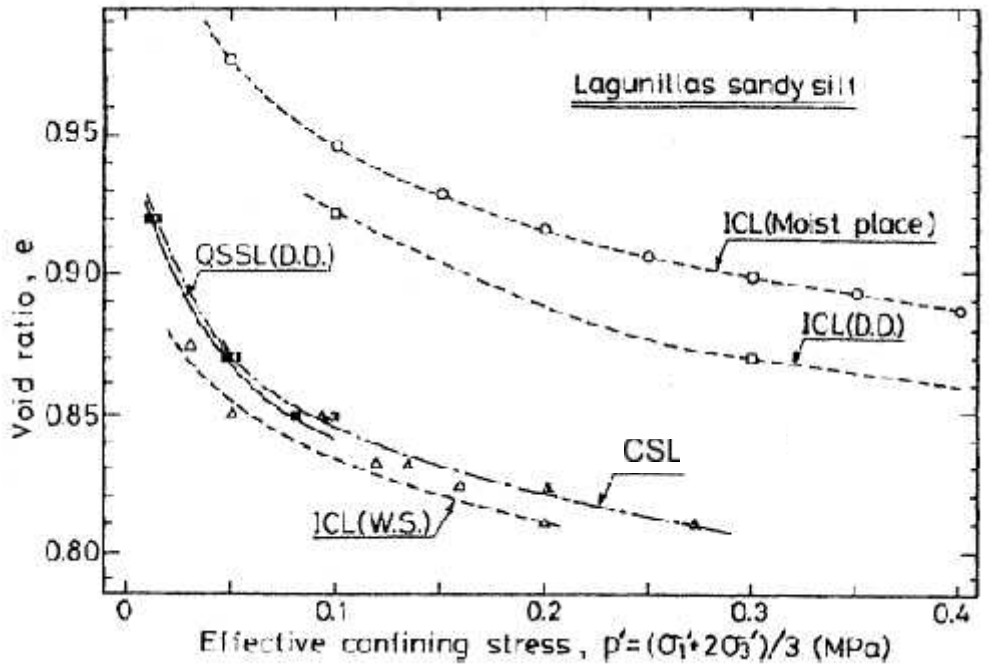

Figure 2.6 Comparison of consolidation behavior and CSL for Lagunillas sandy silt (modified from Ishihara 1993). ICL is isotropic consolidation line, D.D. is dry deposition, QSSL is quasi-steady state line and W.S. is water sedimentation

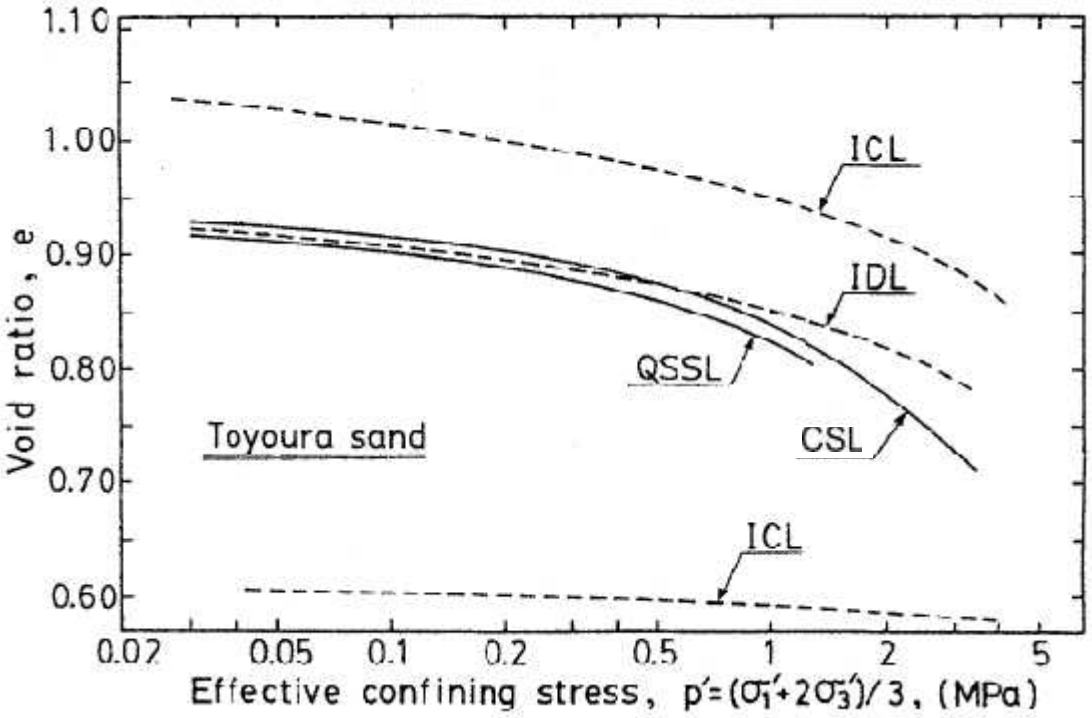

Figure 2.7 Comparison of consolidation behavior and CSL slope Toyoura sand (modified Ishihara 1993). ICL is isotropic consolidation line, IDL is initial dividing line, QSSL is quasi-steady state line

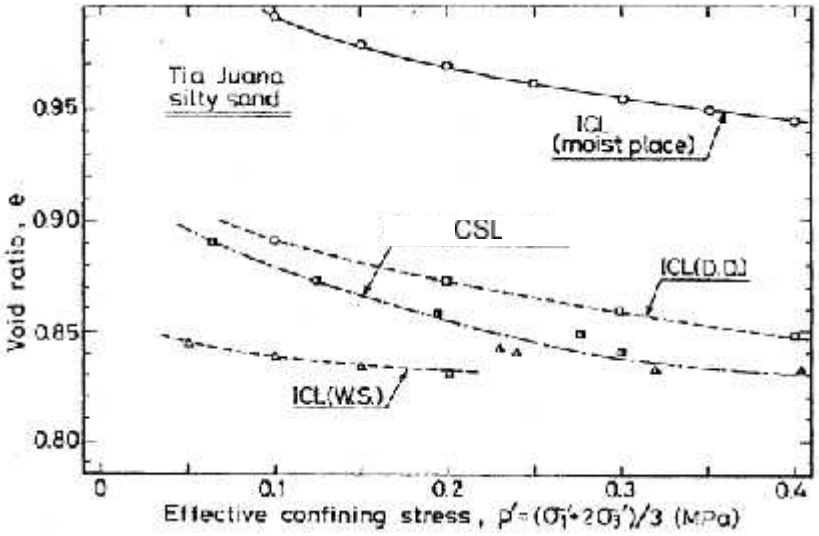

Figure 2.8 Comparison of consolidation behavior and CSL for Tia Juana silty sand (modified from Ishihara 1993). ICL is isotropic consolidation line, D.D. is dry deposition, and W.S. is water sedimentation

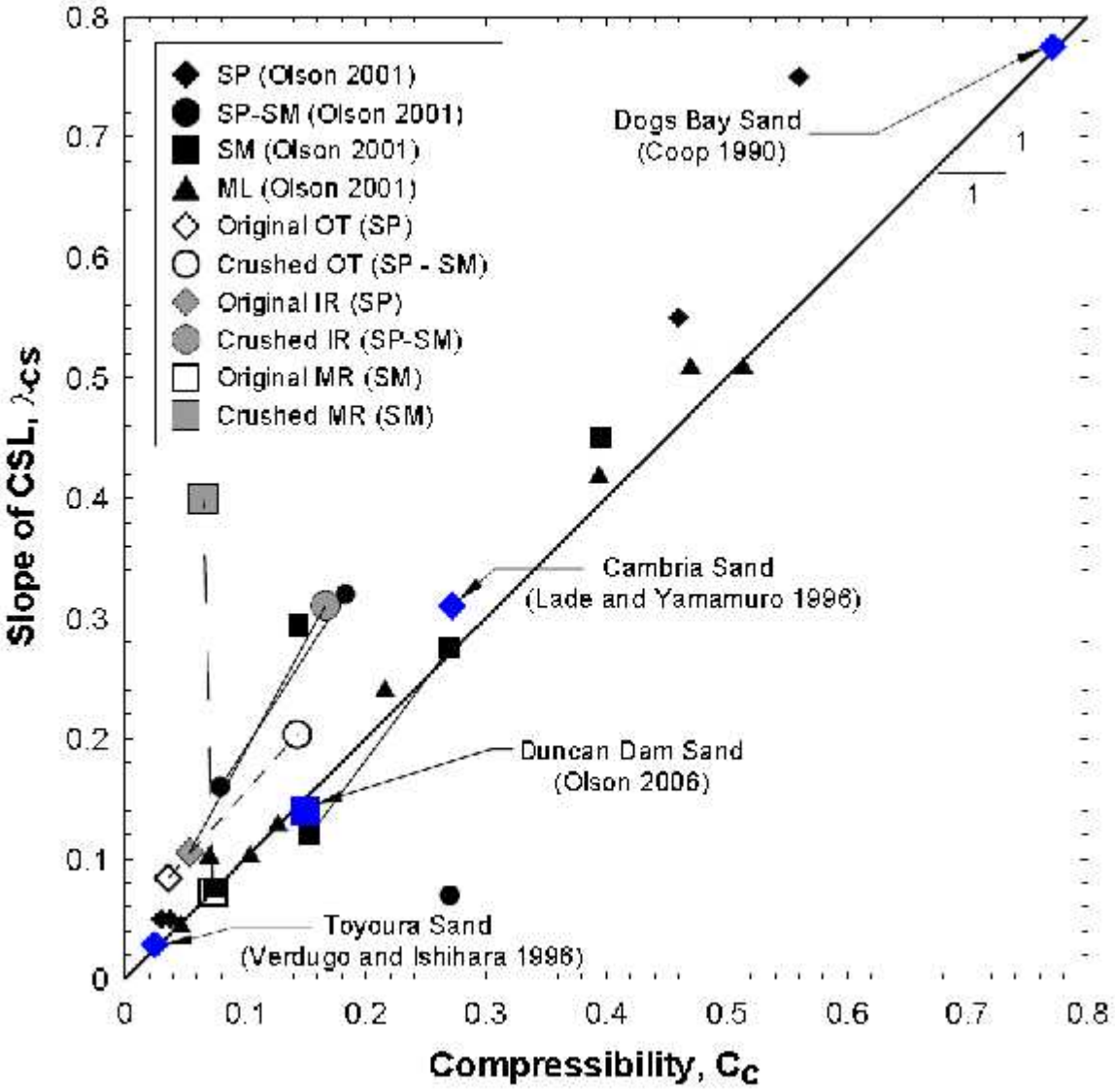

Figure 2.9 Comparison of compressibility and CSL slopes for numerous clean sands, silty sands, sandy silts, and tailings sands with quartz and carbonate mineralogy (from Sadrekarimi 2009)

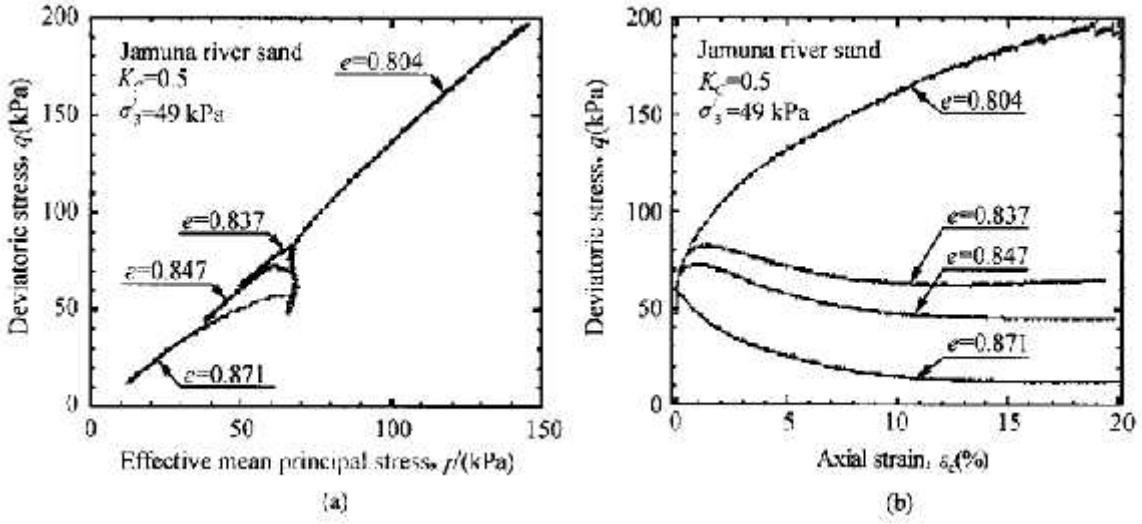

Figure 2.10 Results of undrained triaxial compression tests (from Ishihara 2008)

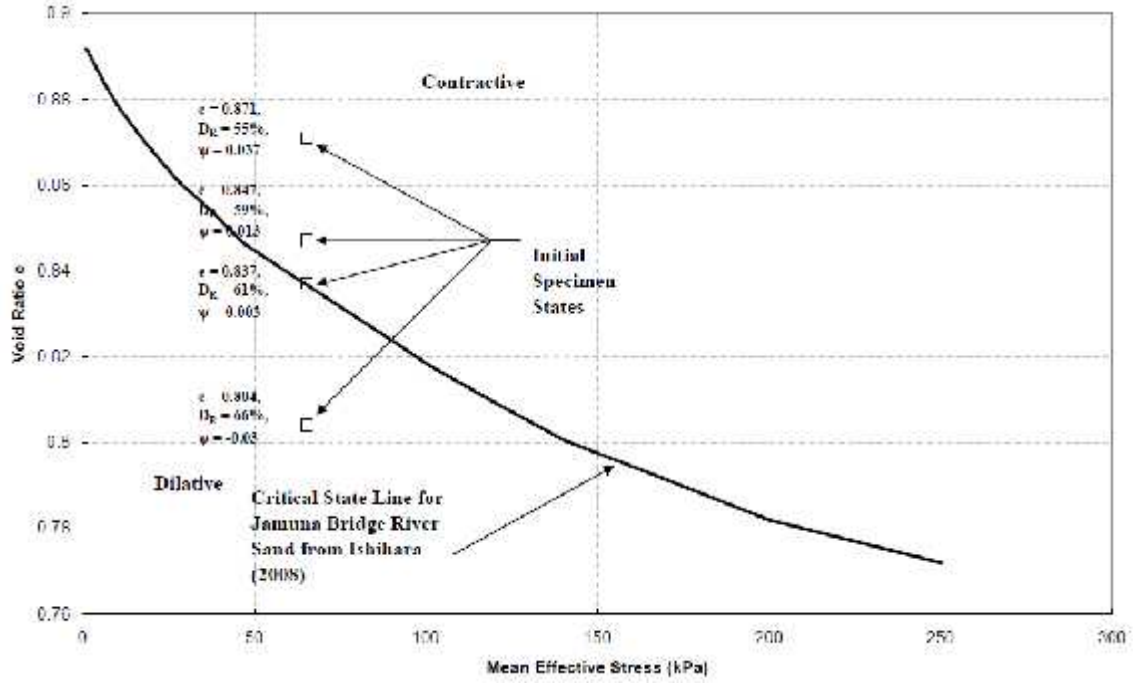

Figure 2.11 Effect of increase in relative density at same confining pressure

CHAPTER THREE:

LITERATURE REVIEW

3.1 Liquefaction Susceptibility

As described in Chapter 2, the CSL represents a boundary between contractive and dilative response to shear. Thus, soils with a state that plots above the CSL boundary will contract during shear. If void ratio with a state that plots above the CSL (or any other measure of density, such as D_R or ψ) is correlated with penetration resistance, e.g., standard penetration test (SPT) blow count or cone penetration test (CPT) tip resistance, the CSL boundary can be expressed as a threshold penetration resistance. That is, soils exhibiting penetration resistance values smaller than the threshold (corresponding to the CSL) will be susceptible to flow liquefaction. These penetration resistance-based boundaries are termed liquefaction susceptibility relationships.

A discussion of liquefaction susceptibility methods described by Olson (2001) (e.g.,Sladen and Hewitt 1989, Ishihara 1993, Baziar and Dobry 1995, and Fear and Robertson 1995) is not repeated here. Rather, the author discusses methods that have been proposed since 2001.

3.1.1 Olson (2001), Stark and Olson (2003a), Olson (2009)

Olson (2001) and later Olson and Stark (2003a) used the susceptibility relationship for Ottawa sand proposed by Fear and Robertson (1995) between overburden-stress normalized SPT blow count and effective vertical stress to evaluate liquefaction flow failure case histories. Because this relationship was developed using theory and laboratory test results, thus Olson and Stark (2003) recommended its use in practice. As illustrated in Figure 3.1, Olson (2001) compared this boundary to the

representative normalized SPT penetration resistances for over 30 flow failure case histories, and found that the boundary encompassed all but two of cases. Olson (2001) also converted the SPT-based liquefaction susceptible relationship from Fear and Robertson (1995) to CPT using $q_c/N_{60} = 0.6$, obtained from Stark and Olson (1995) using a median D_{50} typical for clean sands. As shown in Figure 3.1, the CPT-based boundary encompasses all but one of the flow failure case histories. The recommended liquefaction susceptibility relationships can be approximated as:

$$\left(N_1\right)_{60} = 4.2\pm\,'^{0.21}_{v\text{-}}$$
$$or$$
$$q_{c1} = 2.5\pm\,'^{0.21}_{v\text{-}} \qquad \textbf{Eq. 3.1}$$

where σ'_{vo} and q_{c1} have units of kPa and MPa, respectively.

Based on the concept that soils with same relative density will exhibit different penetration resistances if they have different compressibilities, Olson (2009) tentatively recommended an updated set of liquefaction susceptibility relationships that incorporate compressibility. Olson (2009) proposed to use the CSL slope, λ_{10}, measured in e-$\log_{10}$ σ'_{mean} space as a measure of compressibility (based on the correlation between these parameters illustrated in Figure 3.2). Using relationships among CPT tip resistance, q_c, D_R, and σ'_{vo} from calibration chamber tests on three sands (see Figure 3.2), Olson (2009) proposed a compressibility-based adjustment (termed C_λ) to overburden stress normalized tip resistance values, q_{c1}, to account for sand compressibility. The new susceptibility relationships are presented in Figure 3.3.

3.1.2 Robertson (2010)

Robertson (2010) explained that it is possible to identify a zone on the Robertson (1990) normalized Soil Behavior Type (SBT), based on Q_{tn} and F_r (CPT dimensionless parameters for normalized cone penetration resistance and normalized friction ratio,

respectively) that represents the approximate boundary between dilative and contractive soil response, as shown in Figure 3.4. Figure 3.4 also suggested that the region in the lower left portion of the SBT chart defines soils that are likely susceptible to contractive behavior and strength loss in undrained shear. This region is compared with the approximate boundary between contractive and dilative soil response suggested by Olson and Stark (2003a), but not with that proposed by Olson (2009).

3.2 Liquefaction Triggering

If the liquefaction susceptibility analysis suggests that a soil deposit is contractive, then a liquefaction triggering analysis is performed to determine whether the imposed loading conditions (e.g., gravity and earthquake loads) are sufficient to trigger liquefaction. In other words, a liquefaction triggering analysis for ground subjected to a static shear stress determines whether the applied shear stresses exceed the yield shear strength of the contractive soil.

A discussion of liquefaction triggering methods described by Olson (2001) (e.g., Poulos et al 1985, Seed et al. 1985, Poulos 1988, Seed and Harder 1990, Byrne 1991, Byrne et al. 1992, Harder and Boulanger (1997),) largely is not repeated here. Rather, the author focuses on methods that have been proposed or significantly modified since 2001.

3.2.1 Olson (2001) and Olson et al. (2006)

Olson (2001) analyzed thirty-three flow failure case histories, including cases of: (1) static loading-induced failures, (2) deformation-induced failures, and (3) seismically-induced failures. As explained by Olson (2001), only cases of static loading-induced failure can be used confidently to assess the yield shear strength and strength ratio because the back-calculated shear strength and strength ratio correspond directly to the yield strength envelope. Olson (2001) also suggested that deformation-induced failures may correspond closely to the yield shear strength and strength ratio if the deformation that triggered flow liquefaction in these cases occurred simultaneously with fill

placement during construction. Lastly, Olson (2001) suggested that seismically-induced flow failures may not represent stress conditions that correspond to the yield shear strength and strength ratio.

Plotting yield shear strength ratios back-calculated from five static loading-induced and six deformation-induced flow failures against their representative SPT and CPT penetration resistances, Olson (2001) proposed the following correlations for yield strength ratio (see Figure 3.5 for the SPT-based relationship):

$$\frac{s_u(yield)}{\pm\sigma'_{vo}} = 0.205 + 0.0075\left[(N_1)_{60}\right] \pm 0.04$$

$$\frac{s_u(yield)}{\pm\sigma'_{vo}} = 0.205 + 0.0143(q_{c1}) \pm 0.04 \qquad \textbf{Eq. 3.2}$$

Terzaghi et al. (1996) examined the undrained cyclic shear tests of Monterey No. 0 sand conducted on triaxial and direct simple shear apparatus. As shown in Figure 3. 6 the results suggest that yield shear strength ratios obtained from triaxial tests are larger then the direct simple shear tests. Similarly, Olson and Stark (2003b) compared the yield strength ratio estimated from back-analysis of liquefaction flow failure case histories with the triaxial compression tests (Figure 3.7), and concluded that triaxial tests generally produced yield strength ratios and yield friction angles larger than those back-calculated from flow failures because of the difference in the mode of shear. Olson and Mattson (2008) investigated this postulate, collecting a database of 386 laboratory triaxial compression, direct simple shear, rotational shear, and triaxial extension test results. As illustrated in Figure 3.8, triaxial compression tests exhibited the highest values of yield strength ratio; triaxial extension tests exhibited the lowest values of yield strength ratio; while direct simple shear and rotation (or ring) shear tests yielded intermediate values. Olson and Mattson (2008) concluded that these data clearly illustrated the mode of shear has a significant influence on small strain response, including the yield shear strength. Olson and Mattson (2008) also compared yield strength ratios back-calculated from flow failure case histories (Olson 2001) to those from the laboratory database. This

comparison (Figure 3.8) illustrated that back-calculated yield strength ratios generally agreed with values measured in direct simple shear and rotational shear tests.

Olson et al. (2006) proposed an update to the liquefaction triggering relationships. They collected available triaxial compression, direct simple shear, and rotational shear data from the literature for tests performed with static shear stresses on the horizontal plane. The laboratory results showed that the yield strength ratio increases as the state parameter (ψ) decreases similar to results for Banding sand developed by Terzaghi et al. (1996). But this effect diminishes as the static shear stress ratio increases, as illustrated in Figure 3.9. Olson et al. (2006) used this laboratory data to propose tentative updated relations between yield strength ratio and normalized penetration resistance [q_{c1} and $(N_1)_{60}$] for different static driving shear stress ratios, as shown in Figure 3.10. Combined mobilized shear stress and seismic shear stress ratios from seismically-induced flow failures were used to validate the updated relationships. Figure 3.10 show one such relationship for a static shear stress ratio of about 0.285. Four seismically-induced flow failure case histories exhibited static shear stress ratios close to this value. When the static shear stress ratio was combined with the seismic shear stress ratio induced by the causative earthquakes, the combined stress ratios exceeded the yield strength ratio and liquefaction triggering was predicted. The updated relationships from (2003) successfully predicted the liquefaction triggering for nine flow failure case histories examined by Olson et al. (2006).

3.2.2 Seed (1979, 1983), Seed and Rollins (1988), Seed and Harder (1990), and Harder and Boulanger (1997)

The Seed and Idriss (1971) simplified procedure is used to estimate the cyclic stress ratio (CSR) induced by an M7.5 earthquake at a depth z below a level ground surface using following expression:

$$CSR_{7.5,\sim=0} = \frac{\tau_{avg,seismic}}{\sigma'_{vo}} = 0.65\left(\frac{a_{\max}}{g}\frac{\sigma_{vo}}{\sigma'_{vo}}\right) r_d \qquad \textbf{Eq. 3.3}$$

where a_{max} is the maximum horizontal acceleration at the ground surface (units of g), σ_{vo} is the total vertical stress at depth z, σ'_{vo} is the effective vertical stress at depth z, and r_d is a stress reduction coefficient that accounts for the flexibility of the soil column (e.g., r_d = 1 corresponds to rigid body behavior). The factor 0.65 is used to convert an irregular seismic shear stress time history to an equivalent number of uniform cycles of shear stress, N_c, having an amplitude of 65% of the maximum shear stress, $\tau_{seismic}$, in the irregular time history. The CSR that is required to trigger liquefaction, represented as CSR_{liq}, was estimated from the overburden stress-normalized penetration resistance [e.g., $(N_1)_{60}$] of the soil. The most recent version of this level-ground liquefaction triggering approach was presented by Youd et al. (2001) as shown in Figure 3.11.

Seed (1979, 1983) first observed that dilative soils exhibited greater liquefaction resistance when subjected to a static shear stress than identical samples consolidated under an equal all-around pressure. Based on these results, Seed (1983) proposed a correction to the level ground liquefaction resistance, termed K_α, that accounts for static shear stress greater than zero on horizontal planes. The magnitude of horizontal shear stress is quantified using the static shear stress ratio, $\alpha = \tau_{horizontal}/\sigma'_{vo}$. Later, Seed and Rollins (1988) observed that contractive soils exhibited smaller liquefaction resistance when subjected to a static shear stress than identical samples consolidated under an equal all-around pressure. Seed and Harder (1990) collected available cyclic tests with $\alpha > 0$ and proposed the K_α relationships shown in Figure 3.12. The correction factor obtained from Figure 3.12 is applied to the cyclic resistance ratio (CRR) as follows:

$$CRR_{M\,7.5,\sim>0} = CRR_{M\,7.5,\sim=0} \times K_{\sim} \qquad \textbf{Eq. 3.4}$$

Figure 3.12 shows that for high relative density, the Kα increases with increasing α, while for low relative density Kα decreases with increasing α. It should be noted that Figure 3.12 is limited to σ'_{vo} equal to approximately 3 atmospheres.

Harder and Boulanger (1997) updated the K_α relationships proposed by Seed and Harder (1990) using additional data published between 1990 and 1997. The updated relationships are presented in Figure 3.13. Despite this update, the relationships still exhibit considerable scatter. Nevertheless, Seed et al. (2003) recommend these 1997 relationships for evaluating the triggering of liquefaction in sloping ground.

3.2.3 Boulanger (2002, 2003a); Idriss and Boulanger (2003)

As indicated by Seed and Harder (1990) and Harder and Boulanger (1997), K_α depends on both relative density and effective confining stress. However for effective confining pressures less than about 3 tsf (≈ 3 atm, 300 kPa), the variation in CSR with α depends primarily on relative density. Pillai (1991) clearly illustrated that the scatter in K_α decreases if K_α is interpreted in terms of state parameter rather than relative density. Consistent with this approach, Boulanger (2002, 2003a) proposed using a "relative" state parameter to evaluate K_α based on the work by Bolton (1986). This relative state parameter index is defined mathematically as below:

$$¶_R = \frac{1}{Q - \ln\left(\frac{100\,p'}{P_a}\right)} - D_R \qquad \textbf{Eq. 3.5}$$

where p' is mean effective normal stress, Pa is atmospheric pressure, D_R is relative density, and Q is an empirical constant based on mineralogy as defined by Bolton (1986). The proposed Q values were 10 for quartz and feldspar, 8 for limestone, 7 for anthracite, and 5.5 for chalk. These values were adopted by Idriss and Boulanger (2003).

Idriss and Boulanger (2003) substituted expressions for normalized SPT blow count and CPT tip resistance for D_R in Equation 3.5. The revised equations are presented in Equations 3.6 and 3.7.

$$¶_R = \frac{1}{Q - \ln\left(\frac{100(1+2K_o)\pm'_{vo}}{3P_a}\right)} - \sqrt{\frac{(N_1)_{60}}{46}} \qquad \textbf{Eq. 3.6}$$

$$¶_R = \frac{1}{Q - \ln\left(\frac{100(1+2K_o)\pm'_{vo}}{3P_a}\right)} - (0.086\sqrt{q_{c1N}} - 0.334) \qquad \textbf{Eq. 3.7}$$

Idriss and Boulanger (2003) then derived the following expression relating K_α to ξ_R:

$$K_{\sim} = a + b\exp\left(\frac{-¶_R}{c}\right)$$
$$a = 1267 + 636{\sim}^{2} - 634\exp(\sim) - 632\exp(\sim) \qquad \textbf{Eq. 3.8}$$
$$b = \exp(-1.11 + 12.3{\sim}^{2} + 1.31Ln(\sim + 0.0001))$$
$$c = 0.138 + 0.126\sim + 2.5{\sim}^{3}$$

Figure 3.14 presents the resulting K_α relationships for a range of SPT penetration resistance and σ'_{vo} = 1 and 4 atm.

3.2.4 Terzaghi et al. (1996); Mesri (2007)

Terzaghi et al. (1996) and Mesri (2007) proposed an equation to fit the average K_α relationship for loose sands suggested by Seed and Rollins (1988) and Seed and

Harder (1990). Combining this with the level ground yield strength ratio for clean sand and M = 7.5 published by Seed et al. (1985), Terzaghi et al. (1996) and Mesri (2007) proposed the expression below to estimate the yield strength ratio for sloping ground. and defined as:

$$\frac{s_u(yield)}{\sigma'_{vo}} = \frac{\tau_{static}}{\sigma'_{vo}} + 0.011\left(1 - 2\frac{\tau_{static}}{\sigma'_{vo}}\right)(N_1)_{60} \qquad \textbf{Eq. 3.9}$$

Figure 3.15 graphically presents the relationship in Equation 3.9 for values of $\tau_{static}/\sigma'_{vo}$ = 0, 0.1, 0.2, and 0.3. Note that Terzaghi et al. (1996) observed that for $(N_1)_{60}$ < 20, $s_u(yield)/\sigma'_{vo}$ could be estimated as $0.011(N_1)_{60}$. Yield and mobilized shear strength ratios back-calculated by Olson (2001) for static loading-induced, deformation-induced, and seismically-induced flow failures are included in the Figure 3.15. Because back-calculated yield and mobilized strength ratios showed a range from 0.1 to 0.3 with typical value of 0.2, Mesri (2007) suggested that in absence of information on driving stress ratio, a static shear stress ratio of 0.2 should be used to estimate yield strength ratio.

3.3 Post-Triggering Stability

The third and last step in analyzing liquefaction in sloping ground is to evaluate the post-triggering stability of a structure if liquefaction is triggered in the previous step. As a prerequisite for liquefaction flow failure to occur, the static driving stresses must be greater than the liquefied shear strength of the soil. Several methods are available to estimate the liquefied shear strength. Methods include estimates of liquefied shear strength as a single value (e.g., Seed and Harder 1990; Idriss and Boulanger 2008) and estimates of liquefied shear strength as a strength ratio (e.g., Stark and Mesri 1992; Olson and Stark 2002; Jefferies and Been 2006; Mesri 2007; Idriss and Boulanger 2008; and Robertson 2009).

Again, a discussion of methods to estimate the liquefied shear strength described by Olson (2001) (e.g., Poulos et al. 1985, Seed 1987, Seed and Harder 1990, Stark and Mesri 1992, Ishihara 1993, Konrad and Watts 1995, Fear and Robertson 1995) will not repeated here. Rather, the author will discuss methods that have been proposed or significantly updated since 2001.

3.3.1 Olson (2001); Olson and Stark (2002)

Olson (2001) proposed a systematic procedure to back-calculate liquefied shear strength from liquefaction flow failure case histories. Three different types of stability analyses representing three levels of complexities were conducted to analyze 33 flow failures. Cases with minimum available information were analyzed using a simplified approach, i.e., an infinite slope analysis. For cases with sufficient information about the post-failure geometry and phreatic surface, Olson (2001) performed a more rigorous back-analysis using limit equilibrium method. For cases with appropriate documentation and failure conditions, an additional kinetics analysis was conducted to back-calculate the liquefied shear strength and liquefied shear strength ratio. This work differed from Stark and Mesri (1992) because rather than using a single value of effective vertical stress for the entire length of failure surface, Olson (2001) used a range of effective vertical stresses acting on the liquefied material before failure (i.e., in the prefailure geometry) to back-calculate the liquefied strength ratio. Cases in which the kinetics of failure was incorporated produced "best estimates" of liquefied strength ratios. Despite the uncertainties in the case histories and the analysis methods described in Olson (2001), a reasonable trend between liquefied strength ratio and overburden stress-normalized penetration resistance was observed [see Figure 3.16 for the correlation between liquefied strength ratio and $(N_1)_{60}$]. The trend lines for the SPT-based and CPT-based correlations are described as:

$$\frac{s_u(liq)}{\pm'_{vo}} = 0.03 + 0.0075\left[(N_1)_{60}\right] \pm 0.03 \quad \textbf{for } (N_1)_{60} \leq 12 \qquad \textbf{Eq. 3.10}$$

$$\frac{s_u(liq)}{\pm\,'_{vo}} = 0.03 + 0.0143(q_{c1}) \pm 0.03 \qquad \textbf{for } q_{c1} \leq 6.5 \qquad \textbf{Eq. 3.11}$$

While soils involved in liquefaction flow failures may be subjected to multiple modes of shear, Olson and Stark (2002, 2003a) suggested that the liquefied materials in many of the failures that they analyzed were, on average, subjected approximately to a direct simple shear mode of shear. Olson and Mattson (2008) examined this postulate using a database of 386 laboratory triaxial compression, direct simple shear, rotational shear, and triaxial extension test, as described in Section 3.2.1. Olson and Mattson (2008) concluded that for specimens with state parameters close to zero, but still contractive, triaxial compression yielded the largest upper-bound liquefied strength ratios, simple shear and rotational shear yielded intermediate upper-bound liquefied strength ratios, and triaxial extension yielded the smallest upper-bound liquefied strength ratios. On the other hand, for very loose soil specimens with state parameters considerably greater than zero, all modes of shear yielded similar small liquefied strength ratios. Figure 3.17 presents the laboratory-measured liquefied shear strength ratios collected by Olson and Mattson (2008) and compare these with the liquefied shear strength ratios back-calculated by Olson (2001) from field case histories. Figure 3.17 illustrates that liquefied shear strength ratios back-calculated from field case histories fall near the middle of the range of liquefied strength ratios measured in direct simple shear and rotational shear tests.

3.3.2 Jefferies and Been (2006)

Jefferies and Been (2006) suggested a framework to estimate the normalized liquefied shear strength ratio, $s_u(liq)/\sigma'_{vo}$, using the dimensionless characteristic CPT resistance parameter Q_k, where Q denotes the dimensionless CPT resistance based on vertical stress and ‘k’ subscript denotes characteristic value (80 – 90 percentile). Jefferies and Been (2006) evaluated 12 liquefaction flow failure case histories using this dimensionless framework. In evaluating these case histories, the views of other workers on the mobilized strength in each case, the stress levels involved, and the characteristic

penetration resistances were considered. Figure 3.18 presents a correlation between liquefied strength ratio and dimensionless characteristic Q_k. The bands for each case illustrate the uncertainties in back-analyzed strengths and inferred characteristic Q_k.

In Figure 3.18, the Calaveras Dam case history data lies far from the trend of the other case histories. The author suspects that Jefferies and Been (2006) overestimated the liquefied strength ratio for this case, chiefly because their estimate of about 0.33 is considerably larger than the yield strength ratio (i.e., the shear stress ratio mobilized at the time of failure) of 0.27 backcalculated from the prefailure geometry. Thus the ratio of 0.33 is likely unreasonable for a liquefied strength ratio.

3.3.3 Idriss and Boulanger (2007)

Idriss and Boulanger (2007) recommended relationships for estimating $s_u(liq)$ and $s_u(liq)/\sigma'_{vo}$ of liquefied non-plastic soils based on a review of prior case history studies, laboratory studies, and recent findings regarding void redistribution mechanisms. Void redistribution is defined as void ratio changes that occur locally as a result of liquefaction, while globally an undrained condition is maintained. This local void ratio change occurs as a result of local porewater pressure redistribution that can result in water being captured beneath lower permeable layers of soil. The relationships proposed by Idriss and Boulanger (2007) are given in Figure 3.19 for both sites with significant void redistribution and sites with negligible void redistribution. However, Idriss and Boulanger (2007) provide little guidance on evaluating the occurrence of void redistribution and the position of the curves are poorly constrained by case history data.

3.3.4 Terzaghi et al. (1996), Mesri (2007)

Mesri (2007) proposed that the liquefied strength ratio correlation with overburden stress-normalized penetration resistance should be a function of static shear stress ratio. Mesri used direct simple shear (DSS) test results to develop a baseline

relationship for liquefied strength ratio for tests with $\tau_{static}/\sigma'_{vo} = 0$. Mesri (2007) then used liquefied shear strength ratios back-calculated by Olson (2001) to evaluate the liquefied shear strength ratio for conditions where $\tau_{static}/\sigma'_{vo} > 0$. The proposed relationship is as follows:

$$\frac{s_u(liq)}{\pm'_{vo}} = \frac{1}{4}\frac{\pm^2_{static}}{\pm'_{vo}} + 0.006(N_1)_{60} \qquad \textbf{Eq. 3.12}$$

Figure 3.20 graphically presents the relationship in Eq. 3.12 for values of $\tau_{static}/\sigma'_{vo} = 0$, 0.1, 0.2, and 0.3. The role of $\tau_{static}/\sigma'_{vo}$ and the specific expression for liquefied strength ratio in Equation 3.12 need to be verified by laboratory or field information (Mesri 2007) hence more case histories are needed.

3.3.5 Robertson (2010)

Robertson (2010) reviewed 35 liquefaction flow failure case histories published by Seed (1987), Seed and Harder (1990), Wride et al. (1999), Olson and Stark (2002) and Jefferies and Been (2006), and added one new case history for a total of 36 cases. In reporting the liquefied shear strength ratio, emphasis was placed on the values computed by Olson and Stark (2002). Based on the reviewed cases, Robertson (2010) proposed a lower-bound relationship between the liquefied shear strength and clean sand equivalent normalized penetration resistance as shown in Figure 3.21. So-called Class A case histories represent more relative cases, while Class B cases generally were less reliable cases, particularly the estimated representative values of penetration resistance. The proposed relationship avoids the need to extrapolate beyond the case-history database. Robertson (2010) suggested more detailed field and analytical studies for high risk projects and more conservative estimate of liquefied shear strength for cases where void redistribution could occur. Robertson (2010) recommended that the average value of liquefied shear strength should be applied for stability analyses, since the proposed

relationship was based on average CPT values within non-interlayered deposits from the case histories. A lower bound value of $s_u(liq) = 1$ kPa was assumed at low confining stress.

3.4 References

Baziar, M.H. and Dobry, R. (1995). Residual strength and large-deformation potential of loose silty sands. *Journal of Geotechnical Engineering,* ASCE, vol. 121, iss. 12, p. 896 – 906.

Bolton, M.D. (1986). The strength and dilatancy of sands. *Geotechnique,* vol. 36, p. 65 – 78.

Boulanger, R.W. (2002). Evaluating liquefaction resistance at high overburden stresses. *Proceedings of the 3rd US – Japan Workshop on Advanced Research on Earthquake Engineering for Dams,* Department of Civil and Environmental Engineering, University of California, San Diego.

Boulanger, R.W. (2003). High overburden stress effects in liquefaction analyses. *Journal of Geotechnical and Geoenvironmental Engineering,* ASCE, vol. 129, iss. 12, p. 1071 – 1082.

Byrne, P.M. (1991). A model for predicting liquefaction induced displacements. *Proceedings of the Second International Conference on Recent Advances in Geotechnical Earthquake Engineering and Soil Dynamics,* St. Louis, vol. 2, 1027 – 1035.

Byrne, P.M., Salgado, F., and Jitno, H. (1992). Earthquake induced displacement of soil structure systems. *Proceedings of the Tenth World Conference on Earthquake Engineering,* Madrid, Spain, vol. 3, p. 1407 – 1412.

Fear, C.E. and Robertson, P.K. (1995). Estimating the undrained strength of sand: a theoretical framework. *Canadian Geotechnical Journal,* vol. 32, iss. 4, p. 859 – 870.

Harder, L.F. Jr. and Boulanger, R. (1997). Application of K_σ and K_α correction factors. *Proceedings of NCEER Workshop on Evaluation of Liquefaction Resistance of Soils,* T.L. Youd and I.M. Idriss, eds., NCEER-97-0022, p. 167 – 190.

Idriss, I.M., and Boulanger R.W. (2003). Estimating K_α for use in evaluating cyclic resistance of sloping ground. *In: Hamada, O'Rourke, Bardet (ads), 8th US – Japan Workshop on Earthquake Resistant Design of Lifeline Facilities and Countermeasures against Liquefaction,* Report MCEER-03-0003, MCEER, SUNY Buffalo, N.Y., p. 449 – 468.

Ishihara, K. (1993). Liquefaction and flow failure during earthquakes. *Geotechnique,* vol. 43, iss. 3, p. 351 – 415.

Idriss, I.M. and Boulanger, R.W. (2007). Residual shear strength of liquefied soils. *Proceedings of the 27th USSD Annual Meeting and Conference,* Modernization and Optimization of Existing Dams and Reservoirs March 5-9, 2007.

Jefferies, M., and Been, K. (2006). Soil liquefaction: A critical state approach, *Taylor and Francis,* 512p.

Konrad, J.M. and Watts, B.D. (1995). Undrained shear strength for liquefaction flow failure analysis. *Canadian Geotechnical Journal,* vol. 32, p. 783 – 794.

Mesri G. (2007). Yield strength and critical strength of liquefiable sands in sloping ground, *Geotechnique,* vol. 57, issue 3, p. 309 – 311.

Olson, S. M. (2001). Liquefaction analysis of level and sloping ground using field case histories and penetration resistance, *Ph.D. Thesis,* University of Illinois at Urbana-Champaign, Urbana, Illinois.

Olson, S.M. and Stark, T.D. (2002). Liquefied strength ratio from liquefied flow failure case histories, *Canadian Geotechnical Journal,* vol. 39, p. 629 – 647.

Olson, S.M. and Stark, T.D. (2003a). Use of laboratory data to confirm yield and liquefied strength ratio concepts, *Canadian Geotechnical Journal,* vol. 40, p. 1164 – 1184.

Olson, S.M. and Stark, T.D. (2003b). Yield strength ratio and liquefaction analysis of slopes and embankments, *Journal of Geotechnical and Geoenvironmental Engineering,* ASCE vol. 129, iss. 8, p. 727 - 737

Olson, S. M., Sacks, A. L., Mattson, B. B., and Servigna, D. A. (2006). Role of static shear stress in liquefaction analysis of sloping ground, *Proceedings of the 8th US National Conference on Earthquake Engineering*

Olson, S.M. and Mattson, B.B. (2008). Mode of shear effects on yield and liquefied strength ratios, *Can. Geotechnical Journal,* vol. 45, p. 574 – 587.

Olson, S. M. (2009). Strength ratio approach for liquefaction analysis of tailings dams, *University of Missouri Conference*.

Poulos, S.J., Castro, G. and France, W. (1985a). Liquefaction evaluation procedure. *Journal of Geotechnical Engineering,* ASCE, vol. 111, iss. 6, p. 772 – 792.

Poulos, S.J., Robinsky, E.I., and Keller, T.O. (1985b). Liquefaction resistance of thickened tailings. *Journal of Geotechnical Engineering,* ASCE, vol. 111, iss. 12, p. 1380 – 1394.

Poulos, S.J. (1988). Liquefaction and related phenomena. *In: Advanced Dam Engineering for Design, Construction, and Rehabilitation,* R.B. Jansen, ed., Van Nostrand Reinhold, New York, p. 292 – 320.

Robertson, P.K. (2010). Evaluation of flow liquefaction and liquefied strength using the cone penetration test, *Journal of Geotechnical and Geoenvironmental Engineering,* vol. 136, iss. 6, p. 842 – 853.

Rollins, K.M. and Seed, H.B. (1990). Influence of buildings on potential liquefaction damage, *Journal of Geotechnical Engineering,* ASCE, vol. 116, iss. 2, p. 165 – 195.

Seed, H.B. (1979). Considerations in the earthquake-resistant design of earth and rockfill dams. *Geotechnique,* vol. 29, iss. 3, p. 215 – 263.

Seed, H.B., Idriss, I.M. and Arango, I. (1983). Evaluation of liquefaction potential using field performance data, *Journal of Geotechnical Engineering Division,* ASCE, vol. 109, iss. 3, p. 458 – 482.

Seed, H.B., Tokimatsu, K., Harder, L.F., and Chung, R. (1985). Influence of SPT procedures in soil liquefaction resistance evaluations. *Journal of Geotechnical Engineering Division,* ASCE, vol. 111, iss. 12, p. 861 – 878.

Seed, H.B. (1987). Design problems in soil liquefaction. *Journal of Geotechnical Engineering Division,* ASCE, vol. 113, iss. 8, p. 827 – 845.

Seed, R.B. and Harder, L.F. Jr. (1990). SPT – based analysis of cyclic pore pressure generation and undrained residual strength. *Proceedings of H. Bolton Seed Memorial Symposium,* Bi-Tech Publishing Ltd., vol. 2, p. 351 – 376.

Sladen, J.A. and Hewitt, K.J. (1989). Influence of placement method on the in situ density of hydraulic sand fills. *Canadian Geotechnical Journal,* vol. 26, p. 453 – 466.

Wride (Fear), C.E., McRoberts, E.C., and Robertson, P.K. (1999). Reconsideration of case histories for estimating undrained shear strength in sandy soils. *Canadian Geotechnical Journal*, vol. 36, p. 907 – 933.

Youd, T.L., Idriss, I.M., Andrus, R.D., Castro, G., Christian, J.T., Liam Finn, W.D., Harder, L.F., Hynes, M.E., Ishihara, K., Koester, J.P., Liao, S.S.C., Macuson, W.F., Martin, G.R., Mitchell, J.K., Power, M.S., Seed, R.B., and Stokoe, K.H. (2001). Liquefaction resistance of soils: Summary report from the 1996 NCEER and 1998 NCEER/NSF workshops on evaluation liquefaction resistance of soils. *Journal of Geotechnical and Geoenvironmental Engineering*, vol. 127, iss. 4, p. 297 – 313.

3.5 Figures

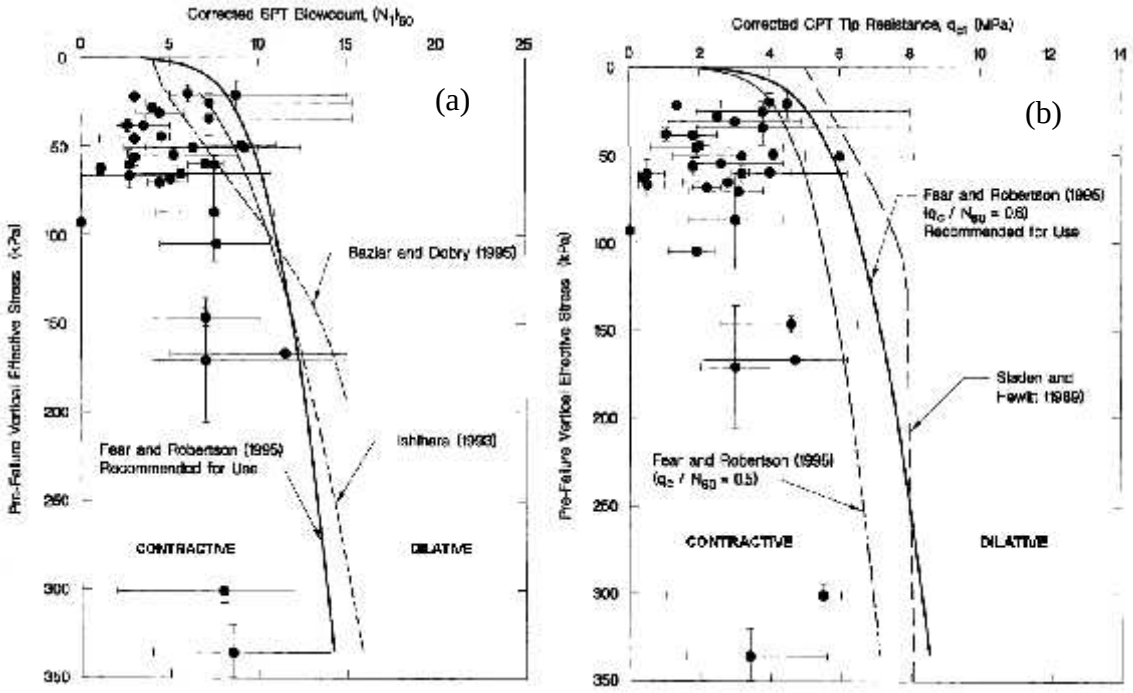

Figure 3.1 Liquefaction susceptibility boundary relationships suggested by various researchers with liquefaction flow failure case histories for SPT and CPT (from Olson 2001)

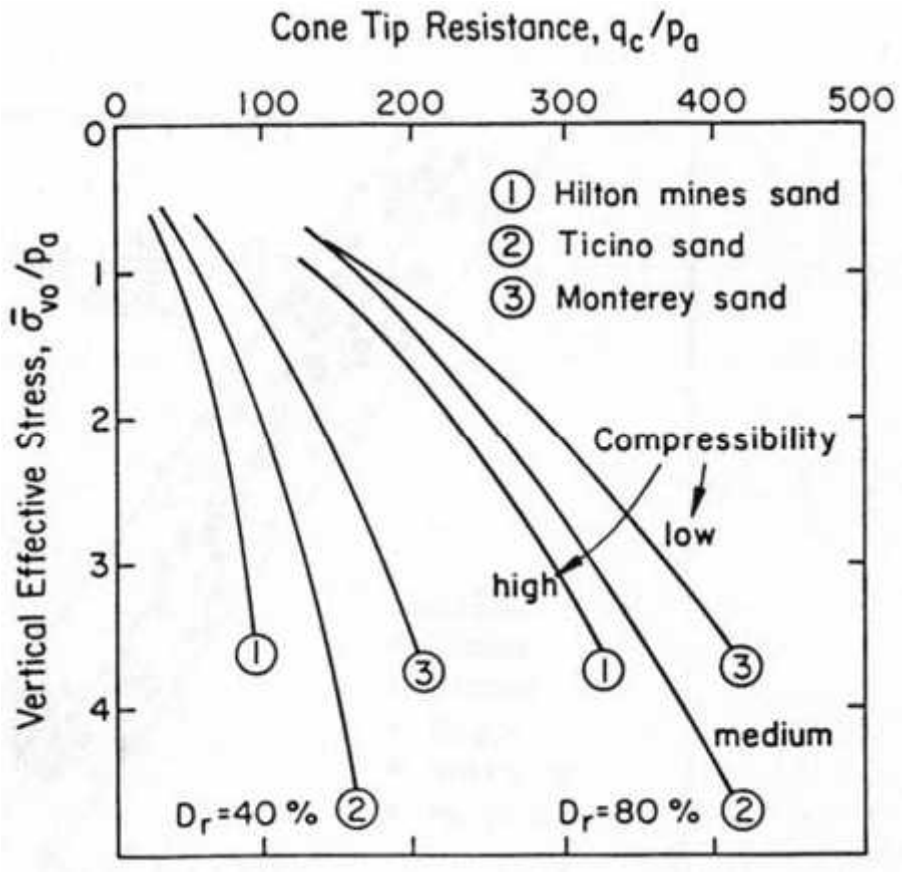

Figure 3.2 Relationships among CPT tip resistance (q_c), relative density (D_r), and effective vertical stress ($\pm'_v$) measured in calibration chamber tests as a function of sand compressibility (from Robertson and Campanella 1983)

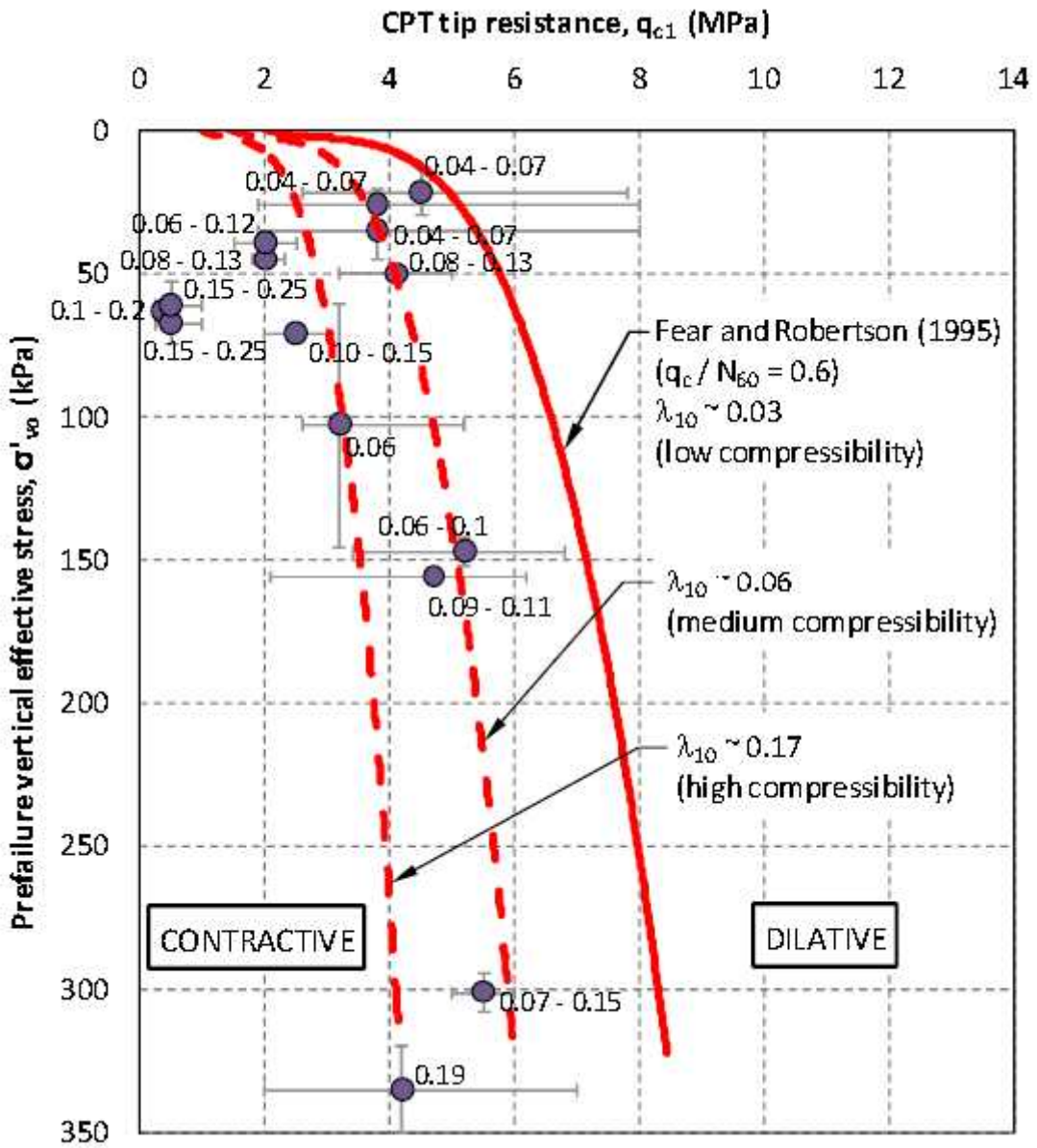

Figure 3.3 Tentative liquefaction susceptibility relationships proposed by Olson (2009) that account for soil compressibility. Soil compressibility is defined as a function of the CSL slope, λ_{10}. Data points in the figure are flow failure case histories

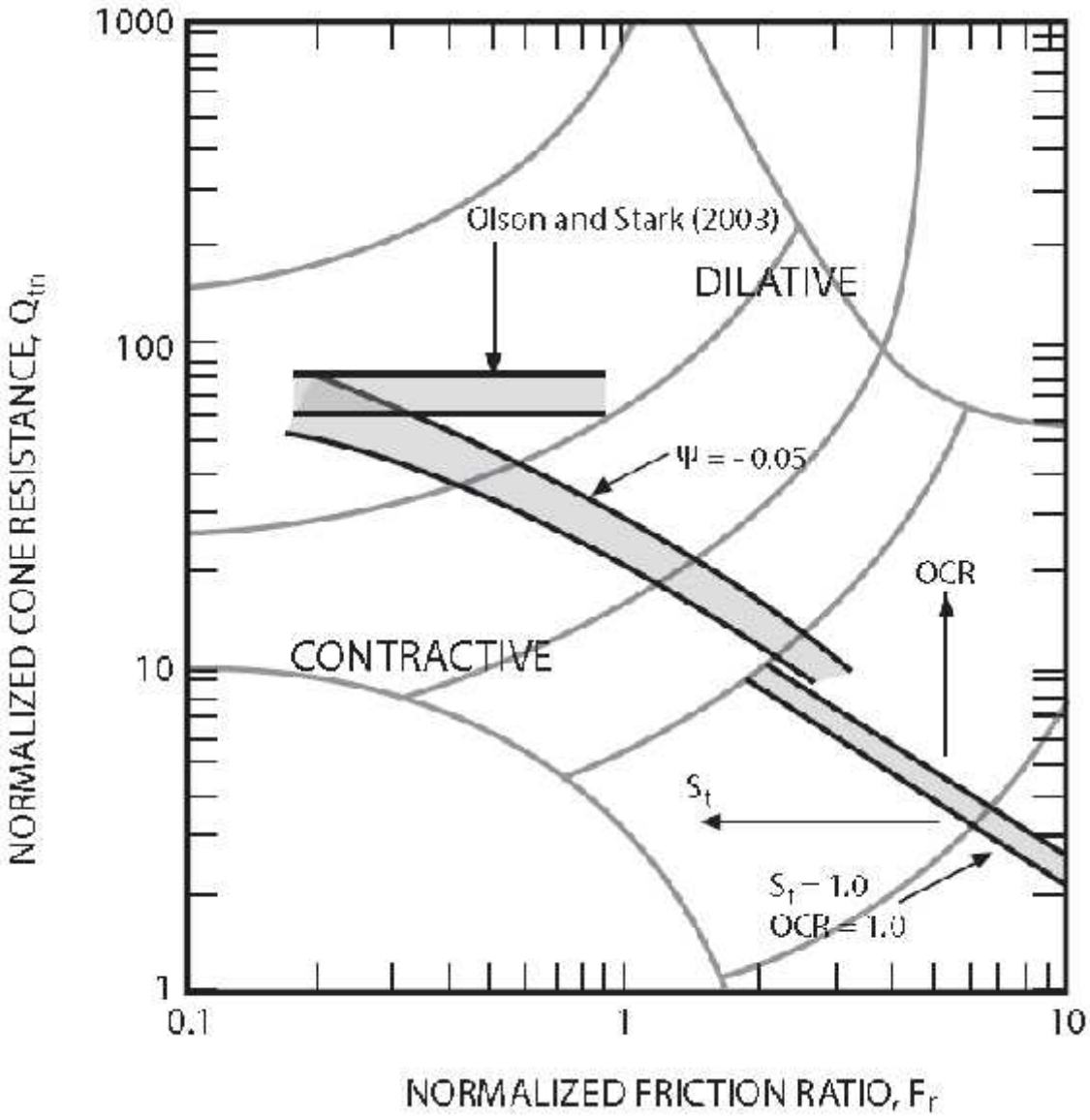

Figure 3.4 Liquefaction susceptibility boundary proposed by Robertson (2010) plotted on chart of normalized net tip stress, Q_{tn} vs. normalized sleeve friction, F_r

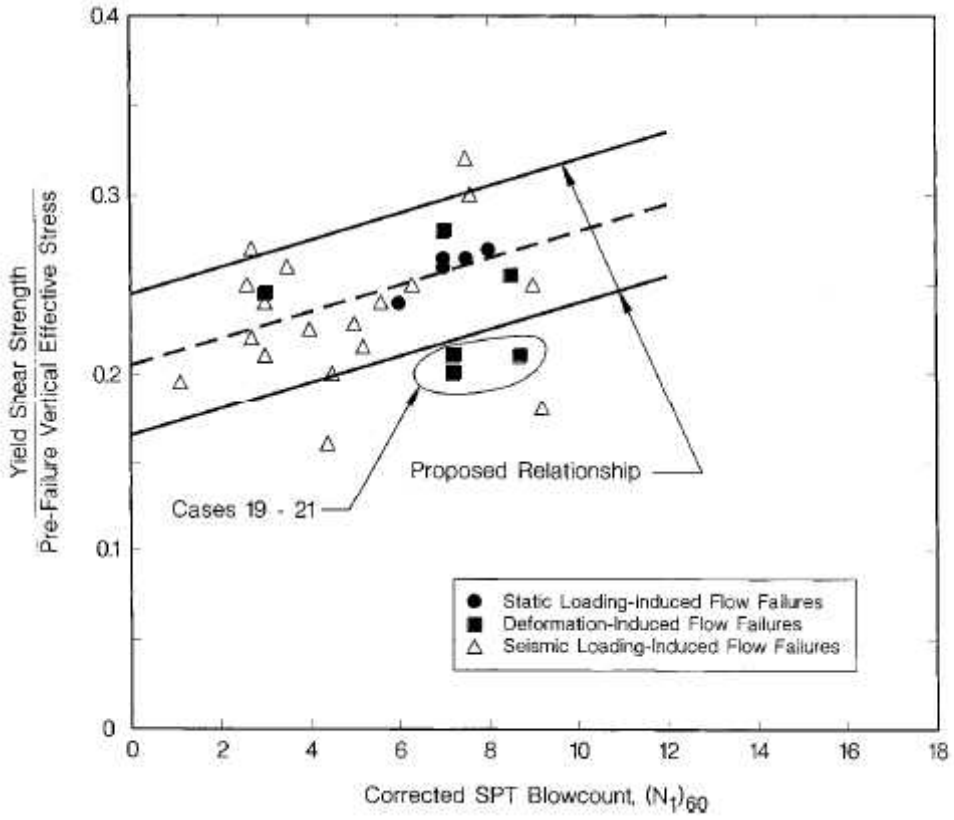

Figure 3.5 Comparison of yield and mobilized strength ratios and corrected SPT blowcount for liquefaction flow failures (from Olson and Stark 2003a)

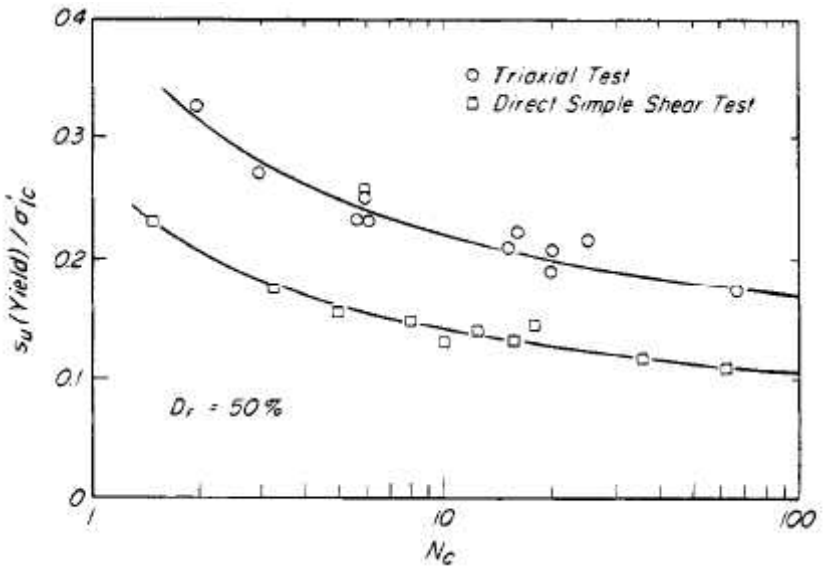

Figure 3. 6 Effect of mode of shear on yield shear strength ratio from cyclic shear tests on Monterey No. 0 sand (Terzaghi et al. 1996)

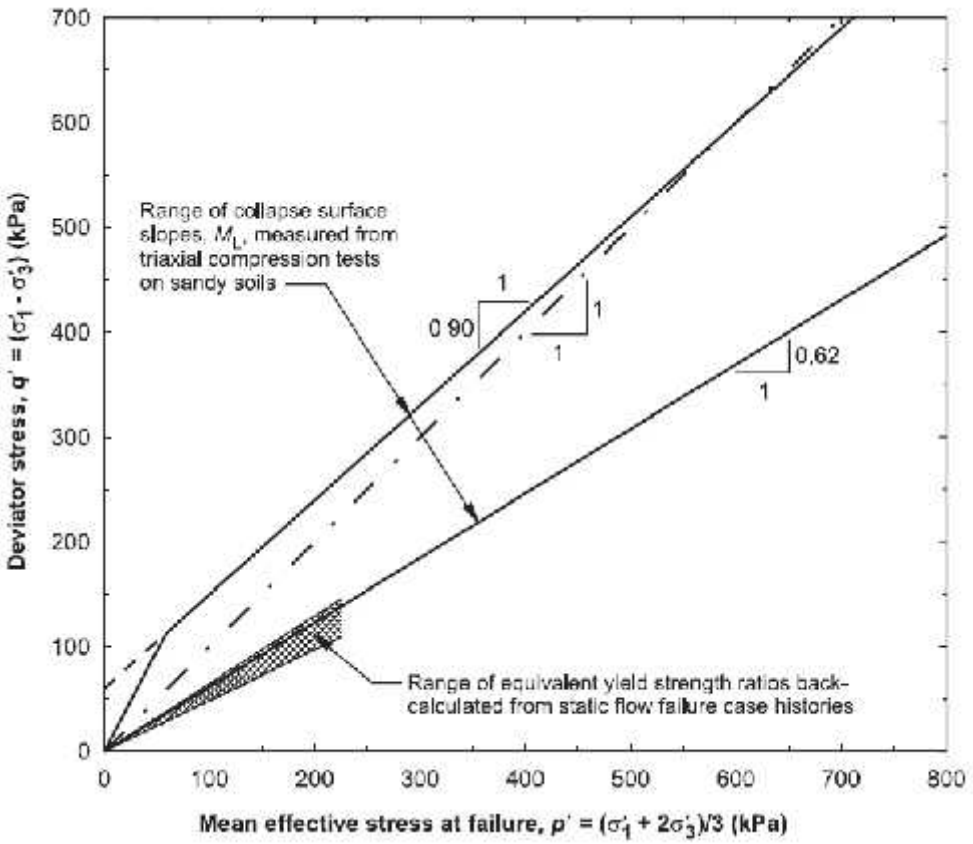

Figure 3.7 Comparison of yield strength envelope data (in stress path space) from laboratory database and static flow failure case histories (from Olson and Stark 2003b)

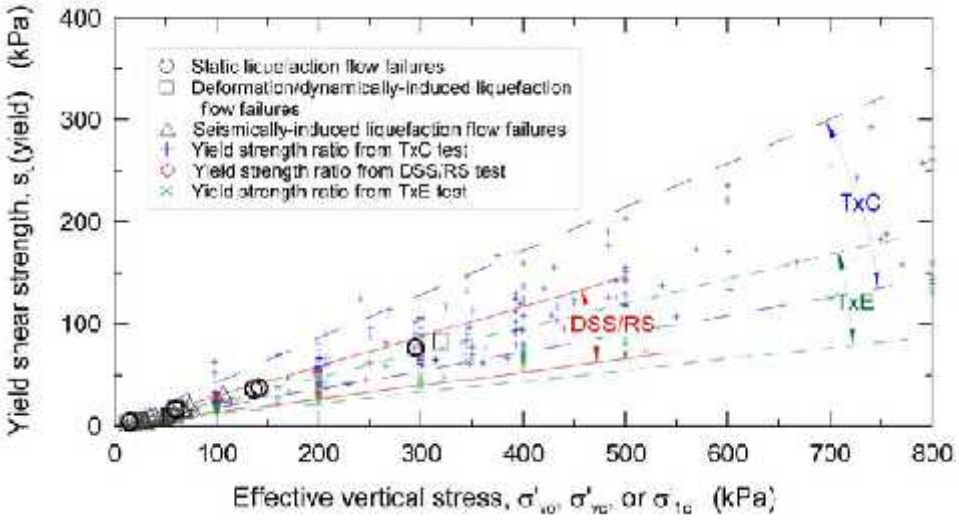

Figure 3.8 Comparison of yield strength ratios measured in triaxial compression (TxC), direct simple shear (DSS) and rotational shear (RS), and triaxial extension (TxE) with yield strength ratios back-calculated from flow failure case histories (from Olson and Mattson 2006).

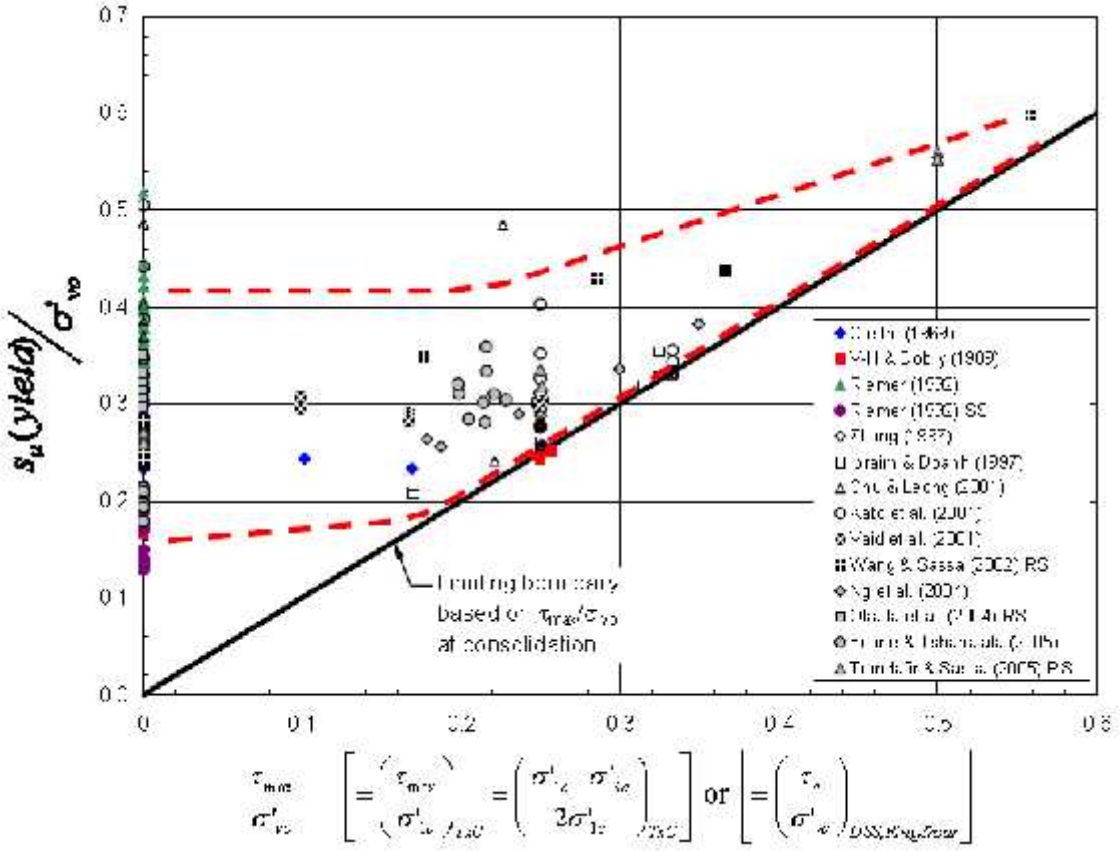

Figure 3.9 Yield strength ratio, $s_u(yield)/\sigma'_{vo}$ vs. static shear stress ratio, $^2{}_{static}/\sigma'_{vo}$ (from Olson et al. 2006)

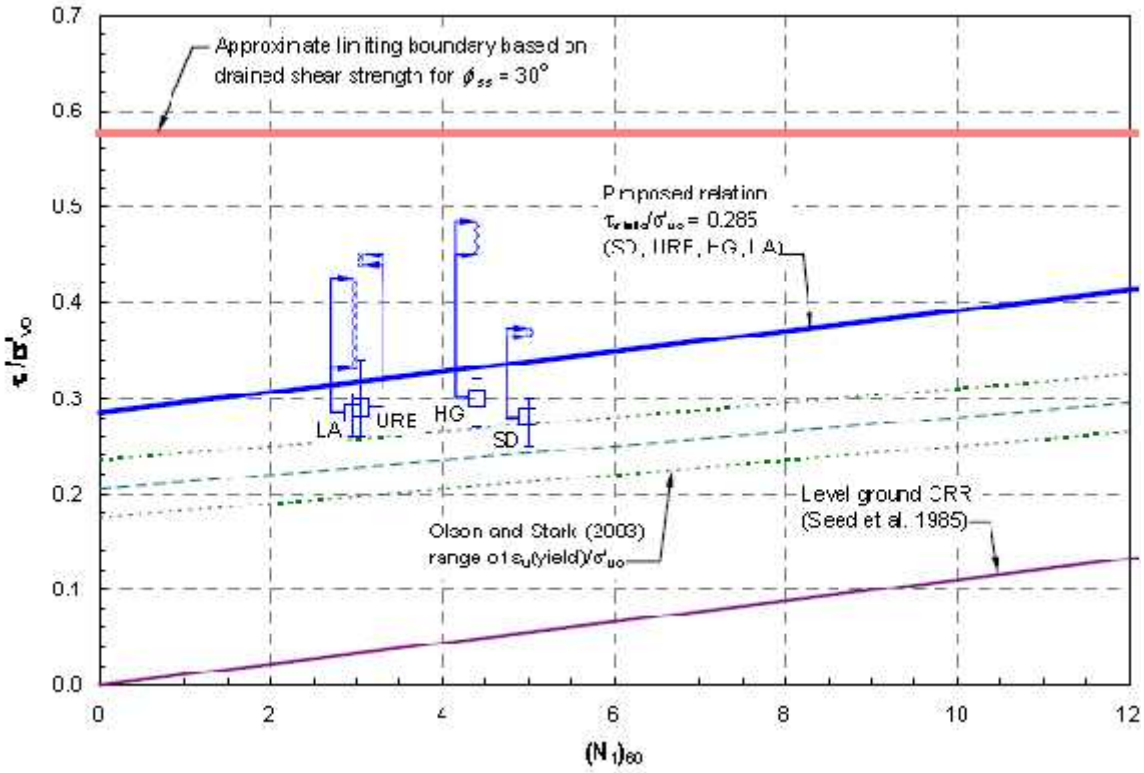

Figure 3.10 Comparison of combined mobilized (static) shear stress and seismic shear stress ratios for seismically-induced flow failures and revised yield strength ratio for a static shear stress ratio, $^{2}_{static}/\sigma'_{vo}$ ~ 0.285 (from Olson et al. 2006)

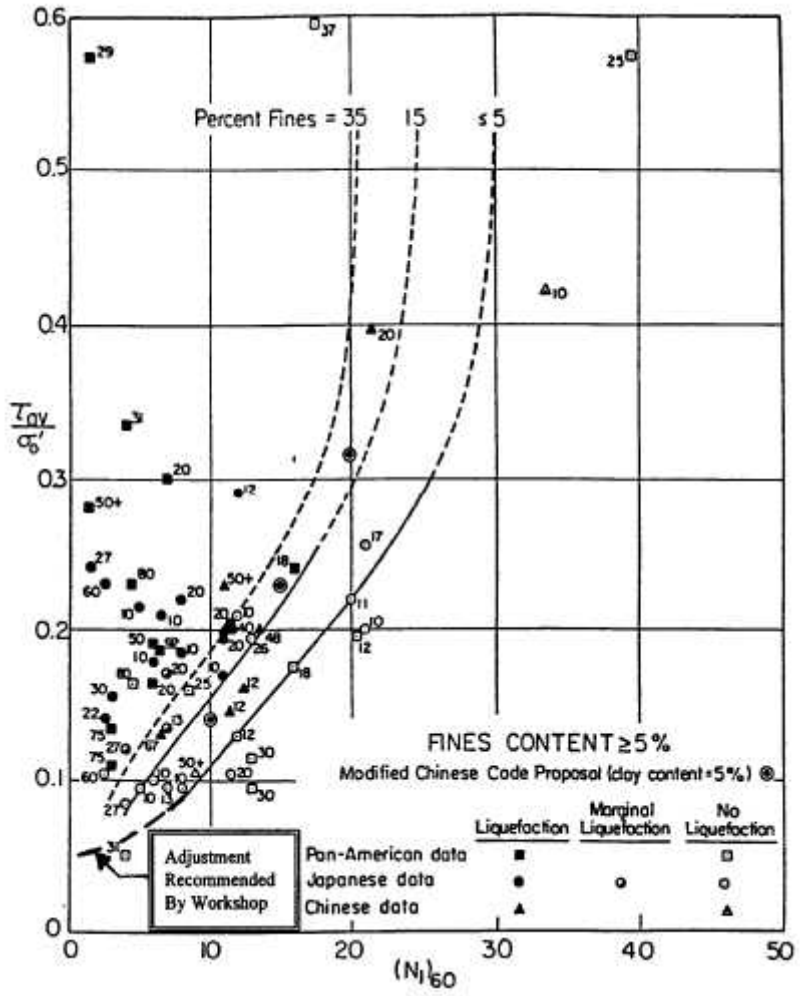

Figure 3.11 Liquefaction resistance curves for level ground conditions and Mw 7.5 earthquakes. Data represent cases of liquefaction and no liquefaction for silty sands (fines content > 10%) recommended by Seed et al. (1985) with adjustment for clean sand curve at low CSR values recommended by Youd et al. (2001)

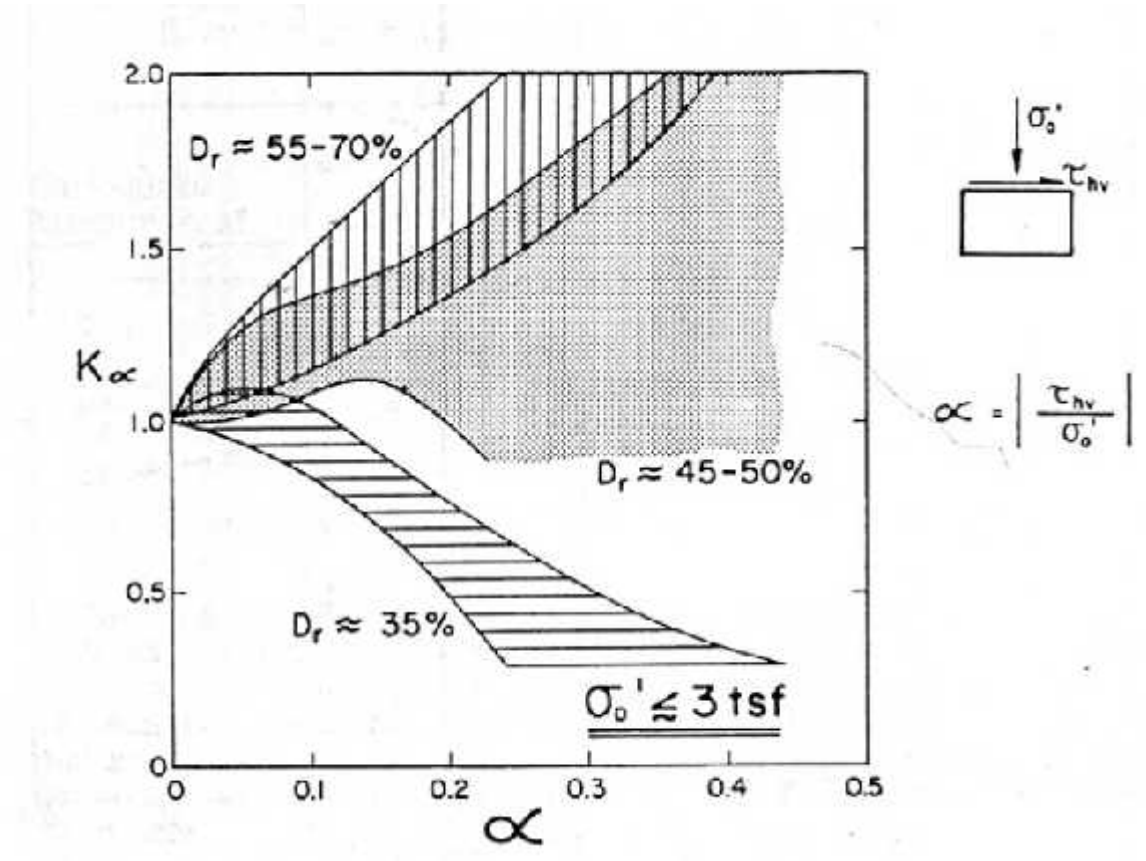

Figure 3.12 Relationship between α and K_α (from Seed and Harder 1990)

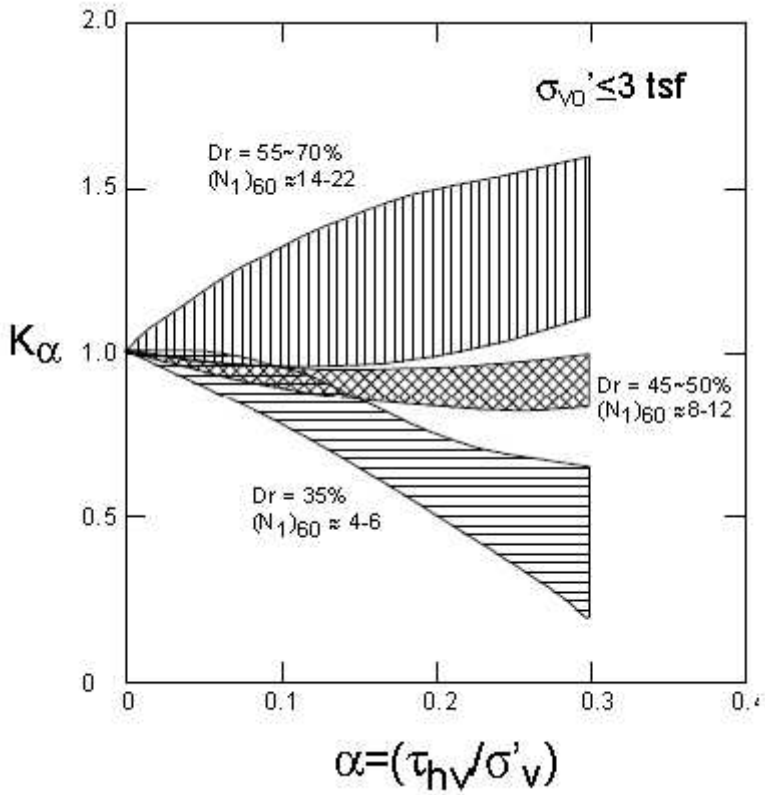

Figure 3.13 Recommended values of K$_\alpha$ as a function of relative density and approximate SPT N-values for effective vertical stresses of less than 3 atmospheres (from Harder and Boulanger 1997)

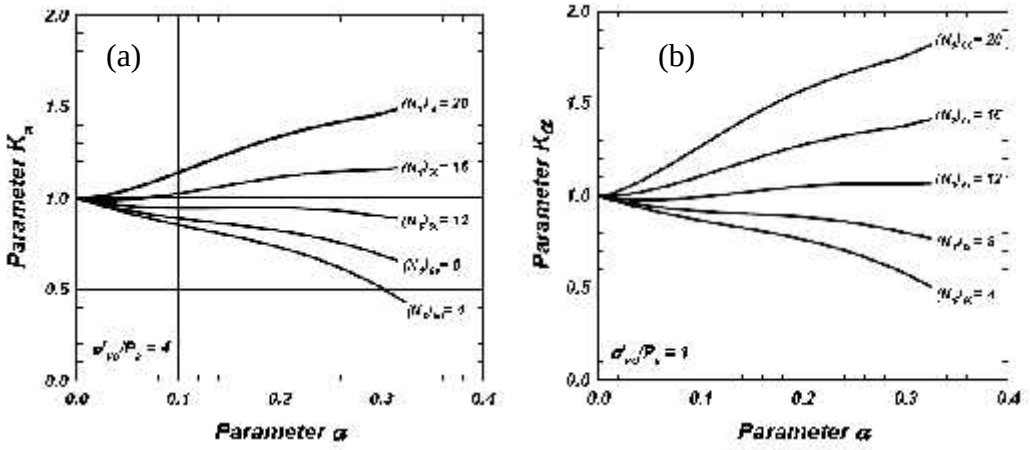

Figure 3.14 Variation of the static shear stress correction factor (K_α) for sands at: (a) an effective overburden stress of 4 atm, and (b) an effective overburden stress of 1 atm. (from Boulanger and Idriss 2004)

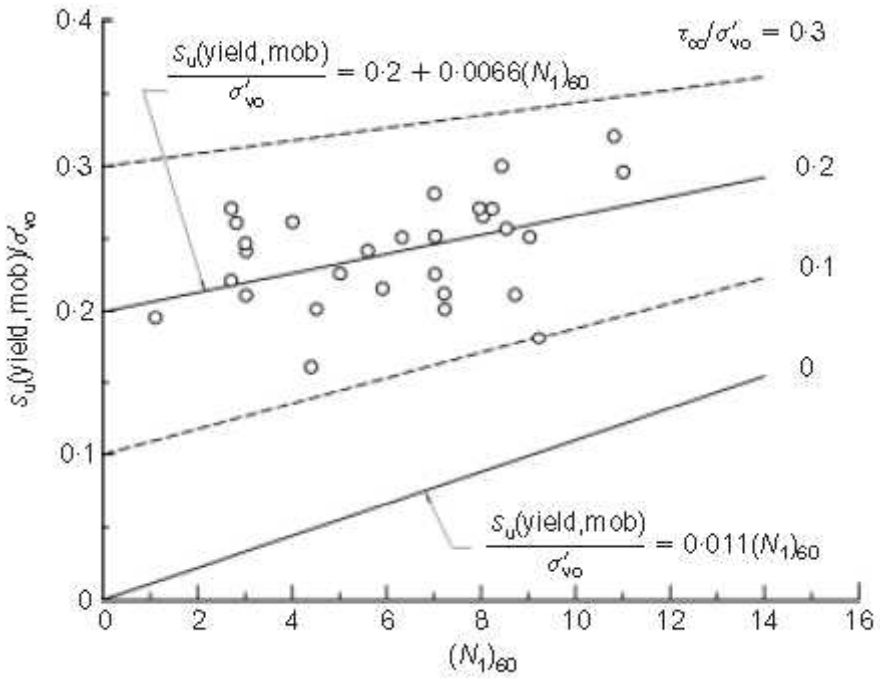

Figure 3.15 Comparison of yield strength ratio relationships proposed by Mesri (2007) with data back-calculated by Olson (2001)

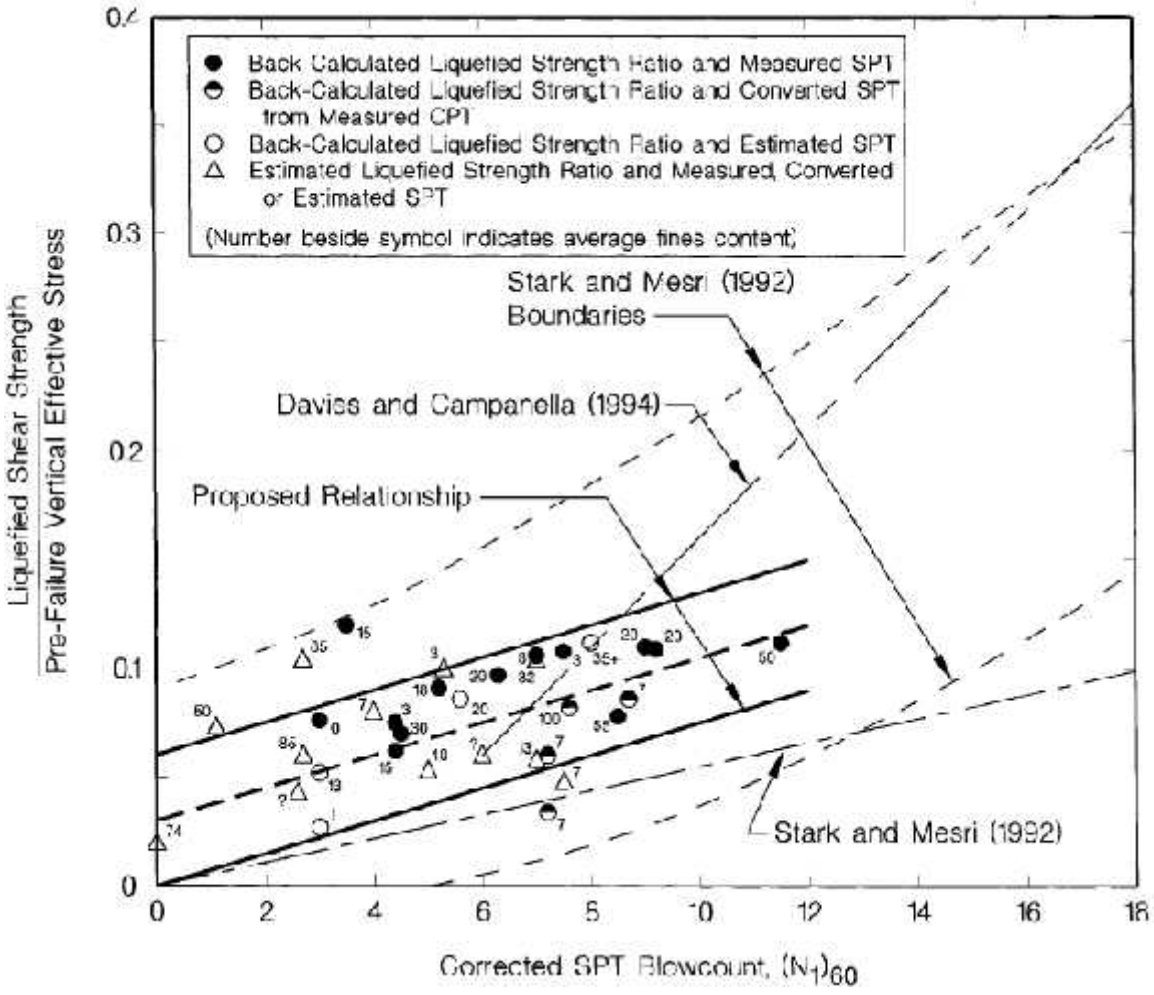

Figure 3.16 Relationship between liquefied strength ratio and corrected SPT blowcount and proposed by Olson (2001) with compared with SPT based liquefied strength ratio relationship from other investigators (from Olson and Stark 2002)

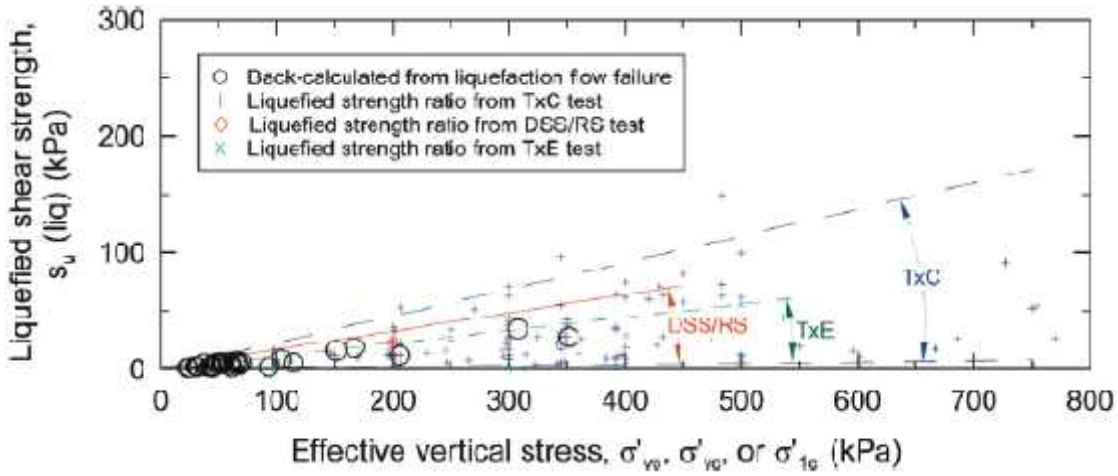

Figure 3.17 Comparison of liquefied strength ratios for field and laboratory data (from Olson and Mattson 2008)

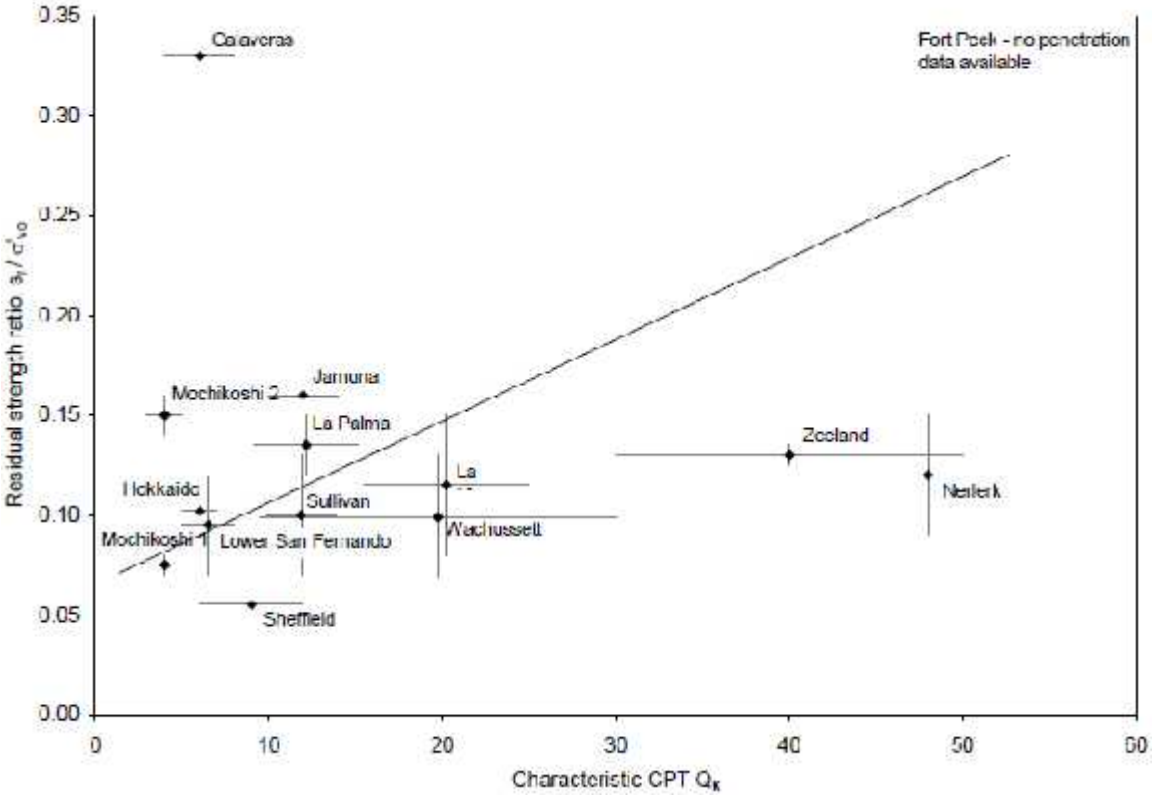

Figure 3.18 Relationship between liquefied shear strength ratio and characteristic CPT tip resistance (from Jefferies and Been 2006)

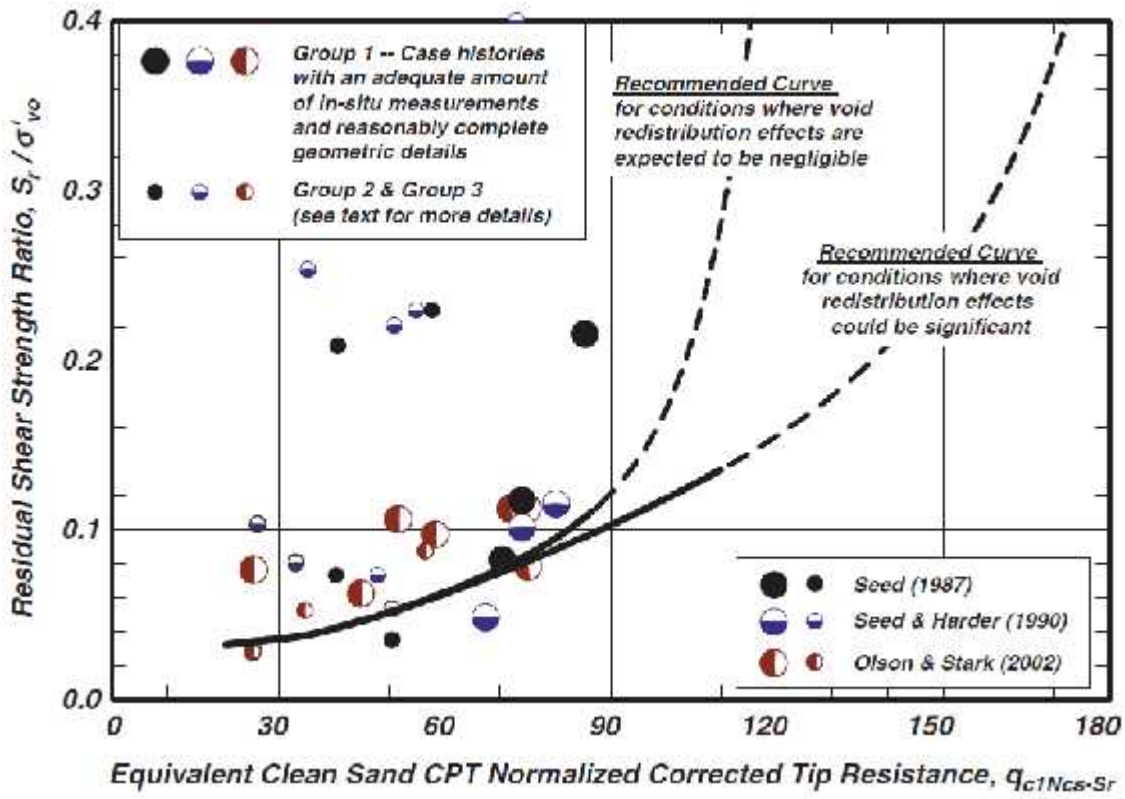

Figure 3.19 Liquefied shear strength ratio versus equivalent clean sand q_{c1} for case histories analyzed by different researchers and curves proposed for relating residual shear strength ratio of liquefied soil to median values of equivalent clean-sand CPT normalize corrected tip resistance for $\pm'_{vo}$ less than 400 kPa (from Idriss and Boulanger 2007)

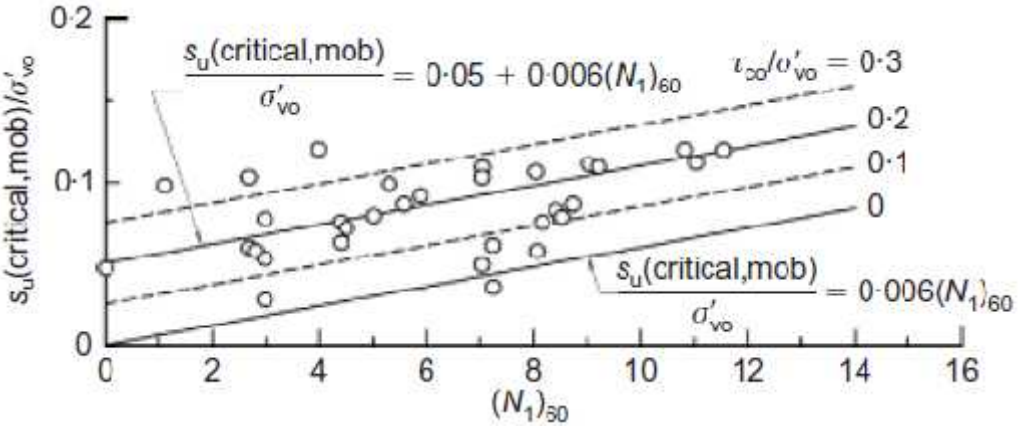

Figure 3.20 Liquefied strength ratio data back-calculated by Olson and Stark (2002) compared with predictions by Eq. 3.12 (from Mesri 2007)

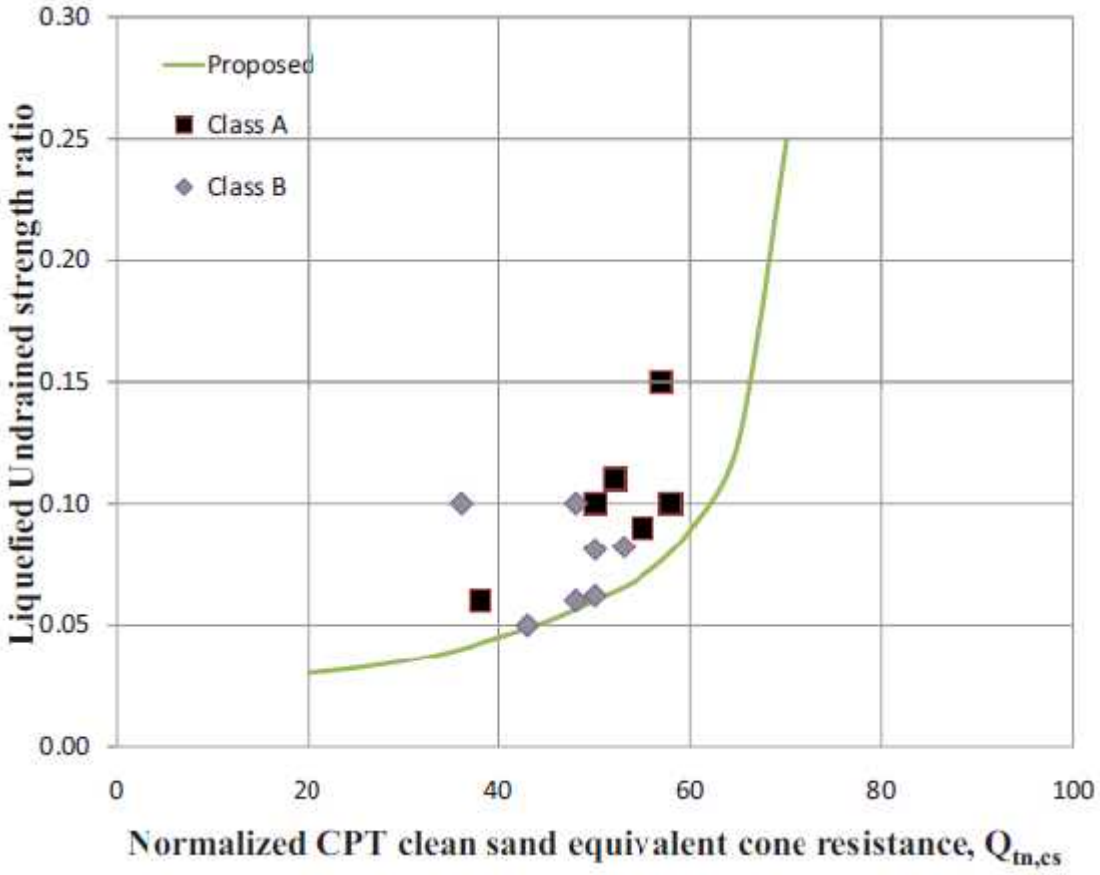

Figure 3.21 Liquefied shear strength ratio and normalized CPT clean sand equivalent penetration resistance from Class A (sites where CPT measurements with sleeve friction values are available) and Class B (sites where only CPT measurements are available) flow liquefaction failure case histories (from Robertson 2010)

.

CHAPTER FOUR:

LIQUEFACTION SUSCEPTIBILITY

4.1 Introduction

The analysis of liquefaction in sloping ground based on case histories can be divided into three steps as defined by Olson (2001): (1) liquefaction susceptibility; (2) liquefaction triggering; and (3) post-liquefaction/flow failure stability. Liquefaction susceptibility refers to identifying potential contractive response to shearing, i.e., strain softening response.

Not all soils are susceptible to flow liquefaction. Soils susceptible to flow liquefaction generally are cohesionless soils loose enough to be contractive and low permeable enough to experience insignificant dissipation of excess porewater pressure generated by static or seismic loading (Terzaghi et al. 1996). This chapter briefly presents compositional, geological, historical, and state criteria for liquefaction susceptibility. Because only contractive soils are susceptible to liquefaction, several existing relationships that distinguish contractive soils from dilative are critically examined in this chapter. Furthermore, the effect of fines content (FC) on empirical liquefaction susceptibility relations is investigated. Following the discussion about the importance of compressibility of sandy soils by Olson (2009), case histories analyzed in this study for which compressibility parameters were estimated by Jefferies and Been (2006) are plotted along with selected case histories from Olson (2001) to evaluate the effect of soil compressibility on liquefaction susceptibility. Finally, a potential relationship between compressibility and fines content of cohesionless soils is explored.

4.2 Liquefaction Susceptibility

Liquefaction susceptibility analysis determines whether a particular soil is contractive (i.e., strain-softening) or dilative (i.e., strain-hardening) when sheared. As discussed below, the contractive or dilative response of a soil is a function of its in situ state, i.e., the combination of the in situ density and effective confining stress. However, there are several additional factors that may influence to liquefaction susceptibility. These include (Kramer 1996): (i) grain characteristics, i.e., particle size, gradation, particle shape, surface roughness, and fabric; (ii) geologic characteristics, i.e., depositional environment and processes, depth of water table, preconsolidation and geologic age; and (iii) seismic history, i.e., whether liquefaction occurred at the same site in the past.

4.2.1 Grain Characteristics

Until the 1975 Haicheng and 1976 Tangshan earthquakes, liquefaction-related phenomena were thought to be limited to relatively clean, fine-grained sands (i.e., with only a small percentage of fines). Fine-grained soils were considered unable to generate excess porewater pressure sufficient to trigger liquefaction, while sands coarser than fine-grained were considered too permeable to sustain excess porewater pressure and liquefy. Tsuchida (1970) conducted sieve analysis on soils that did or did not liquefy during past earthquakes, and chiefly during the 1964 Niigata earthquake. Based on the sieve analysis results, Tsuchida (1970) suggested that soils within the grain size boundaries shown in Figure 4.1 are susceptible to liquefaction. These boundaries are consistent with the concepts above.

However, numerous examples of liquefaction of coarse-grained and fine-grained soils under level and sloping ground conditions have been documented in the literature, including during relatively recent earthquakes of 1988 Armenia, 1994 Northridge, 1999 Adapazari, and 1999 Chi-Chi. Ishihara (1985) proposed finer-grained boundaries based on the liquefaction of fine-grained tailings, as illustrated in Figure 4.1. The current study

also includes some of these sloping ground liquefaction cases, such as the failures of the Merriespruit and Sullivan tailings dams. Fewer cases of sloping-ground liquefaction of coarse-grained soils are available; however, the failure of the Spitak embankment is one example of liquefaction of gravelly soils. Includes the estimated D_{50} for the flow failure case histories studied here as well as the case histories documented by Olson (2001). As illustrated in the figure, these D_{50} data generally are consistent with the Tsuchida (1970) and Ishihara (1985) boundaries.

Well-graded soils generally exhibit small void ratios (compared to uniformly-grained soils) because the void spaces between larger particles in well-graded soils are filled by smaller particles. The lower void ratio generally makes these soils less susceptible to liquefaction. Poorly (uniformly) graded soils, on the other hand, are more likely to be susceptible to liquefaction because voids between the particles remain empty.

Particle shape also affects liquefaction resistance. In general, rounded particles are less resistant to liquefaction than angular particles, primarily because of the interlocking that occurs in angular particle fabrics. However, if the applied loading is sufficiently large to break down the soil fabric, angular soils may become highly contractive. Further, the angular particles are more vulnerable to particle damage due to their angularity.

4.2.2 Geological Characteristics

As stated above, loose, rounded and poorly graded sandy soils are most likely to be susceptible to liquefaction, therefore geological environments that produce such soils influence liquefaction susceptibility. As a result, soil deposits formed under fluvial, colluvial, and aeolian environments are occasionally susceptible to liquefaction (Youd and Hoose 1977; Youd and Perkins 1978; Kramer 1996). Many of the flow failures involving natural soils are alluvial deposits (e.g., failure of Kamenari road embankment during 1979 Montenegro earthquake; Degimendere delta failure during the 1999 Kocaeli earthquake; and the earth dam failures during 2001 Bhuj earthquake). The Okuli

landslide during the 1989 Tajikistan earthquake involved liquefaction of an aeolian deposit. However, most liquefaction flow failures occur in uncompacted manmade deposits.

Geological age of the deposited soils is also important in deciding the susceptibility of soil deposits (Youd and Perkins 1978), with older and overconsolidated soils generally increasing in liquefaction resistance. Table 4. 1 and Table 4. 2 show the depositional environments and approximate geologic age of the soils involved in the liquefaction flow failure analyzed in this study and in Olson (2001) respectively.

Liquefaction occurs only in saturated soils; therefore, the depth of the water table plays an important role in liquefaction susceptibility. Soil deposits with shallow water tables are more susceptible to liquefaction.

4.2.3 Seismic History

Recurrence of liquefaction is possible at the same site during successive earthquakes if the soil and ground water conditions remained unchanged. While reconsolidation causes densification of liquefied soil, this may not result in increased liquefaction resistance. First, upward seepage may cause the upper portion of a liquefied deposit to loosen and remain susceptible to liquefaction (e.g., Youd 1984). Second, liquefaction involves yielding and breaks down of the soil structure. Destroying the soil structure (and effectively re-depositing the soil) may decrease the post-earthquake liquefaction resistance of the deposit, even after reconsolidation (Terzaghi et al. 1996; Olson et al. 2001, 2005; Ha et al. 2011).

Liquefaction case histories are therefore important because they identify the soils that may be susceptible to liquefaction in future earthquakes. Youd (1984) identified several sites in United States and in Japan that experienced liquefaction recurrence. Sloping ground sites that have liquefied multiple times include Lower San Fernando dam,

which liquefied during the 1952 Kern County earthquake, the 1971 San Fernando earthquake, and the 1994 Northridge earthquake. Another example is Yamanaka dam in Japan which liquefied during four separate earthquakes within 26 years. This case history is described in Chapter 7 of this study.

4.2.4 State Criteria

Soil state describes its density and in situ stress. Liquefaction is triggered due to generation of excess porewater pressure which in turn largely depends on the initial stress and density of soil. Therefore, liquefaction susceptibility strongly depends on the initial state of the soil. As discussed in Chapter 2, Casagrande (1936) first illustrated that loose sands tend to contract when sheared while dense sands tend to dilate during shear. Under undrained conditions, loose specimens tend to generate positive excess porewater pressure while dense specimens tend to generate negative excess porewater pressure, as illustrated in Figure 4.2. The critical state line defined by the locus of large strain (e-log σ') conditions is the most important flow liquefaction susceptibility criterion. Even if a particular soil meets all the previously explained criteria it still may not be susceptible to flow liquefaction unless this condition is fulfilled. A detailed discussion about the effect of state on liquefaction susceptibility follows.

4.3 Existing Methods to Evaluate Liquefaction Susceptibility of Sloping Ground

As explained above, liquefaction susceptibility depends strongly on the contractive or dilative nature of the soil. Several relationships have been proposed to differentiate liquefiable and non-liquefiable soils based on their contractive or dilative response to shear. Two liquefaction susceptibility approaches have been used: (i) a state parameter approach; (ii) a penetration resistance approach.

4.3.1 Liquefaction Susceptibility: State Parameter Approach

The state parameter, ψ, is defined as the difference between in situ and critical state void ratios at the same effective confining pressure (see Figure 4.3). The numerical value of state parameter identifies the dilative or contractive nature of the soil. Soils with $\psi > 0$ are contractive and susceptible to liquefaction under any type of loading (Plewes et al. 1992; Jefferies and Been 2006). Plewes et al. (1992) suggested that the soils with $\psi = 0$ to -0.1 represent medium dense soils that may generate positive excess pore pressures and liquefy under dynamic loading. However, medium dense soils are likely to dilate during shearing, and uncontrolled flow failures are highly unlikely.

Jefferies and Been (2006) suggested that the soils with $\psi = 0$ to -0.05 should also be considered as contractive and susceptible to liquefaction. Soils with $\psi < -0.05$ are considered as dilative by Jefferies and Been (2006), while soils with $\psi < -0.1$ are considered as dense or overconsolidated and are predicted to be strongly dilative by Plewes et al. (1992). Been et al. (1986, 1987) proposed a methodology in which normalized CPT resistance could be used to estimate the ψ of a soil. The method was later modified by Plewes et al. (1992) and Shuttle and Jefferies (1998, 2007).

Figure 4.4 catalogs state parameters for selected case histories analyzed by Olson (2001) and in this study, with respect to effective vertical stress (estimated in analyses described in subsequent chapters). Mean state parameters reported in the Figure 4.4 were estimated by Jefferies and Been (2006). In general, these cases illustrate that sites that experienced liquefaction flow failure likely had state parameters greater than zero. Based on the state parameters estimated by Jefferies and Been (2006), only three of the cases in Figure 4.4 plot to the left of the $\psi = 0$ boundary. These cases are the Nerlerk berm failures, the failures along the Zeeland coast (Vleitepolder), and Fort Peck dam. As discussed in Sladen et al. (1985a,b,1987), Been et al. (1987), and Rogers et al. (1990), the in situ value of state parameter at the Nerlerk berm is ambiguous, with Sladen et al. (1985a) suggesting a state parameter that was greater than zero. Very little specific information is available for the Vleitepolder case history; but available penetration

resistance could be interpreted to suggest a state parameter greater than zero. The estimate of Fort Peck dam appears equivocal because other structures consisting of similarly-placed, end-dumped fill, e.g., the North Dike of Wachusett Dam and Calaveras Dam, were assigned much higher values of state parameter by Jefferies and Been (2006). As a result, the author contends that all of the liquefaction flow failure case histories reported in Figure 4.4 may have had in situ state parameters greater than zero. Therefore, it is not possible to evaluate using flow failure case histories the Plewes et al. (1992) and Jefferies and Been (2006) postulated that soils with $\psi < 0$ may be contractive.

4.3.2 Liquefaction Susceptibility: Penetration Resistance Approach

Been and Jefferies (1985) and Been et al. (1986) define the contractive and dilative nature of sands using state parameter. As interpreted by Olson (2001), penetration resistance is inversely related to state parameter (i.e., effective confining stress and void ratio); therefore, it should be possible to develop a boundary curve similar to critical state line that separates contractive from dilative sands.

Sladen and Hewitt (1989) first suggested a relationship between penetration resistance and effective stress separating contractive and dilative conditions as shown in Figure 4.5. Several other relationships based on the same concept were later suggested by Robertson et al. (1992), Ishihara (1993), Baziar and Dobry (1995), Fear and Robertson (1995) as shown in Figure 4.5 and Figure 4.6. The boundary curves reported by Fear and Robertson (1995) for Ottawa sand and Alaska sand represent the $\psi = 0$ condition for these sands.

Table 4. 3 lists the case histories analyzed in this study along with the average and range of penetration resistances for each case. Figure 4. 7 shows the range of $(N_1)_{60}$-values with the corresponding prefailure effective vertical stresses for the case histories analyzed in this study (determined from the pre-failure yield strength analysis described in Chapter 5). As illustrated in the Figure 4. 7, the susceptibility curve adopted by Olson

(2001) based on the work by Fear and Robertson (1995) encompasses all but two cases analyzed in this study. Similarly, Figure 4.8 shows the range of q_{c1}-values with corresponding range of prefailure effective vertical stresses for the case histories analyzed in this study (determined from the pre-failure yield strength analysis described in Chapter 5). Again, the CPT-based susceptibility curve adopted by Olson (2001) based on the work by Fear and Robertson (1995) encompasses all but two cases analyzed in this study.

For a more complete assessment of the SPT-based and CPT-based liquefaction susceptibility boundaries, the author combined the case histories from this study with those studied and documented by Olson (2001). To improve the comparison between the two case history databases, the author developed a matrix for quantifying the "relative confidence" associated with particular "input" data used for the back-analyses performed in this study, including: the pre-failure geometry, the post-failure geometry, the phreatic surface location, and the availability of penetration resistance data. Each "input" was assigned a numerical score. The scores for each "input" were tallied to define a net "relative confidence" in the input data used for the back-analyses. The relative confidence levels are termed: High, Moderate, and Low. The relative confidence (rC) levels are defined as:

High	$rC \geq 4$
Moderate	$3 \leq rC < 4$
Low	$rC < 3$

Table 4. 4 documents the relative confidence levels for each of the case histories studied here and studied in Olson (2001), and Figure 4.9 and Figure 4.10 illustrate SPT $(N_1)_{60}$-values and q_{c1}-values, respectively, against effective vertical stress. These figures include the Fear and Robertson (1995) boundary for Ottawa sand that Olson (2001) adopted for use in evaluating flow failure case histories. As anticipated, the liquefaction susceptibility boundaries adopted by Olson (2001) reasonably envelope the combined

flow failure databases. The figures also illustrate that there is no discernible trend in the position of the cases based on the relative confidence in the "input" data.

4.4 Effect of Soil Compressibility on Liquefaction Susceptibility

A unique relationship between penetration resistance, in-situ effective stress, and relative density does not exist because soil compressibility also influences the penetration resistance, as illustrated in Figure 4.11 based on pressure chamber test (Robertson and Campanella 1983). Robertson and Campanella (1988) suggested that compressibility tends to increase with increasing grain size uniformity, with increasing grain angularity, and with increasing content of compressible mineralogy (e.g., mica and/or carbonate content). Mesri and Verdhanabhuti (2009) summarized compression index (C_c, defined as the slope of the consolidation curve in e-log σ'_v space) data for quartz sands, quartz sands with 10% to 20% fines, and carbonate sands, as shown in Figure 4.12. These data illustrate several key concepts regarding sand compressibility: (1) loose sands are more compressible than dense sands; (2) at effective vertical stresses common for civil engineering projects, i.e., less than 10 MPa where particle damage occurs, quartz sands with 10% to 20% fines generally are more compressible than clean quartz sands; (3) at higher confining stresses (where asperities are sheared off), angular to subangular quartz sands become more compressible; (4) carbonate sands are considerably more compressible than quartz sands, regardless of grain shape, until effective vertical stresses are very high (greater than about 10 MPa). In summary, Figure 4.12 shows that prior to the onset of particle damage at relatively large effective vertical stresses, soil compressibility depends on relative density, mineralogy, and grain shape. In general, these data support the earlier observations by Robertson and Campanella (1983).

High compressibility Hilton Mines sand consists of angular grains of quartz, mica, and feldspar, and has a rather uniform grain size distribution with D_{60} = 0.30 mm and D_{10} = 0.15 mm, yielding a uniformity coefficient, C_U = 2. In contrast, low compressibility Monterey sand consists of subrounded to subangular particles of

primarily quartz with some feldspar, and is also rather uniform with D_{60} = 0.40 mm, D_{10} = 0.25 mm, and C_U = 1.6. Ticino sand, with moderate compressibility, consists of subangular to angular particles of primarily quartz with about 5% mica content (by volume). The sand is also rather uniform, with D_{60} = 0.65 mm, D_{10} = 0.40 mm, and C_U = 1.6. As shown in Figure 4.11, for a given relative density and given effective vertical stress, the CPT tip resistance increases with decreasing compressibility.

4.4.1 Olson (2009) Compressibility Correction Factor, C_a

To account for the effect of compressibility on penetration resistance (not liquefaction resistance), Olson (2009) presented three separate liquefaction susceptibility boundary curves for low, medium, and high compressible soils, as shown in Figure 4.13, developed using a "compressibility" correction factor, C_λ. The original and expanded development of this compressibility factor is detailed below. Figure 4.13 includes data from flow failure case histories studied by Olson (2001). The numbers beside the data are the range of λ_{10} values (i.e., CSL slopes) estimated by Jefferies and Been (2006). The boundaries then represent the upper boundary for contractive-dilative response for soils with various CSL slopes. For example, consider a soil at σ'_{vo} = 100 kPa with q_{c1} = 6 MPa. If this is a moderately compressible quartz sand with 10% feldspar content and λ_{10} ~ 0.06, the soil is predicted to be dilative. In contrast, if this soil is a clean quartz sand with λ_{10} ~ 0.03, the soil is predicted to be contractive. As illustrated in Figure 4.13, most of the data agree reasonably well with the family of susceptibility boundary relationships (i.e., plot to the left of their respective boundary curves).

Olson (2009) developed the compressibility correction factor as follows. The data for the Monterey sand in Figure 4.11 were developed by Villet and Mitchell (1981). As stated by Robertson and Campanella (1988) (and as confirmed by Olson 2009), calibration chamber tests on Ottawa sand performed by Schmertmann (1978) yielded nearly the same q_c curves as the Monterey sand. As discussed above, the boundary relations in Figure 4.9 and Figure 4.10 were based on tests performed by Fear and

Robertson (1995) on Ottawa sand. Therefore, the boundary q_{c1}-σ'_{vo} relations shown in Figure 4.9 and Figure 4.10, which were developed for Ottawa sand can be reasonably applied to Monterey sand, and represents a general boundary relationship for low compressibility sands (with $\lambda_{10} \sim 0.03$).

Referring to the Dr ~ 40% relationships in Figure 4.11 (because these soils are relatively loose and potentially susceptible to flow liquefaction, while soils with $D_r \sim$ 80% are generally too dense to flow liquefaction), Olson (2009) compared q_c values for the three sands at the same values of σ'_{vo} to develop C_λ values.

$$C_a = \frac{q_c(incompressible)}{q_c} \qquad \textbf{Eq. 4.1}$$

where q_c(incompressible) is the q_c-value for low compressibility Monterey sand (and Ottawa sand, both with $\lambda_{10} \sim 0.03$) at a given effective vertical stress and q_c is the q_c-value for another sand (with a different value of λ_{10}) at the same value of effective vertical stress. The calculated C_λ-values for Ticino sand ($\lambda_{10} \sim 0.06$) was about 1.4 and for Hilton Mines sand ($\lambda_{10} \sim 0.17$) was about 2.0. The q_c-values for the boundary curves for $\lambda_{10} \sim 0.06$ and $\lambda_{10} \sim 0.17$ were developed by rearranging Eq. 4.1 and using the C_λ-values noted above with the Fear and Robertson (1995) boundary curve representing the low compressibility "control" curve. Based on these three data, Olson (2009) suggested a relationship between λ_{10} and C_λ, which was defined as:

$$C_a = 4.15\left(\lambda_{10,CS_o}\right)^{0.37} \qquad \textbf{Eq. 4.2}$$

where $\lambda_{10,CSo}$ is the log base 10 slope of the CSL of an undamaged sand (Sadrekarimi 2009).

4.4.2 Updating the Compressibility Correction Factor, C_a

To expand and validate the C_λ factor originally developed by Olson (2009), the author collected calibration chamber test data of different sands from Houlsby and Hitchman (1988), Huang et al. (1999), Jefferies and Been (2006), and included evaluations of C_λ based on some laboratory test data from Sadrekarimi (2009). The calibration chamber test sands are summarized in Table 4.6 and the test results are presented in Figure 4.14.

Baldi et al. (1986) proposed the following equation to evaluate relative density from penetration resistance and effective vertical stress:

$$D_r = \frac{1}{C_2} \ln\left[\frac{q_c}{C_o \left(\pm '_{vo}\right)^{C_1}} \right] \qquad \textbf{Eq. 4.3}$$

where C_0, C_1, and C_2 are constants. As noted above, the C_λ factor is based on comparing qc values for various sands at the same D_r. For a given value of D_r , i.e., D_r is a constant, then Eq. 4.3 can be simplified as:

$$\pm '_v = C(q_c)^n \qquad \textbf{Eq. 4.4}$$

where C and n are constants for a given sand. The calibration chamber test data presented in Figure 4.14 noted above were evaluated in terms of Eq. 4.3. The values of C and n interpreted for similar ranges of D_r for each of the test sands are presented in Table 4.6.

As Olson (2009) used $D_r \sim 40\%$ for initially developing the C_λ factor, this study adopted the same constant $D_r \sim 40\%$ for comparing penetration resistances. Figure 4.15 catalogs the constants C and n with respect to λ_{10} (for $D_r \sim 40\%$) for each of the calibration chamber test sands. For sands where calibration chamber tests were not performed at $D_r \sim 40\%$, the author interpolated values of C and n corresponding to $D_r \sim$

40% based on C and n values interpreted from other D_r values. These interpolated values are included in Figure 4.15. Based on these values of C and n, Figure 4.16 presents the q_c-σ'_v relationships for D_r ~ 40% for each of the calibration chamber test sands.

Using Eq. 4.1 and the q_c-σ'_v relationships (at D_r ~ 40%) shown in Figure 4.16, C_λ values were computed for σ'_v values of 50 to 350 kPa. These values of C_λ for each of the calibration chamber test sands are presented in Figure 4.17 in terms of compressibility expressed as λ_{10}. Figure 4.17 includes data from Sadrekarimi (2009) for Mississippi River sand after particles were damaged during ring shear testing (λ_{10} ~ 0.29). These data very closely followed the trend proposed by Olson (2009):

$$C_a = 4.15\left(a_{10,CS_o}\right)^{0.37} \qquad \textbf{Eq. 4.5}$$

The updated compressibility correction factor in Figure 4.17 confirms the original interpretation by Olson (2009). Figure 4. 18 updates Figure 4.11 with additional flow failure case histories analyzed in this study. The estimates of λ_{10} for the additional case histories were taken from Jefferies and Been (2006). As illustrated in the figure, the case history data are in reasonably good agreement with the proposed liquefaction susceptibility boundaries.

4.5 Effect of Nonplastic Fines on Liquefaction Susceptibility

As anticipated by Robertson and Campanella (1988) and illustrated by Mesri and Verdhanabhuti (2009), sands with FC > 10% tend to be more compressible than clean sands, thereby affecting penetration resistance and influencing the position of the liquefaction susceptibility relationship. Furthermore, FC can be measured easily at any geotechnical lab, while more effort is required to measure either λ_{10} or C_c for reconstituted sand specimens.

To investigate this issue, the author used and divided the flow failure case histories analyzed in this study and those analyzed by Olson (2001) into four FC bins:0 to 10%, 11 to 20%, 21 to 30% and > 30%. The bin ranges were selected to relatively equally divide the available case histories, rather than initially attempting to define physical boundaries. Figure 4.19, Figure 4.21, Figure 4.23 and Figure 4.25 compare flow failure case histories analyzed in this study and by Olson (2001) to the Fear and Robertson (1995) boundary for Ottawa sand (as adopted by Olson and Stark 2003 for evaluating case histories). The moderate and high compressibility boundaries were developed by substituting $(N_1)_{60}$ for the Ottawa sand boundary for q_c(incompressible) and substituting $(N_1)_{60}$ for q_c in Eq. 4.1. Figure 4.20, Figure 4.22, Figure 4.24 and Figure 4.26 compare flow failure case histories analyzed in this study and by Olson (2001) to the Fear and Robertson (1995) boundary for Ottawa sand (converted to q_{c1} by Olson and Stark 2003 for evaluating case histories).

As illustrated in these figures, SPT- and CPT-based cases with FC < 20% show little difference in liquefaction susceptibility, with cases with various relative confidence values falling near the low compressibility boundary. However, at higher fines contents, both the SPT- and CPT-based case histories are enveloped by the moderate compressibility boundary. Interestingly, this change in behavior occurs at a fines content (between 20 and 30%) that is similar to the threshold fines content of 30 to 40% typically associated with changes in liquefaction resistance (Pitman et al. 1994; Zlatovic and Ishihara 1995; Thevanayagam et al. 1996; Thevanayagam et al. 2000; Polito and Martin 2001; Xenaki and Athanaspoulous 2003; Yang et al. 2004; and Papadopoulou and Tika 2008). Furthermore, there are only a few cases with FC > 30% that are not enveloped by the high compressibility susceptibility boundary. These data suggest that compressibility may be directly related to fines content. This is examined in the following section.

4.6 Relationship between Soil Compressibility and Non-Plastic Fines Content

As illustrated in Figure 4.12, an increase in FC generally increases soil compressibility at moderate stress levels. However, there is no unique relationship in the literature between FC and soil compressibility. Some investigators (Been and Jefferies 1985; Hird and Hossana 1990; Chen and Liao 1999; Andrianopoulos et al. 2001; Bouckovalas et al. 2003; Jefferies and Been 2006; among others) have investigated the effect of fines content on the slope and location of the CSL. Been and Jefferies (1985) and Hird and Hossana (1990) reported that λ_{10} increases with increasing FC for a given sand. Chen and Liao (1999) suggested the opposite trend, i.e., λ_{10} decreases with increasing fines content based on the data shown in Figure 4.27. However, in the author's opinion, this data do not show this trend. Rather these data appear to show that λ_{10} is essentially constant for this sand for FC ≤ 15%. Andrianopoulos et al. (2001) and Bouckovalas et al. (2003) collected a larger database of λ_{10} values and FC, and illustrated that λ_{10} values generally increase with increasing FC (Figure 4.28). In contrast, Olson (2001) and Jefferies and Been (2006) collected large databases of λ_{10} for soils with varying FC (Figure 4. 29 and Figure 4.30, respectively), although the Jefferies and Been (2006) reportedly is dominated by uniformly graded soils. These catalogs do not exhibit any discernible trend (particularly the Olson 2001 catalog) and illustrate the considerable scatter between critical state line slope and fines content.

In this study, data compiled by Olson (2001) and Jefferies and Been (2006) are combined in Table 4.5. These data are largely nonplastic sands, silts, and tailings. The grain shapes range from rounded to angular (as noted in Table 4.5 where available). Figure 4.31 presents the portion of the database involving nonplastic quartz sands with rounded to subrounded particles. This subset exhibits a weak trend, again suggesting a weak relationship between fines content and critical state line slope. Figure 4.31 presents the portion of the database involving subangular and angular tailings sands and silts. In

contrast to the data in Figure 4.32, these data do not exhibit any trend between FC and λ_{10}.

4.7 Summary and Conclusions

- Soils that contract upon shearing are susceptible to flow liquefaction.
- Liquefaction susceptibility analysis is performed to separate dilative soils from contractive soils.
- There are some general characteristics, e.g., grain size, depositional environment, liquefaction recurrence, and initial state that can be used to judge liquefaction susceptibility.
- Two methods can be used to evaluate potential contractive or dilative behavior of soils: the state parameter approach and the penetration resistance approach.
- In the state parameter (ψ) approach, soils with $\psi > 0$ are considered contractive while $\psi < 0$ are considered as dilative. However, some researchers suggest that soils with $\psi \geq -0.1$ may be contractive and susceptible to flow liquefaction.
- In the penetration resistance approach, a boundary between contractive and dilative behavior is defined in terms of penetration resistance and effective vertical stress. Soils with penetration resistance lower than this boundary are likely contractive, while soils with penetration resistance higher than this boundary are likely dilative.
- Among several available liquefaction susceptibility relationships based on penetration resistance, Fear and Robertson (1995) SPT-based boundary and the same boundary converted to CPT by Olson (2001) envelope the available flow failure case histories. As a result, recommendation from Olson (2001) to use these relations for evaluating flow failures was confirmed.
- Sands with the same relative density and effective confining stress can exhibit significantly different penetration resistances based on their compressibility.
- Olson (2009) proposed the use of a compressibility correction factor (C_λ) to adjust the location of the penetration resistance-based liquefaction resistance boundary to account for the effect of compressibility on penetration resistance. This study greatly expanded the data used to develop the compressibility correction factor and

confirmed the form of the compressibility correction factor proposed by Olson (2009).

- Using the updated compressibility correction factor, a suite of liquefaction susceptibility curves can be developed for any compressibility conditions of a given soil.
- Effect of fines on liquefaction susceptibility is ambiguous, and a database combined from catalogs collected by Olson (2001) and Jefferies and Been (2006) illustrate that there is no unique correlation between critical state line slope and fines content. The scatter in the comparison results from the effect of relative density, grain shape, and mineralogy on soil compressibility (at a given fines content).
- While no unique correlation between fines content and CSL slope exist, flow failure case histories with FC greater than about 20% are reasonably enveloped by the Olson (2009) "moderate compressibility" ($\lambda_{10} \sim 0.06$) liquefaction susceptibility boundary relation. Soils with FC less than about 20% are enveloped by the low compressibility ($\lambda_{10} \sim 0.03$) liquefaction susceptibility boundary relation.

4.8 References

Ambraseys, N. N. (1988). Engineering seismology, *Earthquake Engineering and Structural Dynamics,* Vol. 17, p. 1-105.

Amini, F., and Qi, G. Z. (2000). Liquefaction testing of sratified silty sands, *Journal of Geotechnical and Geoenvironmental Engineering,* ASCE, vol. 123, issue 3, p. 208 – 217.

Andrianopoulos, K. I., Bouckovalas, G. D., and Papadimitriou, A. G. (2001). A critical state evaluation of fines effect on liquefaction potential, *Proc. Of the 4th Int. Conf. on Recent Advances in Geotechnical Earthquake Engineering and Soil Dynamics and Symposium in Honor of Professor W. D. Liam Finn,* San Diego, California, March 26 – 31, 2001.

Baldi, G., Belloutti, R., Ghionna, V., Jamiolkowski, M., and Pasqualini, E. (1981). Cone resistance of dry medium sand. *10th international Conference on Soil Mechanics and Foundation Engineering,* Stockholm, vol. 2, p. 427 – 432.

Baziar, M. H. and Dobry, R. (1995). Residual strength and large-deformation potential of loose silty sands, *Journal of Geotechnical Engineering,* ASCE, vol. 121, issue 12, p. 896 – 906.

Been, K., and Jefferies, M. G. (1985). A state parameter for sands, *Geotechnique,* vol. 35, issue 2, p. 99 – 112.

Been, K., Crooks, J. H. A., Becker, D. E. and Jefferies, M. G. (1986). The cone penetration test in sands: Part I, state parameter interpretation, *Geotechnique,* vol. 36, issue 2, p. 239 – 249.

Been, K., Jefferies, M. G., Crooks, J. H. A. and Rothenberg, L. (1987). The Cone penetration test in sands: Part II, general inference of state, *Geotechnique,* vol. 37, issue 3, p. 285 – 299.

Bouckovalas G., Andrianopoulos K., Papadimitriou A., (2003), A Critical State interpretation for the cyclic liquefaction resistance of silty sands, *Soil Dynamics and Earthquake Engineering*, vol. 23: p. 115-125.

Casagrande, A. (1936). Characteristics of cohesionless soils affecting the stability of slope and earth fills, *Journal of the Boston Society of Civil Engineers,* January: reprinted in Contributions to Soil Mechanics 1925 – 1940, BSCE, p. 25 J – 276.

Chang, K. T. (1978). An analysis of damage of slope sliding by earthquake on the Paiho Main Dam and its earthquake strengthening, *Tseng-hua Design Section,* Dept. of Earthquake-Resistant Design and Flood Control Command of Miyana Reservoir, Peoples Republic of China.

Chang, N. Y., Yeh, S. T., and Kaufman, L. P. (1982). Liquefaction potential of clean and silty sands, *Proceedings of the 3rd International Earthquake Microzonation Conference,* vol. 2, p. 1017 – 1032.

Chen, Y. C., and Liao, T. S. (1999). Studies of the state parameter and liquefaction resistance of sands, *Earthquake Geotechnical Engineering,* ed. Seco e Pinto, publ. Belkema, Rotterdam, p. 513 – 518.

Coulter, M. and Migliaccio, L. (1996). Effects of the earthquake of March 27, 1964 at Valdez, Alaska, *Professional Paper 542-C,* U.S. Geological Survey, U.S. Department of the Interior, Washington, D.C.

Dezfulian, H. (1982). Effects of silt content on dynamic properties of sandy soils, *Proceedings of the 8th World Conference on Earthquake Engineering,* p. 63 – 70.

Donahue, J. L. (2007). The liquefaction susceptibility, resistance, and response of silty and clayey soils, *Ph. D. Thesis,* University of California, Berkeley.

Evans, M. D. and Seed, H. B. (1987). Undrained cyclic triaxial testing of gravels: the effect of membrane compliance, *Report UCB/EERC-87/08,* Earthquake Engineering Research Center, University of California, Berkeley, California.

Fear, C. E. and Robertson, P. K. (1995). Estimating the undrained strength of sand: a theoretical framework, *Canadian Geotechnical Journal,* vol. 32, issue 4, p. 859 – 870.

Finn, W. D. L., Ledbetter, R. H., and Wu, G. (1994). Liquefaction in silty soils: Design and analysis, *Ground failures under seismic conditions, Geotech. Spec. Publ. No. 44*, ASCE, New York, p. 51–76.

Fourie, A.B., Blight, G.E., and Papageorgiou, G. (2001). Static liquefaction as a possible explanation for the Merriespruit tailings dam failure, *Canadian Geotechnical Journal,* Vol. 38, p. 707 - 719.

Harder, L. F. Jr. (1977). Liquefaction of sand under irregular loading conditions, *M.S. Thesis,* University of California, Davis.

Hird, C.C. and Hassona, F. (1990); Some factors affecting the liquefaction and flow of saturated sands in laboratory tests. *Engineering Geology,* vol. 28, p. 149–170.

Ishihara, K., Sodekawa, M., and Tanaka, Y. (1978). Effects of overconsolidation on liquefaction characteristics of sands containing fines, *ASTM Special Technical Publication,* p. 246 – 264.

Ishihara, K. (1984). Post-earthquake failure of a tailings dam due to liquefaction of the pond deposit, *Proceedings of the International Conference on Case Histories in Geotechnical Engineering,* University of Missouri, St. Louis, Vol. 3, p. 1129-1143.

Ishihara, K. (1985). Stability of natural deposits during earthquakes, *Proceedings of the 11th International Conference on Soil Mechanics and Foundation Engineering,* Vol. 1, p. 321-376.

Jefferies, M., and Been, K. (2006). Soil liquefaction: A critical state approach, *Taylor and Francis,* 512p.

Koester, J. P. (1994). The influence of fine type and content on cyclic resistance, *Ground failures under seismic conditions, Geotech. Spec. Publ. No. 44,* ASCE, New York, p. 17–33.

Kramer, S. L. (1996). Geotechnical earthquake engineering, *Prentice Hall,* New Jersey, 653p.

Kuerbis, R., Negussey, D., and Vaid, V. P. (1988). Effect of gradation and fines content on the undrained response of sand, *Conference Proceedings Hydraulic Fill Structures,* p. 330 – 345.

Lade and Yamamuro. (1997). 'Effects of nonplastic fines on static liquefaction sands, *Can. Geotech. J.*, Ottawa, vol. 34, p. 918–928.

Law, K. T., and Ling, Y. H. (1992). Liquefaction of granular soils with noncohesive and cohesive fines, *Proc., 10th World Conf. on Earthquake Engrg.*, p. 1491–1496.

Mesri, G., and Vardhanabhuti, B. (2009). Compression of granular materials, *Canadian Geotechnical Journal,* vol. 46, p. 369 – 392.

Olson, S. M. (2001). Liquefaction analysis of level and sloping ground using field case histories and penetration resistance, *Ph.D. Thesis*, University of Illinois at Urbana-Champaign, Urbana, Illinois.

Olson, S. M., and Stark, T. D., (2001). Liquefaction analysis of Lower San Fernando Dam using strength ratios, *Proceedings of the 4th International Conference on Recent Advances in Geotechnical Earthquake Engineering and Soil Dynamics and Symposium in Honor of Professor W. D. Liam Finn*, San Diego, California, March 26-31.

Olson, S. M. (2009). Strength ratio approach for liquefaction analysis of tailings dams, *University of Missouri Conference*.

Papadopoulou A., Kallioglou P., Tika Th., Papadopoulos ST. & Batum E. (2010). Liquefaction resistance of silty sands and dynamic properties of cohesive soils from Dúzce, Turkey, *Journal of Earthquake Engineering*, vol. 14, p. 351-362.

Pitman, T.D., Robertson, P.K., and Sego, D.C. (1994); Influence of fines on the collapse of loose sands. *Canadian Geotechnical Journal*, vol. 31, issue 5, p. 728–739.

Plewes, H. D., Davies, M. P., and Jefferies, M. G., 1992. CPT based screening procedure for evaluating liquefaction susceptibility, *Proceedings of the 45th Canadian Geotechnical Conference*, p. 4.1 to 4.9.

Polito, C. P., and Martin II, J. R. (2001). Effects of non-plastic fines on the liquefaction resistance of sands, *Journal of Geotecn. and Geoenv. Engrg.*, vol. 127, issue 5, p. 408 – 415.

Robertson, P.K., Woeller, D.J., and Addo, K.O. (1992). Standard penetration test energy measurements using a system based on the personal computer. *Canadian Geotechnical Journal*, vol. 29, issue 4, p. 551–557.

Robertson, P.K., Campanella, R.G., Gillespie, D., and Rice, A. (1986). Seismic CPT to measure in situ shear wave velocity. *Journal of Geotechnical Engineering,* ASCE, vol. 112, issue GT8, p. 791–803.

Schmertmann, J. H. (1978). Study of feasibility of using Wissa-type piezometer probe to identify liquefaction potential of saturated sands. *U.S. Army Engineer Waterways Experiment Station,* Report S – 78 - 2.

Seed, H. B., Idriss, I. M., and Arango, I. (1983). Evaluation of liquefaction potential using field performance data, *Journal of Geotechnical Engineering,* ASCE, vol. 109, issue 3, p. 458 – 482.

Seed, R. B., Cetin, K. O., Moss, R. E. S., Kammerer, A. M., Wu, J., Pestana, J. M., Riemer, M. F., Sancio, R. B., Bray, J. D., Kayen, R. E., and Faris, A. (2003). Recent advances in soil liquefaction engineering: A unified and consistent framework, *26th Annual ASCE Los Angeles Geotechnical Spring Seminar,* Keynote Presentation, H.M.S. Queen Mary, Long Beach, California, April 30, 2003.

Seed, R. B., and Harder, L. F., Jr. (1990). SPT-based analysis of cyclic pore pressure generation and undrained residual strength, *Proceedings of the H. B. Seed Memorial Symposium,* Bi-Tech Publishing Ltd., vol. 2, p. 351 – 376.

Shen, C. K., Vrymoed, J. L., and Uyeno, C. K. (1977). The effects of fines on liquefaction of sands, *Proc., 9th Int. Conf. on Soil Mech. And Found. Engrg.*, vol. 2, p. 381–385.

Singh, S. (1994). Liquefaction characteristics of silts, *Ground Failures Under Seismic Conditions, Conf. Proc. ASCE National Convention, Geotechnical Special Publication,* vol. 44, S. Prakash and P. Dakoulas eds., ASCE, Reston, Va., p. 105 – 116.

Sladen, J.A., D'Hollander, R.D., Krahn, J., and Mitchell, D.E. (1985). Back analysis of the Nerlerk Berm liquefaction slides. *Canadian Geotechnical Journal,* vol. 22, issue 4, p. 579–588.

Sladen, J. A. and Hewitt, K. J. (1989). Influence of placement method on the in-situ density of hydraulic sand fill, *Canadian Geotechnical Journal,* vol. 26, p. 453 – 466.

Tatsuoka, F., Iwasaki, T., Tokida, K., Yasuda, S., Hirose, M., Imai, T., and Kon-no, M. (1980). Standard penetration tests and soil liquefaction potential evaluation, *Soils and Foundations,* vol. 20, issue 4, p. 95 – 111.

Terzaghi, K., Peck, R. B., and Mesri, G. (1996). Soil mechanics in engineering practice, *John Wiley & Sons, Inc.,* 3rd ed., 549p.

Thevanayagam, S., Ravishankar, K., and Mohan, S. (1996). Steady state strength, relative density and fines content relationship for sands, *TRB 1547,* p. 61 – 67.

Thevanayagam S, Jia W. Liquefaction remediation in silty soils. In: Bruneau M, Inman DJ, editors. Proceedings of the MEDAT-2 Workshop, MCEER, University at Buffalo, SUNY, NY; 2000.p. 23–8.

Tokimatsu, K., and Yoshimi, Y. (1983). Empirical correlation of soil liquefaction based on SPT N – value and fines content, *Soils and Foundations,* vol. 23, issue 4, p. 56 – 74.

Tsuchida, H. (1970). Prediction and countermeans against the liquefaction in sand deposits, *Abstract of the Seminar in the Port and Harbor Research Institute,* Yokohama, Japan, p. 3.1 – 3.33.

Troncoso, J. H., and Verdugo, R. (1985). Silt content and dynamic behavior of tailing sands, *Proc., 12th Int. Conf. on Soil Mech. And Found. Engrg.,* p. 1311–1314.

Vaid, V. P. (1994). Liquefaction of silty soils, *Ground failures under seismic conditions, Geotech. Spec. Publ. No. 44*, ASCE, New York, p. 1– 16.

Villet, W. C. B., and Mitchell, J. K. (1981). Cone resistance, relative density and friction angle. *Symposium on Cone Penetration Testing and Experience, Geotechnical Engineering Division,* ASCE, Oct. 1981, p. 178 – 208.

Wagener, F., Strydom, K., Craig, H., and Blight, G. (1997). The tailings dam flow failure at Merriespruit, South Africa: Causes and consequences, *Tailings and Mine Waste Conference 1997,* Belkem, Rotterdam.

Wagener, F., Craig, H., and Blight, G., McPhail, G., Williams, A.A.B., and Strydom, J.H. (1998). The Merriespruit dam failure – A review, *Tailings and Mine Waste Conference 1998,* Belkem, Rotterdam.

Wong, R. T., Seed, H. B., and Chan, C. K., (1975). Liquefaction of gravelly soil under cyclic loading conditions, *Journal of the Geotechnical Engineering Division,* ASCE, Vol. 101 No. GT6, p. 571-583.

Wong, W. (1984). Earthquake damages to earth dams and levees in relation to soil liquefaction and weakness in soft clays, *Proceedings of the International Conference on Case Histories in Geotechnical Engineering,* Vol. 1, p. 511-521.

Xenaki V.C. and Athanasopoulos G. A., (2003). Liquefaction resistance of sand mixtures an experimental investigation of the effect of fines, *Soil Dynamics and Earthquake Engineering,* vol.23, pp.183-194.

Yamamuro, J. A., and Lade, P. V. (1997). Static liquefaction of very loose sands, *Can. Geotech. J.*, Ottawa, vol. 34, p. 905–917.

Yegian, M. K., Gharaman, V. G., and Harutiunyan, R. N. (1994). Liquefaction and embankment failure case histories, 1988 Armenia earthquake, *Journal of Geotechnical Engineering,* ASCE, Vol. 120, No. 3, p. 581-596.

Youd, T. L., and Hoose, S. N. (1977). Liquefaction susceptibility and geologic setting, *Proceedings of the 6th World Conference on Earthquake Engineering, New Delhi,* Vol. 3, p. 2189 – 2194.

Youd, T. L., (1984). Recurrence of liquefaction at the same site, *Proceedings of the 8th World Conference on Earthquake Engineering,* Vol. 3, p. 231 – 238.

Youd, T. L., Harp, E. L., Keefer, D. K., and Wilson, R. C. (1985). The Borah Peak, Idaho earthquake of October 28, 1983 – Liquefaction, *Earthquake Spectra,* Vol. 2, No. 1, p. 71-89.

Zlatovic, S., and Ishihara, K. (1995). On the influence of non-plastic fines on residual strength, *Proc. IS-TOKOYO'95, 1st International Conf. Earthquake Geotechnical Engrg.,* Tokoyo, eds. K. Ishihara, publs. A. A. Balkema, p. 239 – 244.

Zlatovic, S., and Ishihara, K. (1997). ''Normalized behavior of very loose nonplastic soil: Effects of fabric.'' *Soils and Found.*, Tokyo, vo. 37, issue 4, p. 47– 56.

4.9 Figures and Tables

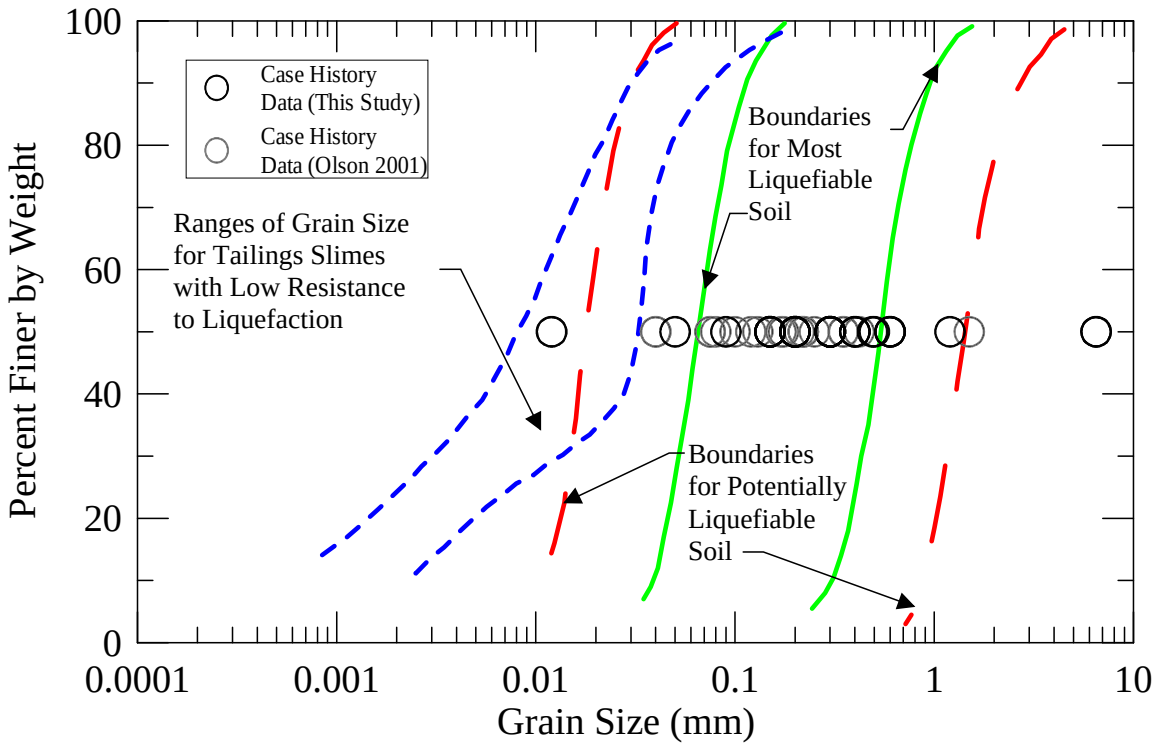

Figure 4.1 Gradation curves defining limits of liquefiable and non-liquefiable soils with case history data from this study and Olson 2001 (from Tsuchida 1970 and Ishihara 1985)

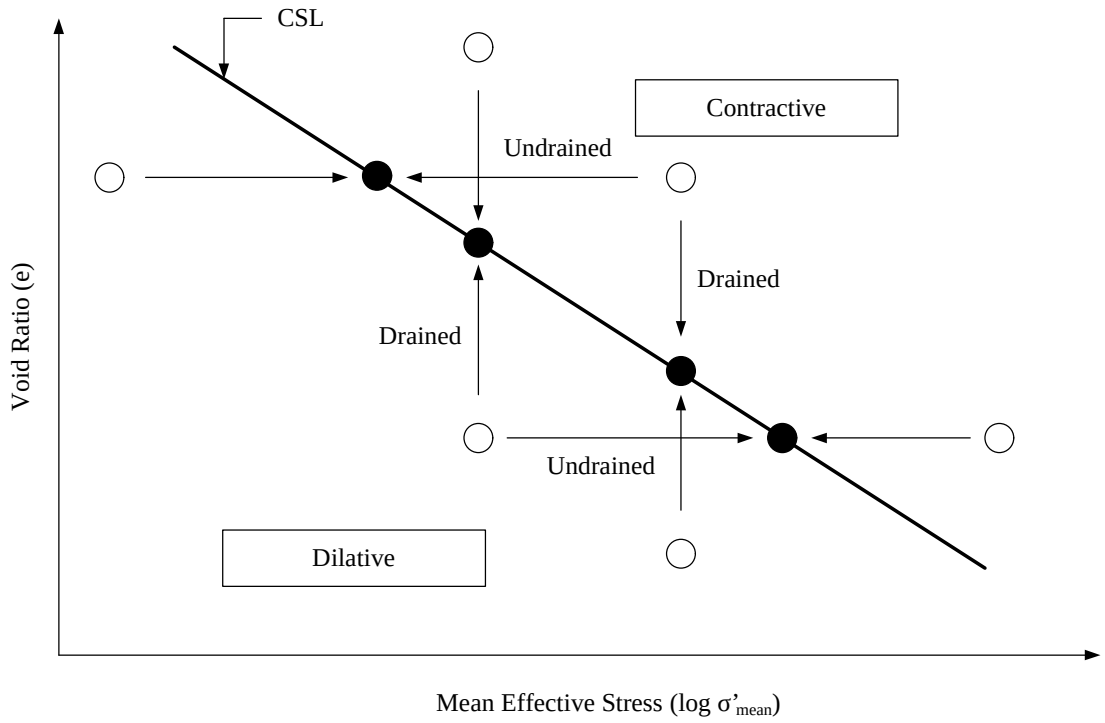

Figure 4.2 Schematic diagram showing the behavior of initially loose and dense specimens under drained and undrained conditions. CSL = critical state line

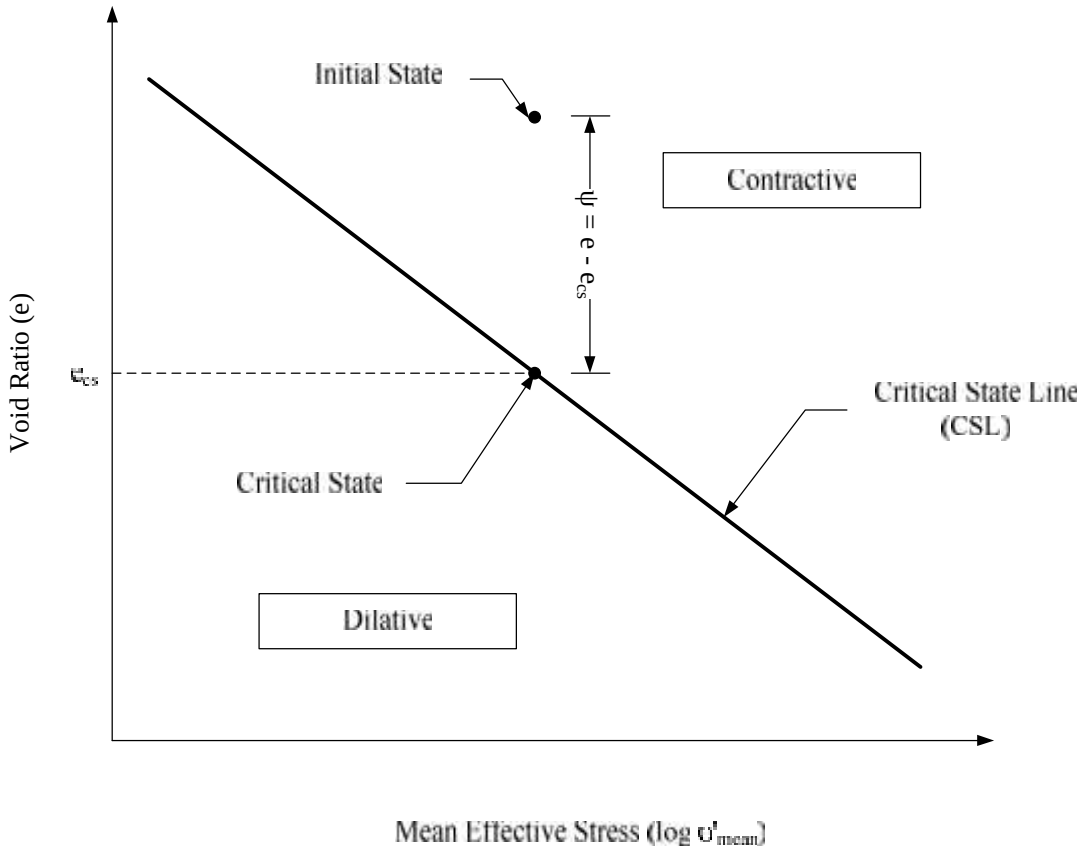

Figure 4.3 Schematic diagram illustrating the definition of state parameter

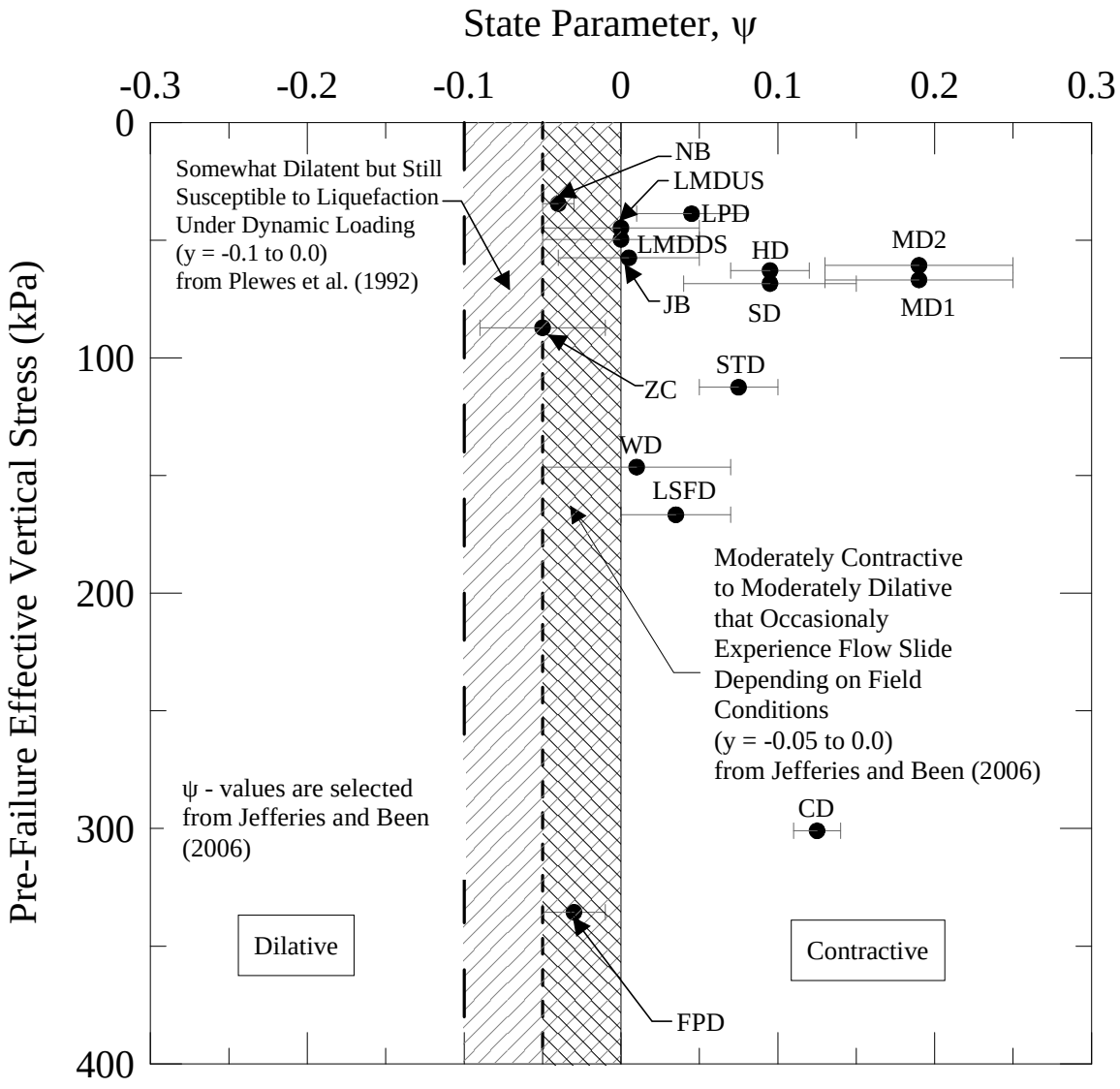

Figure 4.4 State parameter approach with selected analyzed case histories adopted from Plewes et al. 1992, while ψ – values are selected from Jefferies and Been (2006). Abbreviations used are: ZC = Zeeland Coast; WD = Wachusett Dam; CD = Calaveras Dam; SD = Sheffield Dam; FPD = Fort Peck Dam; HD = Hokkaido Dam; LSFD = Lower San Fernando Dam; MD1 = Mochikoshi Dam No. 1; MD2 = Mochikoshi Dam No. 2; NB = Nerlerk Berm; LMDUS = La Marquesa Up-Stream; LMDDS = La Marquesa Down-Stream; LPD = La Palma Dam; STD = Sullivan Tailings Dam; JB = Jamuna Bridge River Embankment

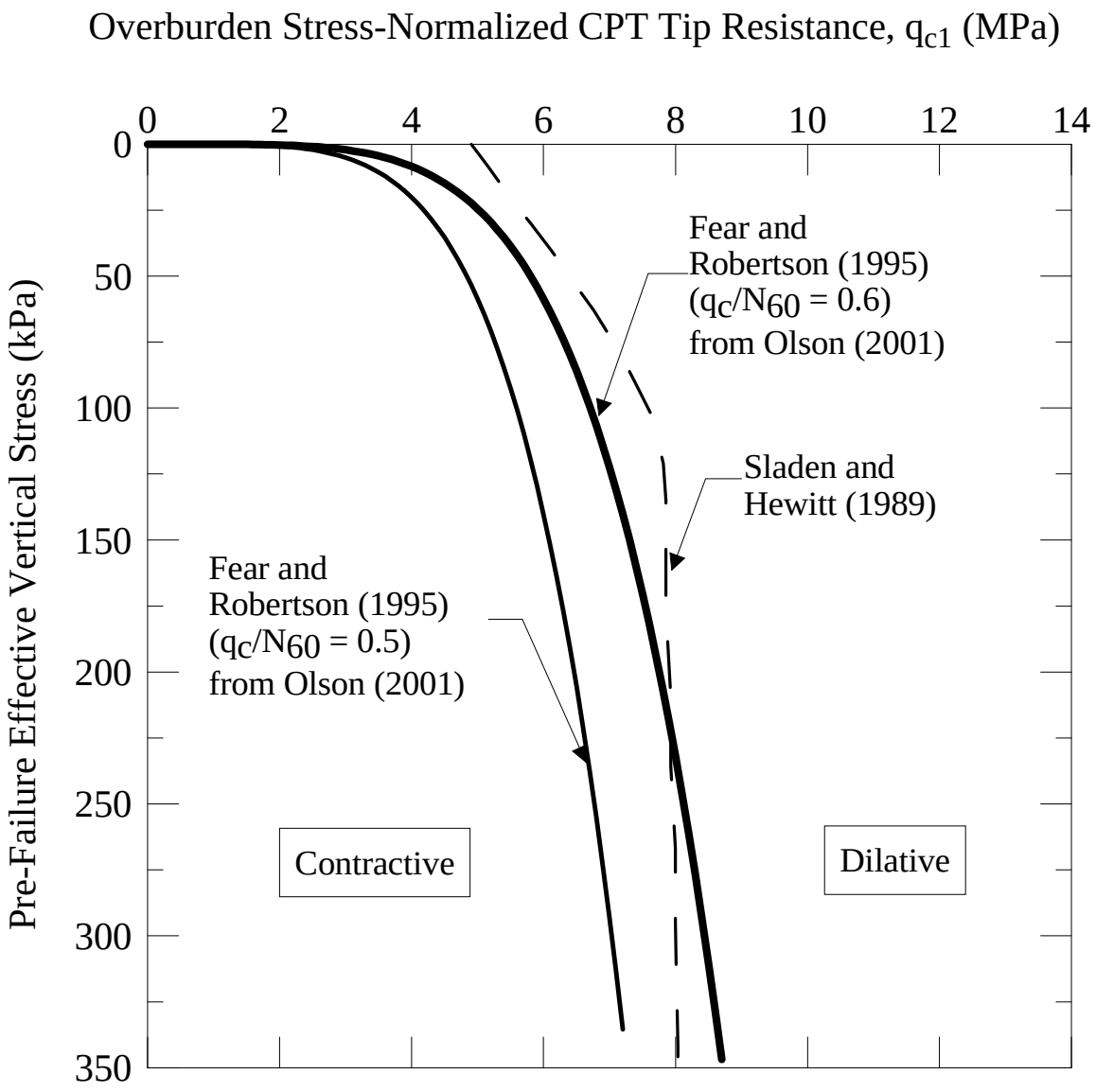

Figure 4.5 CPT-based susceptibility relationship proposed by Sladen and Hewitt (1989), and SPT-based relationship proposed by Fear and Robertson (1995) converted to CPT by Olson (2001)

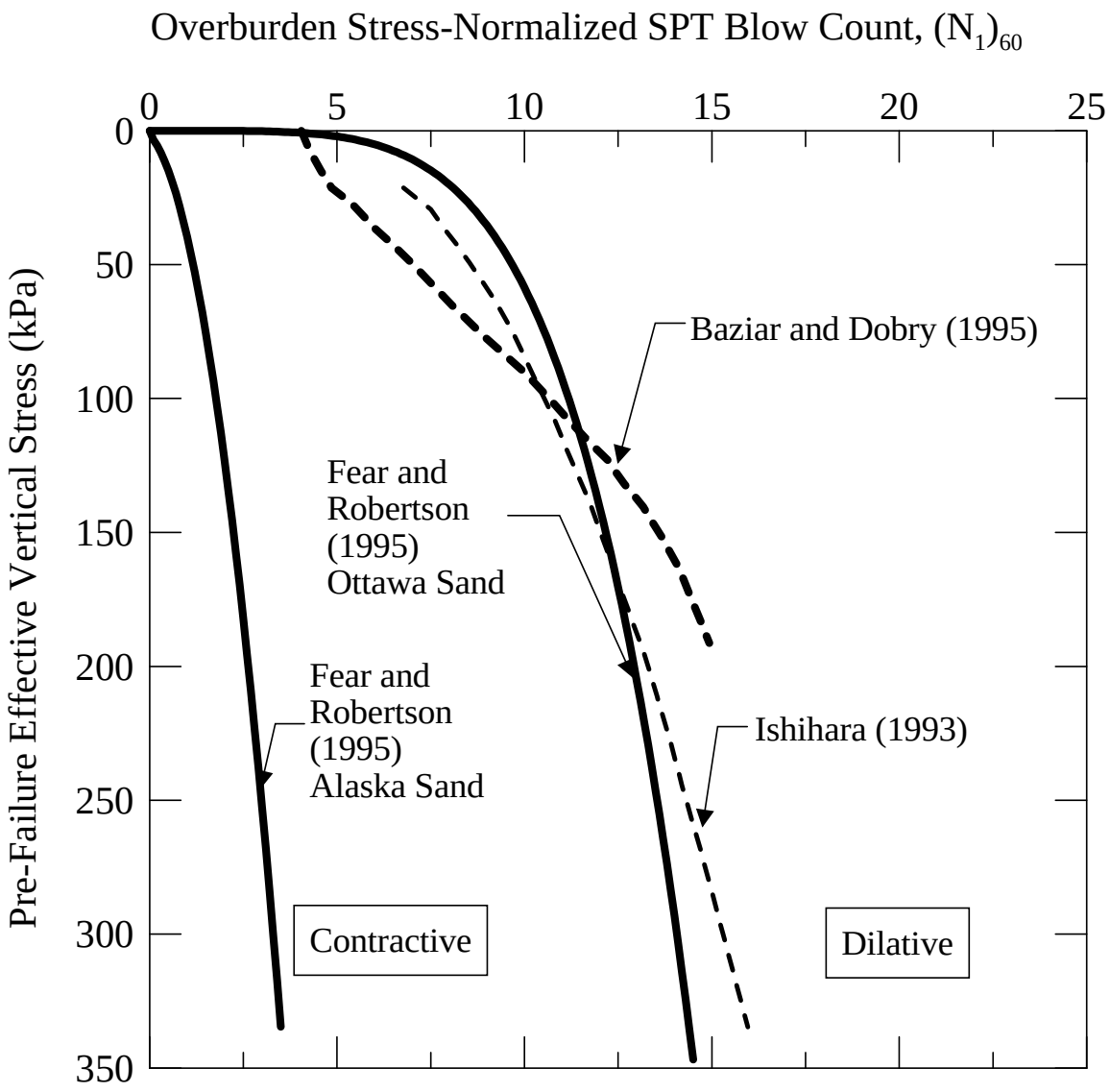

Figure 4.6 SPT-based susceptibility relationships proposed by Ishihara (1993), Baziar and Dobry (1995), and Fear and Robertson (1995)

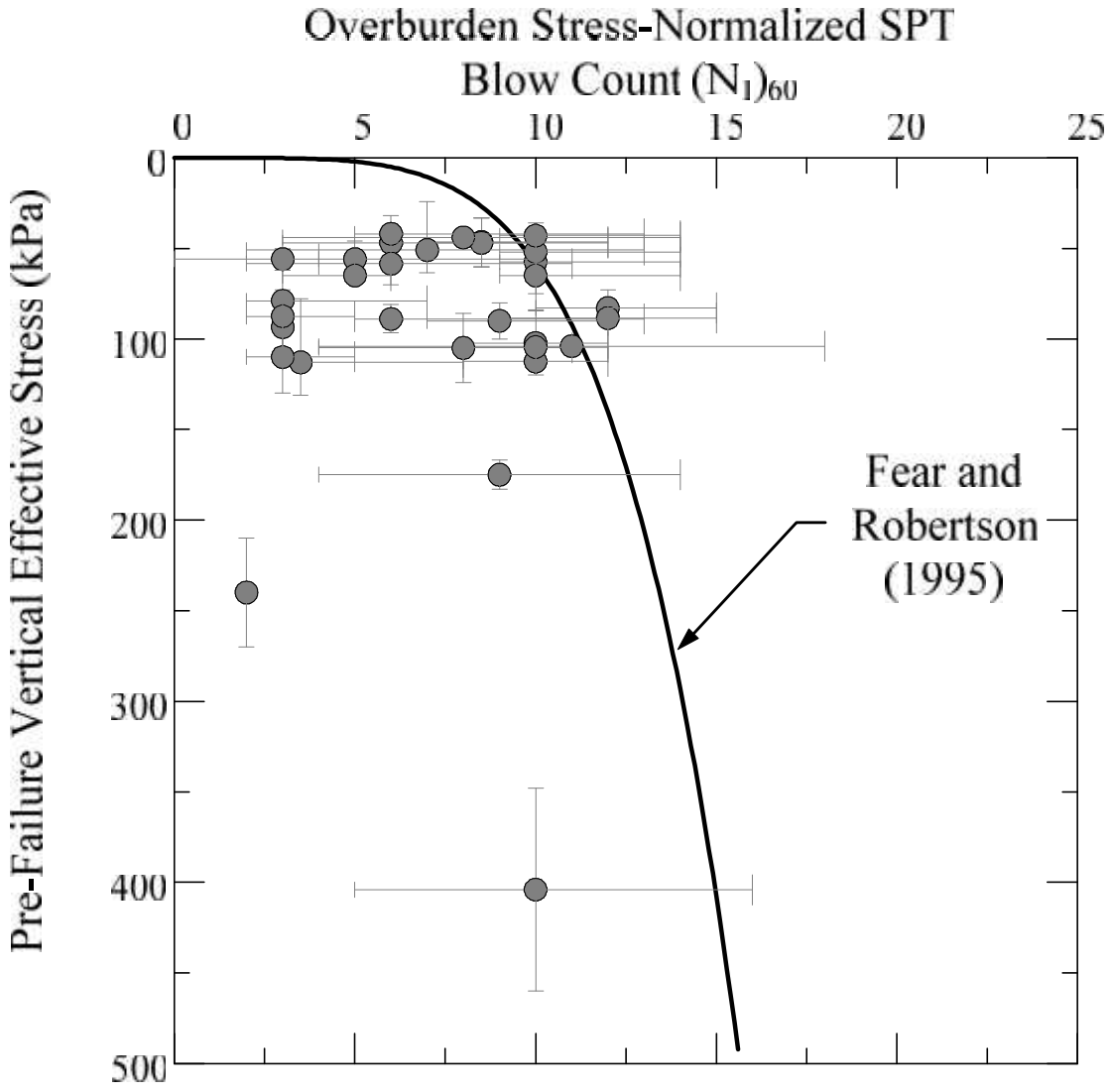

Figure 4. 7 SPT-based liquefaction susceptibility relationship separating contractive from dilative conditions using flow failure case histories analyzed in this study

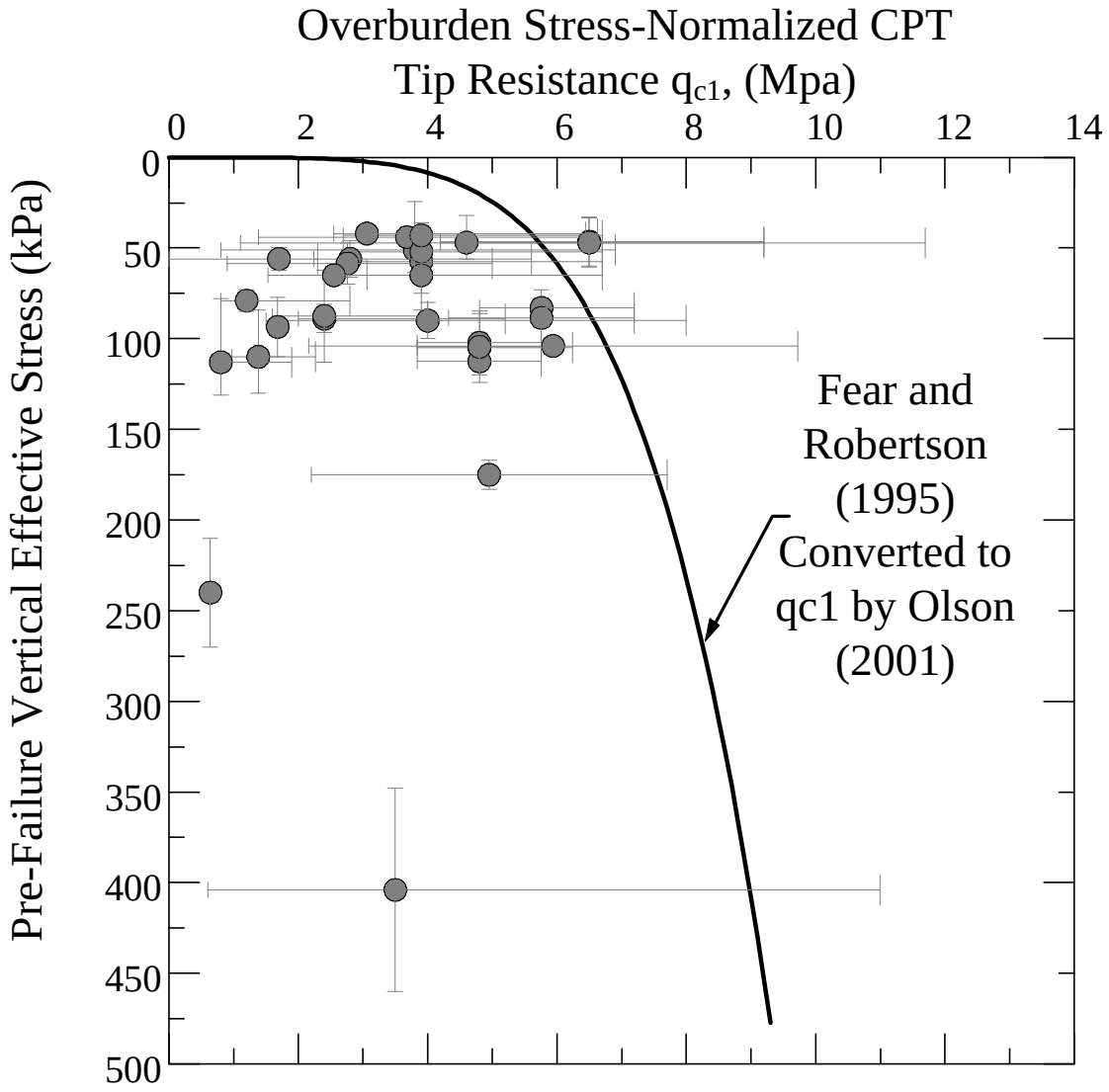

Figure 4.8 CPT-based liquefaction susceptibility relationship separating contractive from dilative conditions using flow failure case histories analyzed in this study

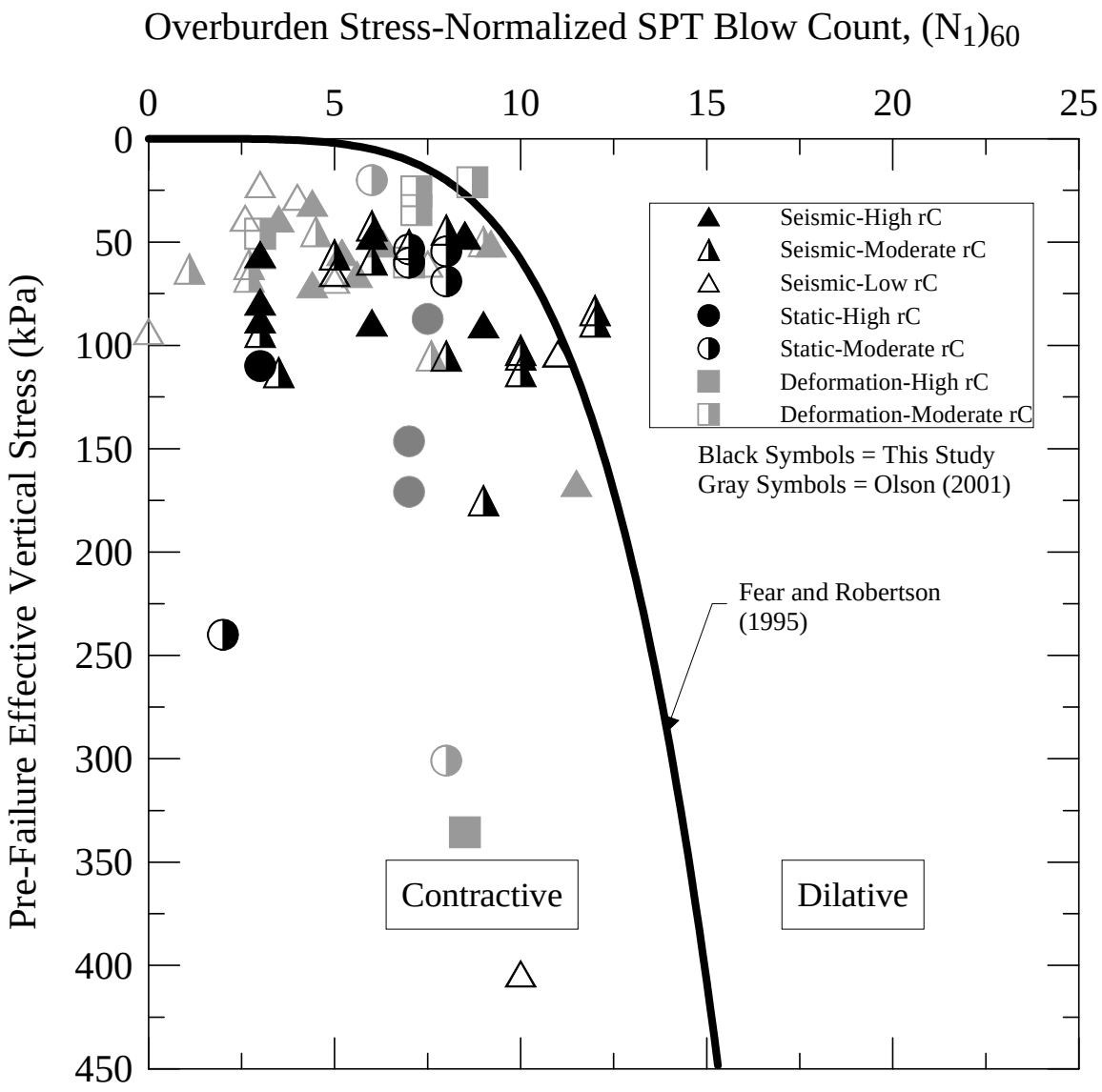

Figure 4.9 Case histories analyzed in this study and in Olson (2001) plotted on Fear and Robertson (1995) susceptibility relationship for corrected SPT blow count

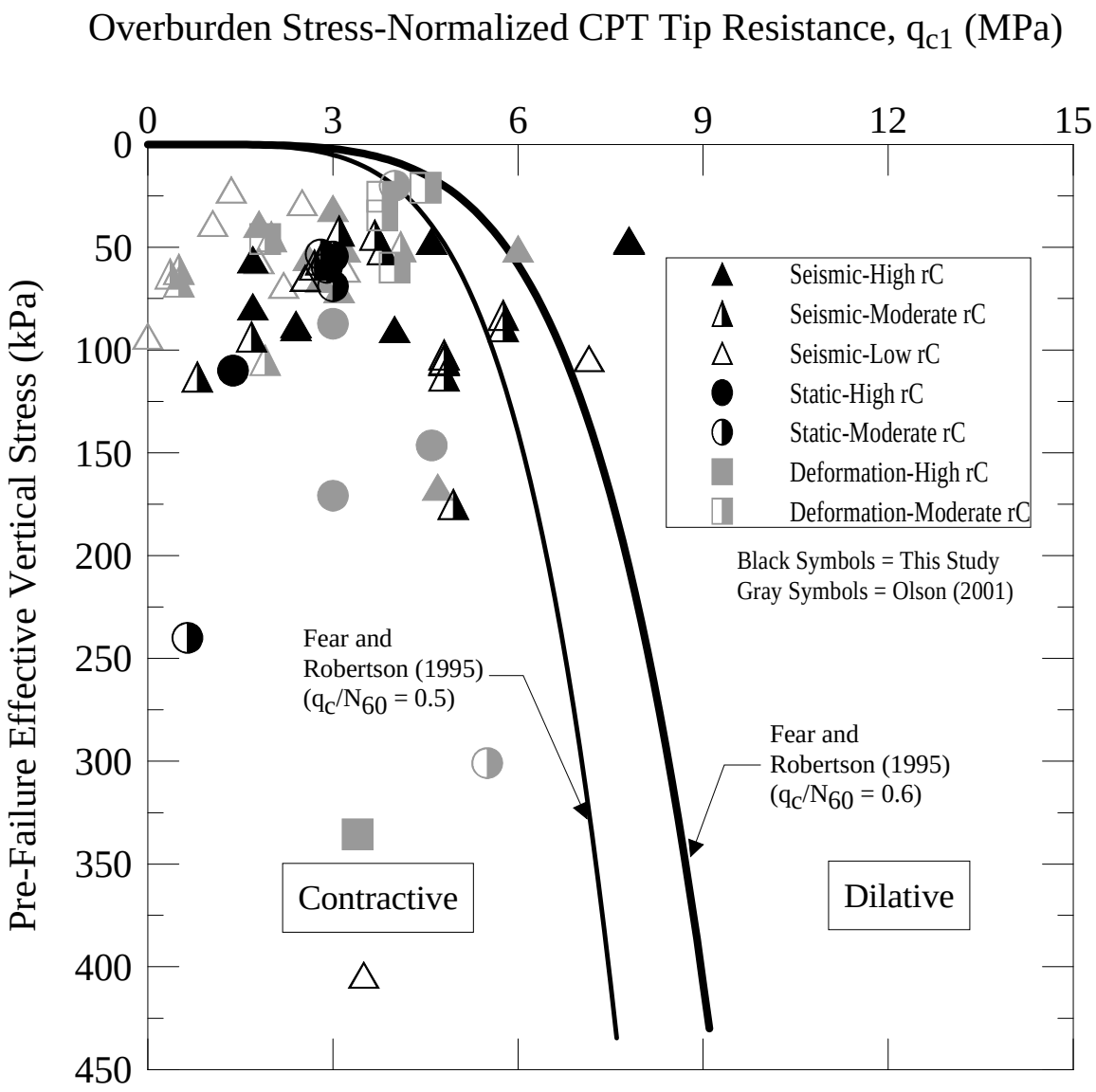

Figure 4.10 Case histories analyzed in this study and in Olson (2001) plotted on Fear and Robertson (1995) susceptibility relationship for corrected CPT tip resistance

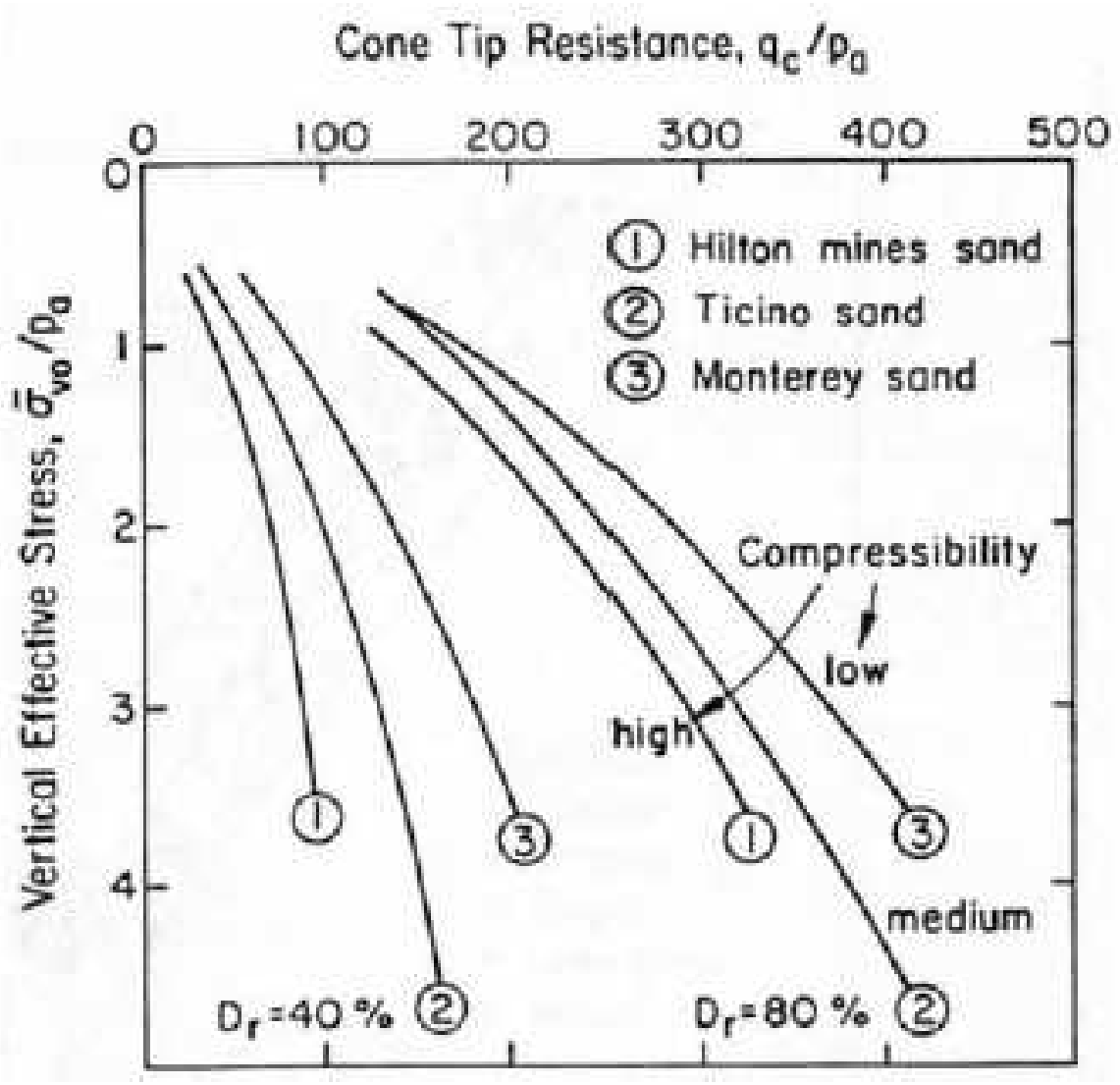

Figure 4.11 Relationship among penetration resistance, effective vertical stress, and relative density for sands of different compressibility (from Robertson and Campanella 1983)

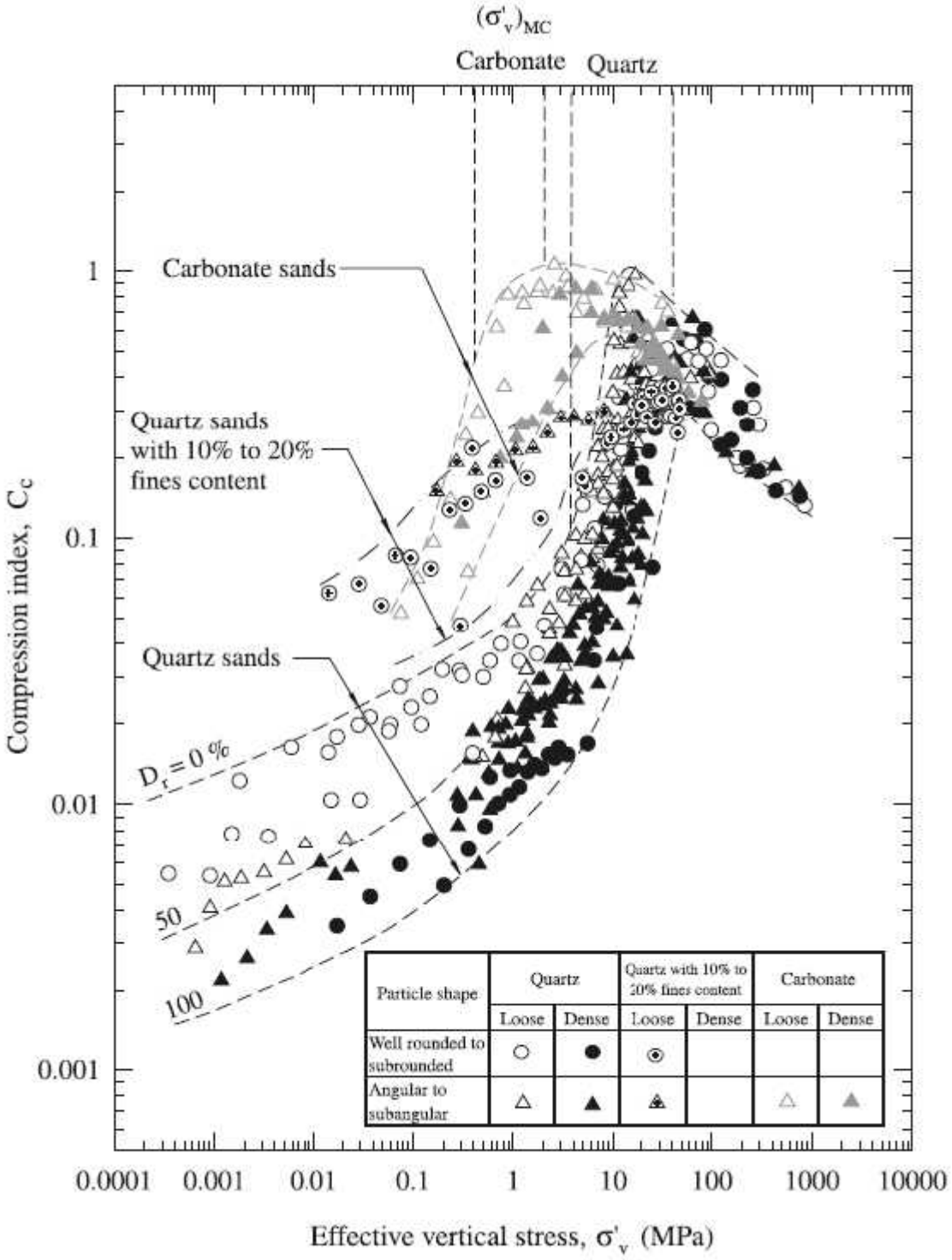

Figure 4.12 Data on soil compressibility for loose (D_r < 50%) and dense (D_r > 50%) quartz sands with particle shapes ranging from rounded to angular, loose quartz sands with 10 to 20% fines contents and particle shapes ranging from rounded to angular, and loose and dense carbonate sands with subangular to angular particles (from Mesri and Verdhanabhuti 2009)

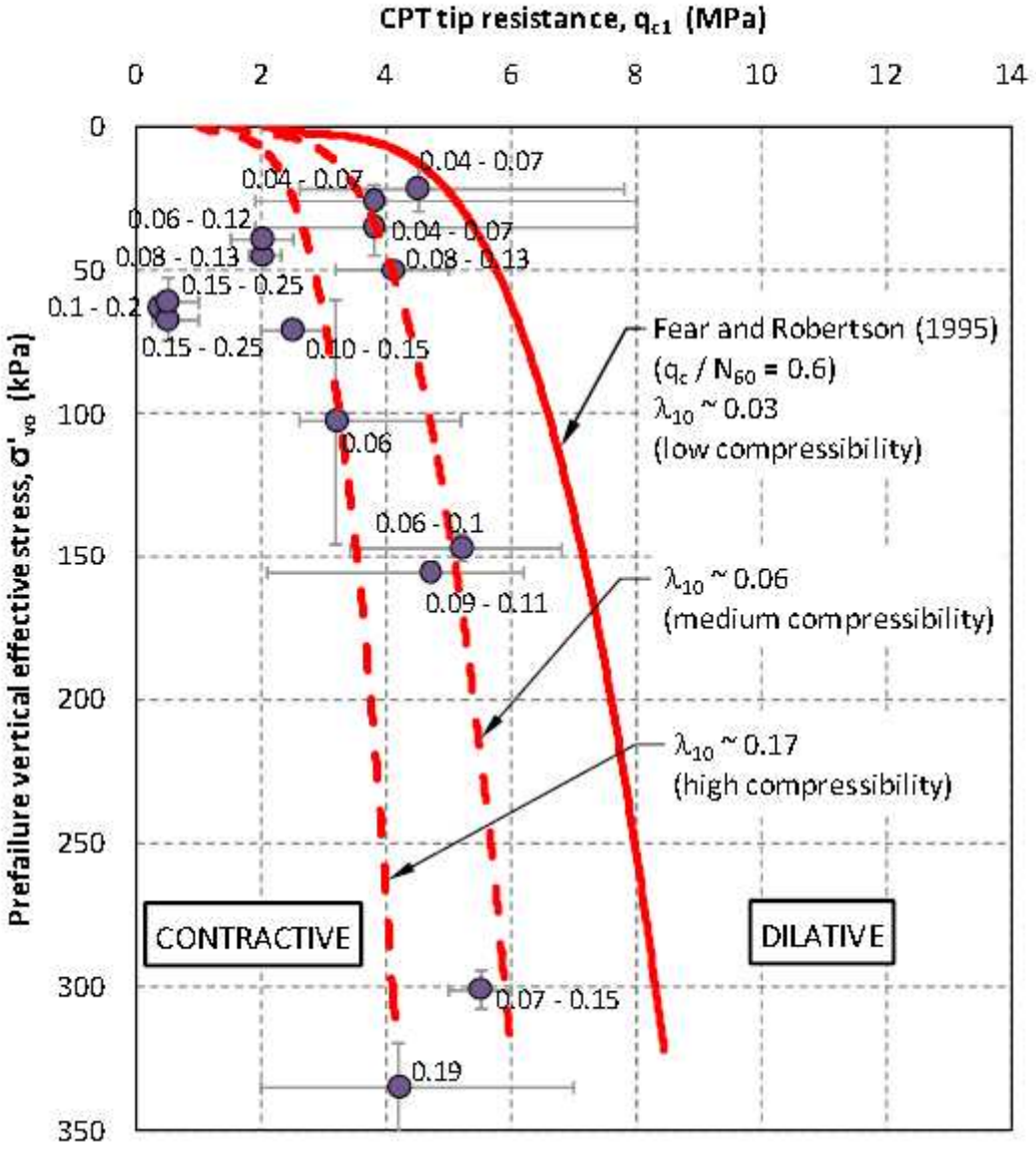

Figure 4.13 Liquefaction susceptibility boundary incorporating the effect of compressibility on penetration resistance. Included in the figure are select flow failure case histories back-analyzed by Olson (2009) for which Jefferies and Been (2006) estimated values of CSL slope, $^{a}{}_{10}$. The ranges for the data indicate the range of CPT tip resistance and pre-failure effective vertical stress for the case histories (from Olson 2009)

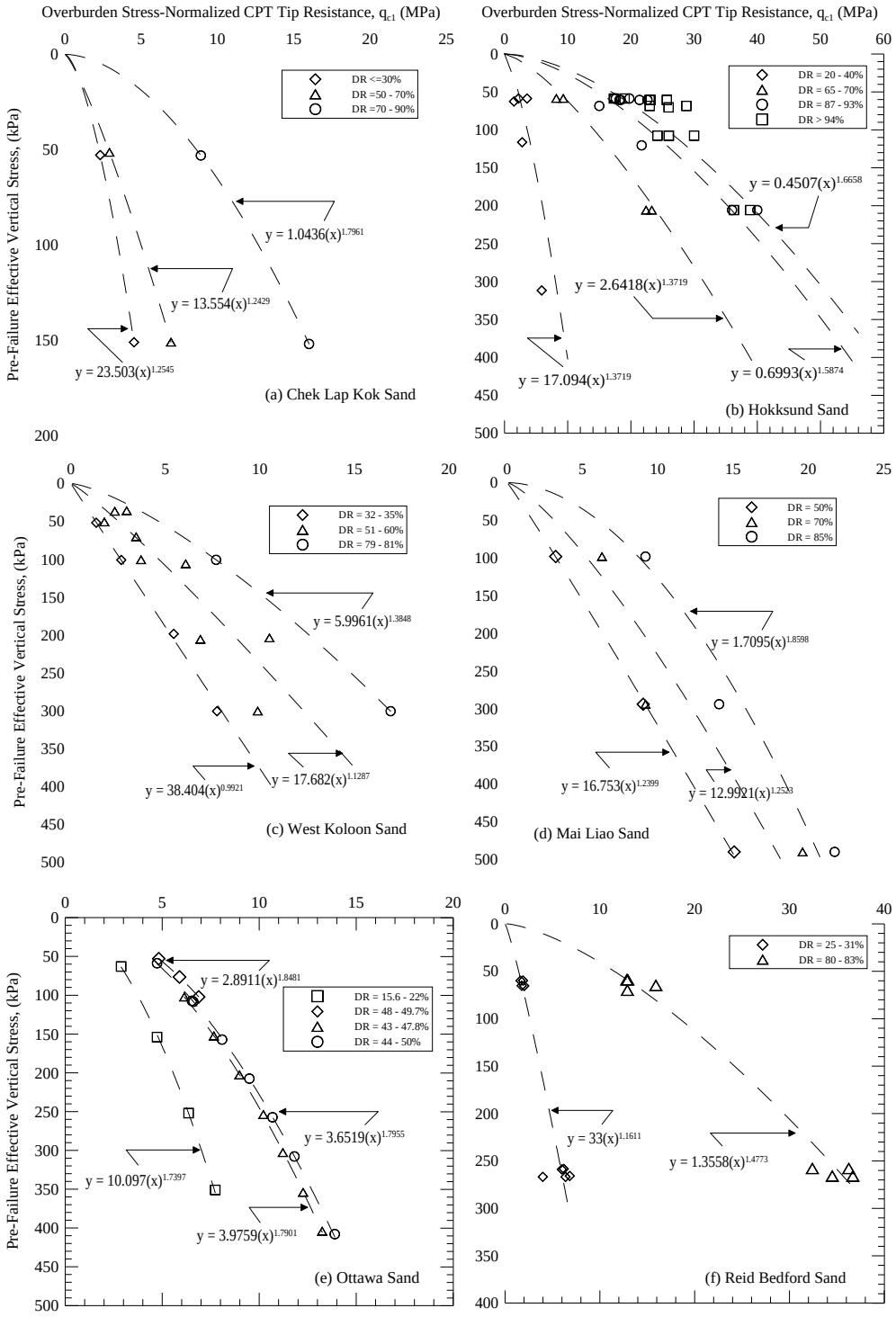

Figure 4.14 Calibration chamber test results for sands data collected in this study with various D_r values. Trend lines for various D_r values used to evaluate constants C and n in Eq. 4.4. (a) Chep Lap Kok sand; (b) Hokksund sand; (c) West Kowloon sand; (d) Mai Liao sand; (e) Ottawa sand; (f) Reid Bedford sand

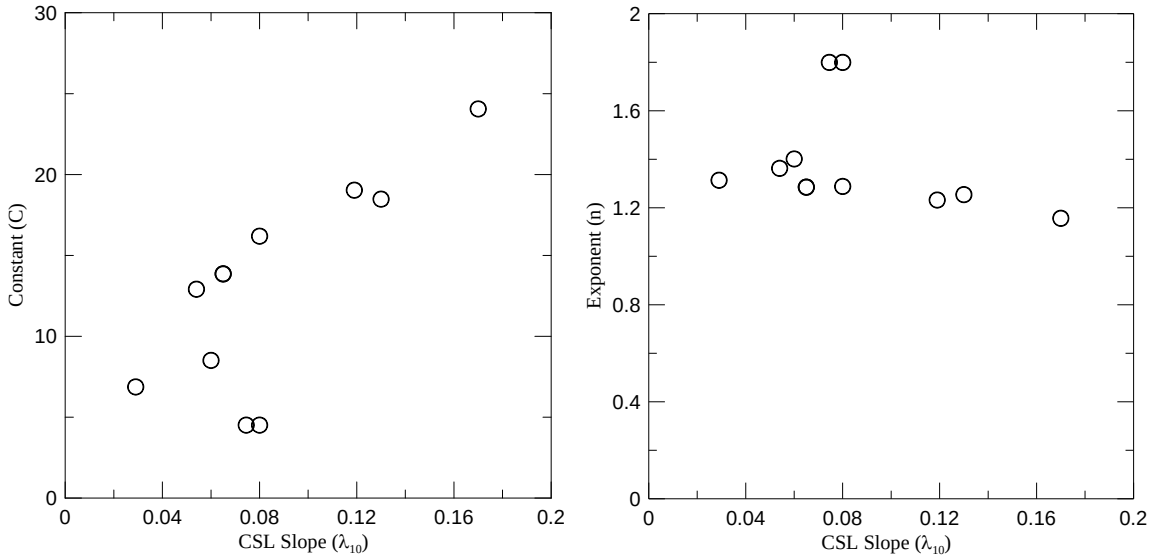

Figure 4.15 Catalog of interpreted and interpolated C and n values for D_r ~ 40% for the calibration chamber test sands with respect to slope of the CSL, $^{a}_{10}$

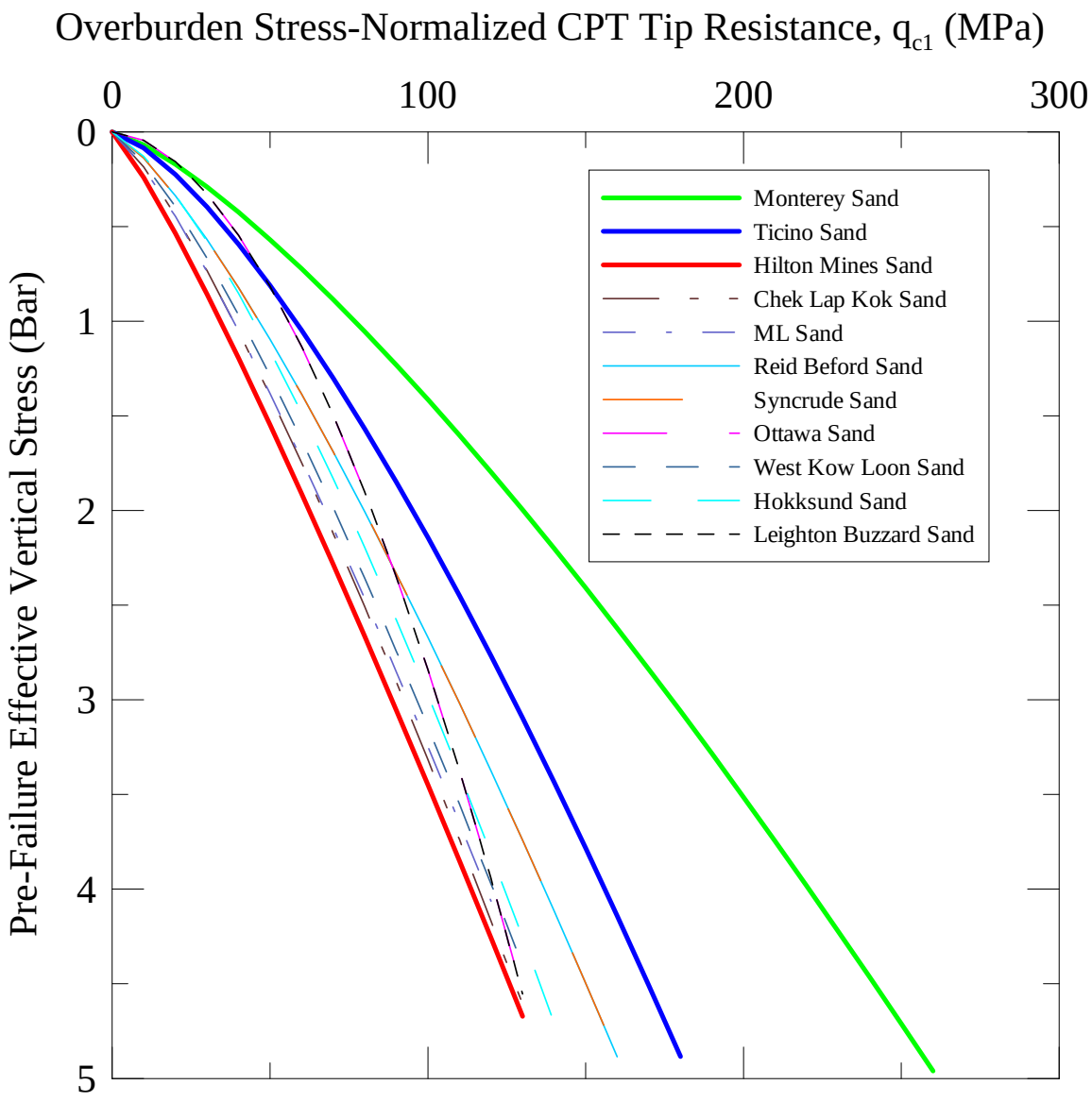

Figure 4.16 Relationships between q_c and $\pm'_v$ for D_r = 40% using C and n values interpreted and interpolated from calibration chamber test sands

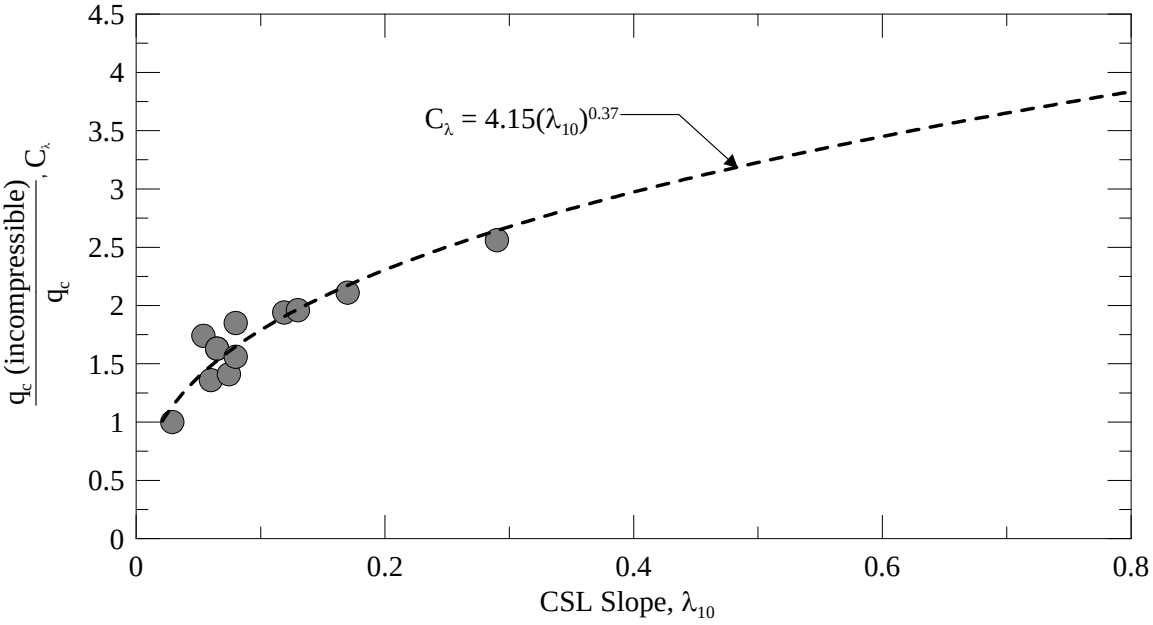

Figure 4.17 Updated compressibility correction factor relationship for cone penetration resistance

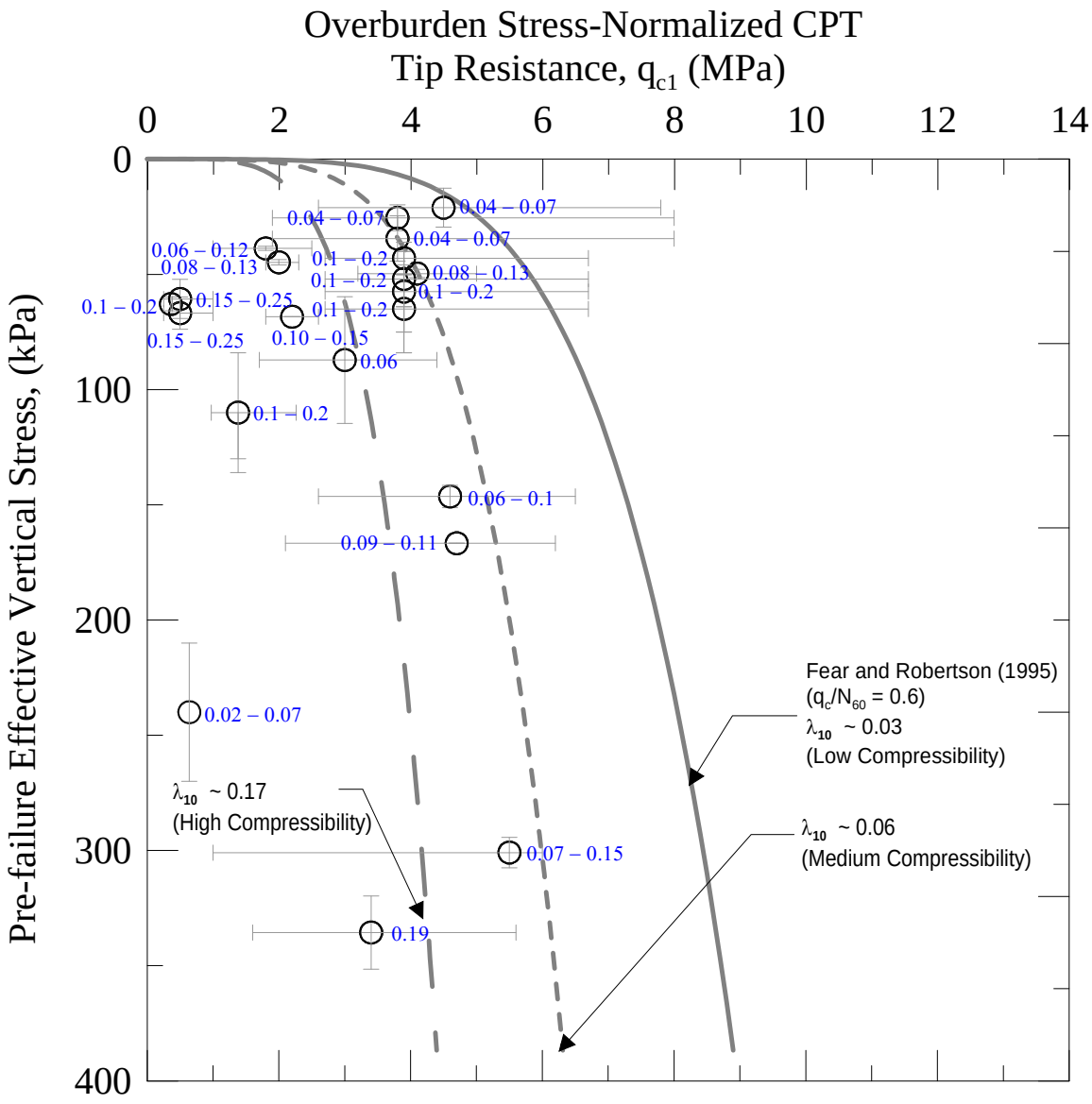

Figure 4. 18 Liquefaction susceptibility curves based on soil compressibility with selected analyzed case histories (from Olson 2009)

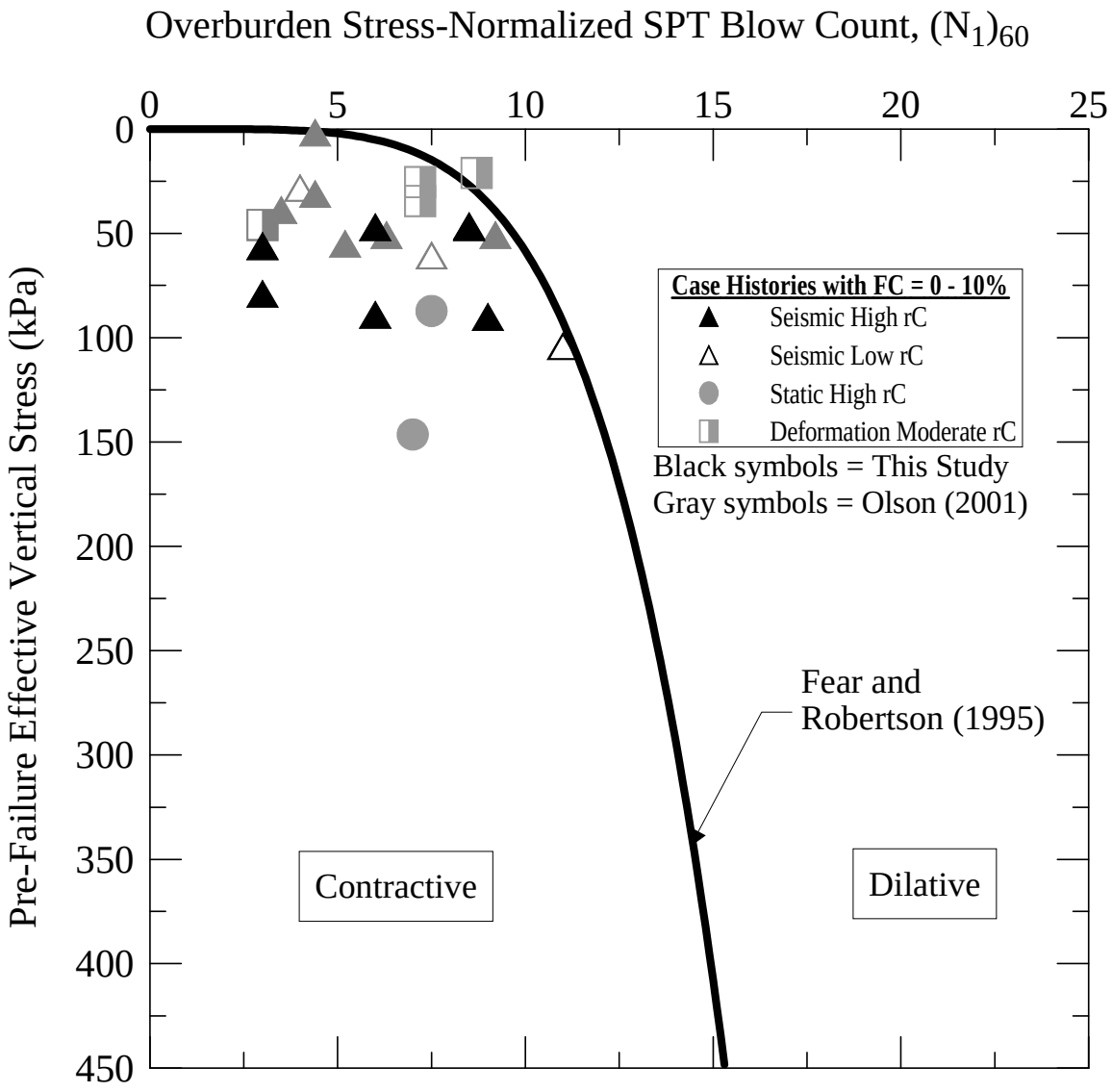

Figure 4.19 Flow failure case histories with FC = 0 to 10% analyzed in this study and by Olson (2001) compared to SPT-based liquefaction susceptibility boundary for Ottawa sand derived by Fear and Robertson (1995) and adopted by Olson (2001) for case history analysis

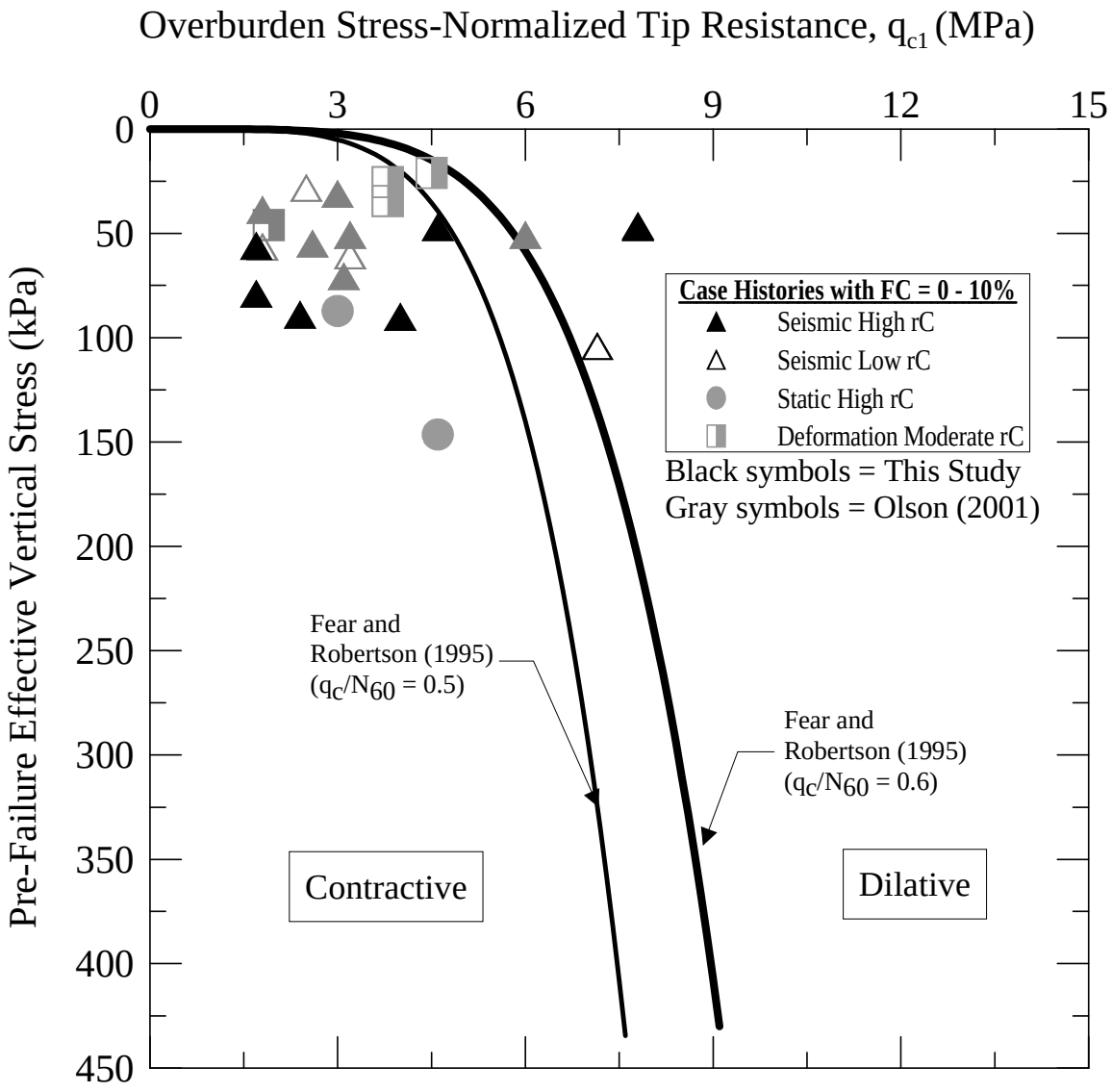

Figure 4.20 Flow failure case histories with FC = 0 to 10% analyzed in this study and by Olson (2001) compared to CPT-based liquefaction susceptibility boundary for Ottawa sand derived by Fear and Robertson (1995) and adopted by Olson (2001) for case history analysis

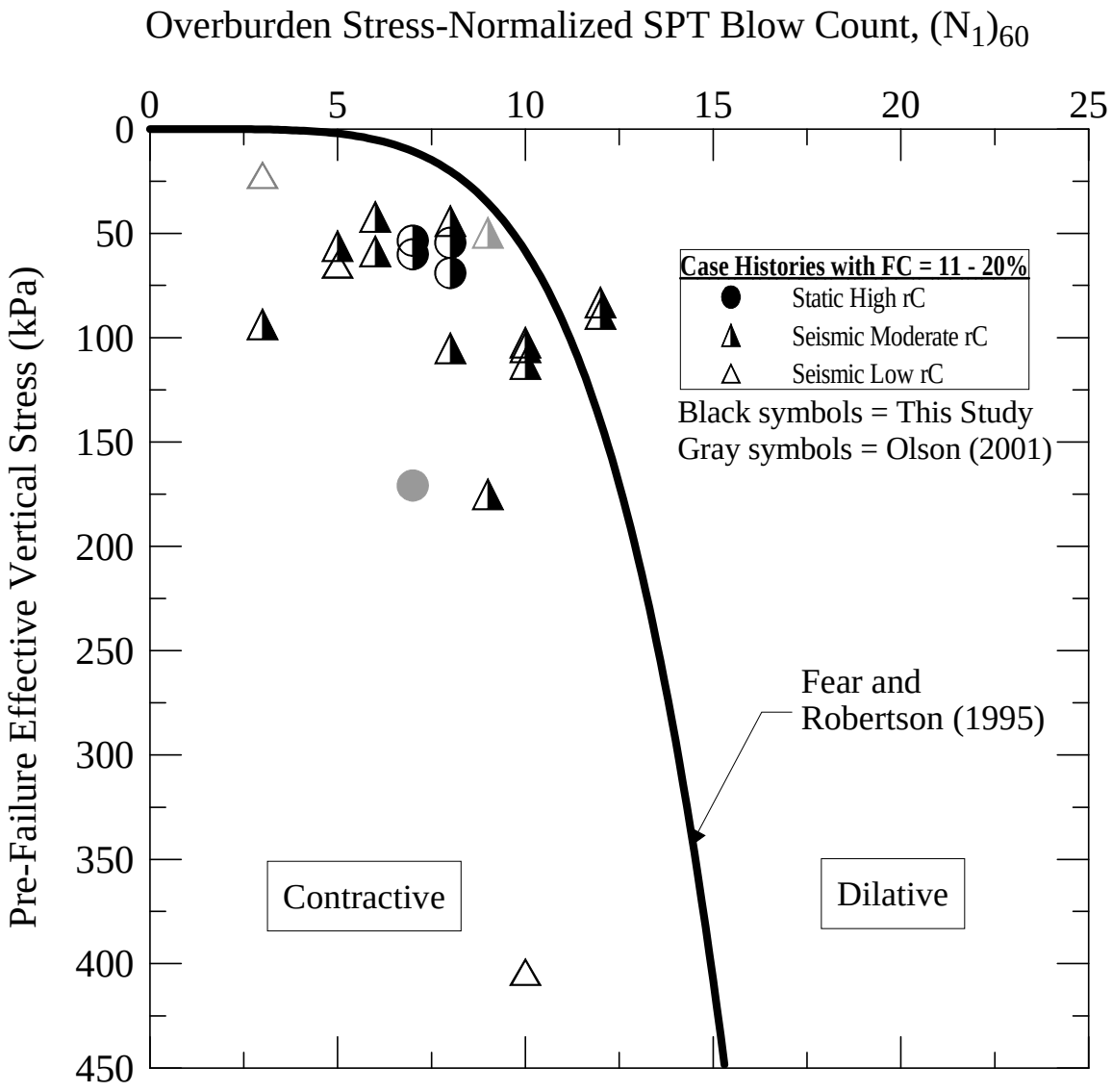

Figure 4.21 Flow failure case histories with FC = 11 to 20% analyzed in this study and by Olson (2001) compared to SPT-based liquefaction susceptibility boundary for Ottawa sand derived by Fear and Robertson (1995) and adopted by Olson (2001) for case history analysis

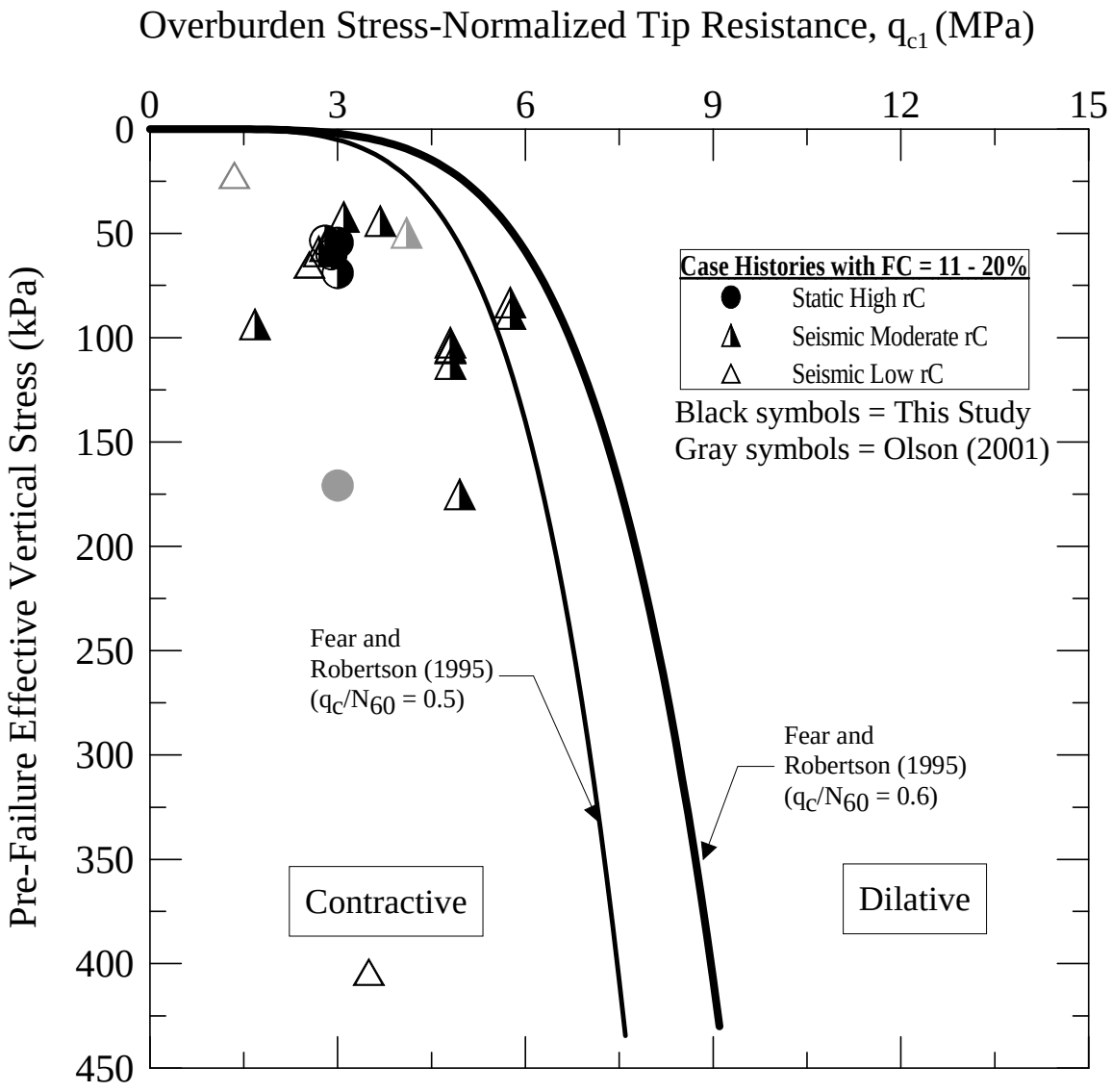

Figure 4.22 Flow failure case histories with FC = 11 to 20% analyzed in this study and by Olson (2001) compared to CPT-based liquefaction susceptibility boundary for Ottawa sand derived by Fear and Robertson (1995) and adopted by Olson (2001) for case history analysis

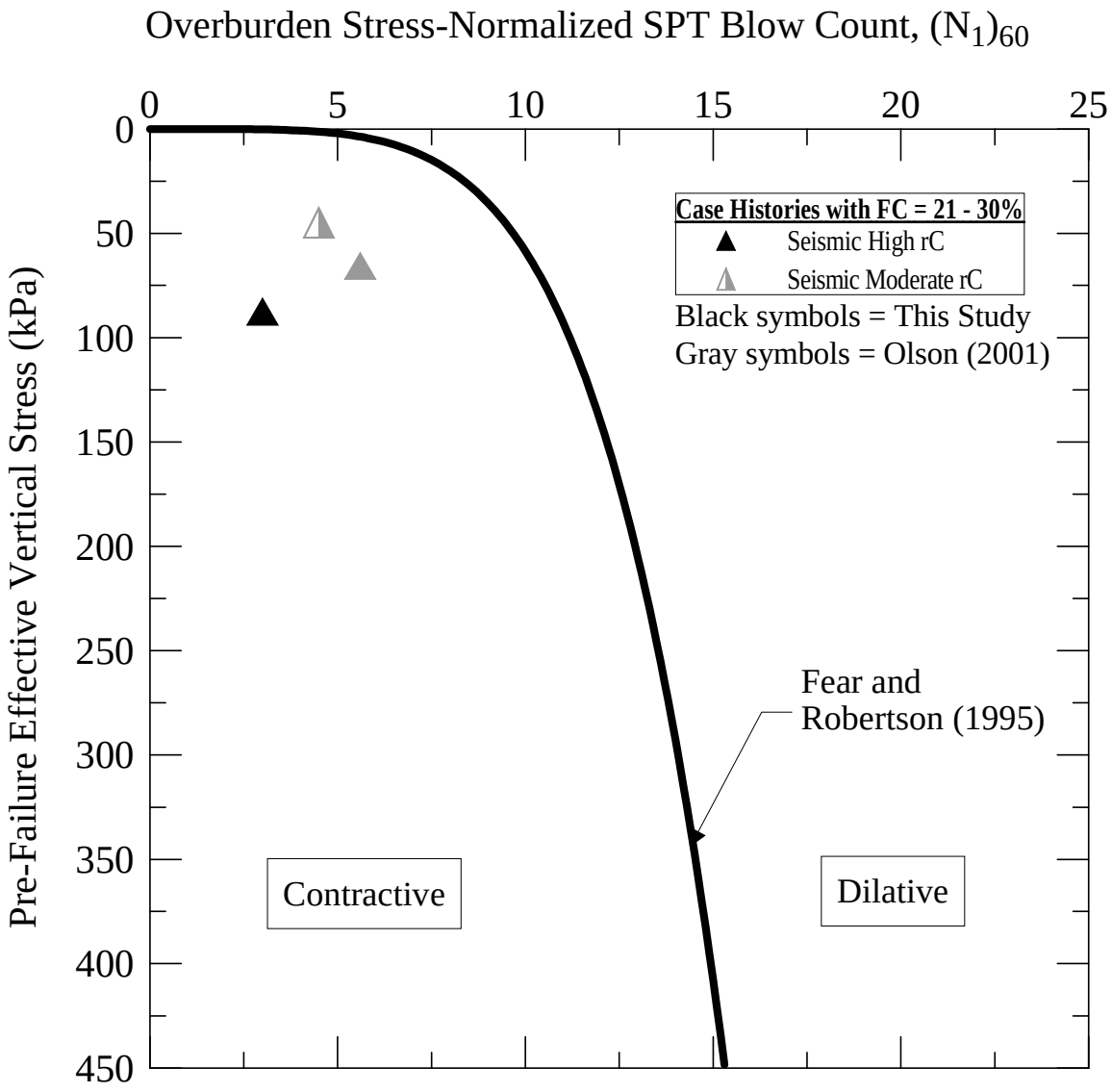

Figure 4.23 Flow failure case histories with FC = 21 to 30% analyzed in this study and by Olson (2001) compared to SPT-based liquefaction susceptibility boundary for Ottawa sand derived by Fear and Robertson (1995) and adopted by Olson (2001) for case history analysis

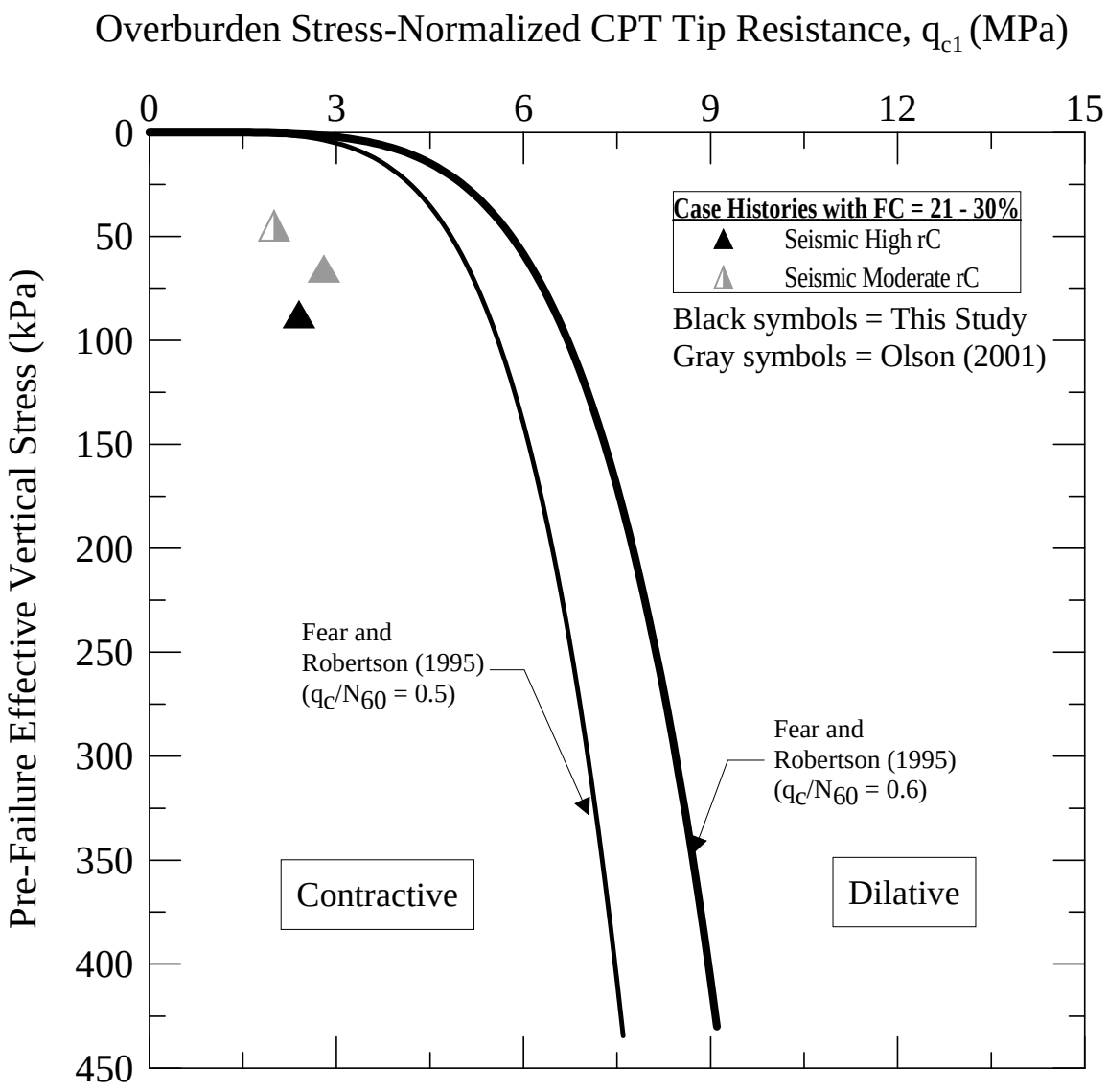

Figure 4.24 Flow failure case histories with FC = 21 to 30% analyzed in this study and by Olson (2001) compared to CPT-based liquefaction susceptibility boundary for Ottawa sand derived by Fear and Robertson (1995) and adopted by Olson (2001) for case history analysis

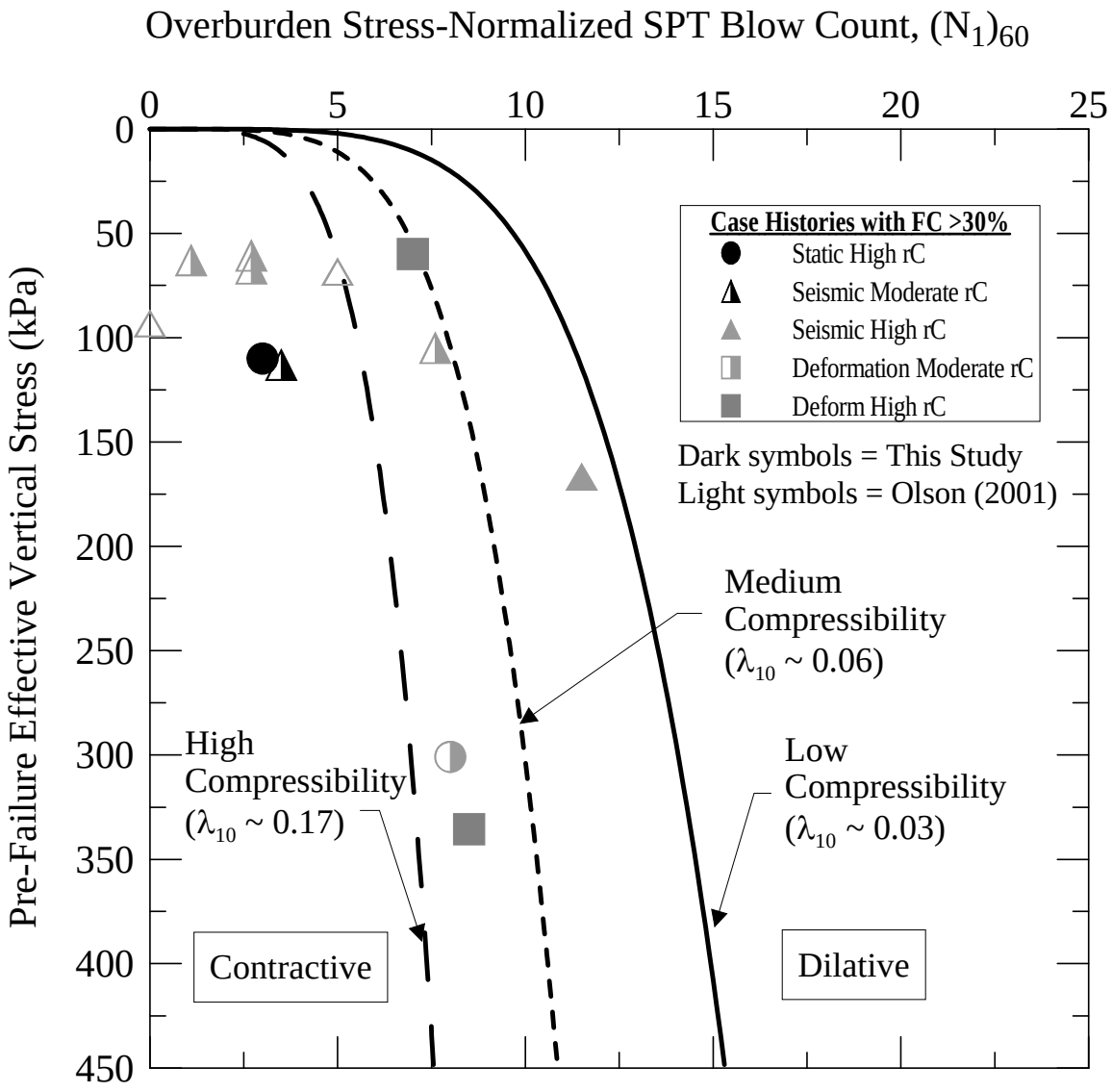

Figure 4.25 Flow failure case histories with FC > 30% analyzed in this study and by Olson (2001) compared to SPT-based liquefaction susceptibility boundary for Ottawa sand derived by Fear and Robertson (1995) and adopted by Olson (2001) for case history analysis

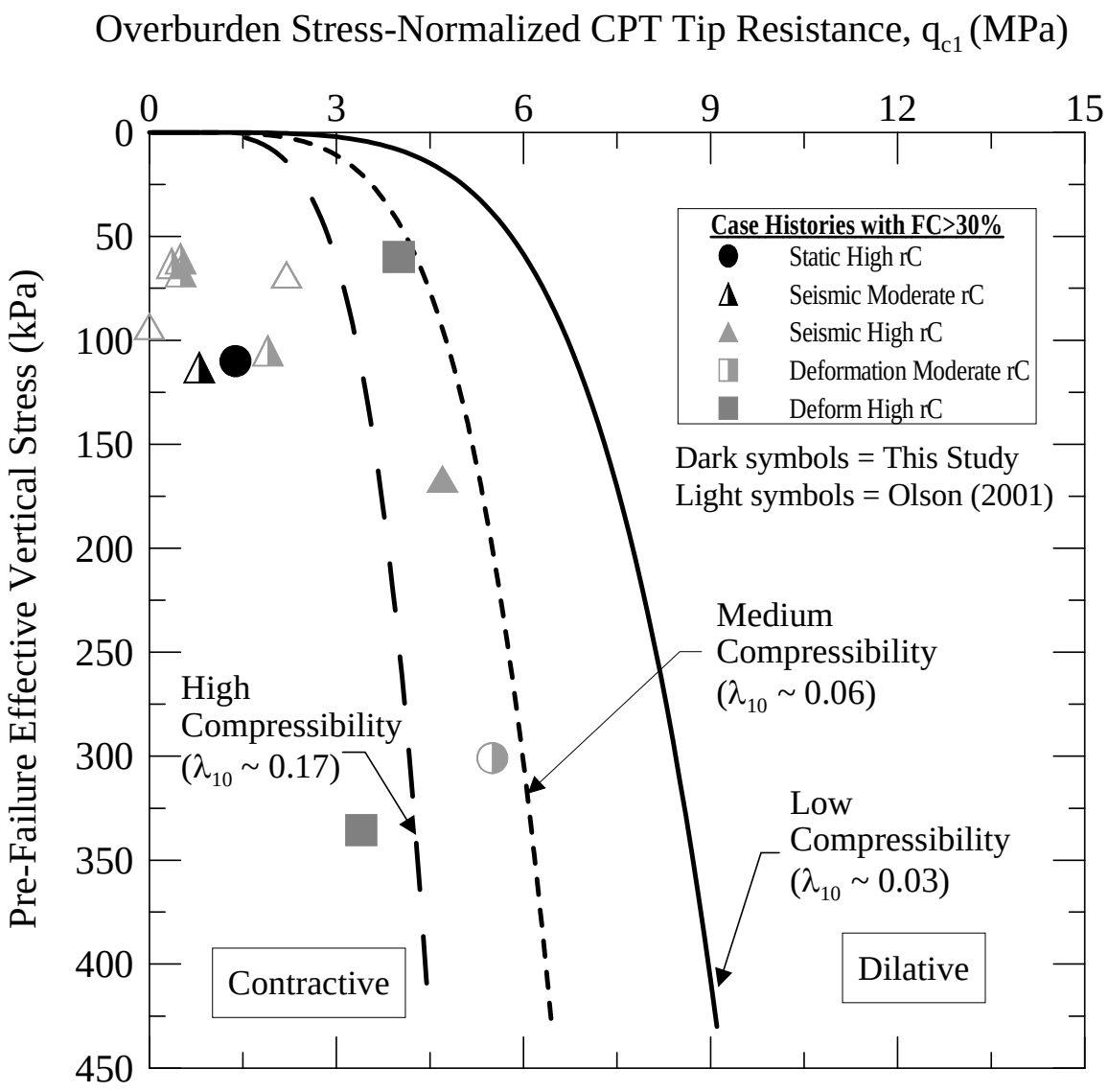

Figure 4.26 Flow failure case histories with FC > 30% analyzed in this study and by Olson (2001) compared to CPT-based liquefaction susceptibility boundary for Ottawa sand derived by Fear and Robertson (1995) and adopted by Olson (2001) for case history analysis

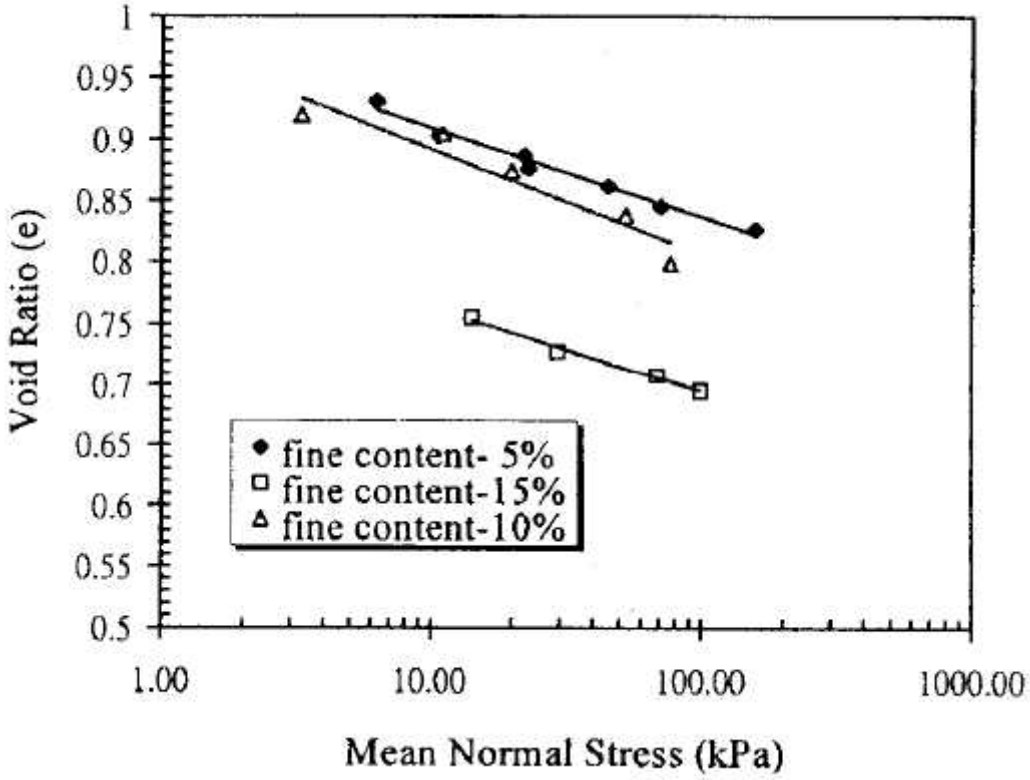

Figure 4.27 Critical state lines for Mailiao sand with different nonplastic fines content (from Chen and Liao 1999)

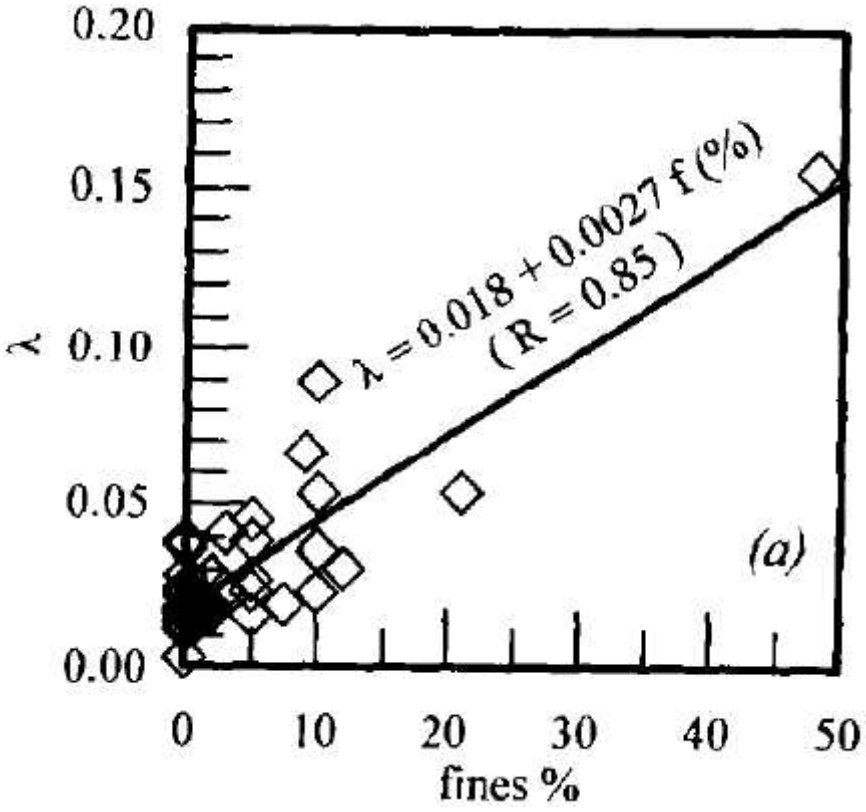

Figure 4.28 Comparison of fines contents and critical state line slopes collected by Andrianopoulos et al. (2001)

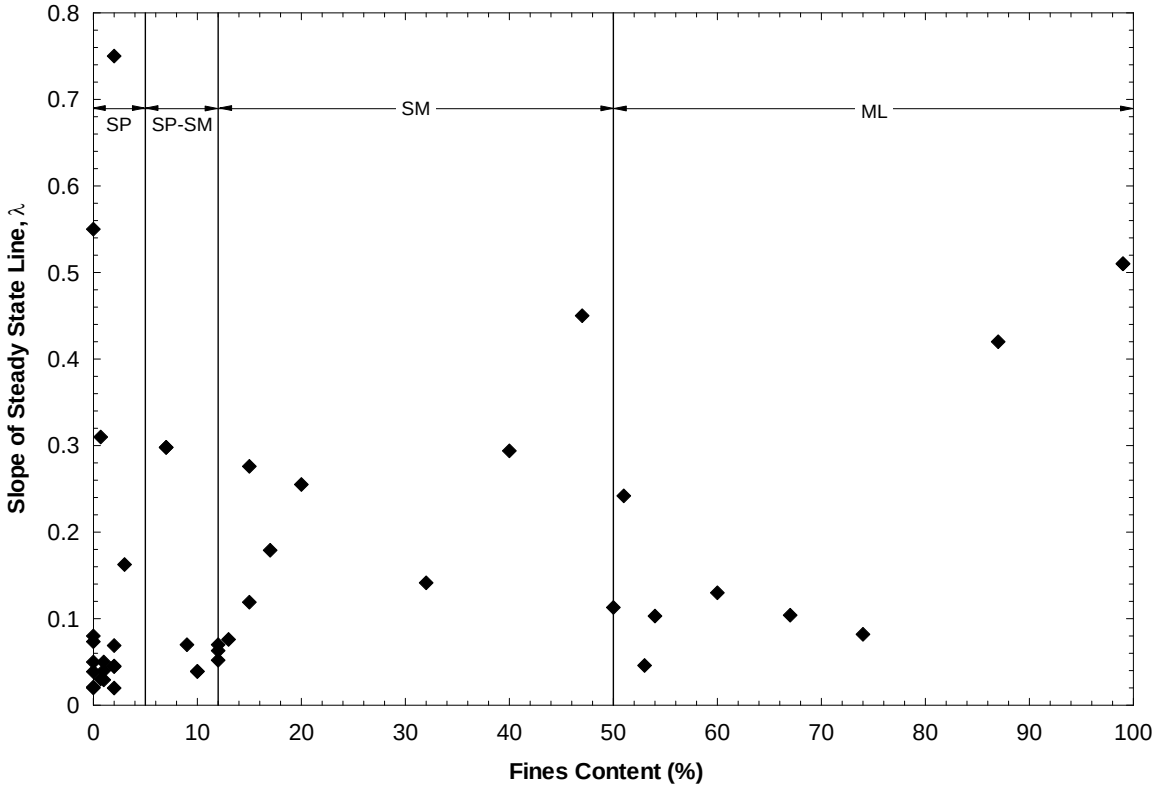

Figure 4. 29 Comparison of fines contents and critical state line slopes collected by Olson (2001)

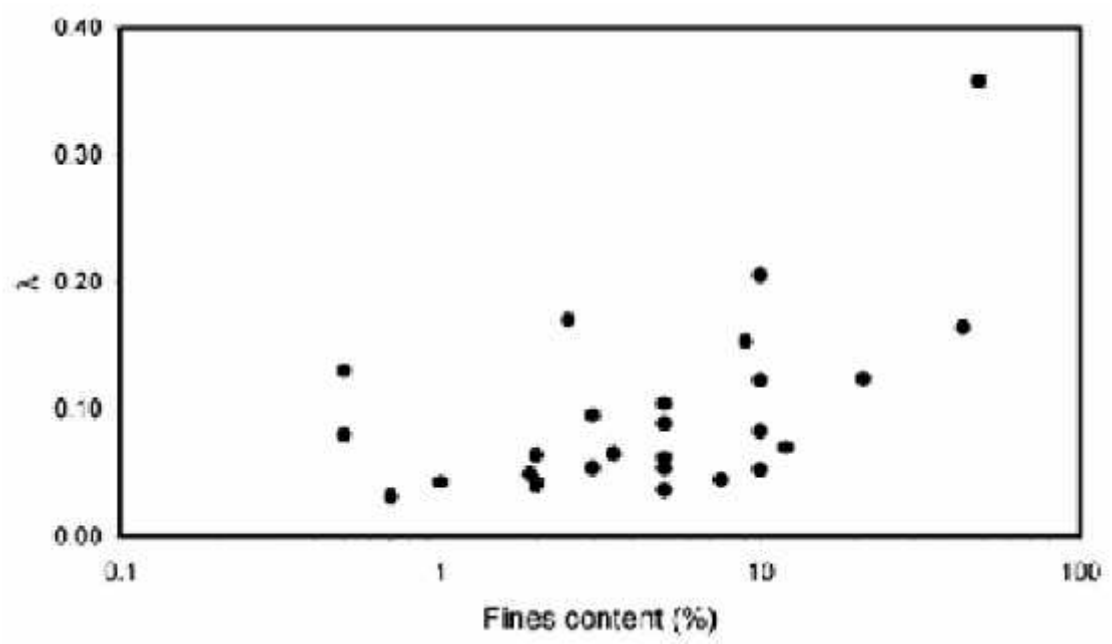

Figure 4.30 Comparison of fines contents and critical state line slopes for uniformly graded soils collected by Jefferies and Been (2006)

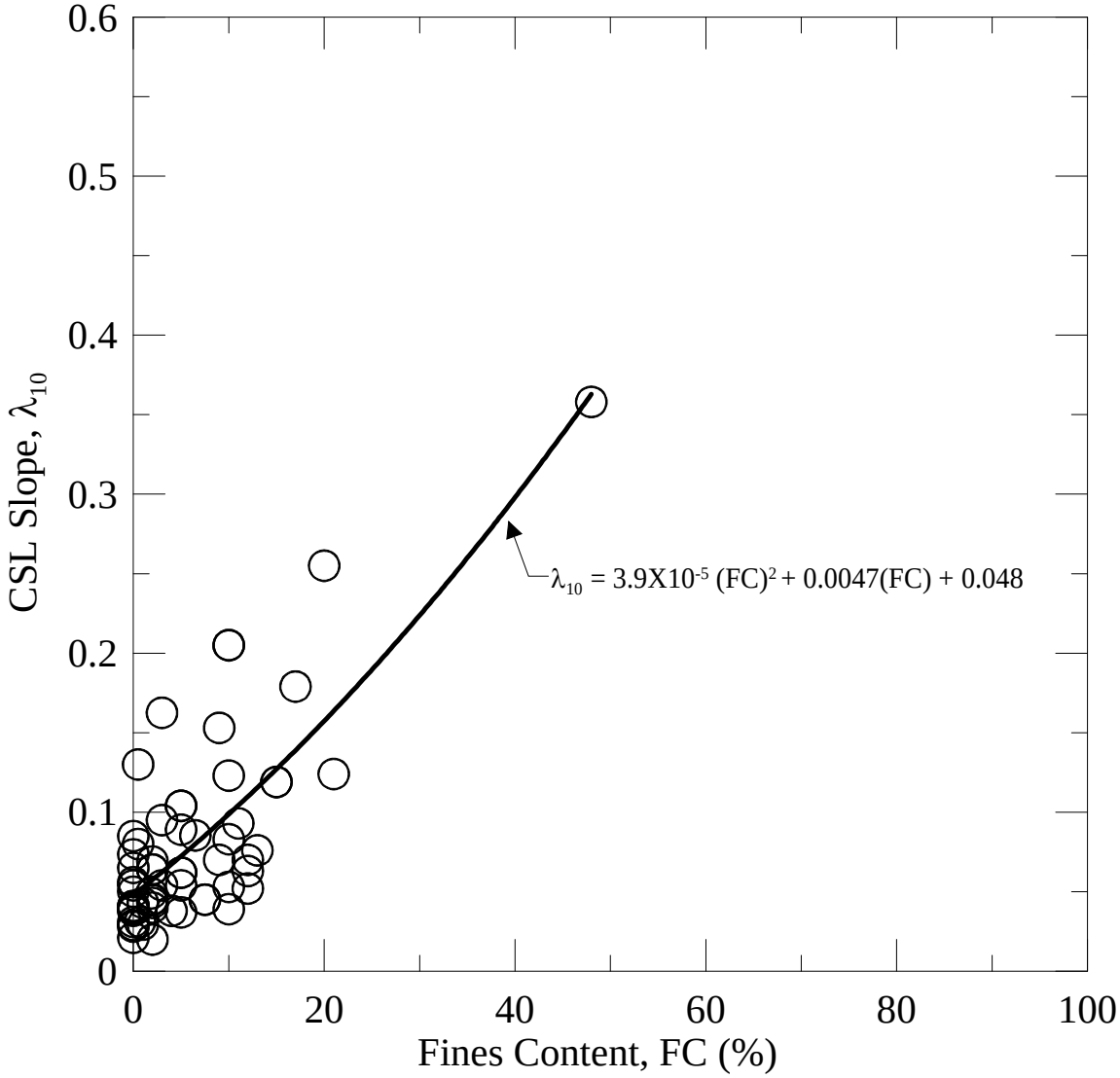

Figure 4.31 Comparison of fines contents and critical state line slopes for rounded to subrounded, nonplastic, quartz sands collected by Olson (2001) and Jefferies and Been (2006)

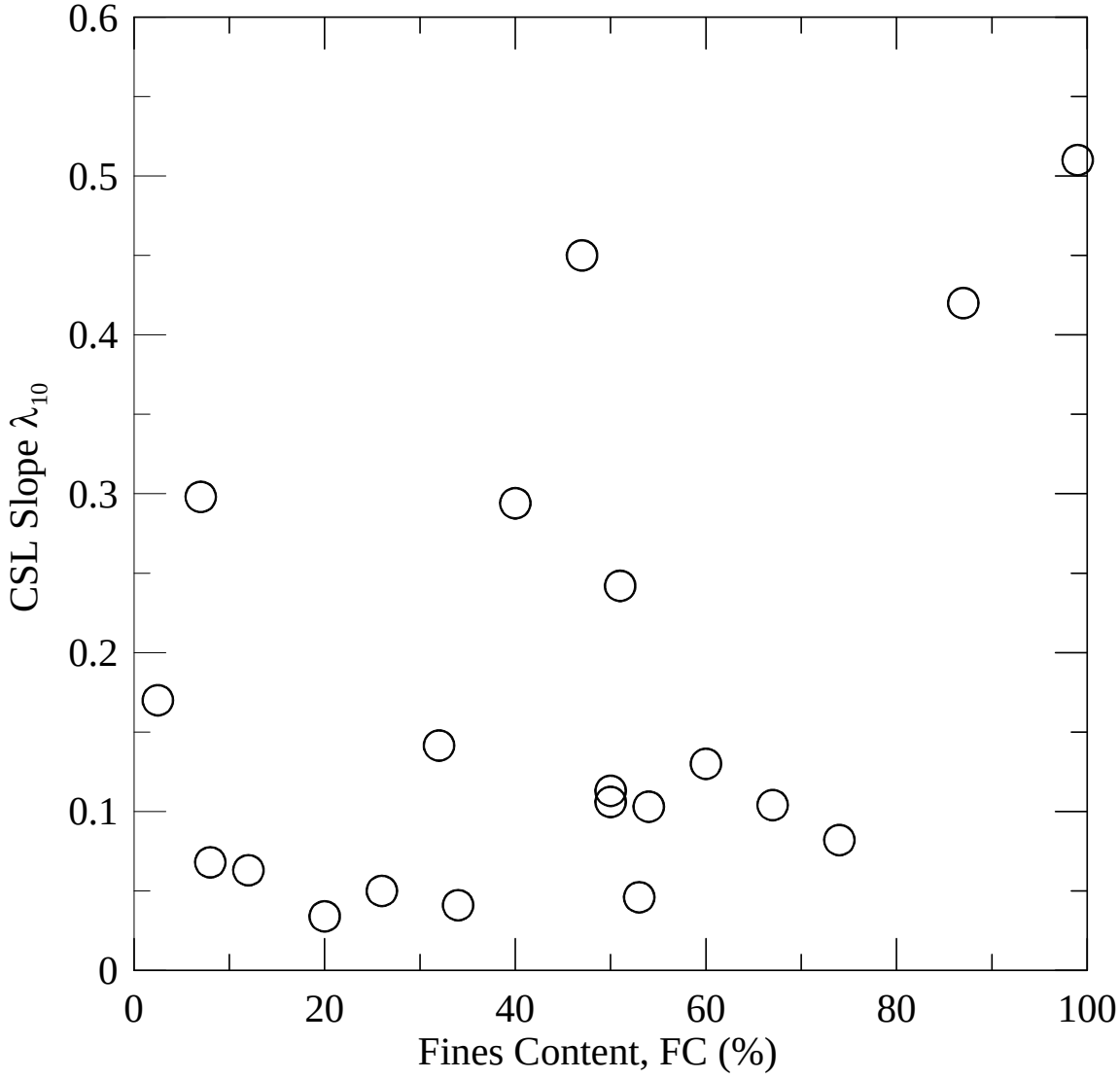

Figure 4.32 Comparison of fines contents and critical state line slopes for subangular to angular, nonplastic, tailings sands and tailings silts collected by Olson (2001) and Jefferies and Been (2006)

Table 4. 1 Depositional environment and age of soils involved in liquefaction failure from the case histories analyzed in this study

Case No.	Year	Structure Name	Apparent Cause of Failure	Triggering Mechanism	Type of Deposit	Distribution of Cohesionless Sediments in Deposits	Approx. Age of Deposit
1	1928	Barahona Dam	1928 Talca, Chile EQ (M_L = 8.2)	Seismic	Artificial Fill	Widespread	<500
2	1979	Kamenari Landslide	1979 Montenagro EQ (M_W = 7.2)	Seismic	Colluvium Talus, Fluvial	Variable	Pleistocene? to Holocene
3	1988	Spitak Embankment slide 1	1988 Armenian EQ (M_S = 6.8)	Seismic	Artificial Fill	Locally Variable	<500
4	1988	Spitak Embankment slide 2	1988 Armenian EQ (M_S = 6.8)	Seismic	Artificial Fill	Locally Variable	<500
5	1989	Okuli Landslide	1989 Tajik USSR EQ (M_L = 5.5)	Seismic	Loess	Widespread	Holocene
6	1991	Sullivan Tailings Dam	1991 During Construction	Static	Artificial Fill	Widespread	<500
7	1993	Kushiro River Left Bank	1993 Kushiro-Oki EQ (M_W = 7.4)	Seismic	Artificial Fill	Locally Variable	<500
8	1993	Kushiro River Right Bank	1993 Kushiro-Oki EQ (M_W = 7.4)	Seismic	Artificial Fill	Locally Variable	<500
9	1993	Tohnai Dike	1993 Kushiro-Oki EQ (M_W = 7.4)	Seismic	Artificial Fill	Locally Variable	<500
10	1993	Pashikuru (Route 38) Road Embankment	1993 Kushiro-Oki EQ (M_W = 7.4)	Seismic	Artificial Fill	Locally Variable	<500
11	1993	Itoizawa (Route 44) Road Embankment	1993 Kushiro-Oki EQ (M_W = 7.4)	Seismic	Artificial Fill	Locally Variable	<500
12	1994	Merrispurit Dam	1994 Overtopping and Erosion	Static	Artificial Fill	Widespread	<500
13	1994	King Harbor Mole B	1994 Northridge EQ (M_W = 6.7)	Seismic	Artificial Fill	Widespread	<500
14	1995	Takarazuka Landslide	1995 Kobe EQ (M_W = 6.9)	Seismic	Marine	Variable	Holocene
15	1995	Upper Niteko Dam	1995 Kobe EQ (M_W = 6.9)	Seismic	Artificial Fill	Locally Variable	<500
16	1995	Middle Niteko Dam	1995 Kobe EQ (M_W = 6.9)	Seismic	Artificial Fill	Locally Variable	<500
17	1995	Nikawa Landslide	1995 Kobe EQ (M_W = 6.9)	Seismic	Marine	Variable	Holocene
18	1995	Torishima Dike	1995 Kobe EQ (M_W = 6.9)	Seismic	Marine	Variable	Holocene
19	1995	Nishijima Dike	1995 Kobe EQ (M_W = 6.9)	Seismic	Marine	Variable	Holocene
20	1995	Idenoshiri Dam	1995 Kobe EQ (M_W = 6.9)	Seismic	Artificial Fill	Locally Variable	<500
21	1995	Jamuna Bridge 1500W3	1995 Toe Excavation	Static	Fluvial	Widespread	<500
22	1996	Jamuna Bridge 1800WT13	1996 Toe Excavation	Static	Fluvial	Widespread	<500
23	1996	Jamuna Bridge 2500WT4	1996 Toe Excavation	Static	Fluvial	Widespread	<500
24	1996	Jamuna Bridge 1800W4	1996 Toe Excavation	Static	Fluvial	Widespread	<500
25	1999	Degimendere Slope	1999 Kocaeli EQ (M_W = 7.4)	Seismic	Delta	Widespread	Holocene
26	2001	Chang Dam	2001 Bhuj EQ (M_W = 7.6)	Seismic	Alluvium	Variable	Holocene
27	2001	Shivlakha Dam	2001 Bhuj EQ (M_W = 7.6)	Seismic	Alluvium	Variable	Holocene
28	2001	Kaswati Dam	2001 Bhuj EQ (M_W = 7.6)	Seismic	Alluvium	Variable	Holocene
29	2001	Fategadh Dam	2001 Bhuj EQ (M_W = 7.6)	Seismic	Alluvium	Variable	Holocene
30	2001	Suvi Dam	2001 Bhuj EQ (M_W = 7.6)	Seismic	Alluvium	Variable	Holocene
31	2001	Tapar Dam	2001 Bhuj EQ (M_W = 7.6)	Seismic	Alluvium	Variable	Holocene

Table 4. 2 Depositional environment and age of soils involved in liquefaction failure from the case histories analyzed in Olson (2001)

Case No.	Year	Structure Name	Apparent Cause of Failure	Triggering Mechanism	Type of Deposit	Distribution of Cohesionless Sediments in Deposits	Approx. Age of Deposit
1	1889	Zeeland-Vlietepolder	1889 High Tide	Static	Delta	Widespread	Holocene
2	1907	Wachusett Dam - North Dike	1907 Reservoir Filling	Static	Artificial Fill	Locally Variable	<500
3	1918	Calaveras Dam	1918 Construction	Static	Artificial Fill	Locally Variable	<500
4	1925	Sheffield Dam	1925 Santa Barbara Eq. (M_L = 6.3)	Seismic	Alluvium	Locally Variable	<500
5	1936	Helsinki Harbor	1936 Construction	Static	Artificial Fill	Locally Variable	<500
6	1938	Fort Peck Dam	1938 Construction	Deformation	Artificial Fill	Locally Variable	<500
7	1940	Solfatara Canal Dike	1940 Imperial Valley Eq. (M_L = 7.1)	Seismic	Artificial Fill & Alluvium	Locally Variable	<500
8	1957	Lake Merced Bank	1957 San Francisco Eq.	Seismic	Artificial Fill	Locally Variable	<500
9	1964	Kawagishi-Cho Building	1964 Niigata Eq.	Seismic	Artificial Fill	Widespread	<500
10	1964	Uetsu Railway Embankment	1964 Niigata Eq.	Seismic	Artificial Fill	Locally Variable	<500
11	1965	El Cobre Tailings Dam	1965 Chilean Eq.	Seismic	Artificial Fill	Widespread	<500
12	1968	Koda Numa Highway Embankment	1968 Tokachi-Oki Eq.	Seismic	Artificial Fill	Locally Variable	<500
13	1968	Metoki Road Embankment	1968 Tokachi-Oki Eq.	Seismic	Artificial Fill	Locally Variable	<500
14	1968	Hokkaido Tailings Dam	1968 Tokachi-Oki Eq.	Seismic	Artificial Fill	Widespread	<500
15	1971	Lower San Fernando Dam	1971 San Fernando Eq.	Seismic	Artificial Fill	Locally Variable	<500
16	1974	Tar Island Dyke	1974 Construction	Static	Artificial Fill	Widespread	<500
17	1978	Mochi-Koshi Tailings Dam - Dike 1	1978 Izu-Oshima-Kinkai Eq.	Seismic	Artificial Fill	Widespread	<500
18	1978	Mochi-Koshi Tailings Dam - Dike 2	1978 Izu-Oshima-Kinkai Eq.	Seismic	Artificial Fill	Widespread	<500
19	1983	Nerlerk Berm - Side 1	1983 Construction	Deformation	Artificial Fill	Widespread	<500
20	1983	Nerlerk Berm - Side 2	1983 Construction	Deformation	Artificial Fill	Widespread	<500
21	1983	Nerlerk Berm - Side 3	1983 Construction	Deformation	Artificial Fill	Widespread	<500
22	1983	Hachiro-Gata Road Embankment	1983 Nihon-Kai-Chubu Eq.	Seismic	Artificial Fill	Locally Variable	<500
23	1983	Asele Road Embankment	1983 Pavement Repairs	Dynamic	Artificial Fill	Locally Variable	<500
24	1985	La Marquesa Dam - U/S slope	1985 Chilean Eq.	Seismic	Alluvium	Locally Variable	<500
25	1985	La Marquesa Dam - D/S slope	1985 Chilean Eq.	Seismic	Alluvium	Locally Variable	<500
26	1985	La Palma Dam	1985 Chilean Eq.	Seismic	Alluvium	Locally Variable	<500
27	1985	Fraser River Delta	1985 Gas Desaturation and Low Tide	Static	Delta	Widespread	<500
28	1987	Lake Ackerman Highway Embankment	1987 Seismic Reflection Survey	Dynamic	Artificial Fill	Locally Variable	<500
29	1987	Chonan Middle School	1987 Chiba-Toho-Oki Eq.	Seismic	Artificial Fill	Locally Variable	<500
30	1988	Nalband Railway Embankment	1988 Armenian Eq.	Seismic	Artificial Fill	Locally Variable	<500
31	1989	Soviet Tajik - May 1 slide	1989 Tajik, Soviet Union Eq.	Seismic	Loess	Widespread	Holocene
32	1993	Shibecha-Cho Embankment	1993 Kushiro-Oki Eq.	Seismic	Artificial Fill	Locally Variable	<500
33	1993	Route 272 at Higashiarekinai	1993 Kushiro-Oki Eq.	Seismic	Artificial Fill	Locally Variable	<500

Table 4. 3 List of case histories along with penetration resistance data analyzed in this study

		Analyzed and Documented Cases			$(N_1)_{60}$ blows/ft			q_{c1} MPa			σ′v
Case No.	Year	Structure Name	SPT/CPT	FC (%)	L/B	BE	U/B	L/B	BE	U/B	(kPa)
1	1928	Barahona Dam	SPT;CPT	15-20	5	10	16	0.6	3.5	11	404
2	1979	Kamenari Landslide	SPT	-	2	7	13	0.8	3.8	6.9	51
3	1988	Spitak Embankment slide 1	SPT;CPT	0	7	8.5	12	4.6	7.8	9.2	46.5
4	1988	Spitak Embankment slide 2	SPT;CPT	0	7	8.5	12	4.6	7.8	9.2	47
5	1989	Okuli Landslide	SPT	100	3	3.5	8	0.66	0.8	1.9	113
6	1991	Sullivan Tailings Dam	SPT;CPT	88	2	3	5	0.97	1.38	2.26	110
7	1993	Kushiro River Right Bank	SPT	10	0	3	4	0	1.7	2.3	56
8	1993	Kushiro River Left Bank	SPT	10	2	3	7	1.14	1.7	4	79
9	1993	Tohnai Dike	SPT	10	5	6	11	2	2.4	5.2	89
10	1993	Pashikuru (Route 38) Road Embankment	SPT	20	-	3	-	-	1.68	-	93.5
11	1993	Itoizawa (Route 44) Road Embankment	SPT	20	4	5	10	2.24	2.8	5.6	56
12	1994	Merrispurit Dam	CPT	1-60	-	2	-	-	0.64	-	240
13	1994	King Harbor Mole B	SPT;CPT	2-7	3	6	10	1.1	4.6	11.7	47
14	1995	Torishima Dike	SPT	20	2	6	11	0.9	2.7	5	58.5
15	1995	Nishiiima Dike	SPT	20	3	8	14	1.38	3.68	6.44	44
16	1995	Upper Niteko Dam	SPT	15	5	6	13	2.6	3.1	6.7	42
17	1995	Middle Niteko Dam	SPT	15	3	5	6	1.53	2.55	3.06	65
18	1995	Takarazuka Landslide	SPT	0	4	11	18	2.6	7.15	11.7	104
19	1995	Nikawa Landslide	SPT	17	4	9	14	2.2	4.95	7.7	175
20	1995	Idenoshiri Dam	SPT	30	4	3	5	1.6	2.4	4	87.5
21	1995	Jamuna Bridge 1500W3	SPT;CPT	15-20	6	7	9	2.5	2.9	3.6	60
22	1996	Jamuna Bridge 1800W4	SPT;CPT	15-20	7	8	10	2.5	3	3.9	54.5
23	1996	Jamuna Bridge 1800WT13	SPT;CPT	15-20	6	8	10	2.4	3	3.5	69
24	1996	Jamuna Bridge 2500WT4	SPT;CPT	15-20	5	7	10	1.9	2.8	4	53.5
25	1999	Degimendere Slope	SPT;CPT	5-10	5	7	10	1.9	2.8	4	53.5
26	2001	Chang Dam	SWS	15-23	4	8	11	3.84	4.8	6.24	105
27	2001	Shivlakha Dam	Estimated	15-23	8	10	12	3.84	4.8	5.8	112.5
28	2001	Tapar Dam	Estimated	15-23	8	10	12	3.84	4.8	5.8	102.25
29	2001	Fategadh Dam	SPT	15-23	10	12	15	4.8	5.76	7.2	83
30	2001	Kaswati Dam	SPT	15-23	9	12	15	4.3	5.76	7.2	88.5
31	2001	Suvi Dam	Estimated	15-23	8	10	12	3.84	4.8	5.8	104.5

Table 4. 4 Evaluation of "relative confidence" in flow failure case histories analyzed (a) in this study and (b) in Olson (2001)

CASE HISTORIES ANALYZED IN THIS STUDY

(a)

Points	1	1	0.5	0	1	0.5	0	1	0.5	0	1	0.5	0	
Case No.	Pre-failure Geometry	Post-failure Geometry Complete	Post-failure Geometry Incomplete [1]	Post-failure Geometry Unavailable	Phreatic Surface Complete	Phreatic Surface Incomplete [2]	Phreatic Surface Unavailable	SPT Full Data Available	SPT Range Available [3]	SPT Not Available	CPT Full Data Available	CPT Range Available [3]	CPT Not Available	Overall Score
1	x			x			x		x			x		2
2	x	x			x				x				x	3.5
3	x	x			x				x			x		4
4	x	x			x				x			x		4
5	x	x				x		x					x	3.5
6	x	x					x	x			x			4
7	x	x			x			x					x	4
8	x	x			x			x					x	4
9	x	x			x			x					x	4
10	x	x				x		x					x	3.5
11	x	x				x		x					x	3.5
12	x			x	x					x	x			3
13	x	x			x			x			x			5
14	x	x				x		x					x	3.5
15	x	x				x		x					x	3.5
16	x			x	x			x					x	3
17	x			x		x		x					x	2.5
18	x	x				x				x			x	2.5
19	x	x				x		x					x	3.5
20	x	x			x			x					x	4
21	x		x		x				x			x		3.5
22	x		x		x				x			x		3.5
23	x		x		x				x			x		3.5
24	x		x		x				x			x		3.5
25	x			x	x			x			x			4
26	x		x		x				x				x	3
27	x	x			x					x			x	3
28	x	x			x					x			x	3
29	x	x			x				x				x	3.5
30	x	x			x				x				x	3.5
31	x	x			x					x			x	3

Table 4. 4Continued

CASE HISTORIES ANALYZED IN OLSON (2001)														
(b)														
Points	1	1	0.5	0	1	0.5	0	1	0.5	0	1	0.5	0	
Case No.	Pre-failure Geometry	Post-failure Geometry Complete	Post-failure Geometry Incomplete[1]	Post-failure Geometry Unavailable	Phreatic Surface Complete	Phreatic Surface Incomplete [2]	Phreatic Surface Unavailable	SPT Full Data Available	SPT Range Available [3]	SPT Not Available	CPT Full Data Available	CPT Range Available [3]	CPT Not Available	Overall Score
1	x	x			x					x	x			4
2	x	x			x			x					x	4
3	x	x			x					x			x	3
4	x			x	x					x			x	2
5	x	x			x					x			x	3
6	x	x			x			x					x	4
7	x			x			x			x			x	1
8	x		x		x					x			x	2.5
9	x	x			x			x				x		4.5
10	x	x					x			x			x	2
11			x				x	x			x		x	2.5
12	x	x					x			x			x	2
13	x		x				x			x		x		2
14	x		x		x					x	x			3.5
15	x	x			x			x			x			5
16	x		x		x			x			x			4.5
17	x		x			x		x				x		3.5
18	x		x			x		x				x		3.5
19	x		x		x					x	x			3.5
20	x		x		x					x	x			3.5
21	x		x		x					x	x			3.5
22	x		x		x			x			x			4.5
23	x		x		x				x				x	3
24	x	x				x		x					x	3.5
25	x	x				x		x					x	3.5
26	x	x			x			x					x	4
27				x	x					x	x			2
28	x		x		x			x					x	3.5
29	x	x			x			x					x	4
30	x	x			x			x					x	4
31	x	x				x				x		x		3
32	x	x			x			x					x	4
33	x	x			x			x					x	4

Notes: Case numbering for Table 4.3(b) taken directly from Olson (2001). 1. Incomplete post-failure geometry was completed by area-balancing method. 2. Sufficient information is available to complete phreatic surface employing the hydrologic concepts or based on nearby groundwater levels. 3. Either range or single value available. Includes sites where penetration tests were performed outside of failed area, non-standard penetration testing equipment was used, or some other issue exists.

Table 4.5 Critical State properties of soils from Jefferies and Been (2006) and Olson (2001) with grain shape and mineralogy

Jefferies and Been (2006) Data

(a) Laboratory Standard Sands	D_{50} *(mm)*	*Fines (%)*	e_{max}	e_{min}	G_s	Γ_1	λ_{10}	M_{tc}	*Source*	*Grain Shape*	*Mineralogy*
Castro Sand B	0.15	0	0.84	0.5		0.791	0.041	1.22	Castro (1969)	Subrounded to Subangular	Uniform Clean Fine Quartz Sand
Castro Sand C	0.28	0	0.99	0.66		0.988	0.038	1.37	Castro (1969)	Angular and Bulky	Basalt Plagioclase Magnetite Olivine
Hokksund	0.39	0	0.91	0.55		0.934	0.054	1.29	Golder Project Files	Subangular	Quartz Feldspar Mica
Leighton Buzzard	0.12	5	1.023	0.665		0.972	0.054	1.24	Golder Project Files	Subrounded	
Leighton Buzzard	0.5	0	0.79	0.515		0.69	0.04		Hird and Hassona (1990)	Subrounded	Uniform Medium Quartz
Leighton Buzzard: 10% Mica	0.5	0	1.07	0.591		0.99	0.145		Hird and Hassona (1990)	Micaceous Sand	Quartz 45%, Feldspar 45% Mica 10%
Leighton Buzzard: 17% Mica	0.47	0	1.32	0.615		1.11	0.16		Hird and Hassona (1990)	Micaceous Sand	
Leighton Buzzard: 30% Mica	0.45	0	1.789	0.823		1.61	0.385		Hird and Hassona (1990)	Micaceous Sand	
Monterey	0.37	0	0.82	0.54		0.878	0.029	1.29	Golder Project Files	Subrounded	Quartz trace of Feldspar
Nevada	0.15	7.5	0.887	0.511		0.91	0.045	1.2	Velacs Project		
Ottawa	0.53	0	0.79	0.49		0.754	0.028	1.13	Golder Project Files	Rounded to Subrounded	Uniform Medium Quartz
Reid Bedford	0.24	0	0.87	0.55		1.014	0.065	1.29	Golder Project Files	Subrounded to Rounded	Quartz some Feldspar Trace of Calcite
Ticino-4	0.53	0	0.89	0.6	2.67	0.986	0.056	1.24	Golder Project Files	Subrounded	Quartz 95%, Feldspar 05%
Ticino-8	0.53	0				0.943	0.031		Golder Project Files	Subrounded	Quartz 95%, Feldspar 05%
Ticino-9	0.53	0				0.97	0.05		Golder Project Files	Subrounded	Quartz 95%, Feldspar 05%
Toyoura	0.21	0	0.873	0.656		1	0.039	1.24	Golder Project Files	Subangular to Angular	Quartz 75% Feldspar 25%
Toyoura	0.16	0	0.981	0.608	0.265	1.043	0.085		Golder Project Files	Subangular to Angular	Quartz 75% Feldspar 25%

Table 4.5 Continued

(b) Natural Sands	D_{50} *(mm)*	*Fines (%)*	e_{max}	e_{min}	G_s	Γ_1	λ_{10}	M_{tc}	*Source*	*Grain Shape*	*Mineralogy*
Amauligak F-24	0.14	10			2.67	0.946	0.083	1.37	Golder Project Files		
Amauligak F-24	0.144	21			2.69	0.966	0.124	1.33	Golder Project Files		
Amauligak I-65	0.08	48			2.65	1.634	0.358	1.29	Golder Project Files		
Amauligak I-65	0.31	9			2.67	1.018	0.153	1.42	Golder Project Files		
Amauligak I-65	0.29	3			2.65	1.023	0.095	1.31	Golder Project Files		
Erksak	0.32	1	0.808	0.614		0.875	0.043	1.27	Golder Project Files	Subrounded	Quartz with some Chert
Erksak	0.355	3	0.963	0.525	2.67	0.848	0.054	1.18	Golder Project Files	Subrounded	Quartz with some Chert
Erksak	0.33	0.7	0.747	0.521	2.66	0.816	0.031	1.27	Golder Project Files	Subrounded	Quartz with some Chert
Isserk	0.21	2	0.76	0.52	2.67	0.833	0.043	1.22	Golder Project Files		
Isserk	0.21	5	0.83	0.55		0.879	0.089	1.24	Golder Project Files		
Isserk	0.21	10	0.86	0.44		0.933	0.123	1.24	Golder Project Files		
Kogyuk	0.35	2	0.83	0.47		0.844	0.064	1.31	Golder Project Files	Subrounded to Subangular	Uniform Medium Quartz
Kogyuk	0.35	5	0.87	0.49		0.924	0.104	1.31	Golder Project Files	Subrounded to Subangular	Uniform Medium Quartz
Kogyuk	0.35	10	0.93	0.46		1.095	0.205	1.24	Golder Project Files	Subrounded to Subangular	Uniform Medium Quartz
Kogyuk	0.28	5	0.87	0.56		0.902	0.062	1.2	Golder Project Files	Subrounded to Subangular	Uniform Medium Quartz
Nerlerk	0.27	1.9	0.812	0.536	2.66	0.849	0.049	1.29	Golder Project Files		
Nerlerk	0.28	2	0.94	0.62		0.88	0.04	1.2	Sladen et al. (1985)		
Nerlerk	0.28	12	0.96	0.43		0.8	0.07	1.24	Sladen et al. (1985)		
Alaskan Beaufort	0.14	5	0.856	0.565	2.7	0.91	0.037	1.22	Golder Project Files		
Alaskan Beaufort	0.14	10	0.837	0.53	2.7	0.92	0.053	1.2	Golder Project Files		
West Kowloon Sand	0.73	0.5	0.685	0.443	2.65	0.71	0.08		Golder Project Files		
Chek Lap Kok	1	0.5	0.682	0.411	2.65	0.905	0.13		Golder Project Files		
Fraser River (Massey)	0.2	4	1.1	0.7	2.68	1.071	0.038		Robertson et al. (2000)	Subrounded	Quartz 70% Feldspar 15% Mica 05%
Duncan Dam	0.2	6.5	1.15	0.76	2.77	1.17	0.0854		Robertson et al. (2000)	Angular to Subangular	Quartz Plagioclase K-Feldspar Calcite-Dolomite
San Fernando 3	0.29	11			2.69	0.869	0.093		Seed et al. (1988)		
San Fernando 7	0.075	50			2.69	0.815	0.106		Seed et al. (1988)		
Bennett Silty Sand (a)	0.27	34	0.678	0.178	2.7	0.457	0.041	1.4	Golder Project Files		
Bennett Silty Sand (b)	0.37	26	0.524	0.332	2.7	0.435	0.05	1.43	Golder Project Files		
Bennett Silty Sand (c)	0.41	20	0.509	0.337	2.7	0.43	0.034	1.43	Golder Project Files		

Table 4.5 Continued

(c) Tailings Sands and Silts	D_{50} *(mm)*	*Fines (%)*	e_{max}	e_{min}	G_s	Γ_1	λ_{10}	M_{tc}	*Source*	*Grain Shape*	*Mineralogy*
Hilton Mines	0.2	2.5	1.05	0.62		1.315	0.17	1.42	Golder Project Files	Angular	Quartz some Feldspar Muscovite Mica Heavy minerals
Highland Valley Copper	0.2	8	1.055	0.544	2.66	0.98	0.068		Robertson et al. (2000)	Angular	Quartz
Faro Lead-Zinc	0.1	30	0.99	0.556	4.48	0.921	0.082	1.19	Golder Project Files	Subrounded to Subangular	
Faro Lead-Zinc	0.05	65	2.017	0.837	3.97	1.076	0.159	1.2	Golder Project Files	Subrounded to Subangular	
Sudbury (nickel)	0.115	35	1.032	0.537	3.03	0.938	0.112	1.45	Golder Project Files	Subrounded to Subangular	
Sudbury (nickel)	0.05	65			2.98	0.868	0.108	1.45	Golder Project Files	Subrounded to Subangular	
Syncrude Oil Sand Tailings	0.207	3.5	0.898	0.544	2.64	0.86	0.065	1.33	Golder Project Files	Angular to Subangular	Quartz small amount of Bitumen as discrete gravel sized lumps
Syncrude (Mildred Lake)	0.16	10	0.958	0.522	2.66	0.919	0.035		Robertson et al. (2000)	Subrounded to Subangular	
Yatesville Silty Sand	0.1	43			2.67	0.653	0.164	1.33	Brandon et al. (1991)	Subrounded	
Merriespruit Gold Tailings	0.14	0	1.221	0.738		1.24	0.07		Fourie & Papageorgiou (2001)		
Merriespruit Gold Tailings	0.13	20	1.326	0.696		1.18	0.05		Fourie & Papageorgiou (2001)		
Merriespruit Gold Tailings	0.11	30	1.331	0.577		0.96	0.035		Fourie & Papageorgiou (2001)		
Merriespruit Gold Tailings	0.06	60	1.827	0.655		0.8	0.02		Fourie & Papageorgiou (2001)		

Table 4.5 Continued

Olson (2001) Data	D_{50} *(mm)*	*Fines (%)*	e_{max}	e_{min}	G_s	Γ_1	λ_{10}	M_{tc}	*Source*	*Grain Shape*	*Mineralogy*
Dune Sand	0.21	3	0.91	0.54		1.1521	0.1625			Angular to Subangular	Quartz and Feldspar
Well-rounded Silica sand (WA)	0.175	1	1.06	0.67		1.0095	0.02932			Rounded	Silica
Fraser River Delta Sand (FRD)	0.25	9	1	0.6		1.11	0.07			Subrounded	Quartz 40% Feldspar 11% Unwathered Rock 45% Other minerals 4%
Duncan Dam Sand (DD)	0.2	6.5	1.15	0.76					Jefferies and Been (2006)		
Hostun RF Sand (HRF)	0.38	0	1	0.656							
Garnet Tailings (GT)	0.17	20	1.52	0.53		1.59	0.255			Angular	Uniform Sand
Zinc Tailings (ZT)	0.2	17	1.43	0.49		1.3275	0.179			Angular	Uniform Sand
Natural Silt (NS)	0.013	98	1.526	0.434							
Fine-Coarse Sand (FCS)	0.33	1	0.796	0.404							
Ottawa Banding Sand (OBS)	0.19	2	0.82	0.51		0.9	0.069			Rounded to Subrounded	Uniform Medium Quartz

Table 4.5 Continued

Olson (2001) Data	D_{50} ***(mm)***	***Fines (%)***	e_{max}	e_{min}	G_s	Γ_1	λ_{10}	M_{tc}	***Source***	***Grain Shape***	***Mineralogy***
Ottawa Banding Sand (OBS)	0.19	2	0.82	0.51		0.856	0.0453			Rounded to Subrounded	Uniform Medium Quartz
Ottawa Banding Sand (OBS)	0.19	2	0.82	0.51		0.849	0.0447			Rounded to Subrounded	Uniform Medium Quartz
Ottawa Banding Sand (OBS)	0.19	2	0.82	0.51		0.789	0.0199			Rounded to Subrounded	Uniform Medium Quartz
Nevada Fine Sand (NFS)	0.12		0.87	0.57		0.832	0.0657		Jefferies and Been (2006)		
Nerlerk 0 - 2% (N2)	0.25	2	0.94	0.62		0.883	0.04		Jefferies and Been (2006)		
Nerlerk 12% (N12)	0.28	12	0.96	0.43		0.8	0.07		Jefferies and Been (2006)		
Leighton Buzzard (LBS)	0.86	0	0.75	0.58		1	0.08		Jefferies and Been (2006)		
Syncrude Tailings Sand (STS)	0.17	10	0.93	0.55		0.845	0.039			Angular to Subangular	Quartz with a trace of silty and clay
							0.039				
Tottori Sand (TS)	0.28	0	1.008	0.638							
Monterey #9 Sand (M9S)	0.35	0	0.86	0.53						Rounded to Subrounded	Quartz Grain
Sydney Sand (SS)	0.3		0.855	0.565							Uniformly Graded Quartz Sand
Arabian Gulf Sand (AGS)		40									
Hostun RF Sand (HRFS)	0.32	0	1	0.655		1.0546	0.0735			Subangular	Siliceous Sand Uniformly Graded
Till Sand (Tills)	0.11	32	0.835	0.3625		0.791	0.1415			Angular	Quartz grain with some Feldspar

Table 4.5 Continued

Olson (2001) Data	D_{50} *(mm)*	*Fines (%)*	e_{max}	e_{min}	G_s	Γ_1	λ_{10}	M_{tc}	*Source*	*Grain Shape*	*Mineralogy*
Massey Tunnel Sand (MTS)	0.25	3	1.102	0.712							Quartz 70% Feldspar 15% Mica 5% Kaolinite 5% Chlorite-Smectite 5%
Quebec Sand (QS)	0.5	0	0.79	0.54		0.757	0.021			Subrounded	
Erksak 330/0.7 (E330)	0.33	0.7	0.753	0.469		0.82	0.0306		Jefferies and Been (2006)		
						1.167	0.31				
Ottowa Sand (C109)	0.34	0	0.82	0.5		0.864	0.0387			Rounded to Subrounded	Quartz grain Uniform Medium Sand
Sand F	0.205	0	1.88	1.23			0.55			Angular	
Sand B	0.16	0	0.84	0.5		0.804	0.05		Jefferies and Been (2006)		
Sand C	0.27	1	0.99	0.66		1.005	0.05		Jefferies and Been (2006)		
Sand H	0.66	13	0.73	0.36			0.076			Subangular	
Sand A	0.2	2	1.88	1.23			0.75			Subangular to Angular	
Alcan Tailings (AT)	0.002	99					0.51			Angular	
							0.51				
Mai-Liao Sand (MLS)	0.105	15	1.06	0.59			0.119			Subrounded to Subangular	Quartz
							0.276				
Star Morning Tailings (SMT)	0.062	51					0.242			Angular	
Bunker Hill Tailings (BHT)	0.0097	87					0.42			Angular	
Coeur Mine Tailings (CMT)	0.06	54					0.103			Angular	
Galena Tailings (GT)	0.086	40					0.294			Angular	
Lucky Friday Tailings (LFT)	0.065	53					0.046			Angular	
Mission Tailings (MT)	0.04	60					0.13			Angular	
Morenci Tailings (MoT)	0.086	47					0.45			Angular	
Climax Tailings (CT)	0.026	67					0.104			Angular	
Lornex Mine Tailings (LMT)	0.256	7					0.298			Angular	
							0.298				
Ottawa Sand F125 (F125)	0.1	12				0.881	0.052				Ground Crystalline Salica (Quartz)
Sand A (SA)	0.15	13									
San Fernando SF7 Sand (SF7)	0.075	50	0.72	0.34			0.113				
Toyoura Sand (ToS)	0.17	0	0.977	0.597			0.02				
Lagunillas Sandy Silt (LSS)	0.05	74	1.389	0.766			0.082				
Tia Juana Silty Sand (TJSS)	0.16	12	1.099	0.62			0.063				

Table 4.6 Sands for which calibration chamber test results are available. Constants C and n for Dr ~ 40% are included

Sand	D_R (%)	λ_{10}	C	n	D_{50}	Γ	Mineralogy	Reference
Monterey	40	0.029	6.8713	1.3134	0.37	0.875	Quartz-Feldspar	Robertson and Campanella (1986)
Hokksund	35	0.054	17.094	1.3719	0.39	0.934	Quartz-Feldspar-Mica	Been and Jefferies (2006)
	67.5		2.6418	1.3719				
	90		0.6993	1.5874				
	97		0.4507	1.6658				
	40		12.9108	1.3625				
Ticino	40	0.06	8.510	1.401	0.53	0.986	Quartz-Feldspar-Calcite	Robertson and Campanella (1986)
Reid Bedford	28	0.065	33	1.1611	0.24	1.014	Quartz-Feldspar-Calcite	Been and Jefferies (2006)
	81.5		1.3558	1.4773				
	40		13.858	1.285				
Syncrude	40	0.065	13.858	1.285	0.207	0.86	Quartz-Bitumen Chunks	Been and Jefferies (2006)
Ottawa	18.5	0.0745	10.097	1.7397	0.53	0.975	Uniform Medium Quartz	Been and Jefferies (2006)
	45		3.9759	1.7901				
	47		3.6519	1.7955				
	49		2.8911	1.8481				
	40		4.510	1.799				
West Kowloon	33.5	0.08	38.404	1	0.73	0.71	-	Been and Jefferies (2006)
	55.5		17.682	1.1287				
	80		5.9961	1.3848				
	40		16.189	1.288				
Leighton Buzzard	40	0.08	16.189	1.288	0.8	1	Uniform Medium Quartz	Houlsby and Hitchman (1988)
MLS	85	0.119	1.7095	1.8598	0.1	-	Quartz-Muscovite-Chlorite	Huang et al. (1999)
	70		12.9921	1.2523				
	50		16.753	1.2399				
	40		19.033	1.232				
Chek Lap Kok	80	0.13	1.0436	1.7961	1	0.905	-	Been and Jefferies (2006)
	60		13.554	1.2429				
	30		23.5032	1.254498				
	40		18.4789	1.254				
Hilton Mines	40	0.17	24.055	1.1565	0.2	1.315	Quartz-Feldspar-Muscovite-Mica	Robertson and Campanella (1986)

Table 4. 7 List of sands collected in this study with compressibility correction factors

	$C_\lambda = q_c(\text{incompressible})/q_c$											
q_c (Bar)	**Monterey**	**Hokksund**	**Ticino**	**Reid Bedford**	**Syncrude**	**Ottawa**	**West Kowloon**	**Leighton Buzzard**	**MLS**	**Chek Lap Kok**	**Hilton Mines**	**MR**
1	1	1.71	1.32	1.65	1.65	1.23	1.87	1.37	2	2	2.24	2.59
2	1	1.74	1.37	1.63	1.63	1.43	1.85	1.58	1.93	1.95	2.09	2.56
3	1	1.76	1.39	1.62	1.62	1.56	1.84	1.72	1.89	1.92	2	2.55
$C_{\lambda(avg.)}$	*1*	*1.74*	*1.36*	*1.63*	*1.63*	*1.41*	*1.85*	*1.56*	*1.94*	*1.96*	*2.11*	*2.57*

CHAPTER FIVE:

LIQUEFACTION TRIGGERING AND YIELD STRENGTH ANALYSIS

5.1 Introduction

As defined in Chapter 4, the second step in liquefaction analysis for sloping ground is liquefaction triggering. In Chapter 4, liquefaction susceptibility was discussed. The fact that a soil deposit is susceptible to liquefaction does not mean that liquefaction will necessarily occur in a given earthquake. Liquefaction triggering requires a disturbance strong enough to initiate undrained yielding of the soil. Evaluation of the nature of that disturbance is one of the most critical parts of a liquefaction analysis for ground subjected to a static shear stress.

This Chapter first discusses some notable methods for liquefaction triggering analysis of sloping ground. Next, the author describes the back-analysis of flow failure case histories in terms of yield shear strengths, yield strength ratios, and yield envelopes. These data are combined with those analyzed by Olson (2001) and compared to liquefaction triggering analyses proposed by Olson et al. (2006) and Mesri (2007). Finally, the back-analysis results are evaluated in terms of the mode of shear, and these results are compared to laboratory data presented by Olson and Mattson (2008).

5.2 Liquefaction Triggering Analysis

Once it is confirmed from liquefaction susceptibility analysis that the soil deposit under consideration is susceptible to liquefaction, liquefaction triggering analysis should be conducted. This involves evaluating whether a particular combination of static and

dynamic loads are sufficient to trigger liquefaction. Triggering is evaluated in terms of a factor of safety against triggering, $FS_{Triggering}$. Olson (2001) defined this term as:

$$FS_{Triggering} = \frac{s_u(yield)}{\tau^2_{driving} + \tau^2_{avg,seismic} + \tau^2_{other}} \qquad \textbf{Eq. 5.1}$$

where s_u(yield) = yield shear strength of the soil; $\tau_{driving}$ = static driving shear stress obtained from limit equilibrium analysis; $\tau_{avg,seismic}$ = average seismic shear stress obtained ground response analysis or the following equation from Seed and Idriss (1971), defined below; and τ_{other} = any other shear stress obtained from an appropriate method. The simplified Seed and Idriss (1971) equation to estimate average seismic shear stress is defined as:

$$\tau^2_{avg,seismic} = 0.65\frac{a_{max}}{g}\pm\sigma_v r_d \Big/ MSF \qquad \textbf{Eq. 5.2}$$

where a_{max} = peak surface ground acceleration; σ_v = total vertical stress; r_d = depth reduction factor to account for soil column flexibility; and MSF = magnitude scaling factor. The terms r_d and MSF used in this study are those proposed in Youd et al. (2001) and adopted by Olson and Stark (2003) for consistency with the latter study.

5.3 Existing Liquefaction Triggering Methods

Several procedures are available to evaluate the triggering of liquefaction in ground subjected to static stresses (or generically, sloping ground). These procedures are: (1) the strain comparison method (Poulos et al. 1985a,b; Poulos 1988; Castro 1994); (2) using correction factors for sloping ground and high effective stresses to modify level ground liquefaction resistance to sloping ground conditions (Seed and Harder 1990; Harder and Boulanger 1997; Idriss and Boulanger 2006); (3) using finite element

methods involving constitutive models of sandy soils (e.g., Byrne 1991; Byrne et al. 1992); and (4) the yield strength ratio approach (Olson 2001; Olson and Stark 2003; Olson et al. 2006). Following sections briefly describe these procedures.

5.3.1 Strain Comparison Method

Poulos et al. (1985a) introduced a procedure where shear strain (or deformation) induced by static or seismic loading is compared with the shear strain required to trigger undrained strain softening (or liquefaction). Poulos et al. (1985b) and Poulos (1988) reasoned that contractive, non-plastic soils are unable to withstand any induced shear strain because of the small level of shear strain required to trigger liquefaction (typically 1.5% shear strain or less); therefore, any disturbance is likely to trigger liquefaction. However, soils with some plasticity can accommodate a finite shear strain prior to reaching their yield (or peak) strength. In order to determine the shear strain induced by static or seismic loading series of laboratory tests need to be performed that can be expensive and time consuming. Further, as stated by Poulos et al. (1985b) and Poulos (1988) that shear strains measured in laboratory do not necessarily correspond shear strains induced in field by static or seismic loading especially for non-plastic soils. This procedure was further elaborated by Castro (1994).

Sample disturbance during sampling and reconsolidation results in considerable uncertainty when using laboratory tests to evaluate liquefaction (Terzaghi et al. 1996)(). To conduct high quality cyclic simple shear testing on relatively undisturbed sampling, expensive and careful handling is required and the tests are also expensive to perform. Cyclic triaxial testing, on the other hand, poorly represents the loading conditions experienced in the field, at least under level ground conditions (Cetin et al. 2004). A relatively undisturbed sample that can reasonably mimic in situ response can however be obtained by use of appropriate “frozen” sampling techniques followed by laboratory testing in cyclic simple shear apparatus. Of course, this procedure requires careful handling during freezing and thawing so that the expansion of the pore water upon

freezing and its contraction upon thawing are accommodated by pore water flow rather than by volumetric straining of the soil structure (Idriss and Boulanger 2008). The cost and level of difficulty to carry out these tests however restrict such testing to large, high profile projects only.

5.3.2 Correction Factors Applied to Level Ground Liquefaction Analysis

Seed et al. (1985) presented an SPT-based level ground liquefaction analysis that employs liquefaction resistance curves for sands with different $(N_1)_{60}$ values and with different fines contents. Seed (1983) and Rollins and Seed (1988) proposed correction factors, K_α, that can be used to modify the level ground liquefaction resistance to account for static shear stresses, which are expressed in terms of $\alpha = \tau_h/\sigma'_v$. Seed (1983) also proposed a correction factor, K_σ for high effective stress conditions (greater than the 50 to 100 kPa effective vertical stresses typical for level ground liquefaction cases).

Seed and Harder (1990) updated these correction factors and incorporated them into a liquefaction triggering analysis for ground subjected to a static shear stress. This method was later updated by Harder and Boulanger (1997), Boulanger (2003), Idriss and Boulanger (2004) and Idriss and Boulanger (2006). Despite the refinements, the data used to develop these corrections and equations exhibit large scatter and hence produce considerable uncertainty when applied in liquefaction triggering analysis. Furthermore, as illustrated by Terzaghi et al. (1996), aging effects also can cause significant uncertainty in interpreting triggering of liquefaction.

5.3.3 Finite Element Methods

Finite element methods to evaluate triggering and post-triggering response of contractive soils rely on constitutive stress-strain models to mimic soil response. Early work by Byrne (1991) indicated that the Newmark (1965) method can be adapted to

estimate liquefaction-induced displacements. However, instead of using a rigid block concept which reflects a constant shear strength and stiffness, Byrne (1991) incorporated the stiffness of the liquefied layer as well as its residual strength. Byrne et al. (1992) and Byrne and Jinto (1992) used finite element code SOILSTRESS, developed by Byrne and Janzen (1981), to estimate the liquefaction-induced deformation of Lower and Upper San Fernando dam. The proposed method is based on the assumption that the strains to trigger liquefaction are small (<1%) and can be neglected when compared to the shear strains (20 to 50%) that are commonly required to mobilize the liquefied shear strength.

Later, Beaty (2001) introduced a simple numerical approach based using a constitutive model UBCsand developed by Byrne et al. 1995 and implemented in the finite-difference code (FLAC). Beaty (2001) termed this the "synthesized approach" because it incorporates analyses for liquefaction triggering, post-triggering stability (flow slide analysis), and limited deformation analysis (in the case that a flow slide is not triggered).

Numerical analyses using UBCsand can perform triggering and post-triggering analyses, as well as estimate liquefaction-induced deformation. However, it is difficult to validate such analyses using field case histories because the soil conditions and input motion are seldom known with sufficient accuracy to properly calibrate the constitutive stress-strain model and properly excite the finite element model. Even with the best-documented case histories (Upper and Lower San Fernando dams during the 1971 San Fernando earthquake), considerable uncertainties remain regarding the constitutive model calibration and loading conditions (Byrne et al. 2004).

5.4 Back-Analysis of Flow Failure Case Histories

The author analyzed 31 reasonably-documented case histories of liquefaction-induced damage to earth dams, tailings dams, and natural slopes. The case histories are divided into two categories: (1) statically-induced failures; and (2) seismically-induced

failures. As explained in Chapter 2, only cases that failed under static loading can be used to reasonably back-calculate the yield shear strength and strength ratio because the shear resistance mobilized at the time of failure corresponds directly to the yield shear strength envelope.

All the cases in this study were analyzed by limit equilibrium to back-calculate the mobilized shear stress and stress ratio. Limit equilibrium types of analyses for assessing the stability of earth slopes have been in use in geotechnical engineering for many decades. Slope/W (GeoStudio 2004) was used for all limit equilibrium analyses in this study. The software is user-friendly, accepts stress ratios as well as strength as inputs, and yields repeatable results. The software offers several slope stability methods, including the Ordinary or Fellenius (1936) method; Bishop's (1955) simplified and generalized methods; Janbu's (1954) simplified and generalized methods; Spencer's (1967) method; the Morgenstern and Price (1965) method; the Corps' of Engineers (1970, 1982) method, and the Lowe and Karafiath (1960) method. Not all methods are accurate; however methods which satisfy all conditions of equilibrium give accurate results for all practical conditions. Despite some required assumptions, the Morgenstern-Price, Spencer, and Janbu generalized procedures are regarded as the most reasonable because they satisfy force and moment equilibrium simultaneously. These methods yield values of FS that differ by no more than ± 5% from the correct answer (Duncan and Wright 1980). This study used the Spencer method for back-analysis of all case histories.

Some cases (cases 3, 4, 25 and 30 in Table 5. 1) showed limited deformation with no unequivocal liquefaction manifestation. As a result, it was possible that the observed deformations resulted from inertial forces. To evaluate whether the observed deformation had resulted from liquefaction, the author performed pseudo-static analyses for these cases. To calculate the yield accelerations, limit equilibrium analyses using Slope/W were conducted. A pseudo-static seismic coefficient was applied and varied until a FS of unity was achieved. A Newmark (1965) sliding block analysis was then conducted using the software developed by Jibson and Jibson (2005). The software contains a large

database of ground motions. Ground motions for the Newmark analysis of a given case was selected using the criteria summarized in Olson and Johnson (2008).

The case histories evaluated in this study are summarized in Table 4.3 (Chapter 4). References for each of the cases are included in this table. The mobilized shear stresses and stress ratios back-calculated for each of these cases are reported in Table 5. 1. Representative penetration resistances and information related to soil properties, such as fines content, are listed in Table 4.3 (Chapter 4). Data reported in these tables are analyzed in the following sections. Detailed discussion for each case is given in Appendix A, including discussion of Newmark analyses conducted for select cases.

5.5 Yield Shear Strength, Yield Strength Ratio, and Yield Strength Envelope

As discussed previously, the shear strength and strength ratio mobilized at the triggering of liquefaction are equal to the yield shear strength and yield strength ratio, respectively, for flow failures triggered by static loading. In this study, six cases of static loading-induced liquefaction flow failure (case histories no. 6, 12, 21, 22, 23 and 24 in Table 5. 1) had sufficient information to conduct back-analysis. Figure 5.1 includes the boundaries of yield strength ratio proposed by Olson (2001). The range of $s_u(\text{yield})/\sigma'_{vo}$ from 0.231 to 0.306 were based on the back-analysis of five statically-induced flow failure cases and four deformation-induced flow failure cases. Mobilized shear stresses and stress ratios back-calculated from deformation-induced case histories may be less than the yield shear strengths and strength ratios, respectively. However, if the pre-failure shear stress and shear stress ratio were close to the yield strength envelope, then only small deformation is needed to trigger liquefaction and the mobilized shear stress and stress ratio will be close to the yield shear strength and strength ratio.

The pre-seismic shear stress seismically-induced flow failures from this study and from Olson (2001) are also presented in Figure 5.1. As illustrated in the figure,

dynamically-loaded cases generally plotted close to or below the yield strength envelope. Cases that plot below the yield strength envelope simply illustrate that the structures were stable prior to the causative earthquake. A few seismic cases pre-seismic shear stress plot above the yield strength envelope. There are at least two possible reasons for this to occur:

(1) because the structures likely were constructed under drained conditions and the drained strength envelope is generally higher than the (undrained) yield strength envelope for contractive soils, these structures were stable under drained conditions, but highly unstable under undrained conditions; and

(2) as discussed in a subsequent section, soil subjected to a static (drained) shear stress will mobilize an (undrained) yield strengths larger than that mobilized by a soil where construction was under undrained conditions (i.e., where void ratio changes associated with drained, construction-induced shear stresses do not occur).

Figure 5.2 compares the seismic cases only, (analyzed in this study and by Olson 2001) with the yield strength envelope from Figure 5.1. Each data pair represents the pre-failure static shear stress (lower point) and the combined static and seismic shear stresses (upper point). The seismic shear stress increment was calculated using Figure 5.1 and Eq. 5.1. As illustrated in the Figure 5.2, all the combined static and seismic shear stresses plot above the yield strength envelope, suggesting that liquefaction was likely to be triggered in each of these cases. However, as discussed in a subsequent section, these data can be used to better define yield strength ratios for cases subjected to static shear stresses. Figure 5.3and Figure 5.4 show the static and deformation cases analyzed in this study and in Olson (2001) on relationship developed by Olson and Zitny (2012). As shown in Figure 5.3and Figure 5.4 the data is reasonable within the proposed range.

5.6 Yield (and Mobilized) Strength Ratio and Penetration Resistance

Olson (2001) speculated that the range of yield strength ratios (from 0.236 to 0.306) varied proportionally with penetration resistance. That is, contractive soils with higher penetration resistance will exhibit higher yield shear strength ratios. To examine this postulate, Figure 5.5 presents best estimates of yield shear strength ratios and overburden stress-normalized SPT blow count for static loading-induced and deformation-induced flow failure case histories documented in this study and in Olson (2001). Similarly, Figure 5.6 presents best estimates of yield shear strength ratios and overburden stress-normalized CPT tip resistance for static loading-induced and deformation-induced flow failure case histories documented in this study and in Olson (2001).

Figure 5.5 and Figure 5.6 include the SPT-based and CPT-based yield strength ratio relationships, respectively, proposed by Olson (2001) and Olson and Stark (2003). As illustrated in figures, the Olson (2001)/Olson and Stark (2003) relationships reasonably envelope most of the static-load and deformation-induced flow failure case histories. The Nerlerk berm case histories back-analyzed by Olson (2001) were excluded from this comparison because as reported by Rogers et al. (1987), it is likely that this flow failure was triggered chiefly by straining of a soft clay layer in the foundation. This induced sufficient shear strains in the sand-fill berm to trigger flow liquefaction. However, at the time of failure, the slopes of the sand berm were relatively flat and likely below their yield strength envelope.

Figure 5.5 and Figure 5.6 repeat Figure 5.3 and Figure 5.4, but include the seismically-induced flow failure case histories where SPT and CPT data were available, respectively. Largely, these cases plot below the yield strength ratio boundaries proposed by Olson (2001) and Olson and Stark (2003). As anticipated, the seismically-induced flow failure case histories plot within, above, and below the Olson (2001)/Olson and Stark (2003) relationship for statically-induced flow failures. This occurs because the embankments and slopes that failed during earthquakes were stable under gravity (i.e.,

static) loads. These structures may have been constructed under drained conditions (where the limiting strength is based on the effective stress (drained) friction angle, or may have been constructed under partially-drained or undrained conditions that did not exceed the (undrained) yield strength envelope (i.e., the yield friction angle). The following section examines these cases using the procedures proposed by Terzaghi et al. (1996) and Olson et al. (2006).

5.7 Seismic Case Histories Confirming Yield Strength Envelope

Olson et al. (2006) analyzed yield strength ratio data for a large number of sands tested under isotropic and anisotropic conditions in triaxial compression, torsional shear/triaxial compression, direct simple shear, and ring shear. These data demonstrated that yield strength ratio tends to increase as static stress ratio increases above values of $\tau_{static}/\sigma'_{vo} > 0.2$. Based on these data, Olson et al. (2006) proposed an updated version of Olson (2001)/Olson and Stark (2003) yield strength ratio relationship. The proposed family of yield strength ratio relationships is presented in Figure 5.7. This figure illustrates yield strength ratio relationships for values of $\tau_{static}/\sigma'_{vo}$ between $s_u(liq)/\sigma'_{vo}$ and 0.2, 0.3, 0.4, and 0.5. The initial relationship is limited to values of $\tau_{static}/\sigma'_{vo} > s_u(liq)/\sigma'_{vo}$ because this is a prerequisite for flow liquefaction to occur.

Olson et al. (2006) performed finite element analyses to more accurately compute static shear stress ratios along the critical failure surface determined from limit equilibrium analysis. The seismic shear stress ratio applied to each segment of the critical failure surface within the zone of liquefiable soil was computed using Eq. 5.2. The cases analyzed by Olson et al. (2006) involved only those cases that were subjected to relatively modest strengths of shaking. As concluded by Olson et al. (2006), the combined static and seismic shear stress ratios exceeded the yield strength ratio for each of these cases, resulting in $FS_{triggering} < 1$ using Eq. 5.1, and suggesting that liquefaction would be triggered for each of the 10 case histories.

Laboratory tests performed at the University of Illinois suggest that the yield strength ratio relationships proposed by Olson et al. (2006) may be slightly unconservative at higher penetration resistances (Olson and Zitny 2012). Olson and Zitny (2012) proposed revised yield strength ratio relationships. The CPT-based, static shear-dependent yield strength ratio relationships can be estimated using the following expression:

$$\frac{s_u(yield)}{\pm'_{vo}} = \frac{\pm_{static}}{\pm'_{vo}} + \left(\frac{0.0034}{\frac{\pm_{static}}{\pm'_{vo}}} \right) q_{c1} \qquad \textbf{Eq. 5.3}$$

and the SPT-based relationships can be estimated using the following expression:

$$\frac{s_u(yield)}{\pm'_{vo}} = \frac{\pm_{static}}{\pm'_{vo}} + \left(\frac{0.0020}{\frac{\pm_{static}}{\pm'_{vo}}} \right) (N_1)_{60} \qquad \textbf{Eq. 5.4}$$

This study provided the opportunity to perform a more comprehensive evaluation of the yield strength ratio relationships reported in Eq. 5.3 and Eq. 5.4, as well as yield strength ratio relationships proposed by Mesri (2007). To evaluate the proposed yield strength ratio relationships, case histories with similar static stress ratios were grouped together and compared to the corresponding yield strength ratio relationship. If the combined static and seismic shear stress ratios exceeds the yield shear strength ratio, liquefaction is predicted to occur (i.e., $FS_{triggering}$ is less than unity).

The Olson and Zitny (2012) yield strength ratio relationships are first compared to available static load-induced and deformation-induced failures in Figure 5.8 and Figure 5.9. While the Olson and Zitny (2012) yield strength ratio relationships are slightly larger than the average relationship from Olson (2001)/Olson and Stark (2003), the updated relationship reasonably follows the case history data.

The seismically-induced flow failure case histories were grouped into static shear stress ratio intervals of $\tau_{static}/\sigma'_{vo} \leq 0.2$, 0.2 - 0.22, 0.22 - 0.24, 0.24 - 0.26, 0.26 - 0.28 and 0.28 – 0.30. Figure 5.10 presents the static shear stress ratios and combined static and seismic shear stress ratios for cases with $\tau_{static}/\sigma'_{vo} \leq 0.2$. Although most of the cases plotted well above the yield envelope after the addition of seismic increment, two case histories plot close to the yield strength ratio relationships proposed by Mesri (2007) and Olson and Zitny (2012), although the Mesri (2007) relationship is slightly more conservative, particularly at higher penetration resistance values. Figure 5.11 presents seismically-induced cases with $\tau_{static}/\sigma'_{vo} = 0.2 – 0.22$. Again, both yield strength ratio relationships capture the seismic case histories, but the Mesri (2007) is more conservative. Similarly, Figure 5.12, Figure 5.13, Figure 5.14 and Figure 5. 15 present the seismically-induced flow failure cases for $\tau_{static}/\sigma'_{vo} = 0.22 – 0.24$, 0.24 – 0.26, 0.26 – 0.28, and 0.28 – 0.30 respectively. No case histories plotted near the yield strength ratio relationships for $\tau_{static}/\sigma'_{vo} = 0.28$; however, its location could be inferred based on the other envelopes. Case histories with $\tau_{static}/\sigma'_{vo} = 0.22$, 0.24 and 0.26 suggest that the Mesri (2007) is more conservative than that proposed by Olson and Zitny (2012). Based on these data, the Olson and Zitny (2012) relationship appears to reasonably account for increases in yield strength ratio with increases in penetration resistance and static shear stress ratio. Therefore, these relationships (i.e., Eq. 5.3 and Eq. 5.4) are recommended for use in practice.

5.8 Mode of Shear Effect on Yield Shear Strength

In general, sands sedimented on level ground under gravity, both in the field and in the laboratory, exhibit anisotropic fabrics, with slightly oblong particles sedimenting with their long axis perpendicular to the direction of gravity (Oda 1972; Oda et al. 2001). This anisotropic fabric produces greater resistance to axial compression as shearing occurs at a high angle to the bedding plane where particle interlocking is most effective. In contrast, shearing parallel to the bedding plane or in extension more readily breaks down particle interlocking and the resulting resistance is lower (Terzaghi et al. 1996). In

other words, the soil response will be more dilative if it is subjected to compression vertically (nearly perpendicular to the bedding plane) and will be more contractive if it is subjected to shearing horizontally (parallel to the bedding plane). During the failure of an embankment on liquefiable soil or of an embankment constructed of liquefiable soil, the liquefiable soil may be subjected to multiple modes of shear, as illustrated in Figure 5.16, including triaxial compression (TxC), triaxial extension (TxE), and direct simple shear (DSS).

For some time, investigators have studied the dependence of mobilized undrained peak shear strength on the mode of shearing. For example, Hanzawa (1980) plotted various undrained strengths, s_u(TxC), s_u(TxE), and s_u(SS) of a sand from strain- and stress-control tests versus vertical consolidation stress (see Figure 5.17). The test results show that for a given value of vertical consolidation pressure, undrained peak shear strengths obtained from triaxial compression are the highest, while undrained peak strengths from simple shear and triaxial extension are 62% and 21%, respectively, of the values in TxC. Similarly, Yoshimine et al. (1998) conducted undrained monotonic TxC and TxE tests on Toyoura sand and found that the shear behavior was more contractive in triaxial extension than in triaxial compression. This difference suggests that the stress conditions, such as the direction of the principal stress and the magnitude of the intermediate principal stress affect the undrained behavior of sand. Laboratory tests conducted by other investigators (e.g. Yamada and Ishihara 1981; Vaid et al. 1990; Nakata et al. 1998; Uthayakumar and Vaid 1998; Yoshimine and Ishihara 1998; Yoshimine et al. 1999; and Olson and Mattson 2008) showed similar results.

Liquefaction flow failure field case histories may represent multiple modes of shear, as shown schematically in Figure 5.16. Olson and Mattson (2008) compiled a large database of triaxial compression, direct simple shear/rotational shear, and triaxial extension test results and compared the yield shear strength measured from laboratory tests with those back-calculated field case histories. Olson (2001) analyzed 33 reasonably-documented liquefaction flow failure case histories that consisted of static loading-, deformation-, dynamic loading-, and seismic loading-induced cases. However,

as explained in Chapter 2, only static loading-induced liquefaction flow failure case histories provide a reasonable estimate of yield shear strength. Olson and Mattson (2008) indicated that three deformation-induced and dynamic loading-induced flow failures exhibited mobilized shear stress ratios close to the yield shear strength ratios. Combining these cases with the static loading-induced failures, they selected eight field case histories from the Olson (2001) case histories database for comparison. In the current study, the author collected 31 reasonably documented case histories. Out of these cases, six static loading-induced case histories were selected and plotted with the eight cases from Olson (2001) in Figure 5.18. As seen in Figure 5.18, the laboratory test data envelope the case histories data. Furthermore, these results confirm the results of Olson and Mattson (2008). As shown in the Figure 5.18, field cases fall within the bounds of DSS/RS, suggesting that it may be the most prevailing failure mode in the field.

5.9 Yield Strength Ratio as a Function of State Parameter

As explained in Chapter 2, state parameter (ψ) is the difference between in situ void ratio and critical state void ratio at the same effective stress. A negative value of ψ generally represents dilative soil behavior while a positive value of ψ suggests contractive behavior. Been and Jefferies (1985) suggested a correlation between yield strength ratio and ψ for Kogyuk 350 sand (see Figure 5.19). The data in Figure 5.19 show a reasonable relationship between yield strength ratio and ψ; however, Kogyuk sand exhibits relatively high undrained shear strengths compared to other sands (Been and Jefferies 1985).

Olson and Stark (2003) and Olson and Mattson (2008) collected a database of TxC, DSS and rotational shear (RS), and TxE tests on saturated, contractive sandy soils. The collected test data was divided into three typical soil responses: purely contractive (type A), contractive then dilative (type B), and dilative (type C). From these databases, the author plotted yield strength ratios versus state parameter for Type A tests only, as shown in Figure 5.20. As expected, a general increase in ψ is observed for decreasing

values of yield strength ratio. The Figure 5.20 also shows the effect of mode of shear on this relationship. For a given ψ value, TxE produces the lowest and TxC gives the highest yield strength ratios while yield strength ratios obtained from DSS-RS plots in the middle. Also in the Figure 5.20, triaxial and ring shear test results of Ottawa 20/40 (OT), Illinois River (IR) and Mississippi River (MR) sand conducted by Sadrekarimi (2009) are shown. As seen in the Figure 5.20 OT, IR and MR sands are plotting within the bounds of DSS and TxC defined by Olson and Stark (2003) and Olson and Mattson (2008). Soil data by Sadrekarimi (2009) also suggests a general decrease in yield strength ratio with increasing values of ψ.

As stated earlier, Olson (2001) back analyzed 33 and the author analyzed 31 reasonably documented case histories to estimate yield and liquefied shear strength ratios. Jefferies and Been (2006) estimated ψ for some of these case histories that are plotted in Figure 5.20 along with yield strength ratios back-calculated by Olson (2001) and this study. The case histories plotted within the bounds of DSS defined by Olson and Stark (2003) and Olson and Mattson (2008). A similar trend of decreasing yield strength ratios with an increase in ψ is observed for the case history data as well.

5.10 Summary and Conclusions

- There are three main procedures to estimate the undrained yield shear strength and undrained strength ratio of a contractive soil: (1) laboratory testing; (2) empirical correlations; and (3) finite element methods.
- Thirty-one reasonably-documented case histories were analyzed in this study and combined with the case histories studied by Olson (2001) to evaluate the yield shear strength ratio relationship based on Olson (2001) data.
- Only cases failed under static loading can reasonably estimate the yield shear strength of soil. Yield shear strength ratios from these cases ranged from 0.231 to 0.306 with an average value of 0.268. Furthermore, these cases reasonably agree with those presented by Olson (2001).

- The mobilized strength of slopes and embankments that failed under seismic loading do not necessarily corresponds to the yield strength at the time of triggering. Olson et al. (2006) suggested that the yield strength ratios are likely to be related to driving stress ratio and presented a family of curves to estimate yield strength ratio as a function of driving stress ratio. These curves were recently updated by Olson and Zitny (2012). The combined database of seismically-induced flow failures appear to support the Olson and Zitny (2012) yield strength ratio relationships.
- The yield shear strength depends on the mode of shear, with triaxial compression generally yielding the largest values, triaxial extension yielding the smallest values, and direct simple shear and ring shear yielding intermediate values. Case histories data from this study plot within the bounds of DSS-RS suggesting that it may be the prevailing mode of shear in the field.

5.11 References

Beaty, M.H. (2001). A synthesized approach for estimating liquefaction-induced displacements of geotechnical structures, *PhD dissertation*, University of British Columbia, Vancouver, B.C., Canada.

Been, K. and Jefferies, M.G. (1985). A state parameter for sands, *Geotechnique*, vol. 35, no. 2, p. 99 – 112.

Bishop, A.W. (1955). The use of the slip circle in the stability analysis of slopes, *Geotechnique*, Great Britain, vol. 5, no. 1, p. 7 – 17.

Byrne, P.M. (1991). A model for predicting liquefaction induced displacements, *Proceedings of the Second International Conference on Recent Advances in Geotechnical Earthquake Engineering and Soil Dynamics*, St. Louis, Vol. 2, p. 1027-1035.

Byrne, P.M., Salgado, F., and Jinto, H. (1992). Earthquake induced displacement of soil structure systems, *Proceedings of the Tenth World Conference on Earthquake Engineering*, Madrid, Spain, Vol. 3, p. 1407 – 1412.

Byrne, P.M., Park, S., Beaty, M., Sharp, M., Gonzalez, L., and Abdoun, T. (2004). Numerical modeling of liquefaction and comparison with centrifuge tests, *Canadian Geotechnical Journal*, vol. 41, iss. 2, p. 193 – 211.

Cetin, K.O., Seed, R.B., Der Kiureghian, A., Tokimatsu, K., Harder, L.F., Kayen, R.E. and Moss, R.E.S. (2004). SPT-based probabilistic and deterministic assessment of seismic soil liquefaction potential, *Journal of Geotechnical and Geoenvironmental Engineering*, ASCE, vol. 130, no. 12, p. 1314 – 1340.

Corps of Engineer (1970, 1982). Stability of Earth and Rock-Fill Dams, *U.S. Army Engineer Waterways Experiment Station,* Viksburg, MS EM 1110-2-1906.

Duncan, J.M. and Wright , S.G. (1980). The accuracy of equilibrium methods of slope stability analysis, *in Proceedings of the International Symposium on Landslides*, New Delhi, vol. 1, p. 247 – 254.

Fellenius, W., (1936). Calculation of the stability of earth dams, *in Proceedings of the 2nd Congress of Large Dams,* vol. 4, p. 445 – 463.

Hanzawa, H. (1980). Undrained strength and stability analysis for a quick sand, *Soils and Foundations,* vol. 20, no. 2, p. 17 – 29.

Harder, L.F. Jr. and Boulanger, R. (1997). Application of K_σ and K_α correction factors, *Proceedings of the NCEER Workshop on Evaluation of Liquefaction Resistance of Soils*, T.L. Youd and I.M. Idriss, eds., NCEER-97-0022, p. 167-190.

Idriss, I.M. and Boulanger, R.W. (2008). Soil liquefaction during earthquakes, *Monograph Series,* No. MNO-12, Earthquake Engineering Research Institue.

Janbu, N. (1954). Applications of composite slip surfaces for stability analysis, *in Proceedings of the European Conference on the Stability of Earth Slopes,* Stockholm, vol. 3, p. 39 – 43.

Jibson, R.W. and Jibson, M.W. (2005). Slope performance during an earthquake – Java Programs for using Newmark's method and simplified decoupled analysis to model slope performance during earthquakes. *USGS Open-File Report 03-005.*

Lowe, J., and Karafiath, L. (1960). Stability of earth dams upon drawdown. *Proceedings of the First PanAmerican Conference on Soil Mechanics and Foundation Engineering.* Mexican Society of Soil Mechanics, Mexico D.F., p. 537-552.

Mesri G. (2007). Yield strength and critical strength of liquefiable sands in sloping ground, *Geotechnique,* vol. 57, issue 3, p. 309 – 311.

Morgensterm, N.R., and Price, V.E., (1965). The analysis of the stability of general slip surfaces, *Geotechnique,* vol. 15, p. 79 – 93.

Olson, S. M. (2001). Liquefaction analysis of level and sloping ground using field case histories and penetration resistance, *Ph.D. Thesis,* University of Illinois at Urbana-Champaign, Urbana, Illinois.

Olson, S.M. and Stark, T.D. (2003). Use of laboratory data to confirm yield and liquefied strength ratio concepts, *Canadian Geotechnical Journal,* vol. 40, p. 1164 – 1184.

Olson, S. M., Sacks, A. L., Mattson, B. B., and Servigna, D. A. (2006). Role of static shear stress in liquefaction analysis of sloping ground, *Proceedings of the 8th US National Conference on Earthquake Engineering*

Olson, S.M. and Mattson, B.B. (2008). Mode of shear effects on yield and liquefied strength ratios, *Can. Geotechnical Journal,* vol. 45, p. 574 – 587.

Olson, S.M., and Johnson, C.I. (2008). Analyzing liquefaction-induced lateral spreads using strength ratios, *Journal of Geotechnical and Geoenvironmental Engineering,* ASCE, vol. 134, no. 8, p. 1035 – 1049.

Petterson, K.E. (1955). The early history of circular sliding surfaces, *Geotechnique,* vol. 5, p. 275 – 296.

Poulos, S.J., Castro, G. and France, W. (1985a). Liquefaction evaluation procedure, *Journal of Geotechnical Engineering,* ASCE, vol. 111, iss. 6, p. 772 – 792.

Poulos, S.J., Robinsky, E.I., and Keller, T.O. (1985b). Liquefaction resistance of thickened tailings, *Journal of Geotechnical Engineering,* ASCE, vol. 111, iss. 12, p. 1380 – 1394.

Poulos, S.J. (1988). Liquefaction and related phenomena, *Advanced Dam Engineering for Design, Construction, and Rehabilitation,* R.B. Jansen, ed., Van Nostrand Reinhold, New York, p. 292 – 320.

Sadrekarimi, A. (2009). Development of a new ring shear apparatus for investigating the critical state of sands, *PhD Thesis,* University of Illinois Urbana Champaign, p. 451.

Seed, H.B. and Idriss, I.M. (1971). Simplified procedure for evaluating soil liquefaction Potential, *Journal of the Soil Mechanics and Foundation Division*, ASCE, vol. 97, issue SM9, p. 1249-1273.

Seed, R.B. and Harder, L.F. Jr. (1990). SPT-based analysis of cyclic pore pressure generation and undrained residual strength, *Proceedings of H. Bolton Seed Memorial Symposium,* Bi-Tech Publishing Ltd., vol. 2, p. 351-376.

Spencer, E. (1967). A method of analysis of embankments assuming parallel inter-slice forces, *Geotechnique,* vol. 17, iss. 1, p. 11 – 26.

5.12 Figures and Tables

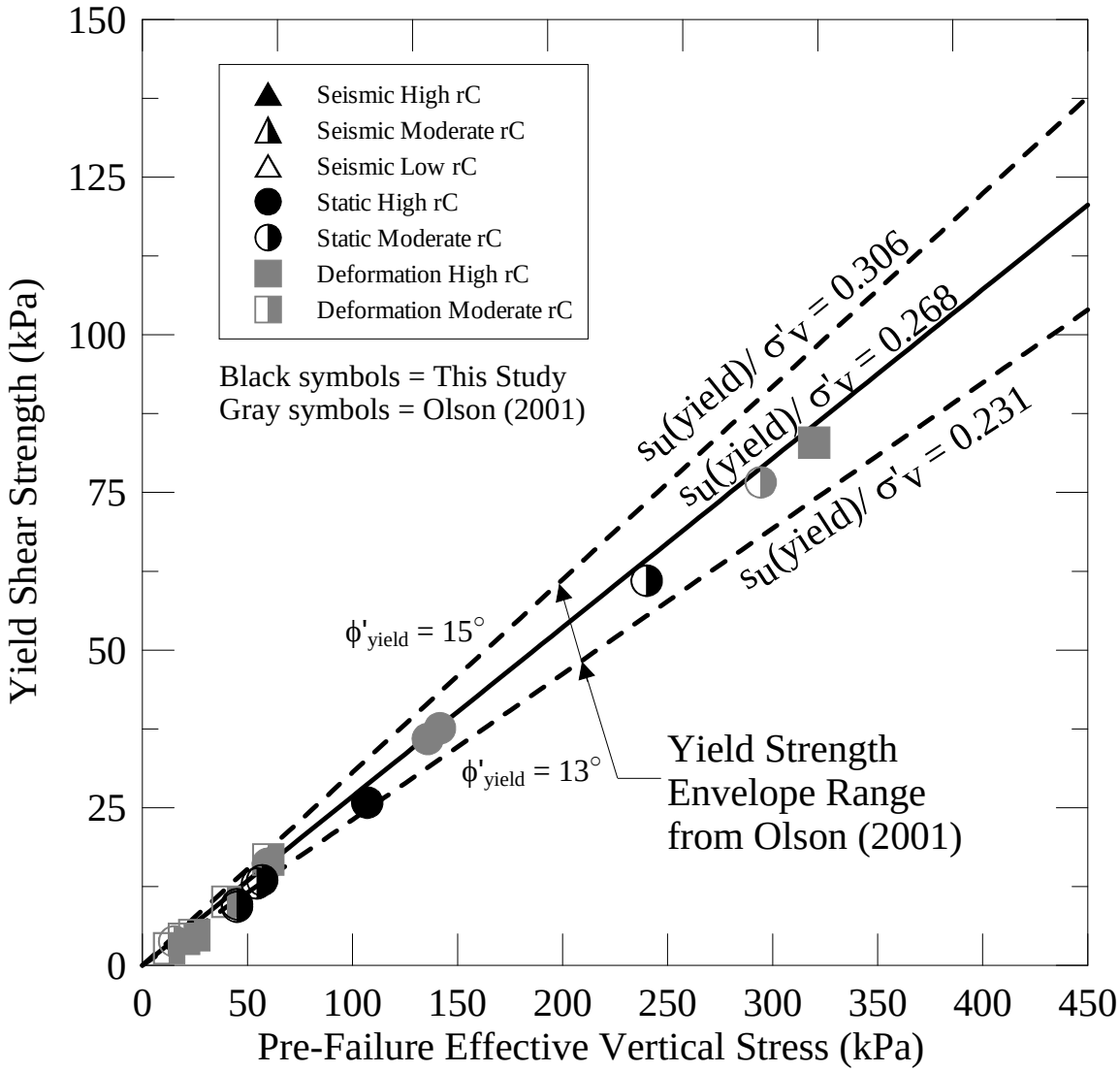

Figure 5.1 Comparison of yield and mobilized shear stress and pre-failure effective vertical stress for statically- and seismically-induced flow failure case histories analyzed in this study and in Olson (2001). Yield strength ratio boundaries proposed by Olson (2001) are included in the figure

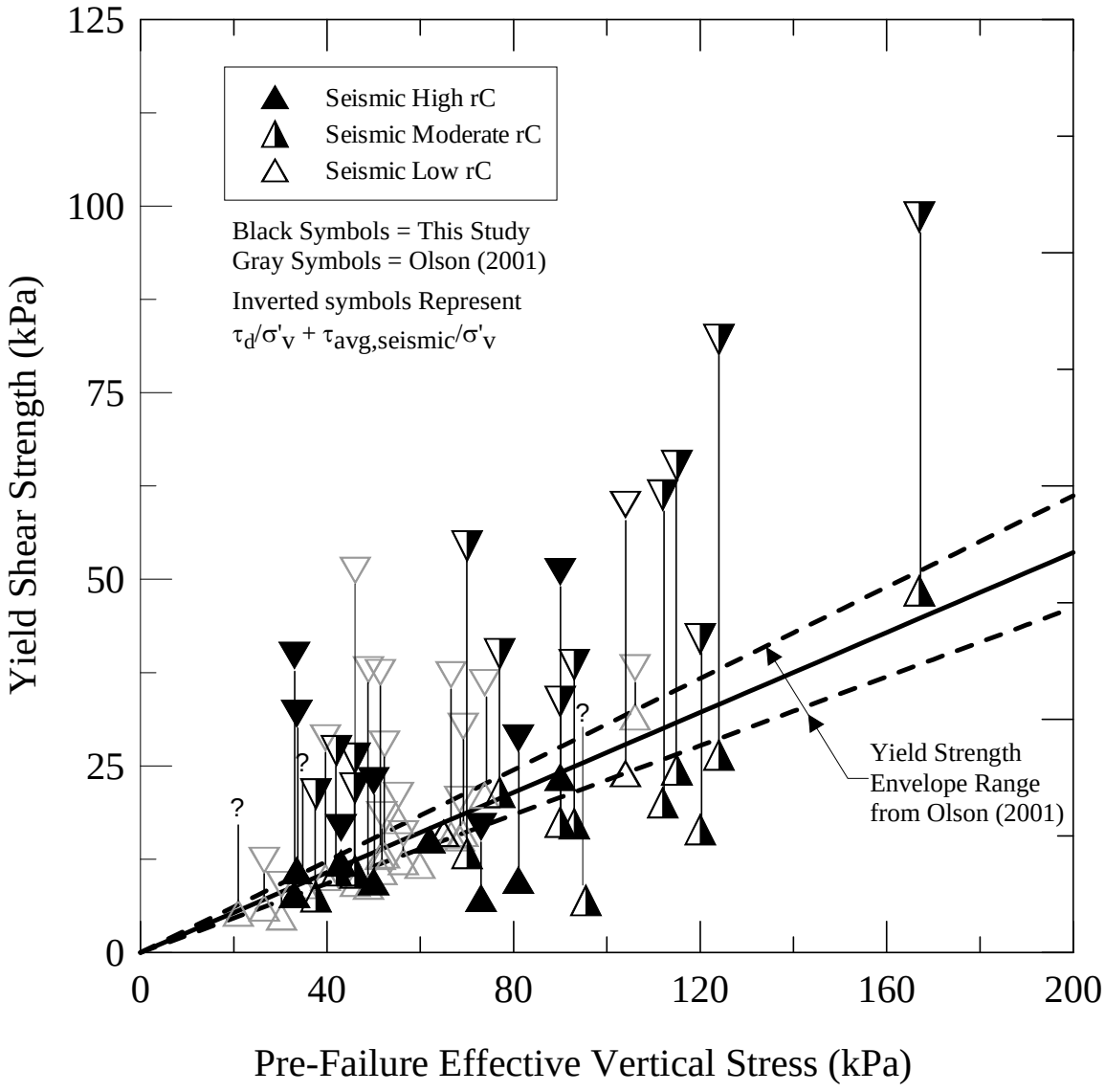

Figure 5.2 Comparison of combined static and seismic shear stresses for seismically-induced flow failures with yield strength envelope for cases analyzed in this study and in Olson (2001). The lower data point of each pair represents the pre-failure static shear stress and the upper data point represents the combined static and seismic shear stresses

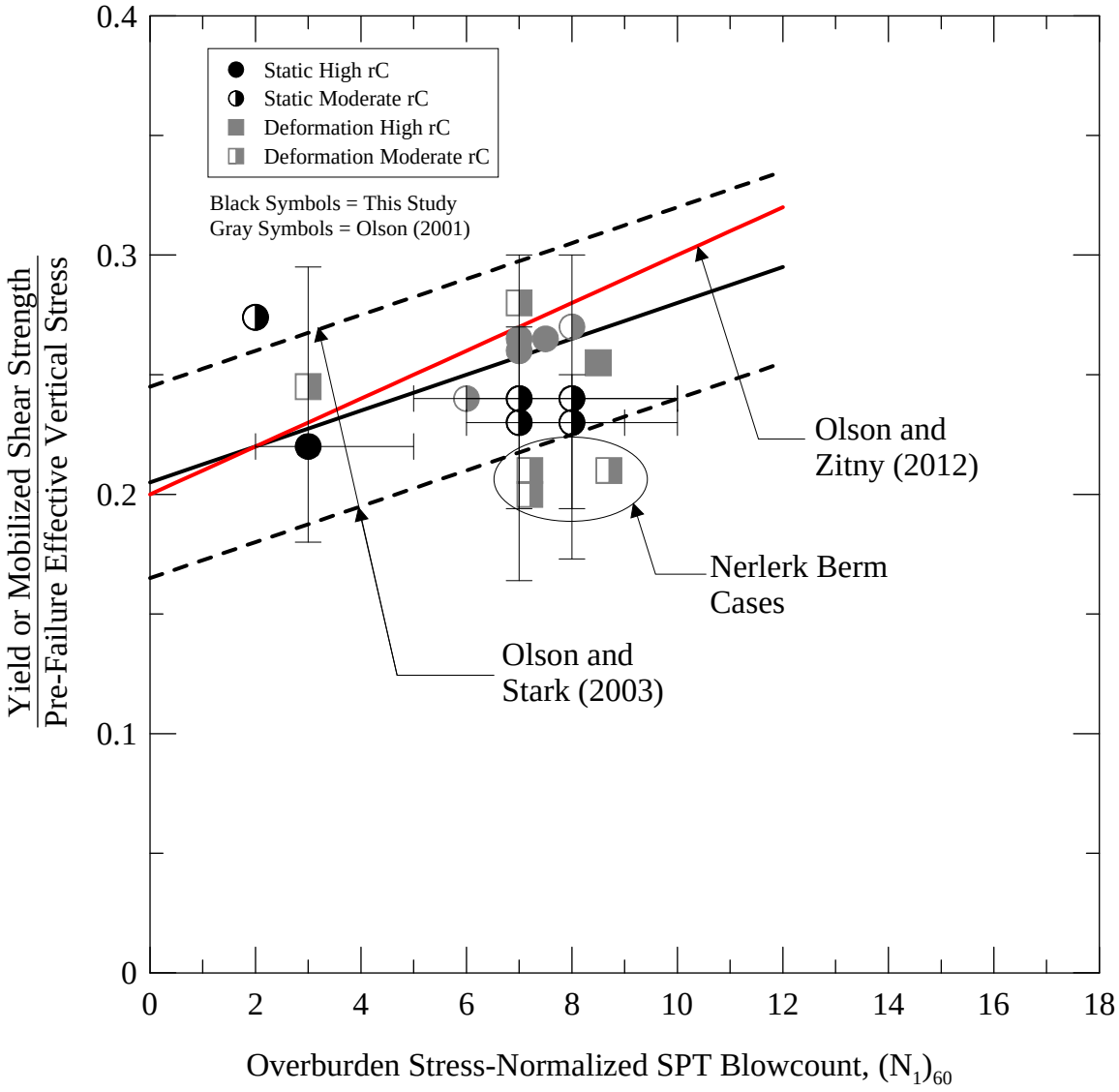

Figure 5.3 Comparison of yield or mobilized shear strength ratios with corrected SPT blow counts for static loading-induced and deformation-induced flow failure cases analyzed in this study and in Olson (2001)

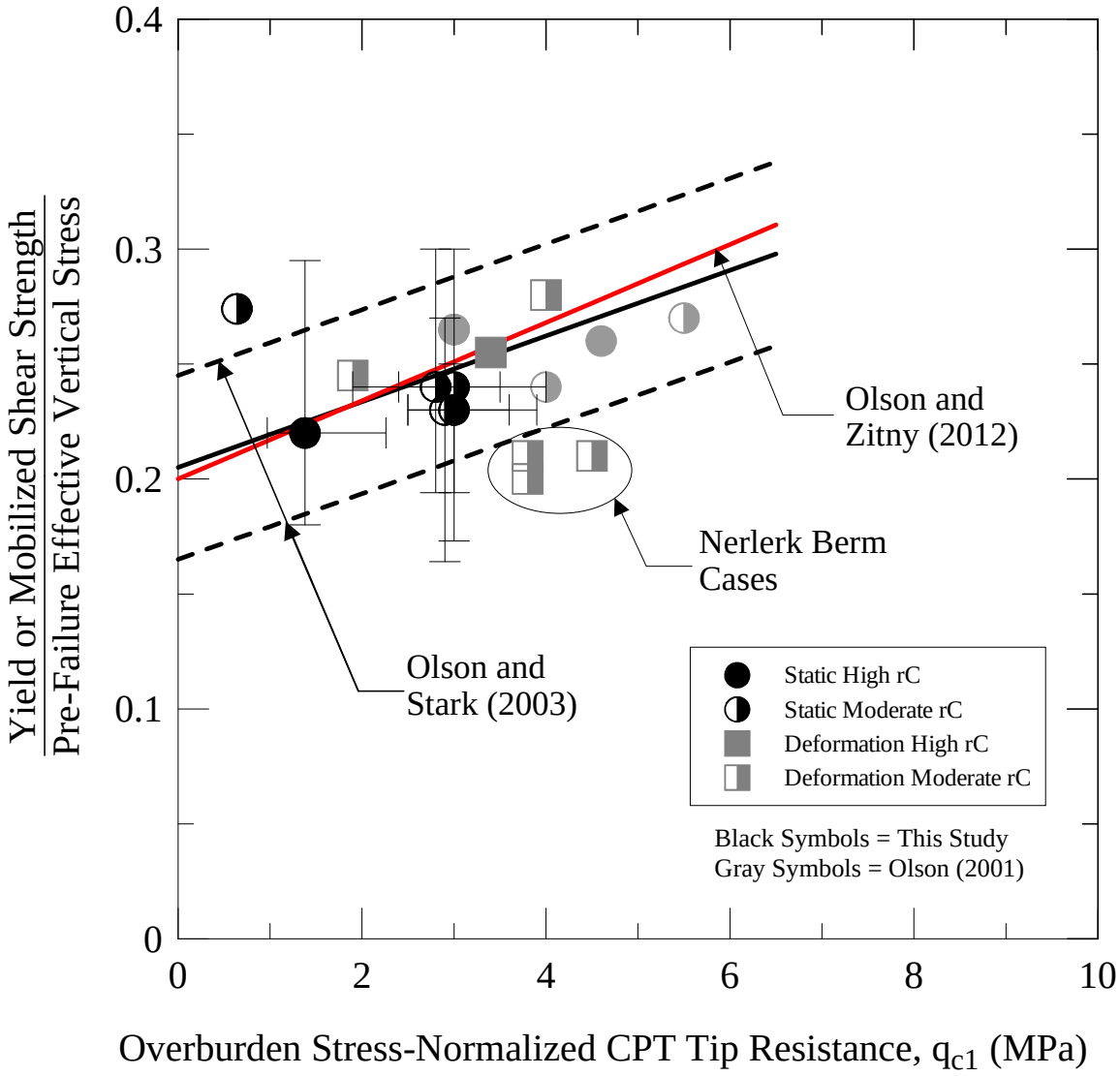

Figure 5.4 Comparison of yield or mobilized shear strength ratios with corrected CPT tip resistances for static loading-induced and deformation-induced flow failure cases analyzed in this study and in Olson (2001)

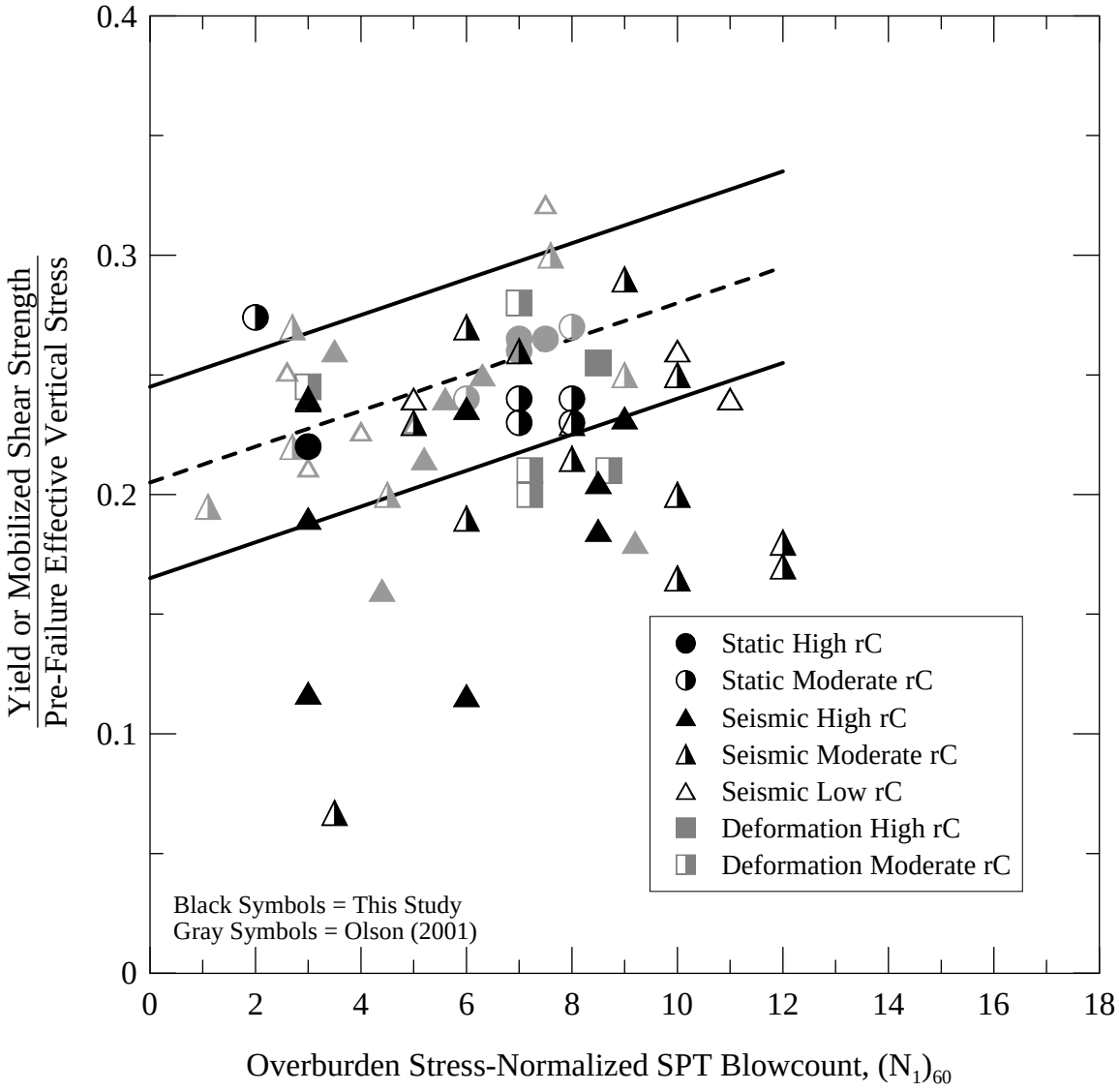

Figure 5.5 Comparison of yield and mobilized strength ratios and overburden stress-corrected SPT blow count for static loading-induced and deformation-induced liquefaction flow failures cases analyzed in this study and in Olson (2001) along with designated relative confidence levels

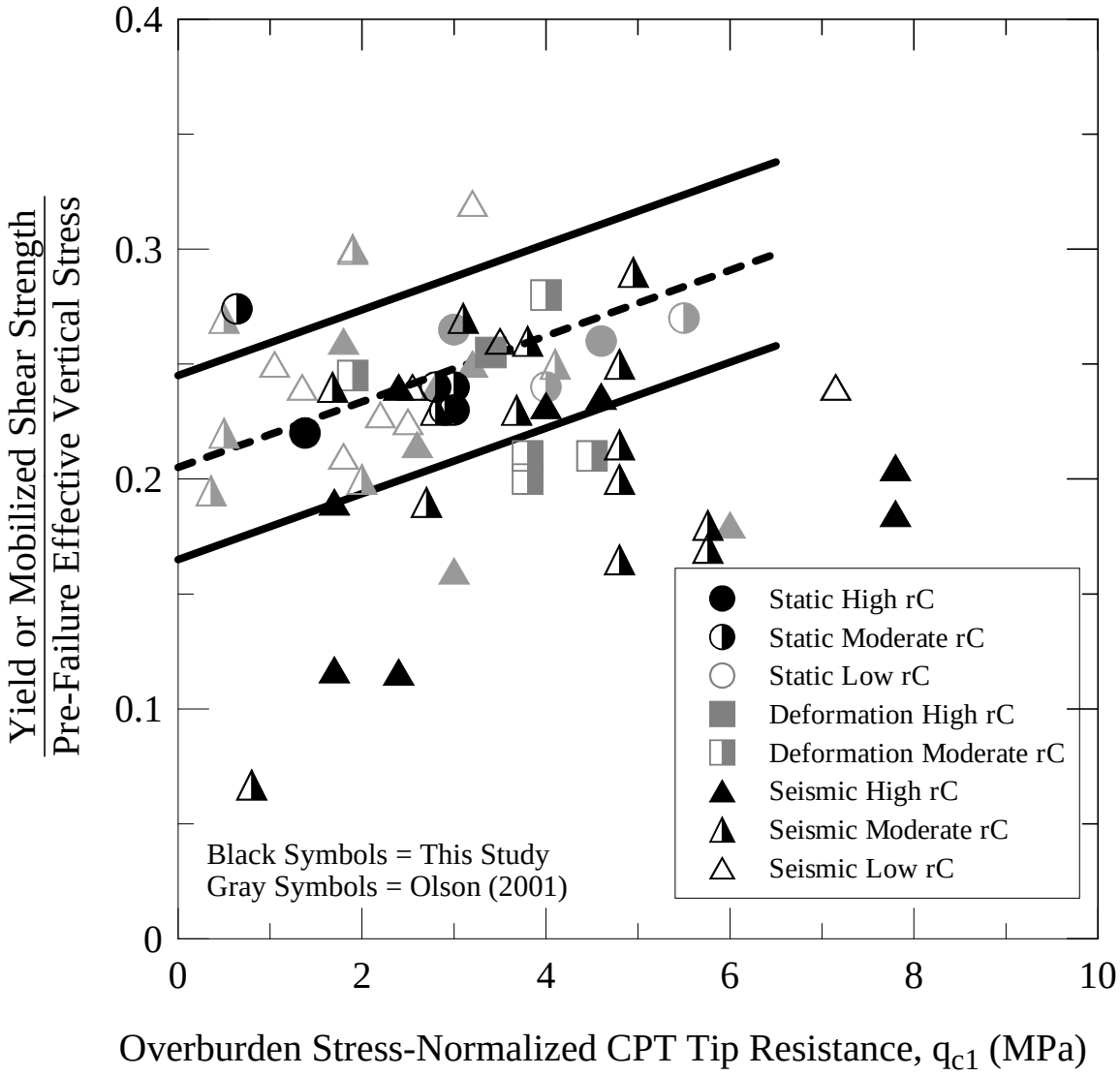

Figure 5.6 Comparison of yield and mobilized strength ratios and overburden stress-corrected CPT tip resistance for static loading-induced and deformation-induced liquefaction flow failure cases analyzed in this study and in Olson (2001) along with designated relative confidence levels

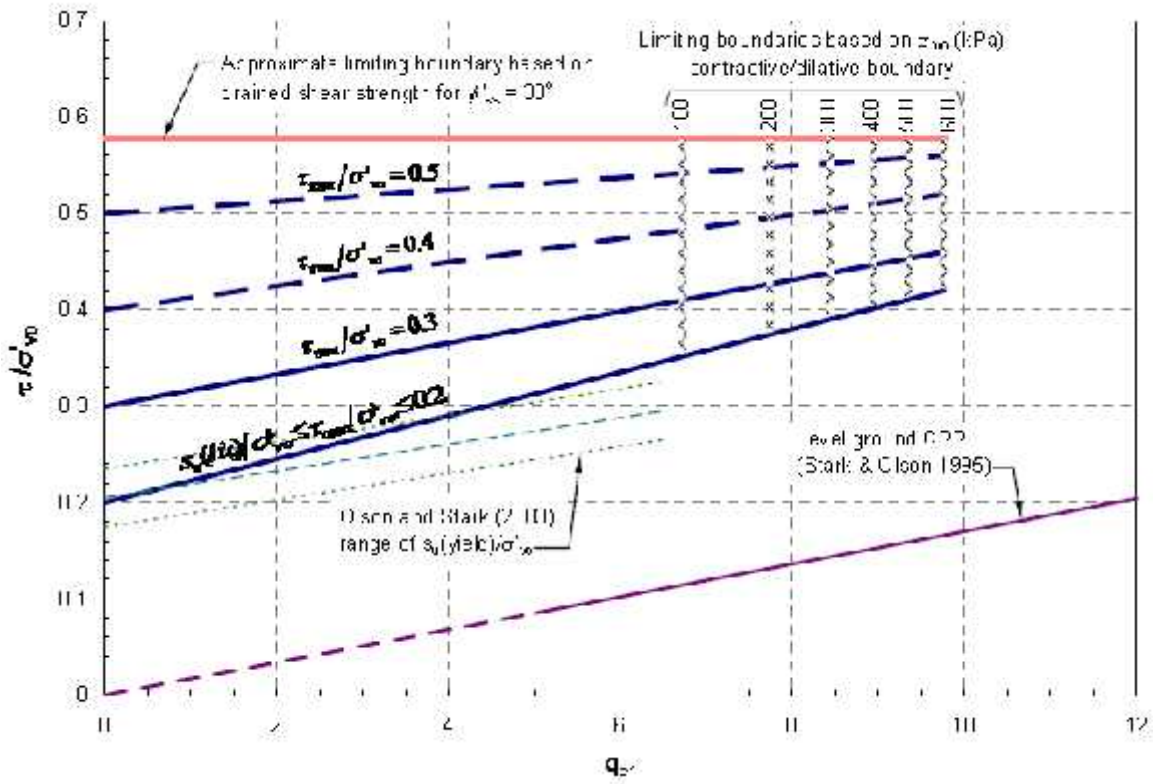

Figure 5.7 Relationships between yield strength ratios and CPT tip resistances for various static shear stress ratios (from Olson et al. 2006)

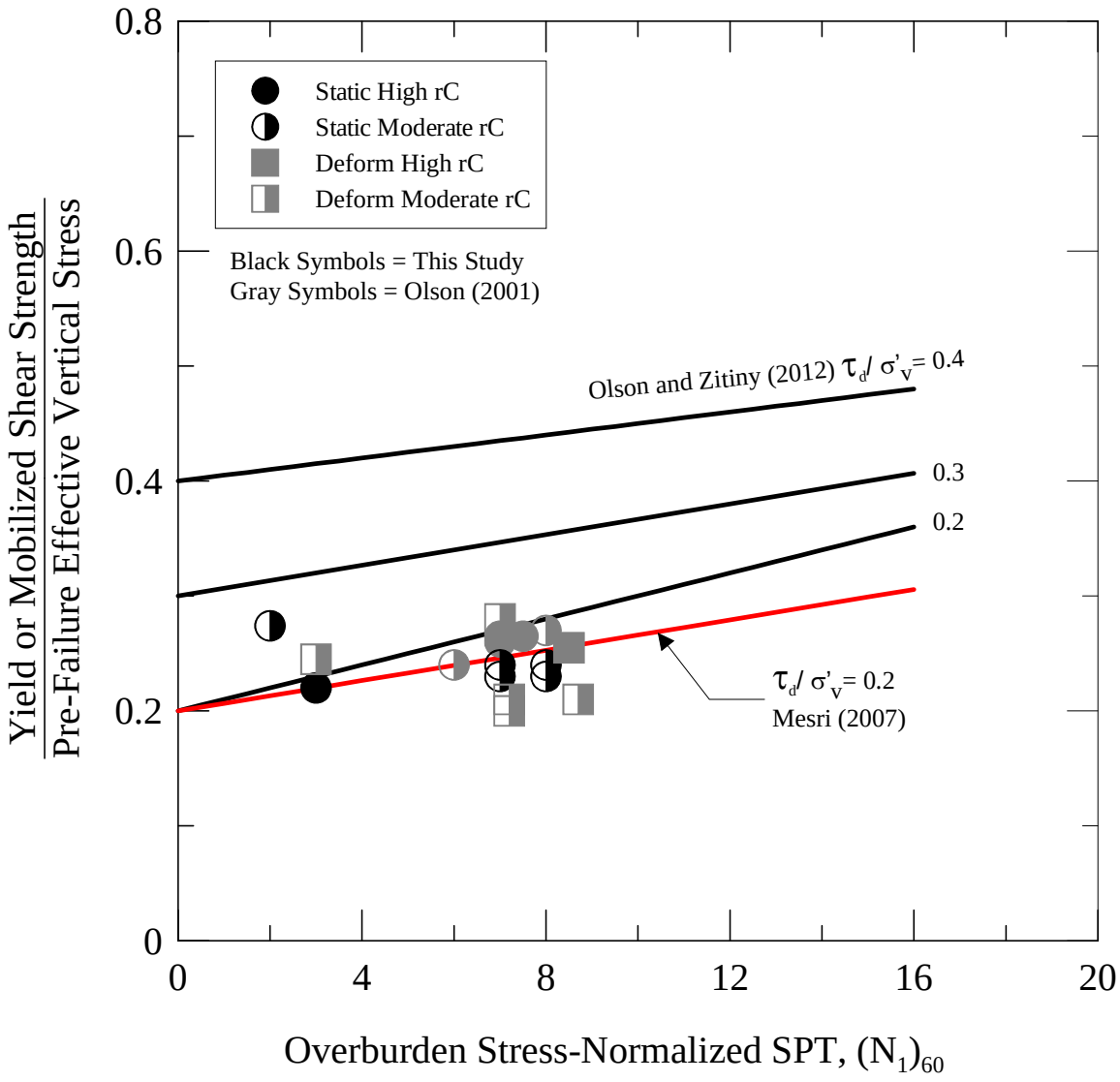

Figure 5.8 SPT-based yield strength ratio relationship proposed by Olson and Zitny (2012) with static and deformation-induced flow failure case histories analyzed in this study and in Olson (2001)

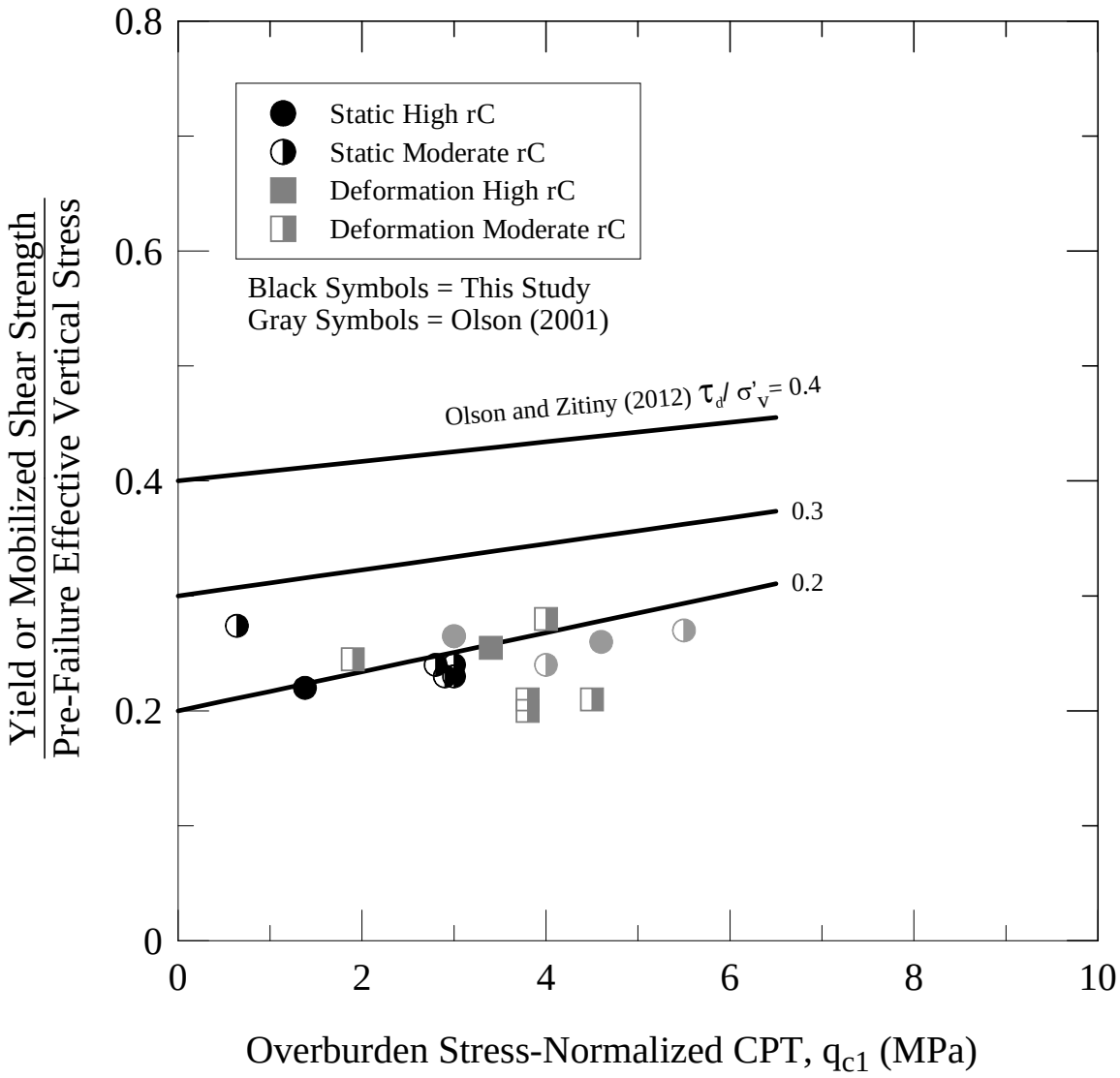

Figure 5.9 CPT-based yield strength ratio relationship proposed by Olson and Zitny (2012) with static and deformation-induced flow failure case histories analyzed in this study and in Olson (2001)

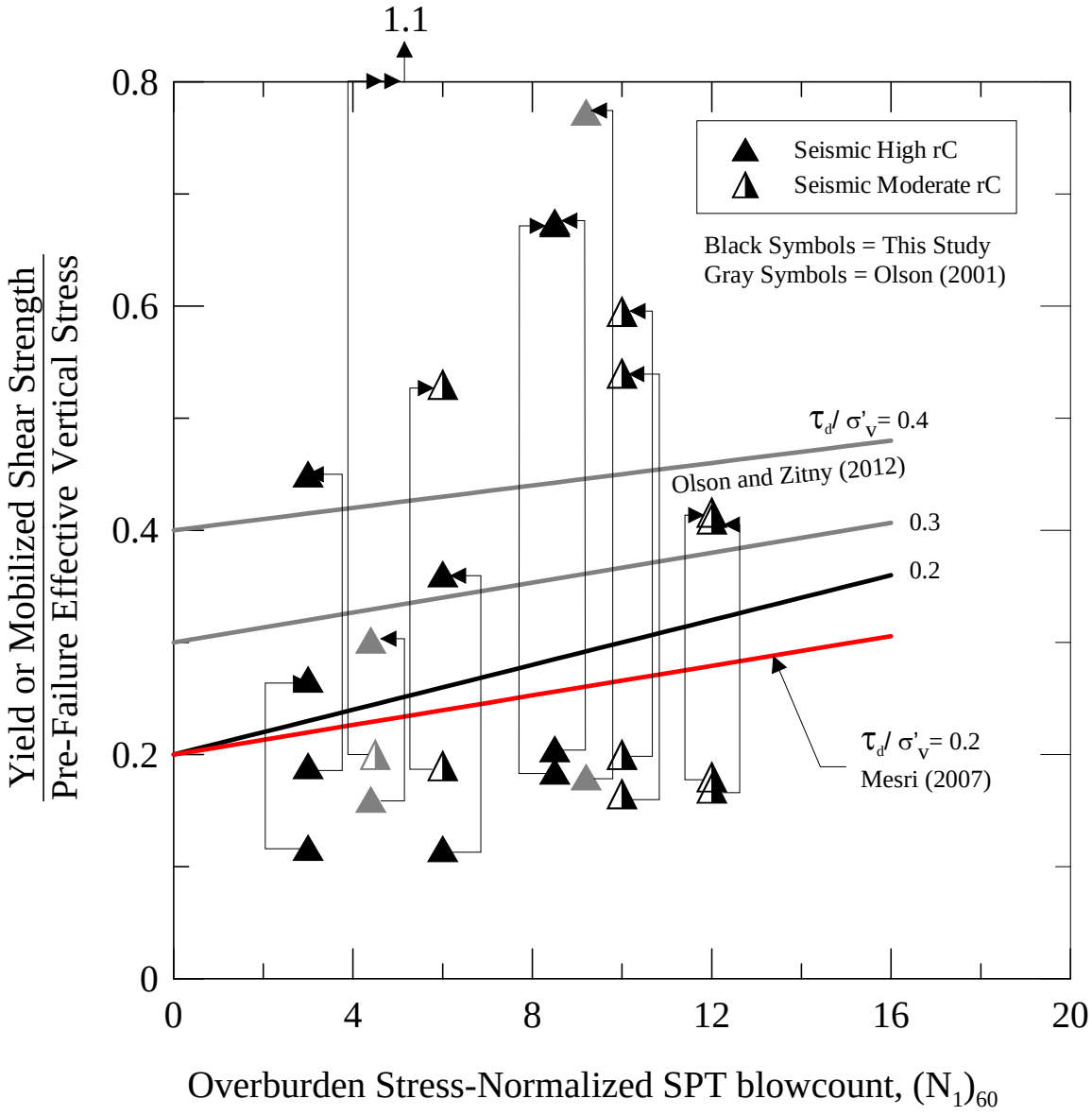

Figure 5.10 Comparison of combined static and seismic shear stress ratios for seismically-induced flow failures with $^{2}_{static}/\pm'_{vo} \leq 0.2$ with SPT-based yield strength ratio corresponding to $^{2}_{static}/\pm'_{vo} = 0.2$ from Olson and Zitny (2012) and from Mesri (2007). Symbols at the tail of arrows represent mobilized $^{2}_{static}/\pm'_{vo}$ back-calculated from prefailure geometry. Symbols at the head of arrows represent $^{2}_{static}/\pm'_{vo}$ + average $^{2}_{seismic}/\pm'_{vo}$

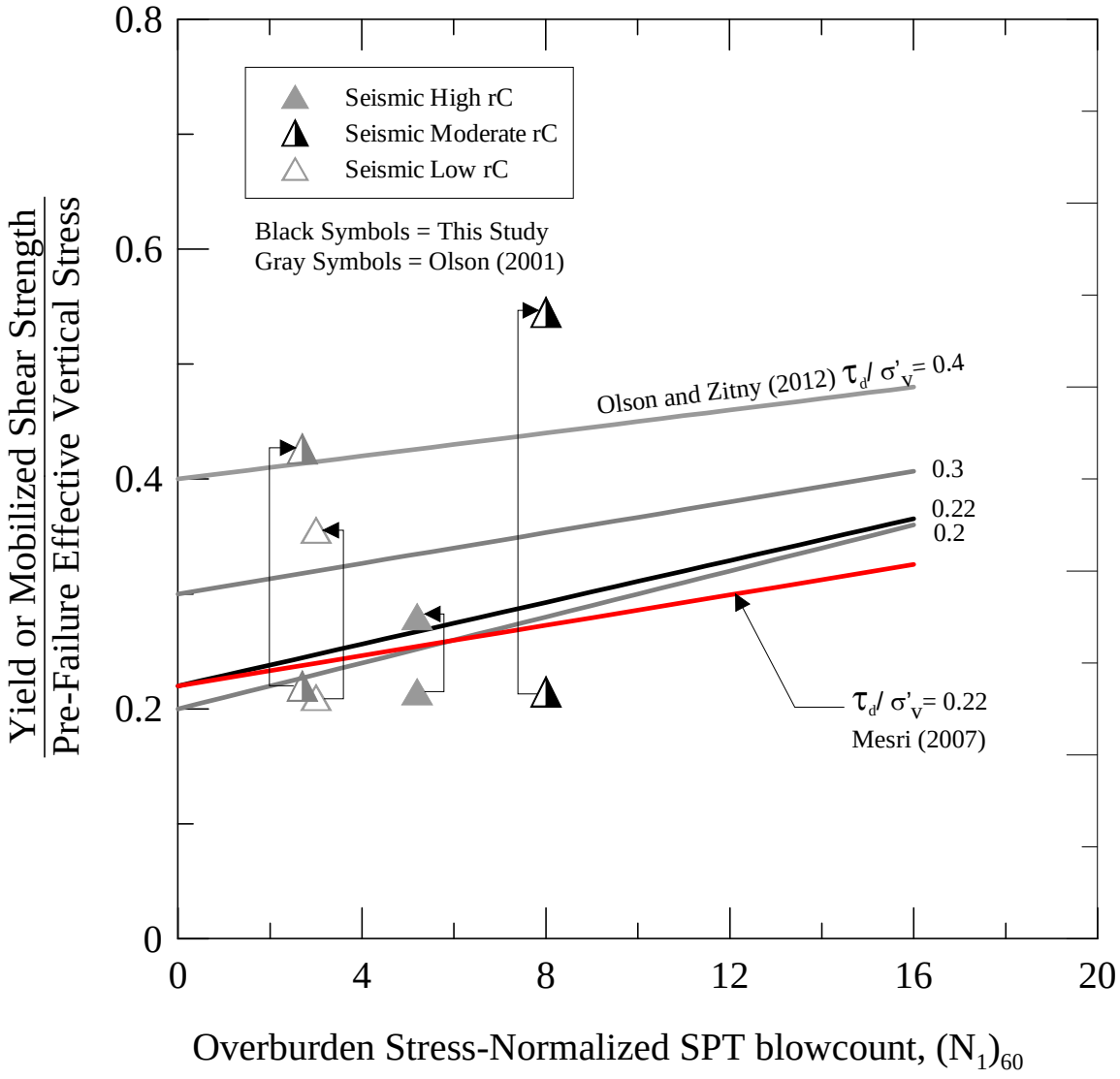

Figure 5.11 Comparison of combined static and seismic shear stress ratios for seismically-induced flow failures with $^{2}_{static}/\pm'_{vo}$ = 0.2 – 0.22 with SPT-based yield strength ratio corresponding to $^{2}_{static}/\pm'_{vo}$ = 0.22 from Olson and Zitny (2012) and from Mesri (2007). Symbols at the tail of arrows represent mobilized $^{2}_{static}/\pm'_{vo}$ back-calculated from prefailure geometry. Symbols at the head of arrows represent $^{2}_{static}/\pm'_{vo}$ + average $^{2}_{seismic}/\pm'_{vo}$

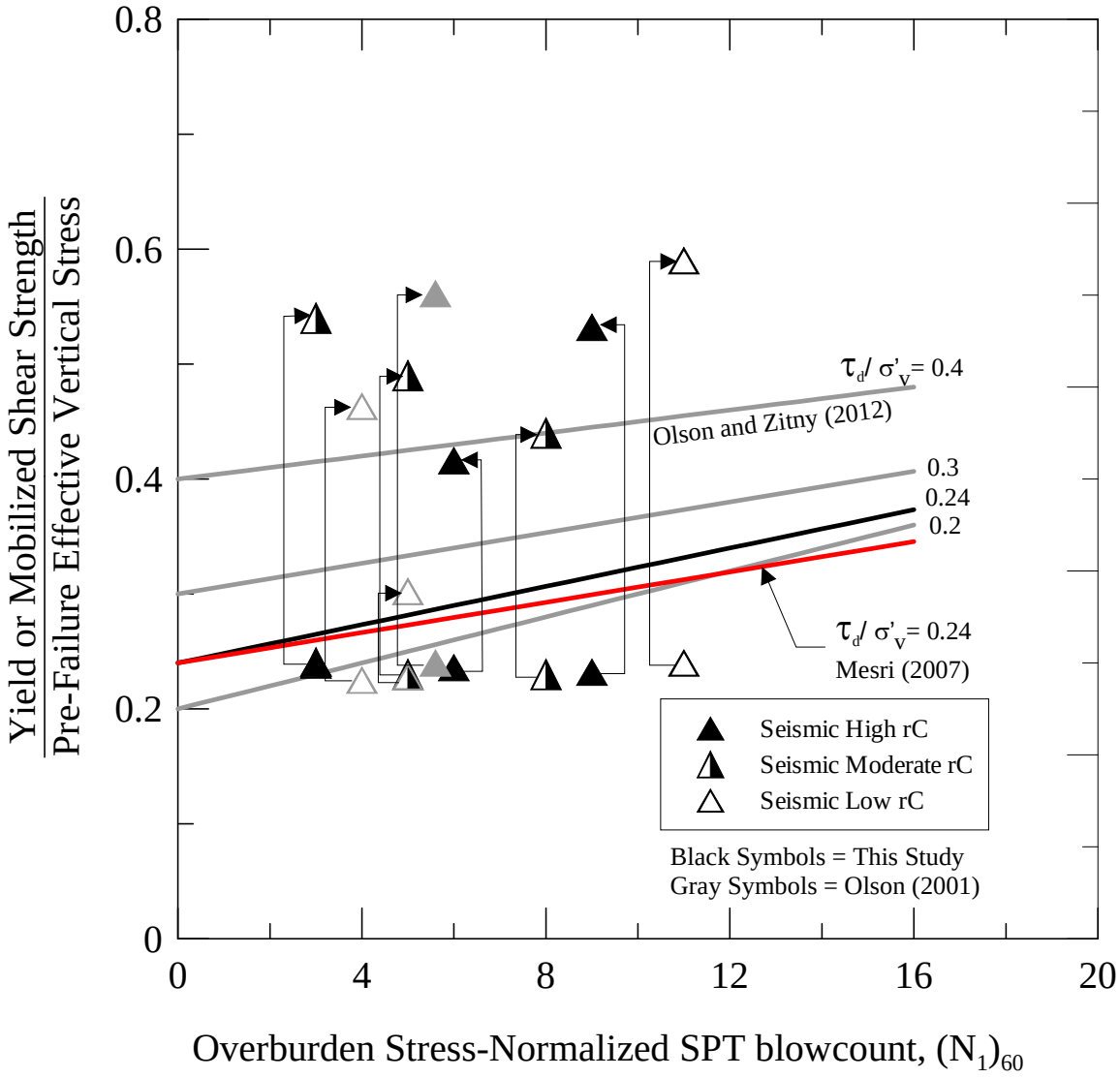

Figure 5.12 Comparison of combined static and seismic shear stress ratios for seismically-induced flow failures with $^{2}_{static}/\pm'_{vo}$ = 0.22 – 0.24 with SPT-based yield strength ratio corresponding to $^{2}_{static}/\pm'_{vo}$ = 0.24 from Olson and Zitny (2012) and from Mesri (2007). Symbols at the tail of arrows represent mobilized $^{2}_{static}/\pm'_{vo}$ back-calculated from prefailure geometry. Symbols at the head of arrows represent $^{2}_{static}/\pm'_{vo}$ + average $^{2}_{seismic}/\pm'_{vo}$

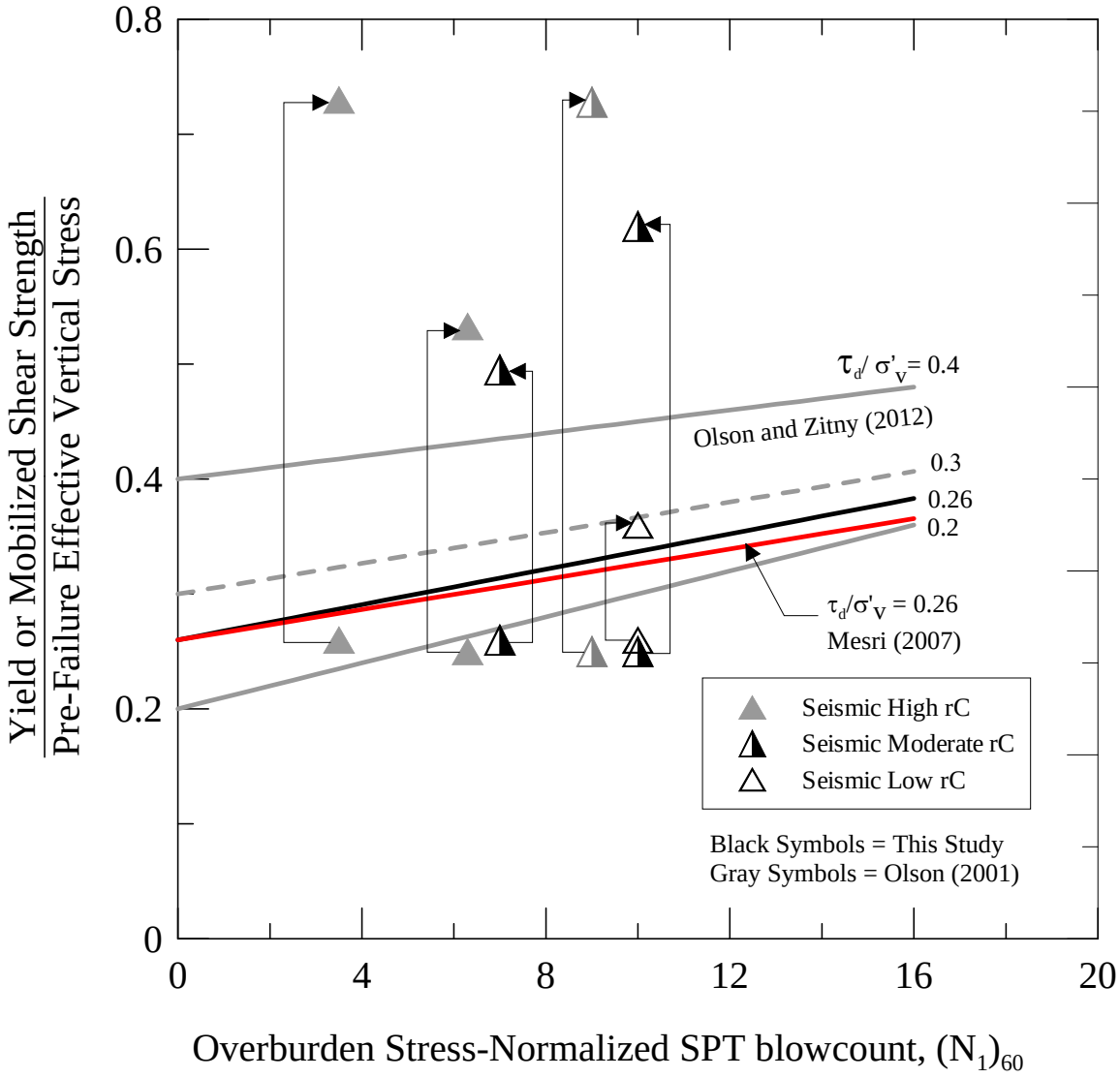

Figure 5.13 Comparison of combined static and seismic shear stress ratios for seismically-induced flow failures with $^{2}_{static}/\pm'_{vo}$ = 0.24 – 0.26 with SPT-based yield strength ratio corresponding to $^{2}_{static}/\pm'_{vo}$ = 0.26 from Olson and Zitny (2012) and from Mesri (2007). Symbols at the tail of arrows represent mobilized $^{2}_{static}/\pm'_{vo}$ back-calculated from prefailure geometry. Symbols at the head of arrows represent $^{2}_{static}/\pm'_{vo}$ + average $^{2}_{seismic}/\pm'_{vo}$

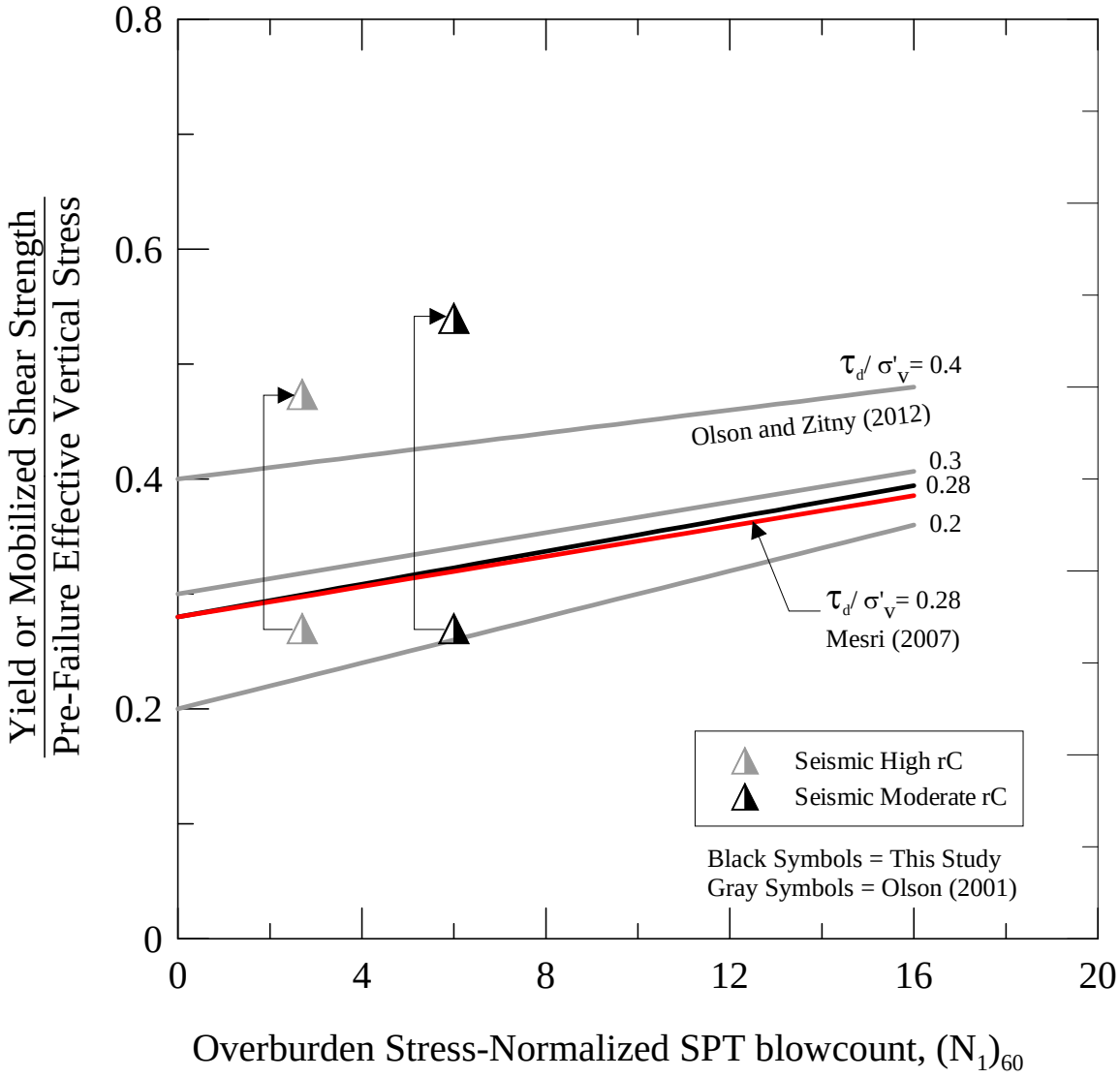

Figure 5.14 Comparison of combined static and seismic shear stress ratios for seismically-induced flow failures with $^{2}_{static}/\pm'_{vo}$ = 0.26 – 0.28 with SPT-based yield strength ratio corresponding to $^{2}_{static}/\pm'_{vo}$ = 0.28 from Olson and Zitny (2012) and from Mesri (2007). Symbols at the tail of arrows represent mobilized $^{2}_{static}/\pm'_{vo}$ back-calculated from prefailure geometry. Symbols at the head of arrows represent $^{2}_{static}/\pm'_{vo}$ + average $^{2}_{seismic}/\pm'_{vo}$

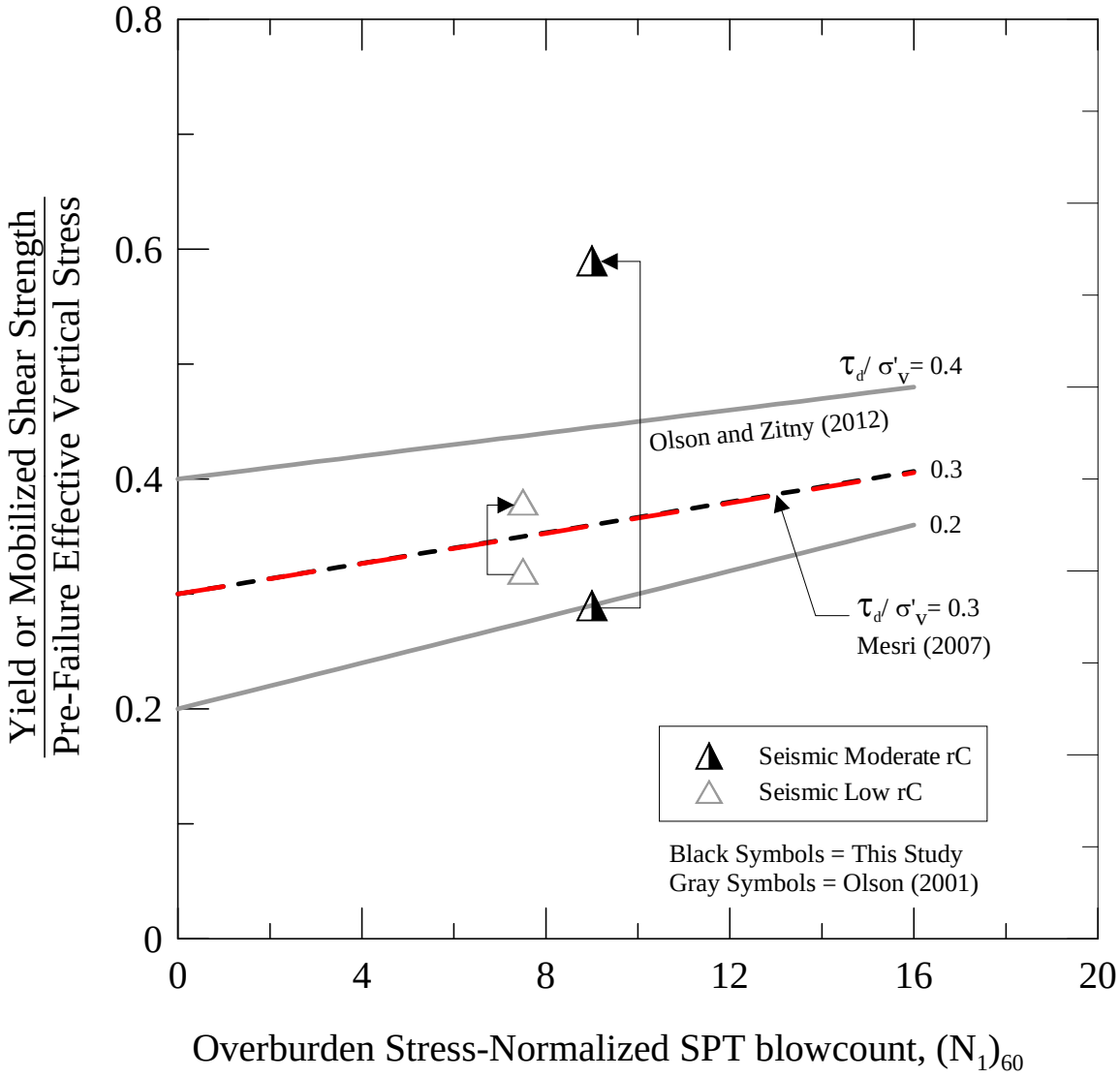

Figure 5. 15 Comparison of combined static and seismic shear stress ratios for seismically-induced flow failures with $\tau_{static}/\sigma'vo$ = 0.28 – 0.30 with SPT-based yield strength ratio corresponding to $\tau_{static}/\sigma'vo$ = 0.28 from Olson and Zitny (2012) and from Mesri (2007). Symbols at the tail of arrows represent mobilized $^{2}{}_{static}/\pm'_{vo}$ back-calculated from prefailure geometry. Symbols at the head of arrows represent $^{2}{}_{static}/\pm'_{vo}$ + average $^{2}{}_{seismic}/\pm'_{vo}$

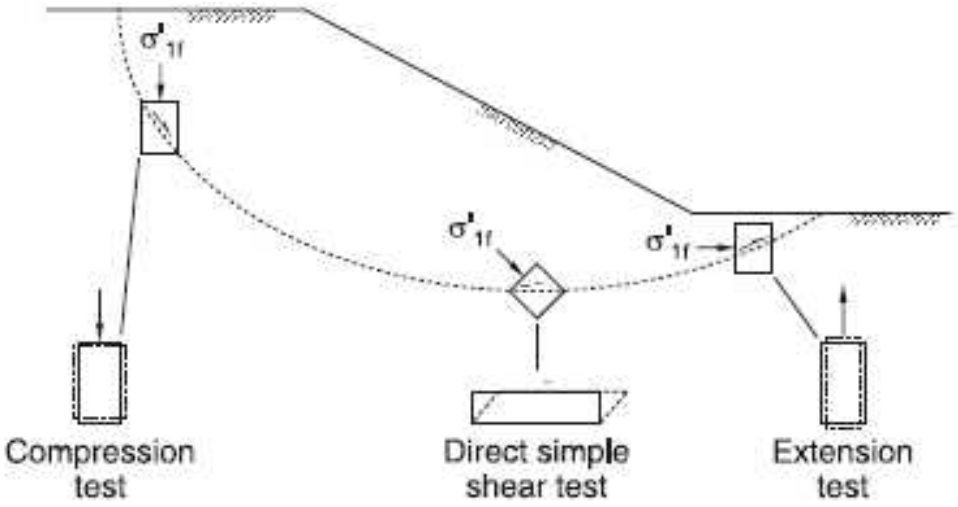

Figure 5.16 Illustration of different modes of shear within an embankment (from Olson and Mattson 2008)

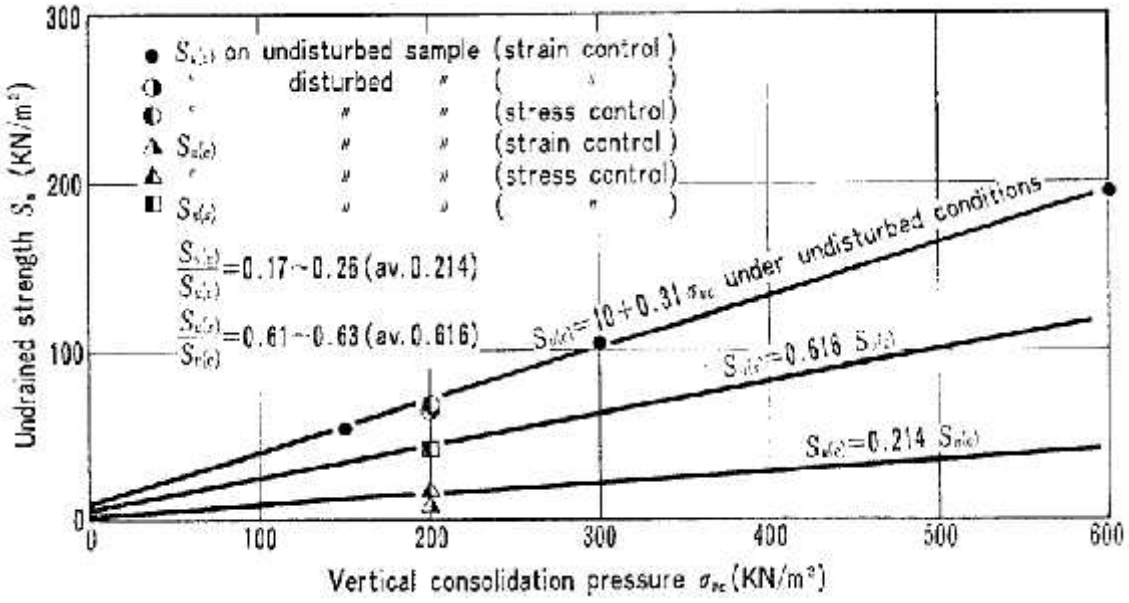

Figure 5.17 Effect of mode of shear on undrained peak (yield) shear strength (from Hanzawa 1980)

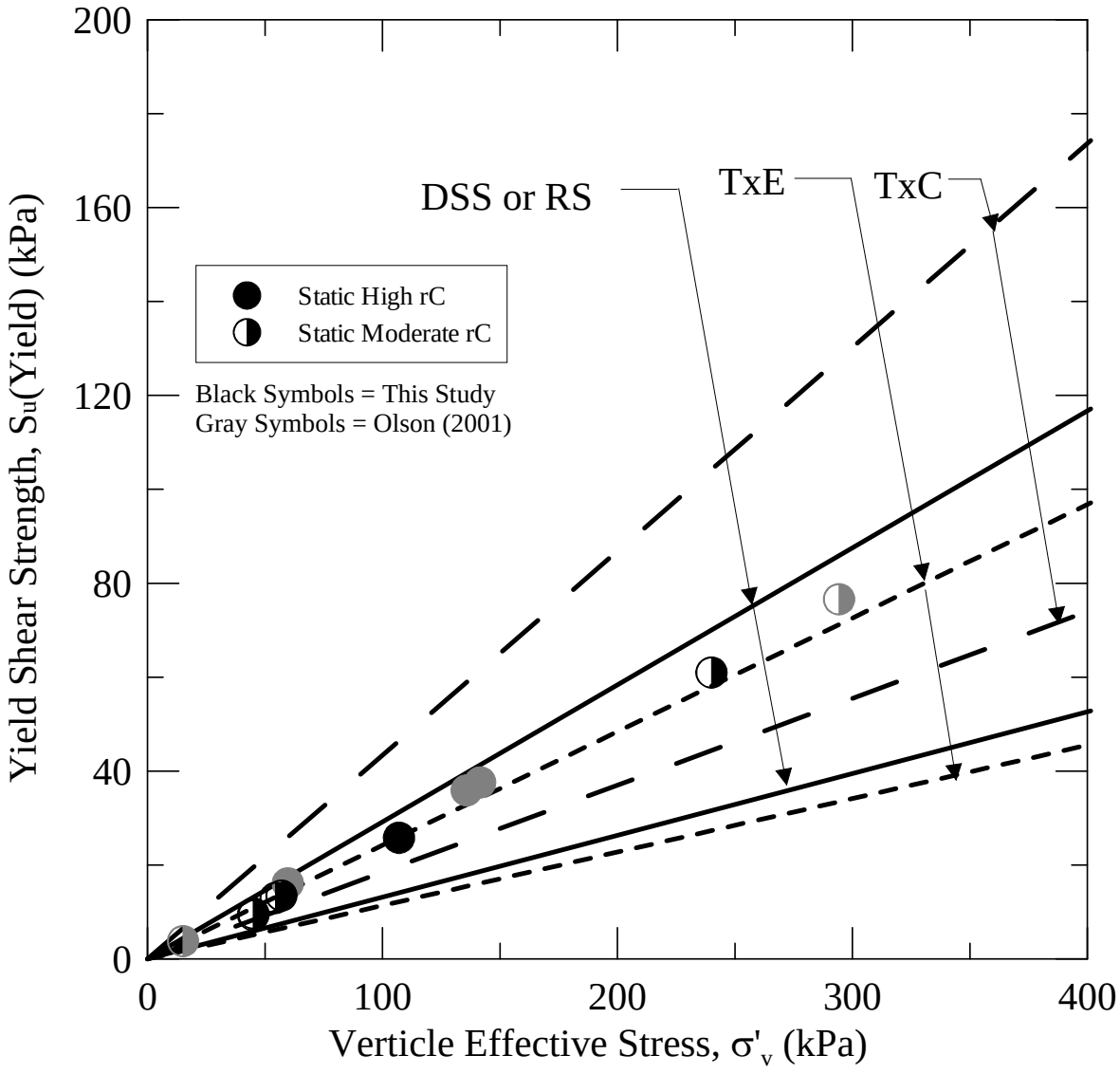

Figure 5.18 Case histories analyzed by Olson (2001) and in this study compared to envelopes of laboratory data reported by Olson and Mattson (2008)

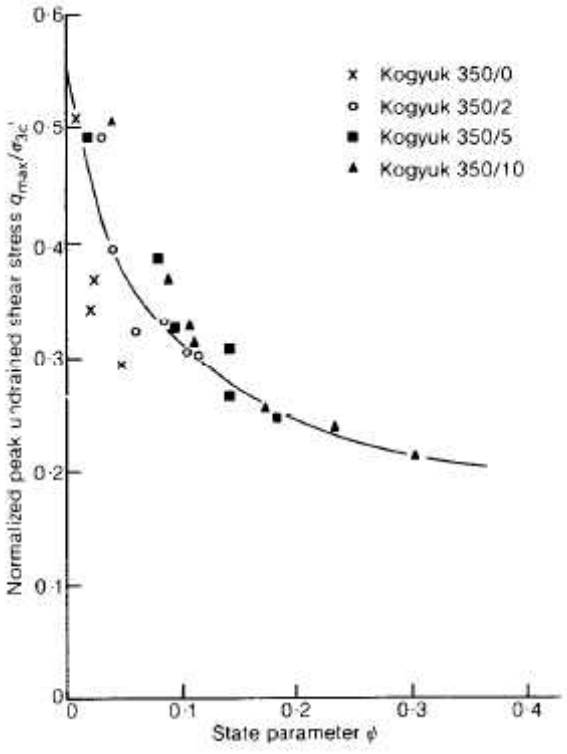

Figure 5.19 Yield strength ratio and state parameter relationship for Kogyuk Sand (from Been and Jefferies 1985) and Bending sand (Terzaghi et al. 1996)

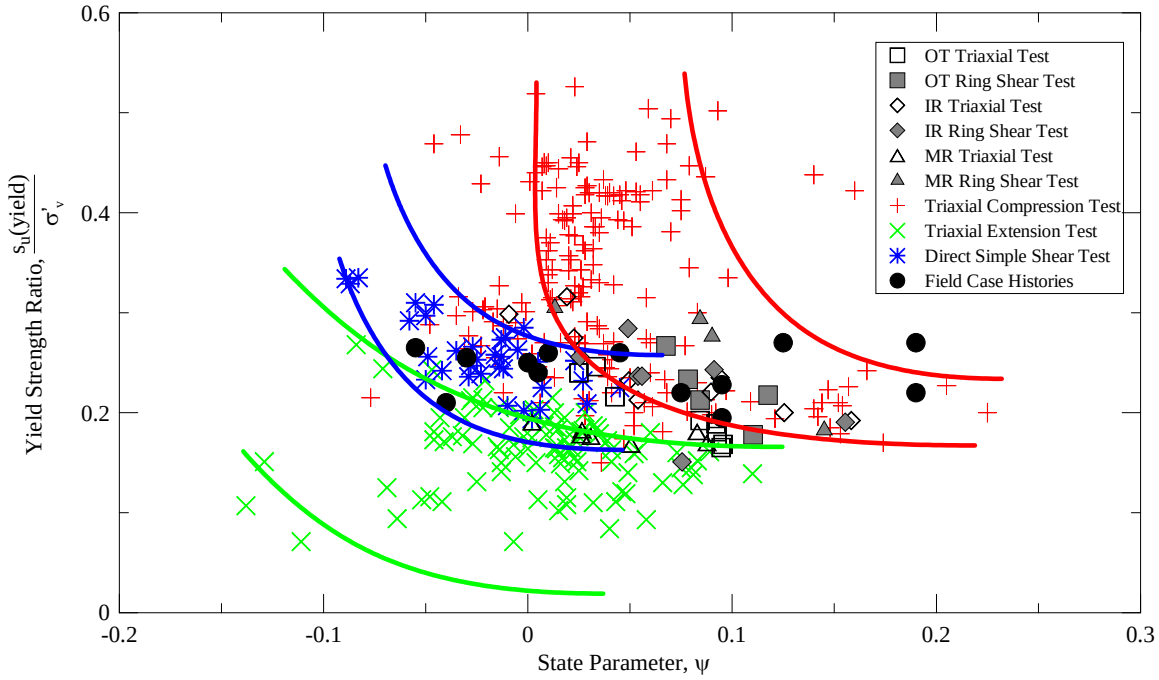

Figure 5.20 General trends of yield strength ratio and state parameter of for TxC, DSS/RS, and TxE laboratory data (data compiled from Olson and Stark 2003; Olson and Mattson 2008; and Sadrekarimi 2009) compared to case histories data from Olson (2001) and this study. State parameters estimated by Jefferies and Been (2006)

Table 5. 1 Back-calculated mobilized or yield shear strengths and strength ratios from analyzed flow failure case histories

Case History (1)	Pre-Failure Geometry Strength Ratio			Pre-Failure Shear Strength			Average Seismic Stress (kPa) (8)	Weighted Average Pre-Failure Vertical Effective Stress (kPa) (9)
	Lowerbound (2)	Best estimate (3)	Upperbound (4)	Lowerbound (kPa) (5)	Best estimate (kPa) (6)	Upperbound (kPa) (7)		
1	0.194	0.26	0.345	103	115	120	34	404
2	0.13	0.26	0.31	6.5	7.5	10.7	13.7	37.6
3	0.165	0.205	0.22	4.7	7.8	9.3	32	33
4	0.184	0.185	0.19	11	11	13.5	21	33.5
5	0.044	0.067	0.077	3.5	7	8.7	189	95.5
6	0.18	0.22	0.295	21.3	25.8	29.7	N/A	107
7	0.16	0.19	0.195	8	9.5	10.5	13.5	50
8	0.007	0.117	0.118	5	7.3	8.2	9.53	73
9	0.107	0.116	0.121	8.5	9.7	10.5	19	81
10	0.22	0.24	0.245	21	21.5	22.5	18.5	77
11	0.16	0.23	0.31	4.5	11	15	15	46
12	-	0.274	-	-	61	-	N/A	240
13	0.193	0.236	0.385	8.2	12	14.5	4.7	43
14	0.112	0.19	0.285	10	13.3	17	41.14	70
15	0.225	0.23	0.24	10	10.7	11	11.3	46
16	0.22	0.27	0.3	8.2	11	13.6	16	42
17	0.18	0.24	0.26	17	16	11.5	-	65
18	0.205	0.24	0.305	22.5	24	36.5	36	104
19	0.21	0.29	0.34	33	48.5	53	50	167
20	0.22	0.24	0.287	11.5	15.1	19	-	62
21	0.164	0.23	0.27	9	9.3	13.3	N/A	45
22	0.173	0.23	0.25	8.4	9.7	10	N/A	45
23	0.194	0.24	0.3	9.3	13	18.5	N/A	54.5
24	0.194	0.24	0.3	9.3	13.5	20	N/A	57
25	0.203	0.232	0.287	21	23.5	25.2	27.5	90
26	0.185	0.215	0.28	20	26.5	36	55.6	124
27	0.165	0.25	0.262	16	24.5	30	40.7	115
28	0.163	0.165	0.17	13.5	16.5	17	25.5	120
29	0.148	0.18	0.215	13.5	17.3	19.5	21.24	93
30	0.145	0.17	0.2	14	17.5	22	16.1	90
31	0.188	0.2	0.275	17.2	20.1	29	41.14	112

CHAPTER SIX:

POST-TRIGGERING STABILITY AND LIQUEFIED SHEAR STRENGTH

6.1 Introduction

As defined in Chapter 4, the third step in liquefaction analysis for sloping ground is a liquefaction flow failure or post-triggering stability analysis. The fact that a liquefaction susceptibility analysis (Chapter 4) shows that a soil is susceptible to liquefaction and a liquefaction triggering analysis (Chapter 5) shows that liquefaction will be triggered by static or dynamic loading does not necessarily mean that liquefaction flow failure will occur, although cyclic mobility and displacements may still occur. A post-triggering liquefaction flow failure analysis evaluates whether a slope will undergo a flow failure. In general, the analysis compares τ_{static} with the soil resistance, including $s_u(liq)$ in the liquefied zone. Liquefaction flow failure can be catastrophic because the failure is sudden and the large loss of shear strength can result in high velocity landslides that can cause significant property damage and fatalities. Therefore, $s_u(liq)$ is a key parameter needed for liquefaction analysis.

A prerequisite for liquefaction flow failure is that the static (prefailure) driving shear stress (τ_{static}) must be greater than the liquefied shear strength [$s_u(liq)$] of the soil. The static driving stress can be calculated from a limit equilibrium analysis of the pre-failure geometry [which is also calculated in the liquefaction triggering analysis (see Chapter 5)]. Several investigators have proposed various methods to determine $s_u(liq)$, including laboratory methods, empirical correlations based on case histories, and combined laboratory and field case history methods. This Chapter first discusses some notable methods for evaluating $s_u(liq)$ and performing liquefaction flow failure analysis. Then, the liquefaction flow failure back-analysis procedure adopted in this study is defined. The results of these back-analyses combined with those from Olson (2001) to

evaluate s_u(liq) and liquefied strength ratio, s_u(liq)/σ'_{vo}. The combined case histories are then compared with the approach proposed by Mesri (2007) where the liquefied strength ratio is considered to vary with τ_{static} /σ'_{vo}. Finally, the effect of the mode of shear on s_u(liq) is studied and the combined case histories are compared with laboratory data compiled by Olson and Mattson (2008) and reported by Sadrekarimi (2009). As a reminder, Chapter 2 provided basic definitions and concepts related to the liquefied shear strength and strength ratio.

6.2 Existing Procedures to Estimate Liquefied Shear Strength

Three general approaches have been proposed to estimate the shear strength of liquefied soil. The first approach, proposed by Poulos et al. (1985a), is based on sampling using fixed piston samplers (and carefully tracking of volume changes during sampling, transport, and specimen preparation) and a suite of laboratory triaxial compression testing. The second approach, initially proposed by Seed (1987), involves empirical correlations between in-situ penetration resistance and liquefied shear strengths back-calculated from liquefaction case histories. Other researchers, including Jefferies et al. (1990), Seed and Harder (1990), Stark and Mesri (1992), Olson and Stark (2002), Mesri (2007), Idriss and Boulanger, Robertson (2009), among others, have proposed other similar empirical correlations. The third approach utilizes both laboratory testing and case histories results. Ishihara (1993), Konrad and Watts (1995), Fear and Robertson (1995), among others, have utilized this approach. Many of these methods were discussed in Chapter 3. A brief review is presented here to identify strengths and shortcomings associated with these approaches.

6.2.1 Laboratory Testing Approach

Poulos et al. (1985a) proposed that liquefied shear strength of cohesionless soils could be determined if a “perfectly undisturbed” sample (i.e., without any disturbance

whatsoever) is consolidated to a high consolidation stress and then shear it under undrained conditions in a triaxial test. Because some disturbance during sampling, transportation, handling and specimen preparation is inevitable, Poulos et al. (1985a) proposed the following step-by-step laboratory procedure to estimate the in-situ liquefied shear strength. The first step is to determine the in-situ void ratio from one or more relatively undisturbed soil samples. The samples can be collected either by fixed-piston sampling, ground freezing and coring, or sampling in test pits. The second step is to locate the critical state line (CSL) by testing 5 to 6 reconstituted samples in triaxial compression. This step assumes that the slopes of the CSL for undisturbed and reconstituted samples is the same. The third step is to perform a consolidated-undrained triaxial test on an undisturbed specimen to measure the liquefied shear strength. The final step is to project the in-situ CSL through the measured liquefied shear strength and corresponding consolidation void ratio, parallel to the slope of CSL developed from reconstituted samples. The in-situ liquefied shear strength is then determined from the in-situ CSL at the in-situ void ratio determined in the first step. The procedure is illustrated in Figure 6.1.

The laboratory-based procedure proposed by Poulos et al. (1985a) utilizes well-defined principles of soil mechanics and can yield a reasonable estimate of liquefied shear strength if properly applied; however, there are a few shortcomings in the procedure. Firstly, the procedure is time-consuming and expensive, making it unfeasible for small projects. Secondly, Kramer (1989) illustrated that the liquefied shear strength of soils that have a flat CSL or soils that exhibit significant scatter in critical state data may be so uncertain that the results of the laboratory-based procedure are difficult to interpret. Poulos et al. (1985a) suggested that the CSL is influenced by grain shape and grain size; however, subsequent studies (e.g., Kuerbis and Vaid 1988; Vaid et al. 1990; Vaid and Thomas 1995; Konrad and Watts 1995) suggest that the CSL may also depend on the mode of shear, effective confining pressure, and sample preparation methods. Lastly Terzaghi et al. (1996) indicated that the values of liquefied shear strength are significantly influenced by the void ratio. A small change in void ratio may cause a considerable change in liquefied shear strength of soil.

6.2.2 pirical Correlations Based on Field Case Histories

An alternative to the laboratory-based procedure suggested by Poulos et al. (1985a) is an empirical correlation based on the back-calculation of field case histories. In this approach, limit equilibrium back-analyses are performed on post-failure geometries (although some studies have also used pre-failure geometries, and some studies incorporate the kinetics of failure for some case histories). The back-analyses yield liquefied shear strengths and/or strength ratios that are commonly related to penetration resistance values in the zone of liquefaction. Olson (2001) critically reviewed the case history-based procedures suggested by Seed (1987), Jefferies et al. (1990), Seed and Harder (1990), and Stark and Mesri (1992). To avoid redundancy, these procedures are not re-reviewed. Two empirical correlations presented in Idriss and Boulanger (2007) and Olson (2009) are shown in Figure 6.2 and Figure 6.3 for illustration purposes. A review of recently developed case history-based correlations is given in Chapter 3.

6.2.3 Empirical Correlations Based on Field Case Histories and Laboratory Tests

The third approach combines laboratory test results and field case histories to develop liquefied shear strength correlations. Incorporating laboratory data allows investigators to incorporate potential effects of mode of shear, grain size, grain shape, fines content and mineralogy on liquefied shear strength. Olson (2001) critically reviewed the combined field and laboratory approaches proposed by Stark and Mesri (1992) Ishihara (1993), Konrad and Watts (1995), and Fear and Robertson (1995), and these methods will not be re-reviewed here. For example, Figure 6.4 shows a relationship suggested by Yoshimine et al. (1999) between normalized CPT tip resistance and liquefied shear strength ratio based on a combination of laboratory tests and case histories. However, there are still a number of uncertainties in this approach, including the similitude of critical state shear strengths measured using reconstituted specimens, estimating the penetration resistance for laboratory tests, among others. Furthermore, there are very few case histories available that have in-situ soils tested elaborately.

6.3 iquefied Shear Strength Back-Analysis Procedures

The author analyzed 31 reasonably well documented case histories to estimate liquefied shear strength and strength ratios. As stated in Chapter 5, case histories collected in this study consist of static loading-induced and seismically-induced flow failures. However unlike yield shear strength analyses, case histories that involve failure under both static and seismic loading can be used to estimate the liquefied shear strength and strength ratio. In this study, three types of stability analyses were performed to back-calculate the liquefied shear strength and strength ratio from the 31 flow failure case histories. The appropriate type of analysis was selected based on the extent and quality of information available for each case history.

Case histories that lack detailed post-failure geometries were analyzed as infinite slopes. Assumptions suggested by Ishihara et al. (1990) were used as guidelines to determine the liquefied shear strength from infinite slope analysis: (1) the ground surface and the surface of the flowed material are approximately parallel when the mass came to rest; (2) side forces were equal, opposite, and co-linear; and (3) the shear strength mobilized at the moment the failed mass came to rest was equal to the liquefied shear strength. Details of the infinite slope analysis performed in this study are provided by Olson (2001). In this study, three case histories (cases 12, 19 and 24 in Table 6.1) lacked detailed post-failure geometries and therefore were analyzed as infinite slopes. Liquefied shear strength ratios, $s_u(liq)/\sigma'_v$, estimated from infinite slope analysis may be smaller than the actual $s_u(liq)/\sigma'_v$ of the liquefied soil because infinite slope analysis does not incorporate the kinetics of failure. Details of these cases are given in Appendix A.

If post-failure geometries is complete (or can be easily completed by area-balancing) and the phreatic surface can be located with reasonable accuracy, then a detailed limit equilibrium analysis was conducted. Limit equilibrium analyses were performed using Spencer's (1967) slope stability method as coded in the computer software Slope/W developed by GEO-SLOPE International. Although these analyses considered the shear strength of each soil (including the liquefied soil) along likely

failure surfaces, limit equilibrium analyses do not explicitly consider kinetics. Therefore, values of s_u(liq) estimated using this method may be smaller than the actual s_u(liq) of the liquefied soil.

To calculate $s_u(liq)/\sigma'_v$, effective vertical stresses were calculated from the pre-failure geometry. This was done by dividing the post-failure geometry in 10 to 15 segments and then estimating the locations of the segments in the pre-failure geometry. Effective vertical stresses for individual segments were then calculated from their locations in the pre-failure geometry. While judgment was used to assign the pre-failure segment positions, segments can be re-arranged reasonably in more than one fashion. For several such cases, the author examined more than one arrangement of post-failure segments in the pre-failure geometry. In each of these cases, minor changes in the pre-failure segment locations had little effect on the back-calculated liquefied shear strength ratios. Similar to the study by Olson (2001), this study considered the effective vertical stresses within the entire zone of liquefaction rather than a single representative value. The limit equilibrium analyses for the case histories (excluding cases 12, 19 and 24 in Table 6.1) are described in Appendix A.

If soil mass flowed a considerable distance (i.e., the post-failure geometry differs considerably from the pre-failure geometry), it is likely that momentum affected the flow slide. In these cases, the back-analysis needs to consider the kinetics of failure. To conduct this analysis, the locations of centroids of the failure mass from the pre- and post-failure geometries must be determined and the travel path of the centroid must be defined. For simplicity, the centroid travel path was typically considered to be parallel to the sliding surface.

As stated earlier, the prerequisite for a liquefaction flow failure is that the static driving stress is larger than shear resistance of the soil (including the liquefied shear strength). Once liquefaction is triggered, the shear resistance of the liquefied soil drops rapidly from the yield strength to the liquefied strength. However because there is no considerable variation in the pre-failure geometry at that stage, the static driving stresses

remain relatively unchanged (Davis et al. 1988). Because of difference between the driving stress and the liquefied strength, the failure mass accelerates and the velocity increases. If the sliding mass moves into a body of water, the shear resistance may be reduced as a result of hydroplaning and mixing with water (Davis et al. 1988; Olson 2001).

As the soil mass continues to displace and deform, the driving shear stress decreases to a value less than liquefied shear strength, and the failure mass decelerates. When the failure mass reaches a velocity of zero and comes to rest, the driving shear stress may be considerably less than the liquefied shear strength. As a result, the back-analysis should consider the kinetics of failure to obtain a reasonable estimate of s_u(liq) (Davis et al. 1988; Olson et al. 2000; Olson 2001). The kinetics analysis procedure used in this study was identical to the procedure detailed by Olson (2001); therefore, the details are not repeated here. In current study, seven case histories (cases 5, 6, 10, 11, 14, 20, and 26 in Table 6.1) had sufficient information to perform a kinetic analysis.

6.4 Liquefaction Flow Failure Case Histories and Uncertainties

The author back-calculated the liquefied shear strength and strength ratio for 31 reasonably well-documented flow failure case histories. Table 6.1 lists the case histories evaluated in this study. Four of the 31 cases histories did not have post-failure geometries reported in the literature; and therefore it was not possible to perform back-analyses for these cases (cases 1, 16, 17 and 25 in Table 6.1). The remaining case histories were analyzed either by infinite slope or by limit equilibrium analysis with or without a kinetics analysis. As described in Chapter 4, case histories uncertainties were qualitatively assessed using a “relative confidence” (rC) factor. These uncertainties included: (1) the “completeness” of the post-failure geometry; (2) the shear strength of the non-liquefied soils, (3) the locations of the initial and final surfaces of sliding; (4) the location of liquefied zone; (5) the location of the phreatic surface; (5) the pre-failure locations of the post-failure segments; and (6) the potential of drainage or pore water

pressure redistribution occurring during flow. As a result of these uncertainties, each case history produced a range of back-calculated liquefied shear strengths and strength ratios. This range is included in Table 6.1.

For cases with an incomplete post-failure geometry, the post-failure geometry was completed by a process termed “area balancing.” This process involved comparing the area of soil in the critical failure mass estimated for the pre-and post-failure geometries. The difference in the failed soil area was then added to the post-failure geometry in a manner consistent with the available post-failure profile and ground conditions. Additional uncertain factors were evaluated on a case-by-case basis, as described in Appendix A.

Seven of the 31 case histories evaluated in this study had sufficient information to perform a kinetics analysis. The kinetics analysis produces the “best estimate” of liquefied shear strength and strength ratio. Table 6.2 lists case histories for which a kinetics analysis was performed. As expected, the “best estimate” liquefied shear strengths and strength ratios estimated from the kinetics analysis were greater than the values estimated from the limit equilibrium analysis (Table 6.1).

To develop correlations to estimate liquefied shear strength and strength ratio, penetration resistance was used. For cases where a profile (or profiles) of SPT and/or CPT data was available, the mean penetration resistance within the liquefied zone was selected as the representative (or “best estimate”) value, consistent with the approach used by Olson (2001). However, in some case histories this information was either incomplete or missing. In these cases, nearby penetration tests were used to estimate penetration resistance at the failure location. Additional uncertainty in the representative penetration resistance resulted for cases where either standard penetration test (SPT) blow count or cone penetration test (CPT) tip resistance were given, and the corresponding values of the other penetration resistance measure was estimated using the median grain size of the liquefied soil (D_{50}) and the average q_c/N_{60} value from the relationships proposed by Robertson and Campanella (1985), Seed and De Alba (1986),

Andrus and Youd (1989), Kulhawy and Mayne (1990) and Stark and Olson (1995). In a few cases, penetration resistance was measured with nonstandard tools (e.g., Swedish weight sounding data in case 26). In this case, the author used available correlations to estimate CPT or SPT values; however, this conversion reduced the relative certainty for the case. Representative penetration resistance values for each case are given in Table 4.3 (Chapter 4). Detailed information about the representative penetration resistance and uncertainties for each case is given in Appendix A.

6.5 Interpretation and Discussion of Results

Figure 6.5 and Figure 6.6 present "best estimate" liquefied strength ratios compared to mean $(N_1)_{60}$ and q_{c1} values, respectively, for each of the cases analyzed in this study. In addition, these figures include the case histories analyzed by Olson (2001). The numbers adjacent to each data point in Figure 6.5 report the fines content of the liquefied soil. This will be discussed in more detail subsequently. As illustrated in the figures, the cases evaluated in this study reasonably agree with the correlations proposed by Olson and Stark (2002), which are included in the figures. The trend lines are expressed as:

$$\frac{s_u(liq)}{\pm'_v} = 0.03 + 0.0075[(N_1)_{60}] \pm 0.03$$

$$\frac{s_u(liq)}{\pm'_v} = 0.03 + 0.0143(q_{c1}) \pm 0.03 \qquad \textbf{Eq. 6.1}$$

Figure 6.7and Figure 6.8 repeat Figure 6.5 and Figure 6.6, but include the relationships proposed by Olson and Stark (2002), Mesri (2007), Idriss and Boulanger (2007), and Robertson (2010) for comparison. Figure 6.7 illustrates that the mean relationship proposed by Olson and Stark (2002), the correlation proposed by Idriss and Boulanger (2007) [for $(N_1)_{60} \leq 12$], and the relationship for $\tau_{static}/\sigma'_{vo} = 0.2$ proposed by Mesri (2007) are nearly identical.

Figure 6.8, based on q_{c1}, illustrates that the relationships from Idriss and Boulanger (2008) and Robertson (2010) provide conservative lower bounds to the case history data. The author used following equation suggested by Robertson (2010) to extend the Robertson (2010) correlation to $q_{c1} = 0$:

$$\frac{s_u(liq)}{\pm '_v} = \frac{[0.02199 - 0.00312 q_{c1}]}{[1 - 0.2676 q_{c1} + 0.0017839 q_{c1}^2]} \qquad \textbf{Eq. 6.2}$$

where q_{c1} is in MPa and $0.03 \leq s_u(liq)/\sigma'_v \leq \tan \phi'$. In addition, Idriss and Boulanger (2008) incorporated a fines content adjustment for the case histories prior to developing their proposed relationship. This may have resulted in the relationship being moved to higher tip resistances compared to the Olson and Stark (2002) and Robertson (2010) relationships, as the latter two relationships do not incorporate fines content adjustments.

The boundary curve suggested by Robertson (2010) becomes vertically asymptotic at an overburden stress-normalized CPT tip resistance of about 7 MPa, while the Idriss and Boulanger (2008) correlations become asymptotic at $q_{c1} \sim 11$ MPa and 17 MPa. (Note that these latter values of CPT tip resistance include a fines content adjustment proposed by Idriss and Boulanger 2008.) As explain in Robertson (2010) soils with overburden stress-normalized CPT tip resistance greater than 7 MPa may exhibit strain-hardening or dilative behavior. This limiting CPT tip resistance is consistent with the contractive/dilative boundary proposed by Olson and Stark (2003) and illustrated by Olson et al. (2006). Olson and Stark (2006) illustrated limiting contractive/dilative boundaries for several vertical effective stresses using the CPT-based liquefaction susceptibility boundary curve shown in Figure 4.8 (Chapter 4). These limiting boundaries illustrate that soils with $q_{c1} > 6.5$ MPa may be contractive at $\sigma'_{vo} > 100$ kPa.

Back-calculated $s_u(liq)$ values from this study and from Olson (2001) are compared to weighted average pre-failure vertical effective stress in Figure 6.9. As

illustrated in Figure 6.9, a reasonable linear relationship exists between s_u(liq) and weighted average pre-failure σ'_{vo}, although the case histories represent differences in relative density, mode of deposition, grain size distribution, grain shape, state parameter, modes of shear and critical state friction angle. The relationship ranges from approximately s_u(liq) = 0.05 to 0.12 σ'_{vo} with an average value (from linear regression) of 0.09 σ'_{vo}.

6.6 Effect of Fines on Liquefied Shear Strength Ratio

Some recent laboratory studies suggest that the liquefied shear strength varies with FC (e.g., Pitman et al. 1994, Zlatovic and Ishihara 1995, Thevanayagam et al. 1996, Thevanayagam 1998, and Naeini and Baziar 2004). For example, Naeini and Baziar (2004) observed that liquefied shear strength decreased with increasing FC for FC less than about 30%, then liquefied shear strength increased with increasing FC, as illustrated in Figure 6.10. In addition, several investigators have observed that most documented liquefaction flow failures involve silty soils (Thevanayagam 1998; Yamamuro and Lade 1998; Olson 2001; Sadrekarimi 2009). As a result, it is feasible that a correlation between laboratory and field case histories liquefied shear strength and FC exists, and a fines content correction would capture this correlation.

Most previous case history-based studies (e.g., Seed and Harder 1990; Stark and Mesri 1992; Ishihara 1993; Mesri 2007; Idriss and Boulanger 2007) have used a fines content correction to penetration resistance to estimate equivalent clean sand penetration resistance. As field case histories with comparable fines contents may have different relative densities and confining pressures, it is difficult to discern any consistent variation in liquefied shear strength with changing FC. Figure 6.5 shows case histories analyzed in this study and by Olson (2001) with the corresponding FC values. As observed by Olson (2001), these case histories exhibit no consistent trend with respect to fines content. Therefore, no correction for FC was used in this study.

6.7 Effect of Driving Stress on Liquefied Shear Strength Ratio

In Chapters 2 and 5, the author investigated the influence of static driving stress on the yield shear strength. As the magnitude of static driving shear stress increases the yield shear strength of soil also increases; however, the increment of shear stress required to trigger liquefaction (or reach the yield shear strength) decreases. Few investigators have specifically studied the role of static shear stress on the liquefied shear strength. One available study is that from Castro (1969). Castro (1969) conducted several undrained triaxial compression tests on Banding sand that suggest no significant role of static-driving shear stress on liquefied shear strength of soil if specimen has same consolidated relative density prior to undrained shear (see Figure 6.11 and Figure 6.12). These figures also illustrate that yield shear strength increases with increasing static shear stress; however, the yield strength envelope does not increase.

Therefore, while these test results are valuable, they are ambiguous for interpreting the role of static shear stress on liquefied shear strength. In these tests, the static shear stress on the 60° plane is applied under drained conditions, which in triaxial compression requires an increase in mean effective stress. An increase in mean effective stress causes a decrease in void ratio, and in turn, should cause an increase in the shear strength mobilized at critical state. However, in these tests, the specimens were prepared at different void ratios such that following application of drained shear stress (i.e., at different mean effective stresses), they exhibited nearly identical void ratios. As a result of the similar void ratios, the specimens exhibited nearly identical shear strengths at the critical state. If it is reasonable to assume that the application of drained shear stress in the field leads to minor particle adjustments and slight density increase such that the yield shear strength increases, it is possible that these minor particle adjustments and slight density increase would result in a slight increase in liquefied shear strength.

Mesri (2007) suggested a possible relationship among static driving shear stress, overburden stress-normalized penetration resistance, and liquefied strength ratio, empirically defined as:

$$\frac{s_u(liq)}{\pm'_{vo}} = \frac{1}{4}\frac{\pm^2_d}{\pm'_{vo}} + 0.006(N_1)_{60} \qquad \textbf{Eq. 6.3}$$

based on a review of the case histories reported by Olson (2001) and Olson and Stark (2002).

To evaluate Eq. 6.3, the author grouped the case histories based on similar values of static shear stress ratio. Figure 6.13 Continued

(a) compare cases with $\tau_{static}/\sigma'_{vo} < 0.1$ with Eq. 6.3 for $\tau_{static}/\sigma'_{vo} = 0.1$. Similarly, Figure 6.13 Continued

(b) - Figure 6.13 Continued

(g) compares cases with $0.2 \leq \tau_{static}/\sigma'_{vo} < 0.22$, $0.22 \leq \tau_{static}/\sigma'_{vo} < 0.24$, $0.24 \leq \tau_{static}/\sigma'_{vo} < 0.26$, $0.26 \leq \tau_{static}/\sigma'_{vo} < 0.28$, and $\tau_{static}/\sigma'_{vo} < 0.3$, respectively, with the corresponding relations from Eq. 6.3. The results of the comparisons illustrate that there is considerable scatter in the values of $s_u(liq)/\sigma'_{vo}$ for each value of $\tau_{static}/\sigma'_{vo}$, inconsistent with Eq. 6.3.

6.8 Effect of Mode of Shear on Liquefied Shear Strength Ratio

The role of the mode of shear on liquefied shear strength is rather ambiguous. Wood (1990) asserted that critical state friction angle is approximately same in triaxial compression and extension. Been et al. (1991) conducted strain-controlled extension and compression tests on Erksak sand. The test results suggested that the CSL is independent of the stress path of the Erksak sand. The same authors showed similar results for Toyoura sand. Other investigators (e.g., Vaid et al. 1990; Riemer and Seed 1997; Yoshimine and Ishihara 1998) have suggested that the minimum shear strength (occasionally termed the critical or steady state shear strength) varied with mode of shear. However, Been et al. (1992) and Jefferies and Been (2006) suggested that this dependence on the mode of shear occurred at the quasi-critical state, not the true critical state.

Using a large database of triaxial compression (TxC), direct simple shear and rotational shear (DSS/RS), and triaxial extension tests (TxE), Olson and Mattson (2008) suggested that TxC show the largest upper-bound liquefied strength ratios, TxE produce the smallest upper-bound liquefied strength ratios, and DSS/RS provided intermediate upper-bound liquefied strength ratios. However, these differences only occurred in specimens with state parameters close to zero (but still positive). For specimens with state parameters greater than zero, the liquefied shear strength ratio was essentially independent of the mode of shear. The liquefied strength ratio boundaries suggested by Olson and Mattson (2008) are shown in Figure 6.14. Flow failure case histories analyzed in this study and in Olson (2001) are included in Figure 6.14. These data suggest that the DSS/RS mode of shear reasonably envelopes the flow failure case histories.

6.9 Brittleness Index and State Parameter Relationship

Soils that experience liquefaction undergo a decrease in shear resistance from the peak strength [s_u(yield)] to the liquefied shear strength [s_u(liq)]. Bishop (1967) used the term "brittleness index" (I_B) to describe the strength drop in terms of a dimensionless ratio, which is defined as:

$$I_B = \frac{s_u(yield) - s_u(liq)}{s_u(yield)} \qquad \textbf{Eq. 6.4}$$

I_B values vary from 0 to 1, where $I_B = 0$ corresponds to perfectly plastic behavior with no loss of shearing resistance, and an $I_B = 1$ implies zero liquefied shear strength.

Sladen et al. (1985) first explored the use of brittleness index to understand undrained behavior of sands. They illustrated that brittleness index measured in triaxial compression was directly related to the ratio of mean consolidation stress, $\sigma'_{mean,c}$, to the

mean effective stress at critical state, $\sigma'_{mean,cs}$. Wride et al. (1999) illustrated that flow failure case histories also roughly followed the relationship observed by Sladen et al. (1985). Yoshimine et al. (1999) inversely related brittleness index to consolidated relative density. Robertson (2004) used the data reported by Yoshimine et al. (1999) to develop a relationship between I_B and $s_u(liq)/ \sigma'_v$. Sadrekarimi and Olson (2011) conducted RS and TxC laboratory tests on a standard Ottawa sand, an Illinois River sand, and a Mississippi River sand, and combined these data with tests performed on Toyoura sand (from Verdugo 1992) and several coal mine wastes (from Dawson et al. 1998). Using these data, Sadrekarimi and Olson (2011) suggested the relationship between I_B and $s_u(liq)/ \sigma'_v$ shown in Figure 6.15.

Figure 6.15 also includes laboratory data from Yoshimine et al. (1999) and Olson and Mattson (2008) with the selected field case histories (case histories that were analyzed by using kinetic analysis) analyzed in this study and in Olson (2001). As illustrated in the figure, the laboratory test and field case histories data are reasonably enveloped by the bounds suggested by Sadrekarimi and Olson (2011). Robertson (2004) reported that the relationship between I_B and $s_u(liq)/\sigma'_v$ was essentially independent of the mode of shear. In general, the additional laboratory data included in Figure Figure 6.15 support the conclusion of Robertson (2004); however, there may be a slight influence of the mode of shear at low values of I_B.

6.10 Summary and Conclusions

- A post-triggering/flow failure stability analysis evaluates whether a soil will undergo flow liquefaction once liquefaction is triggered.
- A prerequisite for liquefaction flow failure to occur is that the static driving stress is greater than liquefied shear strength of the soil. The static driving shear stress for the post-triggering/flow failure stability analysis can be estimated from a limit equilibrium analysis.

- Several procedures are available to estimate the liquefied shear strength or strength ratio for use in post-triggering. These include laboratory-based approaches, empirical correlations based on the back-analysis of flow failure case histories, and combined laboratory-based and case history-based approaches.
- In the current study, the author analyzed 31 well-documented flow failure case histories and combined these cases with 33 cases analyzed in Olson (2001). These cases were used to evaluate liquefied strength ratio relationships proposed by Olson and Stark (2002), Mesri (2007), Idriss and Boulanger (2008) and Robertson (2010). In general, the Olson and Stark (2002) relationship best described the combined liquefied strength ratio database.
- The combined liquefied strength ratio database reasonably agrees with the range of relationships between $s_u(liq)$ and σ'_{vo} proposed by Olson and Stark (2002), although the current data suggest that the linear relationships may be slightly wider than proposed by Olson and Stark (2002).
- The relationship among static driving shear stress ratio, liquefied strength ratio, and overburden stress-normalized penetration resistance proposed by Mesri (2007) was evaluating using the combined liquefied strength ratio database. While the relationship is conceptually feasible, the current database suggests that static shear stress ratio does not directly affect liquefied strength ratio.
- The combined liquefied strength ratio database supports the conclusion from Olson and Mattson (2008) that liquefied shear strengths back-calculated from liquefaction flow failures generally plot in the middle of the range of liquefied strength ratios measured in direct simple shear and rotational shear tests.
- The combined liquefied strength ratio database generally supports the relationship between brittleness index and liquefied strength ratio proposed by Sadrekarimi and Olson (2011).

6.11 References

Andrus, R.D. and Youd, T.L. (1989). Penetration tests in liquefiable gravels, *Proceedings of the 12th International Conference on Soil Mechanics and Foundation Engineering,* Rio de Jenero, Brazil, p. 679 – 682.

Been, K., Crooks, J.H.A., Becker, D.E. and Jefferies, M.G. (1986). The cone penetration test in sands: Part I, state parameter interpretation, *Geotechnique,* vol. 36, iss. 2, p. 239 – 249.

Been, K., Jefferies, M.G., Crooks, J.H.A. and Rothenberg, L. (1987). The cone penetration test in sands: Part II, general inference of state, *Geotechnique,* vol. 37, iss. 3, p. 285 – 299.

Been, K., Jefferies, M.G. and Hachey, J.E. (1991). The critical state of sands, *Geotechnique,* vol. 41, iss. 3, p. 365 – 381.

Been, K., Jefferies, M.G. and Hachey, J.E. (1992). The critical state of sands: Reply to Discussion. *Geotechnique,* vol. 42, iss. 4, p. 655 – 663.

Bishop, A. W. (1967). Progressive failure with special reference to the mechanism causing it, In Proceedings of the Geotechnical Conference Oslo 1967: On Shear Strength Properties of Natural Soils and Rocks, Oslo, Norway, 1967. *Norwegian Geotechnical Institute, Oslo, Norway,* vol. 2. p. 142 – 150.

Castro, G. (1969). Liquefaction of sands, *Harvard Soil Mechanics Series,* No. 81, Cambridge, p. 112.

Castro, G., Seed, R.B., Keller, T.O., and Seed, H.B. (1992). Steady-state strength analysis of Lower Sand Fernando Dam slide, *Journal of Geotechnical Engineering, ASCE,* vol. 118, iss. 3, p. 406 – 427.

Davis, A.P. Jr., Poulos, S.J., and Castro, G. (1988). Strengths backfigured from liquefaction case histories, *Proceedings of the 2nd International Conference on Case Histories in Geotechnical Engineering,* June 1 – 5, St. Louis, MO, p. 1693 – 1701.

Fear, C.E. and Robertson, P.K. (1995). Estimating the undrained strength of sand: a theoretical framework, *Canadian Geotechnical Journal,* vol. 32, iss. 4, p. 859 – 870.

Idriss, I.M. and Ross W. Boulanger (2007). SPT – and – CPT – based relationships for the residual shear strength of liquefied soils, *Proceedings, 27th USSD Annual Meeting and Conference, Modernization and Optimization of Existing Dams and Reservoirs,* United States Society on Dams, Philadelphia, Pennsylvania, March 5 – 9, 2007.

Ishihara, Okusa, S., Oyagi, N., and Ischuk, A. (1990). Liquefaction-induced flow failure of embankments and residual strength of silty sands, *Soils and Foundations,* vol. 30, iss. 3, p. 69 – 80.

Ishihara, K. (1993). Liquefaction and flow failure during earthquakes, *Geotechnique,* vol. 43, iss. 3, p. 351 – 415.

Jefferies, M., and Been, K. (2006). Soil liquefaction: A critical state approach, *Taylor and Francis,* 512p.

Konrad, J.M. and Watts, B.D. (1995). Undrained shear strength for liquefaction flow failure analysis, *Canadian Geotechnical Journal,* vol. 32, p. 783 – 794.

Kramer, S.L. (1989). Uncertainty in steady-state liquefaction evaluation procedures, *Journal of Geotechnical Engineering, ASCE,* vol. 115, iss. 10, p. 1402 – 1419.

Kuerbis, R. and Vaid, Y.P. (1988). Sand sample preparation – the slurry deposition method, *Soils and Foundation,* vol. 28, iss. 4, p. 107 – 118.

Kulhawy, F.H. and Mayne, P.W. (1990). Manual on estimating soil properties for foundation design, *Electric Power Research Institute EL – 6800,* Project 1493 – 6, August, p. 400.

Mesri G. (2007). Yield strength and critical strength of liquefiable sands in sloping ground, *Geotechnique,* vol. 57, issue 3, p. 309 – 311.

Naeini, S.A. and Baziar, M.H. (2004). Effect of fines content on steady – state strength of mixed and layered samples of a sand, *Soil Dynamics and Earthquake Engineering,* vol. 24, p. 181 – 187.

Olson, S.M., Stark, T.D., Walton, W.H., and Castro, G. (2000). Static liquefaction flow failure of the North Dike of Wachusett Dam, *Journal of Geotechnical and Geoenvironmental Engineering, ASCE,* vol. 126, iss. 12, p. 1184 – 1193.

Olson, S. M. (2001). Liquefaction analysis of level and sloping ground using field case histories and penetration resistance, *Ph.D. Thesis,* University of Illinois at Urbana-Champaign, Urbana, Illinois.

Olson, S.M. and Stark, T.D. (2002). Liquefied strength ratio from liquefied flow failure case histories, *Canadian Geotechnical Journal,* vol. 39, p. 629 – 647.

Olson, S. M., Sacks, A. L., Mattson, B. B., and Servigna, D. A. (2006). Role of static shear stress in liquefaction analysis of sloping ground, *Proceedings of the 8th US National Conference on Earthquake Engineering*

Olson, S.M. and Mattson, B.B. (2008). Mode of shear effects on yield and liquefied strength ratios, *Can. Geotechnical Journal,* vol. 45, p. 574 – 587.

Olson, S. M. (2009). Strength ratio approach for liquefaction analysis of tailings dams, *University of Missouri Conference*.

Pitman, T.D., Robertson, P.K., and Sego, D.C. (1994). Influence of fines on the collapse of loose sands, *Canadian Geotechnical Journal,* vol. 31, p. 728 – 739.

Poulos, S.J., Castro, G. and France, W. (1985a). Liquefaction evaluation procedure, *Journal of Geotechnical Engineering,* ASCE, vol. 111, iss. 6, p. 772 – 792.

Poulos, S.J., Robinsky, E.I., and Keller, T.O. (1985b). Liquefaction resistance of thickened tailings, *Journal of Geotechnical Engineering,* ASCE, vol. 111, iss. 12, p. 1380 – 1394.

Riemer, M.F. and Seed, R.B. (1997). Factors affecting apparent position of steady-state line, *Journal of Geotechnical and Geoenvironmental Engineering, ASCE,* vol. 123, iss. 3, p. 281 – 288.

Robertson, P.K., Campanella, R.G. (1985). Liquefaction potential of sands using the CPT, *Journal of Geotechnical Engineering Division, ASCE,* vol. 111, iss. 3, p. 384 – 403.

Robertson, P.K. (2004). Evaluating soil liquefaction and post-earthquake deformations using the CPT, *Proceedings of ISC2 on Geotechnical and Geophysical Site Characterization,* p. 233 – 249.

Robertson, P.K. (2010). Evaluation of flow liquefaction and liquefied strength using the cone penetration test, *Journal of Geotechnical and Geoenvironmental Engineering,* vol. 136, iss. 6, p. 842 – 853.

Sadrekarimi, A. (2009). Development of a new ring shear apparatus for investigating the critical state of sands, *PhD Thesis,* University of Illinois Urbana Champaign, p. 451.

Sadrekarimi, A. and Olson, S.M. (2011). Yield strength ratios, critical strength ratios, and brittleness of sandy soils from laboratory tests, *Canadian Geotechnical Journal*, vol. 48, p. 493 – 510.

Seed, H.B. and de Alba, P. (1986). Use of SPT and CPT tests for evaluating the liquefaction resistance of sands, *Proceedings of the INSITU'86, ASCE Specialty Conference on Use in Situ Testing in Geotechnical Engineering,* Virginia Tech, Blacksburg, VA, Geotechnical Special Publication No. 6, p. 281 – 302.

Seed, H.B. (1987). Design problems in soil liquefaction, *Journal of Geotechnical Engineering Division, ASCE,* vol. 113, iss. 8, p. 827 – 845.

Seed, R.B. and Harder, L.F. Jr. (1990). SPT-based analysis of cyclic pore pressure generation and undrained residual strength, *Proceedings of H. Bolton Seed Memorial Symposium,* Bi-Tech Publishing Ltd., vol. 2, p. 351-376.

Spencer, E. (1967). A method of analysis of the stability of embankments assuming parallel inter-slice forces, *Geotechnique,* vol. 17, iss. 1, p. 11 – 26.

Stark, T.D. and Mesri, G. (1992). Undrained shear strength of liquefied sands for stability analysis, *Journal of Geotechnical Engineering, ASCE,* vol. 118, iss. 11, p. 1727 – 1747.

Stark, T.D., Olson, S.M. (1995). Liquefaction resistance using CPT and field case histories, *Journal of Geotechnical Engineering, ASCE,* vol. 121, iss. 12, p. 856 – 869.

Thevanayagam, S., Ravishankar, K., and Mohan, S. (1996). Steady state strength, relative density and fines content relationship for sands, *Transportation Res. Record 1547,* p. 61 – 67.

Thevanayagam, S. (1998). Effect of fines and confining stress on undrained shear strength of silty sands, *Journal of Geotechnical and Geoenvironmental Engineering, ASCE,* vol. 124, iss. 6, p. 479 – 491.

Tokimatsu, K. (1988). Penetration tests for dynamic problems, *Proceedings of the 1st International Symposium on Penetration Testing,* Rotterdam, p. 117 – 136.

Vaid, Y.P. and Thomas, J. (1995). Liquefaction and post-liquefaction behavior of sand, *Journal of Geotechnical Engineering,* vol. 121, iss. 2, p. 163 – 173.

Vaid, Y.P., Chung, E.K.F. and Kuerbis, R.H. (1990). Stress path and steady state, *Canadian Geotechnical Journal,* vol. 27, iss. 1, p. 1 – 7.

Wood, D.M. (1990). Soil behaviour and critical state soil mechanics, *McGraw Hill,* London.

Yoshimine, M. and Ishihara, K. (1998). Flow potential of sand during liquefaction, *Soils and Foundations,* vol. 38, iss. 3, p. 189 – 198.

Yoshimine, M., Robertson, P.K., and Wride (Fear), C.E. (1999). Undrained shear strength of clean sands to trigger flow liquefaction, *Canadian Geotechnical Journal,* vol. 36, p. 891 – 906.

Zlatovic, S., and Ishihara, K. (1995). On the influence of non-plastic fines on residual strength, *Proceedings IS-TOKYO'95, 1st International Conference on Earthquake Geotechnical Engineering,* K. Ishihara, ed., A.A. Balkema, Rotterdam, The Netherlands, p. 239 – 244.

6.12 Figures and Tables

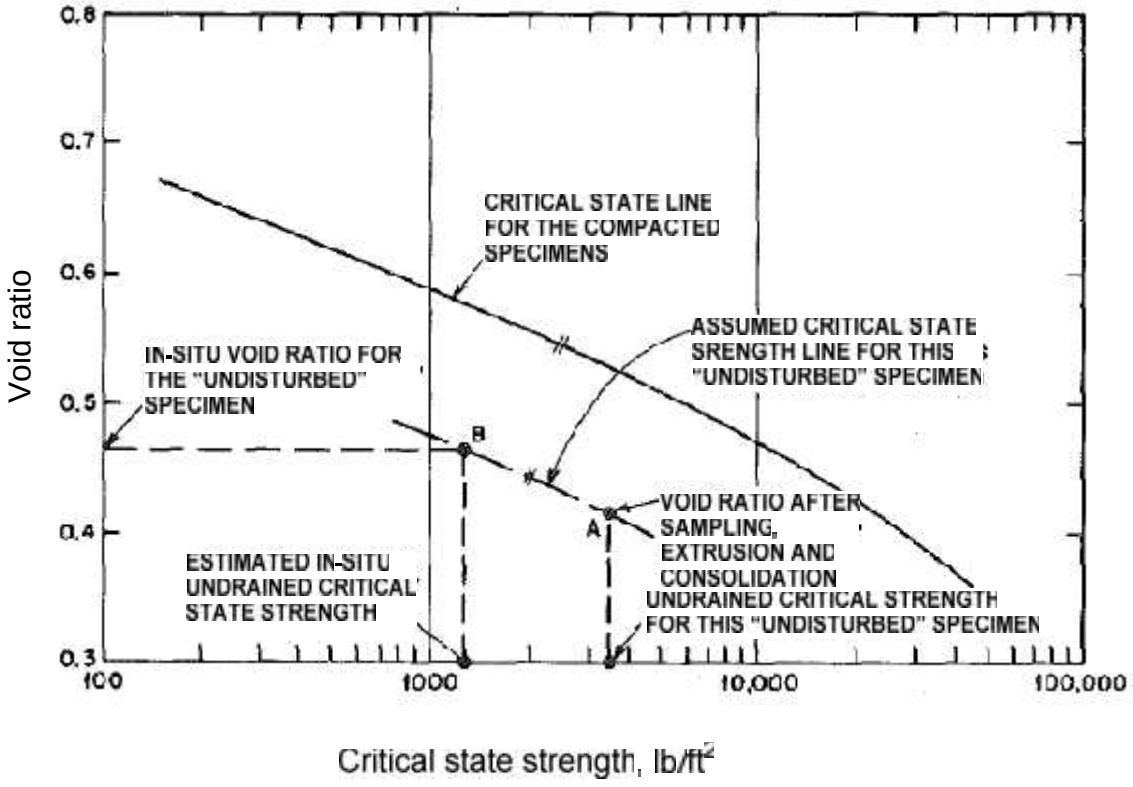

Figure 6.1 Laboratory-based liquefied shear strength estimation procedure (adapted from Poulos et al. 1985)

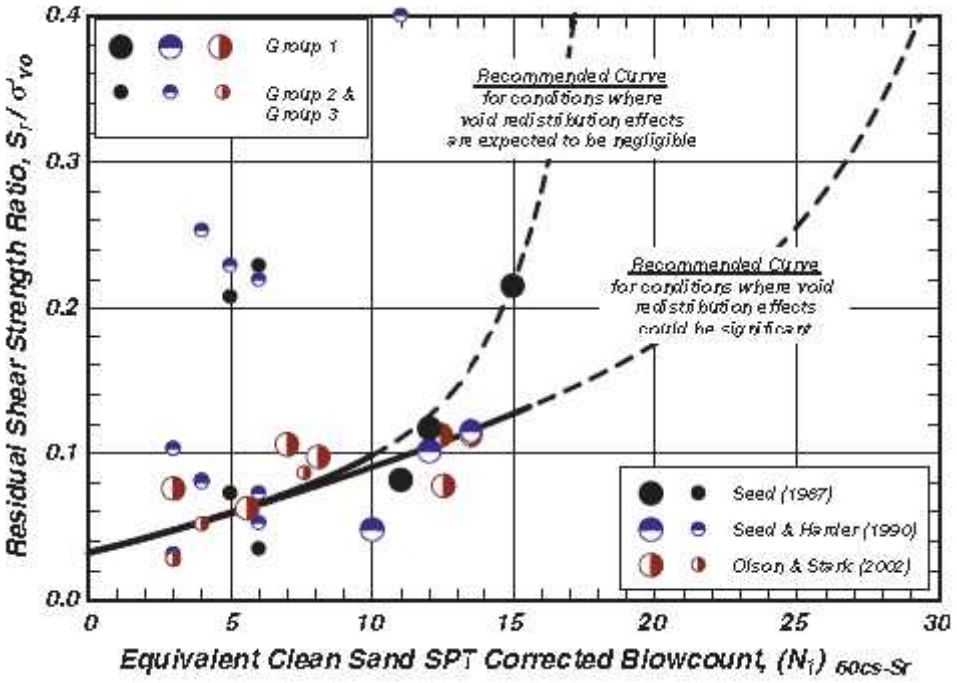

Figure 6.2 Idriss and Boulanger (2007) case history-based correlation to estimate liquefied shear strength

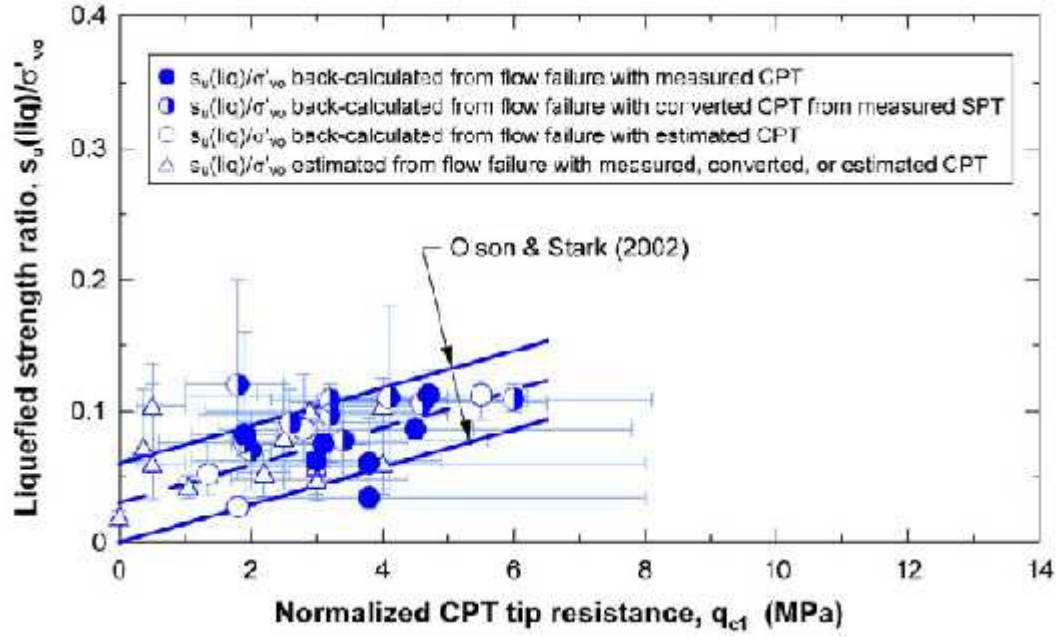

Figure 6.3 Olson and Stark (2002) case history-based correlation to estimate liquefied shear strength (from Olson 2009)

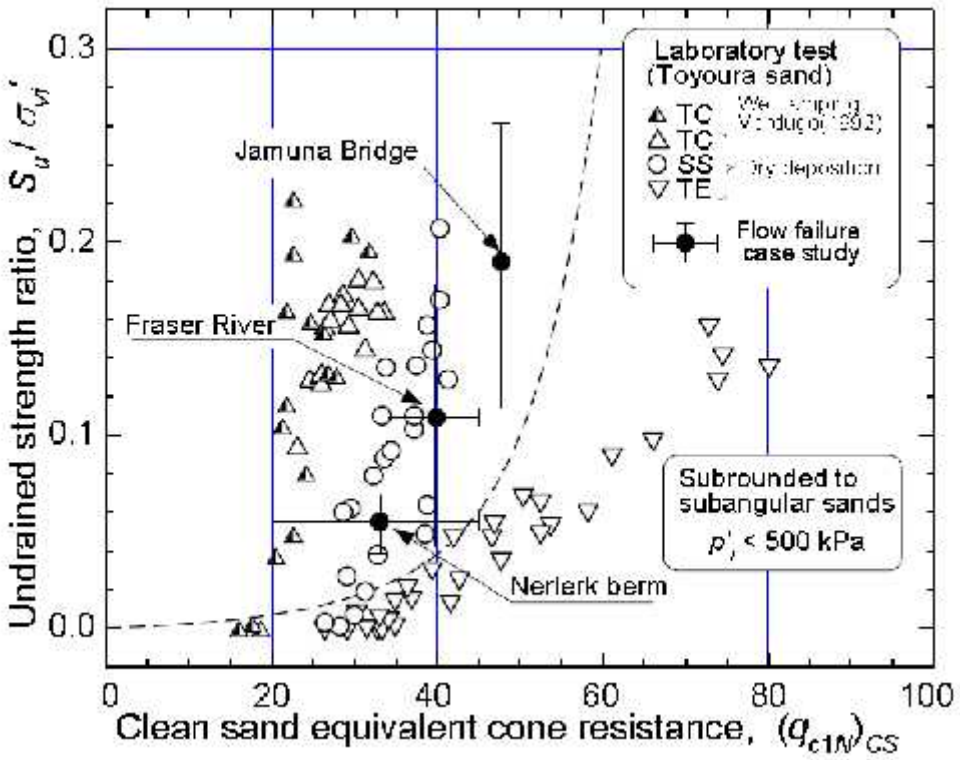

Figure 6.4 Correlation between liquefied shear strength ratio and clean sand equivalent cone resistance based on laboratory tests and field case histories (from Robertson 2004 after Yoshimine et al. 1999)

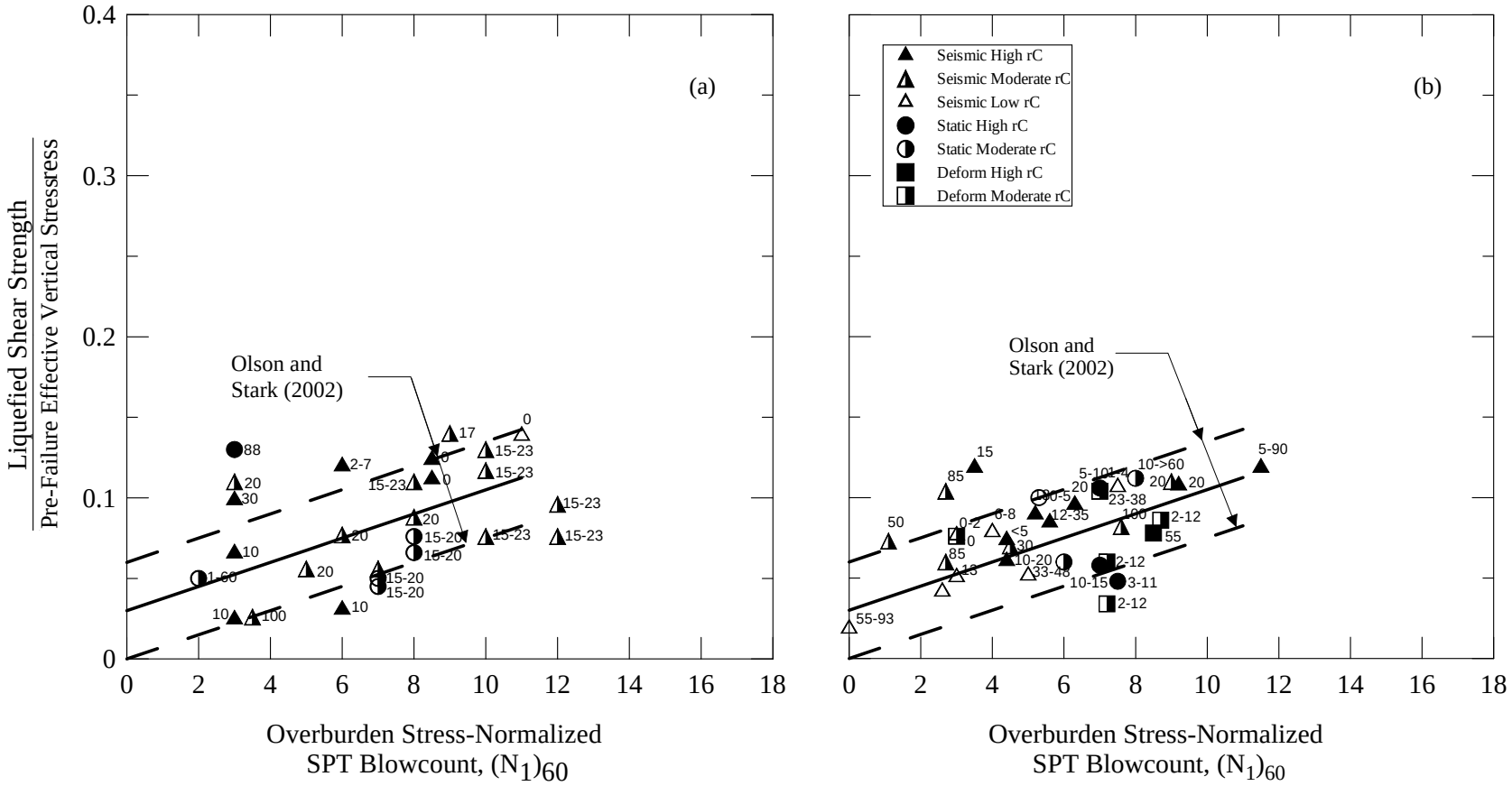

Figure 6.5 Correlation between liquefied shear strength ratio and overburden stress-normalized SPT blow count for case histories from (a) this study and (b) from Olson (2001). Numbers beside data points represent fines content. The figure includes the liquefied shear strength ratio correlation from Olson and Stark (2002)

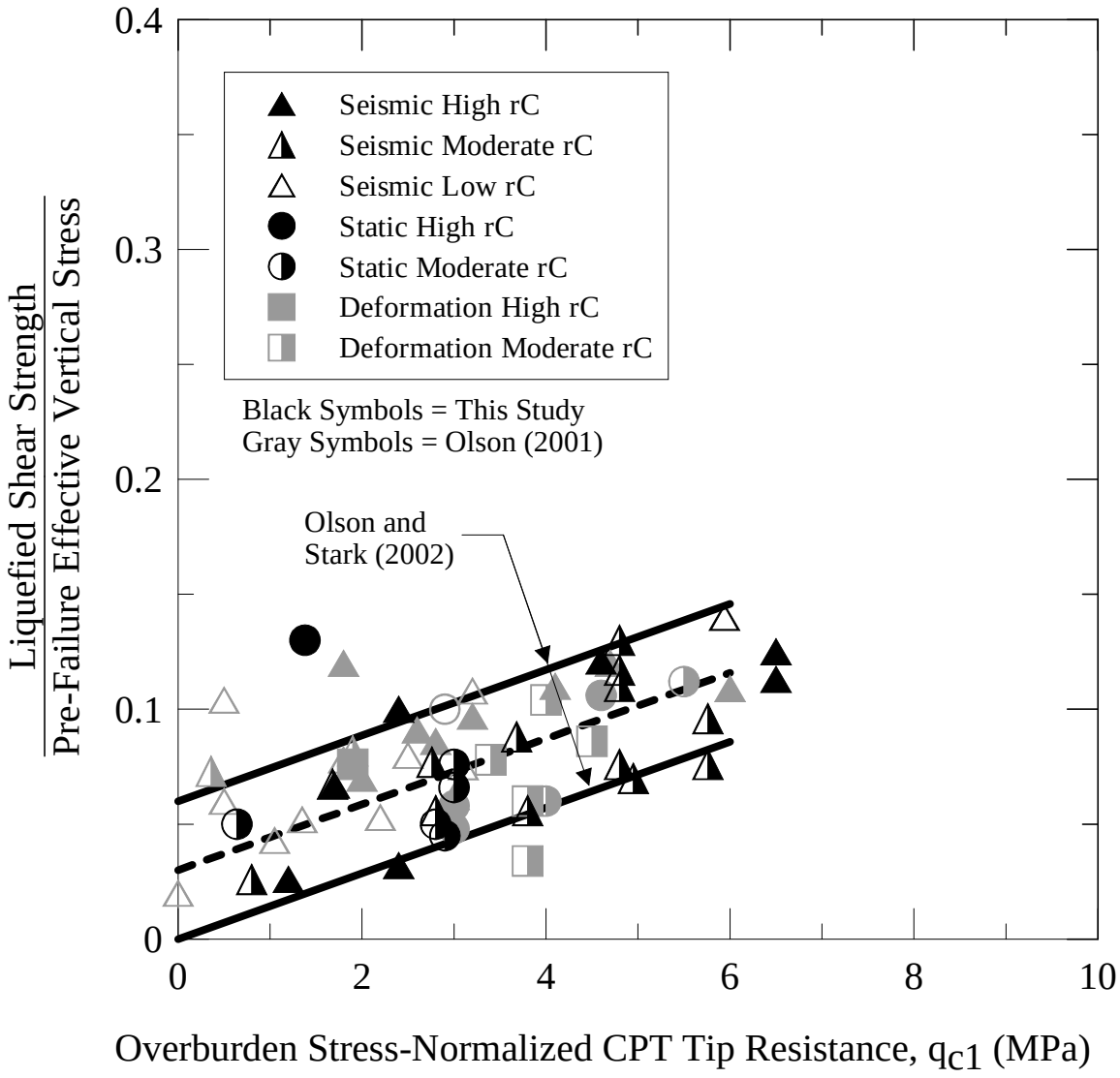

Figure 6.6 Correlation between liquefied shear strength ratio and overburden stress-normalized CPT tip resistance for case histories from this study and from Olson (2001). Numbers beside data points represent fines content. The figure includes the liquefied shear strength ratio correlation from Olson and Stark (2002)

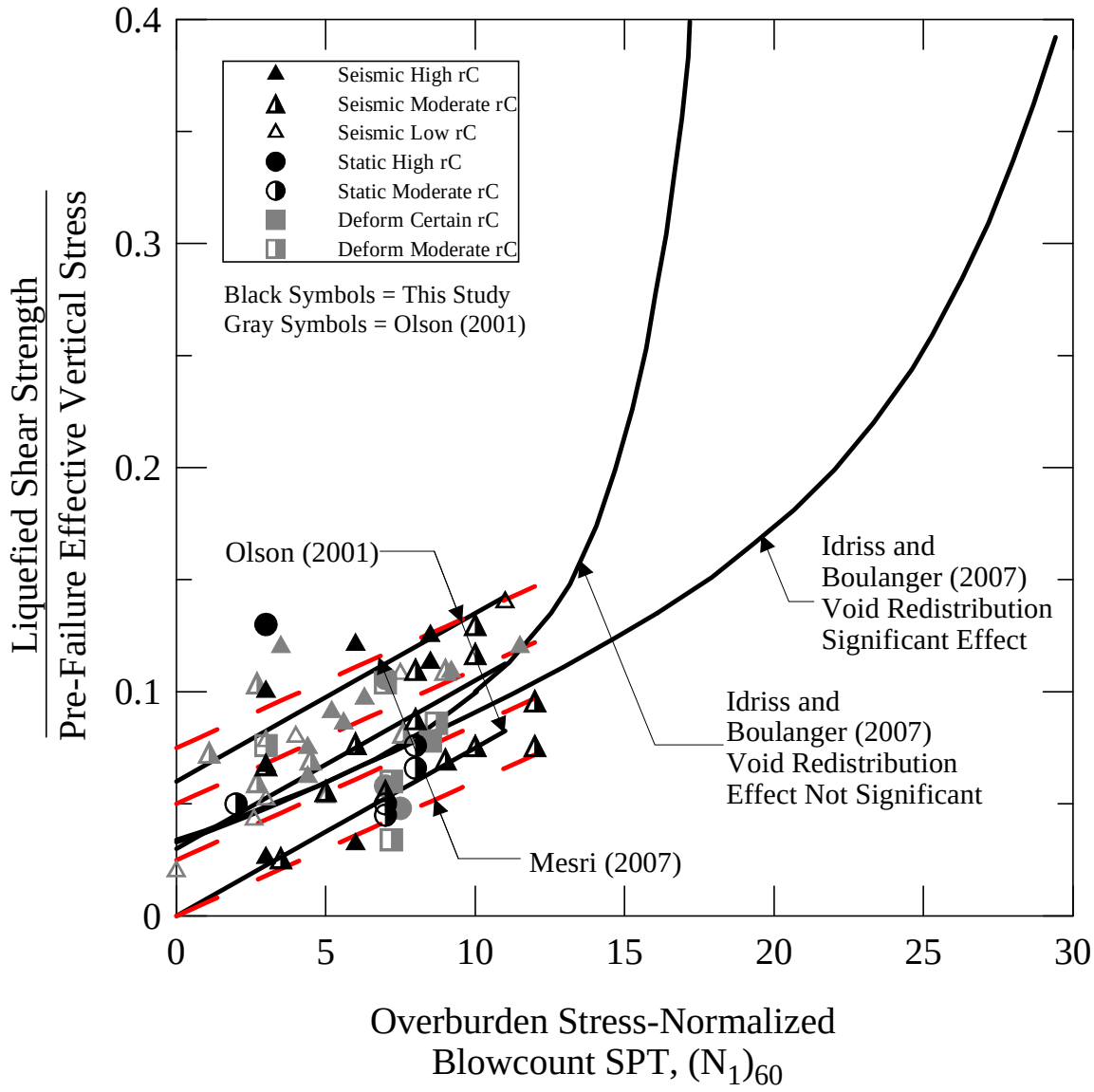

Figure 6.7 Correlation between liquefied shear strength ratio and overburden stress-normalized SPT blow count for case histories from this study and from Olson (2001). The figure includes the liquefied shear strength ratio correlations from Olson and Stark (2002), Mesri (2007), and Idriss and Boulanger (2008)

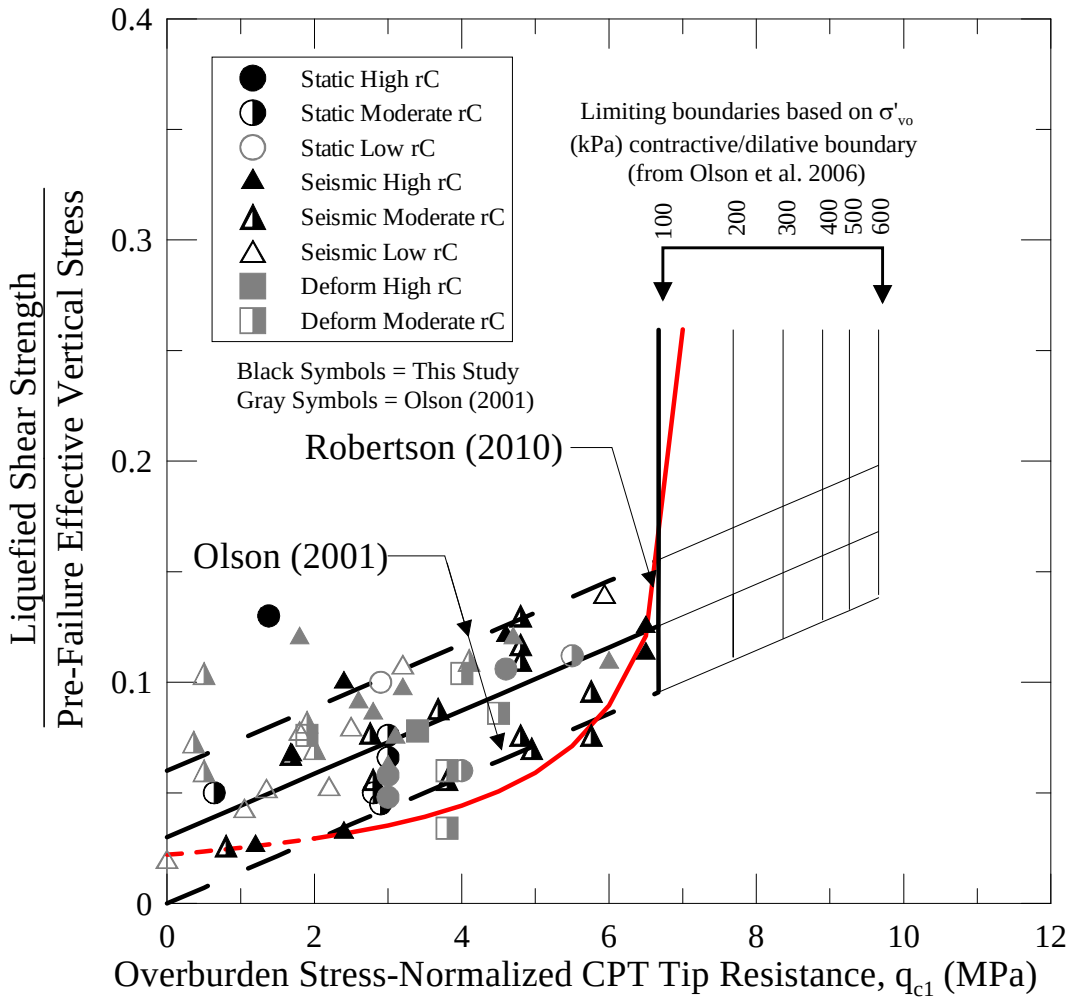

Figure 6.8 Correlation between liquefied shear strength ratio and overburden stress-normalized CPT tip resistance for case histories from this study and from Olson (2001). The figure includes the liquefied shear strength ratio correlations from Olson and Stark (2002), Idriss and Boulanger (2008), and Robertson (2010). In addition, the vertical asymptotes with the Olson and Stark (2002) correlations correspond to the contractive/dilative boundary proposed by Olson and Stark (2003)

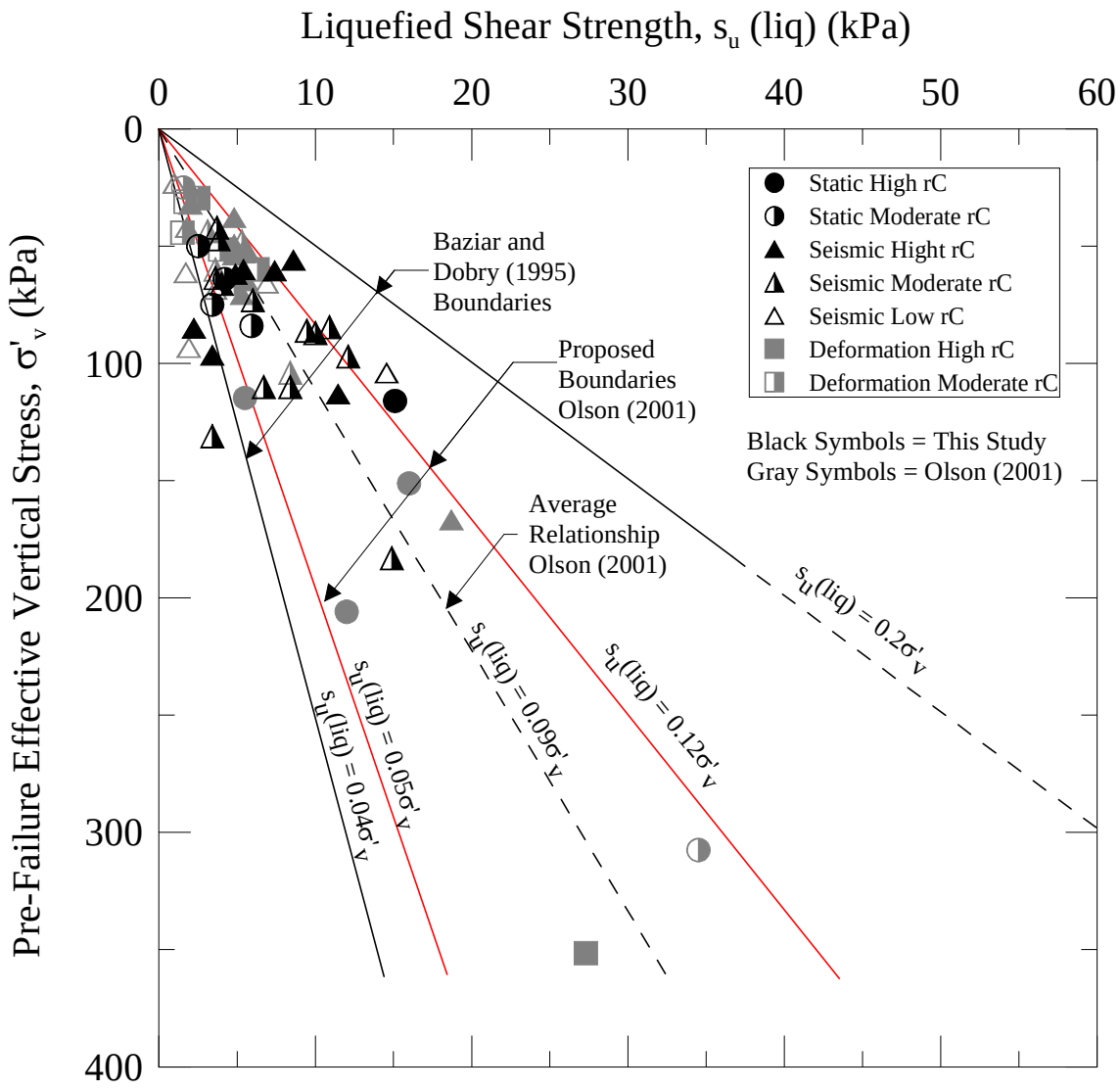

Figure 6.9 Evaluation of strength ratio concept using liquefaction flow failure case histories analyzed in this study and in Olson (2001)

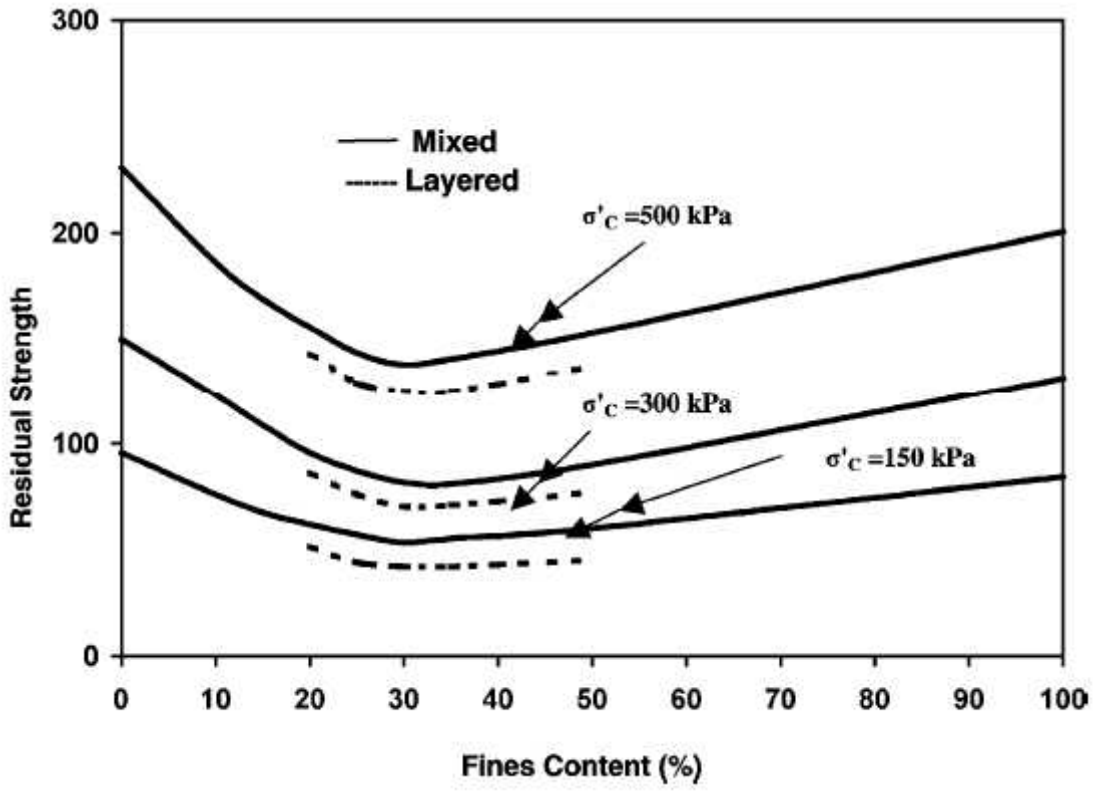

Figure 6.10 Liquefied shear strength of mixed and layered samples versus fines content (from Naeini and Baziar 2004)

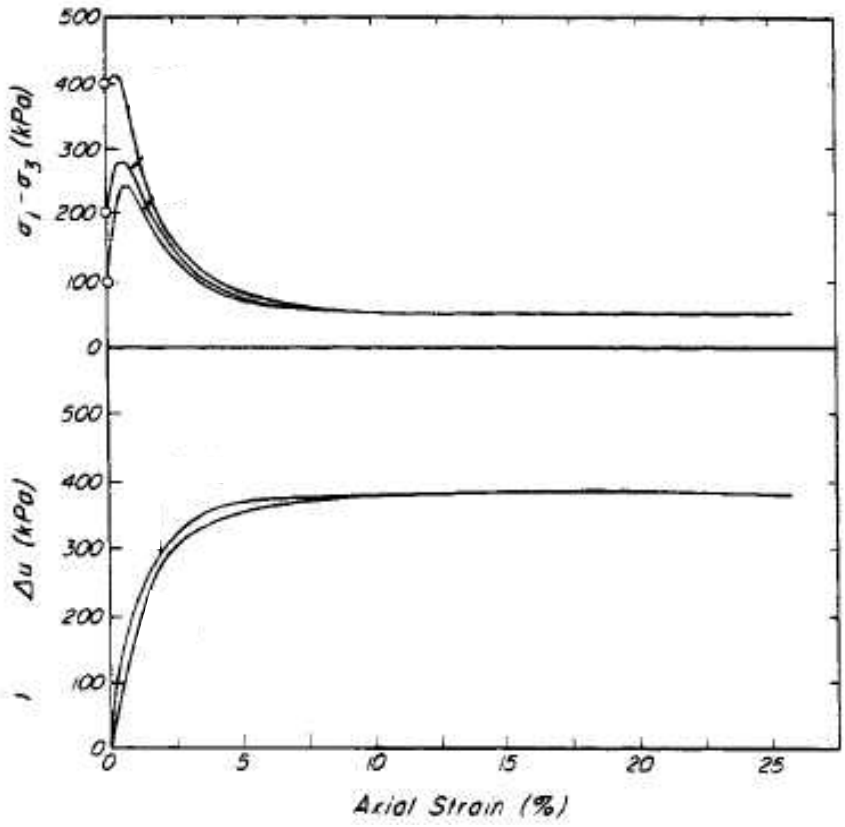

Figure 6.11 Stress-strain and shear-induced porewater pressure behavior of Banding sand tested in undrained triaxial compression with different static driving shear stresses (adapted from Terzaghi et al. 1996 using data from Castro 1969)

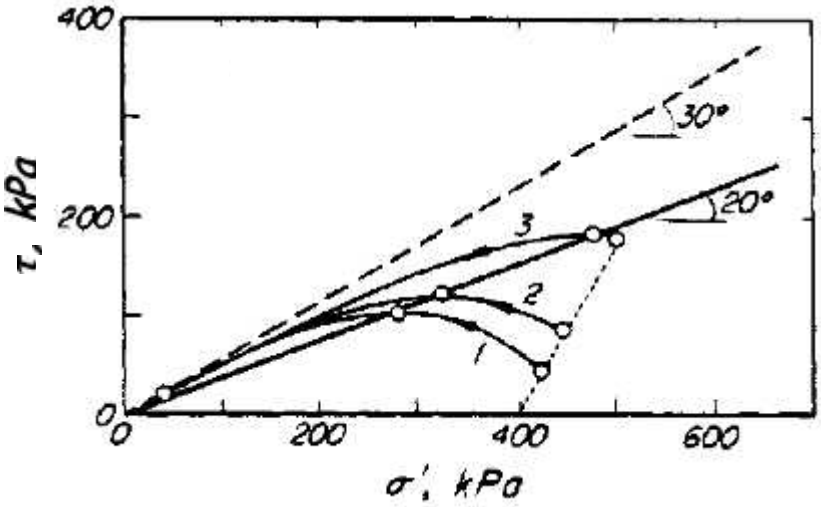

Figure 6.12 Undrained stress paths for 60º plane for tests on Banding sand with different static driving shear stresses (adapted from Terzaghi et al. 1996 using data from Castro 1969)

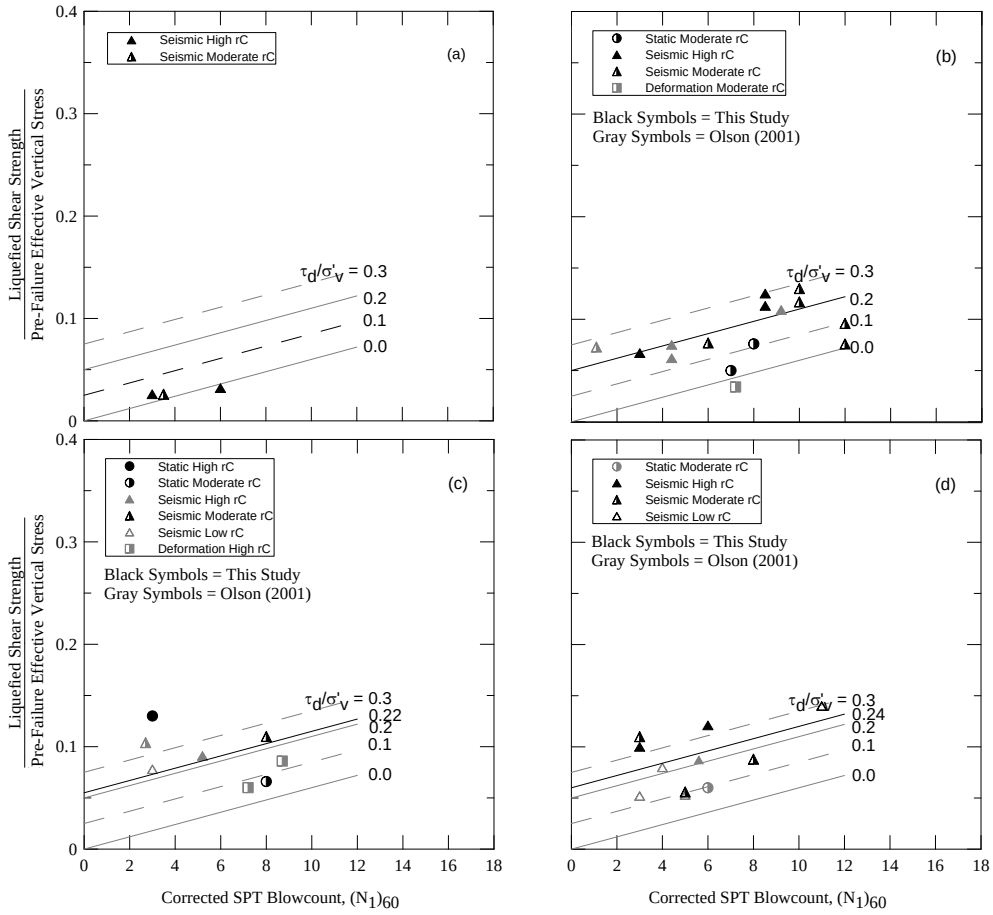

Figure 6.13 Liquefied shear strength ratio and overburden stress-normalized SPT blow count from liquefaction flow failure case histories compared to Eq. 6.3 (from Mesri 2007). (a) $\tau_{static}/\pm'_v = 0.1$; (b) $\tau_{static}/\pm'_v = 0.2$; (c) $\tau_{static}/\pm'_v = 0.22$; (d) $\tau_{static}/\pm'_v = 0.24$; (e) $\tau_{static}/\pm'_v = 0.26$; (f) $\tau_{static}/\pm'_v = 0.28$; (g) $\tau_{static}/\pm'_v = 0.3$

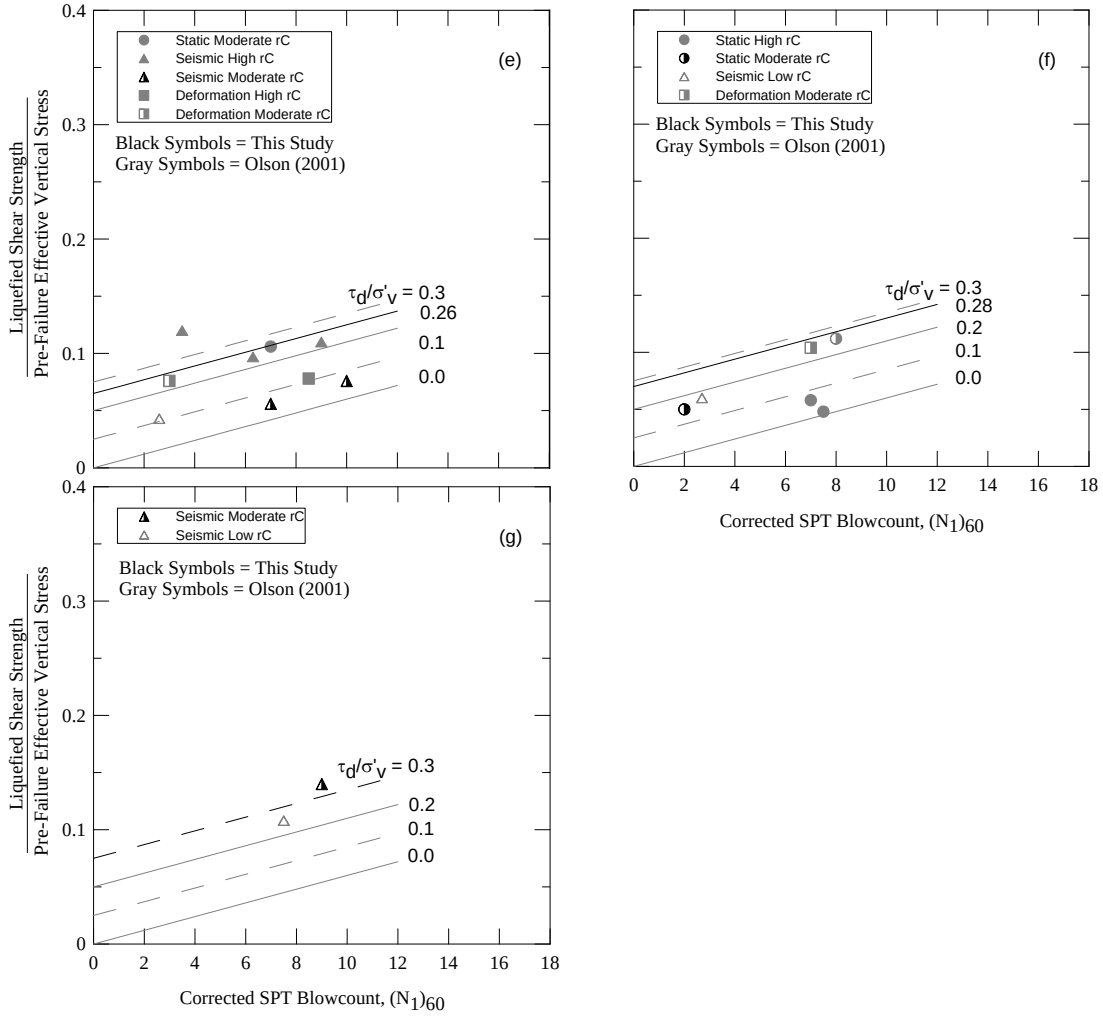

Figure 6.13 Continued

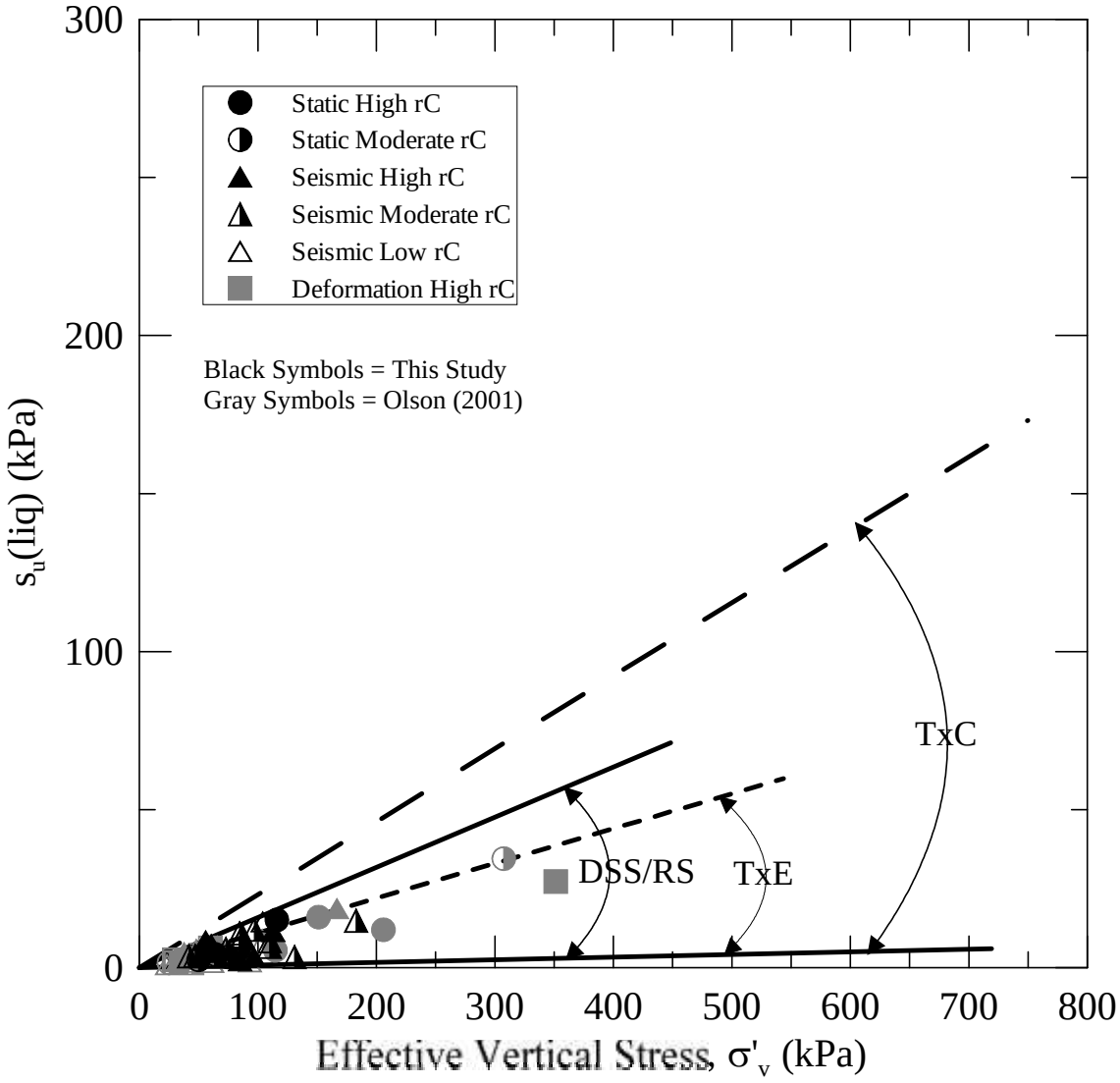

Figure 6.14 Comparison of liquefied strength ratios from field case histories analyzed in this study and in Olson (2001) with the liquefied strength ratio boundaries for various modes of shear from TxC, DSS/RS, and TxE tests collected by Olson and Mattson (2008)

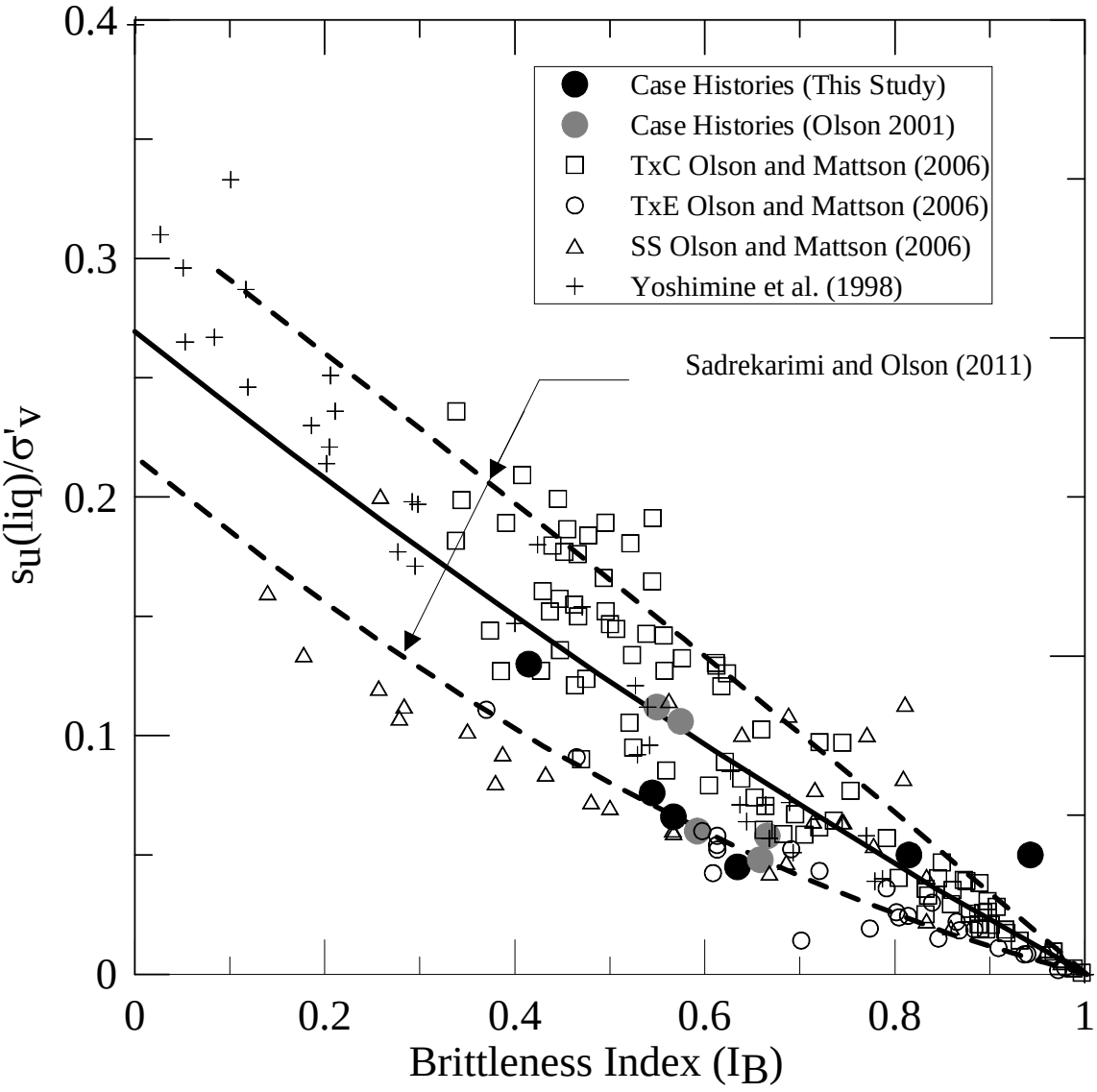

Figure 6.15 Relationship between liquefied strength ratio and brittleness index proposed by Sadrekarimi and Olson (2011) compared with liquefied strength ratios back-calculated from flow failure case histories. Laboratory data from Olson and Mattson (2008) and Yoshimine et al. (1999) are included

Table 6.1 List of flow failure case histories with back-calculated liquefied shear strength and strength ratios. The case history names associated with particular numbers are provided in Table 4.3

Case History (1)	Post-Failure Geometry Strength Ratio			Post-Failure Geometry Shear Strength			Weighted Average Post-Failure Vertical Effective Stress (kPa) (8)
	Lowerbound (2)	Best Estimate (3)	Upperbound (4)	Lowerbound (kPa) (5)	Best Estimate (kPa) (6)	Upperbound (kPa) (7)	
1	-	-	-	-	-	-	-
2	0.04	0.056	0.07	2.7	3.6	4.45	63.5
3	0.107	0.14	0.22	4	6.8	8.2	33.5
4	0.113	0.16	0.25	4.8	7.5	10.2	65.4
5	0.016	0.017	0.019	2.1	2.3	2.5	131
6	0.046	0.064	0.075	4	5.45	6.4	85.5
7	0.065	0.067	0.068	4.7	4.9	5	73
8	0.019	0.026	0.033	1.6	2.2	2.8	85.5
9	0.027	0.032	0.043	2.9	3.4	4.56	106
10	0.038	0.053	0.088	2.65	4.6	5.78	61
11	0.03	0.031	0.04	2.06	2.25	2.8	71
12	0.014	0.05	0.086	1	3.5	6	70
13	0.119	0.15	0.157	6.7	6.8	8	56
14	0.062	0.077	0.091	2.9	3.8	4.3	47
15	0.066	0.088	0.11	2.8	3.7	4.5	42
16	-	-	-	-	-	-	-
17	-	-	-	-	-	-	-
18	0.049	0.07	0.098	9	13.1	18	183.5
19	0.084	0.088	0.089	8.8	9.1	9.3	116
20	0.026	0.038	0.048	2.95	4.4	5.4	113
21	0.04	0.045	0.056	3.05	3.4	4.2	75
22	0.054	0.066	0.08	3.5	4.2	5.1	64
23	0.066	0.076	0.083	5.92	5.37	6.74	84
24	0.04	0.05	0.06	2	2.5	3	50
25	-	-	-	-	-	-	-
26	0.078	0.082	0.126	6.06	8.6	10.43	86
27	0.04	0.076	0.097	4	8.4	9.97	110
28	0.093	0.117	0.155	7.3	10.9	15.6	84.5
29	0.045	0.076	0.11	3.3	6	9.9	73
30	0.092	0.096	0.14	9.2	10	15.3	87
31	0.08	0.13	0.19	7	12.1	19.45	97

Table 6.2 List of cases analyzed incorporating kinetics and the corresponding estimates of liquefied shear strength and strength ratio

Case History (1)	Shear Strength and Strength Ratio Considering Kinetics			
	Best Estimate Shear Strength (kPa) (9)	Lowerbound Shear Strength (kPa) (10)	Upperbound Shear Strength (kPa) (11)	Best Estimate Strength Ratio (12)
5	3.4	-	-	0.026
6	11.3	-	-	0.13
10	6.7	6.44	9.15	0.11
11	4	3.63	5.25	0.056
19	14.9	-	-	0.14
20	11.45	9.95	13.45	0.1
26	9.45	-	-	0.11

CHAPTER SEVEN:

PREDICTING THE PERFORMANCE OF FIELD CASES

7.1 Introduction

As discussed in Chapter 3, liquefaction analysis for sloping ground consists of three steps: (1) liquefaction susceptibility; (2) liquefaction triggering; and (3) post-triggering/flow failure stability analysis. These steps were evaluated and updated in this study using 31 liquefaction failure case histories combined with the 33 liquefaction failure case histories evaluated by Olson (2001) and Olson and Stark (2002; 2003).

A liquefaction susceptibility analysis evaluates whether a soil is contractive or dilative under current the in-situ stress conditions. In Chapter 4, the author evaluated available methods to analyze liquefaction susceptibility using penetration resistance, and an approach that incorporates the compressibility of the potentially liquefiable soil was described.

If the liquefaction susceptibility analysis identifies potentially liquefiable soils, a liquefaction triggering analysis is performed to evaluate whether the combined static and seismic stresses are sufficient to trigger liquefaction. In Chapter 5, the author evaluated several methods to evaluate liquefaction triggering in sloping ground using the 64 liquefaction case histories in the combined case history database.

If the triggering analysis indicates that liquefaction is likely to occur, a post-triggering/flow failure stability analysis is performed to evaluate whether flow failure is likely to occur. In Chapter 6, the author evaluated several methods to estimate the post-triggering liquefied shear strength and strength ratio using the 64 case histories in the combined case history database.

In this Chapter, the liquefaction analysis described in Chapters 4, 5, and 6 are used to evaluate the performance of three separate geostructures: (1) Yamanaka dam in Japan; (2) Mackay dam in Idaho, USA; and (3) a levee in California, USA.

7.2 Case Histories

To evaluate the liquefaction analysis procedure described in Chapters 4, 5, and 6, the procedure was used to predict the performance of three structures subjected to seismic loading: (1) Yamanaka dam in Japan; (2) Mackay dam in Idaho, USA; and (3) a levee site in California, USA. Yamanaka dam was subjected to four strong earthquakes in 1968, 1978, 1983 and 1994, and experienced various severities of failure during each event, including a significant liquefaction-induced slump during the 1968 Tokachi-Oki earthquake. Mackay dam experienced some deformations during the 1983 Borah Peak earthquake. The levee site was shaken during the 1989 Loma Prieta earthquake, but did not fail.

7.3 Yamanaka Dam

The construction of dams in Japan started more than 200 years ago. There are about 90,000 small earth dams used for irrigation purposes. More than 80% of these irrigation dams are less than 10 m high (Tani and Nakashima 1999). Because most of Japan is seismically active, earthquakes often damage these small irrigation dams. Many dams are subjected to several earthquakes; however, only a few earthquakes are strong enough to damage these structures. Yamanaka dam is one of these small irrigation dams that has been subjected to multiple earthquakes.

Figure 7.1 shows the epicenters of several notable earthquakes in Japan. Four earthquakes damaged Yamanaka dam: the 1968 Tokachi-Oki, the 1978 Miyagi-ken-Oki,

the 1983 Nihon-kai-Chubu, and the 1994 Sanriku Haruka-Oki earthquakes. Yamanaka dam is about 5 m high, and is situated near Ogawara Lake on Honshu Island, in the Aomori prefecture, Japan (Figure 7.2).

7.3.1 Site Geology and Soil Conditions

Figure 7.3 shows the longitudinal soil profile at Yamanaka dam based on three borings drilled after the 1983 Nihon-kai Chubu earthquake. The boring logs indicate that the embankment fill thickness ranged from about 4 to 5.5m, and consisted of loose fine sand (with SPT N-values generally less than 10). Below the upper embankment sand fill, a layer of clay (ranging from 0.8 to 1.9m thick) was present. This layer may have served as a cutoff blanket for the reservoir at the site. Below this clay layer, sand (described as fill) was present. The investigators did not indicate whether this was alluvial channel fill sand or artificially-placed fill sand. The failures appear to have been roughly centered over this filled stream channel. The lower sand ranged from about 3 to 9 m thick. Figure 7.4 shows two grain size distributions from the sandy soils below Yamanaka dam. The upper and lower fine sands had a D_{50} of about 0.3 to 0.4 mm and a FC of about 24% to 32%.

Below the lower sandy soil, a silty sand with some lenses of more cohesive material was encountered. The SPT blow counts in this material ranged from about 10 to 30.

7.3.2 Description of Failure

Tani and Nakashima (1999) reported that Yamanaka dam failed during several earthquakes since its initial construction. They argued that the failures likely resulted from liquefaction of the fine sandy fill below the phreatic surface. Specifically, they described damage to the dam during the 1968 Tokachi-Oki, the 1978 Miyagi-ken-Oki, the 1983 Nihon-kai-Chubu, and the 1994 Sanriku Haruka-Oki earthquakes.

The dam suffered severe slumping and flow of the reservoir-side slope during the 1968 Tokachi-Oki earthquake, as illustrated in Figure 7.5. Following the earthquake, the upstream slope and crest were regraded to their pre-earthquake conditions. The upstream slope of Yamanaka dam again failed during the 1978 Miyagi-ken-Oki earthquake, although the failure was not as severe as in 1968. Following this earthquake, the dam slope was regraded, and a sheetpile wall was driven through the slope to mitigate displacements during future earthquakes. Interestingly, during the 1983 Nihon-kai-Chubu earthquake, a part of upstream slope suffered cracking and minor slumping (despite the mitigation effort) and crest settled about 80 cm, as illustrated in Figure 7.6. Following the earthquake, the sheetpile wall was repaired and the slope was regraded. Nevertheless, the upstream slope again suffered cracking and minor slumping during the 1994 Sanriku Haruka-Oki earthquake, as shown in Figure 7.7. Following the earthquake, the upstream slope was again regraded.

As noted above, the most severe failure occurred during the 1968 Tokachi-Oki earthquake, while the other three earthquakes caused less severe damage to the dam. The damage during all four earthquakes was chiefly limited to the upstream slope.

Based on cyclic triaxial tests, Tani and Nakashima (1999) suggested that the liquefaction resistance of the silty sand was adequate to preclude liquefaction and the deformation observed in the dam apparently resulted from liquefaction in the sandy fill present in the embankment and the filled stream channel.

7.3.3 Estimation of Ground Motions

To estimate the peak ground accelerations associated with each earthquake, Tani and Nakashima (1999) utilized the following ground motion prediction equation (although it is not clear if Tani and Nakashima developed Eq. 7.1 or if it was developed by others):

$$a_{\max} = 18.4 * 10^{0.302Mj} * R^{-0.8}$$ **Eq. 7.1**

where M_J = JMA (Japan Meteorological Agency) magnitude scale and R = maximum epicentral distance (in km). Table 7.1 summarizes the seismic data for each of the earthquakes that affected Yamanaka dam. As seen in Table 7.1, Yamanaka dam suffered damage with at peak ground accelerations as small as about 0.04g, suggesting that the soil was near its yield strength envelope in its pre-failure stress condition.

7.3.4 Representative Penetration Resistance

Tani and Nakashima (1999) reported the results of three borings with SPTs performed following the 1983 Nihon-kai Chubu earthquake. Generally SPT N-values were less than 10 to elevation -5 m, with the embankment fill exhibiting SPT N-values typically less than 5, as shown in Figure 7.3. Tani and Nakashima (1999) did not report the SPT hammer type or release mechanism, but Japanese practice commonly employs either donut Tombi or donut slip-rope (with 2 turns) hammers (Skempton 1986). The first method produces a hammer energy ratio (ER) of about 78% while the second method produces ER ~ 65%. These hammer energy ratios yield corrections of 1.3 and 1.1 respectively. Therefore, the author used an average hammer energy correction of 1.2 to calculate N_{60} values. For all vertical effective stress computations, the author used unit weight of 18.5 kN/m^3. Computed $(N_1)_{60}$ values ranged from 5 to 12 with the best estimate of 7 blows/ft as shown in Figure 7.8.

7.3.5 Liquefaction Susceptibility Analysis

Figure 7.9 presents the liquefaction susceptibility analysis for the three borings conducted following the 1983 Nihon-kai Chubu earthquake. This analysis indicates that, with the exception of a few larger N-values, the upper and lower sandy fill soils are

contractive and susceptible to liquefaction. In fact, the silty foundation sand also is marginally susceptible to liquefaction. As a result, a liquefaction triggering analysis is required for each of the earthquakes.

7.3.6 Liquefaction Triggering Analysis

As stated in Section 7.3.4, $(N_1)_{60}$ values in the embankment fill ranged from about 5 to 12 blows/ft with an average of about 7. The lower sandy fill $(N_1)_{60}$ values also ranged from about 5 to 12 blows/ft with an average of about 7 (see Figure 7.8). These values do not include some occasional high blow counts.

As the yield shear strength ratio is a function of $\tau_{static}/\sigma'_{vo}$, the first step of the triggering analysis is to identify the critical sliding surface. Driving stress ratios were computed by limit equilibrium analysis using the software Slope/W from Geo-Slope International (2004). To calculate driving shear stress ratio, a single arbitrary value of driving stress ratio was assigned to the soil in contractive zone and this ratio is modified until a factor of safety of unity is achieved. Non-liquefied soils were assigned a drained friction angle, $\phi' = 33°$. Figure 7.10 and Figure 7.11 present the critical shallow and deep sliding surfaces, respectively, identified by slope stability analysis that involved only the liquefiable embankment sands. Both surfaces were analyzed for all four earthquakes.

Because a sheetpile wall was installed within the upstream slope after 1978 Miyagiken-Oki earthquake, a lateral load of 20 kN representing the pinning effect of the wall was added for the 1983 Nihonkai-Chubu and 1994 Sanriku Haruka-Oki earthquakes. The shallow circular sliding surface in Figure 7.10 yielded $\tau_{static}/\sigma'_{vo} = 0.341$ and 0.162 with and without the sheetpile wall pinning force.

The author also considered a deeper sliding surface that intersected both zones of potentially liquefiable sandy soils as illustrated in Figure 7.11. The deep circular sliding surface shown in Figure 7.11 produced $\tau_{static}/\sigma'_{vo} = 0.200$ and 0.183 with and without the

sheetpile wall pinning force. This sliding surface was considered because the results of the triggering analysis may differ significantly depending on the location of the sliding surface. Yield shear strength ratios were calculated for the liquefiable soils along each of the failure surfaces as shown in Figure 7.12. The results of triggering analysis for these two sliding surfaces are discussed below.

Table 7.2 and Table 7. 3 present the liquefaction triggering analyses for the circular failure surface shown in Figure 7.10. Seismic stresses for all triggering analyses were calculated using Eq. 5.2 (Chapter 5) for each earthquake using a_{max} values listed in Table 7.1. Slices in the sandy soils with vertical effective stresses less than 10.6 kPa were defined as nonliquefiable because they fall in the dilative zone in Figure 7.9 for an average $(N_1)_{60} = 7$. The first five slices near the toe of dam were found to be dilative and therefore considered as nonliquefiable. Different cases were considered based on the $FS_{Triggering}$ value for each slice, as follows:

$FS_{Triggering} < 1$	Liquefaction triggered
$1 \leq FS_{Triggering} \leq 1.05$	Liquefaction triggered marginally
$1.05 > FS_{Triggering} \leq 1.1$	Liquefaction triggered marginally to No liquefaction (decided on case to case basis)
$FS_{Triggering} > 1.1$	Liquefaction not triggered

For the contractive slices, the $FS_{Triggering}$ for the shallow circular failure surface, without the sheetpile wall, ranged from 0.78 to 1.00 during the 1968 earthquake and from 0.96 to 1.09 during the 1978 earthquake. As shown in Table 7.2, the 1968 earthquake triggered liquefaction throughout the contractive zone (slices 6 – 24) Therefore, each slice in the contractive zone was assigned its liquefied shear strengths for post-triggering stability analysis. Table 7.2 also shows that only a portion of the contractive zone (slices 6 – 17) was predicted to liquefy during the 1978 earthquake.

After the sheetpile wall was installed, the $FS_{Triggering}$ for the shallow circular failure surface, ranged from 0.94 to 1.33 during the 1983 earthquake and from 1.07 to 1.4

during the 1994 earthquakes (see Table 7. 3). In these earthquakes, only a portion of the contractive zone (slices 6 – 14 during the 1983 event and slices 6 – 9 during the 1994 event) were predicted to liquefy.

Table 7.4 and Table 7.5 present the liquefaction triggering analysis for the deep circular failure surface shown in Figure 7.11. Again, slices in the sandy soils with vertical effective stresses less than 10.6 kPa were considered dilative and not susceptible for flow liquefaction. Only one slice (slice 3) near the toe of dam was found to be dilative. Slices 1, 2, 24 and 25 intersected in the clay layer and were considered nonliquefiable. For the contractive slices, the $FS_{Triggering}$ (without the sheetpile wall), ranged from 0.70 to 1.08 and 0.97 to 1.22 for the 1968 and 1978 earthquakes, respectively. The $FS_{Triggering}$ for the same failure surface, with the sheetpile wall, ranged from 0.73 to 1.16 and 1.03 to 1.32 for the 1983 and 1994 earthquakes, respectively.

7.3.7 Post-triggering Stability Analysis

As stated in Section 7.3.4, the $(N_1)_{60}$ values ranged from 5 to 12 blows/ft with a best estimate of 7 blows/ft. Slices that liquefied were assigned liquefied strength ratios for post-triggering liquefaction stability analysis, while the slices that did not liquefy (but were still contractive) were assigned their yield strength ratios. The yield and liquefied strength ratios were calculated based on penetration resistance by using Figure 7.12 and Figure 7.13, respectively. Nonliquefied sandy soil (in dilative zone or above phreatic surface) involved in the sliding surface was assigned a friction angle, $\phi' = 33^o$. A mobilized shear strength ratio, $s_u(mob)/\sigma'_v$ of 0.22 was assigned to the clay layer. Slope stability analyses were conducted for the shallow and deep circular slip surfaces shown in Figure 7.10 and Figure 7.11, respectively. The results of post-failure stability analyses are shown in Table 7.6.

The computed values of FS_{Flow} are quite consistent with the observed damage, with the lowest FS_{Flow} of about 0.6 corresponding to the most severe damage to the

embankment during the 1968 earthquake. A value of FS_{Flow} of about 0.9 is consistent with the less severe slump observed following the 1978 earthquake. Similarly, the higher FS_{Flow} of approximately 0.95 to 1.0 and about 1.1, respectively, are consistent with the cracking and minor slumping associated with the 1983 and 1994 earthquakes.

7.4 Mackay Dam

Mackay dam is situated across the Big Lost River, about 6.4 km northwest of the town of Mackay in central Idaho USA. The dam was constructed to store spring runoff so that it can be used for irrigation purposes during summer. It is composed primarily of dumped silty, sandy gravel with a relative density of about 45% (Harder 1992) and was constructed in different phases ranging from 1909 to 1956. The planned height of Mackay dam was about 36.5 m, but due to issues related to excessive seepage the dam was completed to only 21.3 m. During the 1983 Borah Peak earthquake (Ms = 7.3) the dam performed well and only two longitudinal cracks along the crest were observed. The first crack extended about 30.5 m along the downstream edge of the 1.8 m parapet crest fill that was added in 1956. The second crack extended about 61 m, and was located about 3.65 m from the downstream edge of the crest constructed in 1932. The width of both cracks was less than 6.3 mm.

7.4.1 Site Geology and Soil Conditions

Figure 7.14 shows the dam cross-section. The main body of the dam consists of about 10.7 m of sandy gravel fill dumped periodically in several years. Embankment fill came from borrow pits located upstream and above the dam on the Cedar Creek fan forming the left abutment. The foundation of dam consists of gravel, underlain by 1.8 to 3.6 m thick low permeability hardpan with more gravel and sand lying beneath it. Limestone was encountered below the gravel and sand layer (Harder 1992).

To calculate the relative density of the dumped trestle fill gravel on the left abutment, four ring-density tests were performed in August 1984. For each test about 3 to 5 ft^3 (0.085 to 0.141 m^3) of gravel was removed and later dried and weighed in the laboratory. Laboratory dry densities obtained ranged from 125.5 to 134.0 lbs/ft^3 (19.7 to 21 kN/m^3) with an average void ratio of 0.328. The maximum and minimum void ratios were not determined for Mackay dam; however, Seed et al. (1984) reported maximum and minimum void ratios for Livermore gravel as 0.455 and 0.166 respectively. Assuming these to be appropriate for Mackay dam, Seed et al. (1984) computed an average relative density of approximately 45%. This value is reasonably consistent with the fill placement technique.

In addition to the density tests, 27 embankment and 22 foundation samples were obtained from open-bit Becker soundings between Stations 15 and 19. The samples retrieved from the embankment and foundation were predominantly nonplastic, silty, sandy gravel with infrequent lenses of sandy or clayey soil in the upper zone of the foundation. Of the 21 embankment samples, 10 samples were nonplastic, while 7 others had PI < 4. Similarly, three density samples were nonplastic fines while the fourth had PI = 4. Table 7.7 summarizes the grain size characteristics of the soil. As shown in the Table 7.7, the embankment fill in the left abutment and main section of the dam had a gravel content of about 65% and a fines content of about 7%, classifying it as GW-GM.

7.4.2 Description of Failure

On October 1983 at about 8:06am (local time), a large earthquake occurred in a mountainous region of east central Idaho. The epicenter was located in a rural area between the towns of Challis and Mackay, Idaho. The surface magnitude (Ms) of 7.3 for main shock was reported by the National Earthquake Information Service (NEIS). The earthquake caused two fatalities in the town of Challis and an estimated property loss of about $12.5 million caused by structural failure of buildings (Regor and Baldwin 1984, Stover 1985 and Harder 1992).

K. Michael Cline of the EERI reconnaissance team was in Arco, Idaho on the morning of October 28, 1983 and made the following observations (Taylor et al. 1985):

"Mr. Rukavina expressed concern about the Mackay dam, so he and I decided to make a reconnaissance of the dam and reservoir, which are approximately 6.5 km (4mi) north and upstream of Mackay. The reservoir holds approximately 45,000 acre feet when full and at that time was nearly full. The dam, built between 1912 and 1916 and modified in 1930, is an earthen embankment structure with a partial concrete core. The embankment materials consist of local compacted alluvium. It was built on a thick sequence of alluvium, but in a gap in the valley that is bedrock controlled. The right abutment of the dam is against sheared limestone bedrock and the left abutment terminates on alluvial terraces. The dam was originally designed to be approximately twice its present height and, therefore, has a very wide base for its existing height. The dam normally has three to four active springs discharging water at the base of the downstream slope. The spring water flows into a common pool, allowing the discharge to be monitored by a weir. Two hours after the earthquake (approximately 10:00 in the morning), muddy water was observed coming from the spring nearest the discharge tunnel. Muddy water was also coming from another spring located downstream from the dam near the end of the spillway. It was later observed that the spring nearest the discharge tunnel cleared within approximately 2 to 3 hours. However, the other spring, near the end of the spillway, continued to be muddy for approximately 2-1/2 to 3 days. Other observations of the dam included weakly defined concentric cracks suggesting [a] slump of the downstream slope. These cracks may or may not have been caused by the earthquake. My observations were related to the District Irrigation Supervisor and to the State Dam Safety inspectors who arrived that day. Later that day, a local fisherman told me that on the day before the earthquake he was fishing in a boat on Mackay reservoir. The day was calm except for two single waves that went across the lake from north to south. These may have been caused by foreshocks."

As reported above, the Mackay Reservoir was nearly full at the time of earthquake which is at elevation 6058.8 feet (1846.72 m) that comes out to be

approximately 17 feet (5.18 m) below the crest of the dam. Although the earthquake magnitude was 7.3 and Mackay dam was situated approximately 16 km southeast of the epicenter, the dam performed very well with damage restricted to two longitudinal cracks along the crest between stations 15 and 18. The first crack extended about 100 feet (30.5 m) along the downstream edge of the 6-foot (1.8 m) thick parapet crest fill added in 1956. The second crack had a length of approximately 200 feet (61 m). Both cracks were less than about ¼" (6.4 mm) wide.

As indicated by K.M. Cline, the pool at the downstream toe where the seepage is measured turned muddy about two hours after the earthquake. A temporary and slight increase in flow (5%) was also reported in seepage weir (Harder 1992). Most of the cloudiness in the water cleared within a few hours after the earthquake and after a few days, the water was completely clear.

7.4.3 Estimation of Ground Motions

The Borah Peak earthquake occurred near Mackay, Idaho on the Lost River Fault with a length of about 42 km of complex normal-oblique-slip faulting on the Lost River Fault. Figure 7.15 shows the location of Lost River Fault with the epicentral location of the earthquake.

Mackay Dam is located approximately 10 miles southeast of the epicenter while the earthquake ruptured to the northwest, away from Mackay. Based in part on the damage intensities in the area, the earthquake was estimated to have produced a peak ground acceleration of approximately 0.22g in the area of Mackay Dam and a period of strong shaking that lasted between 20 to 30 seconds (Jackson and Boatwright 1985; Harder 1988).

The author utilized the Next Generation Attenuation (NGA) relationships (Powers et al. 2006) to estimate a possible range of peak ground acceleration employing fault

rupture information. Barrientos et al. (1987) and Rudnicki et al. (1991) reported geologic information needed for NGA relationships as shown in

Table 7.8. Because the equivalent SPT N-values exceed 30 blows/ft in the upper 30 m of the foundation, site class D (stiff soil profile) was assigned to the site (IBC 2006). For stiff soil profile the range of shear wave velocity (Vs) suggested by IBC 2006 is 183 to 366 m/s. Employing the information given in

Table 7.8 and Vs-values, PGAs were calculated as shown in Table 7.9. PGAs obtained from the NGA relationship generally ranged from about 0.2 to 0.3g. The author used 0.22g based on the values reported by initial investigators.

7.4.4 Representative Penetration Resistance

No SPT or CPT was performed on Mackay dam site; however, Becker penetration tests (BPT) were conducted in August 1984 and July 1985 within the dam and foundation. Nineteen Becker boreholes were drilled with open and closed bits during these two periods. All of the Becker boreholes were drilled using 6.6 inch (outer diameter) casing with an AP-1000 drill rig owned by Becker Drills, Inc. In general, both open- and closed-bit Becker soundings produced similar results (Harder 1992).

The penetration resistance measured from BPT was converted into equivalent SPT blow counts using the method suggested by Harder and Seed (1986) and Harder (1988). Figure 7.16 shows the equivalent SPT N_{60} blow counts converted from BPT soundings conducted in the main part of the embankment between Stations 16 and 19. The foundation material lies below El. 5995 ft (1827.27 m), and is considerably stronger than the overlying fill materials. The dumped trestle fill is located between El. 5995 (1827.27 m) and 6030 ft (1837.94 m). A relatively loose fill also overlies the trestle fill, as indicated by equivalent SPT N-values in Figure 7.16, above El. 6030 ft (1837.94 m).

Using an overburden correction (C_N) developed by Harder (1988) to normalize blow counts, Harder (1992) reported the average equivalent $(N_1)_{60}$ values for the dumped

fill below El. 6030 ft (1837.94 m) to be approximately 8 to 9 blows/ft. The author calculated average SPT $(N_1)_{60}$ values for every 10 feet of elevation and presented these incremental values in Figure 7.9. The critical deep and shallow sliding surfaces (shown in Figure 7.17 and Figure 7.18) intersect the potentially liquefiable soils below El. 6030. As a result, the average $(N_1)_{60}$ in the depth range intersecting the failure surfaces is about 8.5.

7.4.5 Liquefaction Susceptibility Analysis

As stated in Section 7.4.4, equivalent SPT blow counts converted from BPT were reported by Harder (1992). As illustrated in Figure 7.9, the fill soils (i.e., the dumped trestle fill and newly placed fill) were susceptible to liquefaction. In contrast, the foundation soil was not susceptible to liquefaction.

7.4.6 Liquefaction Triggering Analysis

Figure 7.17 and Figure 7.18 show two possible sliding surfaces that correspond to the cracks observed on the dam crest. Uncorrected blow counts in the saturated fill intersecting the failure surfaces range from about 5 to 30 blows/ft, with an average $(N_1)_{60}$ of about 8.5. Therefore, yield shear strength ratios were calculated for an average $(N_1)_{60}$ = 8.5 as shown in Figure 7.19. The resulting yield strength ratios were calculated as 0.287 and 0.291 based on $(N_1)_{60}$ = 8.5 blows/ft and $\tau_{static}/\sigma'_{vo}$ = 0.203 and 0.21 for the deep and shallow sliding surfaces shown in Figure 7.17 and Figure 7.18, respectively. Non-liquefied soils involved in the sliding surface were assigned a drained friction angle, ϕ' = 33º. Seismic stresses were calculated using Eq. 5.2 and a_{max} = 0.22g.

Tables 7.9 and 7.10 present the results of the liquefaction triggering analysis for the deep and shallow sliding surfaces, respectively. No slices were found to be in the dilative zone (see Figure 7.9) for this case history. All slices (8 – 24) within the contractive zone of deep failure surface (Figure 7.17) were predicted to liquefy, with $FS_{Triggering}$ ranging from 0.87 to 0.97. Similarly, all slices (12 – 22) within contractive

zone of the shallow failure surface (Figure 7.18) were predicted to liquefy, with $FS_{Triggering}$ ranging from 0.87 to 0.95.

7.4.7 Liquefaction Post-triggering Stability Analysis

As stated in Section 7.4, the average $(N_1)_{60}$ intersecting the failure surfaces is about 8.5 blows/ft. This penetration resistance value was used to calculate liquefied shear strength ratio as shown in Figure 7.13. Based on penetration resistance, $s_u(liq)/ \sigma'_{vo}$ was selected as 0.094 and used for both sliding surfaces. Because all the contractive slices were estimated liquefy ($FS_{Triggering} < 1$), each slice was assigned its liquefied shear strengths for post-triggering stability analyses. Non-liquefied soils along the sliding surface were assigned a drained friction angle, $\phi' = 33^o$.

The FS_{Flow} for the deep and shallow failure surfaces were 0.680 and 0.903 respectively. These values suggest the damage at Mackay dam should have been considerably more severe. However, given the high gravel content (65%) of the fill, it is highly likely that several meters of the fill near drainage boundaries would have been drained during shaking and would not have liquefied. Considering a zone of drainage about 2m thick, slices 7 – 9 and 24 in the deep surface were also assigned $\phi' = 33^o$. This analysis yielded $FS_{Flow} = 0.68$. For the shallow failure surface, none of the slices were predicted to liquefy when the drainage zone was included, and the $FS_{Flow} = 0.903$. A high FS_{Flow} for shallow failure surface is quite consistent with the observed minor cracking (but no slumping) observed at the dam.

7.5 Industrial Site Levee

On October 17, 1989 at 5:04pm (PST) a major earthquake occurred in the southern Santa Cruz Mountains near the summit of Loma Prieta Mountain. The epicenter was located at 37º 2.19′N; 121º 52.98′W, about 16 km northeast of Santa Cruz and about 30 km south of San Jose. The Loma Prieta earthquake was $M_w = 6.9$, and ground shaking lasted for 10 to 15 seconds (EERI 1989). The Loma Prieta earthquake caused 62 fatalities and roughly 4,000 injuries. As a consequence of earthquake, 3,000 people were left homeless with around 12,000 homes and 2,600 businesses damaged or destroyed. Total loss of property due to the Loma Prieta earthquake was estimated at $6 billion (Stoffer 2005).

Among other failures, the Loma Prieta earthquake caused ground displacement of the protective levees at many locations along the Pajaro River near Watsonville, CA. Miller and Roycroft (2004) discussed four levee locations: Artichoke Farm, a wastewater treatment plant, a site called the South Side levee, and an industrial site. The industrial site levee was selected for evaluation here as Miller and Roycroft (2004) reported CPT and SPT data for this site only. This is also the only levee described by Miller and Roycroft (2004) that did not experience deformation. Ground cracking within the industrial site landward of the levee did, however, occur. Figure 7.21 shows the cross-section of the industrial site levee.

7.5.1 Site Geology and Soil Conditions

The ancient Pajaro River valley was formed by the scouring of bedrock when the sea level was low and the river likely flowed into Monterey Canyon. The valley was filled with fluvial/alluvial sediments once the sea level rose, drowning the ancient valley. The present day Pajaro River meanders through this valley.

Four levee sites discussed by Miller and Roycroft (2004) are located in the lower reaches of the ancient Pajaro River valley. The old floodplain consists of 60 to 120 m thick heterogeneous deposits of sand and silt with relatively thin layers of clay. The

young floodplain deposits consist of 6 m of sand and silt with discontinuous clay deposits. The young floodplain deposits have been incised by the current river channel, and parts of the young floodplain is filled with channel fill deposits.

The soil layers at the industrial site also follow the similar trend. The recent channel fill is about 2.9 m thick, underlain by 4.3 m thick clay, silt and sand; and 1.4 m of sand and silt. Below this layer was heterogeneous deposits of sand, silt and clay layers. A subsurface profile is given in Figure 7.21.

7.5.2 Estimation of Ground Motions

The Mw = 6.9 Loma Prieta earthquake occurred in a seismically-active section of the San Andreas fault system. The earthquake is the largest earthquake since the 1906 San Francisco earthquake in northern California. The earthquake ruptured a 40 – 45 km (25 – 28 mile) long southernmost segment of the 1906 San Francisco earthquake fault rupture that passes through the southern Santa Cruz mountains (EERI 1989, Miller and Roycroft 2004). The epicenter was about 16 km northwest of Watsonville at a depth of about 19 km. Figure 7.22 shows the location of 1989 Loma Prieta earthquake epicenter.

Table 7. 12 shows the ground motion recording stations near the epicenter. No records were considered “free field” because each record was affected by a structure and by local subsurface conditions. Miller and Roycroft (2004) estimated bedrock acceleration of 0.25g at the industrial site levee based on the Joyner and Boore (1988) attenuation relationship. Using the soft soil site amplification factor proposed by Idriss (1990), Miller and Roycroft (2004) estimated the surface motion of 0.33g. Because of the bilateral propagation of the fault rupture, the duration of strong ground motion during Loma Prieta earthquake was shorter (8 to 10 seconds) than would be expected for M_w 6.9. The shorter duration of strong ground motion more closely resembled an M_w 6.5 event.

7.5.3 Description of the Failure

As stated in Section 7.5, the industrial site levee was the only levee among the four documented by Miller and Roycroft (2004) that did not experience lateral deformation failure. The U.S. Corps' of Engineers (USCOE) inspected the levee after the earthquake, and reported that the levee section did not show any parallel, longitudinal or "en echelon" diagonal cracks that were usually observed at the lateral limits of a deformed embankment. The USCOE inspection report concluded that there no damage occurred within the levee adjacent to the industrial site.

Two distinct semi-circular cracks were observed on the landward side of the levee within the industrial site. These cracks raised concern over the stability of levee, and it was suggested that the cracks resulted from lateral movement toward the Pajaro River, differential settlement at the contact between young and old floodplain deposits, or both. To investigate the nature and dimensions of the cracks, four test pits were excavated. These pits revealed that the cracks were about 25 cm wide at the surface and about 2 m deep. Relic cracks filled with sediments were also discovered at the same location where these cracks were observed. Further, the cracks within the site agreed with the mapped geological limits of the younger floodplain alluvium. Therefore, Miller and Roycroft (2004) concluded that the cracks were related to: (1) differential settlement between young and old floodplain sediments; and (2) pre-existing relic cracks left by previous earthquakes.

7.5.4 Representative Penetration Resistance

Numerous CPT and SPT were conducted at the industrial site levee; however, only boring M-7 and CPT M-6 were reported by Miller and Roycroft (2004). The locations of the boring and CPT are shown in Figure 7.21 and Figure 7.23 presents the penetration data. Boring M-7 shows an approximately 3.5-m thick silt layer from a depth of about 4.5 m to 8 m underlain by silty sand layer about 4 m thick. The N-values of the

silt and silty sand layers were reported as about 10 and 20 to 28 blows/ft, respectively. The location and penetration resistance of the silt is reasonably consistent with the CPT data The CPT tip resistance ranged from about 2.5 to 5.0 MPa from a depth of about 7.5 to 9 m (consistent with the location of the critical sliding surface). The corrected tip resistance q_{c1} ranged from about 1.2 to 5.1 MPa with an average value of 3 MPa while $(N_1)_{60}$ was about 8.5 blows/ft.

7.5.5 Liquefaction Susceptibility Analysis

As stated in Section 7.4.4, both SPT and CPT were conducted at Industrial Site levee as reported by Miller and Roycroft (2004). CPT tip resistances and estimated SPT blow counts below the watertable are plotted in Figure 7.9 to evaluate liquefaction susceptibility. As illustrated in Figure 7.9, the sandy and silty soils above a depth of about 9 m are susceptible to liquefaction, while the denser channel sands are generally dilative and not susceptible to flow liquefaction.

7.5.6 Liquefaction Triggering Analysis

Figure 7.24 shows the critical slip surface (identical to the critical slip surface evaluated by Miller and Roycroft 2004). This surface yielded a value of $\tau_{static}/\sigma'_{vo}$ = 0.075. As this value is less than the minimum $\tau_{driving}/\sigma'_{vo}$ = 0.20 in the Olson and Zitny (2012) relationships, the author checked whether this value was larger than $s_u(liq)/\sigma'_{vo}$ to evaluate whether flow liquefaction was possible [i.e., $\tau_{driving} > s_u(liq)$ is a prerequisite for flow liquefaction]. Using Eq. 6.1 (Chapter 6) for $(N_1)_{60}$ = 8.5 and q_{c1} = 3.0 MPa, the average value of $s_u(liq)/\sigma'_{vo}$ was 0.08. Therefore, because $s_u(liq)/\sigma'_{vo}$ is greater than $\tau_{static}/\sigma'_{vo}$, a sloping-ground liquefaction triggering analysis is not needed, and flow liquefaction is not possible. This finding is consistent with the observed performance of the levee. Of course, a level-ground liquefaction analysis and lateral spreading analysis

should still be conducted for this site. However to illustrate the sloping-ground procedure, the author opted to continue the liquefaction triggering and post-triggering analyses.

As stated in Section 7.5.4, a single $(N_1)_{60}$ value of 8.5 blows/ft and q_{c1}-values ranged from 1.2 to 5.1 MPa with a best estimate of 3 MPa are suggested by the author. These penetration resistance values were used to calculate yield shear strength ratio as shown in Figure 7.25. The relationships shown in Figure 7.25 depend on the driving stress ratio however in this case yield strength ratio was calculated by using the minimum driving stress ratio of 0.2 as suggested by Olson et al. (2006) and Olson (2009). The average yield strength ratio was calculated from the SPT- and CPT-based yield strength ratios. Of course, using a single penetration value to calculate yield strength ratio is a simplification of the procedure. If desired, variations of penetration resistance and yield strength ratio with depth can be considered. Figure 7.25 suggests SPT- and CPT-based yield strength ratios of 0.285 and 0.251, respectively. Therefore, an average yield strength ratio of 0.268 was used in the subsequent analyses. Non-liquefied soils involved in the sliding surface were assigned a drained friction angle, $\phi' = 33^o$. Seismic stresses are calculated using Eq. 5.2 with $a_{max} = 0.33g$.

As described in Section 7.5, the 1989 Loma Prieta earthquake caused no apparent damage to the levee; however, two semi-circular cracks were found within the industrial site landward of the levee. The author selected a failure surface similar to the critical failure surface used by Miller and Roycroft (2004) to evaluate the levee (Figure 7.24). As indicated in Table 7. 13 $FS_{Triggering}$ ranged from 1.04 to 1.21 for the critical failure surface, with only three slices marginally triggered to liquefy.

7.5.7 Liquefaction Post-triggering Stability Analysis

The representative $(N_1)_{60}$ and q_{c1} values of 8.5 blows/ft and 3 MPa, respectively, were used to compute liquefied strength ratios, as shown in Figure 7.26. SPT- and CPT-based liquefied strength ratios of 0.094 and 0.073 resulted in an average liquefied strength ratio of 0.083. This value was used for the liquefied slices in the post-liquefaction triggering analysis, as illustrated in Table 7. 13. Contractive slices that were not predicted to liquefy were assigned their yield shear strength. Non-liquefied soils were assigned a drained friction angle, $\phi' = 33^o$.

The post-triggering slope stability analysis yielded $FS_{Flow} \sim 1.6$. This FS_{Flow} is consistent with the lack of damage and deformations observed along the levee reported by Miller and Roycroft (2004).

7.6 Discussion and Conclusions

- In this Chapter, relationships proposed by Olson and Stark (2002, 2003) and Olson & Zitny (2012) were employed to predict the behavior of three geostructures (subjected to six different earthquakes). These cases included Yamanaka Dam in Japan; Mackay Dam in Idaho, USA; and an industrial site levee in California, USA. All three cases were subjected to earthquake shaking and suffered differing severities of damage ranging from complete failure to no damage.
- Yamanaka dam was subjected to four earthquakes and suffered damage ranging from complete failure to settlement and minor slumping. The sloping ground liquefaction analysis yielded $FS_{Triggering}$ and FS_{Flow} that were completely consistent with the observed performance of the dam during each earthquake, with the FS increasing as the observed performance improved. Table 7.2 through Table 7.6 illustrate the results of the triggering analyses and Table 7.6 presents the results of the post-triggering stability analyses.
- Mackay dam was subjected to the 1983 Borah Peak earthquake and experienced two longitudinal cracks on its crest. No flow failure or slumping was observed, despite the likelihood that liquefaction was triggered within the embankment fill. The sloping

ground liquefaction analysis procedure reasonably predicted the performance of the dam when the high permeability of the sandy, silty gravel fill was considered.

- An industrial site levee reported by Miller and Roycroft (2004) was subjected to 1989 Loma Prieta earthquake and suffered no apparent damage during shaking. However, two semi-circular cracks were observed within the industrial site landward of the levee. The sloping ground liquefaction analysis procedure suggested that flow liquefaction was not possible at the site because $s_u(liq)/\sigma'_{vo}$ was greater than $\tau_{static}/\sigma'_{vo}$ for the critical failure surface. This is consistent with the observed behavior. Nevertheless, the author opted to continue the analysis for the purpose of illustrating the procedure. The completed procedure predicted $FS_{Triggering}$ and FS_{Flow} consistent with the observed lack of damage.

7.7 References

Boatwright, J. (1985). Characteristics of the aftershock sequence of the Borah Peak, Idaho, earthquake determined from digital recordings of the events, *Bulletin of the Seismological Society of America,* vol. 75, no. 5, p. 1265 – 1284, October 1985.

Earthquake Engineering Research Institute (1989). Loma Prieta earthquake October 17, 1989 preliminary reconnaissance report, *Earthquake Engineering Research Institute 89 – 03,* p. 51.

Fear, C.E. and Robertson, P.K. (1995). Estimating the undrained strength of sand: a theoretical framework, *Canadian Geotechnical Engineering,* vol. 32, iss. 4, p. 859 – 870.

Harder L.F.Jr. and Seed, H. Bolton (1986). Determination of penetration resistance for coarse grained soils using the Becker Hammer – Drill, *Report No. UCB/EERC 85/06,* Earthquake Engineering Research Center, University of California, Berkeley, May.

Harder, L.F.JR. (1988). Use of penetration tests to determine the cyclic load resistance of Gravelly soils, *PhD Dissertation,* University of California, Barkeley.

Harder, L.F.JR. (1992). Investigation of Mackay Dam following the 1983 Borah Peak earthquake, *Stability and Performance of Slopes and Embankments II,* ASCE Geotechnical Special Publication No. 31, 2: p. 956 – 972.

Idriss, I.M. (1990). Response of soft soil sites during earthquakes, *Proceedings A Memorial Symposium to Honor Professor H.B. Seed,* University of California, Berkeley, Berkeley, California.

Joyner, W.B. and Boore D.M. (1988). Measurement, characterization and prediction of strong ground motion, *In proceedings of Earthquake Engineering and Soil Dynamics II ,* GT Div/ASCE, Park City, Utah, 27 – 30 June, 1988, p. 43 – 102.

Miller, Eugene A. and Roycroft, Glen, A. (2004). Seismic performance and deformation of levees: four case studies, *Journal of Geotechnical and Geoenvironmental Engineering,* ASCE vol. 130, iss. 4, p. 344 – 354.

Olson, S. M. (2001). Liquefaction analysis of level and sloping ground using field case histories and penetration resistance, *Ph.D. Thesis,* University of Illinois at Urbana-Champaign, Urbana, Illinois.

Olson, S.M. and Stark, T.D. (2002). Liquefied strength ratio from liquefied flow failure case histories, *Canadian Geotechnical Journal,* vol. 39, p. 629 – 647.

Olson, S.M. and Stark, T.D. (2003). Use of laboratory data to confirm yield and liquefied strength ratio concepts, *Canadian Geotechnical Journal,* vol. 40, p. 1164 – 1184.

Olson, S. M., Sacks, A. L., Mattson, B. B., and Servigna, D. A. (2006). Role of static shear stress in liquefaction analysis of sloping ground, *Proceedings of the 8th US National Conference on Earthquake Engineering*

Olson, S.M. and Mattson, B.B. (2008). Mode of shear effects on yield and liquefied strength ratios, *Can. Geotechnical Journal,* vol. 45, p. 574 – 587.

Olson, S.M., and Johnson, C.I. (2008). Analyzing liquefaction-induced lateral spreads using strength ratios, *Journal of Geotechnical and Geoenvironmental Engineering,* ASCE, vol. 134, no. 8, p. 1035 – 1049.

Olson, S. M. (2009). Strength ratio approach for liquefaction analysis of tailings dams, *University of Missouri Conference*.

Reagor, Glen, and Baldwin, F.W. (1984). Intensity survey of the Borah Peak, Idaho, earthquake of October 28, 1983: *U.S. Gelogical Survey Open-File Report 84-166,* p. 67.

Seed, H.B. and Idriss, I.M. (1971). Simplified procedure for evaluating soil liquefaction potential, *Journal of the Soil Mechanics and Foundation Division,* ASCE, vol. 97(SM9), p. 1249 – 1273.

Seed, H. Bolten, Tokimatsu, K., Harder, L.F., and Caung, Riley M. (1985). Influence of SPT procedures in soil liquefaction resistance evaluations, *Journal of the Geotechnical Engineering Division,* ASCE, vol. 111, no. GT12, December.

Skempton, A.W. (1986). Standard penetration test procedures and the effects in sand of overburden pressure, relative density, particle size, ageing, and overconsolidation, *Geotechnique,* vol. 36, p. 425-447.

Stoffer, Philip W. (2005). The San Andreas Fault in the San Francisco Bay area, California, *US Geological Survey*.

Stover, Carl W. (1985). The Borah Peak, Idaho Earthquake of October 28, 1983 – isoseismal map and intensity distribution, *Earthquake Spectra*, *Earthquake Engineering Research Institute,* vol. 2, no. 1, November.

Tani, S. and Nakashima, M. (1999). Earthquake damage to earth dams in Japan – maximum epicentral distance to cause damage as a function of magnitude, *Soil Dynamics and Earthquake Engineering* vol. 18, p. 593 – 602.

Taylor, C.L., Cline K.M., Page, W.D. (1985). The Borah Peak, Idaho Earthquake of October 28, 1983 – surface faulting and other phenomena, *Earthquake Spectra,* vol. 2, no. 1, p. 23 – 49.

7.8 Figures and Tables

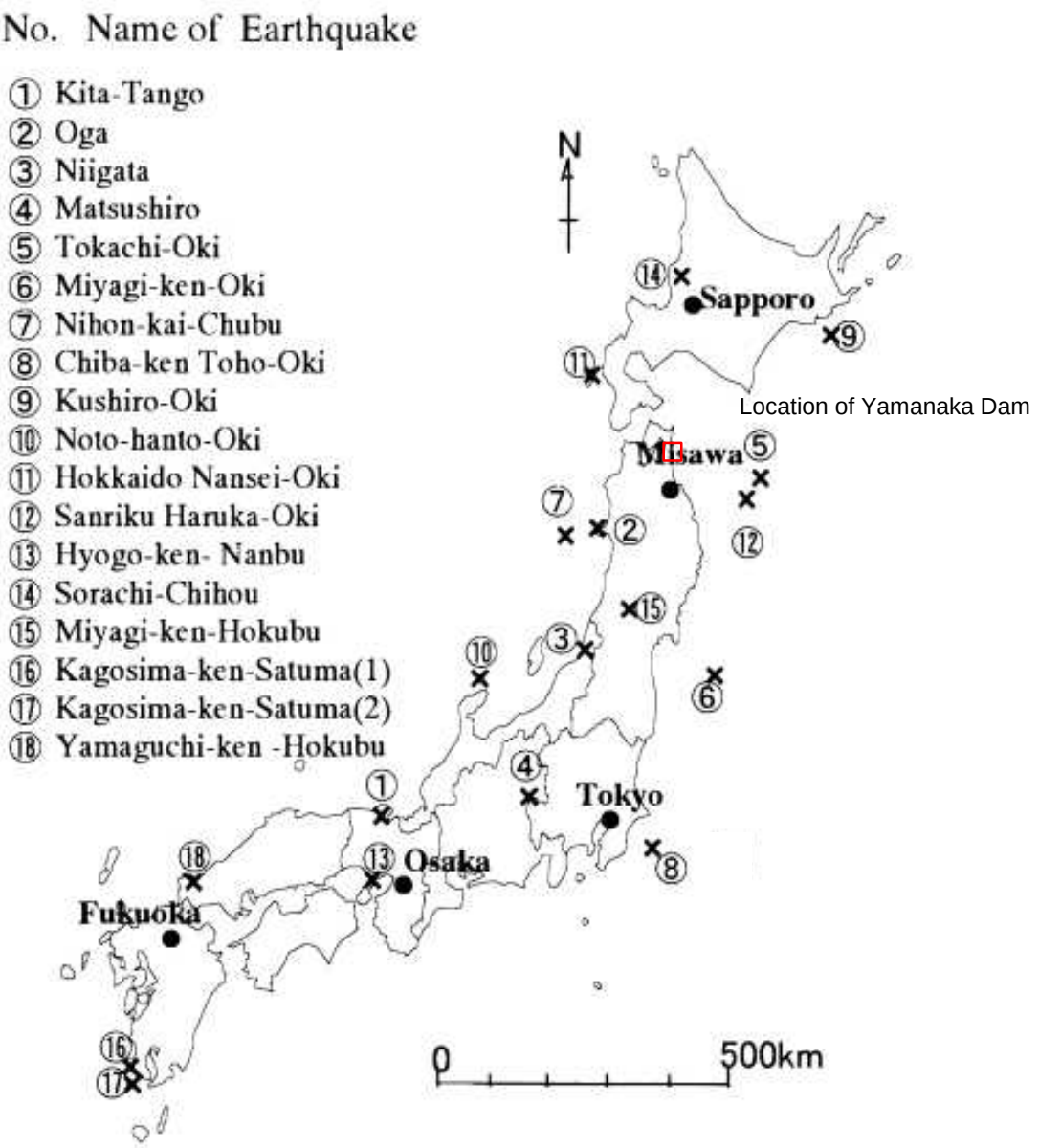

Figure 7.1 The epicenter of notable 20th century earthquakes around Japan. Box shows area of map in Figure 7.2 (modified from Tani and Nakashima 1999)

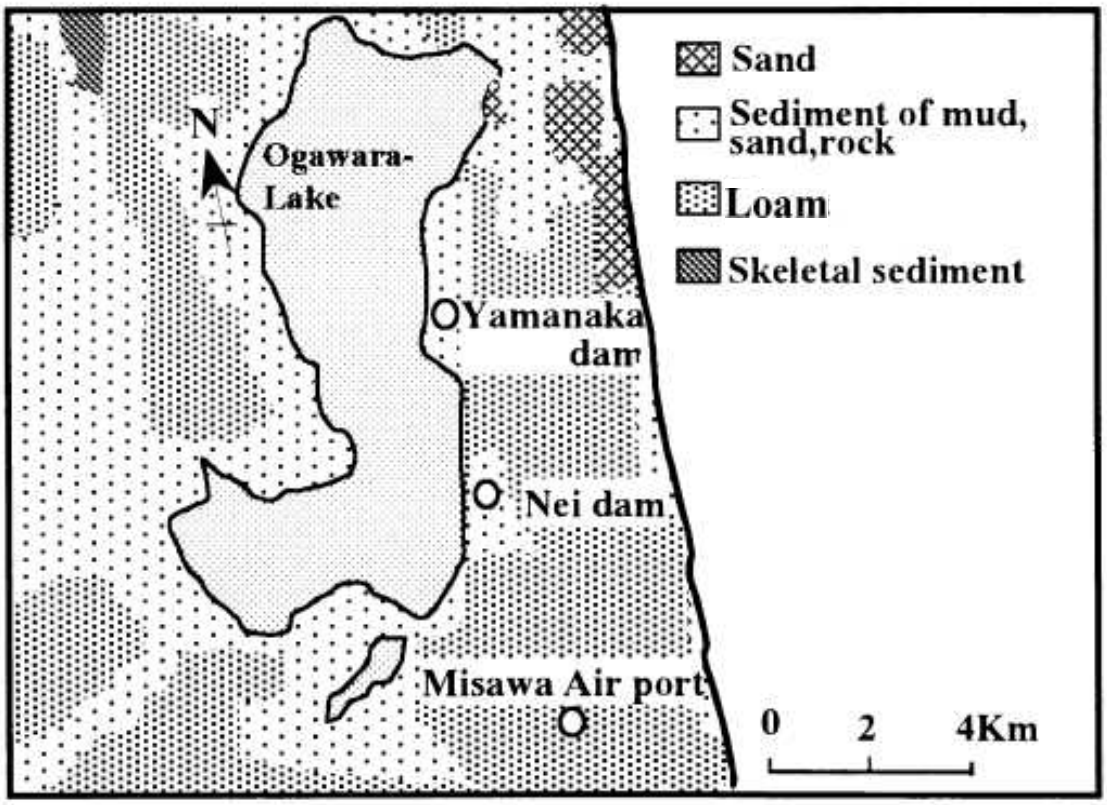

Figure 7.2 Location of Yamanaka dam (Tani and Nakashima 1999)

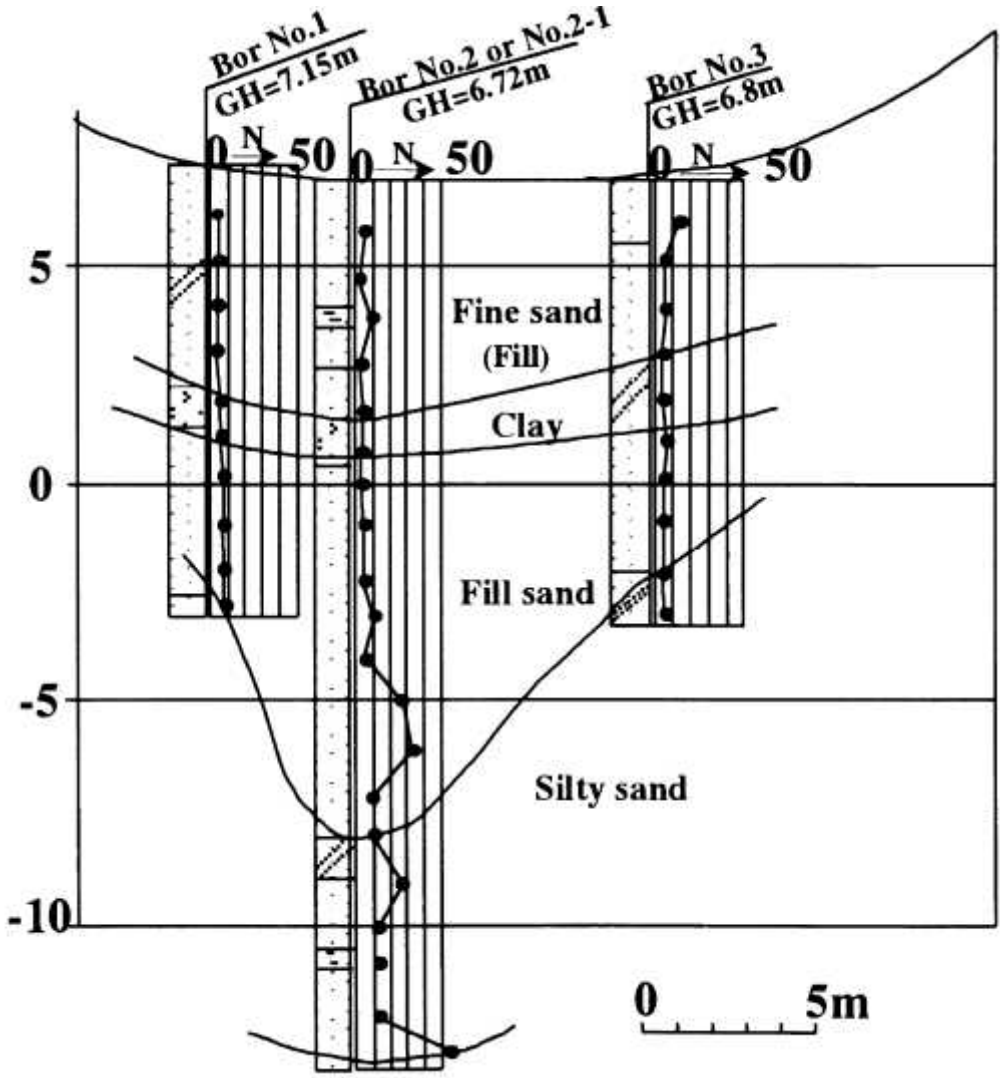

Figure 7.3 Soil profile at Yamanaka dam (from Tani and Nakashima 1999)

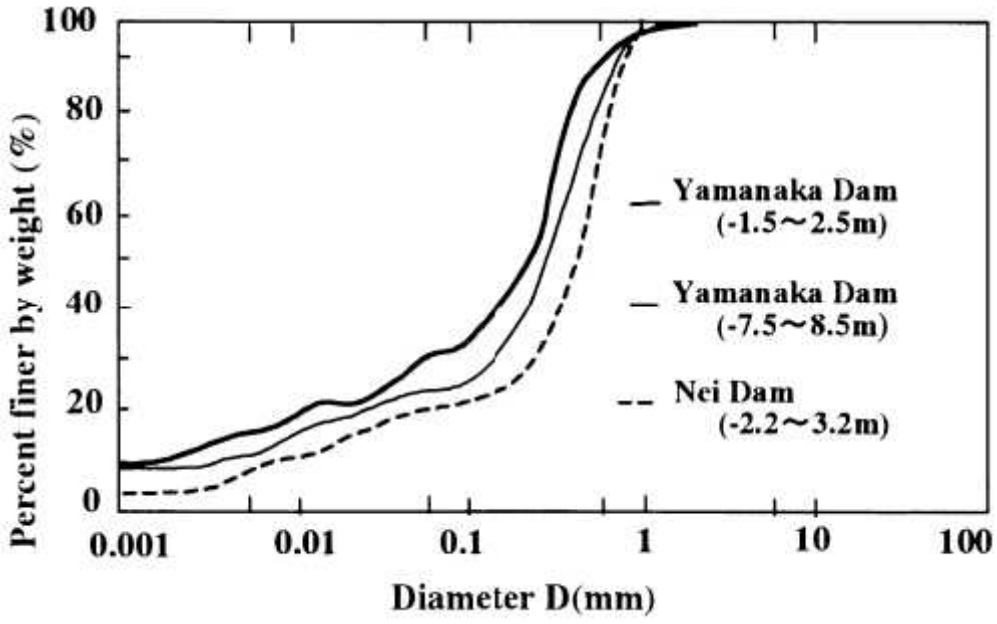

Figure 7.4 Grain size distribution of the embankment and foundation soils of Yamanaka and Nei dams (from Tani and Nakashima 1999)

Figure 7.5 Damage to Yamanaka dam caused by the 1968 Tokachi-Oki earthquake (from Tani and Nakashima 1999)

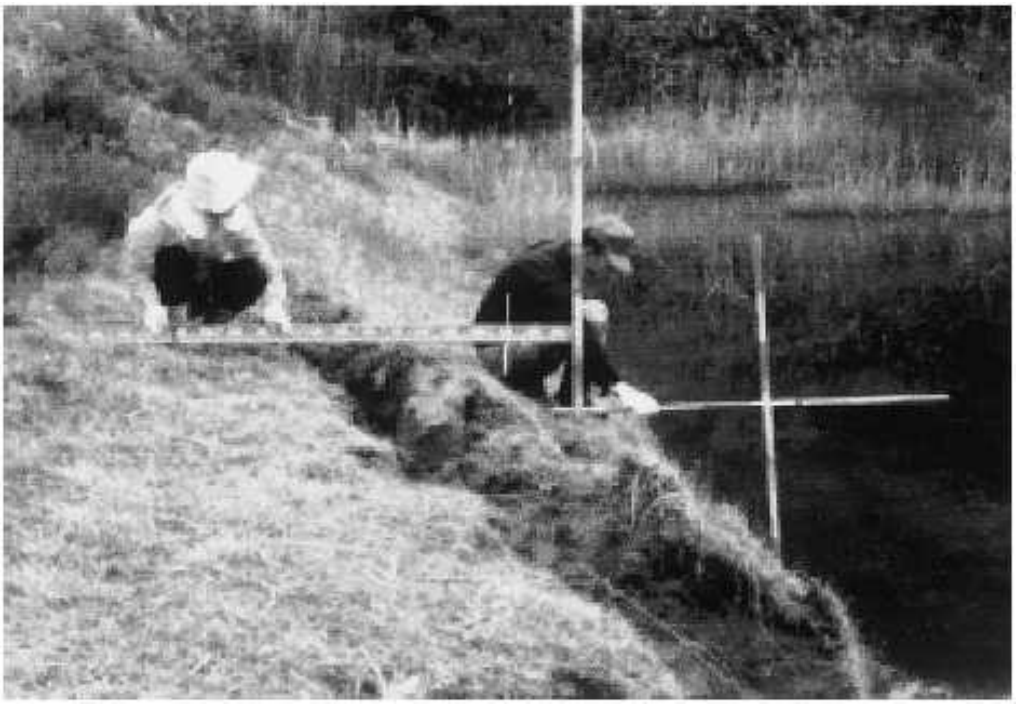

Figure 7.6 Damage to Yamanaka dam caused by the 1983 Nihon-kai-Chubu earthquake (from Tani and Nakashima 1999)

Figure 7.7 Damage to Yamanaka dam caused by the 1994 Sanriku Haruka-Oki earthquake (from Tani and Nakashima 1999)

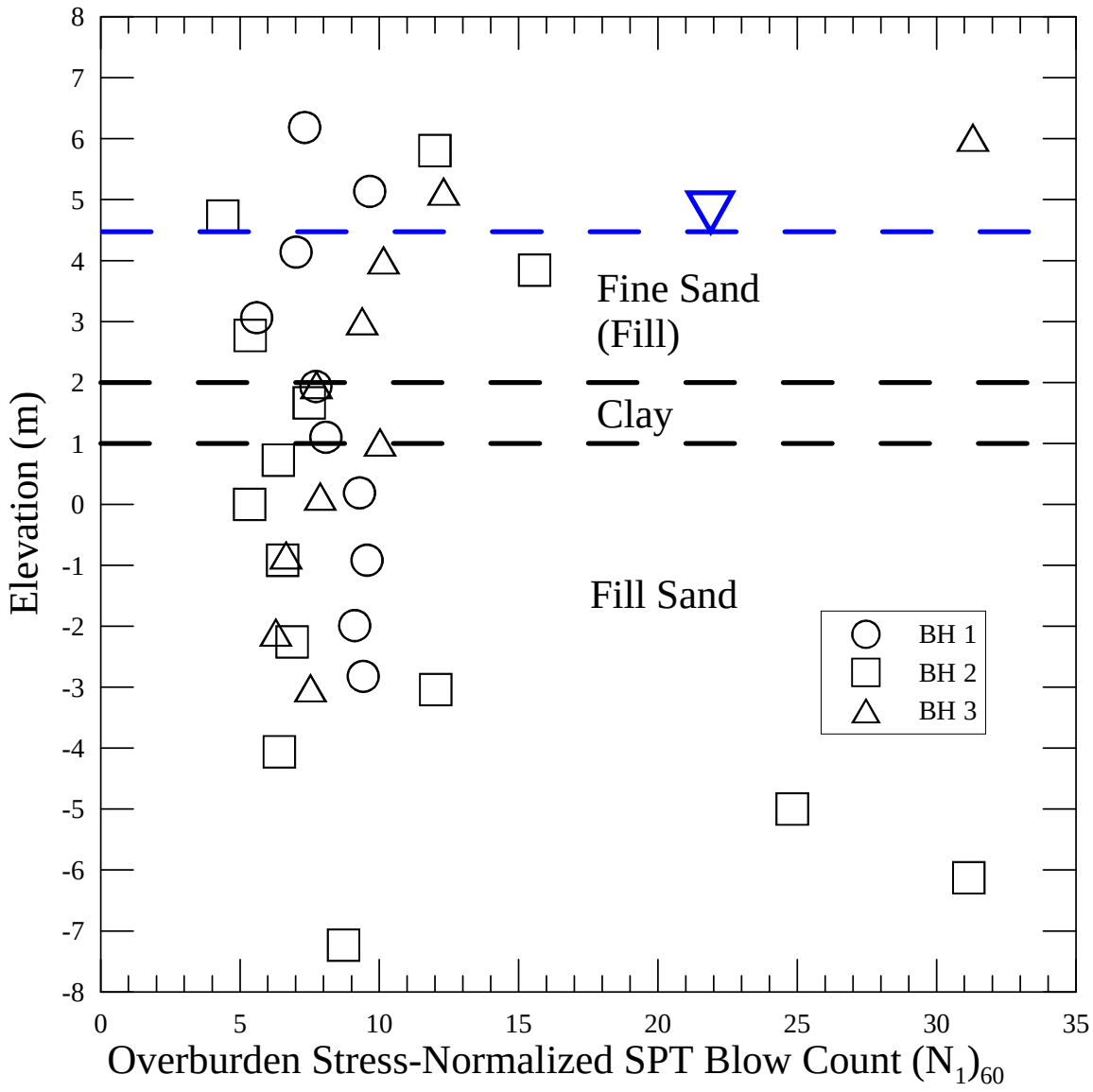

Figure 7.8 Overburden stress-normalized SPT values calculated from SPT borings presented in Figure 7.3. Reservoir level is indicated by inverted triangle and dashed line

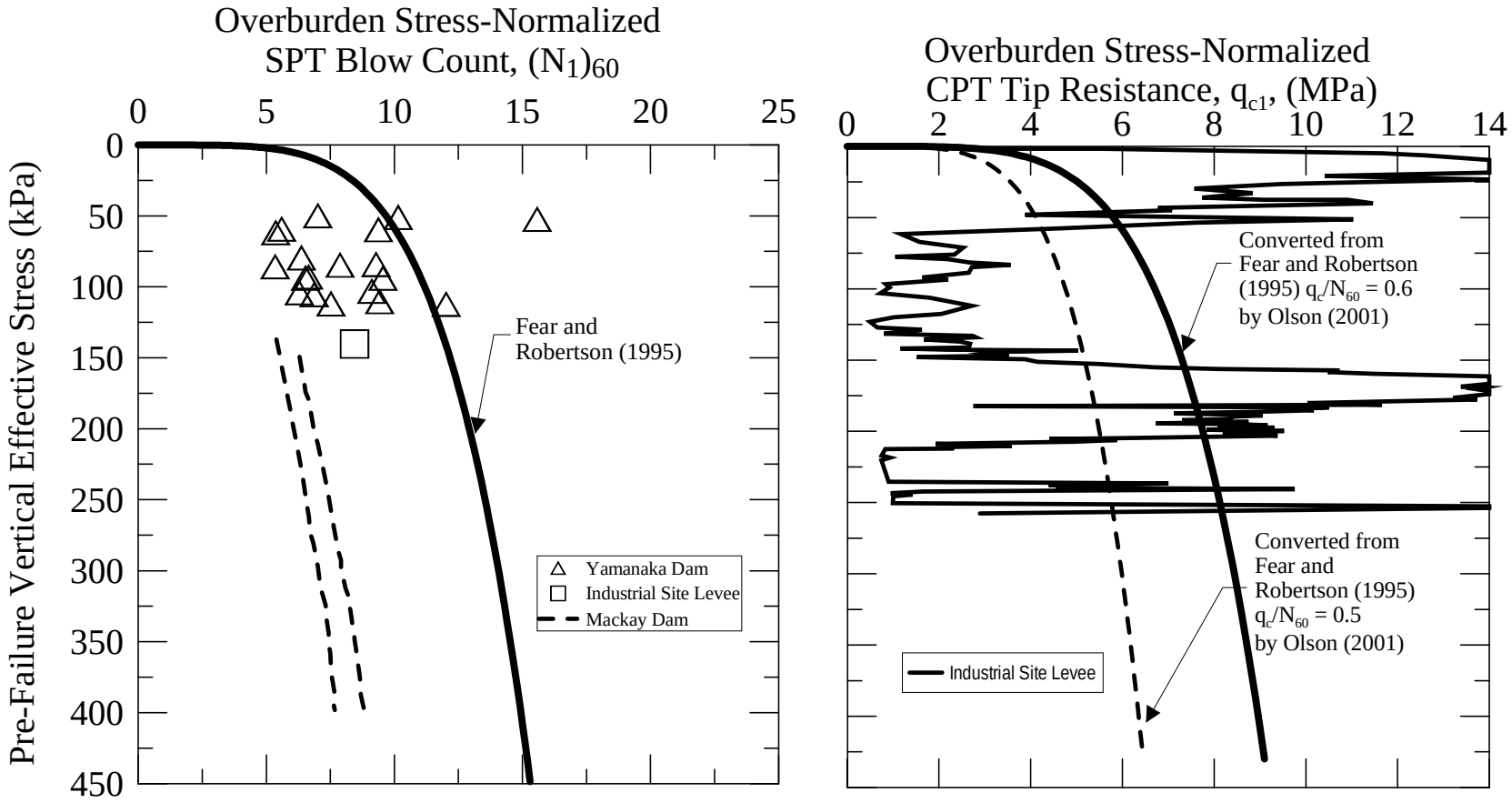

Figure 7.9 Overburden stress-normalized penetration resistances from Yamanaka dam, Mackay dam, and the Industrial Site levee compared to Olson and Stark (2003) recommended liquefaction susceptibility curves using (a) $(N_1)_{60}$; and (b) q_{c1} values

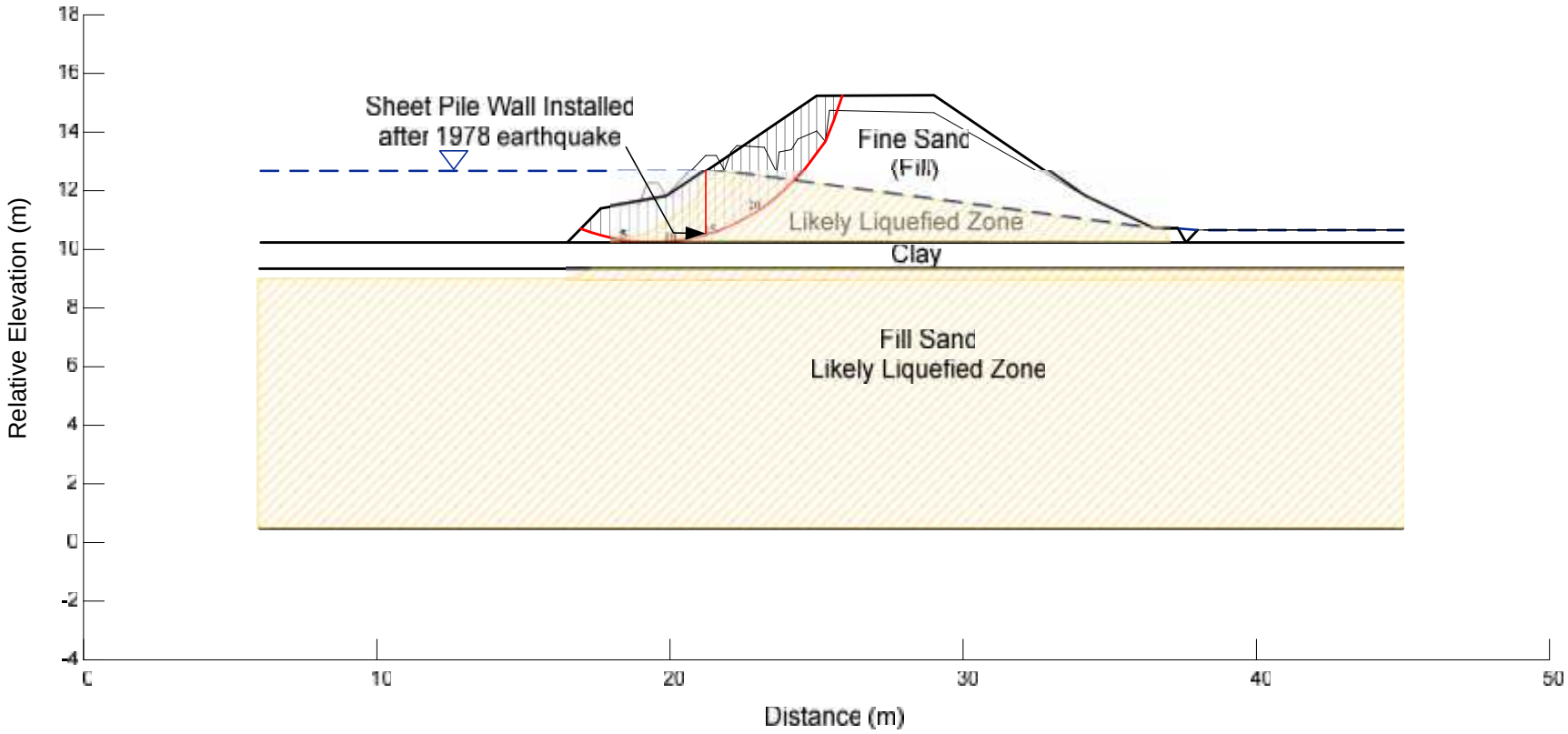

Figure 7.10 Circular sliding surface (shallow surface) for Yamanaka dam that intersects the liquefiable embankment fill soils only. Pinning effect of sheetpile wall is represented by arrow near the base of the sliding surface

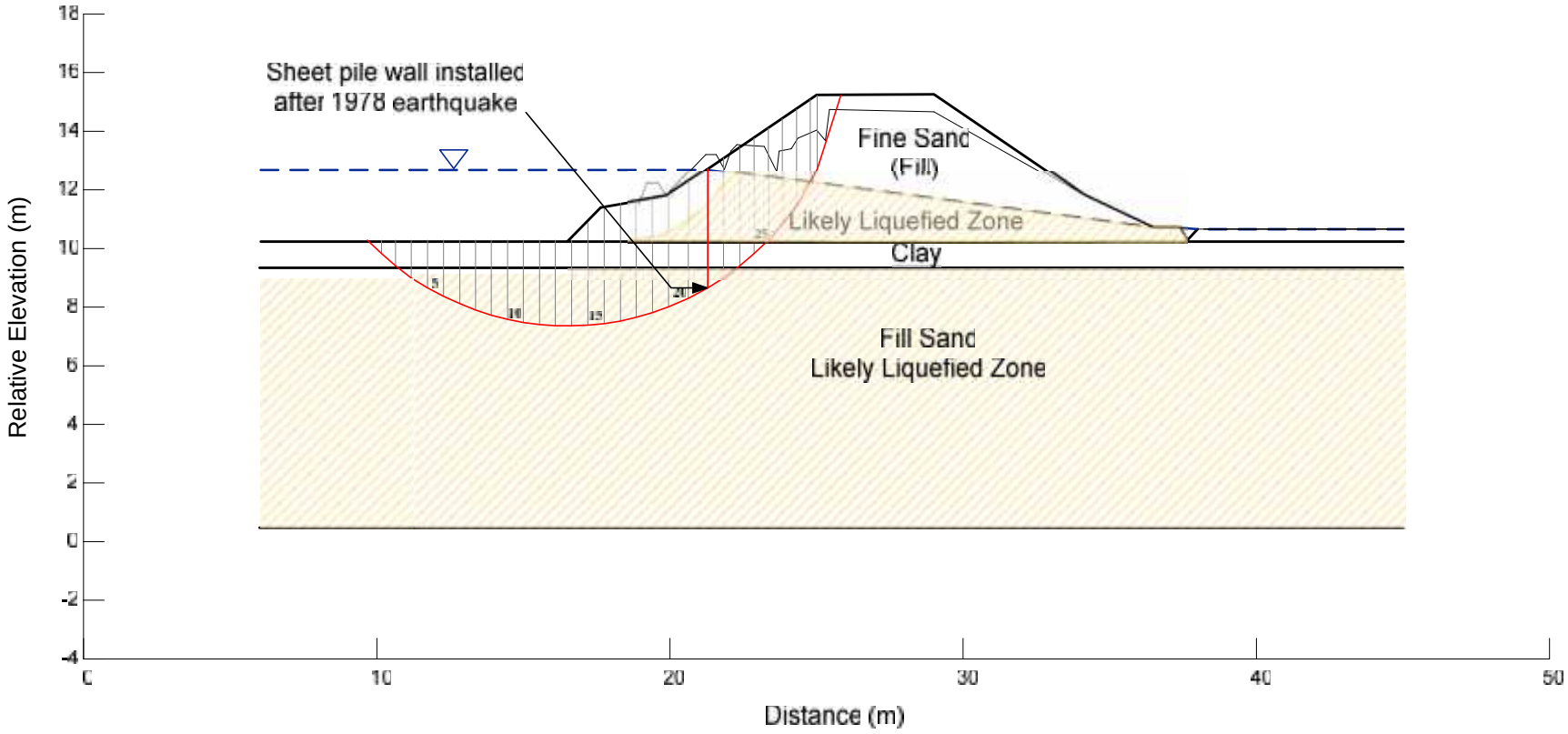

Figure 7.11 Circular sliding surface (deep surface) for Yamanaka dam that intersects both the liquefiable embankment fill soils and lower fill soils

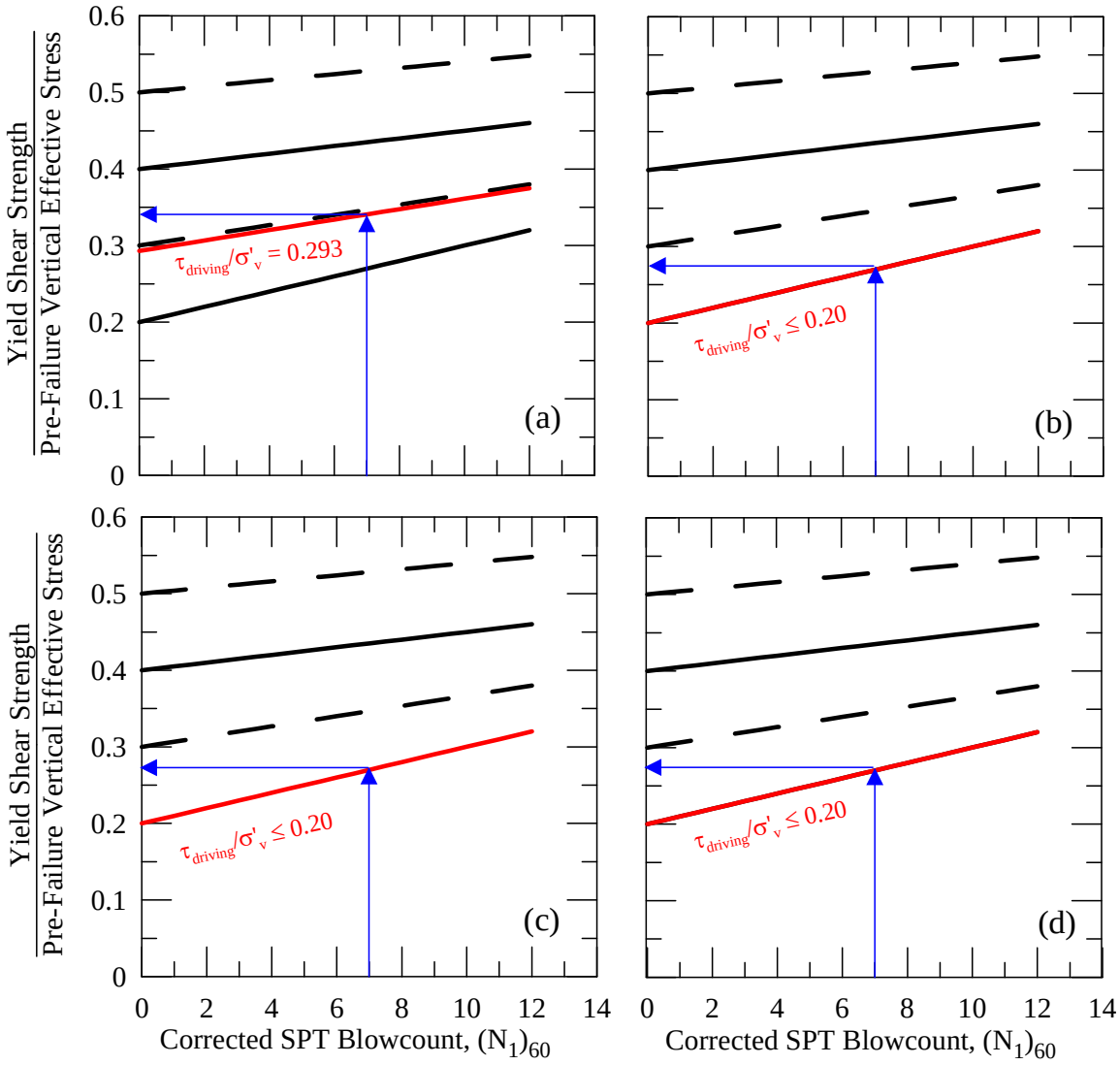

Figure 7.12 Evaluation of yield strength ratio for potentially liquefiable soils at Yamanaka Dam using Olson and Zitny (2012) correlation. (a) Shallow circular failure surface without sheetpile wall; (b) shallow circular failure surface with sheetpile wall; (c) deep circular failure surface without sheetpile wall; and (d) deep circular failure surface with sheetpile wall

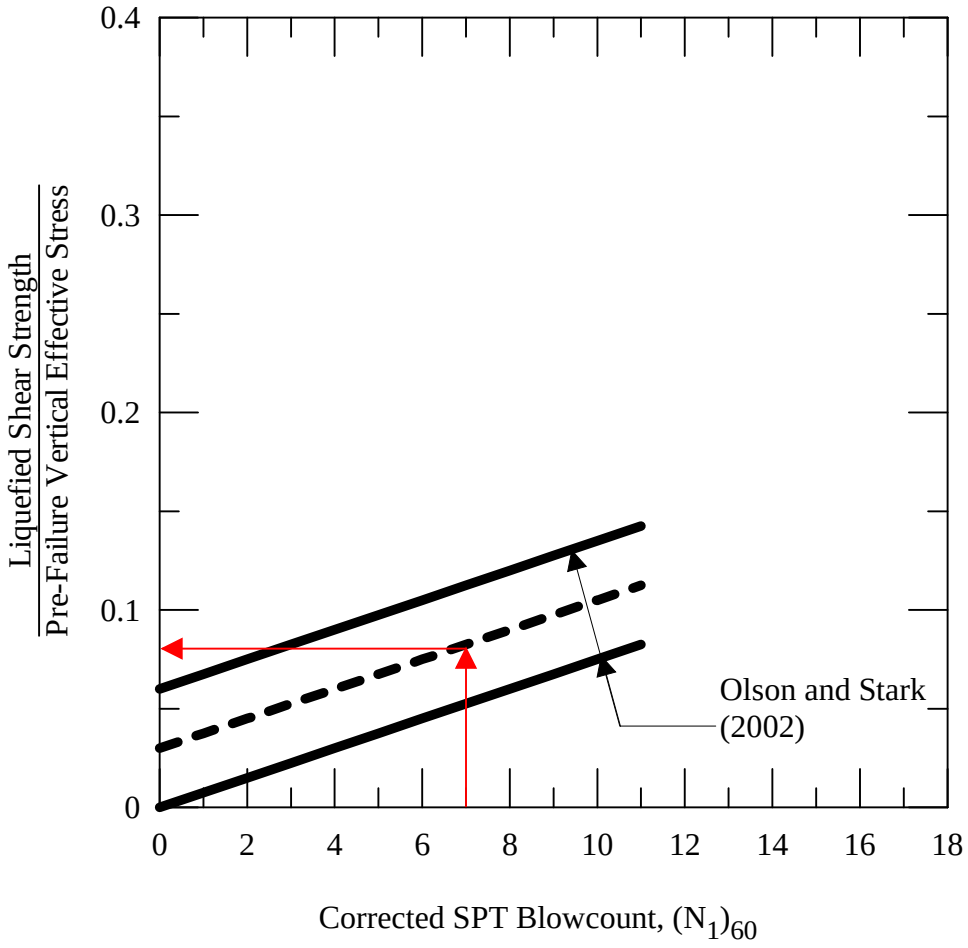

Figure 7.13 SPT-based relationship proposed by Olson and Stark (2002) to estimate liquefied strength ratio. Red arrows indicate estimate for Yamanaka dam

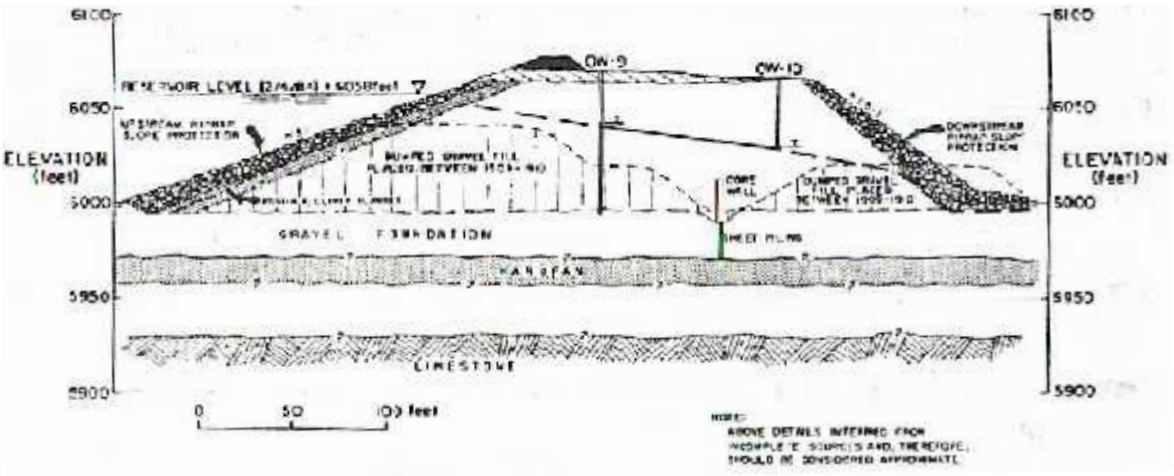

Figure 7.14 Cross-section of Mackay dam at Station 17 (Harder 1992)

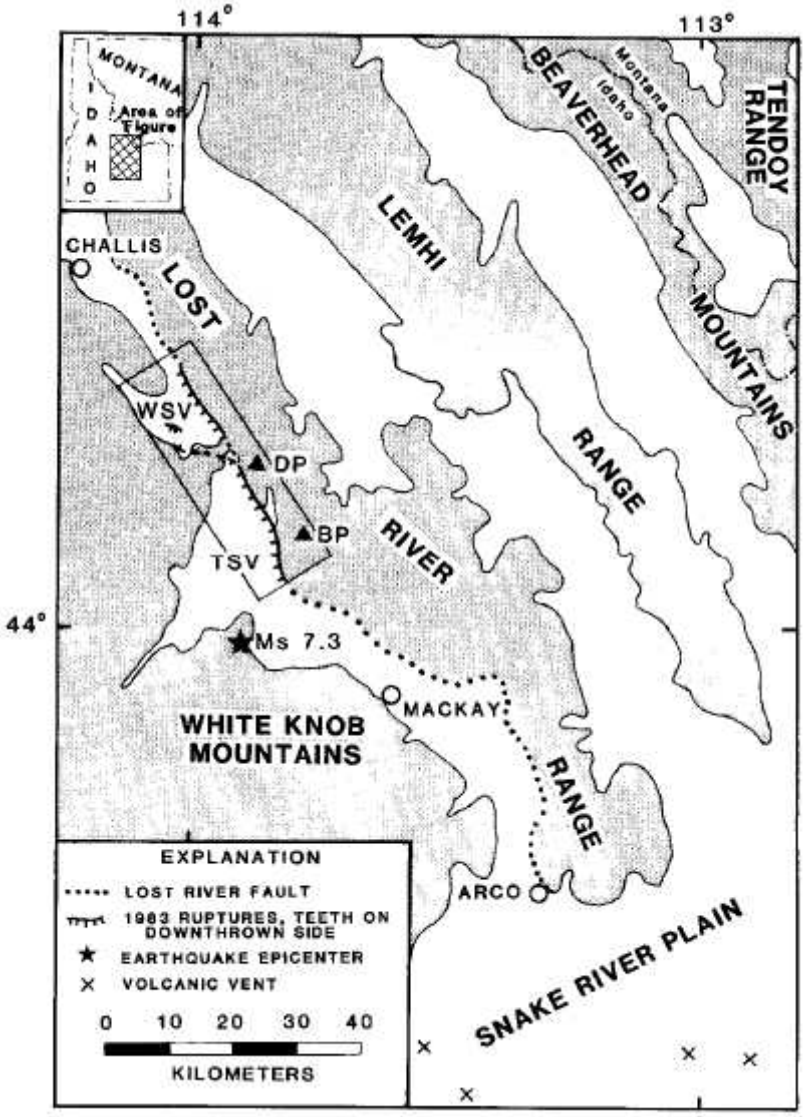

Figure 7.15 Location of Lost River fault. Fault line within rectangle shows the surface scarp during Borah Peak earthquake. Epicentral location is represented as a star. Dickey Peak (DP) and Borah Peak (BP) are shown as solid triangles. Warm Spring Valley (WSV) and Thousand Spring Valley (TSV) are also shown. Shaded regions show the mountainous terrain (from Crone et al. 1987)

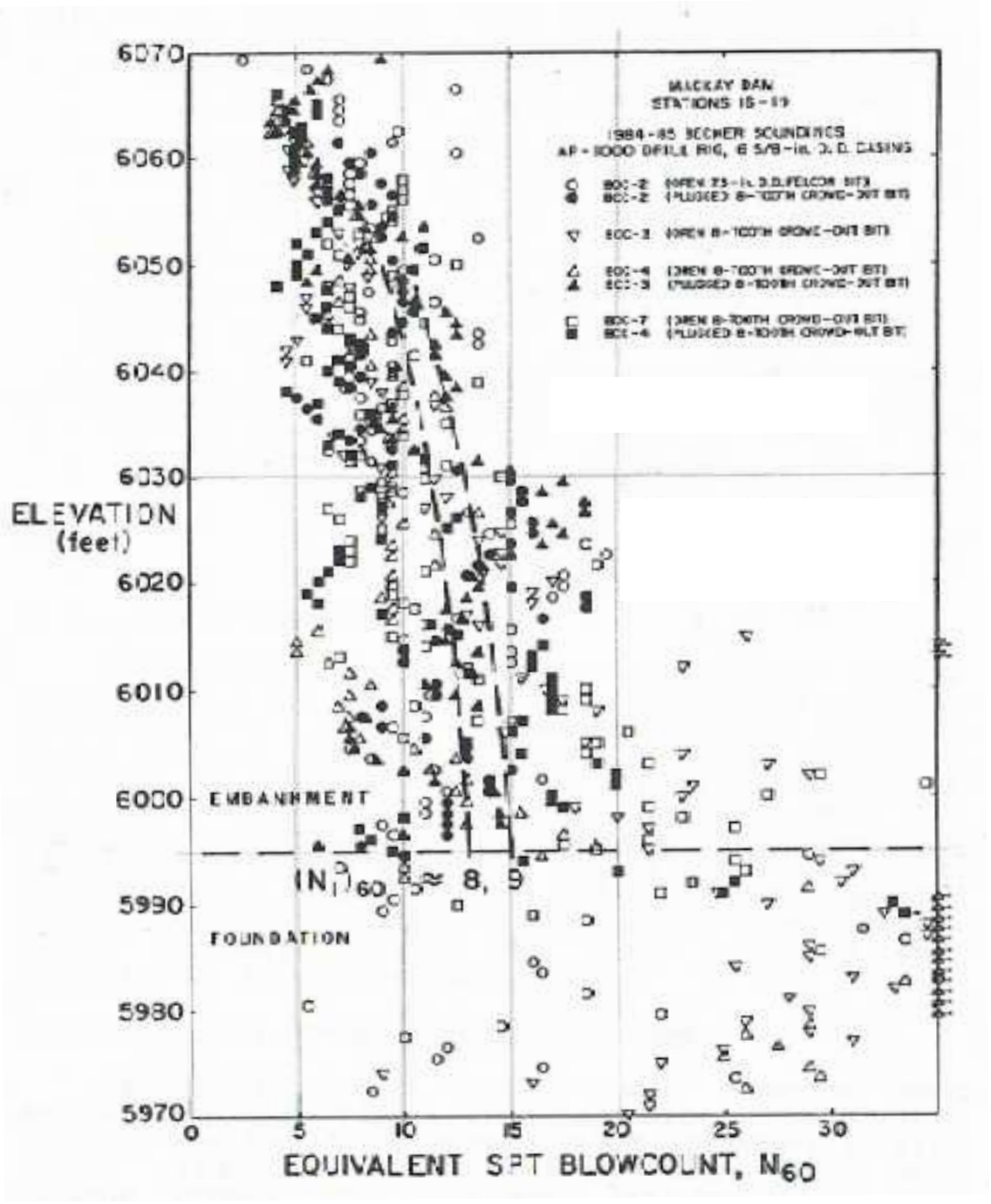

Figure 7.16 Equivalent SPT blowcounts determined in Mackay Dam between Stations 16 and 19 (Harder 1992)

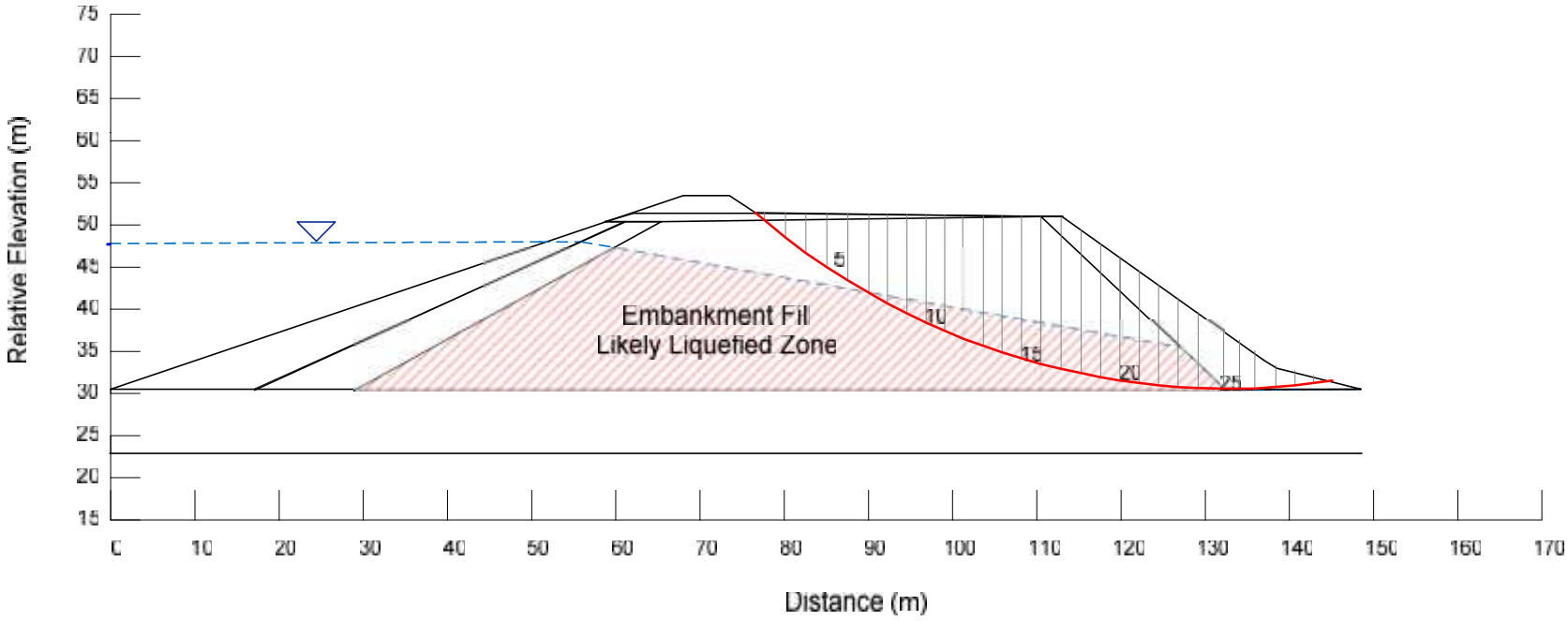

Figure 7.17 Mackay dam with potential failure surface (deep surface) corresponding to cracking near additional crest fill

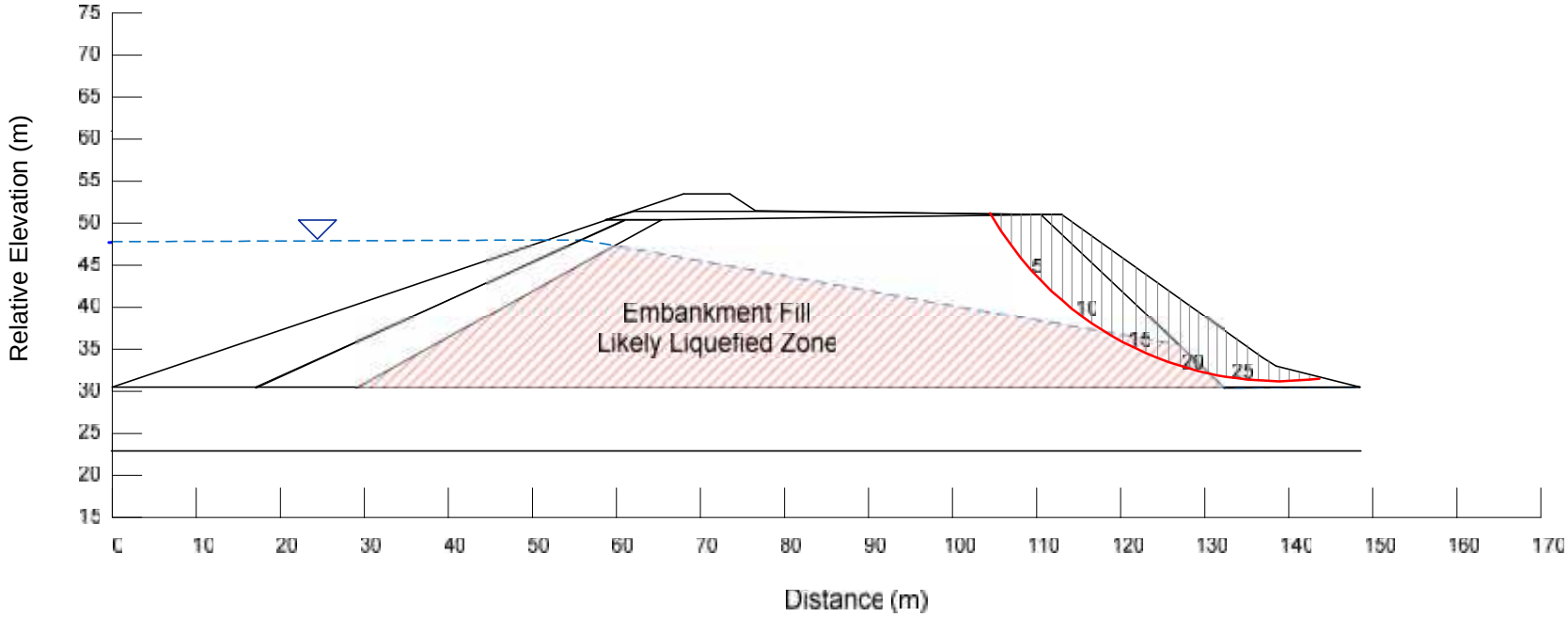

Figure 7.18 Mackay dam with potential failure surface (shallow surface) corresponding to cracking near additional downstream slope

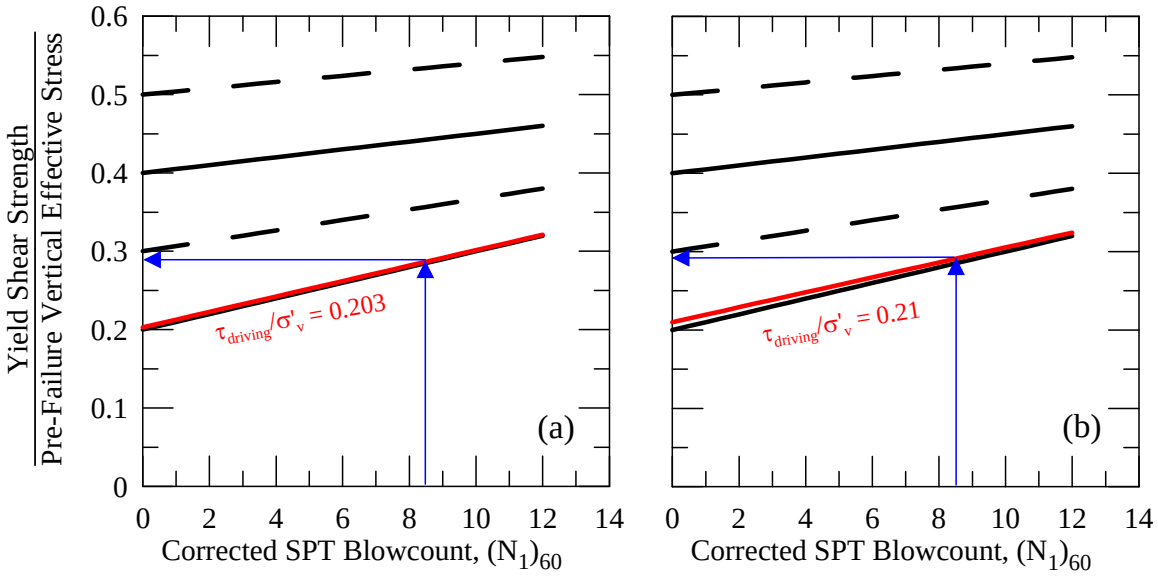

Figure 7.19 Evaluation of yield strength ratio for potentially liquefiable soils at Mackay Dam using Olson and Zitny (2012) correlation. (a) Deep circular failure surface; (b) shallow circular failure surface.

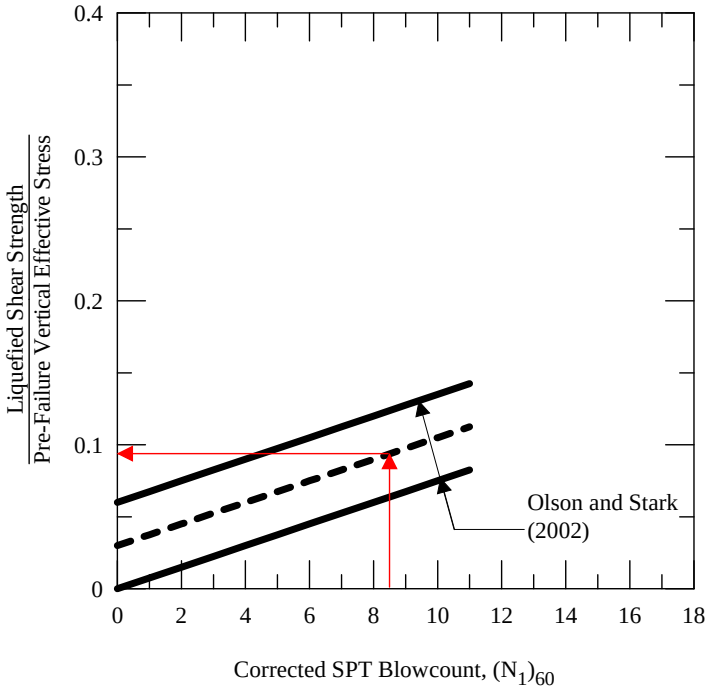

Figure 7.20 SPT-based relationship proposed by Olson and Stark (2002) to estimate liquefied strength ratio. Red arrows indicate estimate for Mackay Dam

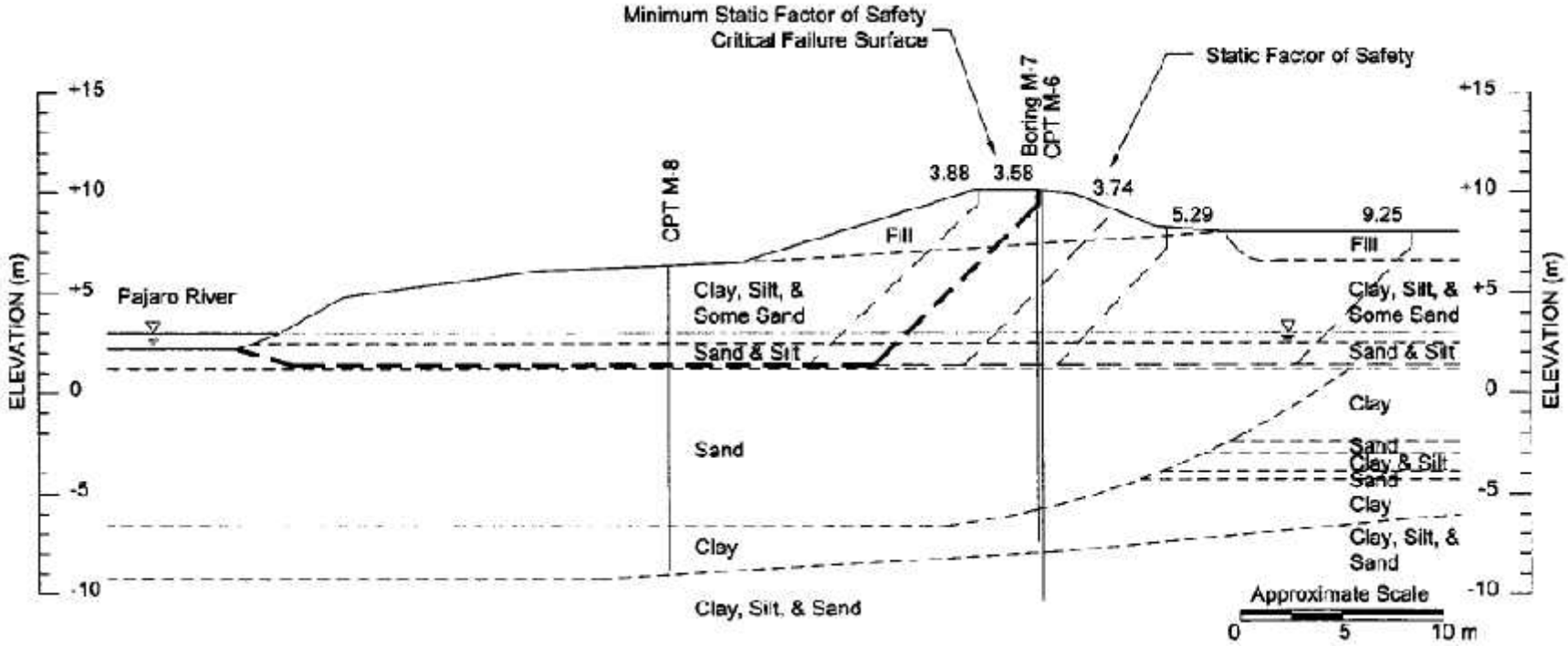

Figure 7.21 Cross-section and subsurface profile of the industrial site levee (from Miller and Roycroft 2004)

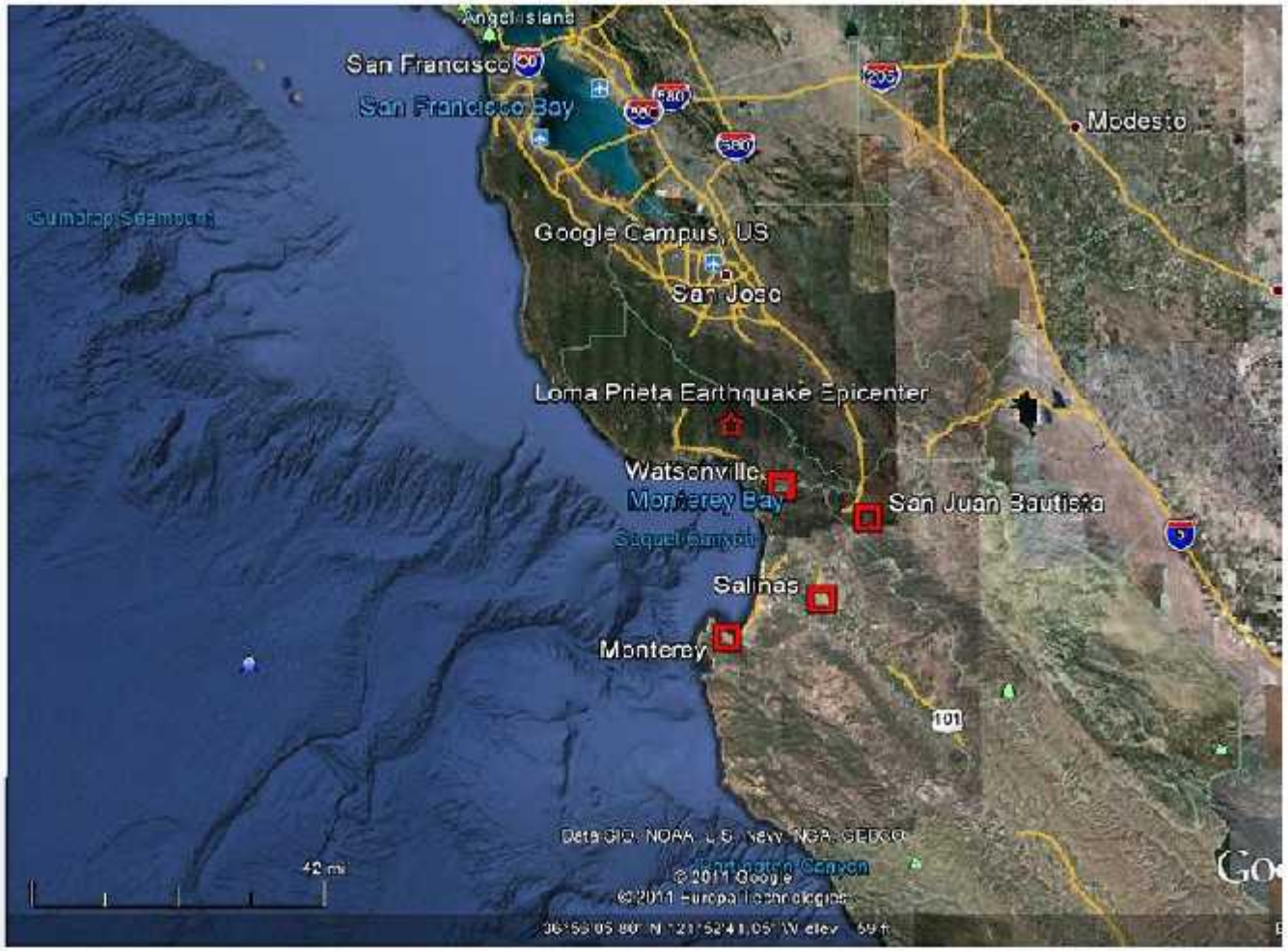

Figure 7.22 Location of Loma Prieta earthquake epicenter with the location of nearby strong ground motion recording stations (background image courtesy of Google Earth 2011)

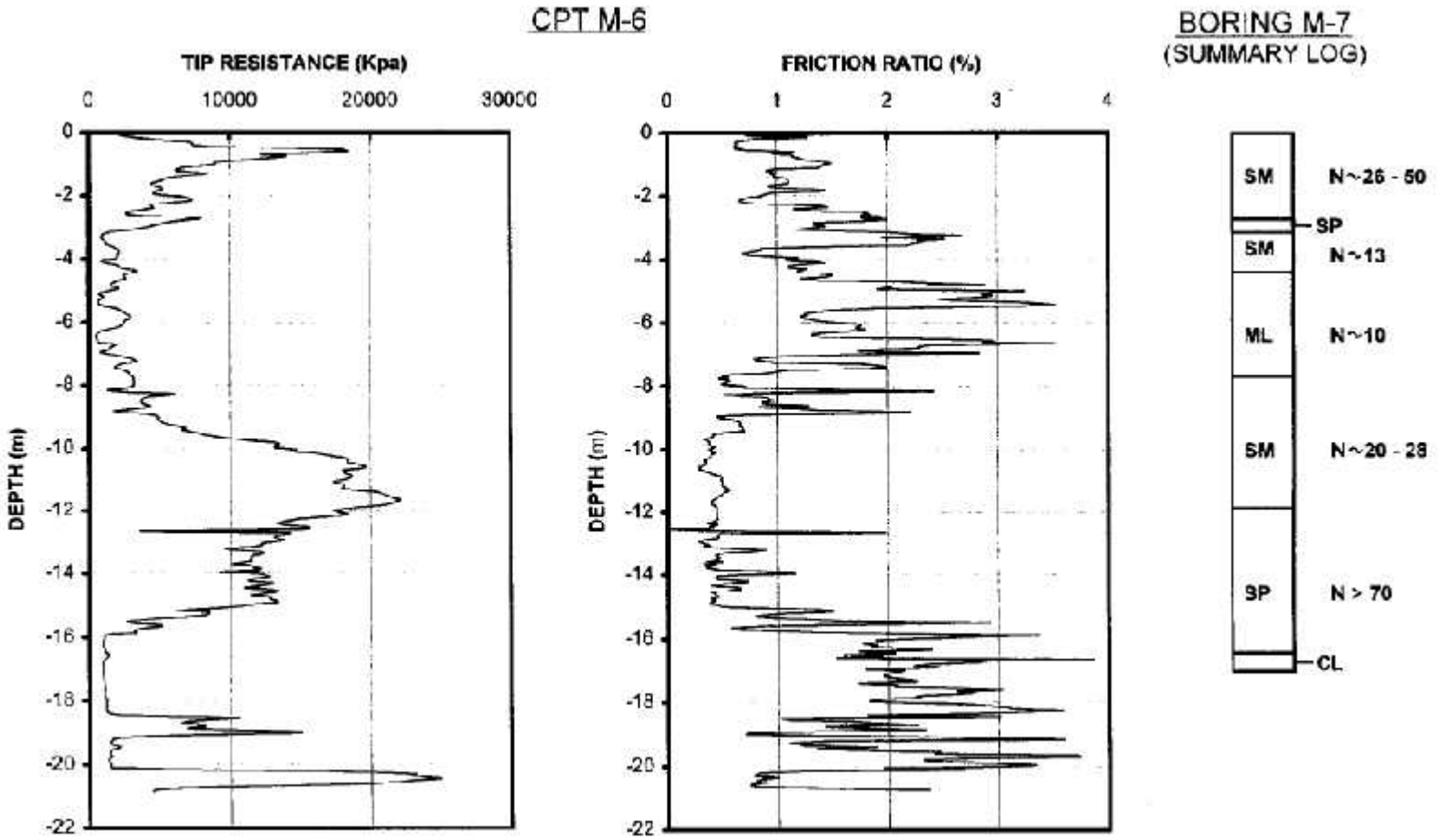

Figure 7.23 Results of CPT M-6, and summary of boring log M-7 with uncorrected SPT values (from Miller and Roycroft 2004)

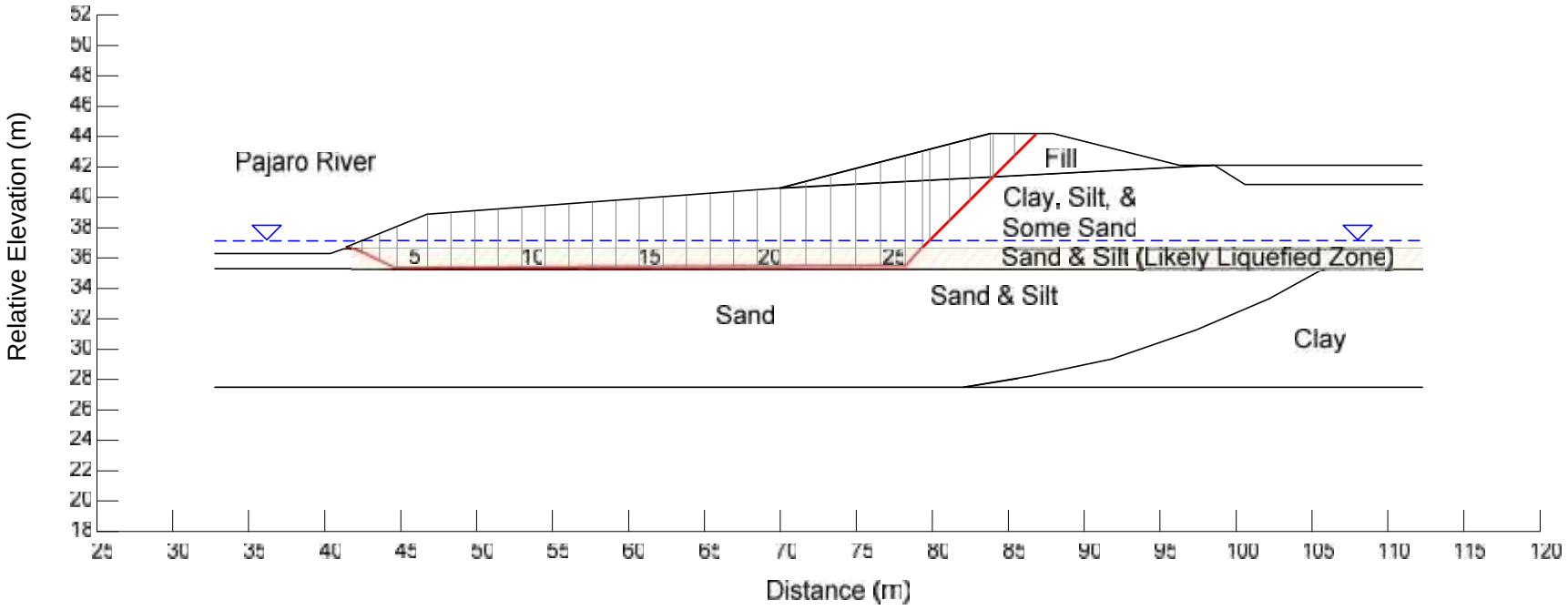

Figure 7.24 Industrial site levee dam with critical failure surface for embankment failure

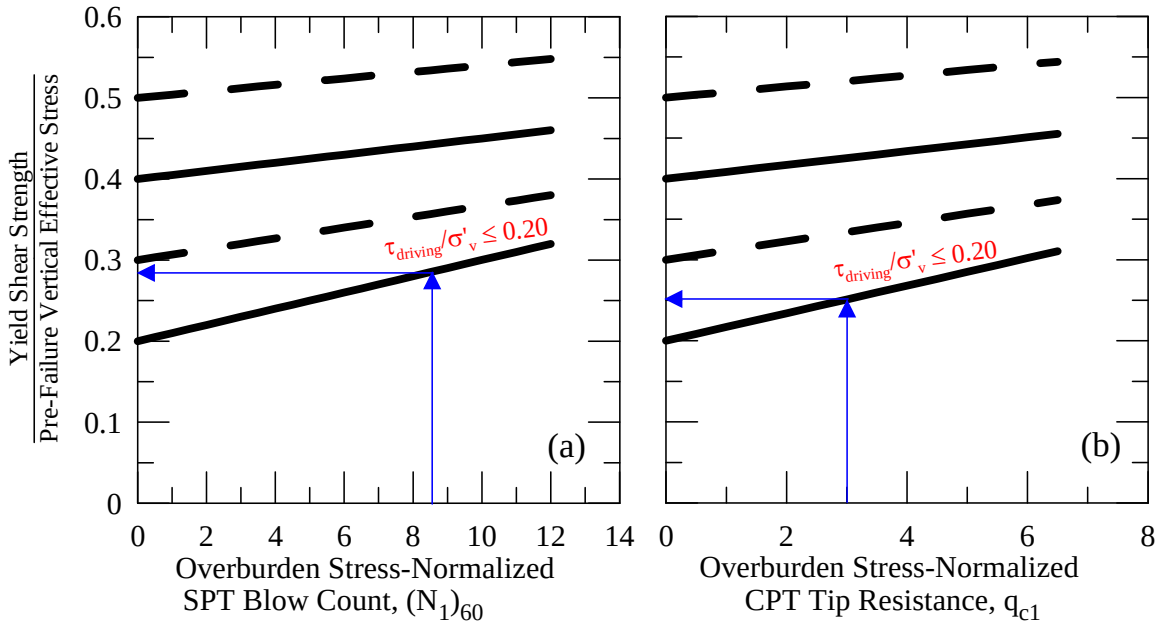

Figure 7.25 Evaluation of yield strength ratio for potentially liquefiable soils at industrial site levee using Olson and Zitny (2012) correlation

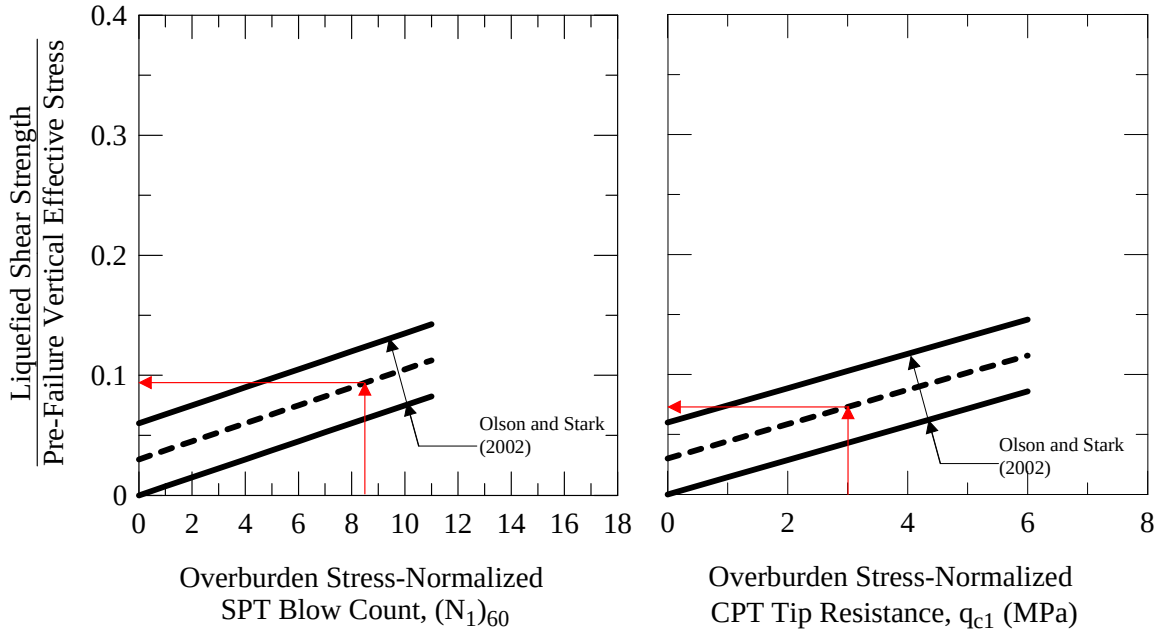

Figure 7.26 SPT- and CPT-based relationships proposed by Olson and Stark (2002) to estimate liquefied strength ratio. Arrows indicate estimate for industrial site levee

Table 7.1 Seismic information for earthquakes experienced by Yamanaka Dam (from Tani and Nakashima 1999)

Earthquake Name	Tokachi-Oki	Miyagiken-Oki	Nipponkai-chubu	Sanriku Haruka-Oka
Year	1968	1978	1983	1994
Epicentral Distance (km)	202	307	199	225
Damage Severity	Severe U/S Slumping Flow Failure	U/S Slump	U/S Cracking and Settlement less severe slumping	U/S Slump
Magnitude in Japanese scale	7.9	7.4	7.7	7.5
Assumed max acceleration (cm/s^2)	55	32	57	45
Seismic Intensity in Japanese scale (Near site)	Hachinohe 5	Hachinohe 4	Hachinohe 4	Hachinohe 6
Acceleration Record (cm/s^2) (Near site)	Hachinohe (Not Available)	Hachinohe (Not Available)	Hachinohe 19	Hachinohe 416

Table 7.2 Liquefaction triggering analysis of Yamanaka Dam for shallow failure surface (without sheetpile wall) shown in Figure 7.10 during 1968 Tokachi-Oki earthquake (a_{max} = 0.056g, MSF* = 0.77) and 1978 Miyagiken-Oki earthquake (a_{max} = 0.032g, MSF = 1.04)

						a_{max}=0.056g					a_{max}=0.032g			
Slice No.	σ'_v (kPa)	σ_v (kPa)	r_d	Avg. s_u(yield) (kPa)	Average $\tau_{driving}/\sigma'_v$	$\tau_{driving}$ (kPa)	$\tau_{avg,seismic}$ (kPa)	$FS_{Triggering}$	Liquefaction Triggered?	Avg. s_u(liq) (kPa)	$\tau_{avg,seismic}$ (kPa)	$FS_{Triggering}$	Liquefaction Triggered?	Avg. s_u(liq) (kPa)
6	11.4	35.1	0.99	3.9	0.29	3.3	1.6	0.78	Yes	0.9	0.7	0.96	Yes	0.9
7	12.1	36.0	0.99	4.1	0.29	3.5	1.7	0.79	Yes	1.0	0.7	0.97	Yes	1.0
8	12.6	36.6	0.99	4.3	0.29	3.7	1.7	0.80	Yes	1.0	0.7	0.97	Yes	1.0
9	13.0	36.9	0.99	4.4	0.29	3.8	1.7	0.80	Yes	1.1	0.7	0.98	Yes	1.1
10	13.9	37.5	0.99	4.7	0.29	4.1	1.8	0.81	Yes	1.1	0.7	0.98	Yes	1.1
11	15.2	38.5	0.99	5.2	0.29	4.4	1.8	0.83	Yes	1.3	0.8	0.99	Yes	1.3
12	16.4	39.4	0.99	5.6	0.29	4.8	1.8	0.84	Yes	1.4	0.8	1.00	Marginal	1.4
13	17.5	40.0	0.98	6.0	0.29	5.1	1.9	0.85	Yes	1.4	0.8	1.01	Marginal	1.4
14	18.5	40.3	0.98	6.3	0.29	5.4	1.9	0.86	Yes	1.5	0.8	1.01	Marginal	1.5
15	20.7	41.5	0.98	7.0	0.29	6.1	1.9	0.88	Yes	1.7	0.8	1.03	Marginal	1.7
16	23.9	43.4	0.98	8.1	0.29	7.0	2.0	0.90	Yes	2.0	0.9	1.04	Marginal	2.0
17	27.0	44.9	0.98	9.2	0.29	7.9	2.1	0.92	Yes	2.2	0.9	1.05	Marginal	2.2
18	30.0	46.2	0.98	10.2	0.29	8.8	2.1	0.94	Yes	2.5	0.9	1.05	No	NA
19	32.8	47.1	0.98	11.2	0.29	9.6	2.2	0.95	Yes	2.7	0.9	1.06	No	NA
20	35.4	47.7	0.98	12.1	0.29	10.4	2.2	0.96	Yes	2.9	0.9	1.07	No	NA
21	37.8	47.8	0.98	12.9	0.29	11.1	2.2	0.97	Yes	3.1	0.9	1.07	No	NA
22	40.0	47.5	0.98	13.6	0.29	11.7	2.2	0.98	Yes	3.3	0.9	1.08	No	NA
23	42.0	46.8	0.98	14.3	0.29	12.3	2.2	0.99	Yes	3.5	0.9	1.08	No	NA
24	43.8	45.4	0.98	14.9	0.29	12.8	2.1	1.00	Yes	3.6	0.9	1.09	No	NA

* Magnitude Scaling Factor, MSF taken as average of equation from Idriss (1995) and Andrus and Stokoe (1997)

Table 7. 3 Liquefaction triggering analysis of Yamanaka Dam for shallow failure surface (with sheetpile wall) shown in Figure 7.10 during 1983 Nihonkai-Chubu earthquake (a_{max} = 0.058g, MSF* = 0.925) and [earthquake name] earthquake (a_{max} = 0.046g, MSF = 1.0)

						a_{max}=0.058g					a_{max}=0.046g				
Slice No.	σ'_v (kPa)	σ_v (kPa)	r_d	Avg. s_u(yield) (kPa)	Average $\tau_{driving}/\sigma'_v$	$\tau_{driving}$ (kPa)	$\tau_{avg,seismic}$ (kPa)	$FS_{Triggering}$	Liquefaction Triggered?	Avg. s_u(liq) (kPa)	$\tau_{avg,seismic}$ (kPa)	$FS_{Triggering}$	Liquefaction Triggered?	Avg. s_u(liq) (kPa)
6	11.4	35.1	0.99	3.1	0.20	1.8	1.4	0.94	Yes	0.9	1.0	1.07	Marginal	0.9
7	12.1	36.0	0.99	3.3	0.20	2.0	1.4	0.96	Yes	1.0	1.1	1.08	Marginal	1.0
8	12.6	36.6	0.99	3.4	0.20	2.0	1.5	0.97	Yes	1.0	1.1	1.09	Marginal	1.0
9	13.0	36.9	0.99	3.5	0.20	2.1	1.5	0.98	Yes	1.1	1.1	1.10	Marginal	1.1
10	13.9	37.5	0.99	3.7	0.20	2.2	1.5	1.00	Yes	1.1	1.1	1.12	No	NA
11	15.2	38.5	0.99	4.1	0.20	2.5	1.5	1.02	Marginal	1.3	1.1	1.14	No	NA
12	16.4	39.4	0.99	4.4	0.20	2.7	1.6	1.05	Marginal	1.4	1.2	1.16	No	NA
13	17.5	40.0	0.98	4.7	0.20	2.8	1.6	1.07	Marginal	1.4	1.2	1.18	No	NA
14	18.5	40.3	0.98	5.0	0.20	3.0	1.6	1.08	Marginal	1.5	1.2	1.19	No	NA
15	20.7	41.5	0.98	5.6	0.20	3.3	1.7	1.11	No	NA	1.2	1.22	No	NA
16	23.9	43.4	0.98	6.5	0.20	3.9	1.7	1.15	No	NA	1.3	1.25	No	NA
17	27.0	44.9	0.98	7.3	0.20	4.4	1.8	1.18	No	NA	1.3	1.28	No	NA
18	30.0	46.2	0.98	8.1	0.20	4.9	1.8	1.21	No	NA	1.4	1.30	No	NA
19	32.8	47.1	0.98	8.8	0.20	5.3	1.9	1.23	No	NA	1.4	1.32	No	NA
20	35.4	47.7	0.98	9.6	0.20	5.7	1.9	1.25	No	NA	1.4	1.34	No	NA
21	37.8	47.8	0.98	10.2	0.20	6.1	1.9	1.27	No	NA	1.4	1.36	No	NA
22	40.0	47.5	0.98	10.8	0.20	6.5	1.9	1.29	No	NA	1.4	1.37	No	NA
23	42.0	46.8	0.98	11.3	0.20	6.8	1.9	1.31	No	NA	1.4	1.39	No	NA
24	43.8	45.4	0.98	11.8	0.20	7.1	1.8	1.33	No	NA	1.3	1.40	No	NA

* Magnitude Scaling Factor, MSF taken as average of equation from Idriss (1995) and Andrus and Stokoe (1997)

Table 7.4 Liquefaction triggering analysis of Yamanaka Dam for deep circular failure surface (without sheetpile wall) shown in Figure 7.11 during 1968 Tokachi-Oki earthquake (a_{max} = 0.056g, MSF* = 0.77) and 1978 Miyagiken-Oki earthquake (a_{max} = 0.032g, MSF = 1.04)

						a_{max}=0.056g					a_{max}=0.032g				
Slice No.	σ'_v (kPa)	σ_v (kPa)	r_d	Avg. s_u(yield) (kPa)	Average $\tau_{driving}/\sigma'_v$	$\tau_{driving}$ (kPa)	$\tau_{avg,seismic}$ (kPa)	$FS_{Triggering}$	Liquefaction Triggered?	Avg. s_u(liq) (kPa)	$\tau_{avg,seismic}$ (kPa)	$FS_{Triggering}$	Liquefaction Triggered?	Avg. s_u(liq) (kPa)
4	12.9	51.7	0.99	3.5	0.20	2.6	2.4	0.70	Yes	1.1	1.0	0.97	Yes	1.1
5	15.8	57.7	0.99	4.3	0.20	3.2	2.7	0.73	Yes	1.3	1.1	0.99	Yes	1.3
6	18.2	62.8	0.98	4.9	0.20	3.6	2.9	0.75	Yes	1.5	1.2	1.01	Marginal	1.5
7	20.2	67.1	0.98	5.5	0.20	4.0	3.1	0.76	Yes	1.7	1.3	1.02	Marginal	1.7
8	21.9	70.7	0.98	5.9	0.20	4.4	3.3	0.77	Yes	1.8	1.4	1.03	Marginal	1.8
9	23.3	73.6	0.98	6.3	0.20	4.7	3.4	0.78	Yes	1.9	1.4	1.03	Marginal	1.9
10	24.3	75.9	0.98	6.6	0.20	4.9	3.5	0.78	Yes	2.0	1.5	1.03	Marginal	2.0
11	25.1	77.6	0.98	6.8	0.20	5.0	3.6	0.79	Yes	2.1	1.5	1.04	Marginal	2.1
12	25.6	78.6	0.98	6.9	0.20	5.1	3.6	0.79	Yes	2.1	1.5	1.04	Marginal	2.1
13	25.8	79.1	0.98	7.0	0.20	5.2	3.7	0.79	Yes	2.1	1.5	1.04	Marginal	2.1
14	28.3	81.5	0.98	7.6	0.20	5.7	3.8	0.81	Yes	2.3	1.6	1.05	No	NA
15	33.0	85.8	0.97	8.9	0.20	6.6	3.9	0.85	Yes	2.7	1.7	1.08	No	NA
16	35.3	87.4	0.97	9.5	0.20	7.1	4.0	0.86	Yes	2.9	1.7	1.09	No	NA
17	35.2	86.2	0.97	9.5	0.20	7.0	3.9	0.87	Yes	2.9	1.7	1.09	No	NA
18	34.8	84.4	0.97	9.4	0.20	7.0	3.9	0.87	Yes	2.9	1.6	1.09	No	NA
19	34.1	81.9	0.97	9.2	0.20	6.8	3.8	0.87	Yes	2.8	1.6	1.09	No	NA
20	34.3	79.8	0.97	9.3	0.20	6.9	3.7	0.88	Yes	2.8	1.5	1.10	No	NA
21	35.4	77.7	0.97	9.6	0.20	7.1	3.6	0.90	Yes	2.9	1.5	1.11	No	NA
22	38.1	76.5	0.97	10.3	0.20	7.6	3.5	0.93	Yes	3.1	1.5	1.13	No	NA
23	42.4	76.4	0.97	11.4	0.20	8.5	3.5	0.96	Yes	3.5	1.5	1.15	No	NA
26	51.0	69.6	0.97	13.8	0.20	10.2	3.2	1.03	Marginal	4.2	1.4	1.19	No	NA
27	52.5	64.6	0.97	14.2	0.20	10.5	3.0	1.05	No	NA	1.3	1.21	No	NA
28	53.0	57.4	0.98	14.3	0.20	10.6	2.6	1.08	No	NA	1.1	1.22	No	NA

* Magnitude Scaling Factor, MSF taken as average of equation from Idriss (1995) and Andrus and Stokoe (1997)

Table 7.5 Liquefaction triggering analysis of Yamanaka Dam for deep circular failure surface (with sheetpile wall) shown in Figure 7.11 during 1983 Nihonkai-Chubu earthquake (a_{max} = 0.058g, MSF* = 0.925) and 1994 Sanriku Haruka-Oki earthquake (a_{max} = 0.046g, MSF = 1.0)

						a_{max}=0.058g					a_{max}=0.046g			
Slice No.	σ'_v (kPa)	σ_v (kPa)	r_d	Avg. s_u(yield) (kPa)	Average $\tau_{driving}/\sigma'_v$	$\tau_{driving}$ (kPa)	$\tau_{avg,seismic}$ (kPa)	$FS_{Triggering}$	Liquefaction Triggered?	Avg. s_u(liq) (kPa)	$\tau_{avg,seismic}$ (kPa)	$FS_{Triggering}$	Liquefaction Triggered?	Avg. s_u(liq) (kPa)
4	12.9	51.7	0.99	3.5	0.20	2.5	2.1	0.77	Yes	1.1	1.5	0.88	Yes	1.1
5	15.8	57.7	0.99	4.3	0.20	3.0	2.3	0.80	Yes	1.3	1.7	0.91	Yes	1.3
6	18.2	62.8	0.98	4.9	0.20	3.5	2.5	0.82	Yes	1.5	1.8	0.93	Yes	1.5
7	20.2	67.1	0.98	5.5	0.20	3.8	2.7	0.84	Yes	1.7	2.0	0.94	Yes	1.7
8	21.9	70.7	0.98	5.9	0.20	4.2	2.8	0.85	Yes	1.8	2.1	0.95	Yes	1.8
9	23.3	73.6	0.98	6.3	0.20	4.4	2.9	0.85	Yes	1.9	2.2	0.95	Yes	1.9
10	24.3	75.9	0.98	6.6	0.20	4.6	3.0	0.86	Yes	2.0	2.2	0.96	Yes	2.0
11	25.1	77.6	0.98	6.8	0.20	4.8	3.1	0.86	Yes	2.1	2.3	0.96	Yes	2.1
12	25.6	78.6	0.98	6.9	0.20	4.9	3.1	0.86	Yes	2.1	2.3	0.97	Yes	2.1
13	25.8	79.1	0.98	7.0	0.20	4.9	3.1	0.87	Yes	2.1	2.3	0.97	Yes	2.1
14	28.3	81.5	0.98	7.6	0.20	5.4	3.2	0.89	Yes	2.3	2.4	0.99	Yes	2.3
15	33.0	85.8	0.97	8.9	0.20	6.3	3.4	0.92	Yes	2.7	2.5	1.02	Marginal	2.7
16	35.3	87.4	0.97	9.5	0.20	6.7	3.4	0.94	Yes	2.9	2.5	1.03	Marginal	2.9
17	35.2	86.2	0.97	9.5	0.20	6.7	3.4	0.94	Yes	2.9	2.5	1.03	Marginal	2.9
18	34.8	84.4	0.97	9.4	0.20	6.6	3.3	0.94	Yes	2.9	2.4	1.04	Marginal	2.9
19	34.1	81.9	0.97	9.2	0.20	6.5	3.2	0.95	Yes	2.8	2.4	1.04	Marginal	2.8
20	34.3	79.8	0.97	9.3	0.20	6.5	3.2	0.96	Yes	2.8	2.3	1.05	Marginal	2.8
21	35.4	77.7	0.97	9.6	0.20	6.7	3.1	0.98	Yes	2.9	2.3	1.07	No	NA
22	38.1	76.5	0.97	10.3	0.20	7.2	3.0	1.00	Marginal	3.1	2.2	1.09	No	NA
23	42.4	76.4	0.97	11.4	0.20	8.1	3.0	1.03	Marginal	3.5	2.2	1.11	No	NA
26	51.0	69.6	0.97	13.8	0.20	9.7	2.8	1.11	No	NA	2.0	1.18	No	NA
27	52.5	64.6	0.97	14.2	0.20	10.0	2.6	1.13	No	NA	1.9	1.20	No	NA
28	53.0	57.4	0.98	14.3	0.20	10.1	2.3	1.16	No	NA	1.7	1.22	No	NA

* Magnitude Scaling Factor, MSF taken as average of equation from Idriss (1995) and Andrus and Stokoe (1997)

Table 7.6 Summary of post-triggering stability stability analyses for Yamanaka Dam

Sliding Surface	Earthquake (a_{max})	Figure No.	Liquefied Slices	Sheet Pile Wall Present?	FS_{FLOW}
Shallow Circular Failure Surface	1968 Tokachi-Oki (0.056)	Figure 7.10	6-24	No	0.598
	1978 Miyagiken-Oki (0.032)		6-17	No	0.892
	1983 Nihonkai-Chubu (0.058)		6-19	Yes	0.985
	1994 Sanriku Haruka-Oki (0.046)		6-15	Yes	1.089
Deep Circular Failure Surface	1968 Tokachi-Oki (0.056)	Figure 7.11	4-26	No	0.83
	1978 Miyagiken-Oki (0.032)		4-13	No	1.07
	1983 Nihonkai-Chubu (0.058)		4-26	Yes	0.947
	1994 Sanriku Haruka-Oki (0.046)		4-13	Yes	1.12

Table 7.7 Grain size summary for Mackay dam samples (from Harder 1992)

Material	Gravel Content (%)	Sand Content (%)	Fine Content (%)
4 Ring Density Samples of Dumped Mackay Dam fill on Left Abutment	Range = 56 - 75 Mean = 64	Range = 18 - 36 Mean = 29	Range = 6 - 8 Mean = 7
21 Becker Samples of Mackay Dam Embankment Material Obtained Beneath Phreatic Surface	Range = 42 - 83 Mean = 69	Range = 13 - 54 Mean = 26	Range = 3 - 10 Mean = 6
16 Becker Samples of Mackay Dam Foundation Material Obtained Beneath Phreatic Surface	Range = 2 - 89 Mean = 57	Range = 8 - 78 Mean = 32	Range = 1 - 75 Mean = 11

Table 7.8 Parameters of Lost River fault that ruptured during the 1983 Borah Peak earthquake

R_{JB} km	Z_{TOR} km	W km	$Z_{1.0}$ m	$Z_{1.0*}$ m	$Z_{2.5}$ m	DIP degree	STRIKE degree
0	0	18	831 to 326	337 to 298	3506 to 1691	50	15

Notes:
* for Chiou and Youngs (2008) relationship
R_{JB} = horizontal distance to surface projection of rupture
Z_{TOR} = depth to top of rupture
W = down-dip rupture width
$Z_{1.0}$ = depth (in m) to the Vs = 1.0 km/s horizon
$Z_{2.5}$ = depth (in m) to Vs = 2.5 km/s horizon

Table 7.9 PGAs (g) calculated from NGA relationships for Mackay dam

Abrahamson & Silva	Boore & Atkinson	Campbell & Bozorgnia	Chiou & Youngs	Idriss
0.2 to 0.22	0.28 to 0.46	0.29 to 0.32	0.23 to 0.24	0.21

Table 7.10 Liquefaction triggering analysis results for Mackay dam for deep failure surface shown in Figure 7.17 during 1983 Borah Peak earthquake (a_{max} = 0.22g, MSF* = 1.27)

Slice No.	σ'_v (kPa)	σ_v (kPa)	r_d	Avg. s_u(yield) (kPa)	Average $\tau_{driving}/\sigma'_v$	$\tau_{driving}$ (kPa)	$\tau_{avg,seismic}$ (kPa)	$FS_{Triggering}$	Liquefaction Triggered?	Avg. s_u(liq) (kPa)
8	189.4	194.1	0.89	54.3	0.20	38.4	19.4	0.94	Yes	17.8
9	204.1	217.6	0.86	58.5	0.20	41.4	21.0	0.94	Yes	19.1
10	218.0	239.2	0.83	62.5	0.20	44.3	22.2	0.94	Yes	20.4
11	231.1	259.0	0.80	66.3	0.20	46.9	23.2	0.94	Yes	21.7
12	243.3	277.1	0.77	69.8	0.20	49.4	24.0	0.95	Yes	22.8
13	254.8	293.6	0.75	73.1	0.20	51.7	24.7	0.96	Yes	23.9
14	265.5	308.4	0.73	76.1	0.20	53.9	25.2	0.96	Yes	24.9
15	275.5	321.9	0.71	79.0	0.20	55.9	25.6	0.97	Yes	25.8
16	285.1	333.9	0.69	81.7	0.20	57.9	25.9	0.98	Yes	26.7
17	279.0	329.7	0.70	80.0	0.20	56.6	25.8	0.97	Yes	26.2
18	257.1	309.0	0.73	73.7	0.20	52.2	25.2	0.95	Yes	24.1
19	234.7	286.8	0.76	67.3	0.20	47.6	24.4	0.93	Yes	22.0
20	211.6	263.3	0.79	60.7	0.20	43.0	23.4	0.91	Yes	19.8
21	187.9	238.7	0.83	53.9	0.20	38.1	22.2	0.89	Yes	17.6
22	163.7	212.6	0.87	46.9	0.20	33.2	20.6	0.87	Yes	15.3
23	147.6	186.3	0.91	42.3	0.20	30.0	18.9	0.87	Yes	13.8
24	137.3	152.1	0.94	39.4	0.20	27.9	16.0	0.90	Yes	12.9

* Magnitude Scaling Factor, MSF taken as average of equation from Idriss (1995) and Andrus and Stokoe (1997)

Table 7. 11 Liquefaction triggering analysis results for Mackay dam for shallow failure surface shown in Figure 7.18 during 1983 Borah Peak earthquake (a_{max} = 0.22g, MSF* =1.27)

Slice No.	σ'_v (kPa)	σ_v (kPa)	r_d	Avg. s_u(yield) (kPa)	Average $\tau_{driving}/\sigma'_v$	$\tau_{driving}$ (kPa)	$\tau_{avg,seismic}$ (kPa)	$FS_{Triggering}$	Liquefaction Triggered?	Avg. s_u(liq) (kPa)
12	218.8	222.1	0.85	63.7	0.21	45.9	21.2	0.95	Yes	20.5
13	209.9	219.4	0.86	61.1	0.21	44.1	21.1	0.94	Yes	19.7
14	200.4	215.1	0.86	58.3	0.21	42.1	20.8	0.93	Yes	18.8
15	190.1	209.4	0.87	55.3	0.21	39.9	20.4	0.92	Yes	17.8
16	179.3	202.4	0.88	52.2	0.21	37.7	20.0	0.91	Yes	16.8
17	167.9	194.2	0.89	48.8	0.21	35.3	19.4	0.89	Yes	15.7
18	155.9	184.7	0.91	45.4	0.21	32.7	18.8	0.88	Yes	14.6
19	143.3	174.1	0.92	41.7	0.21	30.1	18.0	0.87	Yes	13.4
20	135.6	162.2	0.93	39.5	0.21	28.5	16.9	0.87	Yes	12.7
21	132.6	149.1	0.94	38.6	0.21	27.9	15.7	0.89	Yes	12.4
22	129.1	134.8	0.94	37.6	0.21	27.1	14.2	0.91	Yes	12.1

* Magnitude Scaling Factor, MSF taken as average of equation from Idriss (1995) and Andrus and Stokoe (1997)

Table 7. 12 List of nearby strong ground motion stations (from Miller and Roycroft 2004)

Location	Distance (km)	Surface condition	Site condition	Peak horizontal acceleration
Watsonville	8	Alluvium	4 story building	0.39g
San Juan Bautista	20	Stiff alluvium	Bridge	0.15g
Salinas	36	Alluvium	1 story building	0.12g
Monterey	47	Rock	1 story building	0.07g

Table 7. 13 Liquefaction triggering analysis results of Industrial Site levee for failure surface shown in Figure 7.24 (a) during 1989 Loma Prieta earthquake (a_{max} = 0.33g, MSF* = 1.27)

Slice No.	σ'_v (kPa)	σ_v (kPa)	r_d	Avg. s_u(yield) (kPa)	Average $\tau_{driving}/\sigma'_v$	$\tau_{driving}$ (kPa)	$\tau_{avg,seismic}$ (kPa)	$FS_{Triggering}$	Liquefaction Triggered?	Avg. s_u(liq) (kPa)
2	25.5	27.8	0.99	6.8	0.20	1.3	4.6	1.16	No	2.1
3	35.7	41.8	0.98	9.6	0.20	1.8	6.9	1.10	No	3.0
4	42.9	53.0	0.98	11.5	0.20	2.1	8.7	1.06	No	3.6
5	47.2	60.2	0.98	12.7	0.20	2.4	9.9	1.04	Marginal	3.9
6	49.3	62.4	0.97	13.2	0.20	2.5	10.2	1.04	Marginal	4.1
7	51.3	64.5	0.97	13.7	0.20	2.6	10.5	1.05	Marginal	4.3
8	53.3	66.7	0.97	14.3	0.20	2.7	10.9	1.05	No	4.4
9	55.4	68.8	0.97	14.8	0.20	2.8	11.2	1.06	No	4.6
10	57.4	71.0	0.97	15.4	0.20	2.9	11.6	1.07	No	4.8
11	59.5	73.1	0.97	15.9	0.20	3.0	11.9	1.07	No	5.0
12	61.5	75.3	0.97	16.5	0.20	3.1	12.3	1.08	No	5.1
13	63.5	77.4	0.97	17.0	0.20	3.2	12.6	1.08	No	5.3
14	65.6	79.6	0.97	17.6	0.20	3.3	12.9	1.08	No	5.5
15	67.6	81.7	0.97	18.1	0.20	3.4	13.3	1.09	No	5.6
16	69.7	83.9	0.97	18.7	0.20	3.5	13.6	1.09	No	5.8
17	71.7	86.0	0.96	19.2	0.20	3.6	13.9	1.10	No	6.0
18	73.7	88.2	0.96	19.8	0.20	3.7	14.3	1.10	No	6.1
19	75.8	90.3	0.96	20.3	0.20	3.8	14.6	1.10	No	6.3
20	80.3	94.9	0.96	21.5	0.20	4.0	15.3	1.11	No	6.7
21	87.2	102.0	0.96	23.4	0.20	4.4	16.4	1.13	No	7.3
22	94.2	109.1	0.95	25.2	0.20	4.7	17.5	1.14	No	7.8
23	101.1	116.1	0.95	27.1	0.20	5.1	18.6	1.15	No	8.4
24	108.1	123.2	0.95	29.0	0.20	5.4	19.6	1.16	No	9.0
25	115.0	130.2	0.95	30.8	0.20	5.8	20.7	1.17	No	9.6
26	122.0	137.3	0.94	32.7	0.20	6.1	21.7	1.17	No	10.2
27	128.9	144.3	0.94	34.5	0.20	6.4	22.8	1.18	No	10.7
28	129.4	139.5	0.94	34.7	0.20	6.5	22.1	1.21	No	10.8

* Magnitude Scaling Factor, MSF taken as average of equation from Idriss (1995) and Andrus and Stokoe (1997)

CHAPTER EIGHT:

SUMMARY AND CONCLUSIONS

Liquefaction is one of the most interesting and controversial phenomenon in geotechnical engineering. The devastating earthquakes of Prince William Sound, Alaska, USA and Niigata, Japan in 1964 are considered milestones in the study of liquefaction as the occurrence of liquefaction and its consequence were well-documented and publicized following these events. Because of their engineering importance, liquefaction problems have received a great deal of attention among the geotechnical community and many efforts have been made to clarify the basic mechanism and various aspects of the problems associated with liquefaction.

Liquefaction can occur in both level and sloping ground. This research focused on the liquefaction analysis of ground subjected to a static stress, i.e., slopes, embankments, or foundations of structures. Liquefaction analysis of sloping ground typically consists of three primary tasks: (1) a flow failure susceptibility analysis, (2) a triggering analysis, and (3) a post-triggering/flow failure stability analysis.

8.1 Liquefaction Susceptibility Analysis

- Soils that contract upon shearing are susceptible to flow liquefaction.
- Liquefaction susceptibility analysis evaluates whether a soil is dilative or contractive.
- There are general characteristics, e.g., grain size, depositional environment, liquefaction recurrence, and initial state that can be used to judge liquefaction susceptibility.
- Two methods can be used to evaluate directly whether a soil is contractive or dilative: the state parameter and the penetration resistance approaches.

- In the state parameter (ψ) approach, soils with $\psi > 0$ are considered contractive while $\psi < 0$ are considered as dilative. However, some researchers have suggested that soils with $\psi \geq -0.1$ may be contractive and susceptible to flow liquefaction.
- In the penetration resistance approach, a boundary between contractive and dilative behavior is defined in terms of penetration resistance and vertical effective stress. Soils with penetration resistance lower than this boundary are likely contractive, while soils with penetration resistance higher than this boundary are likely dilative.
- Among several available liquefaction susceptibility relationships based on penetration resistance, the Fear and Robertson (1995) boundary based on SPT blow count and the same boundary converted to CPT tip resistance by Olson (2001) reasonably envelope the available flow failure case histories, and can be used in practice.
- Sands with the same relative density and effective confining stress can exhibit significantly different penetration resistances based on their compressibility. Therefore, Olson (2009) proposed the use of a compressibility correction factor (C_λ) to adjust the location of the penetration resistance-based liquefaction resistance boundary to account for the effect of compressibility on penetration resistance. This study greatly expanded the data used to develop the compressibility correction factor and confirmed the compressibility correction factor proposed by Olson (2009).
- Using the compressibility correction factor, a suite of liquefaction susceptibility curves can be developed for any soil compressibility.
- The effect of fines on liquefaction susceptibility is ambiguous, and a database combined from catalogs collected by Olson (2001) and Jefferies and Been (2006) illustrate that there is no unique correlation between critical state line slope (related to compressibility) and fines content because of the role of relative density, grain shape, and mineralogy on soil compressibility (at a given fines content).
- While no unique correlation between FC and CSL slope (or compressibility) exist, flow failure case histories with FC greater than about 20% are reasonably enveloped by the Olson (2009) "moderate compressibility" ($\lambda_{10} \sim 0.06$) liquefaction susceptibility relation. Soils with FC less than about 20% are enveloped by the low compressibility (($\lambda_{10} \sim 0.03$) liquefaction susceptibility boundary relation.

8.2 Liquefaction Triggering Analysis

- There are three main procedures to estimate the yield shear strength and strength ratio of a contractive soil: (1) laboratory testing; (2) empirical correlations; and (3) finite element methods.
- Thirty-one reasonably-documented case histories were analyzed in this study and combined with the case histories studied by Olson (2001) to evaluate the yield shear strength ratio relationship proposed by Olson (2001).
- Only cases failed under static loading can reasonably estimate the yield shear strength of soil. Yield shear strength ratios from these cases ranged from 0.231 to 0.306 with an average value of 0.268. Furthermore, these cases reasonably agree with those presented by Olson (2001).
- The mobilized strength of slopes and embankments that failed under seismic loading do not necessarily corresponds to the yield strength at the time of triggering. Olson et al. (2006) suggested that the yield strength ratios are likely to be related to driving stress ratio and presented a family of curves to estimate yield strength ratio as a function of driving stress ratio. These curves were recently updated by Olson and Zitny (2012). The combined database of seismically-induced flow failures appear to support the Olson and Zitny (2012) yield strength ratio relationships.
- The yield shear strength depends on the mode of shear, with triaxial compression generally yielding the largest values, triaxial extension yielding the smallest values, and direct simple shear and ring shear yielding intermediate values. Case histories data from this study plot within the bounds of DSS-RS suggesting that it may be the prevailing mode of shear in the field.

8.3 Post-liquefaction Triggering Analysis

- A post-triggering/flow failure stability analysis evaluates whether a soil will undergo flow liquefaction after liquefaction is triggered. A prerequisite for liquefaction flow

failure to occur is that the static driving stress exceeds the soil resistance (including the liquefied shear strength). In this study, the static driving shear stress for the post-triggering/flow failure stability analysis was estimated by limit equilibrium analysis.

- Several procedures are available to estimate the liquefied shear strength or strength ratio for use in post-triggering stability analysis. These include laboratory-based approaches; empirical correlations based on the back-analysis of flow failure case histories, and combined laboratory-based and case history-based approaches.
- In the current study, the author analyzed 31 well-documented flow failure case histories and combined these cases with 33 cases analyzed by Olson (2001). These cases were used to evaluate liquefied strength ratio relationships proposed by Olson and Stark (2002), Mesri (2007), Idriss and Boulanger (2008) and Robertson (2010).
- The combined liquefied strength ratio database best agrees with the $s_u(liq)/\sigma'_{vo}$ relationship proposed by Olson and Stark (2002), although the current data suggest that the linear relationships may be slightly wider than that proposed by Olson and Stark (2002).
- The relationship among static driving shear stress ratio, liquefied strength ratio, and overburden stress-normalized penetration resistance proposed by Mesri (2007) was evaluating using the combined liquefied strength ratio database. While the relationship is conceptually feasible, the current database is insufficient to support the proposed relationship.
- The combined liquefied strength ratio database supports the conclusion from Olson and Mattson (2008) that liquefied shear strengths back-calculated from liquefaction flow failures are generally consistent with laboratory-measured strengths using direct simple shear and rotational shear tests.
- The combined liquefied strength ratio database generally supports the relationship between brittleness index and liquefied strength ratio proposed by Sadrekarimi and Olson (2011).

8.4 Predicting the Performance of Field Case Histories

- The relationships proposed by Olson and Stark (2002) and Olson and Zitny (2012) were employed to predict the behavior of several independent case histories: Yamanaka Dam (which was subjected to four earthquakes), Mackay Dam (one earthquake) and and industrial site levee (one earthquake). The observed performance of these geostructures ranged from major flow slide to no displacement.
- Yamanaka dam was subjected to four separate earthquakes (1968, 1978, 1983 and 1994) and each earthquake caused different severities of damage. After the 1978 earthquake, a sheetpile wall was installed along the upstream slope in an attempt to mitigate future damage. Despite this effort, minor to moderate damage still occurred during the 1983 and 1994 earthquakes. Each earthquake, despite accelerations less than 0.06g, triggered liquefaction (at least marginally) in a portion of the loose to very loose sandy embankment fill and channel fill. FS_{FLOW} for shallow and deep circular failure surfaces ranged from about 0.6 when the damage was severe to about 1.0 – 1.1 when damage was minor. These FS are consistent with the observed damage severity.
- Mackay dam was subjected to the 1983 Borah Peak earthquake and experienced two longitudinal cracks on the crest. No flow failure was observed in this case. The proposed procedure predicted that liquefaction would be triggered in the loose embankment fill for both shallow and deep critical failure surfaces. However, because a substantial portion of the embankment was above the phreatic surface and drainage was likely to occur near the phreatic surface (because the fill was chiefly sandy gravel), FS_{Flow} ranged from about 0.68 to 0.90. These FS are consistent with the minor damage observed after the earthquake.
- An industrial site levee that was not damaged by the 1989 Loma Prieta earthquake was documented by Miller and Roycroft (2004). Because of the levee's flatter slope and long sliding surface, the driving stress ratio was less than the liquefied shear strength ratio, indicating that flow failure is not possible. This result is consistent with the lack of damage observed at the levee. However, for illustration, the author continued the analysis and found that while liquefaction was likely to occur below the

levee, a FS_{Flow} = 1.6 suggested that no flow failure should occur as FS_{Flow} >1.1 (consistent with the observed performance).

- Overall, the relationships proposed in this study reasonably predicted the performance of these geostructures, and the analysis procedure was sufficiently sensitive to differentiate the severity of damage suffered in each case.

CHAPTER NINE:

FUTURE RESEARCH

In this study, the author collected and analyzed reasonably well-documented flow failure case histories to investigate the liquefaction susceptibility, liquefaction triggering and post-triggering stability analyses proposed by Olson and his colleagues, as well some aspects of methods proposed by Mesri (2007), Idriss and Boulanger (2008), and others. The number of available field case histories to evaluate liquefaction flow failures was nearly doubled in this study. The effect of fines content and compressibility was investigated on liquefaction susceptibility. In addition, the effect of mode of shear on the yield and liquefied shear strength ratios, and the relationship between brittleness index and state parameter based on laboratory tests results were compared with field case histories. Furthermore, liquefaction susceptibility, liquefaction triggering and post-triggering stability analyses were conducted for select case histories to evaluate the ability of the procedures to predict observed field performance.

The following discussion provides some ideas for future research to further enhance our understanding of liquefaction analysis for sloping ground.

9.1 Increasing Number of Case Histories

Although 31 new case histories were added in this study to the database of 33 case histories analyzed by Olson (2001), more and *better documented* case histories would greatly improve our understanding of several key aspects of liquefaction analysis.

For each case history in the combined database, uncertainties related to penetration resistance, yield or mobilized strength ratio, and liquefied strength ratio were described qualitatively using a new parameter, relative confidence (rC). Occasionally, the

author evaluated these uncertainties quantitatively. Although increasing number of case histories will mitigate these uncertainties on the resulting predictive relationships, the overall uncertainties in the predictive relationships would be better understood if uncertainty specific to each case history were thoroughly quantified.

Increasing the number of well-documented static loading-induced and seismically-induced liquefaction flow failures would likely improve the relationships for liquefaction susceptibility, yield strength ratio, and liquefied strength ratio. Further, an increased number of cases will better define the effect (if any) of driving stress on liquefied shear strength.

9.2 Estimation of Seismic Stress Ratio

To estimate the seismic stress ratio, the current study used the equation suggested by Seed and Idriss (1971). This equation is an approximation of actual cyclic shear stress ratio. Further, the Seed and Idriss (1971) equation was developed for level ground. To obtain actual seismic shear stress along the sliding surfaces of any particular slope, several additional studies would be valuable. These additional studies include: (1) performing site-specific one- and two-dimensional ground response analyses using available tools such as FLAC, Quake/W, OpenSEES, and PLAXIS. These analyses would also highlight the potential uncertainties in the parameters r_d and MSF that were originally developed for level ground.

9.3 Compressibility Correction Factor

The current study illustrates the importance of compressibility sandy soils, particularly with respect to liquefaction susceptibility. More calibration chamber tests, element tests, and field tests are needed to better define and validate this relationship.

9.4 Estimation of State Parameter

For some of the case histories data studied here, Jefferies and Been (2006) suggested values of state parameter (ψ) based on available penetration tests, soil descriptions, and other data. However, these values are not definitive and the conclusions described here based on state parameter are not discussed. More detailed studies related to state parameter at flow failure sites would greatly benefit from more detailed studies at field sites.

9.5 Estimation of Flow Failure Deformation

As illustrated in Chapter 7, there appears to be a recognizable trend between post-triggering factor of safety against flow failure and damage or displacement. Future research would be valuable to better quantify this potential relationship.

APPENDIX A:

DESCRIPTION OF LIQUEFACTION FLOW FAILURE CASE HISTORIES AND ANALYSES

A.1 Barahona Tailings Dam, Central Chile, Chile

A.1.1 Introduction

On December 1, 1928, central Chile was shaken by a M_w 7.6 earthquake, termed the "Talca earthquake." The earthquake occurred on the subduction zone formed between the Nazca and South American plates. This subduction zone is seismically very active, with the 2010 Maule earthquake being the most recent major earthquake on this zone. The Talca earthquake caused casualties and property loss in the towns of Constitución, Talca, and Curicó, which are situated within 70 km from the epicenter, with modified Mercalli intensities in this region ranging from VII to X (Troncoso et al. 1993). About 225 people were killed during the earthquake and numerous buildings, houses, roads, railroads, and bridges were damaged (USGS 2010).

Barahona tailings dam was among the structures that collapsed during the Talca earthquake. Situated about 180 km northeast of the epicenter, the dam was started in 1920 using the upstream construction method and was 65 m high with a 1885 m crest length at the time of earthquake (Troncoso et al. 1993). Figure A.1 shows the location of Barahona Tailings Dam along with the epicenter location. Based on eyewitness reports, the dam catastrophically failed a few minutes after earthquake shaking ceased, unleashing tailings amounting to 4 millions tons (Troncoso et al. 1993). It is believed that the failure occurred as a result of liquefaction of the slimes impounded in an unconsolidated, saturated state.

A.1.2 Site Geology and Soil Conditions

The original design of Barahona Dam utilized a perimeter dyke constructed with clayey gravel from a nearby borrow site. It was decided that the dykes would be constructed in stages with 5 berms, each 15 m wide as necessary. The slope of the retaining dykes was designed as 1.5H:1V and 2H:1V. Construction using this design began in the spring of 1917. Construction material was brought to the site by trains, transferred using horse carts, and compacted by using steam rollers. However, this construction procedure was abandoned when the dam was only 7 m high because of the high costs and difficulty in construction. Troncoso et al. (1993) believed that the construction difficulties may have resulted from the presence of bentonitic clays (derived from laharic deposits) in the fill soils. Soils containing bentonitic clays are widely-known to be very difficult to compact.

A new design was proposed that required a starter dyke to be constructed downstream of the original starter dike so that an upstream method of construction could be adopted using the available coarse tailings. The coarse tailings were to consist of fine sand with a maximum grain size of 0.6 mm and 20% fines. The coarse fraction was separated using a cone-shaped flume separator installed along the crest of the dykes. This was done to obtain a similar grain size distribution along the crest. However, the separation process was modified continuously during dam filling and the fines content of the coarse fill was decreased from 26% fines in 1921 to 15% fines in 1928.

The tailings dam operation was started in March 1921 and deposition of fine tailings in the pond were initiated. Cone penetration tests conducted in impounded slimes and retaining dykes by Troncoso et al. (1993) in November 1991 showed that the tip resistances and sleeve frictions were larger below the failure surface than above it as shown in Figure A.2. A significant increase in blowcounts is observed between the tests conducted in 1981 and 1991 at same depth, illustrating the effect of consolidation and aging in the tailings, as shown in Figure A.2. This suggests that the soil that did not fail during the 1928 earthquake became stronger due to consolidation and aging effects.

A.1.3 Estimation of Earthquake Ground Motions

Details related to the earthquake are as follows (Beck et al. 1998):

Date and Time: 1928 12 01; 04: 06:10 (Local Time)
Location: 35.0ºS, 72.0ºW
Magnitude: 7.6
Region: Central Chile, Chile
Fault Mechanism: Thrust Fault in subduction zone

No strong motion recording stations were available in 1928; therefore, no measured strong motion records are available for the earthquake. Troncoso et al. (1993) suggested PGA from 0.122g to 0.193g, apparently based on epicentral distance of about 180 km, but did not report which ground motion prediction equation was used.

Beck et al. (1998) give some seismotectonic information about the strike, dip and slip angles, fault type, depth to rupture, and duration of motion by analyzing the waveforms of other historical earthquakes. The authors used this information to estimate PGAs using the NGA relationships proposed by Abrahamson and Silva (2008), Boore and Atkins (2008), Campbell and Bozorgnia (2008), and Chiou and Youngs (2008). The fault rupture zone suggested by Beck et al. (1998) is reproduced in Figure A.1. The NGA relations yielded a range of PGA from 0.034g to 0.185g. Details of the parameters used to estimate PGA from attenuation relationships is given in Table A.1.

A.1.4 Description of the Failure

Figure A.3 shows the pre- and post-failure geometries of Barahona Dam. At the time of the failure, the dam was 65 m high, the crest was 1885 m long and 12 m wide, the

slime beach was 400 m wide, and the crest of the dam was 17 m above the slimes. The crest of Barahona tailings dam had a 2% slope descending from east to west to facilitate flow of tailings that were used to construct retaining dykes using the flume separators (Troncoso et al. 1993). Troncoso et al. (1993) reported that during the three months preceding the failure, tailings deposition was very active, with a deposition rate of 17,000 tons/day and a total of 27 million tons deposited.

As a result of 1928 Talca earthquake, Barahona tailings dam collapsed catastrophically, resulting in a flow failure that killed 54 people downstream and destroyed numerous downstream settlements and installations. Eyewitnesses reported that a few minutes after the earthquake a portion of the dam adjacent to the right abutment failed over a length of about 400 m that caused destructive flow of tailings materials. It was believed that impounded, saturated, unconsolidated slimes were liquefied as a result of earthquake (Ishihara 1980, Troncoso et al. 1993) and caused the failure.

Troncoso et al. (1993) included eyewitness statement of G.W. Soady who was the engineer-in-charge of Barahona dam and observed the failure from his house, located about 300 m away from the dam. As reported by Troncoso et al. (1993), "…the dam stood during the occurrence of the earthquake and failed suddenly 2 or 3 minutes after the end of ground motion, estimated because the illumination system first remained working and then it went off in accordance with the stated timing. The telephone line, which crossed the Barahona valley, about 200 to 300 m downstream from the dam, was cut almost immediately indicating that failure was violent."

As soon as the dam failed, 4 million tons of tailings flowed violently down the deep and narrow Barahona creek, which near the dam has a 15% gradient. The flowing tailings destroyed a railway bridge and a significant length of the railway line, several highway bridges, the Barahona station, and other buildings at Coya camp, killing 54 people. Figure A.4 shows the dam after failure and Figure A.5 show the location of failure and other damaged structures. The portion of the tailings that remained in the impoundment formed flat, step-like terraces with steep nearly vertical scarps. Sand volcanoes formed in the horizontal portions of the scarps, and springs of about 0.6 to 1 m diameter in the vertical portions of the scarps were observed after failure, illustrating that the tailings liquefied during the earthquake.

Troncoso et al. (1993) attributed the failure to the decision to change dyke construction from clayey gravel to an upstream construction using coarse tailings. The intrusion of slimes between the coarser dykes played an important role in reducing the overall stability of the dam during undrained loading, allowing excess porewater pressures to be generated but slowing dissipation. As stated above, the last three months before the failure, tailings were placed at very high rates and the slimes may not have been consolidated at the time of earthquake. Seismic loading triggered liquefaction of the slimes in the impoundment, causing the dam to fail catastrophically.

Neither the phreatic surface nor the decant pond is shown in Figure A.3. Penetration-induced porewater pressures were measured in 1991 and suggested that the

water level was about 17 to 22 m below the tailings surface, but these tests do not represent the water level at the time of the earthquake. Based on the high rate of tailings placement, the author believes that the phreatic surface at the time of earthquake likely was near the surface of the tailings.

A.1.5 Representative Penetration Resistance

A field investigation conducted in November 1991 by Troncoso et al. (1993) included 5 CPTu soundings (PC91-1 to PC91-5), three of which were conducted through the perimeter dykes (PC91-1, PC91-4, and PC91-5) while the other two were conducted in the slimes impoundment (PC91-2 and PC91-3). A rotary-wash borehole was also drilled with SPT measurement for soil sampling and classification. These penetration tests were conducted close to penetration tests performed in 1981. Figure A.6 shows the locations of CPTu soundings and SPT borings, while Figure A.2(a) and (b) shows the results of the CPTu soundings, and Figure A.2(c) shows the results of the SPTs conducted in 1981 and 1991.

Analyzing the CPTu results, Troncoso et al. (1993) suggested that the tailings were highly stratified, typical of hydraulic fill tailings. These layers formed as a result of: (1) the heterogeneity of hydraulic fill; (2) the presence of pre- and post-earthquake deposited tailings: and (3) interbedding of slimes and sands due to upstream construction.

Troncoso et al. (1993) indicated that the tip resistance and sleeve friction show higher values below the failure surface than above it, which means that the soils that did not fail during the 1928 earthquake exhibited greater resistance then the younger soils deposited over them. Focusing further on the zone below failure surface, Troncoso et al. (1993) estimated a relatively small range of f_s values from 0.3 – 0.5 kg/cm^2 (29.4 – 49 kPa) for soils in the retaining dyke compared to a larger range of f_s values from 0.16 – 0.81 kg/cm^2 (15.7 – 79.4 kPa) for soils in impoundment. An average f_s value for all the soils below failure surface was estimated as 0.32 kg/cm^2 (31.4 kPa). For CPT tests in impoundment where the water table was encountered, Troncoso et al. (1993) estimated a sharp increase of up to 4.56 kg/cm^2 (447 kPa) in u_d values between the depths of 22.5 and 24.1 m with corresponding decrease in q_c to a value of 9.85 kg/cm^2 (966 kPa), and f_s to a value of 0.21 kg/cm^2 (20.6 kPa).

The SPT (S91-1) results are shown in Figure A.2(c), in which a range of blowcounts from 10 to 20 blows/ft was measured in the upper 16 m, while a range from 22 to 50 blows/ft was measured between depths of 16 to 31 m. This SPT was performed 2 m away from PC91-1. The test was performed at the same location where S81-1 was conducted in 1981 [see Figure A.2(c)]. It can be seen that there is a significant increase in blowcounts after ten years, likely because of aging of the tailings. SPTs conducted in 1981 suggest a weak zone below 35 m which represents the existence of slimes below a sand dyke (Troncoso et al. 1993).

The author suggests that there is a uniform increase in tip resistance with depth, with q_c values of about 35 to 70 kg/cm^2 (3.4 to 6.8 MPa) and sleeve friction values of

about 0.25 to 0.5 kg/cm^2 (24.5 to 49 kPa) for the tests conducted through the retaining dykes. Penetration test PC91-3 performed in impoundment showed a decrease in both tip resistance and sleeve friction and a sharp increase in dynamic porewater pressure after it encountered the water table. These observations suggest that the slimes are contractive.

Because of the time between the failure and the conduct of the penetration tests (i.e., 63 years), aging of the tailings must be considered. Further, the author believes that the phreatic surface at the time of earthquake was much higher than the phreatic surface inferred from the dynamic pore water pressure measured in 1991. Because of the difference in phreatic level, the penetration resistances measured in soundings PC91-1, PC91-4, and PC91-5 are not likely representative of conditions in 1928. Using soundings PC91-2 and PC91-3, the author observed a range of penetration resistance from about 0.6 to 11 MPa, with a best estimate of 3 to 4 MPa. Considering SPT blow counts measured in 1981 (with smaller aging effects) and assuming an energy ratio of 45% (considering typical SPT equipment available in Chile in 1981), the author suggests a range of $(N_1)_{60}$ from 5 to 16, with a best estimate of about 9 to 11.

A.1.6 Yield Shear Strength and Strength Ratio

The mechanism, that likely triggered flow failure of the Barahona tailings dam, was seismic liquefaction of the saturated unconsolidated slimes (Ishihara et al. 1980; Troncoso et al. 1993). As explained in Chapter 2, the shear strength and strength ratios mobilized at the instant of failure in cases where liquefaction is triggered by seismic loading do not necessarily represent yield shear strength and strength ratios.

The pre-failure geometry of the Barahona tailings dam is reproduced in Figure A.7. A slope stability search was conducted to locate an initial failure surface that is consistent with the pre- and post-failure geometry and using the proposed failure surface by Troncoso et al. (1993). All saturated slimes were assumed to liquefy and a single value of shear strength was assigned to the liquefied soil. Sand dykes were considered as non-liquefied and were assigned a drained friction angle of 30º to 38º. The back-calculated upper bound, lower bound and mean values of mobilized shear strength in the zone of liquefaction are 120, 103, and 115 kPa respectively.

A second analysis was conducted to estimate the strength ratio mobilized at the triggering of liquefaction. Identical assumptions regarding the failure surface and shear strength of the non-liquefied soil were used for this analysis. The upper bound, lower bound and mean values of mobilized shear strength ratio in the zone of liquefaction are 0.345, 0.194 and 0.26 respectively, depending on the shear strength of the unsaturated fill and the location of the failure surface. The weighted average pre-failure vertical stress in the liquefied segment was determined as 348 to 460 kPa.

A.1.7 Liquefied Shear Strength and Strength Ratio

Because the liquefied slimes flowed down the valley during the failure, no post-failure geometry was available to conduct a post-failure analysis. Therefore liquefied

shear strength and strength ratios could not be determined for this case. Troncoso et al. (1993) computed liquefied shear strength by analyzing the wedge bounded by the slope of the failure surface shown in Figure A.3, as 0.3 kg/cm^2 (29.4 kPa). The liquefied shear strength calculated by Troncoso et al. (1993) is reported for information only and was not adopted in this study.

A.1.8 Liquefied Shear Strength and Strength Ratio Considering Kinetics

Similarly, no kinetics analysis was performed for this case history.

A.1.9 Sources of Uncertainties

The following sources of uncertainty were involved in estimating the yield shear strength and strength ratio: (1) the initial zone of liquefaction; (2) the position of the initial failure surface; (3) the shear strength of the non-liquefied soils; and (4) the location of the phreatic surface. All of the slimes below the phreatic surface were assumed to be saturated and to liquefy. The position of the initial failure surface was not known; thus the author performed a search using the slope stability software to evaluate the critical surface. The non-liquefied sandy dykes were assigned $\phi' = 30^o$ to 38^o based on the assumption that sand dykes were compacted. The location of phreatic surface at the time of earthquake was not known; however, as discussed above, the author anticipates that it would be close to the surface.

The following sources of uncertainty were involved in determining the "representative" values of penetration resistance: (1) SPT and CPT were conducted about 53 to 63 years after failure; (2) SPT and CPT were conducted on the repaired section; and (3) hammer type was not known for SPT. The SPT and CPT data conducted at Barahona tailings dam were performed more than 50 years after the failure. This time lag has caused significant aging and consolidation. The tests were conducted on repaired section and did not represent original section of the dam present at the time of failure. No information about the SPT hammer system was given; therefore, the author estimated the energy ratio based on practices prevailing in Chile in 1981.

A.2 Kamenari Landslide, Montenegro (Yugoslavia)

A.2.1 Introduction

On April 15, 1979 at about 7:20am, a powerful earthquake struck the coast of present-day Montenegro, a part of the former Yugoslavia. The devastating effects were widespread, reaching from Croatia in the north to Albania in the south (Figure A.8). Tremors were felt in several countries of eastern and central Europe including Germany, Greece, and Italy. Official sources reported 96 fatalities in Yugoslavia and 35 fatalities in Albania. More than 1,000 people were injured and 80,000 others (1/7 of the population of Montenegro at the time of the earthquake) were left homeless (Anicic et al. 1980). Property loss was also widespread. For example, the hotel industry in the region was badly affected. About 5,500 out of 20,000 hotels were completely destroyed, another

5,500 were damaged but repairable in a short time, and 9,000 were slightly damaged. Hospitals, schools, and residential units were also severely damaged. Out of 54 schools, 50 were heavily damaged. About 40,000 apartment units were either damaged or destroyed, and historical buildings and monuments suffered severe damage (Anicic et al. 1980). In addition, substantial damage occurred to transportation facilities including roads, highways, bridges, ports and harbors (Anicic et al. 1980).

Reports differ regarding the epicentral location of this seismic event. The U.S. National Earthquake Information Service (NEIS) suggested an epicentral location at 42.14º N and 19.06º E while the European-Mediterranean Seismological Centre at Strasbourg (CSEM) positioned the epicenter at 42.03º N and 19.04º E, about 12 km away from the NEIS epicenter (see Figure A.9). The surface magnitude (Ms) of this earthquake was assigned as 6.6 while the moment magnitude (Mw) was determined as 7.1 (Anicic et al. 1980, Boore et al. 1981, Benetatos and Kiratzi 2006).

Along with structural damage, ground failures due to liquefaction, landslides, and rockfalls in mountainous regions were also widespread. Figure A.10 shows the area that experienced severe ground failure from liquefaction and landslides, which extended over a roughly 15 km wide zone extending from Ulcinj in the south to Herceg-Novi in the north. The modified Mercalli intensity (MMI) in this region was on the order of VIII to IX (see Figure A.8). Peak ground accelerations in this region were approximately 0.22g (Ishihara 2005). Ground failures observed in the Herceg-Novi area were chiefly associated with liquefaction of alluvial sand deposits along the coastline. In Kamenari, situated about 12 km east of Herceg-Novi, a segment of coastal road slumped into the bay, likely because of liquefaction of the foundation sand deposit (Ishihara 2005). Figure A.11, Figure A.12, and Figure A.13 show photos of the coastal road failure and landslide at Kamenari.

A.2.2 Site Geology and Soil Conditions

The general geology in the northern region of Heceg Novi, Zelenica, Bijela, Kamenari, Kotor and Tivat consists of colluvial talus and fluvial deposits underlain by claystone and limestone (Ishihara 2005). The colluvial talus deposits vary from gravelly sediments near the foot of the limestone cliffs to sandy sediments near the coast. The pattern of the colluvial deposits close to the beach is disrupted by the actions of small rivers and ocean currents and waves. Figure A.14 shows a schematic geological section showing the fluvial and talus deposits present in the area and Figure A.15 shows soil profiles obtained from two boreholes drilled along the coast of the bay. These profiles illustrate that loose sand deposits are present to depths up to 18 m (based on the SPT blow counts that will be discussed in Section A.2.5). It may also be recognized that lower portion of the soil profile consists of fine grained materials that may have been eroded from claystone outcrops on the land and deposited under the sea. The bay area consists of reddish-colored sand that was probably eroded from limestone.

Grain size distributions were not reported in the literature; however, Ishihara (2005) reported that the upper sands were uniform with D_{50} = 0.15 to 0.45 mm.

A.2.3 Estimation of Ground Motions

Details related to the earthquake are discussed below (Anicic et al. 1980, Boore et al. 1981, Benetatos and Kiratzi 2006), but there is conflicting information regarding the epicenter of this event. The U.S. National Earthquake Information Service (NEIS) suggested an epicenter at 42.14º N and 19.06º E, while the European-Mediterranean Seismological Centre at Strasbourg (CSEM) positioned the epicenter at 42.03º N and 19.04º E, about 12 km away from the NEIS epicenter (see Figure A.9). The surface magnitude (Ms) of this earthquake was assigned as 6.6 while the moment magnitude (Mw) was determined as 7.1 (Anicic et al. 1980, Boore et al. 1981, Benetatos and Kiratzi 2006).

Date and Time: 1979 04 15; 07: 20 (Local Time)
Location: 42.14ºN, 19.06ºE or 42.03ºN, 19.04ºE
Magnitude: 7.1
Region: Southeastern part of Adriatic Sea, coastline of Montenegro, southern Croatia and northern Albania
Fault Mechanism: Thrust Fault

Several investigators (Anicic et al. 1980; Boore et al. 1980; Baker et al. 1997; Benetatos and Kiratzi 2006) suggested that the fault mechanism was a low angle thrust to reverse fault motion combined with considerable strike slip motions. The fault movement was in the NW – SE direction, parallel to the coastline with the fault dipping east (Karakaisis et al. 1985). Figure A.8 reproduces the rupture zone from the 1979 Montenegro earthquake as suggested by Viti et al. (2003), and Benetatos and Kiratzi (2006).

The 1979 Montenegro earthquake was recorded by 25 strong motions stations that were part of the seismic network established and maintained by the Institute of Earthquake Engineering and Engineering Seismology (IZIIS) in Skopje (Anicic et al. 1980). Figure A.9 shows peak ground accelerations as high as 0.49g were recorded at these stations (Petrovski et al. 1980, Anicic et al. 1980). Peak ground accelerations were high along the coastline, but decrease substantially going inland.

Unfortunately there were no recorded ground motions available at the Kamenari site. The closest ground motion recording station was at Herceg-Novi, about 12 km away from the Kamenari site. This station recorded PGA values of 0.23g in the NS direction and 0.26g in the EW direction. Viti et al. (2003), and Benetatos and Kiratzi (2006) give some information about the strike, dip and slip angles, fault type, rupture depth, and duration of motion. The author used this information to estimate PGA values using the NGA relationships proposed by Abrahamson and Silva (2008), Boore and Atkins (2008), Campbell and Bozorgnia (2008), and Chiou and Youngs (2008). The NGAs yielded a

PGA range from 0.13g to 0.32g. Details of the parameters used to estimate PGA from attenuation relationships are given in Table A.1.

A.2.4 Description of Failure

The area affected due to earthquake in Montenegro is divided into three zones based on the subsurface soil conditions and abundance (or scarcity) of observed liquefaction-induced ground failures: the central, southern, and northern zones. The central zone includes the cities of Budva, Petrovac, and Bar, where the mountains emerge vertically from the sea. Soft soil deposits were absent in this area and the ground surface consists of claystone and limestone outcrops. In this zone liquefaction-induced ground failures were limited to manmade fills. The southern zone includes the region near Ulcinj. Extensive liquefaction-induced ground failures and mountain slope failures were observed in this zone as well as over the delta region of the Bojana River on the Yugoslavia-Albania border.

The northern zone includes the cities of Herceg-Novi, Zelenika, Djenovici, Bijela, Kamenari and Kotor. Figure A.16 shows the sites that experienced land subsidence, landslides, lateral spreading, building settlement, and sand boil formation caused by liquefaction in fine-grained alluvial sand layers that are present at many locations along the banks. A coastal road near Kamenari failed and slid into the bay, likely due to liquefaction of loose saturated alluvial sandy soil present 3 m below the surface. Records show that prior to failure a peninsula extended several tens of meters into the bay (Anicic et al. 1980). Figure A.17 reproduces the sliding surface and a post-failure geometry suggested by Ishihara (2005). The author believes that the failure was retrogressive based on the small horizontal post-failure "segments" along the surface (see Figure A.17), which may be the crests of individual grabens, horsts, and wedges associated with translational movement. The failed soil mass displaced over 18 to 20 m as measured from the pre-failure to post-failure toe of the slide mass. The author suspects that the first slice slid down and came to rest along a pre-existing slope of about 18º while the other slices failed retrogressively. The slope of headscarp, after the slide came to rest, was about 40º.

A.2.5 Representative Penetration Resistance

Unfortunately no penetration tests were conducted at the Kamenari landslide site either before or after the failure. Ishihara (2005) presented soil profile data and SPT N-values obtained from borings at two locations along the coast of the bay (see Figure A.15). These locations were Bijela and Baosic that are about 2 and 4 km away from the Kamenari landslide site, respectively.

Ishihara (2005) indicated that generally the geological setting in the region of Herceg-Novi, Zelenika, Bijela, Kamenari, Kotor and Tivat can be specified as colluvial talus and fluvial deposits underlain by claystone and limestone. However this setting can be disrupted by the size of individual streams and small rivers feeding that particular area, as well as by the wave action of seawater. The author could not find any active

major streams or rivers in the Kamenari, Bijela, and Baosic areas that would suggest significant differences between the profiles (as a result of very recent deposition) at these three locations. Furthermore, the soil profiles shown in Figure A.15 illustrate that the profiles are similar, although the layer thicknesses are different (likely as a result of differences in the size of the individual streams or rivers that deposited those sediments). Furthermore, the penetration resistances in individual layers are similar across a wide geographic area. The penetration resistances show that upper sand layer in both profiles yielded SPT N-values on the order of 5 to 10 blows/ft, and values generally less than 5 blows/ft in the lower silty sand layers.

In the absence of penetration resistance data specific to the Kamenari landslide, the author elected to choose "representative" values of SPT blow count from those measured in similar deposits along the coast at the Bijela and Baosic sites. The SPT N-values ranged from 2 to 10 blows/ft within the sand and silty sand layers. This range was assigned to the 4 m thick sand layer that was believed to be liquefied at Kamenari site during 1979 Montenegro seismic event, and $(N_1)_{60}$ values were calculated. In the absence of measured SPT hammer energy, the author assumed an energy ratio, ER, of 60%. Based on these assumptions, as well as assuming a saturated unit weight of 18.5 kPa, the author obtained a representative $(N_1)_{60} = 7$, with a range from 2 to 13 blows/ft.

As noted previously, Ishihara (2005) reported that the sand was uniform with D_{50} = 0.15 to 0.45mm. Using this range of D_{50} values yielded q_c/N_{60} ratios from 0.38 to 0.53 based on the average of the correlations from Robertson and Campanella (1985), Seed and de Alba (1986), Andrus and Youd (1989), Kulhawy and Mayne (1990), and Stark and Olson (1995). This q_c/N_{60} range, along with the $(N_1)_{60}$ range reported above, yielded q_{c1} values from 0.8 MPa to 6.9 MPa, with an average value of 3.8 MPa.

A.2.6 Yield Shear Strength and Strength Ratio

The pre-failure geometry of Kamenari landslide along with possible retrogressive failure surfaces are reproduced in Figure A.18. As described above, the failure likely resulted from liquefaction of alluvial sand layer triggered by the 1979 Montenegro earthquake (Anicic et al. 1980; Ishihara 2005). Therefore the slope stability search was constrained to the toe area passing through alluvial sand layer. In the analyses performed in this study, the author assumed that all of the sandy soil below the water table was saturated and liquefiable. The author used a range of friction angles from $\phi' = 30^o$ to 34^o with c' = 0 for soil initially above the phreatic surface. The back-calculated yield shear strengths in the liquefied zone ranged from 6.5 kPa to 10.7 kPa depending on the failure surface locations and to a small degree on shear strength of non-liquefied soil. The best estimate of mobilized shear resistance in the liquefied zone was 7.5 kPa.

A second analysis was conducted to estimate the mobilized shear stress ratio at the triggering of liquefaction. The same trial failure surfaces described above were analyzed here. A shear stress ratio was assigned to the liquefied zone, and this value was varied until a FS of unity was achieved. A best estimate of yield shear stress ratio was

estimated as 0.26, with a possible range of 0.13 to 0.31. The weighted average pre-failure vertical effective stress was determined as 24.2 kPa to 51 kPa.

A.2.7 Liquefied Shear Strength and Strength Ratio

The post-failure geometry of Kamenari landslide is reproduced in Figure A.19. Trial failure surfaces were estimated from the post-failure morphology of the sliding mass, and a slope stability analysis was conducted, as shown in Figure A.19. A single arbitrary value of liquefied shear strength was assigned to liquefied zone. The liquefied shear strength was varied until a factor of safety equal to unity was obtained. The resulting back-calculated liquefied shear strength was 3.6 kPa, with a range of 2.7 kPa to 4.45 kPa.

Using the same post-failure trial sliding surfaces shown in Figure A.19, a limit equilibrium back-analysis of the liquefied strength ratio was conducted. The length of the final failure surface was divided into 11 segments. Segment 1 corresponded to the non-liquefied sand above the phreatic surface. The remaining segments (from 2 to 11) were within the liquefied zone. The post-failure segments were assigned their pre-failure geometry positions, as shown in Figure A.19, to calculate the pre-failure vertical effective stress for each slice. An arbitrary value of liquefied shear strength ratio was assigned to the liquefied zone, which in turn yielded different liquefied shear strength for each segment, and an analysis was run to calculate the factor of safety. The liquefied shear strength ratio was then varied until a factor of safety equal to unity was obtained. Using the same assumptions made in the liquefied shear strength analysis, the liquefied strength ratio was estimated as 0.056, with a range of 0.04 to 0.07. The weighted average of vertical effective stress was estimated as 63.5 kPa.

A.2.8 Liquefied Shear Strength and Strength Ratio Considering Kinetics

A kinetic analysis was not conducted for this case because of the retrogressive mechanism of failure. This failure mechanism made it very difficult to unequivocally clarify similar portions of the pre- and post-failure sliding mass.

A.2.9 Sources of Uncertainty

The following sources of uncertainty were involved in estimating the yield shear strength and strength ratio: (1) the initial zone of liquefaction; (2) the position of the initial failure surface; and (3) the shear strength of the non-liquefied soils. It was assumed that all of the alluvial sand below the phreatic surface liquefied. The position of the initial failure surface was chosen on the basis of sliding surface suggested by Ishihara (2005). The unsaturated fill was assigned $\phi' = 30^o - 34^o$.

The following sources of uncertainty were involved in estimating the liquefied shear strength and strength ratio: (1) the limits of the zone of liquefaction; (2) shape of

final sliding surface and; (3) pre-failure slice positions. As discussed above, all fill below the phreatic surface was assumed to liquefy. There was a pre-existing slope of about 18º on which the failed mass deposited after failure. The final sliding surface therefore included this slope. The positions of post-failure geometry segments are arranged in pre-failure geometry by visualizing how the first slice would have been slid and settled on the pre-existing slope and then other slices followed. Segments were arranged on the final retrogressed sliding surface so that it can accommodate all post-failure segments.

The following sources of uncertainty were involved in determining the "representative" values of penetration resistance: (1) no SPT or CPT data were available, requiring the use of penetration resistance from other local coastal sites; (3) the energy ratio for the SPT hammer system was not measured at any site; and (4) estimating CPT from SPT using q_c/N_{60}. No data for SPT or CPT was available and data from other sites was used to estimate penetration resistance at the site. Blow counts from other sites were used on the site at different depths and overburden calculation was done accordingly. The SPT hammer system details were not reported in the literature, so the author estimated an energy ratio of 60% for these tests. No CPT data were available in the region; therefore, the author converted from SPT to CPT using the average ratio of q_c/N_{60} calculated from the correlations given by Robertson and Campanella (1985), Seed and de Alba (1986), Andrus and Youd (1989), Kulhawy and Mayne (1990), and Stark and Olson (1995).

A.3 Spitak Embankment, Northwestern Armenia, Armenia

A.3.1 Introduction

On December 7, 1988, a surface-wave magnitude Ms ≈ 6.8 earthquake shook northwestern Armenia leaving more than 40,000 dead, over half a million homeless, and causing massive destruction. Historical seismicity records, dating as early as 139 A.D., show high levels of seismic activity in this region. This seismically-active region underlies three main towns that were severely damaged by the 1988 earthquake: Spitak (population of 30,000), Leninakan (population of 300,000) and Kirovakan (population of 200,000). Early reports on geotechnical failures (O'Rourke 1989) focused on the numerous landslides and rockfalls that were observed throughout the affected region, and on the failures of gravity retaining walls in and around Spitak. Being very close to the fault, about 1 to 2 km, 90% of the two-story or taller buildings of Spitak either collapsed or were severely damaged. In Leninakan, about 25 km from the fault, approximately 54% of buildings were damaged. Surprisingly, building performance in Kirovakan, which was only 10 km from the fault, was much better. Here, only 26% of buildings were moderately damaged. Yegian et al. (1994e) documented several cases of liquefaction-induced ground and slope failures, in particular the failure of a roadway embankment near the town of Spitak. The location of this and other failures is shown in Figure A.20(a) and Figure A.20(b) is a photo of the embankment failure near Spitak. Other liquefaction-induced slope failures documented by Yegian et al. (1994e) were studied by Olson (2001) and are not repeated here.

A.3.2 Site Geology and Soil Conditions

The region severely damaged by the 1988 earthquake is situated in the southern portion of the Caucasus mountain range. This region has been subjected to tectonic activity extending back millions of years. The predominant trend of geological features, which includes the 1988 earthquake fault, runs from northwest to southeast, parallel to the main Caucasus mountain range. The region is subjected to north-south tectonic compression from the Eurasian plate in the north and Arabian plate in the south converging at an estimated rate of 3 cm/yr (Yegian et al. 1994e). As a result of this compressive tectonic activity, the prevailing trend of the faults in the region is thrust with strike-slip at some places (Yegian et al. 1994e).

The highway embankment that failed near Spitak was situated along a tributary of the Pambak River, and the ground water table was near the ground surface. A geological map of the region severely damaged by the 1988 earthquake with the geological cross section passing through Spitak town and a geological cross section of Pambak Valley near the failed Spitak highway embankment is given in Figure A.21. The Pambak Valley is filled with up to140m of silty and gravelly alluvial sands with sporadic layers of volcanic tuff. Shortly after the earthquake, the embankment was repaired so that highway could be reopened (Yegian et al. 1994e).

During reconnaissance trips and surveys in the vicinity of the fault, Yegian et al. (1994e) observed sand boils near the failed embankment, with silty sands ejected onto the ground surface and gravels lodged in the sand boil feeder dikes. These sand boils were located as close as 15 m from the toe of the failed section of the highway embankment.

Figure A.22 shows the embankment cross-section before and after the failure as reported by Yegian et al. (1994e). The embankment material is a compacted silty sand fill. The foundation soils of the embankment constitute 30 to 40 cm of organic silt (agricultural soil). This soil, which may have been removed below the embankment, is described as low plasticity sandy silt, and is underlain by at least 3 m of loose to medium-dense gravelly sand. Figure A.23 presents the grain size distribution curves of soil samples recovered from shallow trenches and SPT split spoon samples.

The ground water table at the time of field tests was 20cm below the ground surface and Yegian et al. (1994e) concluded that very little fluctuation occurred in the ground water table during the year.

A.3.3 Estimation of Ground Motions

Details related to the earthquake as reported by USGS (2011) are as follows:

Date and time: 1988 12 07 07:41 UTC

Location: 40.987ºN, 44.185ºE[1]
Magnitude: 6.8
Region: Northwestern region, Armenia
Fault Mechanism: Thrust Fault[2]

Ground motions during the Armenia earthquake were recorded at only two stations: in Ghoukasian, Armenia (25 to 30 km from the main fault rupture), and in the capital city of Yerevan, Armenia (85 km from the fault). The Ghoukasian record was used by Yegian et al. (1994a) in subsequent studies of ground motion attenuation and soil amplification. The two components, north-south (N-S) and east-west (E-W) of the main shock record have peak ground accelerations of about 0.2g and 0.19g, respectively. Using an inverse procedure (deconvolution), Yegian et al. (1994c) computed rock outcrop acceleration time-histories with peak values of about 0.25g in the N-S direction and 0.14g in the E-W direction.

Because only two stations recorded the ground motions during the 1988 Armenia earthquake, the reconnaissance team quantitatively estimated the ground motions by observing grave markers of five cemeteries in the affected region. The grave markers were slender rectangular blocks that were facing approximately east. These grave markers were observed to be rotated about their vertical axis, displaced horizontally, and toppled in some cases. It is interesting to note that such failures and displacements of grave markers were frequent in Spitak, infrequent in Leninakan, and non-existent in Kirovakan. This is consistent with the damage pattern that was observed by Yegian et al. (1994b, e) in these three towns (as described in Section A.3.1). Based on the response of these grave markers, Yegian et al. (1994b) suggested surface PGA values between 0.5 and 1.0g in Spitak.

In addition to the above information, the author used the NGA relationships proposed by Abrahamson and Silva (2008), Boore and Atkinson (2008), Campbell and Bozorgnia (2008), Chiou and Young (2008), and Idriss (2008) to estimate surface PGAs for each of the study sites. The summary of calculated PGAs is given in Table A.1. The PGAs estimated from the NGA relations are quite consistent with the range of values estimated by Yegian et al. (1994b).

A.3.4 Description of Failure

Figure A.20(a) shows the location of three sites studied by Yegian et al. (1994e). At Spitak, 1 to 2km from the fault, a highway embankment failed. Figure A.20(b) shows a photograph of the embankment taken after its failure. The highway supported by this embankment was the primary link between Spitak, Leninakan, and Kirovakan. Its failure seriously hampered the relief efforts immediately after the earthquake. The pre- and post-failure geometry of the failed embankment are shown in Figure A.22, along with limited

[1] The epicentral location was unavailable from USGS (2011), therefore, the epicentral location was taken from Pacheco et al. (1989). However, the author has doubts about the accuracy of their epicentral location because it plots nearly 20km from the surface expression of the Spitak fault.
[2] Yegian et al. (1994e)

SPT and CPT resistances. The earthquake caused a crest settlement of 0.5 m, and a wall at the right embankment toe was tilted. Some cracks on the embankment crest were also visible as shown in Figure A.22. There were minor failures on both sides of highway embankment. Sand boils were observed near the toe of the left side of the embankment. The embankment material is silty, sandy compacted fill.

As stated in Section A.3.2, there was at least about 3m of loose to medium-dense gravelly sands beneath the embankment fill. Yegian et al. (1994e) suggested that liquefaction occurred in the upper portion of these gravelly sands and analyzed circular trial failure surfaces that extended through the liquefied gravelly sands. Although the Spitak highway embankment was situated very close to the fault and the PGA was estimated to be in excess of 0.5g, the high permeability of the gravels and gravelly sands makes them more resistant to liquefaction than clean, fine to medium grained sands (Stark and Olson 1995). In fact a similar site in Spitak did not fail, possibly due to free drainage of the gravelly sands. At the Spitak highway embankment, however, a 30- to 40-cm thick agricultural soil located at the ground surface overlies the loose gravelly sands and likely impeded drainage sufficiently to allow excess porewater pressure to build and eventually trigger liquefaction (Yegian et al. 1994e). However, as discussed in Section A.3.6, liquefaction at the embankment toes alone is unlikely to haved result in the observed embankment damage. Therefore the author suggests that the entire loose gravelly sand layer under the embankment liquefied.

A.3.5 Representative Penetration Resistance

Penetration tests (SPT and CPT) were conducted to shallow depths of only about 2m at the Spitak highway embankment site, partly because of the high gravel content and partly because of limitations of the drilling equipment (Yegian et al. 1994e). This was not a major drawback, as field evidence (i.e., sand boils near the embankment toe) suggested that liquefaction likely occurred at shallow depth in the gravelly sand layer. As shown in Figure A.22, an SPT blow count of 12 was measured in this layer. CPT tip resistance ranged from 9 to 10.8MPa.

Yegian et al. (1994e) used the CPT results to calculate “equivalent” SPT blow counts using the Meigh (1987) q_c/N relationship. Using this interpretation, Yegian et al. (1994e) reported equivalent SPT N-values that ranged from 4 to 16 with an average of 8.

The author used the single available SPT N-value of 12 and applied the gravel content correction proposed by Tokimatsu (1988) (as reported in Terzaghi et al. 1996). A range of D_{50} values from 3 to 10mm (see Figure A.23) were used to calculate a gravel correction factor of 0.3 to 0.5. The N-value after gravel correction ranges from 4 to 6. Unfortunately the SPT hammer type was not reported. Because Olson (2001) assumed a 60% energy ratio for the Armenian earthquake failures, the author adopted the same value. The $(N_1)_{60}$ values are calculated as 7 to 12 with a best estimate of 8.5. (A saturated unit weight of 18.5 kN/m^3 was used for the calculations.)

A range of q_c values from 9 to 10.8 MPa was also reported by Yegian et al. (1994e) as shown in Figure A.22. The author did not find any gravel content correction factor specific to the CPT; therefore the same SPT-based gravel content correction factors were used for the CPT. The q_c-values after gravel correction range from 2.7 to 5.4 MPa. The corresponding q_{c1} values range from 4.6 to 9.2 MPa, with a best estimate of 7.8 MPa. Alternatively, q_{c1} values can be calculated from the single measured N-value by using q_c/N_{60} = 0.59 to 0.95 (average value of Robertson and Campanella 1985, Seed and De Alba 1986, Andrus and Youd 1989, Kulhawy and Mayne 1990, and Stark and Olson 1995) based on the reported D_{50} values. The corresponding q_{c1} values are 5.4 to 9.2 MPa, consistent with the range for the measured, gravel content-corrected CPT values.

A.3.6 Yield Shear Strength and Strength Ratio

The mechanism that likely triggered the embankment failure is seismic liquefaction of the saturated gravelly sand (Yegian et al. 1994e). As explained in Chapter 2, the shear strength and strength ratios mobilized at the instant of failure in cases where liquefaction is triggered by seismic loading do not necessarily represent yield shear strength and strength ratios.

The pre-failure geometry along with the analyzed failure surfaces by Yegian et al. (1994e) is given in Figure A.25. This figure also shows the FS of the slip surfaces analyzed by Yegian et al. (1994e). Yegian et al. (1994e) assigned c' = 5kPa and $\phi' = 30^o$ to the non-liquefied fill to calculate FS. Yegian et al. (1994e) argued that the strength values in their analysis were reasonable because the computed FS of 1.7 was close to a typical design FS of 1.5.

Although Yegian et al. (1994e) suggested that the Spitak highway embankment failed due to liquefaction, the author considered three possibilities that either support or refute the Yegian et al. (1994e) interpretation. Those three possibilities are: (i) the entire gravelly sand foundation liquefied, i.e., both under the entire embankment footprint and outside the toes; (ii) only the gravelly sand outside the embankment toes liquefied; and (iii) no liquefaction occurred and the observed displacements were caused "pseudo-statically" by the large earthquake accelerations. In the following paragraphs each possibility is discussed in detail with the field observations and analyses performed by the author.

Interpretation 1. Entire foundation liquefied. The following arguments support the interpretation that the entire foundation liquefied (i.e., both under the embankment footprint and outside the embankment toes).

- Static slope stability analysis shows that FS >> 1.0. The author conducted slope stability analyses on both sides of embankment with zero shear strength assigned to the gravelly sand outside the embankment toes (as a worst case scenario for liquefied soil) and $\phi' = 30^o$ to the gravelly sand under the embankment (see Figure A.25 and Figure A.26). The FS thus calculated was still significantly larger than unity, which shows that liquefaction of gravelly sand under the toe only is

insufficient to cause failure of the embankment. Because a crest settlement of 0.5m and cracks around 1m deep were observed, the deformation suggests that FS < 1.0 at some point before the embankment became stable again. It is likely that the entire foundation gravelly sand liquefied and the overlain silty sand embankment impede excess porewater pressure for a dynamic load like earthquake.

- The agricultural soil may not have been removed prior to embankment construction. Although Yegian et al. (1994e) indirectly suggest in their figures that the agricultural soil at the site was removed from the embankment footprint prior to embankment construction; it is quite possible that this soil was not removed prior to embankment construction. The author notes that no borings were drilled through the embankment to verify that this silt layer was removed. Furthermore, even if the silt layer was removed, the compacted silty sand fill may have had low enough permeability to cause impeded drainage (at least temporarily) to the gravelly sand foundation such that porewater pressure increase could occur.

- Sand boils formed approximately 15m from the embankment toe, indicating that shaking was sufficiently strong to liquefy the gravelly sand layer when drainage was impeded. In fact, Yegian et al. (1994e) argued based on this observation that, "Our field investigations and observations have led us to the following explanation of the cause of failure of the highway embankment. As stated earlier, failure was limited to the region near a tributary of the Pambak River where the highway was founded on loose gravelly sands with the water table near the ground surface. Because of the proximity of the embankment to the fault, the ground motion at this site was extremely strong (PGA > 0.5g). But even during such high accelerations, free draining gravels and gravelly sands may not be expected to liquefy (as will be demonstrated at site 2). In this case, however, the presence of an overlying 30 – 40 cm relatively impermeable soil layer prevented vertical dissipation of the excess pore-water pressures, as they were being generated by the shaking. As a consequence, high pore-water pressures triggered liquefaction or at least substantially reduced the shearing resistance of this deposit beneath, and particularly near the toes of the embankment. This led to instability of the embankment, resulting in cracking and slip deformations."

Interpretation 2. Only gravelly sand outside toes liquefied. The following arguments support the interpretation that only the foundation soils outside the embankment toes liquefied.

- The sand boil was located outside of the embankment toe and the agricultural soil was only identified via excavations only outside of the embankment footprint. As argued by Yegian et al. (1994e), this low permeability layer was key to impeding the drainage of the gravelly sand sufficiently to trigger liquefaction. If this layer was removed below the embankment footprint, the compacted silty sand may

have been sufficiently permeable that it allowed porewater pressure from the gravelly sand to drain during shaking.

- A pseudo-static analysis conducted by the author shows that along typical failure surfaces the yield acceleration ranges from 0.07g to 0.4g for slide 1 and from 0.33g to 0.5g for slide 2. The pseudo-static analysis was conducted by assigning both, drained and undrained shear strengths to the liquefied soil zone. For drained conditions a range of $\phi' = 30^o - 36^o$ was assigned, while for undrained conditions an undrained yield shear strength ratio of 0.27 was assigned using Olson (2001) relationship for the representative penetration resistance $(N_1)_{60}$ of 8 blows/ft. To calculate the permanent earthquake-induced deformation, Newmark's sliding block analogy was adopted using the software developed by Jibson and Jibson (2005). In order to use Jibson and Jibson (2005) ground motions need to be selected. Unfortunately, ground motions for the 1988 Armenian earthquake were not included in the database used by the software developed by Jibson and Jibson (2005). The author selected the ground motions based on the criteria outlined by Olson and Johnson (2008). The failure surfaces used in the analysis is shown in Figure A.25 and Figure A.26. The results show that the expected permanent deformations ranged from zero to 272cm for slide 1 and from zero to 41cm for slide 2. As the deformations of the embankment were limited to 50cm (vertical), a liquefaction mechanism is not necessary to explain the observed movements.

Interpretation 3. No liquefaction. If one assumes that no liquefaction occurred near the footprint of the embankment (i.e., the sand boil was located far enough from the embankment that it played no role in the observed movement), then pseudo-static deformations would be responsible for the observed embankment deformations. The author performed pseudostatic analyses of the embankment using only drained shear strengths from $\phi' = 30^o$ to 36^o and the same ground motions as described in Interpretation 2. These analyses suggested pseudo-static deformations of about 0 to 68cm for Slide 1 and 0 to 41cm for Slide 2.

Although Interpretation 3 is the most unlikely, each Interpretation is plausible and no single option can be accepted or refuted completely. Although Yegian et al. (1994e) categorized this failure as a liquefaction-induced failure (which is also the author's opinion), the various interpretations related to this case suggest that the case should be classified with a high level of uncertainty. The yield and liquefied shear strength analyses explained in the following paragraphs assume that Interpretation 1 is valid.

The pre-failure geometry of the Spitak highway embankment is reproduced in Figure A.27. A slope stability search was conducted to locate initial failure surfaces on both sides of the embankment that were consistent with the pre- and post-failure geometry as well as the slip surfaces suggested by Yegian et al. (1994e). All saturated gravelly sand below the groundwater table was assumed to liquefy and a single value of shear strength was assigned to the liquefied soil. The compacted silty sand embankment fill initially above the phreatic surface was assigned $\phi' = 30^o$ to 36^o with $c' = 0$. The author also used the strength reported by Yegian et al. (1994e) of $\phi' = 30^o$ with $c' = 5$kPa.

Whenever c' ≠ 0, the author conducted the analysis with and without tension cracks. The resulting back-calculated mobilized shear strength in the zone of liquefaction was 9kPa with a range from 4.7 kPa to 12 kPa for slide 1, and 10kPa with a range from 4.5 kPa to 14.2 kPa for slide 2.

A second analysis was conducted to estimate the strength ratio mobilized at the triggering of liquefaction. Identical assumptions regarding the failure surface and shear strength of the non-liquefied soil were used for this analysis. The resulting back calculated mobilized shear strength ratio was 0.24 with a range from 0.16 to 0.285 for slide 1, and 0.175 with a range from 0.1 to 0.235 for slide 2, depending on the shear strength of the unsaturated fill and the location of the failure surface. The weighted average of pre-failure vertical stress in the liquefied segment was determined as 33kPa and 60kPa for slides 1 and 2, respectively.

A.3.7 Liquefied Shear Strength and strength Ratio

The post-failure geometry along with the analyzed failure surfaces by Yegian et al. (1994e) is given in Figure A.28. This figure also shows the back-calculated undrained shear strength for the liquefied soil for both slip surfaces. Yegian et al. (1994e) assigned c' = 0 to 5kPa and ϕ' = 30º to 36° non-liquefied soil to back-calculate the liquefied shear strengths of the gravelly sand. Again, this analysis was performed for Interpretation 1: that the entire foundation layer liquefied. The post-failure geometry of the Spitak highway embankment is reproduced in Figure A.29. Slope stability searches were conducted to locate the critical failures surface on both sides of embankment that are consistent with the final embankment geometry and the slip surfaces suggested by Yegian et al. (1994e). A single arbitrary value of liquefied shear strength was assigned to liquefied zone and the compacted silty sand embankment fill initially above the phreatic surface was assigned a drained friction angle of 30º to 36º with c' = 0. The author also used the strength reported by Yegian et al. (1994e) of ϕ' = 30º with c' = 5kPa. Whenever c' ≠ 0, the author conducted the analysis with and without tension cracks. The liquefied shear strength was varied until a factor of safety equal to unity is obtained. The resulting back-calculated liquefied shear strength was 6.8kPa with a range from 4.0 kPa to 8.2 kPa for slide 1, and 7.5kPa with a range from 4.8 kPa to 10.2 kPa for slide 2.

Using the same post-failure trial sliding surfaces, limit equilibrium back-analyses of the liquefied strength ratio for slides 1 and 2 were conducted. In slide 1, the length of the final failure surface was divided into 11 segments, as shown in Figure A.29. Segments 1, 10, and 11 correspond to the embankment material in the non-liquefied zone. These segments were assigned ϕ' = 30º - 36º with c' = 0. The author also used the strength reported by Yegian et al. (1994e) ϕ' = 30º with c' = 5kPa. Whenever c' ≠ 0, the author conducted the analysis with and without tension cracks. The remaining segments from 2 to 9 were within the liquefied zone. Because the liquefied soil had limited movement, it was assumed that the pre-failure segment positions were very close to their post failure positions. Therefore these segments were arranged in the liquefied zone of the pre-failure geometry as shown in Figure A.29, along the final sliding surface to calculate the pre-failure vertical effective stress for each slice. An arbitrary value of liquefied shear

strength ratio was given to the liquefied soil zone, which in turn yields different liquefied shear strength for each segment, and a limit equilibrium analysis was run to calculate the factor of safety. The liquefied shear strength ratio was then varied until a factor of safety equal to unity was obtained. Using the same assumptions made in the liquefied shear strength analysis, the liquefied strength ratio for slide 1 was estimated as 0.14 with a range from 0.107 to 0.22. The weighted average of vertical effective stress was estimated as 33.5 kPa.

In slide 2, the length of the final failure surface was divided into 10 segments, as shown in Figure A.30. Segments 1, 2, and 10 correspond to the embankment material in the non-liquefied zone. These segments were assigned $\phi' = 30^o - 36^o$ with $c' = 0$. The author also used the strength reported by Yegian et al. (1994e) of $\phi' = 30^o$ with $c' = 5$kPa. Whenever $c' \neq 0$, the author conducted the analysis with and without tension cracks. The remaining segments from 3 to 9 were within the liquefied zone. Because the liquefied soil had limited movement it was assumed that the pre-failure segment positions were very close to their post failure positions. Therefore these segments were arranged in the liquefied zone of the pre-failure geometry as shown in Figure A.30, along the final sliding surface to calculate the pre-failure vertical effective stress for each slice. An arbitrary value of liquefied shear strength ratio was given to the liquefied soil zone, which in turn yields different liquefied shear strength for each segment, and a limit equilibrium analysis was run to calculate the factor of safety. The liquefied shear strength ratio was then varied until a factor of safety equal to unity was obtained. Using the same assumptions made in the liquefied shear strength analysis, the liquefied strength ratio was estimated as 0.16, with a range from 0.113 to 0.25. The weighted average of vertical effective stress was estimated as 65.4 kPa.

A.3.8 Liquefied Shear Strength and Strength Ratio Considering Kinetics

Due to limited movement of the failed soil mass, kinetics analyses for Spitak highway embankment (both slides) could not be conducted.

A.3.9 Sources of Uncertainty

As described above, several interpretations of the failure mechanisms are plausible for this case. As a result, there is considerable uncertainty in assigning a liquefaction mechanism to this case history. As a result, this case will be reported using the highest level of uncertainty. Other uncertainties related to yield and liquefied shear strengths as well as representative penetration ratios are given in the following.

The following sources of uncertainty were involved in estimating the yield shear strength and strength ratio: (1) the initial zone of liquefaction; (2) the position of the initial failure surface; (3) the shear strength of the non-liquefied soils; and (4) potential drainage during failure. It was assumed that entire gravelly sand layer below the phreatic surface liquefied (i.e., Interpretation 1). (Refer to Section A.3.6 for a detailed discussion of this uncertainty.) The position of the initial failure surface was not known. However, using a slope stability search and comparing this critical slip surface to the embankment

geometry and the initial slip surface reported by Yegian et al. (1994e) allowed some confidence in this item. The unsaturated fill was assigned $\phi' = 30^o - 36^o$ with c' = 0. The author also used the strength reported by Yegian et al. (1994e) of $\phi' = 30^o$ with c' = 5kPa. However, none of these values are based on laboratory test results.

The following sources of uncertainty were involved in estimating the liquefied shear strength and strength ratio: (1) the limits of the zone of liquefaction; (2) the shear strength of the non-liquefied soils; and (3) the potential for void and pore water pressure redistribution. As discussed above, all gravelly sand below the phreatic surface was assumed to liquefy (i.e., Interpretation 1). The unsaturated fill was assigned $\phi' = 30^o - 36^o$ with c' = 0. The author also used the strength reported by Yegian et al. (1994e) of $\phi' = 30^o$ with c' = 5kPa. However, none of these values are based on laboratory test results.

The following sources of uncertainty were involved in determining the "representative" values of penetration resistance: (1) only a single SPT N-value was measured; (2) applying a gravel content correction to the SPT and CPT; and (3) the SPT hammer energy ratio.

A.4 Okuli Landslide, Dushanbe, Tajikistan

A.4.1 Introduction

On January 23, 1989 at about 5:00 am local time, an M 5.5 earthquake hit the southern region of Tajikistan, near Dushanbe (Figure A.31). Ishihara et al. (1990) reported that the focal depth of this event was about 35 km (the USGS reported a focal depth of 33 km). About 274 people were killed and many injured mainly because of mudslides in the Gissar (Hisor) area situated about 20 km west of Dushanbe. There were about 500 farmers' houses and barns in the village of Gissar that were partially damage. The structural damage due to earthquake shaking was moderate and limited to a small area. It is the series of landslides and mud flows that caused a significant number of casualties and large-scale destruction. About 220 villagers died or were missing following the landslides.

Figure A.32 shows locations of four landslides that affected the area of Gissar. These landslides failed catastrophically and turned into mudflows that engulfed more than 100 houses and deposited about 5 m of mud. These landslides are: 1) the Sharara slide; 2) the Firma slide; 3) the May 1 slide; and 4) the Okuli slide. The Sharara and Firma slides do not have available penetration data and the May 1 slide was analyzed by Olson (2001). The Okuli slide is analyzed in this study. Figure A.33 show post-failure photo of the landslide area.

A.4.2 Geological Setting and Soil Conditions

The topography of the Gissar area that experienced damage due to liquefaction-induced landslides during 1989 Tajikistan earthquake is primarily gently-sloping hills, covered by a blanket of loess. These sediments were deposited during the Pleistocene era

by wind from the Karakumy desert located west of Tajikistan and Kyrgyzstan. The loess is a tan to light brown, lightly cemented silty soil and is up to 40m thick. It is underlain by up to 200 m of gravelly sand (Ishihara et al. 1990). Figure A.34 shows the geological parallel to and transverse to the Okuli landslide.

Laboratory tests conducted on the loess yielded liquid limits of about 30 and plastic limits of about 20, which gives plasticity indices of about 10 (Ishihara et al. 1990). The natural water content in the loess prior to failure ranged from 20% to 40% (Ishihara et al. 1990), indicating liquidity indices of 0 to 2. Figure A.35 shows the grain size distribution curve of the loess. It can be seen from Figure A.35 that the loess consists of about 85% silt (primarily quartz and feldspar) and 15% clay (including montmorillonite), with a D_{50} of about 0.012mm.

It is well-understood that loess is an eolian sediment formed by an accumulation of wind-blown silt. These sediments typically are deposited in a very loose state (chiefly as a result of capillarity) and as they age, they develop vertical fractures. The loess soils in Gissar all developed vertical scarps during landsliding. Ishihara et al. (1990) also stated that the loess was very porous, possibly due to root holes. When dry, loess commonly is relatively strong and incompressible. However, if the loess becomes saturated, the bonding readily breaks down and significant settlements and strength loss can occur (e.g., Ishihara et al. 1990). If the natural water content exceeds the liquid limit of soil (i.e., liquidity index > 1), landslides in loess can readily become mudflows.

The village of Gissar is situated in the suburbs of the nation's capital Dushanbe and as the city developed and population increased, the land of Gissar, which was left uncultivated before, was cultivated in order to fulfill the agricultural needs of the city. For the purpose of irrigation a network of water channels was constructed in the hilly areas of Gissar. These water channels were mostly unlined and water had been leaking from them and permeating the ground through the vertical fissures in the loess deposit for many years prior to the earthquake. At the time of the earthquake, a large quantity of absorbed water had saturated the loess. As a result, the ground water table risen to about 5 m below the ground surface. However, the water content of the loess at a depth below about 20 m remained small, likely due to lower permeability at depth, as schematically shown in Figure A.36. Water infiltration had saturated the zone from depths of about 7m to 17m, and the water content in this zone exceeded the liquid limit. As a result, this zone was likely at the verge of hydraulic collapse prior to the earthquake, and the small levels of shaking associated with the earthquake were sufficient to trigger liquefaction and the resulting mudflows.

A.4.3 Estimation of Ground Motions

Details related to the 1989 Tajikistan earthquake are as follows (USGS 2010):

Date and Time: 1989 01 23; 05: 02 (Local Time)
Location: 38.465ºN, 68.694ºE
Magnitude: 5.5

Region: Dushanbe, Tajikistan
Fault Mechanism: Not known

The 1989 Tajikistan earthquake is believed to be associated with a fault movement of the Iliakckin fault on the order of 30 cm, but Ishihara et al. (1990) suggested the fault was a blind fault as no evidence of fault rupture could be traced at the ground surface.

Figure A.31 shows the epicentral location of the 1989 Tajikistan earthquake. The epicenter is located at Gissar near the junction of the Kahirnighan River and the Halaka River (see Figure A.37). Several strong ground motion recording stations around the epicenter recorded the earthquake, and Figure A.37 notes the PGAs measured at these stations. Recorded peak ground accelerations (PGA) ranged from 0.05g in the capital city of Dushanbe, to as high as 0.125g recorded at Cymbulif closest to the epicenter (see Figure A.37). Ishihara et al. (1990) suggested a PGA of 0.153g in epicentral area, where the landslides were located, by extrapolating from the amplitudes of the motions recorded in the region. The shaking intensity in the epicentral area was estimated at MMI 7 (see Figure A.37). Using the attenuation relationship proposed by Trifunac and Brady (1975) and an MMI = 7, a PGA of about 0.15g is obtained, consistent with the locally measured ground motions.

A.4.4 Description of Failure

Unlike other earthquakes where damage commonly occurs in structures as a result of inertial forces, most of the destruction in the area affected by the Tajik earthquake resulted from landslides and mudflows that were triggered by liquefaction of the loess. Figure A.32 shows four landslides in the Gissar area that caused large destruction. The largest and most disastrous landslide was the Okuli landslide. Ishihara et al. (1990) suggested that multiple, smaller landslides participated in the Okuli landslide. At least two landslides from the northern part were triggered independently along with the main slide as indicated by slides B and C in Figure A.32. Ishihara et al. (1990) described these slides as follows: “At least two slides seem to have been triggered independently from the hillsides on the north which then merged into the main stream of the mud flow. The shallow slide indicated by B in [Figure A.32] took place on the terrace of high relief with its scarp located near the hilltop and after the soil moved over the gentle slope the debris flow jumped into the main stream. There were many traces of violent mud flow remaining on the exposed hard soils, indicating evidence of liquefaction and consequent muddy flow of loess soil during the earthquake (see [Figure A.34]). The slides indicated by A and C in [Figure A.32] appear to have been initiated along the line of the water channel. It appears likely that a small slide initially induced at the toe might have retrogressed backwards over a distance of 1.5 km to the east and sidewards to the north as well as to the south.”

The author considered both a continuous sliding surface from head scarp to toe and retrogressive sliding surfaces in this study. Ishihara et al. (1990) reported that the failed ground surface was irregular and broken into number of blocks; and from the middle of the blocks, sand boils consisting of loess were observed. Other portions of the

failed mass turned into a mudflow and covered a distance of about 2 km on a nearly flat ground surface. The failed mass covered an area of about 1.5 million square meters as shown in Figure A.34(a).

Ishihara et al. (1990) showed an incomplete phreatic surface in the Okuli landslide [see Figure A.34(a)]. The phreatic surface is shown in the head scarp area and was not shown in the slope. The author estimated that the phreatic surface would roughly parallel the ground surface, and would approach the ground surface near the toe of the initial failure.

A.4.5 Representative Penetration Resistance

Ishihara et al. (1990) conducted 5 CPT soundings through the failed mass using a portable cone device *after* the failure. Figure A.32 shows the locations of CPT performed on the Okuli landslide failed mass and Figure A.38 shows the CPT data. As can be seen from CPT profiles, tip resistance ranged from 1.2 kgf/cm^2 (0.11 MPa) to 11.1 kgf/cm^2 (1.1 MPa) considering all five penetration tests in the sliding zone at depths of about 7 to 8 m. Ishihara et al. (1990) suggested a range of 1 to 5 kgf/cm^2 (0.1 to 0.5 MPa) for the Okuli landslide.

The author suggests that the "representative" penetration resistance should be similar to the limiting or highest value of penetration resistance for each CPT performed. This limiting value of penetration resistance may correspond to the limiting end bearing suggested by Meyerhof (1976) for axial pile capacity. It is also likely that most of the penetration resistance measured from these tests corresponds to tip resistance, as the side friction likely will be small at depths less than 2 m. Therefore the author selected "representative" q_c-values from 0.4 to 1.1 MPa, which corresponds to q_{c1}-values from 0.66 MPa to 1.9 MPa with a best estimate of 0.8 MPa.

Unfortunately no SPT results were available for this site. Therefore, the author estimated $(N_1)_{60}$ values from the CPT results. Using a D_{50} value of 0.012 mm, correlations by Robertson and Campanella (1985), Seed and De Alba (1986), Andrus and Youd (1989), Kulhawy and Mayne (1990), and Stark and Olson (1995) yield an average q_c/N_{60} ratio of 0.23. Therefore, the estimated $(N_1)_{60}$ values ranged from 3 to 8 blows/ft, with the best estimate of 3.5 blows/ft.

A.4.6 Yield Shear Strength and Strength Ratio

The pre-failure geometry of the Okuli landslide, along with potential retrogressive failure surfaces are presented in Figure A.39. As described above, the failure likely resulted from liquefaction of loess soil layer triggered by 1989 Tajikistan earthquake. Ishihara et al. (1990) suggested that the landslide likely initiated in the toe area and then retrogressed back towards the the final headscarp. The author also considered a single, full-length failure surface as a possible failure mechanism. The slope stability search was therefore constrained first in the toe area and then at the head scarp, as shown in Figure A.39, passing through the loess. In the analyses performed in this study, the author

assumed that all of the loess below the perched water table was saturated and liquefiable. The author used a range of friction angles from $\phi' = 28^o$ to 32^o with $c' = 0$ for soil initially above the phreatic surface based on the low penetration resistance discussed in Section A.4.5. The back-calculated yield shear strengths in the liquefied zone ranged from 3.5 kPa to 8.7 kPa depending on the failure surface location and, to a small degree, on the shear strength of non-liquefied soil. The best estimate of mobilized shear resistance in the liquefied zone was 7.0 kPa.

A second analysis was conducted to estimate the mobilized shear stress ratio at the triggering of liquefaction. The same trial failure surfaces described above were analyzed here. An arbitrary shear stress ratio was assigned to the liquefied zone, and this value was varied until a FS of unity was achieved. A best estimate of yield shear stress ratio was estimated as 0.062, with a possible range of 0.044 to 0.077. The weighted average pre-failure vertical effective stress was determined as 78 kPa to 113 kPa using a unit weight of 15 kN/m^3 as suggested by Ishihara et al. (1990).

A.4.7 Liquefied Shear Strength and Strength Ratio

The post-failure geometry of Okuli landslide is reproduced in Figure A.40. Trial failure surfaces were derived from the post-failure morphology of the sliding mass and a slope stability search, as shown in Figure A.40. A single arbitrary value of liquefied shear strength was assigned to liquefied zone. The liquefied shear strength was varied until a factor of safety equal to unity was obtained. The resulting back-calculated liquefied shear strength was 2.3 kPa, with a range of 2.1 kPa to 2.5 kPa.

Using the same post-failure trial sliding surface shown in Figure A.40, a limit equilibrium back-analysis was conducted to estimate the liquefied strength ratio. The length of the final failure surface was divided into 16 segments. Segment 16 corresponds to the non-liquefied sand above the phreatic surface. The remaining segments from 1 to 15 are within the liquefied zone. The post-failure segments were assigned their pre-failure geometry positions as shown in Figure A.39, to calculate the pre-failure vertical effective stress for each slice. An arbitrary value of liquefied shear strength ratio was given to the liquefied soil zone, which in turn assigns different liquefied shear strength to each segment and an analysis was run to calculate the factor of safety. The liquefied shear strength ratio was then varied until a factor of safety equal to unity is obtained. Using the same assumptions made in the liquefied shear strength analysis, the liquefied strength ratio was estimated as 0.017, with a range of 0.016 to 0.019. The weighted average of vertical effective stress was estimated as 131 kPa.

A.4.8 Liquefied Shear Strength and Strength Ratio Considering Kinetics

The pre- and post- failure geometries are reproduced in Figure A.39 and Figure A.40, respectively. Generally the initial result of the kinetics analysis assumed that all soils along the failure surface mobilized the liquefied shear strength. This inaccurately estimates the actual liquefied shear strength if a portion of the failed soils initially were above the phreatic surface and did not liquefy. Therefore, the liquefied shear strength

needs to be adjusted to account for the strength of the non-liquefied soils, using Eq. A.1 (Olson 2001):

$$s_u(liq) = \frac{s_u(mob) - \left(\frac{L_d}{100} * s_d\right)}{\left[1 - \left(\frac{L_d}{100}\right)\right]} \qquad \textbf{Eq. A.1}$$

where s_u(mob) = shear strength mobilized in the kinetics analysis, i.e., the shear resistance along the entire post-failure sliding surface; L_d = length of the post-failure sliding surface (percent of the total length of the failure surface) that did not liquefy; and s_d = average shear strength of the fill soils that did not liquefy . In this case, the entire sliding surface is passing through liquefied soils and no adjustment is needed.

The centroids illustrated in Figure A.40 consider the failure of the entire slope (i.e., not the individual retrogressive slope failures). The kinetic analysis presented in Figure A.41 yielded the following results:

- Liquefied shear strength = 3.4 kPa
- Liquefied shear strength ratio = 0.026

This liquefied shear strength resulted in a calculated displacement of the centroid of the failure mass of approximately 17 m vertically and 804 m horizontally.

The kinetics analysis only provided a value of liquefied shear strength. Therefore, the liquefied shear strength ratio reported above was determined by dividing the liquefied shear strength of 3.4 kPa by the weighted average vertical effective stress of 131 kPa obtained from the post-failure geometry analysis. These values of liquefied shear strength and strength ratio include the effects of kinetics.

A.4.9 Sources of Uncertainty

The following sources of uncertainty were involved in estimating the yield shear strength and strength ratio: (1) the initial zone of liquefaction; (2) the position of the initial failure surface; (3) the shear strength of the non-liquefied soils and (4) the location of the phreatic surface within the slope. It was assumed that all the loess soil below the phreatic surface liquefied. The position of the initial failure surface was not known. However, it was likely that the failure first occurred in toe area and then retrogressed backwards. The author therefore considered both a single continuous failure and retrogressive failure surfaces. The unsaturated fill was assigned $\phi' = 28^o - 34^o$ based on low penetration resistances. Although Ishihara et al. (1990) showed a phreatic surface in the slope, this surface was shown near the head of the slope and later discontinued. The author continued the same level and profile throughout the rest of the slope.

The following sources of uncertainty were involved in estimating the liquefied shear strength and strength ratio: (1) the limits of the zone of liquefaction; (2) phreatic surface within the slope; and (3) pre-failure slice positions. As discussed above, all loess below the phreatic surface was assumed to liquefy. No phreatic surface for the post failure geometry was given. The author assumed that the water table coincided with the post-failure geometry surface based on the fact that the slide became a mudflow during the failure. The positions of post-failure geometry segments were arranged in pre-failure geometry by estimating the locations of failed mass.

The following sources of uncertainty were involved in determining the "representative" values of penetration resistance: (1) non-standardized cone penetrometer; (2) conversion from CPT to SPT; and (3) shallow depth of CPT. A portable cone device was used to estimate the penetration resistance. No information was given about the device and how the results can be compared with a standard electronic cone. SPT was not conducted at site and therefore $(N_1)_{60}$ values were estimated from CPT using q_c/N_{60} ratio. All the CPTs were conducted from 7 m to 9 m depths through the failed mass.

A.5 Sullivan Tailings Dam, British Columbia, Canada

A.5.1 Introduction

The Sullivan Mine was an underground lead and zinc mine located near the town of Kimberley, British Columbia, Canada (see Figure A.42). The mine was established in 1905 and was closed in 2001. The mine tailings had been hydraulically transported southeast of the concentrator, and several tailings dykes had been constructed as necessary. By the early 1990s, most of the mining operation was shut down and the only active tailings pond was the active iron tailings pond (AIP) which was surrounded by abandoned tailings ponds and dykes (see Figure A.43). Little information is available about the design, construction and operational history of the tailings dam; however, Robinson (1977) stated that the old iron tailings disposal had experienced a number of embankment failures in the past. The most destructive failure occurred in 1948, which resulted in liquefaction of the retention dyke and caused about one million tons of tailings to flow through the valley. From about 1948 to 1975, the old iron tailings were confined in an earth fill structure that was later referred to as the old iron dyke. In 1975, a new starter dyke for the AIP was constructed over the previously placed old tailings and was incrementally raised using the upstream method of construction. The exterior shell was mechanically-placed and compacted progressively over the previously deposited tailings. From 1975 until 1991, each incremental raise was designed and inspected by a consulting engineering firm.

On August 23, 1991, during construction of a 2.4 m incremental raise (fill lift), the southeastern part of the dyke suddenly failed. Figure A.43 shows the location of the failed section and Figure A.44 shows an aerial photo of the failed tailings dam two days after the failure. Fortunately there were no casualties or environmental impact as a result

of this failure, and the slide was contained by another pond. The area was successfully reconstructed after the failure.

A.5.2 Site Geology and Soil Conditions

A field investigation conducted for the old tailings dam showed that the topography of the site was rather flat with less than 12 m of relief over more than a 1.6 km distance. The dam crest was at an elevation of 1006 m ± 6 m, while the iron spill area was at an elevation of 1000 m (see Figure A.45). The field investigation included two borings extending to bedrock, six borings drilled to retrieve relatively undisturbed iron tailings samples, and several soundings at the proposed location of the starter dyke to evaluate the thickness of the tailings (Robinson 1977). Locations of the boreholes and soundings are shown in Figure A.45.

Figure A.46 shows a cross-section (section B-B in Figure A.45) parallel to the containment dike. A relatively low permeable glacial till underlies the tailings, impeding dissipation of any generated excess pore water pressure. During operation of the tailings pond, technicians reported that the tailings liquefied beneath their feet while they conducted probes to evaluate the tailings thickness (Robinson 1977). An average effective friction angle of iron tailings, estimated from consolidated-undrained triaxial and direct shear tests, was about $\phi' = 38^{o}$, consistent with other iron tailings in the region (Davies et al. 1998). A relatively high friction angle for very loose tailings reflects the angular particle shape of the iron tailings (Robinson 1977). Figure A.47 shows the grain size distribution curve for the iron tailings.

A field investigation was conducted for the new iron tailings dam that was constructed in 1975 on the downstream side of the old tailings dam. The starter dyke for this new iron tailings dam was placed on the glacial till. The field investigation included 26 sampled boreholes and 42 piezocone soundings along the AIP dyke alignment. Of these, 11 boreholes and 12 piezocone soundings were conducted in close vicinity to the failed section (Davies et al. 1998).

Field investigations revealed that the failed dyke was founded on the previously deposited iron tailings. About 8 m of old iron tailings existed below the dykes constructed in 1979 and later, and about 7 m of relatively new iron tailings were present under the 1991 dyke addition. Summing the old and newer iron tailings, the total tailings thickness was about 15 m. The iron tailings were underlain by relatively dense and competent glacial till. A cross-section through the transverse to the dam (Figure A.48) shows these units.

As indicated by Robinson (1977), Davies et al. (1998) also designated the foundation iron tailings as very loose and weak. Most of the tailings showed $(N_1)_{60}$ values between 2 to 5 blows/ft although there are some high values on the order of 35 to 40 blows/ft. These high values may represent blow counts through compacted dyke extensions.

A.5.3 Description of Failure

As indicated in Section A.5.1, the old iron tailings dyke had experienced several liquefaction failures throughout its history, with the most devastating failure occurring in 1948. The field investigations conducted for both the old and new tailings dykes suggested that the iron tailings were very loose (Robinson 1977 and Davis 1998). Although each incremental raise was carefully monitored, an incremental raise of 2.4 m placed on August 23, 1991 caused the dyke to fail.

As shown in Figure A.48, portions of the dyke were intact even after the failure and flowed over the underlying tailings, suggesting that the tailings within the foundation underneath the dyke had liquefied. It is likely that the old iron tailings under the dyke liquefied when the new incremental raise was placed.

Davies et al. (1998) suggested that the static instability near the toe caused the flow liquefaction failure. In order to estimate the FS for static stability, a limit equilibrium analysis of pre-failure geometry was conducted. Analysis results show that the computed FS for a deep failure surface was about 1.5. However the FS decreased to unity as the failure surface moved closer to the toe of the tailings dam with the sliding surface passing through the lower portion of 1979 dyke section. Davies et al. (1998) concluded that the toe section of the dyke was already in a state of "losing equilibrium" and the additional load of the incremental raise accelerated the process.

Davies et al. (1998) stated: "Based on the analysis, it appeared that the mechanics of the event likely involved an initial event through the 1979 dyke at the toe. The sudden loss of toe resistance would then have significantly reduced the factor of safety of the remaining dyke section to below unity. This concept was indeed evaluated and it was shown that the computed factor of safety for a typical slip surface through the remaining intact section of the dyke was in the order of about 0.7 or lower, immediately after the toe moves away. Given that the tailings beneath the dyke were loose and saturated, the tailings would be subjected to undrained shear movements as this upper dyke section began moving. Excessive pore pressures would then be generated in response to the rapid shearing, and the tailings would eventually liquefy and undergo a significant loss of strength. Successively larger zones of the tailings would liquefy as the movements became more intense, with the zone of liquefaction progressing backwards into the slope. The entire process of progressive liquefaction can occur in a very short period of time."

Similar to Davies et al. (1998), Jefferies and Been (2006) suggested that the toe of the dyke failed first and then the failure surface retrogressed back in the more recent dykes. Jefferies and Been (2006) stated: "It appears that the toe area comprising the 1979 dyke and part of the 1986 dyke moved first, generally horizontally. The remaining dyke sections then failed by a combination of rotations and sliding, triggered by the loss of support at the toe."

It appears that both investigators, i.e., Davies et al. (1998) and Jefferies and Been (2006), agreed that the toe failed first, causing the large displacement of the 1979 and a

portion of 1986 dykes compared to the newer dyke sections. However, the author suggests another possibility, as follows. Because the 1991 dyke addition was constructed a significant distance upstream from the 1979 dyke (approximately 23 m from the 1991 centerline to the 1979 centerline), it is plausible that liquefaction occurred within the newer and old iron tailings below the 1991 and 1986 dykes. The tailings here were loose and susceptible to liquefaction, and a rapidly placed shear load (from the addition) could trigger an undrained response, liquefying the tailings. If liquefaction occurred over a relatively limited zone initially, yet the global FS remained greater than unity, shear stresses would be transferred downslope to the toe. The rapidly increasing shear stress at the toe of the 1979 dyke likely caused instability there (as the 1979 dyke was only marginally stable before the failure), causing the toe to fail first, consistent with the interpretation by Davies et al. (1988) and Jefferies and Been (2006). The remainder of the dykes then would have failed by rotation as a result of the removal of toe support and because the underlying tailings were already liquefied.

A.5.4 Representative Penetration Resistance

Davies et al. (1998) reported SPT and CPT penetration resistances *after* failure as shown in Figure A.48. Unfortunately, Davies et al. (1998) did not include horizontal penetration scales for the CPT soundings reproduced in Figure A.48, making it difficult to ascertain values of penetration resistance for specific subsurface layers. However, it can be seen clearly from these soundings that low values of CPT and SPT were measured within some zones in the old iron tailings (see Figure A.48). Complete CPT soundings were later published by Jefferies and Been (2006) as discussed below, while low values of $(N_1)_{60}$ ranging from 2 to 5 blows/ft were reported by Davies et al. (1998)for large portions of the tailings. A few high values of $(N_1)_{60}$ on the order of 35 to 40 blows/ft were also reported, which probably correspond to the compacted dykes (Davies et al. 1998).

Jefferies and Been (2006) discussed the CPT data that was part of the extensive investigation *after* failure. Forty-two CPTs were conducted during the investigation, of which 12 were conducted close to the failed zone. Figure A.49(a) shows the result of a CPT sounding that was conducted through the failed mass. Loose and dense layers of tailings are evident from the CPT data, but the zone from 10 to 12 m is consistently loose. Figure A.49(b) shows six CPT soundings in which three soundings were conducted at the pre-failure centerline position of the 1986 dyke while three soundings were conducted at the toe area. Soundings performed at the crest indicate loose tailings from depths of 8 to 14 m, while soundings performed at the toe indicate loose tailings throughout the entire depth of the soundings. Values of q_{c1} in the very loose to loose tailings ranged from 0.97 MPa to 2.26 MPa with a best estimate of about 1.38 MPa, while values of $(N_1)_{60}$ ranged from 2 to 5 blows/ft with a best estimate of 3 blows/ft, as suggested by Davies et al. (1998).

A.5.5 Yield Shear Strength and Strength Ratio

The pre-failure geometry of Sullivan tailings dam along with trial failure surfaces is reproduced in Figure A.50. As described above, the failure likely resulted from

liquefaction of old iron tailings below 1991 dyke when new incremental raise was being placed or due to the toe failure as discussed by Davies et al. (1998) and Jefferies and Been (2006). Therefore the slope stability search was constrained below the dykes in the old iron tailings, and in the toe area passing through 1986 dike, as illustrated in Figure A.50. As shown in Section A.5.2, the friction angle for old tailings was measured as $\phi' = 38^o$ (Robinson 1978). In the analyses performed in this study, the author assumed that all of the tailings below the water table were saturated and liquefiable. The author used a range of friction angles from $\phi' = 30^o$ to 38^o with $c' = 0$ for the mechanically-constructed and compacted dykes. The back-calculated yield shear strengths in the liquefied zone ranged from 21.3 kPa to 29.7 kPa depending on the failure surface locations. The best estimate of mobilized shear resistance in the liquefied zone was 25.8 kPa.

A second analysis was conducted to estimate the mobilized shear stress ratio at the triggering of liquefaction. The same trial failure surfaces described above were analyzed here. A shear stress ratio was assigned to the liquefied zone, and this value was varied until a FS of unity was achieved. A best estimate of yield shear stress ratio was estimated as 0.22, with a possible range of 0.18 to 0.295. The weighted average pre-failure vertical effective stress was determined as 84 kPa to 130 kPa.

A.5.6 Liquefied Shear Strength and Strength Ratio

The post-failure geometry of Sullivan tailings dam is reproduced in Figure A.51. Trial failure surfaces were derived from the post-failure morphology of the sliding mass and a slope stability search, as shown in Figure A.51, was conducted. A single arbitrary value of liquefied shear strength was assigned to liquefied zone and friction angles of $\phi' = 30^o - 38^o$ were assigned to non-liquefied dykes. The liquefied shear strength was varied until a factor of safety equal to unity is obtained. The resulting back-calculated liquefied shear strength was 5.45 kPa, with a range of 4.0 kPa to 6.4 kPa.

Using the same post-failure trial sliding surfaces shown in Figure A.51, a limit equilibrium back-analysis of the liquefied strength ratio was conducted. The length of the final failure surface was divided into 18 segments. All the segments were within the liquefied zone. The post-failure segments were assigned their pre-failure geometry positions based on the failure mode proposed by Davies et al. (1998) and Jefferies and Been (2006), as shown in Figure A.52, to calculate the pre-failure vertical effective stress for each slice. An arbitrary value of liquefied shear strength ratio was given to the liquefied soil zone, which in turn assigns different liquefied shear strength to each segment and analysis was run to calculate factor of safety. The liquefied shear strength ratio was then varied until a factor of safety equal to unity was obtained. Using the same assumptions made in the liquefied shear strength analysis, the liquefied strength ratio was estimated as 0.064, with a range of 0.046 to 0.075. The weighted average of vertical effective stress was estimated as 85.5 kPa.

A.5.7 Liquefied Shear Strength and Strength Ratio Considering Kinetics

The pre- and post- failure geometries were reproduced in Figure A.50 and Figure A.51, respectively. The initial result of the kinetics analysis assumed that all soils along the failure surface mobilized the liquefied shear strength. This inaccurately estimated the actual liquefied shear strength because a portion of the failed soils initially were above the phreatic surface and did not liquefy. Therefore, the liquefied shear strength was adjusted by using Eq. A.1 to account for the strength of the non-liquefied soils.

The analysis was focused on failure of all dykes and centroids were calculated for the pre- and post-failure geometries with the failure surfaces passing under all dykes as shown in Figure A.51. Approximately 5% of the post-failure sliding surface length involved soil mass above phreatic surface that was considered as non-liquefied. This length of the failure surface was assigned average shear strength of 30.7 kPa based on $\phi' = 38^{o}$ which was recommended by Robinson (1977). Further, the effect of the friction angle on the back-calculated shear strength was not very significant.

The kinetics analysis presented in Figure A.53 yielded the following results:

- Liquefied shear strength = 11.3kPa
- Liquefied shear strength ratio = 0.13

This liquefied shear strength resulted in a calculated displacement of the centroid of the failure mass of approximately 2.62 m vertically and 14.77 m horizontally.

The kinetics analysis only provided a value of liquefied shear strength. Therefore, the liquefied shear strength ratio reported above was determined by dividing the liquefied shear strength of 11.3 kPa by the weighted average vertical effective stress of 85.5 kPa obtained from the post-failure geometry analysis. These values of liquefied shear strength and strength ratio include the effects of kinetics and the shear strength of the soils that did not liquefy.

A.5.8 Sources of Uncertainty

The following sources of uncertainty were involved in estimating the yield shear strength and strength ratio: (1) the initial zone of liquefaction; (2) the position of the initial failure surface; (3) the shear strength of the non-liquefied soils and (4) phreatic surface within the dykes. It was assumed that all the tailings below the phreatic surface liquefied. The position of the initial failure surface was not known. Davies et al. (1998) and Jefferies and Been (2006) considered that the toe are liquefied and failed, triggering a retrogressive slope failure. In contrast, the author also considered that liquefaction occurred first under the 1991 dyke raise, and this loss of shearing resistance caused shear stresses to transfer to the toe area and trigger liquefaction below the toe, leading to the initial failure of the toe. The remainder of the dykes then failed as the slides retrogressed into the pond. The unsaturated fill was assigned $\phi' = 30^{o} – 38^{o}$. Although the pore water pressures were regularly monitored in the tailings dam using piezometers, a complete

phreatic surface was not given in the literature. A likely phreatic surface was therefore used in the analysis.

The following sources of uncertainty were involved in estimating the liquefied shear strength and strength ratio: (1) the limits of the zone of liquefaction; (2) the phreatic surface within dykes; (3) the pre-failure slice positions; and (4) the position and path of the centroid. As discussed above, all of the tailings below the phreatic surface were assumed to liquefy. A complete phreatic surface for the post failure geometry was not given. The author therefore considered most likely phreatic surface based on pre- and post-failure geometry. The positions of post-failure geometry segments were arranged in the pre-failure geometry by estimating the locations of the dykes interpreted from failed mass as shown in Davies et al. (1998) and Jefferies and Been (2006). Centroid positions and travel path was considered by the movement of all of the dykes.

The following sources of uncertainty were involved in determining the "representative" values of penetration resistance: (1) the penetration resistance scale for SPT bore logs was missing; (2) the consistency in penetration resistance (i.e., the source of the high values); and (3) the locations of the penetration tests. Because the SPT blow count scale was not given in the literature, the "representative" blow counts were taken directly from the range reported by Davies et al. (1998). Penetration resistance given in Figure A.49 show that tip resistance given by CP91-29 is much lower than the other two, CP91-27 and CP91-28, at the same depth. However, the locations of CP91-27 and CP91-28 are not reported in the literature. Therefore "representative" penetration resistance was based on CP91-29.

A.6 Kushiro-Oki Earthquake Case Histories, Japan[3]

A.6.1 Introduction

The 1993 Kushiro-oki earthquake (Mw = 7.6, Mj = 7.8) of January 15, 1993, caused significant damage to the city of Kushiro, Hokkaido, which is only 14 km from the epicenter, and nearby areas. Two persons were killed, 932 were injured, and 3471 homes were damaged. The total economic loss due to the earthquake was estimated at about US $180 million (EERI 1993, Sasaki et al. 1993). Besides this serious damage, river and road embankments also failed in strongly shaken areas.

Among the river dikes that failed during the earthquake, about 76% of the total damage was suffered by two river dikes: those along the Kushiro River (44%) and those along the Tokachi River (32%). Damage to downstream portions of the Kushiro River dikes occurred at 28 places over a total length of 11.2 km. The Tokachi River dikes suffered some damage along its middle and lower reaches. These failures occurred at 20 locations over a total length of 9.2 km (Sasaki et al. 1993). Three dike failures, at one location along the Kushiro River where dikes on both the left and right banks of the river

[3] Five case histories that failed during Kushiro-Oki earthquake are discussed in this study. A general introduction, geology, estimation of ground motions, and description of the failures is provided here. These sections will not be repeated for individual case histories.

failed, and one location along the Tokachi River where the dike along the right bank of the river failed, are analyzed in this study. Figure A.54 shows the locations of these failures and Table A.1 lists the analyzed river dikes.

Several highways embankments in the affected area also suffered damage from strong shaking. Two embankment locations are studied here: Pashikuru in the city of Shiranuka on Route 38; and Itoizawa in the city of Akkeshi on Route 44. (Sasaki et al. 1993). Figure A.54 includes the locations of these road embankments.

As in past earthquakes, soil liquefaction seemed to be one of the key factors triggering embankment failure, although sand boil were not widely observed because the ground surface was frozen to some depth and covered by snow at the time of the earthquake.

A.6.2 Site Geology and Soil Conditions

The Kushiro River enters the Pacific Ocean at the city of Kushiro running through the Kushiro Marsh, which covers an area of about 204 km^2. Dikes along the Kushiro were constructed using sandy fill on the soft ground of the Kushiro Marsh. The foundation consists of a 3 to 5 m thick peat layer underlain by a thin (less than 1m thick) sand layer and a thick soft clayey soil. The total thickness of the soft layers exceeds 50 m (Sasaki et al. 1993, Finn 1998, and Kano et al. 2007). The peat settled 2 m to 3 m under the weight of dikes before the earthquake. This settlement caused two important effects. First, it raised the water level inside the dike fill, thereby creating a potentially liquefiable zone in the lower portion of embankment fill. Second, because the embankment fill was placed on soft peat layer it is likely that the proper compaction could not be achieved; therefore, low N-values for the embankment fill were observed. Noto and Kumagai (1985) suggested that Hokkaido peat does not lose strength during cyclic loading, suggesting that this layer likely was not directly responsible for the observed failures. Further, lack of uplift of the foundation soils at the toe of the failed masses also suggests that it is unlikely that liquefaction occurred in the alluvial sand layer (Finn 1998).

All of the three failures analyzed in this study consist of flat deposited layers near the ground surface. A 1 to 4 m thick peat layer covers the underlying layers of alluvial sand and clay at the failure locations. The thickness of the upper sand layer varies from 2 m to 10 m at locations along these embankments. Beneath these layers lies a 20-30 m thick clay layer that contains a thin sand layer (Sasaki et al. 1993; Sasaki et al. 1995).

Figure A.55 presents ranges of grain size distributions for the failed reaches of the Kushiro and Tokachi River dikes (Sasaki et al. 1993). The fill sands at the location of the dike failure along the right bank of the Kushiro River show a D_{50} range of about 0.21 to 1.0mm with an average value of 0.6mm. The fill sands at the dike failure along the left bank of the Kushiro River show a D_{50} range of about 0.06 to 1.1mm with an average value of 0.6mm. Sasaki et al. (1995) suggested that the FC of the fill sand ranges from 5 to 25% at the dike failure at the left bank of the Kushiro River. The fill sands used at the failure location of the Tokachi River dike shows a D_{50} range of about 0.1 to 0.2mm with

an average value of 0.15mm. In general, these grain size ranges fall within the range of grain sizes that are easily liquefied (Tsuchida 1970).

The soil profiles under both road embankment fills consist primarily of layers of sand and clay, but a 3 m thick peat layer was present at the original ground surface at Route 44. Sasaki et al. (1993) presented several grain size distribution curves (as shown in Figure A. 56) for the fill materials used for the Route 38, Pashikuru embankment. The D_{50} values ranges from about 0.08 to 1.7 mm with an average value of 0.6mm. The fines content of the fill commonly is about 20%, but can range as high as 50%.

A.6.3 Estimation of Ground Motions

Details related to the earthquake are as follows (Sasaki et al. 1993):

Date and Time: 1993 01 15; 20: 16
Location: 42°51'N, 144°23'E
Magnitude: 7.6
Region: Hokkaido, Japan
Fault Mechanism: Strike-Slip Fault

The source area is one of the major earthquake zones in Japan. The subduction zone between the North American plate and the Pacific Ocean plate runs off Hokkaido's southeast shore, and several damaging earthquakes occurred in this zone, with some as recently as in the past several decades (Sasaki et al. 1993).

Ground motions during Kushiro-Oki earthquake were recorded at more than 180 sites. Sasaki et al. (1993) plotted the PGA observed at the ground floors of buildings or at ground surface against epicentral distance (see Figure A.57). Peak ground accelerations are calculated by using the attenuation relationship developed by PWRI (1985) and given in Sasaki et al. (1993) for different cases analyzed in this study.

A.6.4 Description of the Failures

As stated above, the river dikes were founded on a layer of peat and settled substantially after construction. As a result, a perched watertable formed at the base of the levees (see Figure A.58).Although the peat layer under the dikes had fairly low little strength in its original state, it was consolidated by the dike weight, and Sasaki et al. (1993, 1995) illustrated that Hokkaido peat does not lose strength during cyclic loading (Sasaki et al. 1993 and 1995). Further, there was no evidence of the failure surface passing through the peat layer. Therefore, Sasaki et al. (1995) suggested that it was unlikely that the dike failures were caused by failure in the peat layer. Although heaving was frequently seen in the case of foundation failure of embankments on soft soils, it was not observed along the right bank of Kushiro River, while sand boils were observed along the left bank of the Kushiro River and along the Tohnai dike of Tokachi River (Sasaki et al. 1993).

The two road embankments analyzed here experienced flowslides with toe displacements of several meters. Sasaki et al. (1993) reported that most of the damage was observed in embankment sections at sites with special geomorphology, such as embankments crossing streams from the outlets of small valleys, or embankments in swampy areas.

A.6.5 Dike along the Right Bank of the Kushiro River

The foundation of the dike along the right bank consists of a 3 to 5m-thick peat layer underlain by a thin (less than 1m thick) sand layer and thick soft clayey soil. Total thickness of the soft layers exceeds 50m (Sasaki et al. 1993).

The section of the dike along the right bank of the river before the earthquake was 6.5m high, and 8m and 50m wide at the crest and base, respectively. Figure A.58 illustrates the section after the earthquake. Longitudinal cracks formed at both crest shoulders and on the river side slope, and the crest settled about 0.7m. One of the cracks at the crest was 1.2m wide and more than 4.4m deep. Near the toe, the side slope heaved about 0.6m.

As described by Sasaki et al. (1993), "The ground surface was frozen to a depth of about 60-70cm, judging from observations at the open crack. A covering of snow made it difficult, just after the event, to find evidence of sand boiling." As defined in Section A.6.4, strength loss due to cyclic loading was unlikely in the peat layer, strongly suggested that the liquefaction occurred in the dike fill below the phreatic surface.

A. 6.5.1 Representative Penetration Resistance

Sasaki et al. (1993) presented the results of seven borings with SPT conducted along the dike *after* the failure, as illustrated in Figure A.58. Sasaki et al. (1993) did not report the SPT hammer type. Japanese practice commonly employs either donut Tombi or donut slip-rope (with 2 turns) hammers (Skempton 1986). The first method produces hammer energy of about 78% while the second method produces an energy of about 65%. These hammer energies yield energy ratios of 1.3 and 1.1 respectively. Therefore, the author used an average energy ratio of 1.2 to calculate N_{60} values from raw blow counts. For all stress computations, the author used a saturated unit weight of 18.5 kN/m^3.

The $(N_1)_{60}$-values in the dike fill below the phreatic surface ranged from approximately from 0 to 4 blows/ft, with a best estimate of 3 while N-values as high as 8 blows/ft were obtained in the fill above the phreatic surface.

Cone penetration tests were not conducted at the failed dike along the right bank of the Kushiro River. Therefore, values of q_{c1} were estimated using $q_c/N_{60} = 0.57$ using a $D_{50} = 0.6$ mm (i.e., the average of the q_c/N_{60} ratios from Robertson and Campanella 1985, Seed and De Alba 1986, Andrus and Youd 1989, Kulhawy and Mayne 1990, and Stark and Olson 1995). This value of $D_{50} = 0.6$ mm was selected visually as the average of the grain size distribution curves of the fill soils presented in Figure A.57 (Sasaki et al.

1993). This calculation yielded average, lower bound, and upper bound values of q_{c1} of approximately 1.7, 0, and 2.3 MPa, respectively.

A. 6.5.2 Yield Shear Strength and Strength Ratio

The mechanism that likely triggered flow failure is seismic liquefaction of the saturated sandy fill of the lower, saturated portion of the dike (Sasaki et al. 1993). As explained in Chapter 2, the shear strength and strength ratio mobilized at the instant of failure in cases where liquefaction is triggered by seismic loading do not necessarily represent the yield shear strength and strength ratio.

The pre-failure geometry of the dike along the right bank of the Kushiro River is reproduced in Figure A.59. A slope stability search was conducted to locate an initial failure surface that was consistent with the pre- and post-failure geometry. All saturated fill was assumed to liquefy and a single value of shear strength was assigned to the liquefied soil. Fill soil initially above the phreatic surface was assigned a drained friction angle of 28º to 32º based on its low penetration resistance. The lower bound, upper bound, and mean values of mobilized shear strength in the zone of liquefaction are 8.0, 10.5, and 9.5 kPa, respectively.

A second analysis was conducted to estimate the strength ratio mobilized at the triggering of liquefaction. Identical assumptions regarding the failure surface and shear strength of the non-liquefied soil were used for this analysis. The lower bound, upper bound, and mean values of mobilized shear strength ratio in the zone of liquefaction are 0.16, 0.195, and 0.19 respectively, depending on the shear strength of the unsaturated fill and the location of the failure surface. The weighted average pre-failure vertical stress in the liquefied segment was determined as 50 kPa.

A. 6.5.3 Liquefied Shear Strength and Strength Ratio

The post-failure geometry of the dike along the right bank is reproduced in Figure A.60. The critical failure surface derived from the post-failure morphology of the sliding mass and a slope stability search is shown in Figure A.60. A single arbitrary value of liquefied shear strength is assigned to liquefied zone and a friction angle of $\phi' = 28º$ to 32º was assigned to the non-liquefied zone. The liquefied shear strength was varied until a factor of safety equal to unity was obtained. The resulting back-calculated liquefied shear strength was 4.9 kPa, with a range from 4.7 to 5.0 kPa.

Using the same post-failure trial sliding surfaces shown in Figure A.60, a limit equilibrium back-analysis of the liquefied strength ratio of the failed right bank was conducted. The length of the final failure surface was divided into 12 segments. Segment 1 corresponds to the dike material above the phreatic surface that was assigned $\phi' = 28º$ to 32º. The remaining segments from 2 to 12 are within the liquefied zone. Because the liquefied soil experienced limited movement, it was assumed that the post-failure slice positions were very close to their pre-failure positions. Therefore these segments were arranged in the liquefied zone of the pre-failure geometry as shown in Figure A.60, to

calculate the pre-failure vertical effective stress for each slice. An arbitrary value of liquefied shear strength ratio was given to the liquefied soil zone, which in turn assigns different liquefied shear strength to each segment. A limit equilibrium analysis was run to calculate the factor of safety. The liquefied shear strength ratio was varied until a factor of safety equal to unity was obtained. Using the same assumptions made in the liquefied strength analysis, the liquefied strength ratio was estimated as 0.067, with a range from 0.065 to 0.068. The weighted average vertical effective stress was estimated as 73 kPa.

A. 6.5.4 Liquefied Shear Strength and Strength Ratio Considering Kinetics

Limited movement occurred in the failed dike along the right bank of the Kushiro River in part because of the frozen surface layer which prevented the liquefied material from flowing significantly (Sasaki et al. 1995). Because of this limited movement, a kinetics analysis could not be conducted.

A. 6.5.5 Sources of Uncertainty

The following sources of uncertainty were involved in estimating the yield shear strength and strength ratio: (1) the initial zone of liquefaction; (2) the position of the initial failure surface; (3) the shear strength of the non-liquefied soils; and (4) the potential drainage during failure. It was assumed that all fill soil below the phreatic surface liquefied. The position of the initial failure surface was not known. However, using a slope stability search and comparing this to the post-failure morphology allowed some confidence in locating the yield failure surface. The unsaturated fill was assigned $\phi' = 28^o$ to 32^o.

The following sources of uncertainty were involved in estimating the liquefied shear strength and strength ratio: (1) the limits of the zone of liquefaction; (2) the shear strength of the non-liquefied soils, and (3) the potential for void and pore water pressure redistribution. As discussed above, all fill below the phreatic surface was assumed to liquefy. The unsaturated fill was assigned $\phi' = 28^o$ to 32^o.

The following sources of uncertainty were involved in determining the "representative" values of penetration resistance: (1) effects of flow and reconsolidation on penetration resistance because the penetration tests were conducted after failure; and (2) the conversion of SPT values to CPT values. "Representative" CPT values were obtained by converting SPT blow count to CPT tip resistance. This step involves an unknown level of uncertainty, in part because of the range of grain sizes reported.

A.6.6 Dike along the Left Bank of the Kushiro River

The dike along the left bank of the Kushiro River was about 7m high, 8m at the crest, and 50m wide at the base. The failed dike section was underlain by soil similar to the soils underlying the dike along the right bank, except that sand layer beneath the peat is thicker than that of the right bank foundation (Sasaki et al. 1993). As shown in Figure A.61, the soil profile in this area consists of flat-lying layers near the ground surface. A 3

to 4 m thick peat layer covers the underlying layers of alluvial sand and clay. The thickness of the upper sand layer varies from 2 m to 10 m at below the dike. Beneath these layers, a 20 to 30 m thick clay layer containing a thin sand layer is encountered. The low SPT N-values (5 to 15 blows/ft) of the upper part of the alluvium sand layer indicate that the material is relatively loose, but the lower part of the same layer in some thicker sections had SPT N-values of more than 20 (Sasaki et al. 1995).

As shown in Figure A.61, the failure mode of this section was similar to that of the dike along the right bank. The settlement of the crest ranged from 1.5 to 2m, and cracks along the crest were up to 1.5 to 2m wide and 4 to 5m deep (Sasaki et al. 1993). Longitudinal fissures were found along the shoulders and in the middle of the crest. Fissures along the shoulders approached 0.7m deep with vertical offsets of as much as 1m. The peak ground acceleration at the site was about 0.36g, based on regional recorded ground motions (Figure A.55; Sasaki et al. 1993).

Prior to the earthquake, settlement of dike due to the consolidation of the foundation brought the lower part of the dike below the water level, saturating the lower part of the fill. The ground water level measured in boring after the earthquake is illustrated in Figure A.61. Excavation of some of the damaged spots revealed signs of sand boils from cracks in the lower part of the dike. This indicates that the damage was caused by liquefaction in the part of the dike that had settled into the peat layer, as shown in Figure A.61 (Sasaki et al. 1995). As defined in Section A.6.4, strength loss due to cyclic loading was not likely in the peat layer, strongly supporting a liquefaction triggering mechanism in the fill below the phreatic surface.

A. 6.6.1 Representative Penetration Resistance

Sasaki et al. (1993) presented the results of seven borings with SPT conducted along the dike *after* the failure, as illustrated in Figure A.61. The author used an average energy ratio of 1.2 to calculate N_{60} values as explained in Section A. 6.5.1. For all stress computations, the author used a saturated unit weight of 18.5 kN/m^3. The $(N_1)_{60}$-values in dike fill below the phreatic surface were ranged from approximately 2 to 7 blows/ft, with a best estimate of 3.

Cone penetration tests were not conducted at the site. Therefore, values of q_{c1} were estimated using $q_c/N_{60} = 0.57$ using a $D_{50} = 0.6$ mm (i.e., the average of the q_c/N_{60} ratios from Robertson and Campanella 1985, Seed and De Alba 1986, Andrus and Youd 1989, Kulhawy and Mayne 1990, and Stark and Olson 1995). This value of $D_{50} = 0.6$ mm was selected visually as the average of the grain size distribution curves of the fill soils presented in Figure A.57 (Sasaki et al. 1993). This calculation yielded average, lower bound, and upper bound values of q_{c1} of approximately 1.7, 1.14 and 4 MPa, respectively.

A. 6.6.2 Yield Shear Strength and Strength Ratio

The mechanism that likely triggered flow failure is seismic liquefaction of the saturated sandy fill of the lower portion of the dike (Sasaki et al. 1993, 1995). As explained in Chapter 2, the shear strength and strength ratios mobilized at the instant of failure in cases where liquefaction is triggered by seismic loading do not necessarily represent yield shear strength and strength ratios.

The pre-failure geometry of the dike on the left bank of the Kushiro River is reproduced in Figure A.62. A slope stability search was conducted to locate an initial failure surface that was consistent with the pre- and post-failure geometry. All saturated fill was assumed to liquefy and a single value of shear strength was assigned to the liquefied soil. Fill soil initially above the phreatic surface was assigned a drained friction angle of 28° to 32°, based on its low penetration resistance. The lower bound, upper bound, and mean values of mobilized shear strength in the zone of liquefaction are 5.0 kPa, 8.2 kPa, and 7.3 kPa respectively.

A second analysis was conducted to estimate the strength ratio mobilized at the triggering of liquefaction. Identical assumptions regarding the failure surface and shear strength of the non-liquefied soil were used for this analysis. The mobilized shear strength ratio averaged 0.117, with a range from 0.07 to 0.118, depending on the shear strength of the unsaturated fill and the location of the failure surface. The weighted average pre-failure vertical stress in the liquefied zone was determined as 73 kPa.

A. 6.6.3 Liquefied Shear Strength and Strength Ratio

The post-failure geometry of dike on the left bank of the Kushiro River is reproduced in Figure A.63. The critical failure surface was derived from the post-failure morphology of the sliding mass and a slope stability search, and is shown in Figure A.63. A single arbitrary value of liquefied shear strength was assigned to liquefied zone and friction angles of $\phi' = 28^{o}$ to 32^{o} were assigned to non-liquefied soils. The liquefied shear strength was varied until a factor of safety equal to unity was obtained. The resulting back-calculated liquefied shear strength was 2.2 kPa, with a range from 1.6 to 2.8 kPa.

Using the same post-failure trial sliding surfaces shown in Figure A.63, a limit equilibrium back-analysis of the liquefied strength ratio of the dike on the left bank of the river was conducted. The length of the final failure surface was divided into 12 segments. Segments 1, 2, and 12 correspond to fill above the phreatic surface and were assigned $\phi' = 28^{o}$ to 32^{o}. The remaining segments (3 to 11) are within the liquefied zone. Because the liquefied soil experienced limited movement, it was assumed that the post-failure slice positions were close to their pre-failure positions. Therefore these segments were arranged in the liquefied zone of the pre-failure geometry as shown in Figure A.63 to calculate the pre-failure vertical effective stress. An arbitrary value of liquefied shear strength ratio was given to the liquefied soil zone, which in turn assigned different liquefied shear strength to each segment and analysis was run to calculate factor of safety. The liquefied shear strength ratio was then varied until a factor of safety equal to

unity is obtained. Using the same assumptions made in the liquefied shear strength analysis, the liquefied strength ratio was estimated as 0.026, with a range from 0.019 to 0.033. The weighted average of vertical effective stress was estimated as 85.5 kPa.

A. 6.6.4 Liquefied Shear Strength and Strength Ratio Considering Kinetics

Limited movement occurred in the failed dike along the left bank of the Kushiro River in part because of the frozen surface layer which prevented the liquefied material from flowing significantly (Sasaki et al. 1995). Because of this limited movement, a kinetics analysis could not be conducted.

A. 6.6.5 Sources of Uncertainty

The following sources of uncertainty were involved in estimating the yield shear strength and strength ratio: (1) the initial zone of liquefaction; (2) the position of the initial failure surface; (3) the shear strength of the non-liquefied soils; and (4) the potential for drainage during failure. It was assumed that all of the fill below the phreatic surface liquefied. The position of the initial failure surface was not known. However, using a slope stability search and comparing this to the post failure morphology allowed some confidence in locating the yield failure surface. The unsaturated fill was assigned $\phi' = 28^o$ to 32^o.

The following sources of uncertainty were involved in estimating the liquefied shear strength and strength ratio: (1) the limits of the zone of liquefaction; (2) the shear strength of the non-liquefied soils, and (3) the potential for void and pore water pressure redistribution. As discussed above, all fill below the phreatic surface was assumed to liquefy. The unsaturated fill was assigned $\phi' = 28^o$ to 32^o.

The following sources of uncertainty were involved in determining the "representative" values of penetration resistance: (1) effects of flow and reconsolidation on penetration resistance because the penetration tests were conducted after the failure; and (2) the conversion of SPT values to CPT values. "Representative" CPT values were obtained by converting SPT blow count to CPT tip resistance. This step involves an unknown level of uncertainty, in part because of the range of grain sizes reported.

A.6.7 Tonhai Dike along the Right Bank of the Tokachi River

The failed portion of the Tonhai dike on the right bank of the Tokachi River was 8 to 11m high, 3 to 6m wide at its crest, and about 30m wide at its base. The embankment is underlain by soil similar to that found below the dikes on the right and left banks of the Kushiro River, except that the near surface foundation sand and clay layers are thin. As shown in Figure A.64, the soil profile in this area consists of a 6m thick peat layer, underlain by a 6 to 7m of clayey soil interfingered with sand layers. A gravelly stratum with $N > 50$ (Sasaki et al. 1993) is located below the clay. The Tohnai dike was damaged over a 12.5 km-long reach along the right bank of the Tokachi River. The failure from station 31,774 to station 33,264 is examined here. This section of the Tohnai dike is

located along a channelized section of the river that was excavated from 1929 to 1937 adjacent to a swampy area.

Longitudinal fissures were observed along the dike shoulders, along the crest, and along the landward side berm. The fissures were typically less than 0.4 m wide, but extended from 400 to 500 m along the length of the dike. The depths of the fissures reached 0.7m, and the vertical offsets reached about 1 m (Sasaki et al. 1993).

Blue and black-colored sands boils were found near the toe of the river side slope of the dike between stations 32,000 and 32,200. Adjacent to this reach, from station 32,400 to 33,000, the cracks became wider and deeper, with larger vertical offsets approaching 2 to 3m, as shown in Figure A.64. As defined in Section A.6.4, strength loss due to cyclic loading was not likely in the peat layer, thus it is likely that liquefaction occurred in the dike fill below phreatic surface.

A. 6.7.1 Representative Penetration Resistance

Sasaki et al. (1993) presented the results of five borings with SPT conducted along the embankment *after* the failure, as illustrated in Figure A.64. The author used an average energy ratio of 1.2 to calculate N_{60} values from raw blow counts as explained in Section A. 6.5.1. For all stress computations, author used a saturated unit weight of 18.5 kN/m^3. The $(N_1)_{60}$-values in dike fill below phreatic surface ranged from 5 to 11 blows/ft, with a best estimate of 6 blows/ft.

Cone penetration tests were not conducted at the site. Therefore, values of q_{c1} were estimated using $q_c/N_{60} = 0.4$ using a $D_{50} = 0.15$ mm (i.e., the average of the q_c/N_{60} ratios from Robertson and Campanella 1985, Seed and De Alba 1986, Andrus and Youd 1989, Kulhawy and Mayne 1990, and Stark and Olson 1995). This value of $D_{50} = 0.15$ mm was selected visually as the average of the grain size distribution curves of the fill soils presented in Figure A.57 (Sasaki et al. 1993). This calculation yielded average, lower bound, and upper bound values of q_{c1} of approximately 2.4, 2.0 and 5.2 MPa, respectively.

A. 6.7.2 Yield Shear Strength and Strength Ratio

The mechanism that likely triggered flow failure is seismic liquefaction of the sandy fill in the lower, saturated portion of the dike (Sasaki et al. 1993). As explained in Chapter 2, the shear strength and strength ratios mobilized at the instant of failure in cases where liquefaction is triggered by seismic loading do not necessarily represent yield shear strength and strength ratios.

The pre-failure geometry of the Tohnai dike located along the right bank of the Tokachi River is reproduced in Figure A. 65. A slope stability search was conducted to locate initial failure surface that was consistent with the pre- and post-failure geometries. All saturated fill was assumed to liquefy and a single value of shear strength was assigned to the liquefied soil. Fill soil initially above the phreatic surface was assigned a

drained friction angle of 28º to 32º, based on its low penetration resistance. The lower bound, upper bound, and mean values of mobilized shear strength in the zone of liquefaction are 8.5, 10.5, and 9.7 respectively.

A second analysis was conducted to estimate the strength ratio mobilized at the triggering of liquefaction. Identical assumptions regarding the failure surface and shear strength of the non-liquefied soil were used for this analysis. The lower bound, upper bound, and mean values of mobilized shear strength ratio in the zone of liquefaction are 0.107, 0.121 and 0.116 respectively, depending on the shear strength of the unsaturated fill and the location of the failure surface. The weighted average pre-failure vertical stress in the liquefied zone was determined as 81 kPa.

A. 6.7.3 Liquefied Shear Strength and Strength Ratio

The post-failure geometry of Tohnai dike on the right bank of the Tokachi River is reproduced in Figure A.66. The critical failure surface shown in Figure A.66 was derived from the post-failure morphology of the sliding mass and a slope stability search A single arbitrary value of liquefied shear strength was assigned to the liquefied zone and friction angles of $\phi' = 28º$ to 32º were assigned to the non-liquefied zone. The liquefied shear strength was varied until a factor of safety equal to unity was obtained. The resulting back-calculated liquefied shear strength was 3.4 kPa, with a range from 2.9 to 4.56 kPa.

Using the same post-failure trial sliding surfaces shown in Figure A.66, a limit equilibrium back-analysis of the liquefied strength ratio of the dike was conducted. The final failure surface was divided into 13 segments. Segments 1 and 13 correspond to the embankment material above the phreatic surface and were assigned $\phi' = 28º$ to 32º. The remaining segments from 2 to 12 are within the liquefied zone. Because the liquefied soil experienced limited movement, it was assumed that the post-failure slice positions were close to their pre-failure positions. Therefore these segments were arranged in the liquefied zone of the pre-failure geometry as shown in Figure A.66 to calculate the pre-failure vertical effective stress. An arbitrary value of liquefied shear strength ratio was given to the liquefied soil zone, which in turn assigne different liquefied shear strength to each segment and analysis was run to calculate factor of safety. The liquefied shear strength ratio was then varied until a factor of safety edqual to unity was obtained. Using the same assumptions made in the liquefied shear strength analysis, the liquefied strength ratio was estimated as 0.032, with a possible range from 0.027 to 0.043. The weighted average of vertical effective stress was estimated as 106 kPa.

A. 6.7.4 Liquefied Shear Strength and Strength Ratio Considering Kinetics

Limited movement occurred in the Tohnai dike along the right bank of the Tokachi River in part because of the frozen surface layer which prevented the liquefied material from flowing significantly (Sasaki et al. 1995). Because of this limited movement, a kinetics analysis could not be conducted.

A. 6.7.5 Sources of Uncertainty

The following sources of uncertainty were involved in estimating the yield shear strength and strength ratio: (1) the initial zone of liquefaction; (2) the position of the initial failure surface; (3) the shear strength of the non-liquefied soils; and (4) the potential for drainage during failure. It was assumed that all fill soil below the phreatic surface liquefied. The position of the initial failure surface was not known. However, using a slope stability search and comparing this to the post failure morphology allowed some confidence in locating the yield failure surface. The unsaturated fill was assigned $\phi' = 28^o$ to 32^o.

The following sources of uncertainty were involved in estimating the liquefied shear strength and strength ratio: (1) the limits of the zone of liquefaction; (2) the shear strength of the non-liquefied soils, and (3) the potential for void and pore water pressure redistribution. As discussed above, all fill below the phreatic surface was assumed to liquefy. The unsaturated fill was assigned $\phi' = 28^o$ to 32^o.

The following sources of uncertainty were involved in determining the "representative" values of penetration resistance: (1) effects of flow and reconsolidation on penetration resistance because the penetration tests were conducted after the failure; and (2) the conversion of SPT values to CPT values. "Representative" CPT values were obtained by converting SPT blow count to CPT tip resistance. This step involves an unknown level of uncertainty, in part because of the range of grain size reported.

A.6.8 Pashikuru Embankment (Route 38)

An embankment failed at Pashikuru on Route 38 in the town of Shiranuka (see Figure A.67). This embankment is located at the outlet of a small valley. While defining the failure of Route 38 embankment Sasaki et al. (1993) described as: "A lane for slow vehicles, which was added to the downstream side of two existing lanes, slid down. The original height of the added embankment was about 13m. The length of the slide was about 45m, the depth about 4m. The failed mass of soil flowed about 65m (as measured from the pre-failure crest to post-failure toe). The mass of soil within half of this distance was almost saturated and looked to muddy, while blocks which had kept the original shape of slope surface were mixed in the mass." As an alternate measure of displacement, the failed mass displaced 39 m measured from the pre-failure toe to the post-failure toe. When measured from the midpoint of the slope to the base of sliding surface, the depth of the failure is about 3.8 m.

Fissures up to 100 m long formed parallel to the roadway in the remaining traffic lanes. These fissures were 20 to 30 cm wide with vertical offsets of about 20 to 50 cm. The embankment foundation consists of peat, gravel and cohesive soil layers with SPT blow counts of about 10 (Sasaki et al. 1993). The embankment material was well graded silty, sandy gravel to a gravelly, sandy silt with some clay (FC = 20% to 50%), as shown in Figure A. 56. As defined by Sasaki et al. (1993), "…because this portion of the

embankment was located at the outlet of a small valley, drainage from the embankment was installed. However it did not seem to work well, judging from the muddy state of the failed soil." As discussed in Section A.6.4, strength loss due to cyclic loading was unlikelyin the peat layer, strongly suggesting that liquefaction occurred in the embankment fill below the phreatic surface.

A. 6.8.1 Representative Penetration Resistance

Sasaki et al. (1993) presented the results of two borings with SPT conducted along the embankment *after* the failure, as illustrated in Figure A.67. The author used an average energy ratio of 1.2 to calculate N_{60} values from raw blow counts as explained in Section A. 6.5.1. For all stress computations, the author used a saturated unit weight of 18.5 kN/m^3. Unfortunately there was only a single N-value available in the failed mass; therefore the $(N_1)_{60}$-value of about 3 blows/ft was selected as representative penetration resistance.

Cone penetration tests were not conducted at the site. Therefore, values of q_{c1} were estimated using $q_c/N_{60} = 0.56$ using a $D_{50} = 0.6$ mm (i.e., the average of the q_c/N_{60} ratios from Robertson and Campanella 1985, Seed and De Alba 1986, Andrus and Youd 1989, Kulhawy and Mayne 1990, and Stark and Olson 1995). This value of $D_{50} = 0.6$ mm was selected visually as the average of the grain size distribution curves of the fill soils presented in Figure A.55 (Sasaki et al. 1993). This calculation yielded a q_{c1} of 1.68 MPa.

A. 6.8.2 Yield Shear Strength and Strength Ratio

The mechanism that likely triggered flow failure is seismic liquefaction of the sandy fill in the lower, saturated portion of the embankment (Sasaki et al. 1993). As explained in Chapter 2, the shear strength and strength ratios mobilized at the instant of failure in cases where liquefaction is triggered by seismic loading do not necessarily represent yield shear strength and strength ratios.

The pre-failure geometry of the Route 38 Pashikuru embankment is reproduced in Figure A.68. A slope stability search was conducted to locate initial failure surfaces that are consistent with the pre- and post-failure geometries. Because a complete phreatic surface was not available, several possible ground water tables within the road embankment were considered. In addition, all saturated fill was assumed to liquefy and a single value of shear strength was assigned to the liquefied soil. Fill soil initially above the phreatic surface was assigned a drained friction angle of 28º to 32º, based on low penetration resistance. Different phreatic surfaces employed in this study also account for the drainage at the toe indirectly. The lower bound, upper bound, and mean values of mobilized shear strength in the zone of liquefaction are 21 kPa, 22.5 kPa, and 21.5 kPa, respectively.

A second analysis was conducted to estimate the strength ratio mobilized at the triggering of liquefaction. Identical assumptions regarding the failure surface and shear strength of the non-liquefied soil were used for this analysis. The lower bound, upper

bound, and mean values of mobilized shear strength ratio in the zone of liquefaction are 0.22, 0.245, and 0.24 respectively, depending on the shear strength of the unsaturated fill and the location of the failure surface. The weighted average pre-failure vertical stress in the liquefied zone was determined as 77 kPa.

A. 6.8.3 Liquefied Shear Strength and Strength Ratio

The post-failure geometry of the Route 38 Pashikuru embankment is reproduced in Figure A.69. The critical failure surface shown in Figure A.69 was derived from the post-failure morphology of the sliding mass and a slope stability search. A single arbitrary value of liquefied shear strength was assigned to liquefied zone and friction angles of $\phi' = 28^{o}$ to 32^{o} were assigned to non-liquefied zone. Liquefied shear strength was varied until a factor of safety equal to unity was obtained. The resulting back-calculated liquefied shear strength was 4.6 kPa, with a range from 2.65 to 5.78 kPa.

Using the same post-failure trial sliding surfaces shown in Figure A.69, a limit equilibrium back-analysis of the liquefied strength ratio of the upstream slope was conducted. The length of the final failure surface was divided into 12 segments. Segment 1 corresponds to the embankment material above the phreatic surface and was assigned $\phi' = 28^{o}$ to 32^{o}. Segment 2 was varied between its liquefied shear strength and $\phi' = 28^{o}$ to 34^{o} depending on its position in the pre-failure geometry. The remaining segments from 3 to 12 are within the liquefied zone. These segments were arranged in the liquefied zone of the pre-failure geometry as shown in Figure A.68 to calculate the pre-failure vertical effective stress. An arbitrary value of liquefied shear strength ratio was given to the liquefied soil zone, which in turn assign different liquefied shear strength to each segment and analysis was run to calculate factor of safety. The liquefied shear strength ratio was then varied until a factor of safety equal to unity was obtained. Using the same assumptions made in the liquefied shear strength analysis, the liquefied strength ratio was estimated as 0.053, with a possible range from 0.038 to 0.088. The weighted average of vertical effective stress was estimated as 61 kPa.

A. 6.8.4 Liquefied Shear Strength and Strength Ratio Considering Kinetics

The pre- and post- failure geometries are reproduced in Figure A.68 and Figure A.69, respectively. Figure A.69 also shows the pre- and post-failure centers of gravity and the probable travel path of the center of gravity during flow failure.

The initial result of the kinetics analysis assumed that all soils along the failure surface mobilized the liquefied shear strength. This inaccurately estimated the actual liquefied shear strength because a portion of the failed soils initially were above the phreatic surface and did not liquefy. Therefore, the liquefied shear strength was adjusted using Eq. A.1 (Olson 2001) to account for the strength of the non-liquefied soils. Approximately 13.3% of the post-failure sliding surface length probably involved fill soils initially above the phreatic surface. This length of the failure surface was assigned average shear strength of 18 kPa based on $\phi' = 28^{o}$ to 32^{o}.

The kinetics analysis presented in Figure A.70 yielded the following results:

- Liquefied shear strength ≈ 6.7 (range of 6.44 to 9.15 kPa)
- Liquefied shear strength ratio ≈ 0.11 (range of 0.105 to 0.15)

This liquefied shear strength resulted in a calculated displacement of the center of gravity of the failure mass of approximately 5.63 m vertically and 24.08 m horizontally.

The kinetics analysis only provided a value of liquefied shear strength. Therefore, the liquefied shear strength ratio reported above was determined by dividing the liquefied shear strength of 6.7 kPa by the weighted average vertical effective stress of 61 kPa obtained from the post-failure geometry analysis. These values of liquefied shear strength and strength ratio include the effects of kinetics and the shear strength of the soils that did not liquefy.

A. 6.8.5 Sources of Uncertainty

The following sources of uncertainty were involved in estimating the yield shear strength and strength ratio: (1) the initial zone of liquefaction; (2) the position of the initial failure surface; (3) the shear strength of the non-liquefied soils; (4) phreatic surface within embankment; and (5) the potential for drainage during failure. It was assumed that all fill soil below the phreatic surface liquefied. The position of the initial failure surface was not known. However, using a slope stability search and comparing this to the post failure morphology allowed some confidence in locating the yield failure surface. The unsaturated fill was assigned $\phi' = 28^o$ to 32^o. A complete phreatic surface within the embankment was not given. Therefore, the author considered multiple phreatic surfaces.

The following sources of uncertainty were involved in estimating the liquefied shear strength and strength ratio: (1) the limits of the zone of liquefaction; (2) the shear strength of the non-liquefied soils, (3) phreatic surface within embankment; and (4) the potential for void and pore water pressure redistribution. As discussed above, all fill below the phreatic surface was assumed to liquefy. The unsaturated fill was assigned $\phi' = 28^o$ to 32^o. A complete phreatic surface within the embankment was not given. The author therefore considered several phreatic surfaces.

The following sources of uncertainty were involved in determining the "representative" values of penetration resistance: (1) effects of flow and reconsolidation on penetration resistance because the penetration tests were conducted after the failure; and (2) the conversion of SPT values to CPT values. "Representative" CPT values were obtained by converting SPT blow count to CPT tip resistance. This step involves an unknown level of uncertainty.

A.6.9 Itoizawa Embankment (Route 44)

At Itoizawa in the town of Akkeshi, Route 44 was damaged by the failure of a 10m high embankment. This section was constructed on the border of a hill slope terrace

composed of alternating layers of sandstone and conglomerate, talus, clay, and peat overlying the terrace deposits, as shown in Figure A.71.

In describing the failure of the Route 44 embankment Sasaki et al. (1993) stated, "The embankment failure was 68m long by about 3m deep, as shown in [Figure A.71]. The failed mass of embankment materials flowed out into the swamp about 35-45m. The failed portion of the embankment was not at the outlet of valley, but water was observed to flow out from where the toe of the embankment was before the slide. The source of this water was not clarified; however it was shown that the water content of the embankment had been high at the time of earthquake." As an alternate measure of slope displacement, the author measured a displacement of 29 m from the pre-failure toe position to the post-failure toe position. Measuring from the surface at the mid-slope of the embankment to the assumed sliding surface, the failure mass thickness was 2.9 m. After the failure, ponded water was observed on the failed mass as shown in Figure A.71, suggesting that liquefaction was responsible for the failure. As defined in Section A.6.4, strength loss due to cyclic loading was not likely to occur in the peat layer, thus liquefaction of the embankment fill below phreatic surface was most likely responsible for the failure.

A. 6.9.1 Representative Penetration Resistance

Sasaki et al. (1993) presented the results of two borings with SPT conducted along the embankment *after* the failure, as illustrated in Figure A.71. The author used an average energy ratio of 1.2 to calculate N_{60} values from raw blow counts as explained in Section A. 6.5.1. For all stress computations, the author used a saturated unit weight of 18.5 kN/m^3.

The $(N_1)_{60}$-values in the embankment fill, considering two possible phreatic surfaces, as defined in next section, were approximately from 4 to 10 blows/ft, with a best estimate of 5.

Cone penetration tests were not conducted at the site. Furthermore, a grain size distribution for the embankment fill was not available. The author assumed D50 = 0.6 mm, corresponding to the median grain size for the fill used at the Route 38 Pashikuru embankment. Therefore, values of q_{c1} were estimated using $q_c/N_{60} = 0.56$ (i.e., the average of the q_c/N_{60} ratios from Robertson and Campanella 1985, Seed and De Alba 1986, Andrus and Youd 1989, Kulhawy and Mayne 1990, and Stark and Olson 1995). This calculation yielded an average $q_{c1} = 2.8$ MPa, with a range of 2.24 to 5.6 MPa.

A. 6.9.2 Yield Shear Strength and Strength Ratio

The mechanism that likely triggered flow failure is seismic liquefaction of the saturated sandy fill of the embankment (Sasaki et al. 1993). As explained in Chapter 2, the shear strength and strength ratios mobilized at the instant of failure in cases where liquefaction is triggered by seismic loading do not necessarily represent yield shear strength and strength ratios.

The pre-failure geometry of the Route 44 Itoizawa embankment is reproduced in Figure A.72. A slope stability search was conducted to locate the initial failure surface that is consistent with the pre- and post-failure geometries. Because a complete phreatic surface was not available, two possible ground water tables within the road embankment were considered. All saturated fill was assumed to liquefy and a single value of shear strength was assigned to the liquefied soil. Fill soil initially above the phreatic surface was assigned a drained friction angle of 28º to 32º based on its low penetration resistance. The mobilized shear strength in the zone of liquefaction was approximately 11.0 kPa, with a range from 4.5 to 15 kPa.

A second analysis was conducted to estimate the strength ratio mobilized at the triggering of liquefaction. Identical assumptions regarding the failure surface and shear strength of the non-liquefied soil were used for this analysis. The mobilized shear strength ratio in the zone of liquefaction was approximately 0.23, with a range from 0.16 to 0.31, depending on the shear strength of the unsaturated fill, the position of phreatic surface, and the location of the failure surface. The weighted average pre-failure vertical stress in the liquefied segment was determined as 46 kPa.

A. 6.9.3 Liquefied Shear Strength and Strength Ratio

The post-failure geometry of Route 44 Itoizawa embankment is reproduced in Figure A.73. Trial failure surfaces were derived from the post-failure morphology of the sliding mass and a slope stability search as shown in Figure A.73 was conducted. A single arbitrary value of liquefied shear strength was assigned to liquefied zone and friction angles of $\phi' = 28º$ to 32º was assigned to non-liquefied zone. Liquefied shear strength was varied until a factor of safety equal to unity was obtained. The resulting back-calculated liquefied shear strength was 2.25 kPa, with a range from 2.06 to 2.8 kPa.

Using the same post-failure trial sliding surfaces shown in Figure A.73, a limit equilibrium back-analysis of the liquefied strength ratio of the upstream slope was conducted. The length of the final failure surface was divided into 13 segments as shown in Figure A.73. Segment 1 corresponds to the embankment material above the phreatic surface and was assigned $\phi' = 28º$ to 32º. The remaining segments from 2 to 13 were within the liquefied zone. Because the underlying peat deposit was undisturbed (Sasaki et al. 1993), it was assumed that the liquefied soil flowed on the surface of the foundation soils. Therefore these segments were arranged in the liquefied zone of the pre-failure geometry as shown in Figure A.72, to calculate the pre-failure vertical effective stress. An arbitrary value of liquefied shear strength ratio was given to the liquefied soil zone, which in turn assign different liquefied shear strength to each segment and analysis was run to calculate factor of safety. The liquefied shear strength ratio was then varied until a factor of safety equal to unity was obtained. Using the same assumptions made in the liquefied shear strength analysis, the liquefied strength ratio was estimated as 0.031, with a possible range from 0.03 to 0.04. The weighted average of vertical effective stress was estimated as 71 kPa.

A. 6.9.4 Liquefied Shear Strength and Strength Ratio Considering Kinetics

The pre- and post- failure geometries are reproduced in Figure A.72 and Figure A.73. Figure A.73 also shows the pre- and post-failure centers of gravity and the probable travel path of the center of gravity during flow failure.

The initial result of the kinetics analysis assumed that all soils along the failure surface mobilized the liquefied shear strength. This inaccurately estimated the actual liquefied shear strength because a portion of the failed soils initially were above the phreatic surface and did not liquefy. Therefore, the liquefied shear strength was adjusted by using Eq. A.1 (Olson 2001) to account for the strength of the non-liquefied soils. Approximately 7.7% of the post-failure sliding surface length probably involved fill soils initially above the phreatic surface. This length of the failure surface was assigned average shear strength of 8.43 kPa, based on $\phi' = 28^{o}$ to 32^{o}.

The kinetics analysis presented in Figure A.74 yielded the following results:

- Liquefied shear strength ≈ 4.0 kPa (range of 3.63 to 5.25 kPa)
- Liquefied shear strength ratio ≈ 0.056 (range of 0.051 to 0.074)

This liquefied shear strength resulted in a calculated displacement of the center of gravity of the failure mass of approximately 2.05 m vertically and 15.44 m horizontally.

The kinetics analysis only provided a value of liquefied shear strength. Therefore, the liquefied shear strength ratio reported above was determined by dividing the liquefied shear strength of 4.0 kPa by the weighted average vertical effective stress of 71 kPa obtained from the post-failure geometry analysis. These values of liquefied shear strength and strength ratio include the effects of kinetics and the shear strength of the soils that did not liquefy.

A. 6.9.5 Sources of Uncertainty

The following sources of uncertainty were involved in estimating the yield shear strength and strength ratio: (1) the initial zone of liquefaction; (2) the position of the initial failure surface; (3) the shear strength of the non-liquefied soils; (4) phreatic surface within embankment; and (5) the potential for drainage during failure. It was assumed that all fill soil below the phreatic surface liquefied. The position of the initial failure surface was not known. However, using a slope stability search and comparing this to the post failure morphology allowed some confidence in locating the yield failure surface. The unsaturated fill was assigned $\phi' = 28^{o}$ to 32^{o}. A complete phreatic surface within the embankment was not given. Instead, only a single water level is shown in the embankment. The author considered two possible complete phreatic surfaces within the slope.

The following sources of uncertainty were involved in estimating the liquefied shear strength and strength ratio: (1) the limits of the zone of liquefaction; (2) the shear

strength of the non-liquefied soils, (3) phreatic surface within embankment; and (4) the potential for void and pore water pressure redistribution. As discussed above, all fill below the phreatic surface was assumed to liquefy. The unsaturated fill was assigned $\phi' = 28^o$ to 32^o. A complete phreatic surface within the embankment was not given. Instead, only a single water level is shown in the embankment. The author considered two possible complete phreatic surfaces within the slope.

The following sources of uncertainty were involved in determining the "representative" values of penetration resistance: (1) the effects of flow and reconsolidation on penetration resistance because the penetration tests were conducted after the failure; (2) a grain size distribution for the fill soils was unavailable; and (3) the conversion of SPT values to CPT values. "Representative" CPT values were obtained by converting SPT blow count to CPT tip resistance using an assumed value of D_{50}. This step involves an unknown level of uncertainty.

A.7 Merriespruit Dam, South Africa

A.7.1 Introduction

The Merriespruit tailings dam was a 31 m high gold tailings dam situated 320 m upslope of Merriespruit, a suburb of the town of Virginia, South Africa, which is the part of the Free State Goldfields, in the extreme southern goldfield of the Witwatersrand Basin (Niekerk and Viljoen 2005). Figure A.75 shows the location of the Witwatersrand Basin and the town of Virginia, while Figure A.76 shows a plan view of Merriespruit dam and Merriespruit village, along with flow path of the failed tailings. Figure A.77 shows the breach location, penstock location, as well as the initial flow path of the failed tailings. On the night of February 22, 1994 at about 9 pm, Merriespruit tailings dam catastrophically failed. A late afternoon thunderstorm that lasted for about 30 minutes and produced 30 to 50 mm of rain preceded the failure. The disastrous failure of Merriespruit dam unleashed 600,000 m^3 of tailings that flooded the village of Merriespruit. The failure claimed 17 lives, destroyed 80 houses, and damaged 200 others beyond repair. The tailings flowed for a distance of about 2 km, with some material entering into a small tributary of the Sand River that runs on the northern boundary of Virginia (see Figure A.78 and Figure A.79).

A.7.2 Site Geology and Soil Conditions

The Witwatersrand sedimentary basin is a geological formation in South Africa that carries the world's largest gold reserves in its conglomerate layers. About 50,000 tons of gold have been mined from seven major goldfields in the Witwatersrand basin. The sedimentary basin is overlain by Ventersdorp lava, which in turn is overlain by younger sediments of Paleozoic- and Mesozoic-age (Niekerk and Viljoen 2005). The conglomerate layers contain small quantities of gold that is associated with pyrite (FeS_2). Once the gold is extracted from the ore, the remaining material is deposited in tailings dams. Laboratory testing of the tailings at Merriespruit indicated that their geotechnical

properties are similar to the majority of gold tailings produced in South Africa from quartzitic gold-bearing reefs (Wagener et al. 1998).

In 1985, the tailings dam owners retained an engineering firm to conduct a site investigation. At that time the dam height was 17 m. The site investigation of Merriespruit dam revealed that the foundation consisted of about 1.5 m of aeolian silty sand, underlain by a clayey sand to silty clay alluvium and bedrock. Bedrock was reported to be a weathered mudstone, siltstone, or sandstone. At the breach location, there was a drainage swale in the natural soils where the aeolian sand was not present, and the alluvium was weathered to a very soft sandy clay to a depth of 1.5 m. In addition, the uppermost sandstone bedrock at this location had weathered to a residual sand.

Following the failure, three teams, representing the operator, the owner, and the state, were commissioned by the South African judiciary to investigate the failure. One team noted that while the dam consisted of fairly equal thicknesses of yellow oxidized tailings, grey unoxidized tailings, and dark red (calcine-rich) tailings, there were distinct layers of non-plastic and low plasticity slimes interbedded in the tailings. These interbedded materials exhibited liquid limits between 23 and 43 and plasticity indices (PI) between 1 and 8. It was observed that none of the interbedded materials were high plasticity, but some of the liquid limits were relatively high. The low plasticity materials had shrinkage limits between 3 and 5.

Direct shear tests performed on the nonplastic to low plasticity tailings yielded friction angles of approximately 35° and a nominal cohesion of about 3 kPa. Ring shear tests on this material showed angles of shearing resistance in the range of 27 to 29° and negligible cohesion. The results of consolidated-undrained triaxial shear tests of undisturbed tailings specimens shows friction angle of 38° and c' = 5kPa as reported by (Wagener et al. 1998).

A.7.3 Description of the Failure

There are several conflicting opinions from different investigators regarding the triggering mechanism of the Merriespruit dam failure. Because the tailings that were part of the failed mass were highly disturbed, it was difficult to accept or refute any opinion based on the in-situ response of the undisturbed tailings. A summary of potential triggering mechanisms that were analyzed by Wagener et al. (1998) is given below:

Seismic liquefaction. Seismic liquefaction was considered as to be a potential triggering mechanism because the Free State gold fields, where Merriespruit dam was located, exhibits small levels of seismicity. However, no seismic activity was reported at the time of the failure. As a result, this mechanism is considered highly unlikely.

Piping. Piping may have contributed to the failure because piping was known to occur commonly in gold tailings dams and on-site personnel reported a water jet gushing from the embankment slope during the early stages of the failure. However, the

investigators concluded (somewhat surprisingly to the author) that piping was not considered to be a major triggering mechanism of the Merriespruit dam failure.

Slope Instability. On-site personnel who observed the failure reported that the toe of the starter dike experienced sloughing prior to the main failure. However, the investigative teams concluded that local instability of the lower slope was not the main triggering mechanism of the failure. This conclusion is supported by several slope stability analyses conducted by dam operator and investigators before and after failure using different soil parameters. These analyses all indicated factors of safety greater than unity, although some factors of safety were less than required by design standards.

Static Liquefaction. Static liquefaction of the loose tailings was also considered as a potential triggering mechanism. However, there were conflicting opinions regarding this mechanism. Laboratory tests performed by Blight (1988) showed that the Witwatersrand quartzitic tailings were strongly dilative. Nevertheless, investigators suspected that there may have been pockets or relatively continuous flat-lying layers of contractive soil within the tailings or embankment. Static liquefaction of these contractive soils was assumed to explain the distance that the failed tailings flowed, even if it was not the primary cause of the failure. Another factor that may have contributed to the mobility of the tailings was gravitational (i.e., vertical) segregation. Vertical layering, consisting of coarser-grained tailings and finer-grained slimes, developed within the fill as a result of the hydraulic deposition methods used at the pond. It was also observed from satellite imagery that a water pool commonly stretched from the penstock to the daywall at the breach location (see Figure A.77) around the time of the failure. This allowed little time for the newly-deposited tailings to drain, dry, and desiccate compared to the tailings in other parts of the containment dam. It was assumed by the investigators that the tailings at this location probably exhibited about half the strength of the more consolidated tailings elsewhere in the facility.

Based on their analysis of potential triggering mechanisms, Wagener et al. (1997, 1998) reported the following events ultimately led catastrophic failure of Merriespruit tailings dam. About 15 months before failure it was decided by the mine owner and contractor that further tailings deposition in the impoundments near the north wall should be discontinued (see Figure A.76). This precautionary step was taken because the north wall, which is where the failure eventually occurred, was showing signs of distress for several years in the form of seepage and sloughing near the toe. A buttress was constructed using coarse tailings in an attempt to stop this sloughing. At the time of the decision to stop deposition in the impoundment, the free board along the north perimeter wall was at least 1 m, which was acceptable according to the prevailing design practice. The raising of outer wall was also stopped after the decision to retire the impoundment.

It was observed that sloughing near the toe continued after the deposition of tailings was supposedly stopped and construction of the buttress was initiated. Investigators found that despite the decision to stop depositing tailings in the impoundment, excess water from the facility was still being delivered to the impoundment, and this water likely contained tailings. Although the water was

occasionally decanted as required, tailings continued to accumulate and reduce the free board. At the time of failure, the available freeboard had been reduced to just 0.3 m. This unauthorized pumping of water from the mill to the impoundment, which was actually continued even on the day of failure, not only resulted in reduced freeboard but also pushed the water pool away from the penstock and caused it accumulate near the north wall (Wagener et al. 1997, 1998).

Based on this chronology, Wagener et al. (1997, 1998) suggested the following mode of failure, and Figure A.79 describes the failure mechanism schematically. A late afternoon rainstorm on February 22, 1994 caused the pool to overtop the crest of the tailings dam. The overtopped water from the impoundment started to erode the loose tailings near the toe resulting in local slips in the outer berms of the dam. Eventually the overtopped water eroded or triggered a stability failure of the tailings buttress. This failure, in turn, triggered retrogressive slides in the oversteepened tailings dam slopes, leading to a massive overall slope failure that released the loose, saturated tailings. As pointed out by Wagener et al. (1997, 1998), this mode of failure is consistent with both eyewitness accounts as well as results of the technical investigation conducted by the investigating teams.

In addition to mode of failure suggested by Wagener et al. (1997, 1998) the author considers that the first few slides may be failed under drained condition and then it retrogressed under undrained condition causing a static liquefaction failure. This is particularly true for shallower sliding surfaces where undrained shear strength analysis yields mobilized friction angles in excess to the tailings friction angles.

As briefly stated above, laboratory tests by Blight (1988) suggested that the quartzitic tailings were in a dilative state and, thus the catastrophic failure came as a shock for geotechnical community of South Africa. Fourie et al. (2001) suggested that the dilatant response of the tailings observed during previous laboratory tests was misleading because laboratory tests may not capture the correct mode of shear, rate of shear, and drainage conditions. In particular, Fourie et al. (2001) pointed out that Blight (1988) reported drained test results while the failure likely was undrained. In contrast to the earlier studies, Fourie et al. (2001) stated that a large portion of the tailings were highly contractive, with $\cdot > 0.1$. Fourie et al. (2001) collected bulk samples of tailings from different locations close to the failure scar. These recovered samples had FC ~ 60% and are denoted as group M4 in Figure A.81. Other sample groups, i.e., M1, M2, and M3 (see Figure A.81), were created by sieving M4 samples to yield samples with FC = 1%, 20%, and 30%, respectively. Critical state lines defined by Fourie et al. (2001) for the soil samples with various FCs are shown in Figure A.81.

Blight and Fourie (2005) conducted consolidated-undrained shear tests on 16 specimens from Merriespruit dam with various void ratios. Nine of the samples showed dilative behavior while seven demonstrated contractive or almost neutral behavior (see Figure A.82). However, it is important to note that the authors did not report the method of sample preparation, and these void ratios might not represent the void ratios of the insitu tailings. Nevertheless, Blight and Fourie (2005) speculated that some layers of the

tailings likely were in a contractive state and would have liquefied and flowed during the catastrophic failure, carrying the denser layers with them.

Another argument that supports the contractive behavior of the tailings in the impoundment is shown in Figure A.83(a). In this sounding, the upper limit of the penetration-induced porewater pressures measured in the CPT sounding performed in the pond are more than 2.5 times greater than the hydrostatic pressures in the pond. This is only possible if the tailings are in the contractive state (Lunne et al. 1997). These penetration-induced porewater pressures strongly suggest that there are interbedded contractive (high penetration-induced porewater pressures) and dilative (low or negative penetration-induced porewater pressures) layers of tailings.

A.7.4 Representative Penetration Resistance

Wagener et al. (1998) reported five piezocone test results that were conducted by owner's investigator at different locations *after* the failure (see Figure A.83). As described earlier, the tailings near the penstock had the least opportunity to drain, consolidate, and desiccate; therefore, it was expected that the tip resistance in the impounded tailings near the penstock would be lower. It was also anticipated that the piezocone test results would be of a similar order of magnitude as the tailings at the slope near the breach location. As a result, CPT soundings were performed at the following locations (Wagener et al. 1998):

- Tests PE5A and PE5B were conducted to the east of the breach on the middle and upper berms respectively.
- Tests PE7A and PE7B were conducted to the west of the breach on the middle and upper berms respectively.
- Test PE2D was conducted in the impoundment close to penstock.

It should be noted that the piezocone typically used in South Africa does not include a friction sleeve, and results are thus only obtained for end resistance and penetration-induced porewater pressure (with a ceramic piezoelement located behind the shoulder of the cone).

It can be seen from sounding PE7A (Figure A.83c) that the tip resistance at depths from 2 to 9m is significantly lower than the tip resistance of the tailings at other locations on the slope. The tip resistance is however similar to the tip resistance measured in the tailings near the penstock within the tailings, as represented by sounding PE2D (see Figure A.83a). The investigators concluded that there was indeed poorly-consolidated material in the slope of the tailings dam and that this material could be expected to flow in the event of disturbance or a removal of support. The investigators ascribed the existence of poorly-consolidated tailings in the facility to the particular deposition practices prevalent in the industry at the time of placement (Wagener et al. 1998). The q_c value observed from Figure A.83c from a depth of 2 to 9 m is 0.6 MPa, which yields a q_T value of 0.64 MPa for an assumed a_n value of 0.75. Penetration resistances are as high as 3 MPa at other locations.

No SPTs were conducted at the Merriespruit tailings dam site. Therefore values of $(N_1)_{60}$ were estimated using $q_c/N_{60} = 0.31$ (i.e., the average q_c/N_{60} ratio from Robertson and Campanella 1985, Seed and De Alba 1986, Andrus and Youd 1989, Kulhawy and Mayne 1990, and Stark and Olson 1995). This q_c/N_{60} ratio corresponds to $D_{50} = 0.056$ mm, which was selected from the grain size distribution curve of the original tailings material (FC ~ 60%) reported by Fourie et al. (2001) and shown in Figure A.84. The resulting $(N_1)_{60}$ is approximately 2 blows/ft.

A.7.5 Yield Shear Strength and Strength Ratio

The pre-failure geometry of Merriespruit dam along with the likely mode of failure was given in Figure A.80. As described in Section A.7.3, the initial slides may have been shallow sloughs that occurred under drained conditions. As a result, the author considered some shallow trial failure surfaces to estimate yield strength and yield strength ratio. However, the critical failure surfaces were relatively deep, as illustrated in Figure A.85.

Coincidentally, a few months prior to the failure, the tailings dam operator had carried out a stability analysis for the section of the dam that ultimately failed. Using an angle of internal friction, $\phi' = 35°$ and an assumed cohesion c' = 2 kPa below and 11 kPa above the phreatic surface, a stability analysis using circular failure surfaces and the Bishop (1955) method of analysis was carried out. A minimum FS of 1.34 was calculated. The rationale for using a higher apparent cohesion above the phreatic surface than below was presumably to account empirically for the contribution of matric suction to the shear strength of the unsaturated tailings. In the analyses performed in this study, the author assumed that all of the tailings below the watertable were saturated and liquefiable; however the compacted dikes were drained during failure. Drained shear strength was assigned to the compacted dikes. The author used range of friction angles from $\phi' = 33^o$ to 38^o with c' = 0, 5 and 11 kPa based on the test results by Wagener et al. (1998) and earlier analysis performed by dam operator. The back-calculated yield shear strengths in the liquefied zone ranged from 59 kPa to 90 kPa depending on the failure surface locations, values of friction angle and cohesion intercept. The best estimate of mobilized shear resistance in the liquefied zone was 61kPa. This value is reasonably consistent with the range of peak shear strengths of 16 to 62 kPa measured by vane shear tests (Fourie et al. 2001).

A second analysis was conducted to estimate the mobilized shear stress ratio at the triggering of liquefaction. The same retrogressive failure surfaces described above were analyzed here. An arbitrary shear stress ratio was assigned to the liquefied zone, and this value was varied until a FS of unity was achieved. A best estimate of yield shear stress ratio was estimated as 0.274, with a possible range of 0.252 to 0.47. The weighted average pre-failure vertical effective stress was determined as 210 kPa to 270 kPa.

A.7.6 Liquefied Shear Strength and Strength Ratio

A complete post-failure geometry was not available for this case history. Therefore, it was not possible to conduct liquefied shear strength and strength ratio analyses by limit equilibrium analysis. However, infinite slope analysis was conducted by estimating the thickness of the tailings from eyewitness accounts. Eyewitnesses reported that the flowing tailings were just below the eaves of the roofs of homes. This height is assumed to be about 3m high (Fourie et al. 2001). Using Google Earth ©2011, the slope of the ground was estimated from 1º to 6º (see Figure A.86). This range of slopes suggests the liquefied shear strength ranged from 1 to 6 kPa with average liquefied shear strength of 3.5 kPa. These values are consistent with the shear strengths of 3 to 13 kPa measured using the vane shear test after large rotation (Fourie et al. 2001).

A.7.7 Liquefied Shear Strength and Strength Ratio Considering Kinetics

No kinetics analysis was conducted for this case as no post-failure geometry was available.

A.7.8 Sources of Uncertainty

The following sources of uncertainty were involved in estimating the yield shear strength and strength ratio mobilized at the time of failure: (1) the location of the initial failure surface; (2) the triggering mechanism; (3) the potential for failure through the foundation; and (4) the potential for drainage during triggering of liquefaction. Initial failure surfaces used in the analyses are the critical limiting equilibrium surfaces and are consistent with those proposed by previous researchers. As explained in Section A.7.3 the triggering mechanism of this slide is most likely the sloughing of the toe of the perimeter dike and static liquefaction of the materials behind the perimeter dike, but there may be other contributing factors. As indicated in Section A.7.2 the site was covered with silty sand which is also susceptible to liquefaction. It may be possible that a shallow failure could have occurred through the foundation and the foundation soil was replaced by the tailings from the impoundment after failure.

The following sources of uncertainty were involved in estimating the liquefied shear strengths and strength ratios: (1) the complete post-failure geometry was not available; (2) the thickness of the failed mass during flow was estimated from eyewitness accounts; and (3) the slope for the ground surface prior to the failure was estimated using Google Earth tools.

The following sources of uncertainty were involved in estimating the "representative" penetration resistance: (1) the conversion of CPT tip resistance to SPT blow count; (2) possible differences between soil conditions where penetration tests were conducted and the conditions where the failure occurred. A representative SPT value was obtained by converting CPT tip resistance based on the D_{50} values. Three of the four piezocone soundings that were conducted on the perimeter dike slope showed relatively higher penetration resistances than the sounding performed in the impounding. And only

one sounding yielded tip resistances similar to the tip resistances measured in the impoundment. Nevertheless, the penetration resistances measured along the perimeter dike are only 3 MPa maximum, which is still susceptible to liquefaction.

A.8 King Harbor Mole B, California, USA

A.8.1 Introduction

On January 17, 1994 at 4:30 am, greater Los Angeles was jolted by the Northridge earthquake. It was the first earthquake to hit an urban area of United States since the 1933 Long Beach earthquake. The earthquake occurred on a blind thrust fault and had $M_W = 6.7$ ($M_L = 6.6$) (Trifunac et al. 1994). Because the epicenter of Northridge earthquake was located in an urban area, it killed 60 people, injured more than 7,000 others and left 20,000 homeless. Property loss was also widespread with more than 40,000 buildings damaged in Los Angeles, Ventura, Orange and San Bernardino counties (USGS 2011). Damage included the collapse of major freeways sections, parking structures, as well as office and apartment buildings. As expected, most of the damage occurred near the epicenter, but significant ground and structural deformation also occurred at sites tens of kilometers away from the epicenter. Preliminary studies of these sites revealed that the ground and structural deformation were likely due to geologic and topographic characteristics of the failed areas (Kerwin and Stone 1997)

Figure A.87 shows an aerial image of Redondo Beach King Harbor, located about 42 km south of the epicenter. Liquefaction occurred over an area of King Harbor Mole B approximately 150 m long and 50 m wide, severely damaging the marina facilities. Figure A.88 shows an aerial view of the failed section of Mole B with two graben-like features visible on the surface. Mole B consisted of fill soils, with a seawall around it and rock revetment on the slopes. Buildings to the east and west of the failed zone were supported on deep foundations. As a result of earthquake shaking, the fill liquefied and displaced the seawall and rock-armored slope southward as much as 5.5 m. The central portion of the Mole settled about 1.2 m. Interestingly, the prefailure slopes were reestablished during reconstruction.

A.8.2 Site Geology and Soil Conditions

The fill soil that was used to construct Mole B was excavated from a borrow area situated about 1.5 km east-northeast of the site. The borrow soil was excavated from a backshore area to construct the adjoining boat basin, and the borrow fill likely was supplemented by beach deposits. During construction of Mole B, the fill soil was delivered from the borrow area by truck, dumped into the basin, and later pushed by bulldozers along an east-west axis perpendicular to shoreline. Kerwin and Stone (1997) reported that the fill consisted of sand with clay and silt particles that were washed away during placement. Kerwin and Stone (1997) stated that, “Available aerial photographs of the dumping and spreading process show large plumes of dirty water in the harbor basin, suggesting that silt and clay sizes present in the sandy fill soils tended to wash out as the fill was placed.” Only the fill soil that was above sea level was compacted mechanically.

To define the stratigraphy, six test borings were drilled about three weeks after the earthquake at various locations on the Mole. These layers are shown in Figure A.89. The test borings revealed four distinct stratigraphic units at the site: (1) artificial fill placed as a part of Mole construction; (2) beach deposits of Recent or Holocene age; (3) lagoonal deposits of Holocene age; and (4) fluvial and/or marine deposits, possibly of Pleistocene age. Other than the lagoonal deposit, the near surface soils are chiefly sands. These layers differ in depth, stratigraphic position, age of deposition, and penetration resistance. A brief summary of these soil units is given below. These descriptions are repeated from Kerwin and Stone (1997).

Artificial fill. The artificial fill is a uniform fine- to medium-grained sand and was about 6.4 m to 7 m thick, increasing in thickness to about 8 m on the seaward side of the Mole. The grain size distribution of the artificial fill is shown in Figure A.90. The layer is categorized as very loose to loose based on SPT blow counts, as discussed below.

Beach and Lagoonal deposits. Beach and lagoonal deposits are interlayered and underlay the artificial fill. The interlayering of these units likely resulted from the cyclic nature of beach-bar systems. The essential difference between these two layers is their depositional environment and primary grain size. Beach deposits result from wave action and are chiefly sandy, while lagoonal deposits reflect a still-water environment and are chiefly clayey.

A large portion of Mole B is underlain by beach deposits that increase in thickness from west to east. The variation in thickness appears to be due to erosion as stated in Kerwin and Stone (1997) after the construction of breakwater wall in 1938. Fill soils in the south-central portion of Mole B were placed directly over the eroded surface in the lagoonal deposits. Beach deposits consist of fine-grained sand and fine- to medium-grained silty sand and are categorized as loose to dense (generally grading denser with depth) according to SPT blow counts.

Thin layers of lagoonal deposits ranging from 0.5 m to 3 m thick were found in the samples recovered from the test borings. Lagoonal deposits generally consisted of gray-brown to gray-green clayey silt with some thin lenses of silty clay or fine silty sand (Kerwin and Stone 1997). The thickness of the lagoonal deposits decreased towards the sea, and apparently none of these fine-grained deposits were encountered in the seaward borings. Lagoonal deposits were found at depths of about 8 m to 11.7 m. This unit is classified as very soft to stiff on the basis of SPT blow counts.

Fluvial and/or marine deposits. Fluvial and/or marine deposits consist of fine- to medium-grained sand without shells or shell fragments. The presence of these Pleistocene deposits is recognized by an abrupt increase in penetration resistance between the depths of approximately 11 m and 14 m. This stratigraphic unit is identified as dense to very dense on the basis of SPT blow counts (Kerwin and Stone 1997).

A.8.3 Estimation of Ground Motion

Details related to the earthquake are as follows (Trifunac et al. 1994):

Date and Time: 1994 01 17; 04: 30:55 (Pacific Standard Time)
Location: 34º12.80' N, 118º32.22' W
Magnitude: 6.7
Region: Greater Los Angeles, USA
Fault Mechanism: Blind Thrust Fault

Maximum horizontal accelerations measured during the 1994 Northridge earthquake were used to develop a surface acceleration contour plot as shown in Figure A.91. Unfortunately there were no strong motion recording stations in Redondo Beach, but there were several stations located near the site. The closest strong motion recording station was situated 4.5 km north of the site. The maximum horizontal ground acceleration was recorded as 0.16g at this recording station. The recording station is situated on ancient dune deposits about 2 km east of the shoreline. Based on these recordings, Kerwin and Stone (1997) estimated a peak horizontal ground acceleration at King Harbor Mole B of about 0.15g.

Kerwin and Stone (1997) postulated that the ground motions at Mole B were probably amplified because of the long slender topography of the site, which was perpendicular to the primary component of the ground motion. The loose saturated fill soils also may have caused additional amplification. The author considers that invoking topographic effects is unnecessary here because the estimated ground motions at the site (Kerwin and Stone 1997) and the ground motions recorded at the nearest station are about the same. Furthermore, considering further amplification does not change the susceptibility or triggering of liquefaction at this site.

A.8.4 Description of Failure

Liquefaction due to the 1994 Northridge earthquake is considered responsible for the failure of King Harbor Mole B (Kerwin and Stone 1997) because of the morphology of the failure and because sand boils were observed around the mole. Liquefaction the fill caused the south side of the mole to displace southward into the nearby basin. A southward inclination of 1.5 to 2.0% of the preconstruction harbor bottom under the fill soil directed the movement of failed mass (see Figure A.89). The direction of movement also coincides with the primary direction of ground motion propagation. Furthermore, the underlying lagoonal deposits had low permeability and low frictional strength, which may have influenced the movement of the failed mass (Kerwin and Stone 1997).

Liquefaction-induced deformation is shown in Figure A.89. The fill soil and the southern seawall displaced as much as 5.5 m laterally southward. Two graben-like fissures, parallel to the long axis of the mole, were also observed (see Figure A.89). Cars parked in the displaced area sunk into the liquefied fill and had to be removed by tow trucks (see Figure A.92 and Figure A.93). Several boats were also damaged by the lateral

displacement of the mole. Settlement in the middle portion of the mole was about 1 m whereas as much as 1.5 m to 2 m of settlement was observed within portions of the graben-like features. Utility pipes that passed across the mole were broken as a result of this deformation. Although most of the sand boils were washed away either by the water released by the utility pipes or tidal inflow, at least one sand boil was observed in the larger northern graben area (Kerwin and Stone 1997).

The seawall settled as much as 0.5 m at its south end, while the northern seawall experienced only about 30 to 50 mm of deformation. Concrete buildings located near the eastern and western ends of the mole were also severely damaged by extension and settlement. Differential settlement of about 0.7 m was observed from west to east across the western building, while no significant deformations were observed in the eastern building (Kerwin and Stone 1997).

A.8.5 Representative Penetration Resistance

Kerwin and Stone (1997) reported that no significant difference was observed in penetration resistance in the fill soil within and outside of the failed area of Mole B. Therefore, $(N_1)_{60}$ values measured outside the failed area can be assumed to apply to the failed mass. Uncorrected blow counts from 2 to 10, with an average value of 6 were measured at this site (see Figure A.94). The $(N_1)_{60}$-values range from 3 to 10 with an average value of 6.

Figure A.94 also shows CPT results at the site before and after ground improvement. Uncorrected tip resistance ranged from about 1.5 to 5.7 MPa (ignoring one high reading of 11.2 MPa). An average uncorrected tip resistance of about 5 MPa is observed within fill soil before improvement. It is important to note that q_c/N_{60} ratios for the measured data were unusually high, with values as large as 1.0. Furthermore, a range of N-values were reported while only one CPT sounding was reported. Thus, the CPT sounding may not be "representative" of the fill. As a check on the reported CPT tip resistance, the author used D50 values from 0.28 to 0.7 mm (Figure A.91) to estimate an approximate q_c/N_{60} ratio for the site. Correlations from Robertson and Campanella (1985), Seed and de Alba (1986), Andrus and Youd (1989), Kulhawy and Mayne (1990), and Stark and Olson (1995) yielded average q_c/N_{60} ratios from 0.39 to 0.74. The average of this range is 0.54. Considering this average q_c/N_{60} ratio, the author computed qc1 values of 1.1 to 11.7 MPa, with an average of 4.6 MPa. These values are fairly consistent with the measured CPT values, but present a wider (and more conservative) range, and will be used for this study. Interestingly, post-improvement q_c/N_{60} ratios ranged from 0.42 to 0.56, which is consistent with most qc/N60 correlations.

A.8.6 Yield Shear Strength and Strength Ratio

The mechanism that likely triggered flow failure is seismic liquefaction of the saturated sandy fill comprising the mole (Kerwin and Stone 1997). As explained in Chapter 2, the shear strength and strength ratios mobilized at the instant of failure in

cases where liquefaction is triggered by seismic loading do not necessarily represent yield shear strength and strength ratios.

The pre-failure geometry of King Harbor Mole B is reproduced in Figure A.95. A slope stability search was conducted to locate initial failure surfaces that were consistent with the pre- and post-failure geometries. All saturated fill was assumed to liquefy and a single value of shear strength was assigned to the liquefied soil. Fill soil initially above the phreatic surface was assigned a drained friction angle of 30º to 35º, based on its low penetration resistance. The back-calculated mobilized shear strength in the zone of liquefaction ranged from 8.2 to 14.5 kPa, with a best estimate of 12 kPa.

A second analysis was conducted to estimate the strength ratio mobilized at the triggering of liquefaction. Identical assumptions regarding the failure surface and shear strength of the non-liquefied soil were used for this analysis. The best estimate of mobilized shear strength ratio in the zone of liquefaction was 0.236, with a range from 0.193 to 0.385, depending on the shear strength of the unsaturated fill and the location of the failure surface. The pre-failure vertical stress in the liquefied zone was ranged from 54 to 32 kPa.

A.8.7 Liquefied Shear Strength and Strength Ratio

The post-failure geometry of King Harbor Mole B is reproduced in Figure A.96. Trial failure surfaces similar to the pre-failure sliding surface were adopted, and a slope stability search was conducted. A single arbitrary value of liquefied shear strength was assigned to the liquefied zone and friction angles of $\phi' = 30º$ to 35º were assigned to the non-liquefied zone. The liquefied shear strength was varied until a factor of safety equal to unity was obtained. The resulting back-calculated liquefied shear strength was 6.8 kPa, with a range from 6.7 to 8.0 kPa.

Using the same post-failure trial sliding surfaces shown in Figure A.96, limit equilibrium back-analyses were conducted to estimate the liquefied strength ratio of the liquefied zone. The critical circular failure surface was divided into 10 segments. Segment 1 corresponds to the embankment material above the phreatic surface, which was then assigned $\phi' = 30º$ to 35º. The remaining segments from 2 to 10 were within the liquefied zone. These segments were arranged in the liquefied zone of the pre-failure geometry as shown in Figure A.95, along the critical sliding surface to calculate the pre-failure vertical effective stress for each segment. An arbitrary value of liquefied shear strength ratio was given to the liquefied soil zone, which in turn assigned different liquefied shear strengths to each segment, and a limit equilibrium slope stability analysis was performed to calculate the factor of safety. The liquefied shear strength ratio was then varied until a factor of safety equal to unity was obtained. Using the same assumptions made in the liquefied shear strength analysis, the liquefied strength ratio was estimated as 0.15, with a possible range from 0.119 to 0.157. The weighted average vertical effective stress was estimated as 56 kPa.

A.8.8 Liquefied Shear Strength and Strength Ratio Considering Kinetics

Mole B experienced somewhat limited movement because of the bounding seawall on its southern side. The seawall bulged outward to accommodate the soil displacement (Kerwin and Stone 1997). Because of this limited movement, a kinetic analysis could not be conducted.

A.8.9 Sources of Uncertainty

The following sources of uncertainty were involved in estimating the yield shear strength and strength ratio: (1) the initial zone of liquefaction; (2) the position of the initial failure surface; (3) the shear strength of the non-liquefied soils; and (4) potential drainage during triggering of liquefaction. It was assumed that all fill soil below the phreatic surface liquefied. The position of the initial failure surface was not known. However, using a slope stability search and comparing this to the post failure morphology allowed some confidence in locating the yield failure surface. The unsaturated fill was assigned $\phi' = 30^o$ to 35^o.

The following sources of uncertainty were involved in estimating the liquefied shear strength and strength ratio: (1) the limits of the zone of liquefaction; (2) the shear strength of the non-liquefied soils; (3) the role of the seawall in potentially limiting the flow deformations; and (4) the potential for void and pore water pressure redistribution. As discussed above, all fill below the phreatic surface was assumed to liquefy. The unsaturated fill was assigned $\phi' = 30^o$ to 35^o.

The following sources of uncertainty were involved in determining the "representative" values of penetration resistance: (1) only a single CPT sounding was reported, which yielded fairly high q_c/N_{60} ratios; and (2) the location of the tests was not reported.

A.9 Hyogoken-Nanbu (Kobe) Earthquake Case Histories, Japan[4]

A.9.1 Introduction

The 1995 Hyogoken-Nanbu, or Kobe, earthquake ($M_w = 6.9$) was one of the most devastating earthquakes ever to hit Japan. There were more than 5,500 fatalities and over 26,000 injured. The economic loss was estimated at about US$200 billion. The proximity of the epicenter and propagation of rupture directly beneath a highly populated region helped explain the loss of life and widespread damage.

[4] Seven case histories are discussed that are failed during Kobe earthquake. A general introduction, geology, estimation of ground motions, and description of failure is given. These headings will not be repeated for individual case histories.

The Hyogoken-Nanbu earthquake caused extensive damage to river dikes, levees and revetments, agricultural facilities, earth dams, subway stations, tunnels, water supply pipelines, public sewerage systems, and soil retaining walls for railway embankments. In this study, the author analyzed the following structures:

- Torishima dike
- Nishijima dike
- Idenoshiri dam
- The Upper and Middle Niteko dams
- Takarazuka landslide
- Nikawa landslide

Figure A.97 shows the locations of these earth structures along with the location of epicenter. All of these failures were attributed to soil liquefaction induced by the 1995 Hyogoken-Nanbu earthquake (Tani 1996; Sasaki et al. 1997; Ozutsumi et al. 2002).

A.9.2 Site Geology and Soil Conditions

Nakagawa et al. (1996) described the geological characteristics of the Osaka Basin in detail. They theorized that Quaternary crustal movement and sea level change were chiefly responsible for the extensive distribution of inland alluvial deposits. Similarly, at many locations along the Japanese island arc, sedimentary basins have formed as a result of tectonic movements since the Neogene period. Because the Pleistocene basement has been subjected to active fault movements, the Holocene sedimentary deposits have been divided into smaller blocks. These Holocene deposits consist mainly of the sediments deposited during sea level rise, and correspond to a geological event called the Flandrian Transgression, which occurred about 4000 to 7000 years ago Nakagawa et al. (1996).

Topographically, Osaka Basin is a wide alluvial plain facing Osaka Bay on the west, bounded by high mountain ranges, which consist of Mts. Rokko, Hokusetsu, Ikoma, Kongo, Izumi-Katsuragi, and Awaji Island. A thick soil column has accumulated in Osaka Basin since late Tertiary time. Basement rocks consist of mainly the Ryoke granitic rocks and partially of Paleozoic, Mesozoic and Miocene sedimentary rocks and some volcanic rocks. These basement rocks are widely exposed in the surrounding mountain ranges. The sedimentary cover overlying the basement rock consists of the Osaka Group, the upper Pleistocene and Holocene alluvial deposits. Figure A.98 shows the geological cross section of Osaka Basin. The Osaka Group is divided into three sub-groups: the lower, middle and upper sub-groups. The stratigraphy and lithology of area around Osaka Bay is presented in Figure A.99, along with geological column.

Starting in the 1960’s, four artificially-placed islands were constructed in the eastern part of the city of Kobe (Towhata et al. 1996). The borrow soil consisted of Holocene alluvial soil deposits. Since 1967, additional land reclamation projects involved the construction of Port Island and Rokko Island. The cities of Ashiy and Nishinomiya

also were constructed on reclaimed land. As discussed subsequently, these young artificial fills liquefied extensively during the earthquake.

A.9.3 Estimation of Ground Motions

Details related to the earthquake are as follows (Ozutsumi et al. 2002):

Date and Time: 1995 01 16 20:46:52 UTC
Location: 34.58N, 135.01E
Magnitude: 6.9
Region: Near South Coast of Western Honshu
Fault Mechanism: Strike-Slip

Estimates of peak ground acceleration (PGA) were provided by the original investigators for all the earth structures that are analyzed in this study. Ozutsumi et al. (2002) estimated PGA based on the recorded motions at the Ooyodo Station for analyzing the Torishima and Nishijima dikes. Ooyodo Station was situated 6.5 km and 45 km from the dike-protected estuary and earthquake epicenter, respectively, and located on one of the dikes of the Yodogawa River (Sasaki and Shimada 1997). This dike was constructed using the same fill as the dikes studied here (i.e., Torishima and Nishijima dikes) and has alternating layers of alluvial sand and clay in the foundation. A surface PGA exceeding 0.36g was recorded at the station. Akai et al. (1995) stated that the earthquake was estimated to have induced surface accelerations of approximately 0.3 to 0.5g in this area.

No acceleration record was obtained on Awaji Island, where Idenoshiri Dam was located; therefore, Uchida et al. (2001) used the record obtained at Kobe University as an input motion for effective stress analysis of the dam. The maximum acceleration was adjusted to 0.45g based on the maximum accelerations evaluated from the toppling of tombstones at local graveyards (Uchida et al. 2001).

Gerolymos and Gazetas (2007) reported a PGA of about 0.6g at level ground very close to Nikawa, the location of the Nikawa landslide. Sassa et al. (2001) suggested that the attenuation relationship proposed by Fukushima and Tanaka (1992) could be used to estimate the surface PGA at the Nikawa and Takarazuka landslide sites. The attenuation relationship is:

$$\log PGA = 0.42Mw - \log(R + 0.025 \times 10^{0.42Mw}) - 0.0033R + 1.22 \qquad \textbf{Eq. A.2}$$

where PGA (in cm/s^2) is the average of the orthogonal peak horizontal accelerations; Mw is moment magnitude; and R is distance to fault rupture (in km). As this attenuation relation was developed for stiff soil conditions, Sassa et al. (2001) suggested that the PGA at the Nikawa landslide site was about 1.4 times that at the Takarazuka Station. The location of Takarazuka Station is indicated in Figure A.97. The preferred Vs_{30} at the Takarazuka Station is reported as 312 m/s by the PEER Strong Motion database (http://peer.berkeley.edu/peer_ground_motion_database). Therefore, a NEHRP-based

Site Class D can be assigned to this site. Furthermore, Fukushima and Tanaka (1990) also found that, in general, the mean attenuation relationship for loose soil sites was approximately 1.4 times the average attenuation relation. Considering these two factors, Sassa et al. (2001) suggested that the PGA at the Nikawa landslide site should be about 2 times the value measured at the Takarazuka Station.

In addition to the above information, the author used attenuation relationships proposed by Abrahamson and Silva (2008), Boore and Atkinson (2008), Campbell and Bozorgnia (2008), Chiou and Young (2008), and Idriss (2008) (where applicable) to estimate surface PGAs for each of the study sites. Table A.1provides the PGA estimates from the various sources, as well as the value used in this study.

A.9.4 Descriptions of the Failures

During the 1995 Hyogoken-Nanbu earthquake, several engineered and non-engineered structures, i.e., embankments, levees, landslides, and dams were damaged. In this study two river dikes, three dams, and two landslides were analyzed.

Damage was observed at 32 locations along six rivers, with a total damaged length of nearly 9.3 km (Matsuo 1996). The most severely damaged were the dikes of the Yodo-gawa River, which flows through Osaka and is the largest river in the Kansai area. At most of the damaged sites, sand boils were observed near the dikes, indicating that liquefaction occurred (Matsuo 1996). Major damage to the Yodo-gawa River dikes occurred at two locations: Torishima dike at kilopost 1.4 and Nishijima dike at kilopost 1.7. These sections were analyzed in this study.

In Nishinomiya City, a complex of three reservoirs was badly damaged. Two of its dams were completely destroyed by the earthquake, while the third dam was significantly damaged (Towhata et al. 1996). The two dams designated as Upper and Middle Niteko Dams were analyzed in this study.

The northern part of Awaji Island, which was near the epicenter, experienced severe damage to various earth structures. One important dam damaged in this region was Idenoshiri Dam, which was analyzed in this study. The central part of the embankment failed and liquefaction-induced sand boils were observed within the reservoir (Tani 1996).

In addition to the damage to all types of engineered structures, the earthquake triggered nearly 400 landslides (Gerolymos and Gazetas 2007). Two landslides, the Nikawa and Takarazuka landslides, were analyzed in this study. Both of these landslides experienced rapid and long run-outs. A complete discussion of all of these failures is given below.

A.9.5 Torishima Dike

Torishima dike is situated on the left bank of the Yodo-gawa River with a length of 2.0 km (kilopost 0.2 to 2.2), and was designed to protect the population against the high sea tide of 5.2 m above mean sea level. The core of the dike was a soil embankment, and the river side surface was protected by a concrete facing and parapet wall, the design height of which was 8.1 m above sea level. The rear slope and crest were faced with concrete blocks and asphalt pavement, respectively.

The dike was severely damaged during the 1995 Hyogoken-Nanbu earthquake. Figure A.100 illustrates the Torishima dike before and after the earthquake and Figure A.101 shows the pre- and post-failure cross-sections. The concrete parapet wall can be clearly seen in pre-earthquake photo. This wall tilted and slid about 8 m into the river after the earthquake. Damage to the dike crest can also be seen in the photo, showing significant cracking and vertical movement exceeded 2 m, with a maximum of 3 m, from kilopost 0.5-1.9. Sand boils were observed along fissures on the ground surface. Lateral movements and heaving of the ground surface occurred in residential areas at low elevations. These facts suggest that soil liquefaction triggered the damage.

Figure A.101 includes the subsurface profile at the Torishima dike. Generally, the dike is underlain by the 30 m-thick Holocene Umeda formation. This formation consists of (from the surface): an upper sandy layer (As2), a clay layer (Ac), and a lower sandy layer (As1). The thickness of the Umeda formation decreases downstream, with occasional additional clay lenses. Layer As2 is divided into an upper sublayer (As2-2) and a lower sublayer (As2-1) based on density inferred from the SPT. Detailed soil parameters are given in Table A.2. Grain size comparisons suggest that the sand boils observed after the earthquake originated from Layer As2.

A. 9.5.1 Representative Penetration Resistance

Matsuo (1996) presented the results of five borings with SPT conducted along the failure, as illustrated in Figure A.101. Bore logs represented by 1.4k-2, 1.4k-3, and 1.4k-4 were conducted within the failed zone. Matsuo (1996) did not report the SPT hammer type, but Japanese practice commonly employs either donut Tombi or donut slip-rope (with 2 turns) hammers (Skempton 1986). The first method produces a hammer energy ratio (ER) of about 78% while the second method produces ER ~ 65%. These hammer energy ratios yield corrections of 1.3 and 1.1 respectively. Therefore, the author used an average hammer energy correction of 1.2 to calculate N_{60} values. For all vertical stress computations, the author used a saturated unit weight of 18.5 kN/m^3.

The average N-value in Layer As2-2 was approximately 4 blows/ft, while Layer As2-1 exhibited an average of 12 bpf. This suggests that Layer As2-2 likely liquefied first. The computed $(N_1)_{60}$ in Layer As2-2 averaged 6 to 7, with a range of 2 to 11.

Cone penetration tests were not conducted at Torishima dike. Therefore, values of q_{c1} were estimated using $q_c/N_{60} = 0.46$ (i.e., the average value of correlations by

Robertson and Campanella 1985, Seed and de Alba 1986, Andrus and Youd 1989, Kulhawy and Mayne 1990, and Stark and Olson 1995), corresponding to D_{50} ~ 0.25 mm. This D_{50} value was selected visually as the rough average of the large number of grain size distributions presented in Figure A.102 (the majority of D_{50} values range from about 0.15 to 0.45mm). Therefore the average q_{c1} value is 2.7 MPa, with a range from 0.9 to 5.0 MPa.

A. 9.5.2 Yield Shear Strength and Strength Ratio

As stated in Section A.9.4, widespread sand boils along the dikes suggest that seismically-induced liquefaction was responsible for the severe damage to the Yodo-gawa River dikes. Moreover, low SPT N-values strongly suggest that Layer As2-2 liquefied during shaking.

The pre-failure geometry of Torishima dike is reproduced in Figure A.103. Constraints for the initial failure surface were ascertained by carefully reviewing the pre- and post-failure geometries, establishing the zones of looser soil identified by in-situ testing, and considering the mode of failure suggested by Sasaki and Shimada (1997). A search of failure surfaces was then performed to obtain the critical failure surface giving the minimum mobilized shear stress with a FS of unity.

Several investigators (e.g., Matsuo 1996; Ozutsumi et al. 2002) stated that sand layer As2-2 was likely to liquefy and did not consider that the lower saturated portion of embankment soil could have liquefied, despite the fact that Ozutsumi et al. (2002) classified the embankment fill as sandy. Investigators also did not explain why only the foundation would have liquefied and the lower portion of the embankment would not when there is no physical difference (i.e., color, density, and grain size) between the As2-2 sandy soil and the sandy embankment soil. Lastly, the N-values presented by Matsuo (1996) and reported by Ozutsumi et al. (2002) (see Figure A.101 and Table A.2) show that there is no meaningful difference in blow count between the two soils. As a result, the author conducted analyses considering: (i) that only unit As2-2 liquefied; and (ii) that both unit As2-2 and the embankment fill below the phreatic surface liquefied.

A single value of yield shear strength mobilized at the triggering of liquefaction was assigned to the liquefied soil. Ozutsumi et al. (2002) suggested strength parameters of $\phi' = 25°$ and $c' = 20$ kPa for the embankment fill soils above the phreatic surface (see Table A.2). These values are recommended by Japanese design guidelines for road earth works on soft foundation ground. However, these values appear unusual for coarse-grained fill (e.g., Terzaghi et al. 1996). Therefore, the author varied ϕ' from 28° to 35° with $c' = 0$ for the analyses performed here. To account for the short drainage path in the embankment, the author considered a 0.5- to 1-m thick soil layer beneath the water level to be drained. This thin zone was assigned the same strength parameters as the embankment soil above the phreatic surface.

Trial failure surfaces encompassing the critical failure surface (i.e., the surface requiring the lowest mobilized shear stress or stress ratio in the liquefied zone for

stability) is shown in Figure A.103. The mobilized shear stress in the liquefied zone ranged from 10 to 17.2 kPa depending on the assumptions regarding limits of liquefied zone, drained layer thickness, position of the phreatic surface, shape and location of failure surface, and the value of ϕ'. The best estimate of mobilized shear stress in the liquefied zone corresponding to assumption (ii) was 13.3 kPa.

The same failure surfaces that were used to estimate mobilized shear stress at liquefaction triggering were also used to estimate mobilized shear stress ratio in the assumed liquefied zones (i.e., Layer As2-2 and lower saturated portion of embankment fill). The mobilized shear stress ratio assigned to these units was varied until a FS equal to unity was obtained. A best estimate of mobilized shear stress ratio was determined as 0.19, with a possible range of 0.112 to 0.285 based on assumptions for the failure surface, non-liquefied soil strength ($\phi' = 28^o$ to 35^o), drained layer thickness, and phreatic surface position. The weighted average pre-failure vertical effective stress was estimated as 70 kPa.

A. 9.5.3 Liquefied Shear Strength and Strength Ratio

The post-failure geometry is reproduced in Figure A.104. The final sliding surface was ascertained from the failed mass shape and the mode of failure suggested by Sasaki and Shimada (1997). Layer As2-2 and the sandy embankment fill below the phreatic surface were assumed to liquefy, and a single value of shear strength was assigned to the liquefied soil. The back-calculated shear strength was approximately 3.8 kPa, with a possible range from 2.9 to 4.3 kPa.

Using the same assumptions made in the liquefied shear strength analysis and same post-failure sliding surface shown in Figure A.104, a limit equilibrium analysis was conducted to estimate the liquefied strength ratio. The post-failure geometry was divided into 12 segments. Segment 1 was above the phreatic surface and considered non-liquefiable. A range of friction angle from 28° to 35° was assigned to this segment. The remaining segments, i.e., from 2 to 12, were arranged in the pre-failure geometry, as shown in Figure A.104. From these segments, the pre-failure vertical effective stress for each segment was determined. An arbitrary value of liquefied shear strength ratio was assigned to the liquefied soil segments, which in turn defines the liquefied shear strength for each segment. The liquefied strength ratio was varied until a FS of unity was achieved. The best estimate of liquefied strength ratio was 0.077, with a possible range from 0.062 to 0.091. The weighted average of pre-failure vertical effective stress was estimated as 47 kPa for the critical failure surface.

A. 9.5.4 Liquefied Shear Strength and Strength Ratio Considering Kinetics

The crest of the dam displaced vertically about 2 to 3 m (Ozutsumi et al. 2002) and the centroid moved 1.8 m vertically and 3.6 m horizontally. The centroid path was rather steep and difficult to track parallel to the final sliding surface. For this reason, a kinetics analysis was not conducted.

A. 9.5.5 Sources of Uncertainty

The following sources of uncertainty were involved in estimating the mobilized shear stress and shear stress ratio at liquefaction triggering: (1) limits of the liquefied zone; (2) shear strength of the non-liquefied soils; (3) location of the initial sliding surface; (4) drainage at the toe; and (5) phreatic surface location within the embankment. Although SPT results suggested that Layer As2-2 and the lower portion of the fill likely liquefied, the exact zone the liquefied soils is not known. Therefore author conducted two studies: first considering liquefaction in the foundation only; and second considering liquefaction in both the lower portion of the embankment and in the foundation. As discussed in Section A. 9.5.2, the shear strength of the non-liquefied soil (embankment fill above phreatic surface) given in Table A.2 suggested by Ozutsumei et al. (2002) was not used. Instead, the author used a range of friction angles with zero cohesion in the analysis. The initial sliding surface was not know as there were no eyewitnesses of the failure, therefore numerous sliding surfaces were studied to estimate the mobilized shear stress and stress ratio. The phreatic surface inside Torishima dike was not reported; therefore, the author used two possible phreatic surface positions, i.e., a more reasonable position and a highest-likely position.

The following sources of uncertainty were involved in estimating the liquefied shear strength and strength ratio: (1) shear strength of the non-liquefied soils; (2) the potential for porewater pressure or void redistribution; and (3) final sliding surface location. The shear strength of the non-liquefied soil was taken as 28° to 35°. The final sliding surface location was ascertained based on visual examination of the pre-and post-failure geometries. Several trial failure surfaces that incorporated the entire slide mass that was shown in the post-failure geometry were considered.

The following sources of uncertainty were involved in estimating the "representative" penetration resistance: (1) the use of Japanese SPT equipment; and (2) conversion from SPT to CPT. The type of SPT hammer was not reported; therefore, the author considered two methods that are commonly used in Japanese practice to calculate energy ratio. The average of the two was used to calculate N_{60} from raw N-values. No CPTs were conducted for Torishima dike and hence SPT blow counts were converted to CPT tip resistance. Based on the grain size distribution curve of Layer As2 given by Matsuo (1996), the D_{50} and q_c/N_{60} values are given in Section A. 9.5.1.

A.9.6 Nishijima Dike

Nishijima dike is situated on the right bank of the Yodo-gawa River with a 750m length (kilopost 1.2-2.0). Nishijima dike is located opposite to Torishima dike, both of which were damaged during the 1995 Hyogoken-Nanbu earthquake. During this event, the entire 750-m length of the tributary river side slope failed, with a 1.5-m wide longitudinal fissure developing along the dike crest, the crest moving 1.2 m vertically, and the mainstream river side toe displacing approximately 1.2 m, as illustrated in Figure A.105. Sand boils were observed along the bench on the side of the dike opposite the parapet wall. Interestingly, although the structure of the dike was similar to that of

Torishima dike, the failure occurred on the tributary river side rather than the mainstream river side, and there was no damage to the parapet wall. Layer As2-2 exhibited the same low SPT blow counts along both banks of the Yodo-gawa River (Matsuo 1996). Original investigators, including Matsuo (1996), Sasaki and Shimada (1997), and Ozutsumi et al. (2002), suggested that Layer As2-2 at Nishijima dike liquefied and lost strength. Again though, investigators did not explain why only the foundation would have liquefied and the lower portion of embankment would not have liquefied when there was no physical difference (i.e., color, density and grain size) between Layer As2-2 and the sandy embankment soil.

A. 9.6.1 Representative Penetration Resistance

Matsuo (1996) reported the results of 5 borings with SPT conducted on different parts of dike, as shown in Figure A.106. Borings 1.7k-3, and 1.7k-4 were performed through the failed mass. Similar to Torishima dike, both the lower portion of the embankment and foundation soil layer As2-2 were considered potentially liquefied. Again, the SPT hammer type was not reported; therefore, the average of the energy ratios from both common Japanese hammer methods was used (see Section A. 9.5.1). A saturated unit weight of 18.5 kN/m^3 was used to normalize the raw blow counts. Measured N-values in the lower portion of the embankment and in Layer As2-2 ranged from 4 to 6, while in As2-1, N-values exceeded 10 (Matsuo 1996; Sasaki and Shimada 1997). Again, this suggests that the lower part of the embankment and Layer As2-2 liquefied first. Values of $(N_1)_{60}$ in layer As2-2 averaged 8, with a range of 3 to 14.

Values of CPT were not measured at Nishijima dike. Therefore, values of q_{c1} were estimated using the average of the q_c/N_{60} ratios proposed by Robertson and Campanella (1985), Seed and de Alba (1986), Andrus and Youd (1989), Kulhawy and Mayne (1990), and Stark and Olson (1995). For D_{50} = 0.25 mm, the average q_c/N_{60} from the five correlations is 0.46. Therefore, the average q_{c1} value is 3.68 MPa, with a range of 1.38 to 6.44 MPa.

A. 9.6.2 Yield Shear Strength and Strength Ratio

As stated in Section A.9.4, widespread sand boils along the dikes suggests that seismically-induced liquefaction was responsible for the severe damage to the Yodo-gawa River dikes, i.e., the Torishima and Nishijima dikes. Moreover, low SPT N-values suggest that Layer As2-2 and the lower portion of the embankment fill may have liquefied.

The pre-failure geometry of Nishijima dike is reproduced in Figure A.107. Constraints for the initial failure surface were ascertained by carefully reviewing the pre- and post-failure geometries, establishing the zones of loose soil identified by in-situ testing, and the considering the mode of failure suggested by Sasaki and Shimada (1997). A slope stability search was then performed to define a critical failure surface giving a minimum mobilized shear stress with a FS of unity.

As noted above, several investigators (e.g., Matsuo 1996; Sasaki and Shimada 1997; and Ozutsumi et al. 2002) stated that the Layer As2-2 was likely to liquefy, but apparently did not consider that the lower saturated portion of the embankment fill could have liquefied despite the fact that Ozutsumi et al. (2002) classified the embankment fill as sandy. Given the similarities in physical characteristics (i.e., color, density and grain size) and N-values (e.g., Matsuo 1996; Ozutsumi et al. 2002; Figure A.106) between Layer As2-2 and the sandy embankment fill, the author conducted analyses considering the following two scenarios: (i) only Layer As2-2 liquefied; and (ii) both Layer As2-2 and the embankment fill below the phreatic surface liquefied.

A single value of yield shear strength mobilized at the triggering of liquefaction was assigned to the liquefied soil. Ozutsumi et al. (2002) suggested strength parameters of $\phi' = 25°$ and $c' = 20$ kPa for the embankment fill above the phreatic surface (see Table A.2). These values are recommended by the Japanese design guidelines for road earth works on soft foundation ground. However, these values appear unusual for coarse-grained fill (e.g., Terzaghi et al. 1996). Therefore, the author varied ϕ' from 28° to 35° with $c' = 0$ for the analyses performed here. To account for the short drainage path in the embankment, the author considered a 0.5 to 0.8 m thick soil layer beneath the water level to be drained. This thin zone was assigned the same strength parameters as the unsaturated embankment fill.

Several trial failure surfaces, including the critical failure surface (i.e., the surface requiring the lowest mobilized shear stress or stress ratio in the liquefied zone for stability), are shown in Figure A.107. The mobilized shear stress in the liquefied zone ranged from 10 to 11 kPa depending on the assumptions regarding limits of liquefied zone, drainage layer thickness, position of the phreatic surface, shape and location of failure surface, and the shear strength of non-liquefied soils. The best estimate of mobilized shear stress in the liquefied zone was 10.7 kPa.

The same failure surfaces that were used to estimate mobilized shear stress at liquefaction triggering were also used to estimate mobilized shear stress ratio in the assumed liquefied zones (Layer As2-2 and the lower saturated portion of the embankment fill). The mobilized shear stress ratio assigned to this unit was varied until a FS equal to unity was obtained. A best estimate of mobilized shear stress ratio was determined as 0.23, with a possible range of 0.225 to 0.25 based on the assumptions for the failure surface, non-liquefied soil strength ($\phi' = 28^o$ to 35^o), drained layer thickness, size of the liquefied zone, and the phreatic surface position. The weighted average pre-failure vertical effective stress was determined as 46 kPa.

A. 9.6.3 Liquefaction Shear Strength and Strength Ratio

The post failure geometry is reproduced in Figure A.108. The critical circular sliding surface was ascertained using a selective slope stability search constrained by the shape of the failed mass and the mode of failure suggested by Sasaki and Shimada (1997). Again, based on SPT N-values, Layer As2-2 and the lower portion of the embankment were assumed to liquefy and a single value of shear strength was assigned

to the liquefied soil. The author found essentially no difference in s_u(liq) for assumptions (i) and (ii). The back-calculated shear strength was approximately 3.7 kPa, with a possible range from 2.8 to 4.5 kPa.

Using the same assumptions made in the liquefied shear strength analysis and same post-failure sliding surface shown in Figure A.108, a limit equilibrium analysis for liquefied strength ratio of Nishijima Dike was conducted. The post-failure geometry was divided into 13 segments. Segment 1 was located in the non-liquefiable soil, and assigned $\phi' = 28°$ to 35°. The remaining segments (i.e., from 2 to 13) experienced somewhat limited movements, and were assigned the same pre-failure and post-failure positions. Pre-failure vertical effective stresses were determined for these segments. Using a single value of liquefied shear strength ratio, values of liquefied shear strength were assigned to each segment in the liquefied zone. The liquefied shear strength ratio was varied to achieve a FS of unity. The liquefied strength ratio was estimated as 0.088, with a possible range from 0.066 to 0.11. The weighted average vertical effective stress was estimated as 42 kPa.

A. 9.6.4 Liquefied Shear Strength and Strength Ratio Considering Kinetics

The centroid moved 0.04 m vertically and 1.11 m horizontally. Due to the limited movement of the centroid, a kinetic analysis was not conducted.

A. 9.6.5 Sources of Uncertainty

The following sources of uncertainty were involved in estimating the mobilized shear stress and stress ratio at liquefaction triggering: (1) the limits of the liquefied zone; (2) the shear strength of the non-liquefied soils; (3) the location of the initial sliding surface; (4) potential drainage at the toe of the slope and along the base of the embankment; and (5) the phreatic surface location within the embankment. Although Matsuo (1996), Sasaki and Shimada (1997), and Ozutsumi et al. (2002) suggested that liquefaction occurred in Layer As2-2, it appears likely that the saturated portion of the embankment fill (Bs) also liquefied. As discussed earlier, the shear strength of the non-liquefied soil (unsaturated embankment fill) suggested by Ozutsumei et al. (2002) (see Table A.2) was not used. Instead, a range of friction angles were used to conduct the analysis. The initial sliding surface was not known; therefore, numerous sliding surfaces were studied to determine the best estimate of yield shear strength and strength ratio.

The following sources of uncertainty were involved in estimating the liquefied shear strength and strength ratio: (1) the shear strength of the non-liquefied soils; (2) the potential for porewater pressure or void redistribution during failure; and (3) the location of the final surface of sliding. The shear of the non-liquefied soils was taken as 28° to 35°, as explained above. The location of the final surface of sliding was ascertained based on visual examination of the pre-and post-failure geometries. Several trial failure surfaces that incorporated the entire slide mass were considered.

The following sources of uncertainty were involved in estimating the "representative" penetration resistance: (1) the use of Japanese SPT equipment; and (2) the conversion from SPT to CPT. The type of SPT hammer was not reported; therefore, the author considered two methods that are commonly used in Japanese practice to define an average energy ratio. The average of the two was used to calculate N_{60} from raw N-values. No CPTs were conducted for Nishijima Dike and hence SPT blow counts were converted to CPT tip resistance. Based on the grain size distribution curve of soil As2 given by Matsuo (1996), the D_{50} and qc/N_{60} values are given in Section A. 9.6.1.

A.9.7 Upper Niteko Dam

The Upper Niteko dam had a maximum height of approximately 6.3 m and a crest length of about 80 m prior to the earthquake. The crest was 3.5 m wide and the dam had 1V:2.2H upstream and downstream slopes. Figure A.109 shows a plan view of the Upper, Middle, and Lower Niteko dams which were severely damaged during the 1995 earthquake. The upper two-thirds of the central portion of Upper Niteko dam appeared to have flowed as much as 60 to 70 m downstream of its centerline (Akai et al. 1995).

Figure A.110 shows the pre- and post-failure geometries of Upper Niteko dam. The figure also shows the foundation soils below the fill and SPT values measured in the foundation. The Upper Niteko dam consists of (from the ground surface): sandy fill, alluvial sand, diluvial sand, diluvial clay, and diluvial sand. The post-failure morphology of the Upper Niteko dam, along with the extensive failures of the perimeter fills, strongly suggest that liquefaction was responsible for the flow failure, despite the fact that sediment boils were not observed within the reservoirs during the reconnaissance (Akai et al. 1995). However, in the residential neighborhood to the west there was ample evidence of liquefaction in the form of sand ejecta and boils. All of the fill soils were believed to originate from decomposed granite (Akai et al. 1995).

A. 9.7.1 Representative Penetration Resistance

Towhata et al. (1996) presented logs and SPT data obtained from boreholes drilled through the embankment shortly after the earthquake. The SPT N-values are presented in Figure A.110. As can be seen from the borehole data, SPT N-values within the dam embankment generally ranged from 2 and 10, with a median value between 2 and 3. Blow counts in the foundation soils, other than in the upper alluvial and diluvial sands, were generally greater than 25 blows/ft as shown in Figure A.110. These results suggest that the saturated lower portion of the embankment, the alluvial sand, and perhaps the diluvial sand were potentially liquefiable. The SPT hammer used for these tests was not reported; therefore an average energy ratio for Japanese hammers (see Section A. 9.5.1), with a saturated unit weight of 18.5 kN/m^3 was used to normalize the blow counts. The values of $(N_1)_{60}$ in this soil layer averaged 6, with a range of 5 to 13.

CPTs were not performed at Upper Niteko dam; therefore, q_{c1} values were estimated using the average of the q_c/N_{60} ratios proposed by Robertson and Campanella (1985), Seed and De Alba (1986), Andrus and Youd (1989), Kulhawy and Mayne (1990),

and Stark and Olson (1995). For D_{50} = 0.4 mm (see Figure A.111), the average of the five correlations yielded q_c/N_{60} = 0.51. Therefore, the average q_{c1} value is 3.1 MPa, with a range of 2.6 to 6.7 MPa.

A. 9.7.2 Yield Shear Strength and Strength Ratio

The mechanism that likely triggered flow failure of the Upper Niteko dam was seismically-induced liquefaction of the sandy embankment fill and alluvial sand below the phreatic surface. Although liquefaction manifestations were not observed within the reservoirs during the reconnaissance, the flow failure of the dam strongly suggests that seismically-induced liquefaction was responsible for this failure. Moreover, a nearby neighborhood west of the dam exhibited liquefaction-induced sand boils and sand ejecta. As discussed in Chapter 2, the shear strength and strength ratio mobilized at the instant of failure in cases of liquefaction flow failure triggered by seismic loading do not necessarily represent the yield shear strength and yield strength ratio, respectively.

The pre- and post-failure geometry of the Upper Niteko dam is reproduced in Figure A.112. As indicated in the cross-section of the dam given in Figure A.110, the only reservoir level shown is the high water level (HWL). However, this likely was not the water level at the time of earthquake. Towhata et al. (1996) stated that at the time of earthquake both upper and middle Niteko dams were roughly 80% full. This could be interpreted as 80% of total crest height or 80% of the HWL. Therefore, the author performed two sets of analyses using these two potential reservoir levels. Coincidentally, 80% of the crest height yields about the same reservoir level as the HWL shown.

A slope stability search was conducted to determine the critical initial failure surface. The initial critical failure surface was estimated after establishing the zone of liquefaction (lower portion of embankment fill and alluvial sand as indicated by SPT N-values). The post-failure ground surface suggests that the failure did not occur deep into the diluvial sand but rather remained relatively shallow, i.e., within the embankment fill and alluvial sand.

Several trial circular and noncircular failure surfaces were searched for Upper Niteko dam. Three of the failure surfaces are shown in Figure A.112. A single value of shear strength was assigned to liquefied foundation soil, and a drained friction angle of 28° to 34° was assigned to the embankment material above the phreatic surface. Relatively low friction angles were selected because the penetration resistance of the sandy embankment fill was low. Calculations showed that the presence of a drained layer below the phreatic surface did not significantly affect the back-calculated shear strength; therefore, drainage was not considered in the analysis. Mobilized shear stresses in the liquefied zone ranged from 8.2 to 13.6 kPa depending on the failure surface location. The best estimate of mobilized shear resistance in the liquefied zone was 11 kPa.

A second analysis was conducted to estimate the mobilized shear stress ratio at the triggering of liquefaction. Several trial circular and non-circular failure surfaces were searched, with the critical surfaces shown in Figure A.112. A shear stress ratio was

assigned to the liquefied zone, and this value was varied until a FS of unity was achieved. The best estimate of mobilized shear stress ratio was estimated as 0.27, with a possible range of 0.215 to 0.3 determined using various failure surfaces. The weighted average pre-failure vertical effective stress was determined as 42 kPa.

A. 9.7.3 Liquefied Shear Strength and Strength Ratio

The post-failure geometry was not reported; therefore, it was not possible to conduct liquefied shear strength and strength ratio analyses.

A. 9.7.4 Liquefied Shear Strength and Strength Ratio Considering Kinetics

Similarly, no kinetics analysis was conducted for this case.

A. 9.7.5 Sources of Uncertainties

The following sources of uncertainty were involved in estimating the yield shear strength and strength ratio: (1) the location of the initial sliding surface; (2) the limits of liquefaction; (3) the location of phreatic surface; and (4) the potential for drainage at the toe. The position of the initial sliding surface is not known with certainty; therefore, numerous circular and noncircular sliding surfaces were analyzed. The sliding surfaces were evaluated by establishing the zone of liquefaction (as indicated by SPT N-values) and visual comparisons of the pre- and post-failure geometry. The reservoir level presented in Figure A.110 corresponds to the design high water level (HWL). It was not reported in the literature where the reservoir level was at the time of failure. Therefore, the author performed analyses for two alternative reservoir levels as explained in Section A. 9.7.2.

The following sources of uncertainty were involved in determining the "representative" values of penetration resistance: (1) the use of Japanese SPT equipment; and (2) the conversion of SPT blow counts to CPT tip resistance. The type of SPT hammer was not reported; therefore, the author considered two methods that are commonly used in Japanese practice to calculate energy ratio. The average of the two was used to calculate N_{60} from raw N-values. No CPT was conducted for Upper Niteko dam and hence conversion from SPT to CPT was necessary.

A.9.8 Middle Niteko Dam

The Middle Niteko dam had a maximum height of approximately 7.6 m and a crest length of about 80 m prior to the earthquake. It had a crest width of about 3 m and was estimated to have had 1V:2.2H upstream and downstream slopes. Akai et al. (1995) stated that the upper two-thirds of the dam in the central portion appeared to have flowed as much as 70 m downstream of the dam's centerline. Figure A.109 shows an aerial and plan view of the reservoir complex, which indicates the position of the dams and damage due to earthquake. Figure A.113 shows the pre-failure geometry with an incomplete post-failure geometry. A complete post-failure geometry with the final position of the failed

soil mass was not available in the literature. A small flow of reservoir water was still passing through the breach at the time of the field reconnaissance, 17 days after the earthquake (Akai et al. 1995 and Towhata et al. 1996).

The movement of the Middle Niteko dam appeared to be almost entirely in the downstream direction, although examination of the remaining portions of upstream slope near the abutments indicated minor slumping toward the upstream reservoir (see Figure A.109). A small outlet structure at the upstream toe near the center of the dam appeared to be nearly vertical with a possible slight upstream tilt, although the catwalk to the structure had collapsed. Exposures of the upper portion of the embankment fill near the abutments indicated a layered fill composed of sandy silt and silty sand with gravel. However, the slide debris appeared to be composed mostly of sandy silt. All of the fill soils were believed to originate from decomposed granite (Akai et al. 1995).

A. 9.8.1 Representative Penetration Resistance

Towhata et al. (1996) presented logs and SPT data obtained from boreholes drilled through the embankment shortly after the earthquake. Figure A.113 provides the measured SPT N-values. Two N-values of 2 and 4 were measured in the remaining sandy fill, yielding an average of 3. Blow counts in the foundation soils beneath the embankments were greater than 10, and most greater than 20. These results suggest that the saturated portions of the embankments were more likely to liquefy than the foundation soils.

The SPT hammer type was not reported; therefore, an average energy ratio for both common Japanese hammer systems was used to compute $(N_1)_{60}$ values (see Section A. 9.5.1). A saturated unit weight of 18.5 kN/m^3 was used to normalize the raw blow counts. Using these parameters, $(N_1)_{60}$ values were 3 and 6, with an average of about 5.

Values of CPT were not measured at Middle Niteko dam. Therefore, q_{c1} values were estimated using the average of the q_c/N_{60} ratios proposed by Robertson and Campanella (1985), Seed and De Alba (1986), Andrus and Youd (1989), Kulhawy and Mayne (1990), and Stark and Olson (1995). Because the embankment construction material was same for both dams, the same grain size distribution curve as given in the Upper Niteko Dam was used. For D_{50} = 0.4 mm (see Figure A.111), the average q_c/N_{60} from the five correlations is 0.51. Therefore, the average q_{c1} was 2.55 MPa, with a range from 1.53 to 3.06 MPa.

A. 9.8.2 Yield Shear strength and Strength Ratio

The mechanism that likely triggered the flow failure of Middle Niteko dam is seismically-induced liquefaction of the sandy embankment fill below the phreatic surface. As in the case of Upper Niteko dam, liquefaction manifestations were not observed at the dam site, but the flow failure of the dam strongly suggests that liquefaction was responsible for this failure. As discussed in Chapter 2, the shear strength and strength ratio mobilized at the instant of failure in cases of liquefaction flow failure

triggered by seismic loading do not necessarily represent the yield shear strength and yield strength ratio, respectively.

The pre- and post-failure geometries of the Middle Niteko dam are reproduced in Figure A.114. This figure illustrates the design HWL; however as discussed in Section A. 9.7.2, the HWL likely was not the water level at the time of earthquake. Similar to the analyses performed for the Upper Niteko dam, the author conducted analyses for reservoir levels at 80% of the crest height and at 80% of the HWL. A slope stability search was conducted to determine the critical initial failure surface, and the search was constrained by the assumed zone of liquefaction (i.e., the saturated portion of embankment fill). As seen in Figure A.113, the post-failure geometry is nearly flat. A single value of shear strength was assigned to liquefied embankment fill soil, and a range of friction angles from 28° to 34° were assigned to the embankment material above the phreatic surface. Relatively low friction angles were selected because the penetration resistance of the sandy embankment fill was low. Calculations showed that the presence of a drained layer below the phreatic surface did not significantly affect the back-calculated shear strength; therefore, drainage was not considered in the analysis.

Several circular and non-circular trial failure surfaces were searched. Two failure surfaces representing the critical circular and non-circular slip surfaces are shown in Figure A.114 for the Middle Niteko dam. The values of mobilized shear resistance in the liquefied zone ranged from 11.5 to 17 kPa depending on the failure surface location. The best estimate of mobilized shear resistance in the liquefied zone was obtained from the critical failure surface as 16 kPa.

A second analysis was conducted to estimate the mobilized shear stress ratio at the triggering of liquefaction. Several circular and non-circular surfaces were searched, and the critical circular and non-circular slip surfaces are illustrated in Figure A.114. A shear stress ratio in the liquefied zone was varied until FS of unity was achieved. A best estimate of yield shear strength ratio was determined as 0.24, with a possible range of 0.18 to 0.26. The weighted average pre-failure vertical effective stress was determined as 65 kPa.

A. 9.8.3 Liquefied Shear Strength and Strength Ratio

The postfailure geometry was not reported; therefore, it was not possible to conduct liquefied shear strength and strength ratio analyses.

A. 9.8.4 Liquefied Shear Strength and Strength Ratio Considering Kinetics

For the same reason, no kinetics analysis was conducted for this case.

A. 9.8.5 Sources of Uncertainties

The following sources of uncertainty were involved in estimating the yield shear strength and strength ratio: (1) the location of the initial sliding surface; (2) the reservoir

level and phreatic surface within the embankment; and (3) the potential for drainage at the embankment toe. The initial sliding surface location is not known with certainty; therefore, several circular and noncircular sliding surfaces were considered that are consistent with the initial and final geometry and the assumed zone of liquefaction. Two reservoir levels were considered that are consistent with the site description provided by Towhata et al. (1996). The water level on the downstream side was not given. It was assumed that the water level was at the interface of the fill and clay layer (see Figure A.114).

The following sources of uncertainty were involved in determining the "representative" values of penetration resistance: (1) the use of Japanese SPT equipment; and (2) the conversion of SPT blow counts to CPT tip resistance. The type pf SPT hammer was not reported; therefore, the author considered two methods that are commonly used in Japanese practice to calculate energy ratio. The average of the two was used to calculate N_{60} from raw N-values. No CPT was conducted for Middle Niteko dam and hence conversion from SPT to CPT was necessary.

A.9.9 Nikawa Landslide

The 1995 Hyogoken-Nanbu earthquake occurred in a very dry season following the dry summer of 1994. Compared to the number of earthquake-induced ground failures in artificial fills near the coast, landslides in natural slopes were much less numerous. The Nikawa landslide was associated with the Osaka formation layer that consists of limnic and marine sands and clays of Pliocene- to middle Pleistocene-age, of low permeability. Within these low permeability layers, porewater could have been preserved despite the dry season (Gerolymos and Gazetas 2007). Because the low permeability retained the ground water during the dry season, the Nikawa landslide likely involved seismically-induced liquefaction. Table A.1 provides relevant seismic data about the Nikawa landslide.

The Nikawa landslide was one of the largest ground failures triggered by the earthquake, destroying 11 houses and causing 34 fatalities. The landslide volume was 110,000 to 120,000 m^3, and the sliding mass displaced 175 m. No observations are available regarding the slide velocity. However, it is believed that it was a high speed landslide, because no one evacuated the destroyed houses and all 34 residents were killed (Wang et al. 2000). Concerning the time of the landslide, Mr. Tsunehito Tanaka, a witness who lived near the Nikawa landslide, said, "…the announced occurrence time of the Hyogoken-Nanbu earthquake is from 5:46:51.6, on the morning of January 17, 1995. The occurrence time of the landslide was one or two minutes later. I can also remember there were two strong shocks of the earthquake. It is difficult to tell the exact time of the landslide, I can just say that the landslide occurred as soon as the second shock of the earthquake came (Wang et al. 2000)."

Figure A.115 shows an aerial photograph and plan view of the Nikawa landslide. Figure A.116 illustrates the central longitudinal section of the landslide. Investigative borings revealed that the soils at the site are underlain by granite bedrock. Overlying

granite bedrock, Pliocene- to middle Pleistocene-aged Osaka Group limnic and marine granitic sands and clays were encountered. Alluvial terrace and uncompacted old artificial sand fill deposits overlay the Osaka Group soils, which are in turn overlain by artificially-placed fill consisting of Osaka Group sands. Ground water was observed at a depth of 6 to 7 m from February to March 1995 in three boreholes drilled near the landslide mass. The groundwater table was assumed to be subparallel to the ground surface, at a depth consistent with the borehole observations. Sliding occurred at a maximum depth of about 14 m. Therefore the sliding surface was saturated. The average angle of the slope prior to failure was about 20°.

A. 9.9.1 Representative Penetration Resistance

Sassa et al. (1996) performed a detailed investigation of the landslide, including 28 borings, exploratory trenches, in situ testing, and sampling. Sassa et al. (1996) stated that the SPT N-values measured in the embankment were almost always less than 10, while Loukidis et al. (2001) stated that SPTs performed in the lower portion of the sand fill adjacent to the failure exhibited blow counts ranging from 4 to 16, with an average value close to 10. (Regrettably, the raw SPT results and SPT hammer type were not reported in the literature.) To normalize these raw blow counts, the effective vertical stress was calculated at the middle of the embankment (183.5 kPa), with a total and saturated unit weight of 19 kN/m^{3}as reported by Loukidis et al. (2001). The hammer energy was assumed to be 72%, the average of the two hammer types commonly used in Japan. Using the corrections for overburden pressures and hammer energy, $(N_1)_{60}$ values ranged from 4 to 14 with a best estimate of 9.

CPTs were not performed at the site; therefore, q_{c1} values were estimated using the average of the q_c/N_{60} ratios proposed by Robertson and Campanella (1985), Seed and de Alba (1986), Andrus and Youd (1989), Kulhawy and Mayne (1990) and Stark and Olson (1995). For D_{50} = 0.5 mm (see Figure A.117), the average q_c/N_{60} from the five correlations is 0.55. Therefore, the average q_{c1} is 4.95 MPa, with a range of 2.2 to 7.7 MPa.

A. 9.9.2 Yield Shear Strength and Strength Ratio

Given the dry conditions prior to the earthquake, investigators were surprised with the significant distance and speed of the Nikawa landslide because, as reported in Gerolymos and Gazetas (2007): (a) the slope inclination barely exceeded 20°; and (b) the water table was not high (although there was evidence that it was above the sliding surface over a significant length of the surface).

The pre-failure geometry of the Nikawa Landslide is reproduced in Figure A.118. Several trial circular and noncircular failure surfaces were searched, and some of the more critical surfaces are shown in Figure A.118. The critical surfaces are similar to the failure surface suggested by Sassa et al. (1995, 1996) and Loukidis et al. (2004), which is at a maximum depth of about 14 to 15 m in the embankment. The maximum height of water above the sliding surface was about 7 m as reported by Sassa et al. (1995, 1996,

2004) and Loukidis et al. (2001). The liquefied zone was assumed to correspond to the fill soils below the phreatic surface, where $(N_1)_{60}$ values were approximately 9. The values of mobilized shear strength in the zone of liquefaction ranged from 33 to 53 kPa depending on the assumptions regarding failure surface shapes used. The best estimate of mobilized shear strength in the zone of liquefaction was 48.5 kPa.

A second analysis was conducted to estimate the mobilized shear stress ratio at the triggering of liquefaction using the sliding surfaces shown in Figure A.118. The shear stress ratio in the liquefied zone was varied until FS of unity was achieved. A best estimate of yield shear strength ratio was determined as 0.29, with a possible range of 0.21 to 0.34 determined using other failure surfaces. The weighted average prefailure vertical effective stress was determined as 167 kPa.

A. 9.9.3 Liquefied Shear Strength and Strength Ratio

Because the post-failure geometry is discontinuous and some of the mass is deposited in a stream channel, the liquefied shear strength was estimated using the infinite slope analysis described in Chapter 2. The failed mass was divided into several sections that have similar top and bottom slope angles. Using a slope of the failed material and slope of the ground surface of 8.6°, an average thickness of failed mass of 4.5 m (see Figure A.119), and the liquefied shear strength was estimated to be 13.1 kPa. Lower and upper bound values were estimated using failed mass slope angles from 8° to 12° and a failed mass thickness of of 2.5 m and 4.5 m. The resulting lower and upper bound liquefied shear strengths are 9 and 18 kPa, respectively.

To estimate the liquefied shear strength ratio using an infinite slope analysis, the pre-failure effective vertical stress needs to be determined first. As can be seen from Figure A.119, the entire embankment mass failed and was deposited at the foot of slope. Therefore, it is likely that liquefaction occurred in the embankment fill below the water table and that the embankment mass above the phreatic surface also moved with the liquefied fill. The vertical effective stress at this location was calculated as 183.5 kPa for the SPT-based overburden stress correction. Using the liquefied shear strength and prefailure vertical effective stress above, the best estimate of liquefied strength ratio was approximately 0.07, with a range of 0.049 to 0.098.

A. 9.9.4 Liquefied Shear Strength and Strength Ratio Considering Kinetics

Because the deformed soil mass was discontinuous and deposited in a stream channel, the actual path of centroid movement can not be determined and a kinetics analysis could not be conducted.

A. 9.9.5 Sources of Uncertainty

The following sources of uncertainty were involved in estimating the yield shear strength and strength ratio: (1) the limits of the zone of liquefaction; (2) the location of the initial sliding surface; and (3) the location of the phreatic surface within the slope.

Although from SPT results it was determined that the lower portion of the embankment fill is liquefiable [$(N_1)_{60}$-values ~ 9), the exact location of soil mass that liquefied is not known. Therefore it was assumed that the entire fill beneath the water table was loose enough to liquefy. The initial sliding surface was consistent with that suggested by Sassa et al. (1996). Alternative circular and noncircular surfaces were also considered. Available studies provide only a portion of the phreatic surface within the fill. The author completed the phreatic surface by assuming that it is subparallel to the ground surface. This is a minor uncertainty because it is likely that the phreatic line will be parallel to the ground surface, moreover, Loukidis et al. (2001) interpreted the same phreatic surface.

The following sources of uncertainty were involved in estimating the liquefied shear strength and strength ratio: (1) variations in the slope angles of the failed material and the ground surface; (2) the thickness of failed mass; (3) the potential for porewater pressure or void redistribution; and (4) the final geometry of the failed mass. Because there was some variation in the slope angles of both failed material and the ground surface on which the soil was deposited, a range of slope angles were considered. There was some variation in the thickness of the failed mass, therefore two thicknesses (2.5 m and 4.5m) were considered in the analysis. The flow of the failed mass was impeded by stream channel and a building near the toe (see Figure A.116), suggesting that the mass may have flowed farther (and to a flatter slope) if unimpeded.

The following sources of uncertainty were involved in estimating the "representative" penetration resistance: (1) the raw N-values were not reported in the literature; (2) the use of Japanese SPT equipment; and (3) the conversion from SPT to CPT. Sassa et al. (1996) and Loukidis et al. (2001) reported typical raw N-values, but did not report the actual N-values and the depths at which these values correspond. As a result, it was assumed that the N-values correspond to the depth of the failure plane. It was not reported in the literature which hammer type was used for SPTs; therefore an average of energy ratios of two common Japanese methods was used to correct N-values. Because CPT was not conducted on this site, SPT values were converted to CPT values using the average of five q_c/N_{60} correlations.

A.9.10 Takarazuka Landslide

The Hyogoken-Nanbu earthquake triggered an unusually long-runout landslide at the Takarazuka Golf Club. Figure A.120 shows plan and sectional views of the landslide. The landslide took place on a moderately-inclined slope, and it moved over a flat golf course, transporting some trees (which remained standing). The landslide caused no fatalities, and it was preserved in its failed state for several months. The 1995 Hyogoken-Nanbu earthquake (M_W = 6.9) was estimated to have produced a peak ground surface acceleration of 0.3g at this site.

The 1995 Takarazuka Landslide is a typical example of a rapid long-runout landslide, which flowed a total distance of about130 m measured from the pre-failure toe to the post-failure toe position on a moderately inclined slope. As noted above, trees on the slope remained upright; indicating that the landslide mass remained coherent. The

landslide traveled along a small valley that had been artificially filled with weathered Osaka Group coarse-grained sandy soils to develop the golf course. The groundwater level was about 2 m below the ground surface. Estimating from the rapid, long-runout movement and the field investigation of the source area, the base of the landslide mass was saturated and sliding occurred under nearly undrained conditions (Okada et al. 2004).

Based on descriptions of the failed mass (Sassa et al. 1996), the landslide seemed to have slid along the ground surface, scraping and mounding the surface soil layer in front of the sliding mass. The toe of the initial landslide is not clear; however Sassa et al. (1995) suggested that the intial toe was located between P11 and P13 (Figure A.120). To explain the undrained loading mechanism, Fukuoka et al. (1997) stated the following: (1) the landslide mass "bulldozed" the original ground surface to a depth of 2 to 3 m; (2) the landslide traveled along a reclaimed valley filled with loose sandy soil; and (3) the observed water table was 2 to 3 m below the ground surface.

The Takarazuka Landslide is an interesting case history as the failed mass traveled nearly 130m while carrying trees that remained upright and were essentially undisturbed. Sassa et al. (1995, 1996) described the failure as *self-undrained loading mechanism* in which the failed mass from a steeper portion of the slope induced undrained loading within the saturated soil layer a few meters beneath the ground surface as the landslide mass moved downslope. The moving landslide mass "bulldozed" the surface soil layer above the sliding surface, causing significant heave and buckling of the soil at the toe. Figure A.121 shows a photograph of the Takarazuka Landslide. Trees that were moved by the landslide can be clearly seen, and brown soil (above the failure surface) was scraped off and pushed downslope in front of the main body of the sliding mass. Figure A.122 schematically illustrates the longitudinal central section of the landslide toe. This figure shows several markers, e.g., forests/trees, a sand bunker, and lawn sections that were moved from their original position. The upward shear surfaces shown in Figure A.122 suggest that the "bulldozed" soil essentially buttressed the main body of the landslide mass, limiting the downslope movement. Further, the GWT is located about 0.7 m (Figure A.122) above the sliding surface. The original ground surface (marked as 'G.S.' in Figure A.122) is about 2.7 m above the sliding surface. Figure A.123 shows a sketch of trench T1. A remolded brown soil matrix is shown in this figure. This sheared/remolded soil likely represents the shear zone developed during the landslide, located at a depth of about 2.7 m below the ground surface. This information helped to constrain the stability analyses described below.

Although Sassa et al. (1995, 1996) suggested that the weight of the landslide mass moving over the ground was required to trigger undrained loading and liquefaction, the author believes that the cohesionless soil below the GWT should have been undrained and, if so, would have liquefied during shaking. The evidence for this postulate is: (i) the soil below the GWT was in a loose state (as estimated from penetration resistance described below); and (ii) the reported PGA at the Nikawa landslide site (which is located in close proximity to the Takarazuka landslide site) was 0.6g (Gerolymos and Gazetas 2007). If this soil liquefied during shaking, the sliding mass would likely have moved downslope on this surface, rather than flowing onto the existing ground surface. The

unsaturated soil above the sliding surface would have been "bulldozed" in front of the sliding mass, eventually acting as a buttress and decelerating the sliding mass.

A. 9.10.1 Representative Penetration Resistance

Trenches were excavated at locations T1, T2 and T3, three borings were drilled and 20 CPTs were performed after the earthquake (see Figure A.120), although the results of the CPTs were not reported in the literature. The sliding surface was observed to be about 2.7 m below the original ground surface and the side walls were nearly vertical.

In the absence of penetration data and relative density, it is hard to determine the "representative" penetration resistance for this case. Fukuoka et al. (1997) stated that Nikawa landslide was situated just 1 km south of Takarzuka landslide site and the subsurface profiles at both sites were similar, i.e., both landslides consisted of artificially-placed fill overlying Osaka Group sand. Each landslide exhibited long run-out and low apparent friction angles. Because of the lack of other reasonable options, the author opted to use N-values reported by Loukidis et al. (2001) for the Nikawa landslide to interpret this case history. From the Nikawa landslide, the average, lower bound and upper bound N-values were 10, 4, and 16, respectively. For the approximate depth of sliding of 3 m at the Takarazuka landslide site and a total and saturated unit weight of 18.5 kN/m^3, the approximate mean $(N_1)_{60}$-value is 11, with a range of approximately 4 to 18.

Portable cone penetration tests were performed at the Takarazuka site, but the results were not published. Therefore, author used converted the approximate SPT result to CPT tip resistance. The D_{50} of the Osaka group soil, as shown in Figure A.124, is approximately 1.2 mm, corresponding to $q_c/N_{60} = 0.65$ based on the average of the five correlations from Robertson and Campanella (1985), Seed and de Alba (1986), Andrus and Youd (1989), Kulhawy and Mayne (1990) and Stark and Olson (1995). Note that the correlations from Robertson and Campanella (1985), Seed and de Alba (1986), and Olson and Stark (1995) were extrapolated to $D_{50} = 1.0$ for computing this average ratio. The average qc1 value becomes 7.15 MPa, with a range from 2.6 to 11.7 MPa.

A. 9.10.2 Yield Shear Strength and Strength Ratio

The mechanism that likely triggered flow failure at the Takarazuka Golf Course was seismically-induced liquefaction of the saturated, loose, sandy fill by the 1995 Hyogoken-Nanbu earthquake. As shown in Figure A.120, the initial landslide took place on the steepest portion of the slope. This mass slid onto a lower, gentler slope and traveled more than 130 m. Figure A.120 shows that this landslide traveled along the golf course and that the runout path was not straight. As discussed in Chapter 2, the shear strength and strength ratio mobilized at the instant of failure in cases of liquefaction flow failure triggered by seismic loading do not necessarily represent the yield shear strength and yield strength ratio, respectively. Therefore, back-calculated values of shear strength and strength ratio likely do not represent the yield shear strength and yield shear strength ratio.

The pre-failure geometry is reproduced in Figure A.125. A slope stability search considering several circular and noncircular surfaces was conducted to determine the critical initial failure surface that was consistent with descriptions by Sassa et al. (1995, 1996) and Fukuoka et al. (1997). As stated above, Fukuoka et al. (1997) reported that the water table was 2 to 3 m below the ground surface. It was not clear whether Fukuoka et al. (1997) was referring to the water level at the toe of the deposited mass as illustrated in Sassa et al. (1996), or the water table was 2 to 3 m below the embankment which would correspond to a water table 0.6 to 0.7 m above the sliding surface.

Using the pre-failure geometry and the failure surface shown in Figure A.125, values of shear strength below the phreatic surface were varied until a FS of unity was achieved. Fukuoka et al. (1997) suggested a drained friction angle of 28.8° from ring shear tests. As a result, the friction angle of the non-liquefied soil above the phreatic surface was varied from 28° to 32° in this study. The resulting yield shear strength ranged from 22.5 to 36.5 kPa, with a best estimate of 24 kPa.

Using the same initial failure surfaces that were used in yield strength analysis, a limit equilibrium analysis was performed to evaluate the yield strength ratio. The yield strength ratio varied until a FS of unity was achieved. The yield strength ratio ranged from 0.205 to 0.305, with a best estimate of 0.24. This range was obtained using the assumptions regarding shape of failure surface, variation in ground water table, and strength of non-liquefiable soil discussed above.

A. 9.10.3 Liquefied Shear Strength and Strength Ratio

The post-failure geometry is reproduced in Figure A.126. The failure surfaces shown in the figure was determined from the stability search and is consistent with the undrained loading mechanism as suggested by Sassa et al. (1996) and Fukuoka et al. (1997). The final sliding surface is likely to pass through the junction of the surface soil that was “bulldozed” during failure and the failed embankment fill that was deposited during the slide. Considering various failure surfaces, the back-calculated shear strength ranged from 8.8 to 9.3 kPa, with a best estimate of approximately 9.1 kPa. The weighted average vertical effective stress was estimated as 116 kPa.

Using the same post-failure sliding surface shown in Figure A.126, a limit equilibrium analysis was conducted to estimate the liquefied strength ratio. The landslide traveled a total distance of 130 m and transported a standing forest without significant disturbance. A detailed explanation of the failure mechanism is given in Section A.9.10. The description of failure suggests that the soil along the entire sliding surface liquefied as soon as earthquake hit the region. Thus, the segments did not originate from the source area, but rather remained in their pre-failure locations. Because the water table was 2 to 3 m below the surface, the same thickness should be used to calculate the pre-failure vertical effective stress for estimating the liquefied shear strength ratio. To calculate the pre-failure vertical effective stress for liquefied shear strength ratio analysis, the post-failure geometry was divided into number of segments and the pre-failure effective

vertical stress was calculated for each segment. The liquefied strength ratio was varied until a FS equal to unity was achieved. The average value of liquefied shear strength ratio obtained from the analysis is 0.088 with a possible range of 0.084 to 0.089.

A. 9.10.4 Liquefied Shear Strength and Strength Ratio Considering Kinetics

The pre- and post-failure geometries are reproduced in Figure A.126. Figure A.126 also shows the pre- and post-failure centers of gravity, the final sliding surface, and the possible center of gravity travel path during flow failure. The initial kinetics analysis assumed that all soils along the failure surface mobilized the liquefied shear strength.The kinetics analysis in Figure A. 127 yielded the following results:

- Liquefied shear strength ≈ 14.9 kPa
- Liquefied shear strength ratio ≈ 0.14

The acceleration, velocity,and displacement time histories of the failed mass are shown in Figure A. 127, along with the back-calculated driving shear stress and liquefied shear stress along the entire length of the failure surface. This liquefied shear strength resulted in a calculated displacement of the center of gravity of the failure mass of approximately 17.70 m vertically and 98.90 m horizontally. The initial kinetics analysis assumed that all soils along the failure surface mobilized the liquefied shear strength. However, as shown in Figure A.126, segment 1 was located above the phreatic surface and was therefore non-liquefiable. Therefore, the liquefied shear strength was adjusted to account for the strength of the non-liquefied soils using Eq. A.1 (Olson 2001).

Because the upward shear surfaces shown in Figure A.122 suggest that the "bulldozed" soil essentially buttressed the main body of the landslide mass, limiting the downslope movement, the effects of passive forces at the toe of the sliding mass were considered in a separate analysis. In this analysis, it was assumed that the soil in front of the sliding mass was initially 2.5 m thick, and this thickness was increased incrementally with unit change in displacement until it reached its final thickness of 9 m. This passive force was used to reduce the driving force. The results of this analysis are shown in Figure A. 127.

The kinetics analysis only provides a value of liquefied shear strength. Therefore, the liquefied shear strength ratio reported above was determined by dividing the liquefied shear strength of 14.9 kPa by the weighted average vertical effective stress of 104 kPa determined from the corresponding locations of the post-failure segments in the pre-failure geometry.

These values of liquefied shear strength and strength ratio include the effects of kinetics, and therefore are considered best estimates. These values are roughly one-half of the sum of the shear resistances backcalculated from the pre-and post-failure geometries. This result is reasonable because as illustrated in Figure A. 127, the driving shear stress is approximately equal to the liquefied shear strength when the center of gravity of the

failed mass has moved approximately halfway between its pre-failure and post-failure position.

A. 9.10.5 Sources of Uncertainties

The following sources of uncertainty were involved in estimating the yield shear strength and strength ratio: (1) the location of the phreatic surface within the embankment; (2) the limits of the zone of liquefaction; (3) location of the initial sliding surface; and (4) the shear strength of the non-liquefied soils. The water table in the upper portion of the slope was not reported. However, Sassa et al. (1996) reported the watertable depth near the toe of post-failure geometry. The remainder of the phreatic surface was assumed. No specific liquefied zone(s) was defined in the literaure. This study assumed that all of the loose sandy soil below the phreatic surface was liquefiable. A sliding surface covering the entire slope was suggested by Sassa et al. (1996); however, no initial sliding surface was clearly defined. As stated by Sassa et al. (1996), the location of the toe of the initial landslide likely was between P11 and P13 (see Figure A.120). Therefore, both circular and non-circular trial sliding surfaces were considered. Fukuoka et al. (1997) suggested a drained friction angle of 28.8° from ring shear tests. In this study, the author considered a range of potential friction angles from 28° to 32° for the non-liquefied soil above the phreatic surface.

The following sources of uncertainty were involved in estimating the liquefied shear strength and strength ratio, including the kinetics analysis: (1) the location of phreatic surface; (2) the limits of the liquefied zone; (3) the shear strength of non-liquefied soils; (4) the pre-and post-failure position of toe; (5) the location of final surface of sliding; and (6) the travel path for the center of gravity.

The following sources of uncertainties were involved in estimating the "representative" penetration resistance: (1) the unavailability of raw SPT and CPT measurements; (2) the use of Japanese SPT equipment; and (3) the conversion from SPT to CPT, particularly for a D_{50} value slightly outside the range of data for three of the five qc/N60 correlations considered in this study. No penetration data or in-situ measured relative density were available for this site. As explained earlier, the landslide site was located 1 km north of the Nikawa landslide for which N-values were reported. These N-values were used here because the geology and fill soils involved in the Nikawa and Takarazuka landslides were similar. It was not indicated in the literature what hammer type was used, therefore an average of energy ratio of two common Japanese methods, as indicated above, was used to estimate $(N_1)_{60}$- values. Because CPT results were not reported for this site, the author converted SPT blow count to CPT tip resistance.

A.9.11 Idenoshiri Dam

The Idenoshiri Dam had a maximum height of approximately 5.5 m and a crest length of approximately 155 m prior to the earthquake. Its crest was about 4 m wide and it had an approximately 1V:2H upstream and downstream slopes. The Idenoshiri Dam

was a homogeneous earth-fill dam with a reservoir storage capacity of 17,500 m^3. At the time of earthquake, the center part of the dam collapsed completely; and many cracks in the longitudinal direction appeared.

Figure A.128 and Figure A.129 show the pre- and post-failure geometries of Idenoshiri Dam, as well as the soil profile and SPT data measured in a borehole drilled after the earthquake. The Idenoshiri Dam consists of (from the surface): embankment fill, fine sand, alluvial sandy gravel, and the Osaka Group soil. Tani (1996) reported that the embankment fill consisted of 6.4% gravel, 76.4% sand, 2.9% silt, and 14.3% clay. Following the earthquake, sand boils were observed in the reservoir suggesting that seismically-induced liquefaction was responsible for the failure (Tani 1996). Liquefaction most likely occurred in the sandy embankment fill and fine sand below the phreatic surface because these soils exhibited SPT blow counts less than 5.

A. 9.11.1 Representative Penetration Resistance

Tani (1996) presented borehole data with SPTs that were obtained after the earthquake, as illustrated in Figure A.129. SPT N-values within the lowest portion of the embankment and the fine sand foundation generally ranged between 3 and 5 with a mean value around 4. Blow counts in the alluvial sandy gravel and Osaka Group soils all exceed 35. These results suggest that the saturated portion of the embankment and the fine sand foundation were likely to liquefy. Uchida et al. (2001) provided percentage passing various sieves for the embankment soil. Based on this information, a reconstructed grain size curve suggests that the D_{50} value is about 0.2 mm for embankment soil. The equipment used to drill the borings and perform the SPTs is unknown. Therefore the energy ratio used here (i.e., 72%) was taken as the average of the hammer energies for the two hammer types commonly used in Japan. The total and saturated unit weight was assumed to be 18.5 kN/m^3.

CPTs were not performed at Idenoshiri Dam. Therefore, q_{c1} values were estimated using the average q_c/N_{60} ratio from the following five correlations: Robertson and Campanella (1985), Seed and de Alba (1986), Andrus and Youd (1989), Kulhawy and Mayne (1990) and Stark and Olson (1995). For the estimated D_{50} of 0.2 mm, the average $q_c/N_{60} = 0.43$. Thus, the average q_{c1} value is 2.4 MPa, with a range from 1.6 to 4.0 MPa.

A. 9.11.2 Yield Shear Strength and Strength Ratio

As stated above, the mechanism that likely triggered the flow failure of Idenshiri Dam is seismically-induced liquefaction of the saturated sandy embankment fill and fine sand foundation. As discussed in Chapter 2, the shear stress and stress ratio mobilized at the instant of failure in cases of liquefaction flow failure triggered by seismic loading do not necessarily represent the yield shear strength and yield strength ratio, respectively.

The pre- and post-failure geometries of Idenoshiri Dam are reproduced in Figure A.130. Because two relatively different cross-sections of the pre- and post-failure geometries are given in Tani (1996) and Uchida (2001), as shown in Figure A.128 and

Figure A.129, respectively, the author combined the cross-sections to produce a single-cross section that is reasonably consistent with the information given by different investigators. Although, saturated embankment fill and foundation both are likely to trigger liquefaction, Uchida et al. (2001) emphasized on possible liquefaction of the foundation soil because several sand boils were observed on the reservoir bed and at the downstream paddy field. A slope stability search was conducted to determine the critical initial failure surface that is consistent with the failed geometry and the location of the liquefied soils. A single value of shear strength was assigned to liquefied soil, and this value was varied until a FS of unity was achieved. A range of drained friction angles from 28º to 34º were assigned to the embankment material above the phreatic surface.

Several trial circular and non-circular failure surfaces were searched, and Figure A.130 presents two trial circular and noncircular failure surfaces. The values of mobilized shear strength in the zone of liquefaction ranged from 11.5 to 19 kPa depending on the shape of the failure surface, with a best estimate of 15.1 kPa.

A second analysis was conducted to estimate the mobilized stress ratio at the triggering of liquefaction. Several trial failure surfaces, including the critical failure surface from the mobilized shear strength analysis were considered, as shown in Figure A.130. The shear stress ratio in the liquefied zone was varied until FS of unity was achieved. A best estimate of mobilized shear strength ratio was determined as 0.24, with a possible range of 0.22 to 0.287 using other failure surfaces. The weighted average pre-failure vertical effective stress was determined to be 62 kPa.

A. 9.11.3 Liquefied Shear Strength and Strength Ratio

The post-failure geometry is reproduced in Figure A. 131. Because the complete post-failure geometry was not reported, area balancing was used to complete the post-failure geometry. As indicated in Figure A. 131, area balancing suggests that the soil mass flowed approximately 30 to 35 m from its original toe position. The final sliding surface was constrained by the shape of the failed mass. Again, the embankment fill and fine sand foundation were assumed to liquefy and a single value of shear strength was assigned to the liquefied soil. This value was varied until a FS of unity was achieved. The back-calculated shear strength was approximately 4.4 kPa, with a possible range from 2.95 to 5.4 kPa. This range is obtained due to the assumptions regarding shape of failure surface. Varying the friction angle did not have a significant effect on the liquefied shear strength as many of the failure surfaces do not pass through the non-liquefied soil.

Using the same assumptions made in the liquefied shear strength analysis and same post-failure sliding surface shown in Figure A. 131, a limit equilibrium analysis was conducted to estimate the liquefied strength ratio at Idenoshiri Dam. The post-failure geometry was divided into 12 segments, all of which involved liquefied soil, as illustrated in Figure A. 131 The pre-failure vertical effective stress was determined for each of these segments and applied to the segment in its assumed final location. The value of liquefied shear strength ratio was varied until a FS of unity was achieved. The liquefied strength

ratio was estimated as 0.038, with a possible range from 0.026 to 0.048. The weighted average of prefailure vertical effective stress was estimated as 113 kPa.

A. 9.11.4 Liquefied Shear Strength and Strength Ratio Considering Kinetics

Figure A. 131 also shows the pre-and post-failure centers of gravity, the final sliding surface, and the probable center of gravity travel path during flow. The initial kinetics analysis assumed that all soils along the failure surface mobilized the liquefied shear strength. In the case of Idenoshiri Dam, the entire failure surface was within the liquefied zone and therefore an adjustment for the non-liquefied soil strength was not necessary. The kinetics analysis in Figure A.132 yielded the following results:

- Liquefied shear strength ≈ 11.45 kPa (range of 9.95 to 13.45 kPa)
- Liquefied shear strength ratio ≈ 0.10 (range of 0.088 to 0.12)

The liquefied shear strength range results from incorporating the potential effect of hydroplaning (reductions of 0%, 50%, and 100% were used here). This liquefied shear strength resulted in a calculated displacement of the center of gravity of the failed mass of approximately 2.33 m vertically and 12.53 m horizontally, consistent with the movement shown in Figure A. 131.

The kinetics analysis only provides a value of liquefied shear strength. Therefore, the liquefied shear strength ratio reported above was determined by dividing the liquefied shear strength of 11.45 kPa by the weighted average vertical effective stress of 113 kPa determined from the liquefied strength analysis.

These values of liquefied shear strength and strength ratio include the effects of kinetics and hydroplaning, and therefore are considered best estimates. These values are roughly one-half of the sum of the upper and lower bounds computed from the pre-and post-failure geometries, respectively. This result is reasonable because as illustrated in Figure A.132, the driving shear stress is approximately equal to the liquefied shear strength when the failed mass has moved approximately half-way between its pre-failure and post-failure position.

A. 9.11.5 Sources of Uncertainties

The following sources of uncertainty were involved in estimating the mobilized shear stress and stress ratio at the triggering of liquefaction: (1) the initial failure surface location; (2) the actual limits of the initial zone of liquefaction; (3) the phreatic surface within the embankment; and (4) the potential for drainage at the triggering of liquefaction. Because the failure surfaces shown in Figure A.130 were inferred from the observed damage and the exact location of the initial failure surface cannot be identified, a number of trial failure surfaces, both circular and non-circular, were analyzed until best-estimate values of yield strength and yield strength ratio could be obtained. Because the exact limits of the liquefied zone were not known it was assumed that the entire

embankment soil below phreatic surface and fine soil was liquefied during this event, as suggested by the SPT N-values. The phreatic surface shown in Figure A.130 is suggested by some investigators, but this is an assumed phreatic surface.

The following sources of uncertainty were involved in estimating the liquefied shear strength and strength ratio: (1) the complete post-failure geometry was not available; (2) the phreatic surface for post failure geometry; and (3) the location of the final surface of sliding. Because the complete post-failure geometry was not available for Idenoshiri Dam, area balancing was used to infer the remaining part of the failed mass. Information about the phreatic surface for the post-failure geometry was not given in the literature, and it was assumed to follow the surface of the post-failure geometry. The final failure surface for the post-failure geometry was inferred from the post-failure geometry and initial sliding surface.

The following sources of uncertainty were involved in estimating the "representative" penetration resistance: (1) SPT borehole drilling equipment; and (2) the conversion of SPT blow counts to CPT tip resistance. No CPTs were conducted at Idenoshiri Dam, and hence SPT blow counts were converted to CPT tip resistance.

A.10 Jamuna Bridge Landslides, Bangladesh

A.10.1 Introduction

The Jamuna River, which is one of the world's largest rivers, physically divides Bangladesh into two halves: east and west. The eastern half of the country is more developed than the western half, partly because of its access to the capital Dhaka and to international market through Chittagong port. The western half, which has fertile agricultural land with higher average yields for major crops than the rest of the country, is dependent on agriculture as the dominant sector of the economy. A higher proportion of poor people live in the western half; particularly in northwestern part of Bangladesh (ADB 2000).

The Jamuna Multipurpose Bridge, or Bangabandhu Bridge, hastened the economic and social development of the west zone of Bangladesh. Constructed in the middle reach of the Jamuna River, the Bangabandhu Bridge is situated 110 km northwest of Dhaka and has a length of 4.8 km. Connecting the towns of Sirajganj and Bhuapur (see Figure A.133); the bridge was planned and constructed between 1995 and 1999 (Hight et al. 1999).

The Jamuna River is a braided river, consisting of numerous channels that change their width and course significantly with the seasons (Ishihara 2008). Thus, channeling the river to ensure that it would continue to flow under the bridge corridor was the most difficult technical challenge of the project. Construction of the Bangabandhu Bridge across the Jamuna River in Bangladesh required the formation of extensive river channelization. In addition it was considered necessary to protect the bridge abutment from scour and erosion. Ishihara (2008) reported that riverbed elevation could change by

more than 10m daily during heavy flows. The channels were excavated by dredging river sand from barges. The aim was to reinforce the underwater slope with stones and geotextiles to protect the abutments. The West Guide Bund was constructed at the site of a recently formed sand island (see Figure A.133). Therefore, the material forming the dredged slopes consisted of young, rapidly-deposited sediments. The slope on the west side was to be protected against scour by geotextiles and stone armor, because the bridge abutment was to be installed due west of the West Guide Bund. Thus the underwater slope on the west side was designated as a "permanent slope" and was designed with slope varying from 5H:1V to 3.5H:1V. In contrast, the slope on the east side of the dredged channel was considered temporary and was to be left unprotected. Even though slides were expected to occur in the temporary slope, and it was expected that the temporary slope would be eroded over time, designers considered this to be acceptable. Thus, the eastern slope was designed with a 3H:1V grade. Both permanent and temporary slopes are shown in Figure A.134. During construction, a number of slips occurred in both the permanent and temporary slopes. The locations of the slips that occurred in the permanent and temporary slopes are shown in Figure A.135. Four slides, two each on the permanent and temporary sides of the West Guide Bund are analyzed in this study. The locations of these slides are marked on Figure A.135.

A.10.2 Site Geology and Soil Conditions

Over 30 submarine flow slides occurred along the West Guide Bund of the Jamuna Bridge in Bangladesh. The slides occurred on relatively gentle slopes (1V:3H and 1V:3.5H, i.e., slope angles from 11° to 16°), involved large volumes of soil, and resulted in very flat final slopes (approx. 1:10 to 1:20, i.e., slope angles from 2.9° to 5.7°). The Guide Bund slopes were formed in very young (< 200 years) sandy sediments deposited by the Jamuna River consisting chiefly of micaceous sands. The mica consists of thin plates of fine to medium sand size, which varied in their distribution and orientation. Based on grain counting, the mica content also varied, but generally was 5 to 10% (Hight et al. 1999; Ishihara 2008). Apart from the mica, the sand was mainly composed of siliceous material.

A typical grain size distribution curve is shown in Figure A.136. As can be seen from the grain size distribution curve the percent passing the 0.075 mm grain size (mostly silt) was approximately 5 to 20%, and the median grain size was approximately 0.1 to 0.2 mm. The specific gravity was about Gs = 2.75 and the maximum and minimum void ratios (as measured by the Standard of the Japanese Geotechnical Society) were e_{max} = 1.202 and e_{min} = 0.602, respectively (Ishihara 2008). Jefferies and Been (2006) suggested a large range of in situ state parameter (ψ), ranging from -0.04 to +0.05 for the sands in the upper 7 m. Ishihara (2008) suggested a range of ψ = -0.081 to +0.04. The saturated unit weight is estimated as 18.5 kN/m^3.

A.10.3 Description of the Failures

On December 3, 1995, the largest slide (denoted as W3 in Figure A.135) took place on the permanent slope at station 1550. This slide covered an area of about 150 m

wide by 150 m long over the permanent slope. This slope was third in a sequence and followed by slides on November 19 and November 22, 1995 at stations 1270 and 1410 respectively. The second slide analyzed in this study (denoted W4) occurred on December 15, 1995, on the permanent slope at station 1800. The other two slides on the temporary slopes that are analyzed in this study failed on May 5, 1996 and April 20, 1996 at stations 1800 and 2500, and are denoted as WT13 and WT4, respectively.

It is difficult to determine a single triggering mechanism for the slides because they occurred rapidly in underwater environments. Several triggering mechanisms are proposed for Jamuna Bridge River slides by researchers, but the most obvious triggering mechanism for the slides is dredging at the slope toe (Hight et al. 1999). As explained in Section A.10.1, the initial design of the permanent slope included 1V:3.5H slopes at the top and bottom with a 1V:5H slope in the middle (see Figure A.134). A number of failures occurred during dredging of the bottom slope. The dredging might have been carried out so fast that the rapid change in the state of stress created an undrained condition, triggering a local failure that retrogressed into a larger slide. These slips occurred over approximately 50% of the constructed length. In general, the slides involved large volumes of soil, and resulted in very flat slopes (approximately 1V:10H to 1V:20H, i.e., slope angles from 2.9 to 5.7º).A significant reduction in the number of slides, i.e., only three minor slips representing less than 5% of the excavated length of the slope, occurred after the temporary slope was flattened to 1V:6H, as shown in Figure A.134.

Prior to the 1st slide, the temporary slope was being dredged at 1V:3H (see Figure A.134) and slips affected almost 100% of its dredged length (Hight et al. 1999). As noted above, a significant reduction in the number of slides occurred after the permanent slope was flattened to 1V:6H. In contrast, the temporary slope was flattened to 1V:5H and the slope continued to fail. Hight et al. (1999) attributed 61% of the slides to dredging, 30% with storm activity, and 9% to drops in river level (~1.0m/day over a 5-day period). The dredging and storm activity, which contributed to more than 90% of the slides, dredged or scoured the toe of the slopes causing initial failures that then retrogressed backward.

A.10.4Representative Penetration Resistance

Both SPTs and CPTs were performed on the West Guide Bund of the Jamuna River Bridge prior to excavation. Following the failures, numerous additional CPTs were performed along the West Guide Bund. Hight et al. (1999) presented typical SPT results carried out in the vicinity of the West Guide Bund apparently *before* the failure as shown in Figure A.137. SPT-N values were corrected to $(N_1)_{60}$ following Skempton (1986) and converted to relative density, using a correlation suggested by Skempton (1986). These blow counts illustrate that loose to medium dense pockets of sand were present in the upper 25m of the alluvial sediments. The loose pockets exhibit $(N_1)_{60}$-values ranging from 9 to 14, with a typical value of about 10. However, these values were based on an assumed (not measured) energy ratio of 80% as suggested on Ishihara (2008) for the drop system used in Bangladesh. However, if the energy ratio were closer to 60%, the $(N_1)_{60}$-

values decrease to a range of 7 to 11, with a typical value of about 8 in the elevation range from 0 to -17m.

Dutch cone penetration tests (CPT) were carried out at 15 locations for design. Ishihara (2008) reported that the Dutch CPT yielded tip resistances of 4 to 5 MPa at depths from 6 to 8m at a location close to the east section of the West Gude Bund, indicating loose pockets similar to those observed from the SPT. Unfortunately, the Duch CPT soundings performed *before* failure are not available in the literature.

Following the failures, Fugro Engineers performed 22 electronic CPTs at the locations shown in Figure A.135. Prof. Yoshimine kindly provided the author with the CPT sounding data on personal request. Yoshimine et al. (1999) indicated that the slides typically occurred between Elevation -7m and Elevation +8m, i.e., within 15m of the ground surface. Because the soundings were performed from the top of the Bund, the author selected penetration resistance values within the upper 15 m to represent the conditions within 15 m of the surface where the failures occurred. **Figure A.138** presents the CPT soundings performed near the slides studied here.

- Station 1500W3, sounding C150WRD, 8 to 13m below grade.
  q_{c1} = 2.5 to 3.6 MPa, average value = 2.9 MPa.
- Station 1800W4, soundings C170W and C190W, 6.5 to 9m below grade.
  q_{c1} = 2.5 to 3.9 MPa, average value = 3.0 MPa.
- Station 1800WT13, sounding C190E, 4.3 to 10.3m below grade.
  q_{c1} = 2.4 to 3.5 MPa, average value = 3.0 MPa.
- Station 2500WT4, sounding C250E, 4.8 to 10m below grade.
  q_{c1} = 1.9 to 4.0 MPa, average value = 2.8 MPa.

Because the SPT values were not measured at the failure locations, the author also estimated $(N_1)_{60}$ values from the measured q_{c1} values. The D_{50} values of Jamuna Bridge sands ranged from 0.1 to 0.2 mm which yields q_c/N_{60} ratios of 0.35 to 0.43 using the average of the five qc/N60 correlations proposed by Robertson and Campanella (1985), Seed and de Alba (1986), Andrus and Youd (1989), Kulhawy and Mayne (1990) and Stark and Olson (1995).

- Station 1500W3, $(N_1)_{60}$ = 6 to 9, average value = 7.
- Station 1800W4, $(N_1)_{60}$ = 7 to 10, average value = 8.
- Station 1800WT13, $(N_1)_{60}$ = 6 to 10, average value = 8.
- Station 2500WT4, $(N_1)_{60}$ = 5 to 10, average value = 7.

These values are slightly lower than those reported in Figure A.137 for ER = 80%, but are consistent with the values for ER = 60%. Because of the uncertainty in ER at the site, and because the available SPT data are not specific to individual slides, the $(N_1)_{60}$ values listed here will be used for analyzing these slides.

A.10.5 Yield Shear Strength and Strength Ratio

As described in Section A.10.3, multiple events were cited to have been possible causes for initiating the slide. A summary of these triggering mechanisms is as follows:

1. Removal of material at the toe of the underwater slope by dredging.
2. Shear stresses induced in the slope as a result of pressure differences on its surface associated with passing waves during storms.
3. Outward directed seepage forces in the slope as a result of drawdown.
4. The mica content of the sand (Ishihara 2008).

Ishihara (2008) suggested that the lowering of water levels and the potentially susceptible nature of the mica-containing sand were the two most likely triggering mechanisms. In contrast, Hight et al. (1999) considered the most likely triggering mechanism to be dredging at the toe. However, Hight et al. (1999) illustrated that adding small percentages of mica greatly increased the soil void ratio and compressibility making the soil highly susceptible to liquefaction. The dredging mechanism is strongly supported by the following information: (i) slope failures occurred on the permanent slope in November as the dredging proceeded (Ishihara 2008); (ii) once the permanent slope was modified to more stable slope of 1V:6H, the number of slides dropped drastically from 50% of the excavated length to only 5% (Hight et al. 1999), and (iii) if wave action or lowering of the water level were responsible for these slides, the failure of two adjacent slides on both sides of W3, i.e., W2 and W4, would not be 10 and 12 days apart. Furthermore, as defined in Section A.10.1 the temporary slopes were left unprotected and it was already expected that the slopes would fail due to scour and erosion.

The pre-and post-failure geometries of cross section 1500 W3 are shown in Figure A.139. The pre-failure geometry of the 1500 W3 slide is reproduced in Figure A.140. As described above, the failure likely resulted from toe excavation; therefore the search was limited to the toe area. Both circular and noncircular sliding surfaces were considered, as shown in Figure A.140. The regression of the slide was halted when the back scarp of the slip emerged above the water level, where capillary forces in the partially saturated sands provided stability and the sand was unable to liquefy. A friction angle of 30° (as used by Ishihara 2008) was used here for the non-liquefied soil. The entire soil under the water table was considered liquefiable. The back-calculated yield shear strengths in the liquefied zone ranged from 9.0 to 13.3 kPa depending on the failure surface location. The best estimate of mobilized shear resistance in the liquefied zone was 9.3 kPa.

A second analysis was conducted to estimate the mobilized shear stress ratio at the triggering of liquefaction. Several trial failure surfaces, both circular and noncircular, were considered. A shear stress ratio was assigned to the liquefied zone, and this value was varied until a FS of unity was achieved. A best estimate of yield shear stress ratio was estimated as 0.23, with a possible range of 0.164 to 0.27. The pre-failure vertical effective stress ranged from 40 to 50 kPa.

The pre-and post-failure geometries of cross section 1800 W4 are shown in Figure A.142. The pre-failure geometry of the 1500 W3 slide is reproduced in Figure A.143. As described above, the failure likely resulted from toe excavation; therefore a search was limited to the toe area. Both circular and noncircular sliding surfaces were considered, as shown in Figure A.143. The regression of the slide was halted when the back scarp of the slip emerged above the water level, where capillary forces in the partially saturated sands provided stability and the sand was unable to liquefy. A friction angle of 30° (as used by Ishihara 2008) was used here for the non-liquefied soil. The entire soil under the water table was considered liquefiable. The back-calculated yield shear strengths in the liquefied zone ranged from 8.4 to 10 kPa depending on the failure surface location. The best estimate of mobilized shear resistance in the liquefied zone was 9.7 kPa.

A second analysis was conducted to estimate the mobilized shear stress ratio at the triggering of liquefaction. Several trial failure surfaces, both circular and noncircular, were considered. A shear stress ratio was assigned to the liquefied zone, and this value was varied until a FS of unity was achieved. A best estimate of yield shear stress ratio was estimated as 0.21, with a possible range of 0.173 to 0.27. The pre-failure vertical effective stress was ranged from 40 to 50 kPa.

As described above, the failures along the temporary slope likely resulted from toe excavation; however, the slope inclinations at the time of failure are unknown. Hight et al. (1999) and Ishihara (2008) reported that the failures were retrogressive. Slide regression halted when the back scarps of the slips emerged above the water level, where capillary forces in the partially saturated sands provided stability and the sand was unable to liquefy. Hight et al. (1999) reported that the temporary slopes dredged at 1V:3H failed nearly 100% of the time. This suggests that a 1V:3H slope is unstable and represent an upper bound of the yield shear strength and strength ratio. Because of the instabilities associated with the 1V:3H slopes, the designers flattened the temporary slopes to 1V:5H, as illustrated in Figure A.134. As the dredging work resumed to flatten the slopes to 1V:5H, slides occurred over about 50% of the dredged length (Hight et al. 1999). Hight et al. (1999) further reported that slopes cut at 1V:6H did not fail. This suggests that slopes of 1V:5H may represent a yield shear strength and strength ratio between the lower bound and the average value. The best estimate of yield shear strength and strength ratio falls somewhere between these two slope inclinations, but likely closer to 1V:5H. The author assumed the best estimate to correspond to 1V:4H slopes for simplicity. Because of the uncertainty regarding the actual slope geometries at the time of the failures, the author opted to perform only infinite slope analyses for the failures in the temporary slope.

The pre-and post-failure geometry of cross section 1800WT13 is shown in Figure A.145.The depth of the failure surface (z) was considered to be 5.5 to 7 m based on the post-failure geometry shown in Figure A.145. The back-calculated yield shear strength ranged from 9.3 to 18.5 kPa, with a best estimate of 13kPa. The average pre-failure vertical effective stress was 54 kPa, with a range from 48 to 61 kPa for depths of 5.5 and 7 m, respectively. The yield shear strengths and vertical effective stresses produced an average yield strength ratio of 0.24, with a range from 0.194 to 0.30.

The pre-and post-failure geometry of cross section 2500WT4 is shown in Figure A.148. The analyses performed for this slide are identical to those performed for 1800WT13. The depth of the failure surface (z) was considered as 5.5 to 7.6 m based on the post-failure geometry shown in Figure A.148. The back-calculated yield shear strength ranged from 9.3 to 20 kPa, with a best estimate of 13.5kPa. The average vertical effective stress was 57 kPa, with a range from 48 to 66 kPa for depths of 5.5 and 7.6 m, respectively. Theyield shear strengths and vertical effective stresses produced an average yield strength ratios of 0.24, with a range from 0.194 to 0.30.

A.10.6 Liquefied Shear Strength and Strength Ratio

As can be seen from Figure A.139, Figure A.143, Figure A.145, and Figure A.148, all of the post-failure geometries are incomplete. To conduct liquefied strength analyses, the incomplete post-failure geometries for slides 1500 W3 and 1800 WT13 were completed by area balancing. Area balancing is a tool used to estimate the post-failure geometry of a failed soil mass by adjusting the area of post-failure soil mass to match the area of the pre-failure geometry. The post-failure geometry for slide 1800 W4 was inferred by extending the surface of the failed mass to the pre-failure geometry surface. No attempt was made to complete the post failure geometry of slide 2500W4 because the mass missing from the pre-failure geometry appeared to be much greater than the size of the post-failure geometry. As a result, the author employed only an infinite slope analysis for this case.

The post-failure geometry of slide 1500 W3 is reproduced in Figure A.141. The final sliding surface was ascertained from the failure mass, the back scarp, and the post-failure geometry completed by area balancing. The sliding surface shown in Figure A.141 is the critical final sliding surface for this post-failure geometry. The soil under the phreatic surface was assumed to liquefy and a single value of shear strength was assigned to the liquefied soil. The back-calculated shear strength was approximately 3.4 kPa, with a possible range from 3.05 to 4.2 kPa.

Using the same final sliding surface, a limit equilibrium analysis was conducted to estimate the liquefied shear strength ratio. The post-failure geometry was divided into 15 segments, with all the segments under the phreatic surface. The post-failure segments are arranged in the pre-failure geometry to calculate the pre-failure effective vertical stress as shown in Figure A.140. As discussed in Chapter 6, the author considered several arrangements of the pre-failure geometry segments for this case. The various arrangements had little effect on the back-calculated liquefied shear strength ratio.

Using individual σ'_{vo} values for each segment and a single value of $s_u(liq)/\sigma'_{vo}$, individual values of liquefied shear strength were assigned to each segment of the post-failure geometry for stability analysis. This allows the variation in pre-failure σ'_{vo} within the zone of liquefaction to be reflected in variable liquefied shear strengths along the final sliding surface. The best estimate of liquefied shear strength ratio is back-calculated as 0.045 with a possible range of 0.04 to 0.056.

The post-failure geometry of slide 1800 W4 is reproduced in Figure A.144. The final sliding surface was ascertained from the failure mass, the back scarp, and the post-failure geometry completed by area balancing. The sliding surface shown in Figure A.144 is the critical final sliding surface for this post-failure geometry. The soil under the phreatic surface was assumed to liquefy and a single value of shear strength was assigned to the liquefied soil. The back-calculated shear strength was approximately 4.2 kPa with a possible range from 3.5kPa to 5.1kPa.

Using the same final sliding surface, a limit equilibrium analysis was conducted to estimate the liquefied shear strength ratio. The post-failure geometry was divided into 12 segments with all the segments under the phreatic surface. The post-failure segments were arranged in the pre-failure geometry to calculate the pre-failure effective vertical stress as shown in Figure A.144. As discussed in Chapter 6, the author considered several arrangements of the pre-failure geometry segments for this case. The various arrangements had little effect on the back-calculated liquefied shear strength ratio, as noted below.

Using individual σ'_{vo} values for each segment and a single value of $s_u(liq)/\sigma'_{vo}$, individual values of liquefied shear strength were assigned to each segment of the post-failure geometry for stability analysis. This allows the variation in pre-failure σ'_{vo} within the zone of liquefaction to be reflected in variable liquefied shear strengths along the final sliding surface. The best estimate of liquefied shear strength ratio is back-calculated as 0.066 with a possible range from 0.054 to 0.08.

The post-failure geometry of slide 1800 WT13 is reproduced in Figure A.147. The final sliding surface was ascertained from the failure mass, the back scarp, and the post-failure geometry completed by area balancing. The sliding surface shown in Figure A.147 is the critical final sliding surface for this post-failure geometry. The soil under the phreatic surface was assumed to liquefy and a single value of shear strength was assigned to the liquefied soil. The back-calculated shear strength was approximately 5.92 kPa, with a possible range from 5.37 to 6.74 kPa.

Using the same final sliding surface, a limit equilibrium analysis was conducted to estimate the liquefied shear strength ratio. The post-failure geometry was divided into 12 segments, with all segments except segment 1 under the phreatic surface. The post-failure segments were arranged in the pre-failure geometry to calculate the pre-failure effective vertical stress as shown in Figure A.146. As discussed in Chapter 6, the author considered several arrangements of the pre-failure geometry segments for this case. The various arrangements had little effect on the back-calculated liquefied shear strength ratio.

Using individual σ'_{vo} values for each segment and a single value of $s_u(liq)/\sigma'_{vo}$, individual values of liquefied shear strength were assigned to each segment of the post-failure geometry for stability analysis. This allows the variation in pre-failure σ'_{vo} within the zone of liquefaction to be reflected in variable liquefied shear strengths along the final

sliding surface. The best estimate of liquefied shear strength ratio was back-calculated as 0.076 with a possible range of 0.066 to 0.083.

The post-failure geometry of slide 2500 WT4 is shown in Figure A.148. Because the post-failure geometry is incomplete and infinite slope analysis was used to calculate liquefied shear strength and strength ratio. The average post-failure geometry thickness ranged from about 4 to 7m, and the post-failure slope angle (β) was about 2.86º (1V:20H). The back-calculated liquefied strength ranged from 2 to 3 kPa with the best estimate of 2.5 kPa. Using a pre-failure geometry vertical effective stress of 50 kPa, the back-calculated liquefied shear strength ratio ranged from 0.04 to 0.06 with the best estimate of 0.05.

A.10.7 Liquefied Shear Strength and Strength Ratio Considering Kinetics

The failed soil mass was incomplete in all four slides studied here. The post-failure geometry was completed in two slides by using area balancing. In the fourth slide it was not possible to balance the sliding mass in the post-failure geometry. Also in slide 1500 W3 soil mass was halted by the other temporary excavation slope. For these reasons, it was not possible to conduct the kinetics analyses for the Jamuna bridge slides.

A.10.8 Sources of Uncertainties

The following sources of uncertainty were involved in estimating the yield shear strengths and strength ratios mobilized at the time of the failures: (1) excavation slope geometries near the toes; (2) the locations of the initial failure surfaces; (3) the triggering mechanisms; and (4) the potential for drainage during triggering of liquefaction. As explained above, the slope geometries at the time of failure are not known with certainty because of the active dredging operation. For the temporary slope, this uncertainty resulted in the author resorting to an infinite slope analysis. Initial failure surfaces used in the analyses were the critical sliding surfaces that were consistent with the postulated triggering mechanism and a retrogressive slope failure. As explained in Section A.10.3, the triggering mechanism of these slides are most likely the excavation of the toes. Alternate triggering mechanisms as described by Ishihara (2008) are mentioned in Section A.10.3.

The following sources of uncertainty were involved in estimating the liquefied shear strengths and strength ratios: (1) the post-failure geometries; and (2) the potential for porewater pressure redistribution during flow. By far, the largest source of uncertainty for the Jamuna River Bridge slides is the post-failure geometries. As the entire post failure geometries were not available in the literature, the author estimated post-failure geometries using area balancing or judgment. The estimated post-failure geometries also considered the location of the slope on the opposing side of the excavation.

The following sources of uncertainty were involved in estimating the "representative" penetration resistances: (1) conversion of raw N-values to corrected N-values, i.e., the energy ratio of the SPT hammer system; (2) the available CPT soundings

were performed after the failures; and (3) conversion between CPT and SPT (which was used to validate the measured SPT N-values). As stated in Section A.10.4, corrected SPT N-values were reported by Hight et al. (1999). Although Hight et al. (1999) did not thoroughly explain how the N-values were corrected, it appears that the hammer energy used in Japan for tombi donut type hammers (ER ~ 80%) was used to calculate N_{60}.

A.11 Degirmendere Slope Failure, Kocaeli, Turkey

A.11.1 Introduction

On August 17, 1999, a M_w 7.4 earthquake jolted the northwestern part of Turkey along the North Anatolian fault. This earthquake, which was later called the "Kocaeli" or "Izmit" earthquake, is one of the most devastating earthquakes of the 20th century with respect to the number of casualties and damage. Reported casualties vary from about 15,000 (official sources) to about 45,000 (unofficial sources), with about 44,000 injured and 600,000 left homeless. Property loss was also widespread with more than 120,000 houses collapsed and 50,000 others heavily damaged. About 2,000 other buildings collapsed, and 4,000 were damaged beyond repair (USGS 2010). Along with the structural loss, extensive landslides, ground subsidence, and liquefaction-induced ground deformations occurred along the coast of Izmit Bay.

The epicenter of the Kocaeli earthquake was near the Gulf of Izmit, near the cities of Izmit (5 km northeast) and Kocaeli (6.7 km northwest) (see Figure A.149). The hypocenter was located at a depth of 17 km and earthquake caused right lateral strike-slip movement on the fault. As noted above, the earthquake occurred on four different segments of the North Anatolian fault system. These segments are separated by stepovers that are associated with unique, sediment filled pull-apart basins. These pull-apart basins are recognized as Karamursel, Golcuk, and Spanca (Rathje et al. 2004). A pull-apart basin is a type of structural basin that forms between two offset segments in a strike slip fault system. As defined by Rathje et al. (2004), "Pull-apart basins are formed as a result of extension within the basins that is accommodated by vertical displacement along basin-bounding normal faults and causes structural downdropping and warping," (see Figure A.150). Over time, these basins were filled with thick Quaternary deposits. During the Kocaeli earthquake, these basins experienced extensive ground subsidence and sea inundation which caused severe damage to coastal areas and facilities. A likely liquefaction flow failure occurred within the Karamursel pull-apart basin at Degirmendere. Figure A.151 shows aerial photographs of the pre-and post-failure conditions at the Degirmendere site.

A.11.2 Site Geology and Soil Conditions

Izmit Bay is located in an east-west trending graben system with two horsts (Cetin et al. 2004): the Kocaeli Peninsula to the north and Armutlu Peninsula to the south. Both horsts manifest different geomorphological characteristics and well-defined fault scarps (Cetin et al. 2004). The graben varies between 6 and 10 km in width and forms large,

long and narrow basins that are filled with young sediments of marine and continental deposits (Cetin et al. 2004).

The Karamursel pull-apart basin is one of the three pull-apart basins that developed by the right extension of the strike-slip stepover (see Figure A.149). Situated on the southern coastline of Izmit Bay, Karamursel basin consists mainly of Plio-Pleistocene sedimentary bedrock overlain in some parts by Pleistocene marine terrace deposits and sandy Holocene sediments that become more silty and clayey toward the north (Cetin et al. 2004a). Figure A.152 shows a geological map of the Armutlu peninsula.

The city of Degirmendere is situated on the border of the Karamursel pull-apart basin. Degirmendere creek flows through the northern part of the city of Degirmendere and forms a delta fan into Izmit Bay. Generally, prograding deltaic sediments along Izmit Bay are saturated and consist of loose sand and silty sand layers deposited with a relatively steep slope, greater than 10º to 15º (Rathje et al. 2004, Cetin et al. 2004). At Degirmendere, the upper 10 m of the fan consists of sand and gravel with 5% to 10% fines with an overall slope angle of about 12.7º and a toe angle of 18º.

A.11.3 Estimation of Ground Motion

Details related to the earthquake are as follows (USGS 2010):

Date and Time: 1999 08 17; 03: 02:00 (Local Time)
Location: 40.74N, 29.86E
Magnitude: 7.6
Region: Izmit/Kocaeli, Turkey
Fault Mechanism: Strike-Slip Fault

The North Anatolian fault is 1500-km long strike-slip fault passing through northern and western Turkey. The 1999 Kocaeli earthquake ruptured a 126-km long section of the North Anatolian fault. A large number of strong ground motions were recorded within 20 km of the fault rupture area, at the stations shown in Figure A.153. As shown in Figure A.153, the Yarimca (YPT) station is closest to the Degirmendere site. The YPT recording station was about 4.4 km away from the rupture plane and situated on deep alluvium. The east-west components recorded at this station are 0.262 and 0.298, respectively, producing a geometric mean of 0.27g. Cetin et al. (2004a) used SHAKE'91 to deconvolve the YPT record and then propagated the resulting bedrock motion through the soil profile at Degirmendere. This analysis yielded a surface PGA of 0.35g. Collectively, Cetin et al. (2004a,b) and Rathje et al. (2004) suggested a range of PGA from 0.3g to 0.4g.

A.11.4 Description of Failure

As shown in pre-failure geometry (see Figure A.154), the Degirmendere delta fan had a steep slope of about 18º at the toe located about 100 m offshore. About 175 m away

from the coastline the seafloor was almost flat. The post-failure geometry (see Figure A.154) shows a considerable change in the slope and coastline. The slope near the coastline was locally steepened after the failure and the seafloor inclination was reduced to about 5º after the failure. Comparison of the pre-and post-failure geometries illustrates that the maximum depth of the failed soil mass was about 25 m.

Cetin et al. (2004a) conducted a dynamic slope stability analysis using limit equilibrium analysis, and also performed a finite element analysis of the Degirmendere delta fan. The soil parameters were chosen based on the penetration resistances. PGA was chosen as 0.35g based on the strong motion acceleration records at YPT. The results of these analyses showed that the FS was less then unity even without considering the excess pore water pressure due to earthquake. Cetin et al. (2004a) then conducted liquefaction triggering analysis using the cyclic stress method (Seed and Idriss 1971) along with the liquefaction triggering correlations proposed by Cetin (2000) and Cetin et al. (2004c) in order to investigate the potential effects of soil liquefaction. A peak ground acceleration was chosen as 0.35g to estimate CSR, and SPT blow counts from Figure A.158 were used to estimate CRR. The investigation results suggested that soil liquefaction may have contributed to the failure. As reported by Cetin et al. (2004a), "As suggested by the analyses results for SPT DN1, soil layer at depth range of 8 – 11 m has a small margin of safety against liquefaction triggering and is believed to have suffered from significant shear strength loss due to pore pressure generation. Remembering the fact that the site investigations were done on actually nonfailed soils, after the earthquake, it is believed that the soils that slid into the bay as a result of slope instability are more prone to liquefaction and likely to exhibit lower SPT blowcounts if site investigation studies had been performed on these soils before the earthquake (landslide). Thus, it can be concluded that liquefaction of the soil layer below 8 m depth have also played a major role in the observed instability."

Although the cross-section used in this study differs slightly from the cross-section used by Cetin et al. (2004a), the post-failure geometry strongly suggests that flow failure (i.e., significant strength loss) occurred. While earthquake-induced inertial forces likely played a role in triggering the failure, the displacements associated with inertial forces alone, while significant, do not explain the very large displacements associated with the failure.

Rathje et al. (2004) also disagreed with the theory that the failure of Degirmendere slope resulted from inertial forces only. They suggested that the earthquake triggered liquefaction in the deltaic soils and resulted in a deep-seated failure (25 to 30 m deep). Rathje et al. (2004) stated, "Analyses with residual strengths assigned to both the shallow [5 – 10 m below grade] and deep [25 – 30 m below grade] liquefiable layers predicted a deep-seated failure with a factor of safety equal to 1.05. The yield seismic coefficient for this slip surface (using drained strengths) is 0.19. Considering a PGA of 0.3g and reducing that value to $k_{max} = 0.2$ to correct for averaging effects over the depth of the sliding mass results in a k_y/k_{max} close to 1.0, suggesting that inertial effects alone, without soil strength reduction by liquefaction, could not have triggered the failure at Degirmendere. The failure appears to have initiated on a deep liquefied soil

layer in the steeper part of the offshore delta nose, and may have expanded laterally in a progressive mode. The zone of cracking inland of the failure scarp suggests that this zone was quasi-stable and experienced some minor external movements in response to formation of the slide head scarp and partial liquefaction of underlying soil layers."

Cetin et al. (2004b) reported three cracks parallel to the coastline with crack widths of 9, 50, and 28 cm respectively, with the zone of cracking roughly illustrated in Figure A.155. Rathje et al. (2004) reported a total amount of 45 cm lateral seaward movement in the zone of primary cracking. No other ground manifestation in the form of sand boils and/or soil ejecta was observed in the failure zone; however, buildings inland close to failure zone experienced slight to moderate levels of settlement. In the absence of differential settlement and observed failure pattern, Rathje et al. (2004) concluded that the Degirmendere slope failure was deep-seated slide rather than a liquefaction-induced lateral spread.

Because both investigators, Cetin et al. (2004a) and Rathje et al. (2004), suggested that liquefaction was primarily responsible with inertial effects playing a secondary role in the Degirmendere slope failure, the author considered both potential failure mechanisms in this study. As suggested by Rathje et al. (2004), the author considered the primary failure mechanism to be a deep-seated slope failure near the steep toe of the slope followed by retrogressive failure of the resulting oversteepened delta slopes.

A.11.5 Representative Penetration Resistance

Rathje et al. (2004) reported three SPT borings and two CPT soundings conducted at the failure site by a local company. The locations and results of these penetration tests are given in Figure A.154 to Figure A.158. The boring results show that in the top 30 m consist primarily of medium dense sand and fine gravel with some layers of silty clay and silty sand. CPT tip resistances generally were on the order of 10 to 20 MPa in the sand layer while SPT blowcounts were in the range of 10 to 30. An increase in penetration resistance was observed beyond 10 m depth which was also confirmed by shear wave velocity. Rathje et al. (2004) suggested that the soil between the depths of about 5 to 10 m was liquefiable with $q_c \approx 8$ to 12 MPa and $(N_1)_{60} \approx 10$ to 20, yielding a factor of safety against liquefaction triggering between 0.5 and 0.9. Below 10 m, Rathje et al. (2004) suggested that the CPT and SPT data do not predict the same liquefaction potential.

Cetin et al. (2004) reported two SPT borings, two seismic piezocone (sCPTu) soundings, and one CPT sounding at Degirmendere. Locations of these penetration tests with the location of the cross section are shown in Figure A.157. SPT borehole data and CPT soundings, along with the cross section of Degirmendere slope are shown in Figure A.158. Although Cetin et al. (2004a) did not conduct liquefaction triggering analyses using CPT data, most of the corrected tip resistances are above 10 MPa.

Both investigators, Cetin et al. (2004a) and Rathje et al. (2004), collectively suggested the presence of liquefiable soil between the depths of 5 to 11 m. However,

Cetin et al. (2004a) and Rathje et al. (2004) did not explain why the failure was deep-seated. Because the sediments were deposit in prograding delta environment, the sediments were likely deposit in successive, subparallel beds from grading from gravelly sand near the coastline to fine silty sand towards the bay, as shown schematically in Figure A.159. Therefore it is likely that alternate pockets of coarse and fine sand would be encountered in borings and penetration tests.

The author suggests that rather than averaging the penetration resistance over thick zones of potentially liquefiable soils, as suggested by Rathje et al. (2004) and Cetin et al. (2004a), individual and isolated beds of sand and silty sand exhibiting low tip resistance should be considered to estimate "representative" CPT tip resistance. The reasoning for this is that sediments in delta fan are deposited in downward accretion (see Figure A.159), and fairly loose sediments may be continuous in subparallel beds that are not vertically continuous. Furthermore, because SPTs may miss these individual loose sand and silty sand beds, the lowest N-values regardless of their depths should be used to estimate "representative" SPT N-values. Further, as Cetin et al. (2004a) suggested, the failed soil may have had lower penetration resistances than the penetration resistance measured close to the coastline. Using a unit weight of 20 kN/m^3, $(N_1)_{60}$ values ranged from 7 to 12 blows/ft with the best estimate of 9 blows/ft, and q_{c1} values ranged from 1.5 to 8 MPa with the best estimate of 4 MPa.

A.11.6 Yield Shear Strength and Strength Ratio

The mechanism that may have played a contributing part and likely triggered flow failure is seismic liquefaction of the saturated delta fan, especially in the steeper toe area (Cetin et al. 2004a, Rathje et al. 2004). As explained in Chapter 2, the shear strength and strength ratios mobilized at the instant of failure in cases where liquefaction is triggered by seismic loading do not necessarily represent yield shear strength and strength ratios.

As discussed in Section A.11.4, the delta slope was steeper near the toe and the soil was saturated and loose to medium dense. On the other hand, the delta site was about 5 km away from the fault rupture. Cetin et al. (2004a) considered the failure mechanism to result from both inertial loading and liquefaction. Although the author believes that the slope likely failed as a result of liquefaction, inertial forces may have played some role in the failure. Therefore, the author investigated both mechanisms in this study. Undrained strength pseudo-static analysis exhibited yield accelerations ranging from 0.017g to 0.045g, while drained strength pseudo-static analyses exhibited yield accelerations ranging from 0.135g to 0.258g. Potential failure surfaces considered in this analysis are illustrated in Figure A.160. For the undrained analyses, the author assigned an undrained yield strength ratio of 0.295 to the sands below the water level based on the Olson and Stark (2003) correlation and $(N_1)_{60} = 9$. For the drained analyses, the author assigned $\phi' = 30^o$ to 38^o to the sands (these values envelope the $\phi' = 35^o$ suggested by Rathje et al. 2004). PGAs between 0.3g and 0.4g were used, as suggested by Cetin et al. (2004a,b) and Rathje et al. (2004). To calculate the permanent earthquake-induced deformation, Newmark's sliding block analysis was adopted using the software developed by Jibson and Jibson (2005). The Jibson and Jibson (2005) software requires ground motions.

Several ground motions recorded during the Kocaeli earthquake ground motions were available in the software and were used by the author for this analysis. Each motion was linearly-scaled to the target PGA of either 0.3 or 0.4g. The results show that the expected permanent deformations ranged from 9 cm to 327 cm for typical failure surfaces. As the slope completely failed after the earthquake, with displacements probably exceeding tens of meters, these displacements (i.e., about 0.1 to 3m) can not satisfactorily explain the morphology of the failure.

The pre-failure geometry of the Degirmendere slope is reproduced in Figure A.160. A slope stability search was conducted to locate an initial failure surface that was restricted to the toe area. All of the saturated soil in the toe area was assumed to liquefy Sandy above phreatic surface was assigned range of friction angles from $\phi' = 30^o$ to 38^o. The back-calculated mobilized shear strength averaged about 23.5 kPa, with a range from 21.0 to 25.2 kPa.

A second analysis was conducted to estimate the strength ratio mobilized at the triggering of liquefaction. Identical assumptions regarding the failure surface and shear strength of the non-liquefied soil were used for this analysis. The mobilized shear strength ration in the zone of liquefaction averaged 0.232, with a range from 0.203 to 0.287, depending on the shear strength of the unsaturated fill and the location of the failure surface. The weighted average pre-failure vertical stress in the liquefied segment was determined as 90 kPa.

A.11.7 Liquefied Shear Strength and Strength Ratio

No post-failure geometry is available for this case history because the soil mass flowed into the bay. Therefore, it was not possible to conduct a liquefied shear strength analysis.

A.11.8 Liquefied Shear Strength and Strength Ratio Considering Kinetics

Similarly, no kinetics analysis was conducted for this case.

A.11.9 Sources of Uncertainty

The following sources of uncertainty were involved in estimating the shear strength and strength ratio mobilized at the triggering of liquefaction: (1) the initial zone of liquefaction; (2) the position of the initial failure surface; and (3) the shear strength of the non-liquefied soils. All of the sandy soil in toe area was assumed to liquefy because the location of the subparallel beds of looser soils was unknown. The position of the initial failure surface was not known. However, as defined by Cetin et al. (2004a) and Rathje et al. (2004) as well as observed from post-failure geometry, several deep-seated failure surfaces were considered. The non-liquefied sandy soil was assigned $\phi' = 30^o$ to 38^o.

The following sources of uncertainty were involved in determining the "representative" values of penetration resistance: (1) identifying penetration resistances that are consistent with the liquefied zones and consistent with the depositional environment; and (2) the tests were conducted in non-liquefied soil. The deltaic environment likely deposited looser sandy beds in subhorizontal, subparallel sets, making them difficult to correlate among penetration tests. As defined by Cetin et al. (2004a), the failed soil likely to exhibit lower penetration resistance than the non-liquefied soil nearer to the coastline.

A.12 Bhuj Earthquake Case Histories, Gujarat, India[5]

A.12.1 Introduction

On January 26, 2001 a moment magnitude (Mw) 7.7 earthquake occurred in Bhuj, state of Gujarat, India. Several small- to moderate-sized earth dams in the vicinity of the epicenter were damaged during this event. The state of Gujarat is arid, does not have any perennial rivers, and depends on rain for agriculture. The greater Kachchh region receives less than 35 cm of annual rainfall on average (Krinitzsky and Hynes 2002). In order to collect water for agricultural and drinking purposes, the state of Gujarat constructed a large number of small- to moderate-sized earth dams on ephemeral streams that carry low or discontinuous flow, except during the rainy season (which usually begins in June). The damage to the dams during the Bhuj earthquake was widespread and extensive, but no flooding was reported because the dams were at unusually low levels at the time of the earthquake. The low reservoir levels resulted from a two-year drought that preceded the event.

Most of the damage was observed on the upstream sides and crests of the dams, and involved slope displacements and longitudinal cracking ranging from significant to minor. The damage likely resulted from liquefaction of the foundation soils. Although a number of such structures were located within 150 km of the epicenter (Figure A.161), the consequences of the damage caused by the earthquake to these dams and ancillary structures were relatively light.

A.12.2 Site Geology and Soil Conditions

The stratigraphy of the Gujarat region is broadly characterized by Precambrian crystalline basement rocks overlain by Jurassic through Quaternary sedimentary deposits within the basins. One of the most widespread deposits of the region is the upper Cretaceous Deccan Trap basalt and related intrusive rocks. The Deccan Trap forms a massive deposit of flood basalts that covers more than 500,000 km^2. The Deccan basalts are more than 3 km thick in places. Tertiary sediments that overlie the Deccan Traps are also several kilometers thick within basins and are source rocks for the extensive Gujarat Alluvium that occupies large portions of central and northern Gujarat State.

[5] Six case histories are discussed that failed during Bhuj earthquake. A general introduction, geology, and description of the failures are given. These headings will not be repeated for individual case histories.

Holocene marine deposits occur along the coast of Gujarat. These deposits are comprised of raised mudflats, stabilized coastal ridges and shelly beach rock, and are reported by Merch (1995) to be related to an early Holocene marine transgression that raised the sea level 6 to 10 m about 6,000 years ago. A coastal ridge related to this marine transgression is mapped as far as 5 km inland. Shell and coral materials are radiometrically dated at a number of sites in Gujarat and range in age from last interglacial (120,000 yrs before present) to mid-Holocene (6000 yrs before present) (Gupta 1972; Gupta and Amin 1974). It is not known whether the elevation of these coral and shell beds are the result of eustatic sea level rise, cyclonic storm surge, and/or differential tectonic uplift of the region. Much of the Indian geological literature attributes these raised marine deposits to sea level high stands. Recent cyclones, however, demonstrate that large areas may be inundated and marine sediments and organisms can betransported and deposited far inland during severe storms. This process could account for the mixture of late Pleistocene and Holocene age deposits at elevations of several meters above current sea level. The foundation soils underneath the dams are products of recent tectonism that Kachchh has experienced and of effects on river erosion that were caused by changes in sea level (Krinitzsky and Hynes 2002).

As a result of the Bhuj earthquake, widespread liquefaction-induced failures occurred over an area greater than 15,000 km^2 and possibly as far away as 250 to 300 km from its epicenter. Surface manifestations of liquefaction included sand blows, sand blow craters, and lateral spreading. Areas where widespread liquefaction occurred include the Great Rann of Kachchh, Little Rann, Banni Plain, Kandla River and Gulf of Kachchh (see Figure A.162). These areas contain low-lying salt flats, estuaries, intertidal zones, and young alluvial deposits, which are typically considered to have a very high susceptibility to liquefaction (EERI 2001). Soil samples ejected onto the ground surface from the liquefied layer of the deposit were collected by Sitharam et al. (2004) from two locations close to the epicenter of the earthquake. Figure A.163 presents the grain size distributions of the samples collected from the Bhuj area and Table A.3 shows the grain characteristics of these two soil samples. Sitharam et al. (2004) considered these samples to be representative of the alluvium at the dam sites examined in this study.

A.12.3 Estimation of Ground Motions

Details related to the earthquake are as follows (Krinitzsky and Hynes 2002):

Date and Time: 2001 01 26 03: 16:40
Location: 23.41N 70.23E
Magnitude: 7.7
Region: Bhuj, Gujarat
Fault Mechanism: Thrust Fault

Because there were no strong motion recordings in the epicentral region, Krinitzsky and Hynes (2002) and Singh et al. (2003) used empirical relationships to estimate PGA. Krinitzsky and Hynes (2002) estimated PGA, peak horizontal ground

velocity (PGV), and shaking duration from observed level of damage using correlations with Modified Mercalli Intensities (MMI). Figure A.164 shows the MMI distribution in the Bhuj area and Figure A.165 shows the relationship between MMI and PGA proposed by Krinitzsky and Chang (1988). Predicted values of PGA proposed by Krinitzsky and Hynes (2002) are given in Table A.1.

Singh et al. (2005) estimated PGA by using attenuation relationships created with an Approximate Finite Source Model (AFSM) and a Finite Source Model (FSM). The combined attenuation relationship using these models is shown in Figure A.166, and it applies to hard rock conditions. Available recordings at source-to-site distances greater than 565 km are included in Figure A.166. As illustrated in Figure A.166, measured and predicted PGAs agree well. One exception is a recording in the city of Ahmedabad, where a PGA of 0.1g was recorded on the ground floor of a 10-story building. The predicted PGA at an R = 240 km is about 0.03g. Singh et al. (2003) attributed this difference to soft soil amplification and soil-structure interaction effects at the building site. They also noted that there is also some doubt about the performance of the accelerograph. The Singh et al. (2003) attenuation relationship was developed for hard rock conditions, and therefore soft soil amplification must be considered for softer sites. They used the Idriss (1990) soft soil amplification relationship for this purpose (shown in Figure A.167). The resulting site-specific PGA values estimated by Singh et al. (2005) are given in Table A.1.

In addition to the above information, the author used the NGA relationships proposed by Abrahamson and Silva (2008), Boore and Atkinson (2008), Campbell and Bozorgnia (2008), Chiou and Young (2008), and Idriss (2008) (where applicable) to estimate surface PGAs for each of the study sites. These estimates are presented in Table A.1.

A.12.4 Description of the Failures

The performance of six embankment dams affected by the Bhuj earthquake is examined here. The dam locations are identified in Figure A.161. Among these, Chang Dam experienced severe upstream and downstream slope failures as a result of liquefaction of shallow foundation soils. The upstream slope of Shivlakha Dam was also severely damaged, presumably because of liquefaction of the upstream foundation soils. Damage to Suvi, Tapar, Fatehgadh, and Kaswati Dams was less severe and confined near the upstream toe, upstream slope, and dam crest. Details of each dam and the earthquake-induced damage are provided below.

A.12.5 Chang Dam

Chang Dam was constructed in 1959 with reservoir storage capacity of 6.9×10^6 m^3. The dam height at the maximum section was 15.5 m and the crest length was 370 m (EERI 2001; Singh et al. 2005a,b; Babu et al. 2007). No specific information is available about the subsurface soils other than that the site is underlain by loose to medium dense alluvial sand-silt mixtures over shallow sandstone bedrock (Singh et al. 2005a). The

reservoir at Chang Dam was nearly empty at the time of Bhuj earthquake; however the foundation soils were saturated.

EERI (2001) reported a large translational slide in the upstream shell and minor movement in the downstream shell, as illustrated in Figure A.168. Translation of the upstream shell produced large cracks and fissures on the upstream face and caused the crest to drop as a series of graben-like blocks, with a maximum vertical displacement of 6.5 m, while the downstream toe experienced minor bulging or lateral translation. The upstream slide was approximately 85 m wide along the dam axis, extending over the full length of the maximum height section of the dam. In addition, relatively minor longitudinal cracking occurred along much of the crest of the lesser height embankment sections away from the highest section.

Silty sand ejecta was observed at the upstream toe, supporting a liquefaction mechanism for the slope failure. Fine sand and silty sand boils were also observed adjacent to a small agricultural pond near the downstream toe.

A. 12.5.1 Representative Penetration Resistance

Towhata et al. (2002) conducted Swedish weight soundings (SWS) near the toe of the failed upstream mass at Chang Dam, as illustrated in Figure A.169. The SWS clearly demonstrates that the foundation was loose to a depth of 2.5 m. Inada (1982) suggested a correlation between SPT blow count and SWS measurements as:

$$N = 0.02W_{sw} + 0.067N_{sw} \qquad \textbf{Eq. A. 3}$$

where N = raw (unadjusted) SPT blow count; W_{sw} = weight (in kg) used for the static phase of SWS penetration; and N_{sw} = number of half-revolutions of the rod in the rotating phase of the SWS test. Using Figure A.169 and Eq. A 3, the weighted average SPT N-value is 4 with a reasonable range from 2 to 5. Because the correlation shown above was established using Japanese data, an average energy ratio of 72% (i.e., the average of 65% and 78% hammer energies common for Japanese hammers) was assumed, and the equivalent $(N_1)_{60}$ values range from 4 to 11, with a best estimate of about 8. The author notes that the correlation between SWS and SPT (or CPT) exhibits large scatter, as illustrated by Moss and Hollenback (2008), who showed a correlation coefficient (ρ) of 0.235 (where perfectly correlated measurements would render $\rho = 1.0$). They argue that the process of converting from SWS to SPT or CPT involves compounding uncertainties, to the point where the median value becomes ambiguous. Nevertheless, this correlation provides a means to estimate the penetration resistance at the site, and was used for this purpose.

Electronic CPT values were not measured at any Indian dam site. Therefore, corresponding values of q_{c1} were estimated using the average q_c/N_{60} ratio from the five correlations proposed by Robertson and Campanella (1985), Seed and de Alba (1986), Andrus and Youd (1989), Kulhawy and Mayne (1990), and Stark and Olson (1995). For

D_{50} = 0.3 mm (see Figure A.163), the average q_c/N_{60} = 0.48. Therefore, the average q_{c1} is 2.88 MPa, with a range of 0.96 to 6.24 MPa.

A. 12.5.2 Yield Shear Strength and Strength Ratio

The pre-failure geometry is reproduced in Figure A.170. Based on sand boils observed at the site, EERI (2001), Singh et al. (2005a,b), and Babu et al. (2007) suggested that earthquake-induced liquefaction and strength loss in the foundation alluvium were responsible for the observed damage.

Limit equilibrium stability analyses of the pre-failure geometry were conducted using the software Slope/W (GEO-SLOPE International 2004). This software allows direct input of a strength ratio (i.e., τ/σ'_v) for the potentially liquefiable soils. Therefore it was not necessary to evaluate the pre-failure vertical effective stress for the mobilized strength ratio analyses of the prefailure geometry. Numerous potential failure surfaces, both circular and non-circular, that are consistent with the observed failure pattern were searched to determine the critical failure that requires the minimum value of shear resistance for equilibrium, i.e., factor of safety equal to unity. The critical circular and noncircular slip surfaces were similar to the failure surfaces reported by other researchers (EERI 2001; Singh et al. 2005a, b; Babu et al. 2007).

For each case, the upstream alluvium was assumed to be liquefiable because the water table was just above the foundation alluvium and the alluvium was loose to medium dense. Soils above the phreatic surface, including the semi-pervious shells, impervious cores, and masonry walls were assigned appropriate drained or undrained shear strengths, as given in Table A.4. The best estimate of mobilized shear strength for Chang Dam was 26.5 kPa, with a range from 20 to 36 kPa. Similarly, the best estimate of mobilized strength ratio was 0.215, with a range from 0.185 to 0.28. As explained in Chapter 2, the shear strength and strength ratios mobilized at the instant of failure in cases where liquefaction is triggered by seismic loading do not necessarily represent yield shear strength and strength ratios.

A. 12.5.3 Liquefied Shear Strength and Strength Ratio

The post-failure geometry of Chang Dam is reproduced in Figure A.171. Failure surfaces that are consistent with the final position of the failed mass were searched to define the critical post-failure noncircular failure surface. The critical final failure surface passed through both liquefied and nonliquefied soils, where nonliquefied soils included soils above the phreatic line (e.g., shell material) and soils too plastic to experience significant strength loss due to shaking. For the liquefied soil, the shear strength was varied until a factor of safety equal to unity was achieved. Figure A.171 shows two potentially critical failure surfaces. The analyses considered two possible scenarios to evaluate liquefied shear strength and liquefied shear strength ratio. These scenarios are: (1) no drainage occurred prior to failure and the liquefied shear strength was used along the entire length of the final sliding surface within the liquefied zone; and (2) drainage occurred at the toe segment prior to (or during) failure and a drained friction angle

(ranging from 28º to 32º) was assigned to this segment. Different combinations of these two possible scenarios were used along both sliding surfaces. Considering these possibilities, the best estimate of liquefied shear strength for Chang Dam was 8.6 kPa, with a range from 6.06 to 10.43 kPa.

Using the same post-failure sliding surface, an analysis to back-calculate the liquefied strength ratio was conducted. Each of the two potential post-failure sliding surfaces was divided into a number of segments as shown in Figure A.171. Because it was assumed that the entire foundation liquefied, the post-failure segments are assumed to be located at the pre-failure position (segments 1 to 9 and 1 to 10 for shorter and longer surfaces, respectively, in Figure A.171).

Using individual σ'_{vo} values for each segment and a single value of $s_u(liq)/\sigma'_{vo}$, individual values of liquefied shear strength were assigned to each segment of the post-failure geometry for stability analysis. This allows the variation in pre-failure σ'_{vo} within the zone of liquefaction to be reflected in variable liquefied shear strengths along the final sliding surface. Appropriate drained or undrained strengths were assigned to nonliquefiable soils based on the strengths given in Table A.4. The best estimate of liquefied strength ratio for Chang Dam was 0.082, with a range from 0.078 to 0.126.

A. 12.5.4 Liquefied Shear Strength and Strength Ratio Considering Kinetics

The pre- and post-failure geometries are reproduced in Figure A.171. Figure A.171 also includes the pre- and post-failure centers of gravity and the assumed travel path of the center of gravity during flow failure. The acceleration, velocity, and displacement of the center of gravity computed in the kinetics analysis is shown in Figure A.172 along with the back-calculated driving shear stress and liquefied shear stress along the entire length of the failure surface.

The kinetics analysis assumed that all soils along the failure surface mobilized the same shear strength. This procedure overestimates the actual liquefied shear strength because a portion of the failed soils initially were above the phreatic surface and did not liquefy. Therefore, the mobilized shear strength was adjusted by using Eq. A.1 (Olson 2001) to account for the strength of the nonliquefied soils. Approximately 24% of the post-failure sliding surface length involved soils that did not liquefy. These soils (i.e., segments 10 through 13 in Figure A.171) were assigned average shear strength of 51.2 kPa, using a non-liquefied shear strength given in Table A.4 based on a $\phi' = 30^{\circ}$. After adjustment, the kinetic analysis shown in Figure A.172 yielded the following results:

- Liquefied shear strength ≈ 9.45 kPa
- Liquefied shear strength ratio ≈ 0.11

Only single values of liquefied shear strength and strength ratio are reported here because stress reduction due to water mixing or hydroplaning was not significant, as failure likely occurred through the foundation soils. Lastly, the kinetics analysis only provides a value of liquefied shear strength. Therefore, the liquefied strength ratio was

computed by dividing the liquefied shear strength of 9.45 kPa by the weighted average vertical effective stress of 86 kPa obtained from the post-failure geometry analysis. These values of liquefied shear strength and strength ratio include the effects of kinetics and the shear strength of the soils that did not liquefy and are considered best estimates.

A. 12.5.5 Sources of Uncertainties

The following sources of uncertainty were involved in estimating the shear strength and strength ratio mobilized at the time of failure: (1) the location of the initial failure surface; (2) the actual limits of liquefied soil; (3) the shear strength of nonliquefied soils; (4) the reservoir level outside the embankment; (5) the phreatic surface within the embankment; and (6) the potential for drainage at the toe during liquefaction triggering. Numerous trial failure surfaces that were consistent with the observed damage were analyzed until best-estimate values of mobilized strength and strength ratio were obtained. Because the exact limits of the liquefied zone were not known, the author assumed that the entire foundation liquefied during this event, as suggested by different researchers. Singh et al. (2005a) reported shear strengths for non-liquefiable soils used in their analysis, but they did not report laboratory tests to support these values. The accuracy of the reservoir level reported by Singh et al. (2005a) is unknown (as the method of determination was not reported), and therefore represents an uncertainty. The phreatic surface (and reservoir level) reported by Singh et al. (2005a) is at the same elevation, suggesting that there was no head loss through the dam. This seems unlikely because of the presence of impervious clay core and masonry wall in the dam.

The following sources of uncertainty were involved in estimating the liquefied shear strength and strength ratio: (1) the upslope limit of the failed mass geometry; (2) the location of the final surface of sliding; (3) shear strength of non-liquefiable soil; and (4) potential porewater pressure redistribution (or drainage) during flow failure. Because the complete post-failure geometry was not available for Chang Dam, area-balancing was used to estimate the geometry of the remaining part of the failed mass. Area balancing is a tool used to define any incomplete toe portion of the post-failure geometry by comparing the areas of soil in the pre- and post-failure geometries, and adjusting the toe region of the post-failure geometry to balance the pre- and post-failure areas. The final failure surface for post-failure geometry was constrained by cracks in dam slope and the locations of graben blocks. Singh et al. (2005a) reported shear strengths for non-liquefiable soils used in their analysis, but they did not report laboratory tests to support these values. As defined in NRC (1985), there may be drainage or void redistribution during the failure (e.g., Liu and Qiao 1984; Stark and Mesri 1992; Fiegel and Kutter 1994; Kokusho 2000; Olson 2001; Kulasingam et al. 2004).

The following sources of uncertainty were involved in estimating the "representative" penetration resistance: (1) conversion from Swedish weight soundings to SPT; and (2) conversion from SPT to CPT. Towhata et al. (2002) conducted Swedish weight sounding *after* failure for Chang Dam. The soundings suggest soft soil in the upper 2.5m of foundation layer. The Swedish weight soundings were converted to SPT N-values by using Equation A.3 suggested by Inada (1982). As discussed by Moss and

Hollenback (2008), there are multiple uncertainties involved if a correlation is used to convert from one index test to another. These uncertainties involve certain amount of measurement uncertainty associated with the process of testing and uncertainty that is a function of the conversion. A weak correlation exists between SWS and CPT, resulting in a coefficient of variation of approximately 123%. This large uncertainty means that converting from SWS to CPT produces ambiguous results, and there is considerable uncertainty in the median value.

A.12.6 Shivlakha Dam

Shivlakha Dam was constructed in 1954 with an unusually large reservoir capacity as part of a second minor irrigation scheme. The crest length was approximately 300 m and the height at its maximum section was 18 m (EERI 2001; Singh et al. 2005a). Although the reservoir was nearly empty at the time of earthquake, the foundation alluvium was saturated. The earthquake caused the failure of the upstream slope and development of large fissures near the upstream toe, with vertical cracks on the order of 3m deep. In addition, a bulge occurred at the upstream toe. A smaller rotational slump occurred at the downstream toe. The majority of the slip surface at Shivlakha Dam appears to have passed upstream of the central core. Figure A.173 presents the pre- and post-earthquake configurations of the dam. A local farmer just upstream of the dam reported that water issued from ground fissures for approximately ½ hour on the day of the earthquake (Bardet et al. 2001), strongly suggesting that liquefaction was responsible for the failure.

A. 12.6.1 Representative Penetration Resistance

No penetration data is available for Shivlakha Dam. The range of uncorrected SPT N-values given for Fatehgadh and Kaswati Dams (see Sections A. 12.8.1 and A. 12.9.1, respectively) was used to estimate $(N_1)_{60}$-values for this site. N-values before dam construction (13 to 19) were used to compute representative $(N_1)_{60}$ values below the mid-height of the upstream slope. In typical Indian practice, the energy ratio typically is taken as 55% (Singh et al. 2005a). However, EERI reconnaissance team member Prof. R. Seed suggested an energy ratio of 45% for the SPT data (2009 email communication between R. Seed, University of California-Berkeley, and David R. Gillette, Bureau of Reclamation). Therefore the author used an average energy ratio of 50% for computing $(N_1)_{60}$. This calculation yielded average, upper bound and lower bound $(N_1)_{60}$ values of 10, 12, and 8, respectively.

CPTs were not perfromed at any Indian dam site. Therefore, corresponding values of q_{c1} were estimated using the average q_c/N_{60} ratio from the five correlations proposed by Robertson and Campanella (1985), Seed and de Alba (1986), Andrus and Youd (1989), Kulhawy and Mayne (1990), and Stark and Olson (1995). For D_{50} = 0.3 mm (see Figure A.163), the average q_c/N_{60} = 0.48. Therefore, the average q_{c1} value is 4.8 MPa, with a range from 3.8 to 5.8 MPa.

A. 12.6.2 Yield Shear Strength and Strength Ratio

Similar to Chang Dam, liquefaction likely occurred beneath the upstream shell of Shivlakha Dam, leading to the observed slope failure towards the reservoir. The pre-failure geometry is reproduced in Figure A.174. Because the failure surface shown in Figure A.174 is only constrained by the observed damage and the exact location of the initial failure surface cannot be identified, a number of trial failure surfaces were analyzed until best-estimate values of mobilized stress and mobilized stress ratio were obtained. Both circular and non-circular failure surfaces were searched using a limit equilibrium slope stability analysis to determine the critical failure surface that is consistent with the observed failure pattern and requires the minimum value of shear resistance for equilibrium, i.e., a factor of safety equal to unity. The critical circular slip surfaces were similar to the failure surfaces reported by other researchers (EERI 2001; Sing et al. 2005a, b; Babu et al. 2007).

For each case, the upstream alluvium was assumed to be liquefiable because the water table was just above the foundation alluvium and the alluvium was loose to medium dense. In contrast, EERI (2001) and Singh et al. (2005a, b) considered only a portion of this foundation to be liquefiable. The apparent reason for Singh et al. (2005a,b) suggesting a limited zone of liquefaction was their calculation of cyclic stress ratio (CSR) and cyclic resistance ratio (CRR), which shows that foundation soil under the toe of each dam is susceptible to liquefaction while foundation soil under the crest is not susceptible to liquefaction at each dam, except for Chang Dam. However, this interpretation appears unreasonable to the author because: (1) their calculation potentially used the wrong CRR curve (they used FC = 5 to 15%, while the FC shown in Figure A.163 ranges from 15 to 23%); (2) they provide no justification for their selection of K_α; and (3) more importantly, their CRR values (0.32 by Singh et al. 2005a and 0.34 by Singh et al. 2005b) corresponds to an $(N_1)_{60}$ value of 21 to 22, and their reported yield and liquefied strength ratios of 0.37 and 0.195, respectively (although both were incorrectly derived) correspond to $(N_1)_{60} = 22$. These values are inconsistent with the N-values reported earlier for Shivlakha Dam. Furthermore, Singh et al. (2005a) attributed this variation in liquefaction triggering to partial saturation of the soil, yet they report no change in water level from the upstream to the downstream side of the dam. Therefore, the author considered the entire upstream foundation to be liquefiable.

Soils above the phreatic surface, including the semi-pervious shells, impervious core, and masonry wall were assigned appropriate drained or undrained shear strengths, as shown in Table A.4. The best estimate of mobilized shear strength was 24.5 kPa, with a range from 16 to 30 kPa. Similarly, the best estimate of mobilized strength ratio was 0.25, with a range from 0.165 to 0.262. As explained in Chapter 2, the shear strength and strength ratios mobilized at the instant of failure in cases where liquefaction is triggered by seismic loading do not necessarily represent yield shear strength and strength ratios.

A. 12.6.3 Liquefied Shear Strength and Strength Ratio

The post-failure geometry of Shivlakha Dam is reproduced in Figure A.175. Failure surfaces that are consistent with the final position of the failed mass were searched to define the critical post-failure noncircular failure surface. The critical final failure surface passed through both liquefied and non-liquefied soils, where non-liquefied soils included soils above the phreatic line (e.g., shell material) and soils too plastic to experience significant strength loss due to shaking. For the liquefied soil, the shear strength was varied until a factor of safety equal to unity was achieved. The best estimate of liquefied shear strength back-calculated for Shivlakha Dam was 8.4 kPa, with a range from 4.0 to 9.97 kPa.

Using the same critical post-failure sliding surface, an analysis to back-calculate the liquefied strength ratio was conducted. The post-failure sliding surface was divided into number of segments as shown in Figure A.175. Because it was assumed that the entire foundation liquefied, the pre-failure and post-failure positions of each segment were assumed to be essentially unchanged (segments 1 to 9 in Figure A.175). Using the individual σ'_{vo} values for each segment and a single value of $s_u(liq)/\sigma'_{vo}$, individual values of liquefied shear strength were assigned to each segment of the post-failure geometry for stability analysis. This allows the variation in pre-failure σ'_{vo} within the zone of liquefaction to be reflected in variable liquefied shear strengths along the final sliding surface. Appropriate drained or undrained strengths (given in Table A.4) were assigned to nonliquefied soils. The best estimate of liquefied strength ratio for Shivlakha Dam was 0.076, with a range from 0.04 to 0.097.

A. 12.6.4 Liquefied Shear Strength and Strength Ratio Considering Kinetics

The center of gravity of the failed mass covered little distance during failure, making it difficult to track. Therefore, a kinetics analysis for Shivlakha Dam was not conducted.

A. 12.6.5 Sources of Uncertainties

The following sources of uncertainty were involved in estimating the mobilized shear strength and strength ratio: (1) the location of the initial failure surface; (2) the actual limits of the zone of liquefaction; (3) the shear strength of non-liquefiable soils; (4) the reservoir level at the time of earthquake; and (5) the phreatic surface within the embankment. Because the failure surfaces shown in Figure A.174 were estimated from the observed damage and the exact location of the initial failure surface cannot be identified, a number of circular and non-circular trial failure surfaces were analyzed until best-estimate values of mobilized strength and strength ratio could be obtained. Singh et al. (2005a) suggested that only a portion of the upstream soil liquefied (see Figure A.173). The author believed that the entire upstream foundation should have liquefied, as the entire foundation below the upstream slope was saturated and consists of loose to medium dense alluvial soil. Singh et al. (2005a) reported shear strengths for non-liquefiable soils used in their analysis, but they did not report laboratory tests to support

these values. The phreatic surface (and reservoir level) reported by Singh et al. (2005a) is at the same elevation, suggesting that there was no head loss through the dam. This seems unlikely because of the presence of impervious clay core and masonry wall in the dam.

The following sources of uncertainty were involved in estimating the liquefied shear strength and strength ratio: (1) the location of the final surface of sliding; (2) the shear strength of non-liquefiable soils; and (3) the potential for porewater pressure redistribution during flow failure. The final failure surface for post-failure geometry was ascertained based on the cracks in dam slope or from graben blocks. Singh et al. (2005a) reported shear strengths for non-liquefiable soils used in their analysis, but they did not report laboratory tests to support these values. As suggested by Stark and Mesri (1992), there may be drainage or void redistribution during the failure (e.g., Liu and Qiao 1984; Fiegel and Kutter 1994; Kokusho 2000; Kulasingam et al. 2004).

No penetration tests were conducted either before or after the failure for this case. Therefore, "representative" values of penetration resistance had to be estimated for this site from the range of penetration resistance values given for Kaswati and Fatehgadh Dams.

A.12.7 Tapar Dam

Originally constructed in 1976, Tapar Dam has a large reservoir capacity of 46 x 10^6 m^3, and is used as municipal water source for the Gandhidam metropolitan area and the Port of Kandla. Tapar dam was 15.5 m high with a crest length of 1350 m (EERI 2001; Singh et al. 2005a). In the 1990's, the dam was raised an additional 2.5 m. Figure A.176 shows the geometric configuration of Tapar Dam before and after the earthquake.

EERI (2001) suggested that liquefaction occurred in the alluvium beneath several sections of the main embankment. Cracks and fissures were observed on all three parts of the dam, i.e., the upstream face, crest, and downstream face. On the upstream face, large cracks and fissures, some with scarp-like vertical offsets occurred, and moderate slippage towards the upstream toe at two separate sections was also observed. One of the slips occurred principally through the two lower berms at the upstream toe, and sand and silty sand ejecta was noted in fissures over a considerable area at this location. Liquefaction beneath the upstream toe section caused lateral spreading and translational movements of several sections of the upstream face and berms. On the crest along several hundred meters, longitudinal cracks with apertures as wide as 0.3 to 0.5 m and depths of up to 5 m occurred. At the top of the downstream face, a minor shallow slip occurred at one station. Liquefaction, as manifested by sand and silty sand boils, was also observed in an agricultural field immediately downstream of the toe, and ejecta issued from several of the relief wells near the downstream toe. There was minor cracking at several locations on the downstream faces, but distress to the downstream faces was less pronounced than on the upstream side (Figure A.176). All of the distress and deformation that was visible on the entire dam surface, especially the sand boils observed near the upstream slope, suggest that foundation liquefaction was responsible for the movements observed at the dam.

A. 12.7.1 Representative Penetration Resistance

No penetration data is available for Tapar Dam. The range of uncorrected SPT N-values reported for Kaswati and Fatehgadh Dams was used to estimate the $(N_1)_{60}$-values for this site. Therefore N-values before dam construction (13 to 19) reported elsewhere were used to compute representative $(N_1)_{60}$ values below the mid-height of the upstream slope. This calculation yielded an average $(N_1)_{60}$-value of 10, with a range from 8 to 12.

As stated above, CPTs were not performed at any Indian dam site. Therefore, corresponding values of q_{c1} were estimated using the average q_c/N_{60} ratio from the five correlations proposed by Robertson and Campanella (1985), Seed and de Alba (1986), Andrus and Youd (1989), Kulhawy and Mayne (1990), and Stark and Olson (1995). For D_{50} = 0.3 mm (see Figure A.163), the average q_c/N_{60} = 0.48. Therefore, the average qc1 was 4.8 MPa, with a range from 3.84 to 5.76 MPa.

A. 12.7.2 Yield Shear Strength and Strength Ratio

As explained in Section A.12.1, seismically-induced liquefaction of the foundation alluvium underneath the embankment likely triggered movement in the upstream slope of Tapar Dam. The pre-failure geometry is reproduced in Figure A.177. Because the failure surface shown in Figure A.177 is only constrained by the observed damage and the exact location of the initial failure surface cannot be identified, a number of trial failure surfaces were analyzed until best-estimate values of mobilized stress and mobilized stress ratio were obtained. Both circular and non-circular failure surfaces were searched using a limit equilibrium slope stability analysis to determine the critical failure surface that is consistent with the observed failure pattern and requires the minimum value of shear resistance for equilibrium, i.e., a factor of safety equal to unity.

The critical slip surface determined for Tapar Dam is similar to the failure surface used by other researchers (EERI 2001; Singh et al. 2005a; Babu et al. 2007). For each case, the foundation alluvium below the upstream slope was assumed to liquefy because the water table was above the foundation alluvium and the alluvium was loose to medium dense. Singh et al. (2005a) suggested that only a portion of the upstream soil liquefied (Figure A.176). The author believed that the entire upstream foundation should have liquefied, as the entire foundation below the upstream slope was saturated and consisted of loose to medium dense alluvial soil. For further explanation, see Section A. 12.6.2. Soils above the phreatic surface, including the semi-pervious shells, impervious core, and masonry wall were assigned appropriate drained or undrained shear strengths, as shown in Table A.4. The average mobilized shear strength was 16.5 kPa, with a range from 13.5 to 17 kPa. Similarly, the average strength ratio was 0.165, with a range from 0.163 to 0.17. As explained in Chapter 2, the shear strength and strength ratios mobilized at the instant of failure in cases where liquefaction is triggered by seismic loading do not necessarily represent yield shear strength and strength ratios.

A. 12.7.3 Liquefied Shear Strength and Strength Ratio

The post-failure geometry of Tapar Dam is reproduced in Figure A.178 Post-failure geometry of Tapar Dam with critical final sliding surfaces and locations of post-failure geometry segments Following a slope stability analysis search, a critical noncircular failure surface was selected that was consistent with the final position of the failed mass. The critical failure surface was divided into segments that consisted of liquefied soils and non-liquefied soils, where the non-liquefied soils can be either soils above the phreatic line (e.g., shell material) or soils too plastic to experience significant strength loss. For the liquefied soil, the shear strength was varied until a factor of safety equal to unity was achieved. The representative value of liquefied shear strength back-calculated for Tapar Dam was 10.9 kPa, with a range from 7.3 to 15.6 kPa.

Using the same post-failure sliding surface, an analysis to back-calculate the liquefied strength ratio was conducted. The post-failure sliding surface was divided into number of segments as shown in Figure A.178. Because the movements were small and the embankment soils may not have liquefied, the pre- and post-failure segment positions are assumed to be in the same positions (segments 1 to 8 in Figure A.178). Using the individual σ'_{vo} values for each segment and a single value of $s_u(liq)/\sigma'_{vo}$, individual values of liquefied shear strength were assigned to each segment of the post-failure geometry for stability analysis. This allows the variation in pre-failure σ'_{vo} within the zone of liquefaction to be reflected in variable liquefied shear strengths along the final sliding surface. Appropriate drained or undrained strengths based on the strengths given in Table A.4. The best estimate of liquefied strength ratio back-calculated for Tapar Dam was 0.117, with a range from 0.093 to 0.155.

A. 12.7.4 Liquefied Shear Strength and Strength Ratio Considering Kinetics

The movements at Tapar Dam and of its center of gravity were small. Because there was almost no change in the center of gravity position, a kinetics analysis could not be conducted.

A. 12.7.5 Sources of Uncertainties

The following sources of uncertainty were involved in estimating the yield shear strength and strength ratio: (1) the location of the initial failure surface; (2) the actual limits of liquefied soil; (3) the shear strength of nonliquefied soils; (4) the reservoir level at the time of earthquake; and (5) the phreatic surface within the embankment. Because the failure surfaces shown in Figure A.177 were only constrained by the observed damage and the exact location of the initial failure surface cannot be identified, a number of trial failure surfaces were analyzed until best-estimate values of mobilized stress and mobilized stress ratio were obtained. Singh et al. (2005a) suggested that only a portion of the upstream soil liquefied (Figure A.176), while the author believes that the entire upstream foundation should have liquefied, as explained in Section A. 12.6.2.

The following sources of uncertainty were involved in estimating the liquefied shear strength and strength ratio: (1) the location of the final surface of sliding; and (2) the shear strength of non-liquefied soils; and (3) porewater pressure redistribution (or drainage) during flow failure. The final failure surface for post-failure geometry was ascertained based on the cracks in dam slope or from graben blocks, but is not known with certainty. Singh et al. (2005a) reported shear strengths for non-liquefiable soils used in their analysis, but they did not report laboratory tests to support these values. As defined in Stark and Mesri (1992), there may be drainage or void redistribution during the failure (e.g., Liu and Qiao 1984; Fiegel and Kutter 1994; Kokusho 2000; Kulasingam et al. 2004).

No penetration tests were conducted either before or after the failure for this case. Therefore, "representative" values of penetration resistance had to be estimated for this site from the range of penetration resistance values given for Kaswati and Fatehgadh Dams.

A.12.8 Fatehgadh Dam

Constructed in 1979, Fatehgadh Dam had a design reservoir capacity of 7.5×10^6 m^3, a crest height of 11.6 m, and crest length of 4050 m. The reservoir was nearly empty at the time of earthquake; however, the upstream foundation alluvium was saturated. Figure A.179 presents the pre- and post-earthquake configuration of the dam.

EERI (2001) reported that the embankment crosses two recently active stream channels, and upstream slope movement occurred at both of these locations. Longitudinal cracking occurred along much of the crest, and was most severe at the location of the upstream slope failure. Open fissures were observed on the upstream face of the dam. EERI (2001) also reported the development of cracks as deep as 1.5 to 1.7 m within the upstream portion of the dam, bulging of the upstream toe, and settlement of the crest and uppermost portion of the downstream shell of 0.5 to 1 m along a length of 280 m. Fine, silty sand boil ejecta was observed in the bulged soil at the upstream toe, illustrating that liquefaction occurred in the foundation soils and was likely responsible for the observed movements.

A. 12.8.1 Representative Penetration Resistance

Although detailed boring logs were not available, investigators did provide some information about subsurface conditions in the upper 10 m of the foundations (Krinitzsky and Hynes 2002) at this site. Singh et al. (2005a) reported that SPT blow counts in the foundation alluvium below the dam footprint generally ranged from 13 to 19. The raw N-values are corrected as explained in Section A. 12.6.1. This calculation yielded average $(N_1)_{60}$ of 12, with a range from 10 to 15.

As stated above, CPTs were not performed at any Indian dam site. Therefore, corresponding values of q_{c1} were estimated using the average q_c/N_{60} ratio from the five correlations proposed by Robertson and Campanella (1985), Seed and de Alba (1986),

Andrus and Youd (1989), Kulhawy and Mayne (1990), and Stark and Olson (1995). For D_{50} = 0.3 mm (see Figure A.163), the average q_c/N_{60} = 0.48. Therefore, the average q_{c1} was 5.76 MPa, with a range from 4.8 to 7.2 MPa.

A. 12.8.2 Yield Shear Strength and Strength Ratio

As described above, seismically-induced liquefaction of the foundation alluvium below the embankment likely triggered minor movement in the upstream slope of Fatehgadh Dam. The pre-failure geometry is reproduced in Figure A.180. Because the failure surface shown in Figure A.180 is only constrained by the observed damage and the exact location of the initial failure surface cannot be identified, a number of trial failure surfaces were analyzed until best-estimate values of mobilized stress and mobilized stress ratio were obtained. Both circular and non-circular failure surfaces were searched to determine the critical failure surface that is consistent with the observed failure pattern and requires the minimum value of shear resistance for equilibrium, i.e., a factor of safety equal to unity. The slip surface determined for Fatehgadh Dam is similar to the failure surface reported by other researchers (EERI 2001; Singh et al. 2005a; Babu et al. 2007). For this case, the foundation alluvium soil underneath the upstream slope was assumed to have liquefied because the water table was just above the foundation alluvium and the alluvium was loose to medium dense. Singh et al. (2005a) suggested that only a portion of the upstream soil liquefied (Figure A.179). The author believes that the entire upstream foundation should have liquefied, as the entire foundation below the upstream slope was saturated and consists of loose to medium dense alluvial soil. For further explanation, see Section A. 12.6.2. Soils above the phreatic surface, including the semi-pervious shells, impervious core, and masonry wall were assigned appropriate drained or undrained shear strengths, as shown in Table A.4.

It should be noted that various investigators reported different foundation thicknesses, ranging from 2 to 5 m, for Fatehgadh Dam. Therefore, the author performed slope stability analyses for three different foundation layer thicknesses: 2 m, 3.5 m and 5 m. The best estimate of mobilized shear strength was 17.3 kPa, with a range from 13.5 to 19.5 kPa. Similarly, the best estimate of mobilized strength ratio was 0.18, with a range from 0.148 to 0.215. As explained in Chapter 2, the shear strength and strength ratios mobilized at the instant of failure in cases where liquefaction is triggered by seismic loading do not necessarily represent yield shear strength and strength ratios.

A. 12.8.3 Liquefied Shear Strength and Strength Ratio

The post-failure geometry of Fatehgadh Dam is reproduced in Figure A.181. Following a slope stability analysis search, a final failure surface was selected that was consistent with the final position of the failed mass. The critical final failure surface was divided into segments that consist of both liquefied soils and non-liquefied soils, where the non-liquefied soils can be either soils above the phreatic line (e.g., shell material) or soils too plastic to experience significant strength loss during shaking. For the liquefied soil, the shear strength was varied until a factor of safety equal to unity was achieved.

The best estimate of liquefied shear strength back-calculated for Fatehgadh Dam was 6.0 kPa, with a range from 3.3 to 9.9 kPa.

Using the same post-failure sliding surface, an analysis to back-calculate the liquefied strength ratio was conducted. Similar to the yield strength and strength ratio analyses, liquefied shear strength and strength ratio analyses were conducted using three different thicknesses: 2, 3.5, and 5 m. The post-failure sliding surface was divided into number of segments as shown in Figure A.181. Because it is assumed that the entire foundation liquefied, the pre- and post-failure segment positions were assumed to be the same (segments 1 to 9 in Figure A.181).

Using the individual σ'_{vo} values for each segment and a single value of $s_u(liq)/\sigma'_{vo}$, individual values of liquefied shear strength were assigned to each segment of the post-failure geometry for stability analysis. This allows the variation in pre-failure σ'_{vo} within the zone of liquefaction to be reflected in variable liquefied shear strengths along the final sliding surface. Appropriate drained or undrained strengths were assigned to nonliquefied soils as reported in Table A.4. The best estimate of liquefied strength ratio back-calculated for Fatehgadh Dam was 0.076, with a range from 0.045 to 0.11.

A. 12.8.4 Liquefied Shear Strength and Strength Ratio Considering Kinetics

The center of gravity of the failed mass covered little distance making it difficult to track. Therefore, a kinetics analysis for Fatehgadh Dam could not be conducted.

A. 12.8.5 Sources of Uncertainties

The following sources of uncertainty were involved in estimating the yield shear strength and strength ratio: (1) the locations of the initial failure surface; (2) the actual limits of liquefied soil; (3) the shear strength of nonliquefied soils; (4) the reservoir level at the time of earthquake; and (5) the phreatic surface within the embankment. Singh et al. (2005a) reported shear strengths for non-liquefiable soils used in their analysis, but they did not report laboratory tests to support these values. The phreatic surface (and reservoir level) reported by Singh et al. (2005a) is at the same elevation, suggesting that there was no head loss through the dam. This seems unlikely because of the presence of impervious clay core and masonry wall in the dam.

The following sources of uncertainty were involved in estimating the liquefied shear strength and strength ratio: (1) the location of the final surface of sliding; (2) the shear strength of non-liquefied soils; and (3) porewater pressure redistribution (or drainage) during flow failure. The final failure surface for post-failure geometry was ascertained based on the cracks in dam slope or from graben blocks, but is not known with certainty. Singh et al. (2005a) reported shear strengths for non-liquefiable soils used in their analysis, but they did not report laboratory tests to support these values. As defined in Stark and Mesri (1992), there may be drainage or void redistribution during the failure (e.g., Liu and Qiao 1984; Fiegel and Kutter 1994; Kokusho 2000; Kulasingam et al. 2004).

The following sources of uncertainty were involved in estimating the "representative" penetration resistance: (1) the absence of raw SPT or CPT data. There are no boring logs available, only a range of uncorrected SPT-N values were reported (Singh et al. 2005a). The locations of these SPT borings are unknown and hence uncorrected SPT-N values were corrected for overburden pressures underneath the toe, mid-slope, and crest of the embankment dam.

A.12.9 Kaswati Dam

Kaswati Dam was constructed in 1973 on the Kaswati River. The dam has a design reservoir capacity of 8.86×10^6 m^3 and crest length of 1455 m (EERI 2001; Singh et al. 2005a,b; Babu et al. 2007). However, there is some confusion regarding the dam height, which is reported as 8.8 m (EERI 2001, Singh et al. 2005a), 12.9 m (Singh et al. 2005b), and 15.74 m (Babu et al. 2007). For the analysis described subsequently, the author used a maximum height of 11.5 m based on the height measured from the scaled diagram of Singh et al. (2005a) and because this height is near the average of values reported by others. Like other dams in this area, Kaswati Dam is underlain by loose to medium-dense, alluvial silt-sand mixtures.

Kaswati Dam reservoir was nearly empty at the time of earthquake, but the foundation soils were saturated (EERI 2001). During the earthquake, longitudinal cracking developed along much of the crest, as well as the upstream slope. In addition, the upstream toe bulged approximately 1.6 m above the pre-earthquake ground surface, likely as a result of shallow sliding. Such distress may have been due to localized liquefaction near the upstream toe of the dam; however, because most of the toe remained below the reservoir surface, it was not possible to ascertain whether sand boils developed during the earthquake (EERI 2001). The downstream slope, on the other hand, remained largely unaffected. Figure A.182 presents the pre- and post-earthquake configuration of the dam.

A. 12.9.1 Representative Penetration Resistance

While no detailed boring logs were available, investigators did provide some information about subsurface conditions in the upper 10 m of the foundations (Krinitzsky and Hynes 2002). Singh et al. (2005a) reported that SPT blow counts in the foundation alluvium below the dam footprint generally ranged from 13 to 19. The raw N-values are corrected as explained in Section A. 12.6.1. This calculation yielded an average $(N_1)_{60}$ of 12, with a range of 9 to 15.

As stated above, CPTs were not performed at any Indian dam site. Therefore, corresponding values of q_{c1} were estimated using the average q_c/N_{60} ratio from the five correlations proposed by Robertson and Campanella (1985), Seed and de Alba (1986), Andrus and Youd (1989), Kulhawy and Mayne (1990), and Stark and Olson (1995). For D_{50} = 0.3 mm (see Figure A.163), the average q_c/N_{60} = 0.48. Therefore, the average q_{c1} was 5.76 MPa, with a range from 4.3 to 7.2 MPa.

A. 12.9.2 Yield Shear Strength and Strength Ratio

As explained in Section A.12.1, seismically-induced liquefaction of the foundation alluvium sand underneath the embankment likely triggered the movement in the upstream slope of Kaswati Dam. Neither liquefaction flow failure nor liquefaction manifestations were observed at dam site, suggesting that the observed deformation may have resulted from inertial forces. To evaluate whether the observed deformation resulted from liquefaction or inertial forces, a Newmark sliding block analysis is conducted by the author using the Jibson and Jibson (2005) Newmark sliding block analysis software. To conduct a Newmark sliding block analysis, yield accelerations need to be determined first. A limit equilibrium analysis was performed using Slope/W (GEO-SLOPE International 2004) with initial value of horizontal seismic coefficient (k_h) of zero and factor of safety (FS) was calculated. This process was repeated several times, incrementing k_h until FS reached unity. Analyses were run for both drained and undrained conditions using circular and non-circular sliding surfaces as shown in Figure A.182. For drained conditions, drained friction angles of 28° and 30° were used for both non-liquefied and assumed liquefied soil. For undrained condition, drained friction angles of 28° and 30° were used for non-liquefied soils while undrained mobilized shear strength ratio from Olson and Stark (2003a) was assigned to the liquefiable soil.

A range of yield accelerations, a_y, (k_h values with FS of unity) from 0.104g to 0.362g was obtained from these analyses. Ground motions for the analyzed earthquake cases need to be used in Jibson and Jibson (2005) software in order to calculated deformations. Unfortunately, ground motions from Bhuj earthquake were not available in the software database and therefore alternate ground motions were selected from those available in the software using the criteria summarized in Olson and Johnson (2008). Newmark sliding block analyses were performed for various combinations of PGA values, as given in Table A.1, and a range of yield accelerations, as calculated above. Calculated mean displacements ranged from 0.0 to 116.1 cm. It should be noted that the majority of the computed mean deformations ranged from about 5 cm to 80 cm when undrained yield strength ratios were used, while computed mean deformations ranged from 0 to 5 cm when drained strengths were used for the liquefiable soils. These calcuations suggest that at the time of earthquake, when undrained conditions are assumed to prevail, the deformations are likely the result of liquefaction. The observed deformation based on pre-and post-failure geometries showed a horizontal displacement of 3.8 m, a vertical displacement of 1 m, and a rotational displacement of 2.6 m. Regardless of drained or undrained conditions, this disparity strongly suggests that the displacements were produced by liquefaction and not by inertial forces.

The pre-failure geometry is reproduced in Figure A.183. Because the failure surface shown in Figure A.183 was only constrained by the observed damage and the exact location of the initial failure surface cannot be identified, a number of trial failure surfaces were analyzed until best-estimate values of mobilized stress and mobilized stress ratio were obtained. Both circular and non-circular failure surfaces were searched using a limit equilibrium slope stability analysis to determine the critical failure surface that is

consistent with the observed failure pattern and requires the minimum value of shear resistance for equilibrium, i.e., a factor of safety equal to unity. The slip surface determined for Kaswati Dam is similar to the failure surface reported by others (EERI 2001; Singh et al. 2005a; Babu et al. 2007).

For this case, the foundation alluvium soil underneath the upstream slope was assumed to have liquefied because the water table was just above the foundation alluvium and the alluvium was loose to medium dense. Singh et al. (2005a) suggested that only a portion of the upstream soil liquefied (Figure A.182). The author believed that the entire upstream foundation should have liquefied, as the entire foundation below the upstream slope was saturated and consists of loose to medium dense alluvial soil. For further explanation, see Section A. 12.6.2. Soils above the phreatic surface, including the semi-pervious shells and impervious core were assigned appropriate drained and undrained shear strengths, as shown in Table A.4. The best estimate of mobilized shear strength was 17.5 kPa, with a range from 14 to 22 kPa. Similarly, the best estimate of mobilized strength ratio was 0.17, with a range from 0.145 to 0.2. As explained in Chapter 2, the shear strength and strength ratios mobilized at the instant of failure in cases where liquefaction is triggered by seismic loading do not necessarily represent yield shear strength and strength ratios.

A. 12.9.3 Liquefied Shear Strength and Strength Ratio

The post-failure geometry of Kaswati Dam is reproduced in Figure A.184. Following a slope stability analysis search, a final failure surface was selected that was consistent with the final shape and position of the failed mass. The critical final failure surface was divided into segments that consisted of both liquefied and non-liquefied soils, where the non-liquefied soils can be either soils above the phreatic line (e.g., shell material) or soils too plastic to experience significant strength loss during shaking. For the liquefied soil, the shear strength was varied until a factor of safety equal to unity was achieved. The best estimate of liquefied shear strength back-calculated for Kaswati Dam was 10 kPa, with a range from 9.2 to 15.3 kPa.

Using the same post-failure sliding surface, an analysis to back-calculate the liquefied strength ratio was conducted. The post-failure sliding surface was divided into number of segments as shown in Figure A.184. Because it is assumed that the entire foundation liquefied, the pre- and post-failure segment positions were assumed to be the same (segments 1 to 9 in Figure A.184). Using the individual σ'_{vo} values for each segment and a single value of $s_u(liq)/\sigma'_{vo}$, individual values of liquefied shear strength were assigned to each segment of the post-failure geometry for stability analysis. This allows the variation in pre-failure σ'_{vo} within the liquefied zone to be reflected in variable liquefied shear strengths along the final sliding surface. Appropriate drained or undrained strengths were assigned to nonliquefied soils as reported in Table A.4. The best estimate liquefied strength ratio back-calculated for Kaswati Dam was 0.096, with a range from 0.092 to 0.14.

A. 12.9.4 Liquefied Shear Strength and Strength Ratio Considering Kinetics

The center of gravity of the failed mass covered little distance making it difficult to track. Therefore, a kinetics analysis for Kaswati Dam could not be conducted.

A. 12.9.5 Sources of Uncertainties

The following sources of uncertainty were involved in estimating the yield shear strength and strength ratio: (1) whether the observed displacements were caused by liquefaction; (2) the location of the initial failure surface; (3) the actual limits of liquefied soil; (4) the shear strength of nonliquefied soils; (5) the reservoir level at the time of earthquake; and (6) the phreatic surface within the embankment. Although it may be possible that the longitudinal cracks observed on the dam crest resulted from localized liquefaction at the toe, the toe remained below the reservoir surface making it impossible to ascertain whether liquefied soil ejected to the surface. Because the failure surfaces shown in Figure A.184 were estimated from the observed damage and the exact location of the initial failure surface cannot be identified, a number of trial failure surfaces were analyzed until best-estimate values of yield strength and yield strength ratio could be obtained. Singh et al. (2005a) suggested that only a portion of the upstream soil liquefied (Figure A.184). The author believed that the entire upstream foundation should have liquefied, as the entire foundation below the upstream slope was saturated and consists of loose to medium dense alluvial soil. For further explanation, see Section A. 12.6.2. Singh et al. (2005a) reported shear strengths for non-liquefiable soils used in their analysis, but they did not report laboratory tests to support these values. The phreatic surface (and reservoir level) reported by Singh et al. (2005a) is at the same elevation, suggesting that there was no head loss through the dam. This seems unlikely because of the presence of impervious clay core in the dam.

The following sources of uncertainty were involved in estimating the liquefied shear strength and strength ratio: (1) the location of the final surface of sliding; (2) the shear strength of non-liquefiable soils; and (3) porewater pressure redistribution (or drainage) during flow failure. The final failure surface for post-failure geometry was ascertained based on the cracks in dam slope or from graben blocks. Singh et al. (2005a) reported shear strengths for non-liquefiable soils used in their analysis, but they did not report laboratory tests to support these values. As defined in Stark and Mesri (1992), there may be drainage or void redistribution during the failure (e.g., Liu and Qiao 1984; Fiegel and Kutter 1994; Kokusho 2000; Kulasingam et al. 2004).

No penetration tests were conducted either before or after the failure for this case. Therefore, “representative” values of penetration resistance had to be estimated for this site from the range of penetration resistance values given for Kaswati and Fatehgadh Dams because the soil stratum is relatively consistent throughout the Bhuj area (Sitharam and Govindaraju 2004).

A.12.10 Suvi Dam

Suvi Dam was constructed in 1959 with a crest length of 2100 m and a maximum crest height of 16.5 m. In the 1990's, the crest was raised 1 m and an upstream parapet wall was added. Although the reservoir was nearly empty at the time of the earthquake, the foundation alluvium was saturated (EERI 2001). Significant bulging at the upstream toe, as well as settlement and fissuring of the upstream shell and crest occurred during the earthquake. The vertical settlement reached 1 m along roughly a 200 m long segment of the crest. The parapet collapsed along approximately 60% of the crest length. Figure A.185 presents the pre- and post-earthquake configurations of the dam. No sand boils were observed at or near the dam, but other researchers (e.g., EERI 2001; Singh et al. 2005a,b) suggested that the foundation soils likely liquefied.

A. 12.10.1 Representative Penetration Resistance

No penetration data either in terms of SPT, CPT, or Swedish weight sounding is available for Suvi Dam. The range of uncorrected SPT N-values given for Kaswati and Fatehgadh Dams were used to estimate the $(N_1)_{60}$-values for this site. Therefore N-values before dam construction (13 to 19) were used to compute representative $(N_1)_{60}$ values below the mid-height of the upstream slope. This calculation yielded an average $(N_1)_{60}$ of 10, with a range from 8 to 12.

As stated above, CPTs were not performed at any Indian dam site. Therefore, corresponding values of q_{c1} were estimated using the average q_c/N_{60} ratio from five correlations proposed by Robertson and Campanella (1985), Seed and de Alba (1986), Andrus and Youd (1989), Kulhawy and Mayne (1990), and Stark and Olson (1995). For D_{50} = 0.3 mm (see Figure A.163), the average q_c/N_{60} = 0.48. Therefore, the average q_{c1} was approximately 4.8 MPa, with a range from 3.8 to 5.8 MPa.

A. 12.10.2 Yield Shear Strength and Strength Ratio

The pre-failure geometry is reproduced in Figure A.186. Because the failure surface shown in Figure A.186 is only constrained by the observed damage and the exact location of the initial failure surface cannot be identified, a number of trial failure surfaces were analyzed until best-estimate values of mobilized stress and mobilized stress ratio were obtained. Both circular and non-circular failure surfaces were searched to determine the critical failure surface that was consistent with the observed failure pattern and requires the minimum value of shear resistance for equilibrium, i.e., a factor of safety equal to unity. The slip surface determined for Suvi Dam was similar to the failure surface reported by others (EERI 2001; Singh et al. 2005a; Babu et al. 2007).

For this case, the foundation alluvium soil underneath the upstream slope was assumed to have liquefied because the water table was just above the foundation alluvium and the alluvium was loose to medium dense. For detailed discussion see section A. 12.6.2. Soils above the phreatic surface, including the semi-pervious shells, impervious core, and concrete wall were assigned appropriate drained or undrained shear strengths, as shown in Table A.4. The best estimate of mobilized shear strength was 20.1 kPa, with a range from 17.2 to 29 kPa. Similarly, the best estimate of mobilized strength ratio was

0.20 with a range from 0.188 to 0.275. As explained in Chapter 2, the shear strength and strength ratios mobilized at the instant of failure in cases where liquefaction is triggered by seismic loading do not necessarily represent yield shear strength and strength ratios.

A. 12.10.3 Liquefied Shear Strength and Strength Ratio

The post-failure geometry of Suvi Dam is reproduced in Figure A.187. Following a slope stability analysis search, a critical failure surface was selected that was consistent with the final position of the failed mass. The critical final failure surface was divided into segments that consist of both liquefied and non-liquefied soils, where the non-liquefied soils can be either above the phreatic line (e.g., shell material) or too plastic to experience significant strength loss during shaking. For the liquefied soil, the shear strength was varied until a factor of safety equal to unity was achieved. The best estimate of liquefied shear strength for Suvi Dam was 12.1 kPa, with a range from 7.0 to 19.45 kPa.

Using the same post-failure sliding surface, an analysis to back-calculate the liquefied strength ratio was conducted. The post-failure sliding surface was divided into number of segments as shown in Figure A.187. Because it is assumed that the entire foundation liquefied, the pre- and post-failure segment positions were assumed to be the same (segments 1 to 8 in Figure A.187). Using the individual σ'_{vo} values for each segment and a single value of $s_u(liq)/\sigma'_{vo}$, individual values of liquefied shear strength were assigned to each segment of the post-failure geometry for stability analysis. This allows the variation in pre-failure σ'_{vo} within the liquefied zone to be reflected in variable liquefied shear strengths along the final sliding surface. Appropriate drained or undrained strengths were assigned to nonliquefied soils as reported in Table A.4. The best estimate of liquefied strength ratio for Suvi Dam was 0.13, with a range from 0.08 to 0.19.

A. 12.10.4 Liquefied Shear Strength and Strength Ratio Considering Kinetics

The center of gravity of the failed mass covered little distance making it difficult to track. Therefore, a kinetics analysis for Suvi Dam could not be conducted.

A. 12.10.5 Sources of Uncertainties

The following sources of uncertainty were involved in estimating the yield shear strength and strength ratio: (1) the location of the initial failure surface; (2) the actual limits of liquefied soil; (3) the shear strength of nonliquefied soils; (4) the reservoir level at the time of earthquake; and (5) the phreatic surface within the embankment. Although it may be possible that the longitudinal cracks observed on the crest of the dam are due to localized liquefaction at the toe, it was not possible to ascertain whether or not liquefied soil was ejected from the toe because it remained submerged. Because the failure surfaces shown in Figure A.186 were estimated from the observed damage and the exact location of the initial failure surface cannot be identified, a number of trial failure surfaces were analyzed until best-estimate values of yield strength and yield strength ratio could be obtained. Singh et al. (2005a) suggested that only a portion of the upstream soil liquefied

(Figure A.185). The author believed that the entire upstream foundation should have liquefied, as the entire foundation below the upstream slope was saturated and consists of loose to medium dense alluvial soil. Singh et al. (2005a) reported shear strengths for non-liquefiable soils used in their analysis, but they did not report laboratory tests to support these values. The phreatic surface (and reservoir level) reported by Singh et al. (2005a) was at the same elevation, suggesting that there was no head loss through the dam. This seems unlikely because of the presence of impervious core in the dam.

The following sources of uncertainty were involved in estimating the liquefied shear strength and strength ratio: (1) the location of the final surface of sliding; (2) the shear strength of non-liquefiable soils; and (3) porewater pressure redistribution (or drainage) during flow failure. The final failure surface for post-failure geometry was ascertained based on the cracks in dam slope or from graben blocks. Singh et al. (2005a) reported shear strengths for non-liquefiable soils used in their analysis, but they did not report laboratory tests to support these values. As defined in Stark and Mesri (1992), there may be drainage or void redistribution during the failure (e.g., Liu and Qiao 1984; Fiegel and Kutter 1994; Kokusho 2000; Kulasingam et al. 2004).

No penetration tests were conducted either before or after the failure for this case. Therefore, “representative” values of penetration resistance had to be estimated for this site from the range of penetration resistance values given for Kaswati and Fatehgadh Dams because the soil stratum is relatively consistent throughout the Bhuj area (Sitharam and Govindaraju 2004).

A.13 Figures

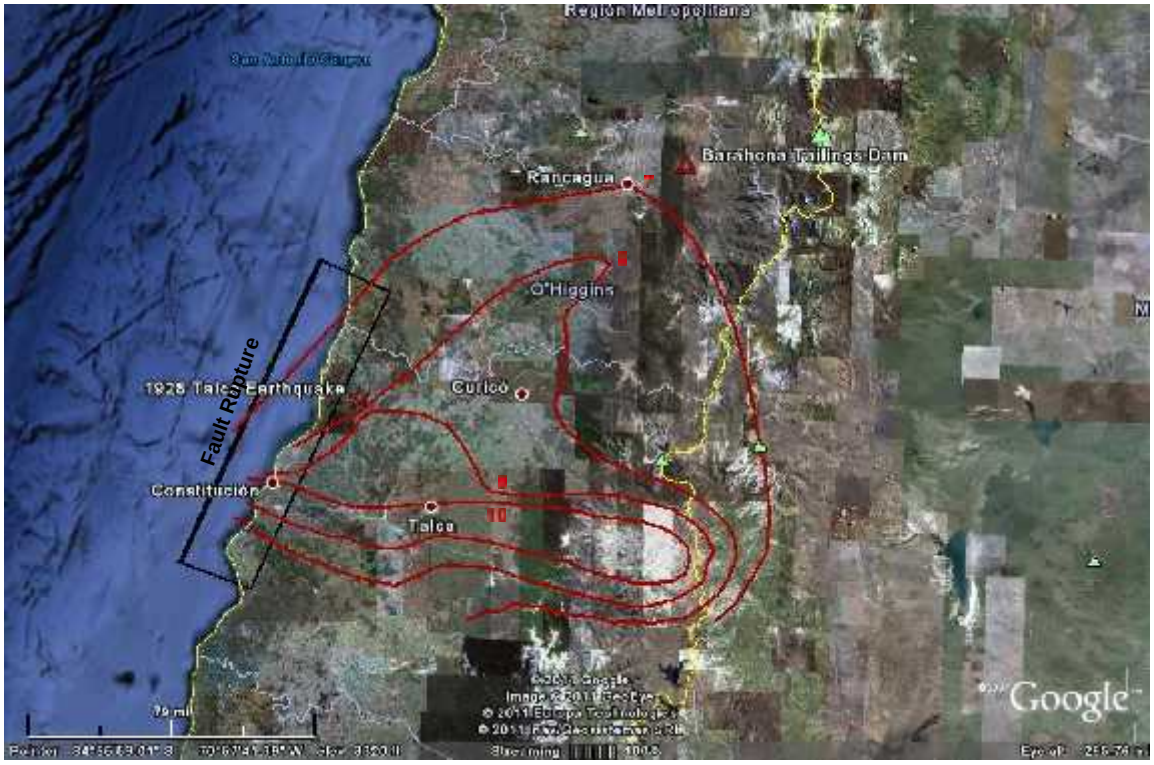

Figure A.1 Location of 1928 Talca earthquake epicenter, fault rupture, and Barahona tailings dam with contours of modified Mercalli intensity from Toncoso et al. (1993) (background image courtesy of Google Earth © 2011)

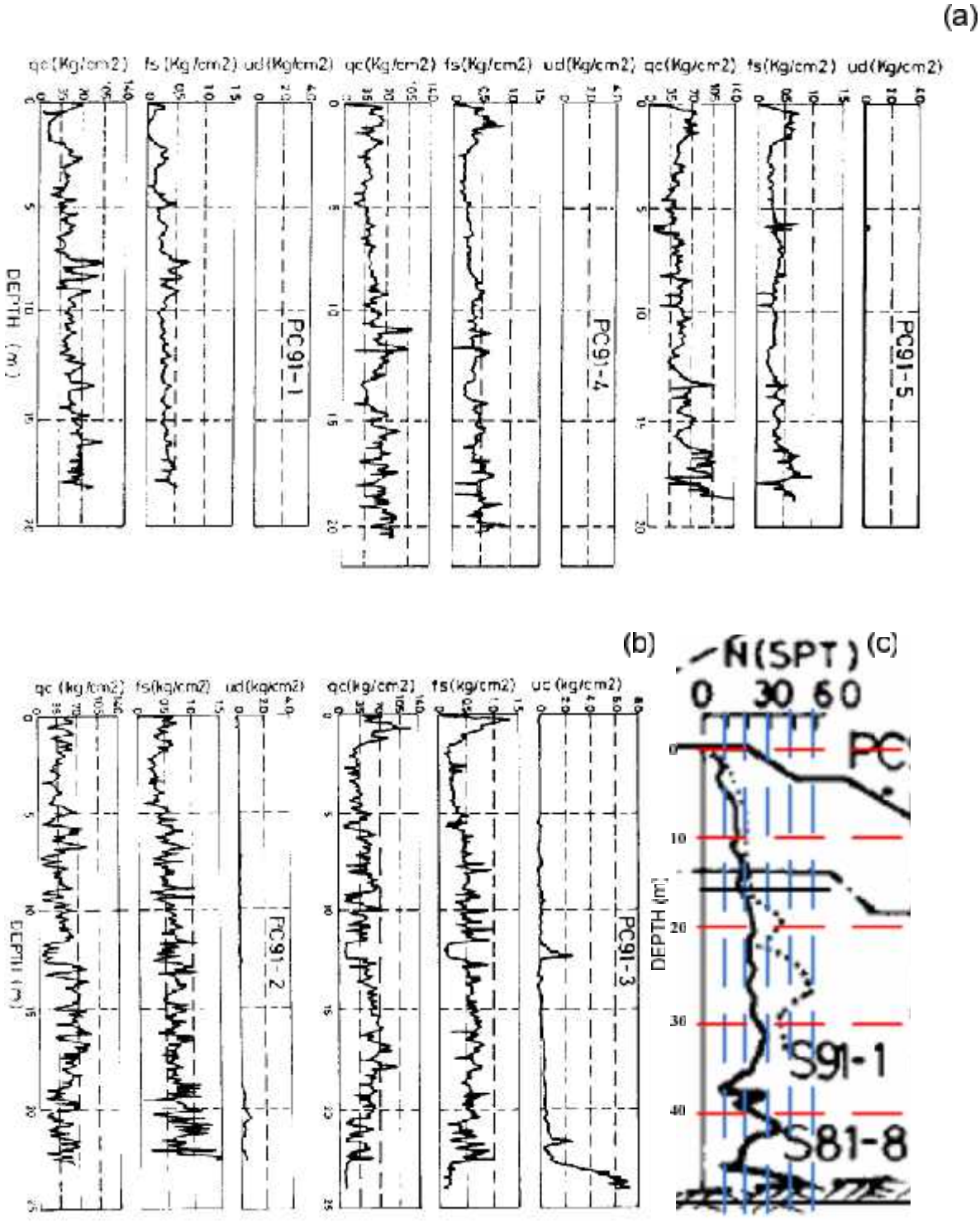

Figure A.2 Penetration resistance data of Barahona tailings dam (a) CPT on retaining dykes conducted in 1991 (b) CPT on impoundment conducted in 1991, (c) SPT on retaining dykes conducted in 1981 and 1991 (from Troncoso et al. 1993)

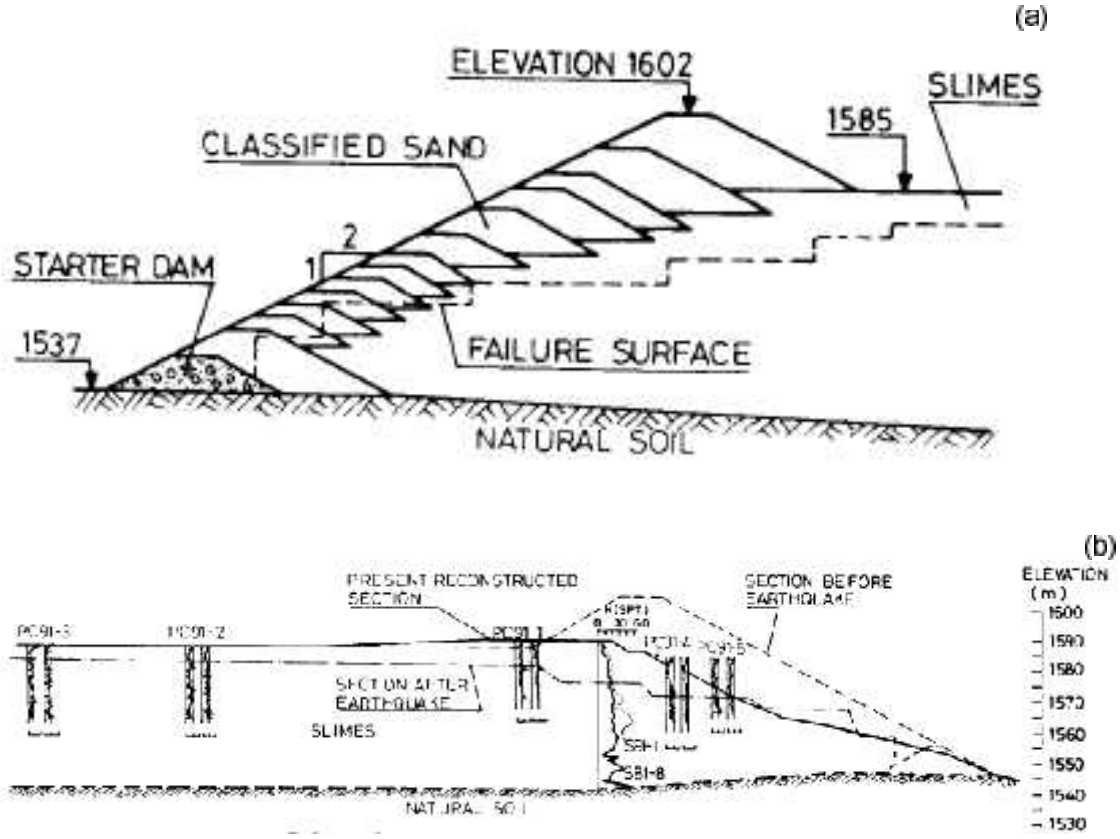

Figure A.3 Pre- and post-failure geometry of Barahona Tailings Dam with sand dykes, (b) pre- and post-failure geometry of Barahona Tailings Dam with locations of in situ tests (from Troncoso et al. 1993)

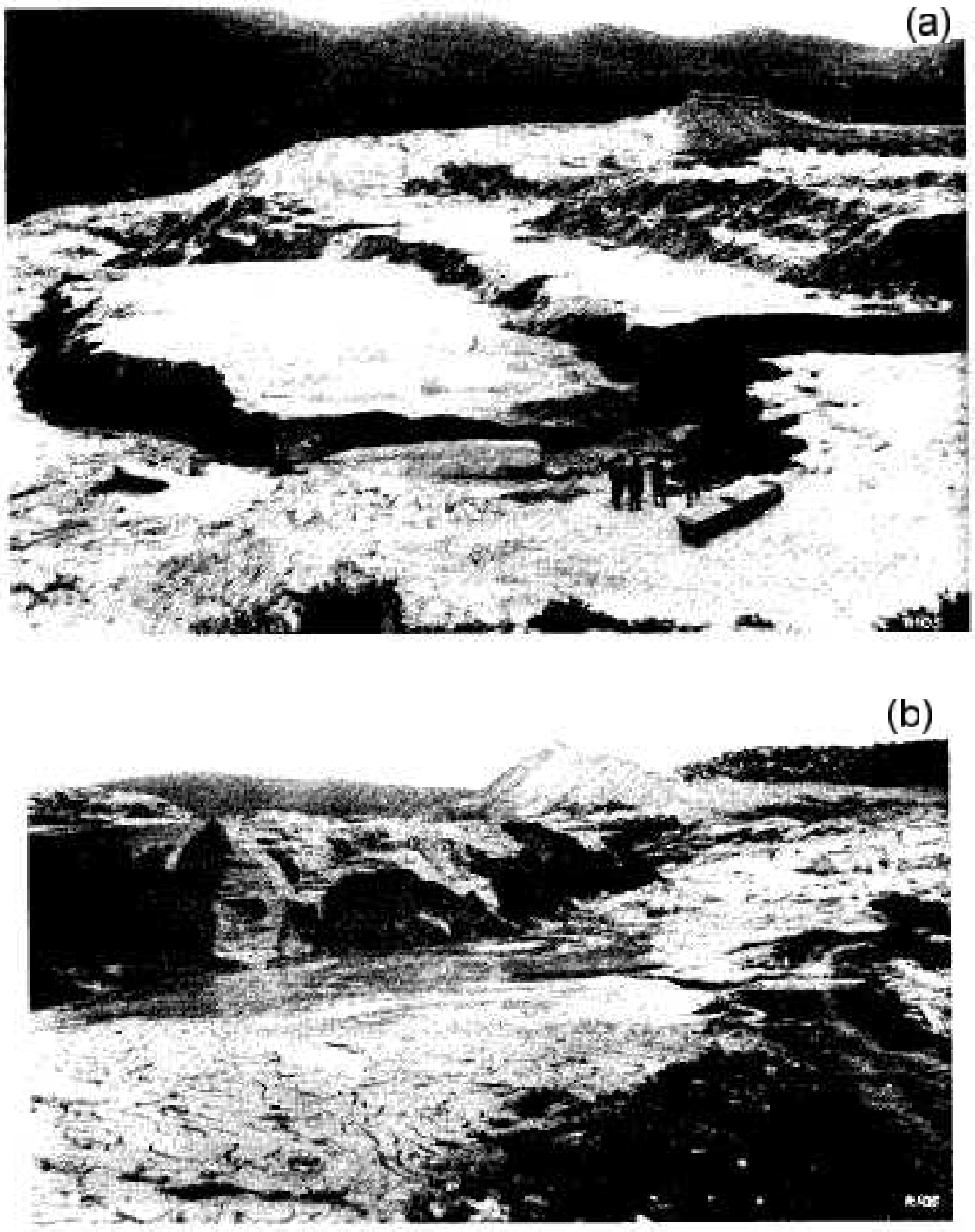

Figure A.4 Photographs of failed dam sections (a) terraces left after failure of the tailings; and (b) liquefied tailings soils (from Troncoso et al. 1993)

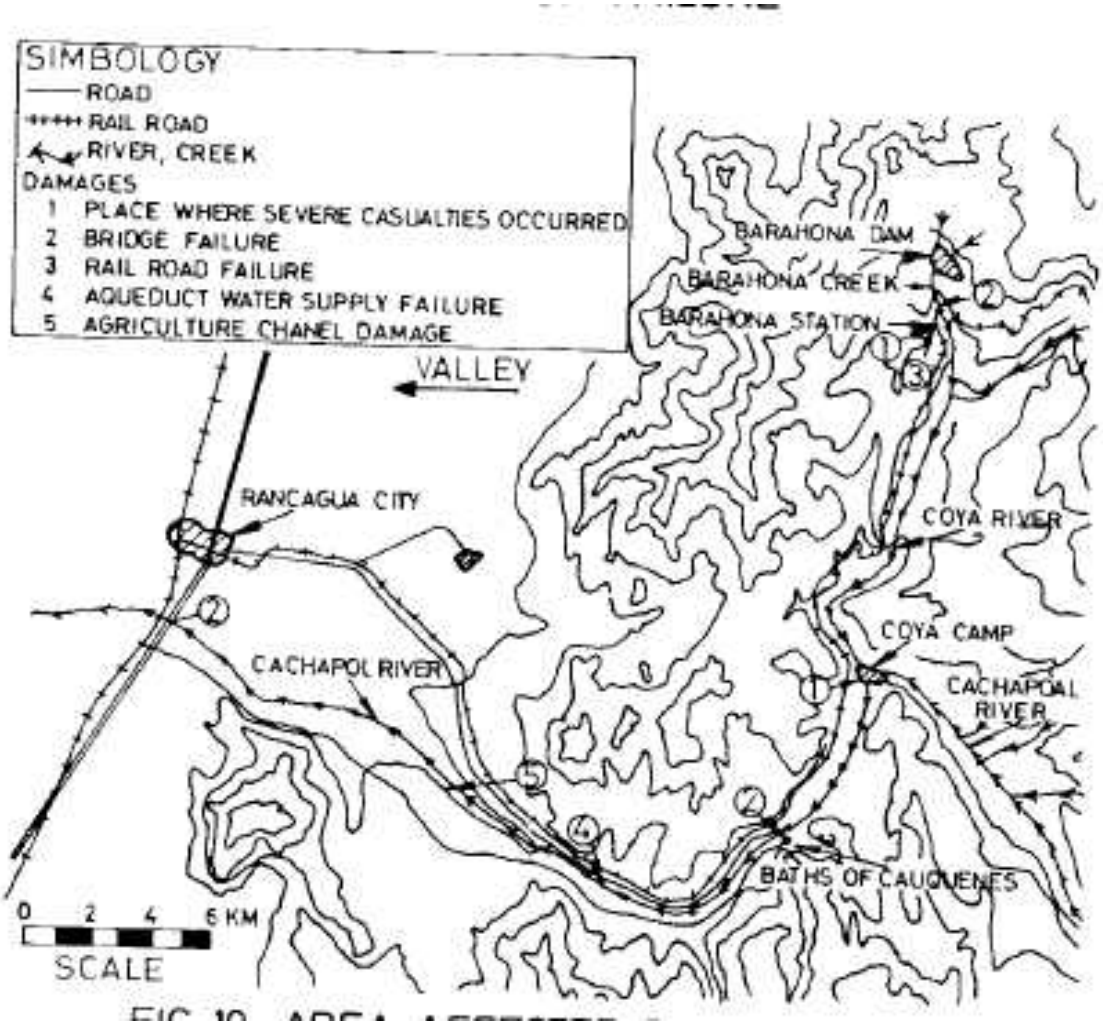

Figure A.5 Area affected by failure of dam and flow of tailings (from Troncoso et al. 1993)

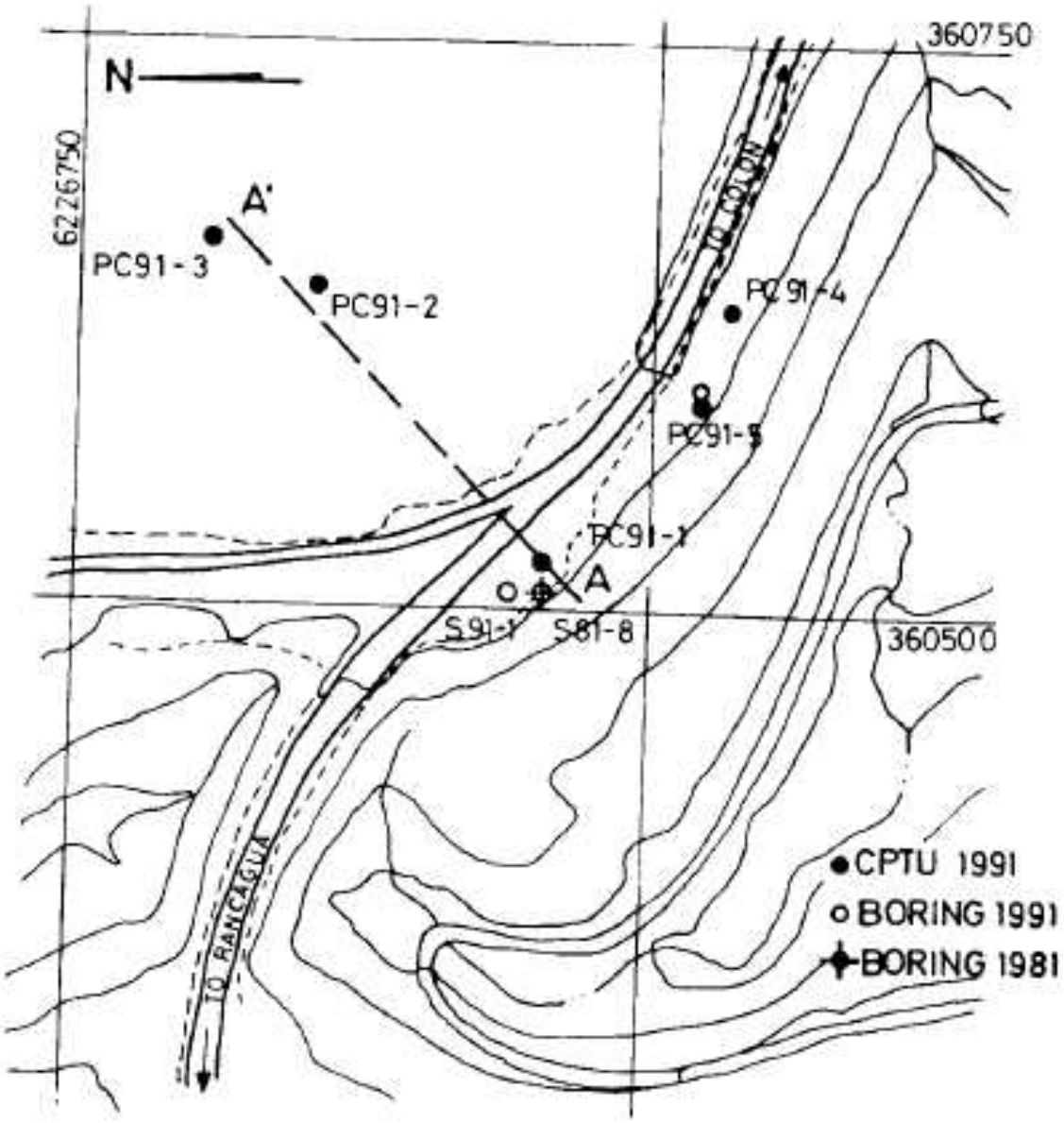

Figure A.6 Location of CPTs, SPT, and borings (from Troncoso et al. 1993)

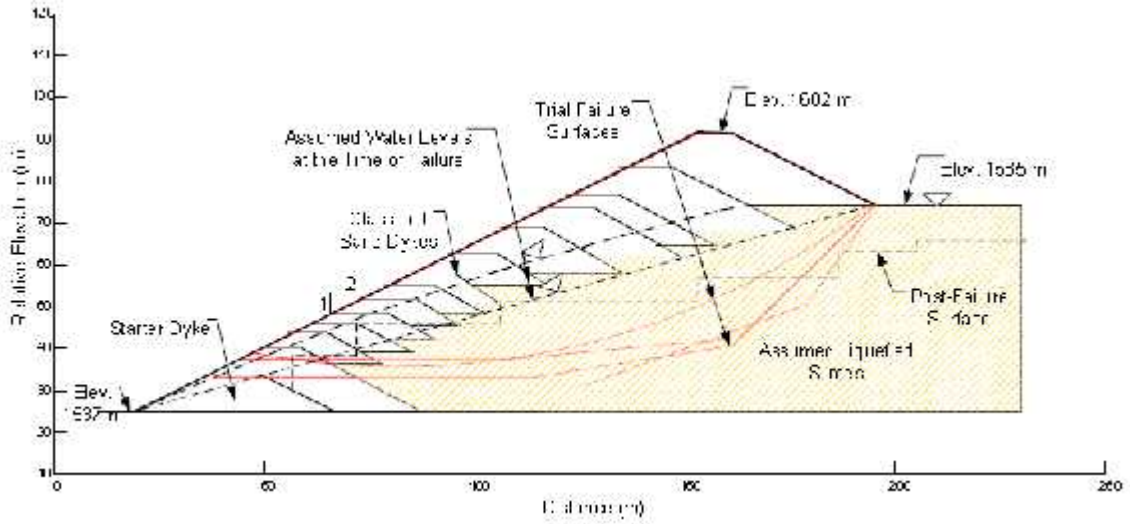

Figure A.7 Pre-and post-failure geometry of Barahona tailings dam with trial failure surfaces and assumed phreatic surfaces

Figure A.8 Map of Adriatic Sea, fault rupture from 1979 Montenegro earthquake, and isoseismic map of the intensity of shaking (reproduced from Ishihara 2005; background image courtesy of Google Earth ©2011)

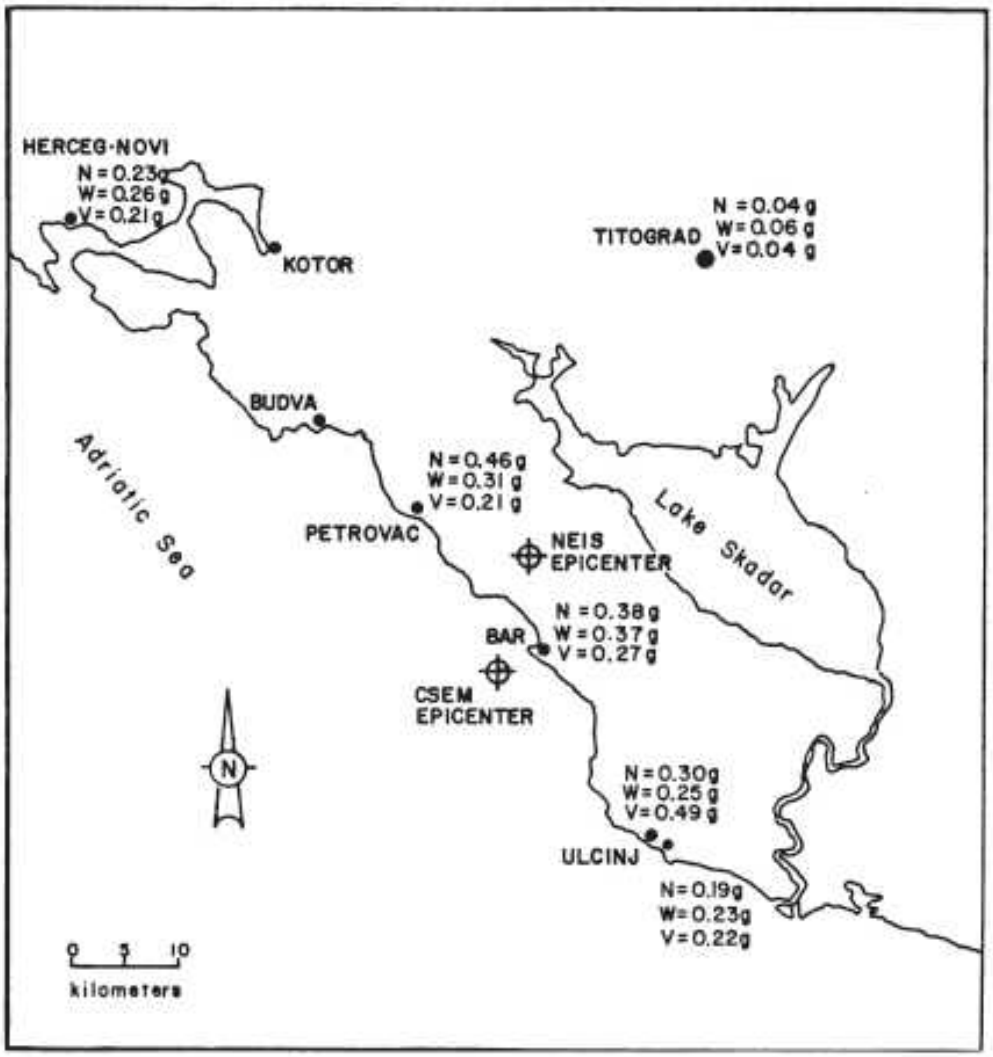

Figure A.9 Locations of reported epicenters and highest recorded accelerations during the Montenegro earthquake of April 15, 1979 (from Anicic et al. 1980).

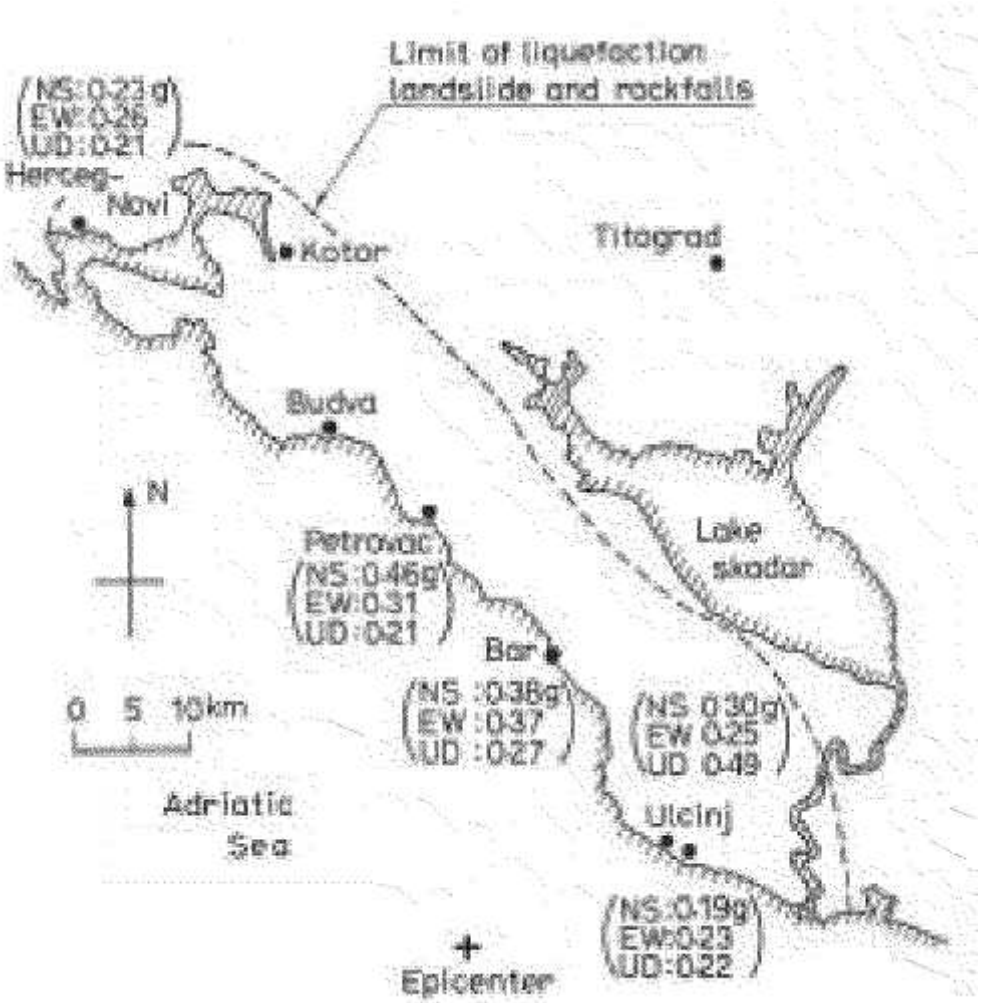

Figure A.10 Area affected by the Montenegro earthquake of April 15, 1979 (from Ishihara 2005)

Figure A.11 Landslide and road failure at Kamenari (from Anicic et al. 1980)

Figure A.12 Landslide and coastal road failure at Kamenari (from Anicic et al. 1980)

Figure A.13 Coastal road failure at Kamenari (from Anicic et al. 1980)

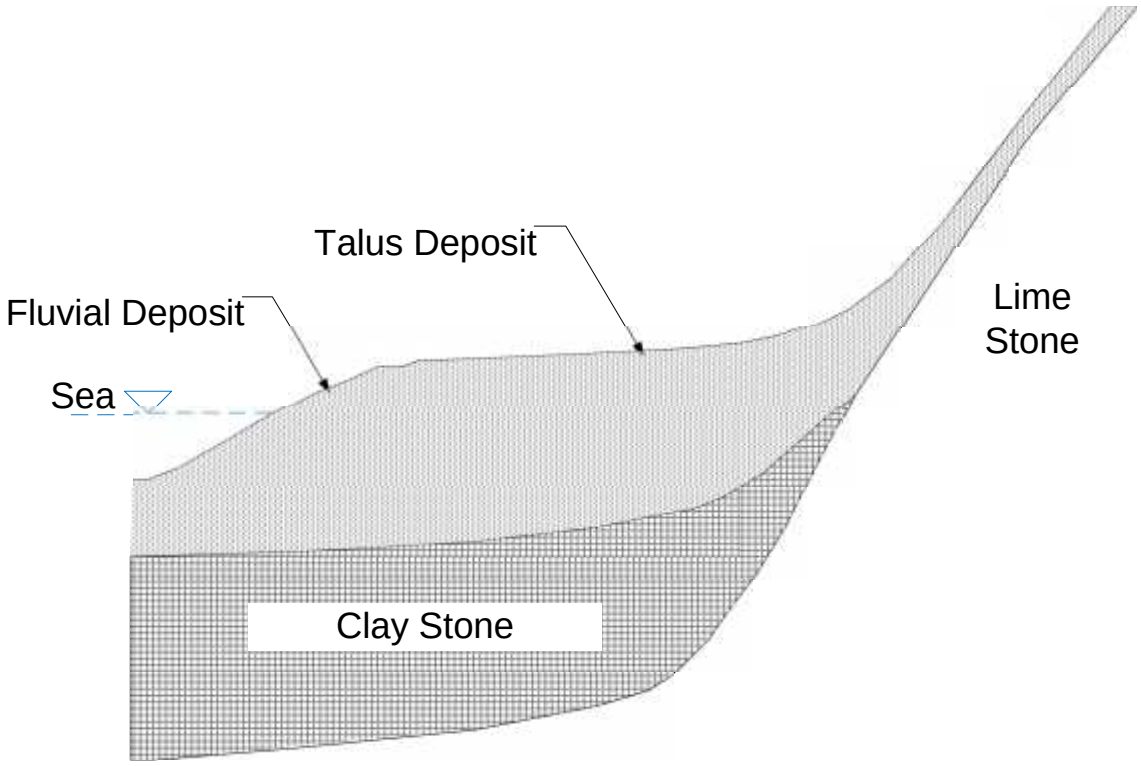

Figure A.14 Talus and fluvial deposits in the region along the Adriatic coast affected by the 1979 Montenegro earthquake (reproduced from Ishihara 2005)

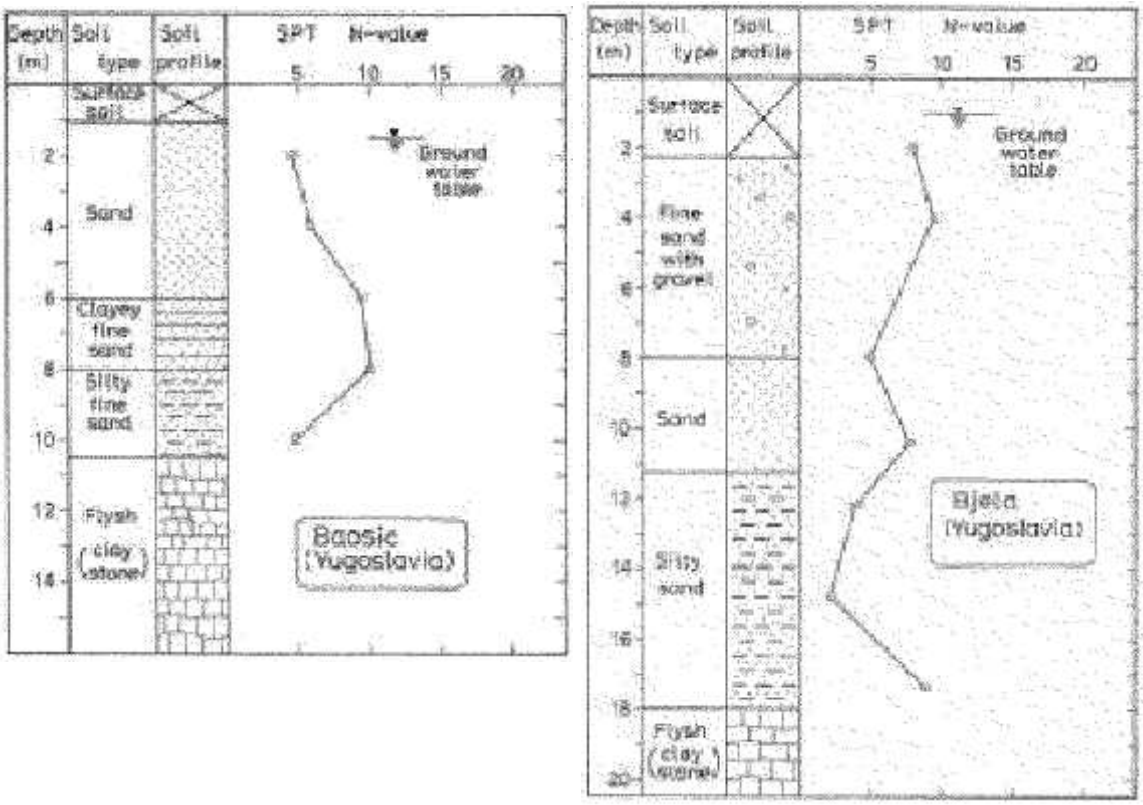

Figure A.15 Typical soil profiles at Baosic and Bijela along with SPT N-values (from Ishihara 2005)

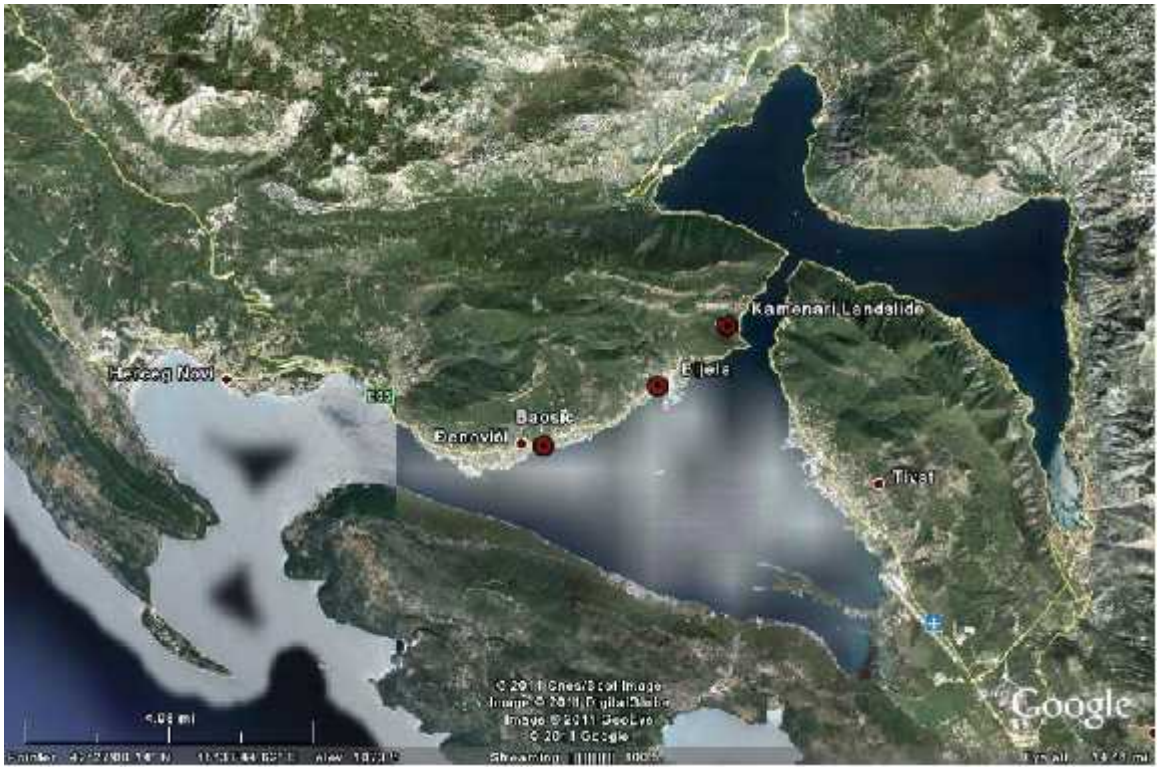

Figure A.16 Area of coastal landsliding, lateral spreading and liquefaction in Herceg-Novi (from Ishihara 2005; background image courtesy of Google © 2011)

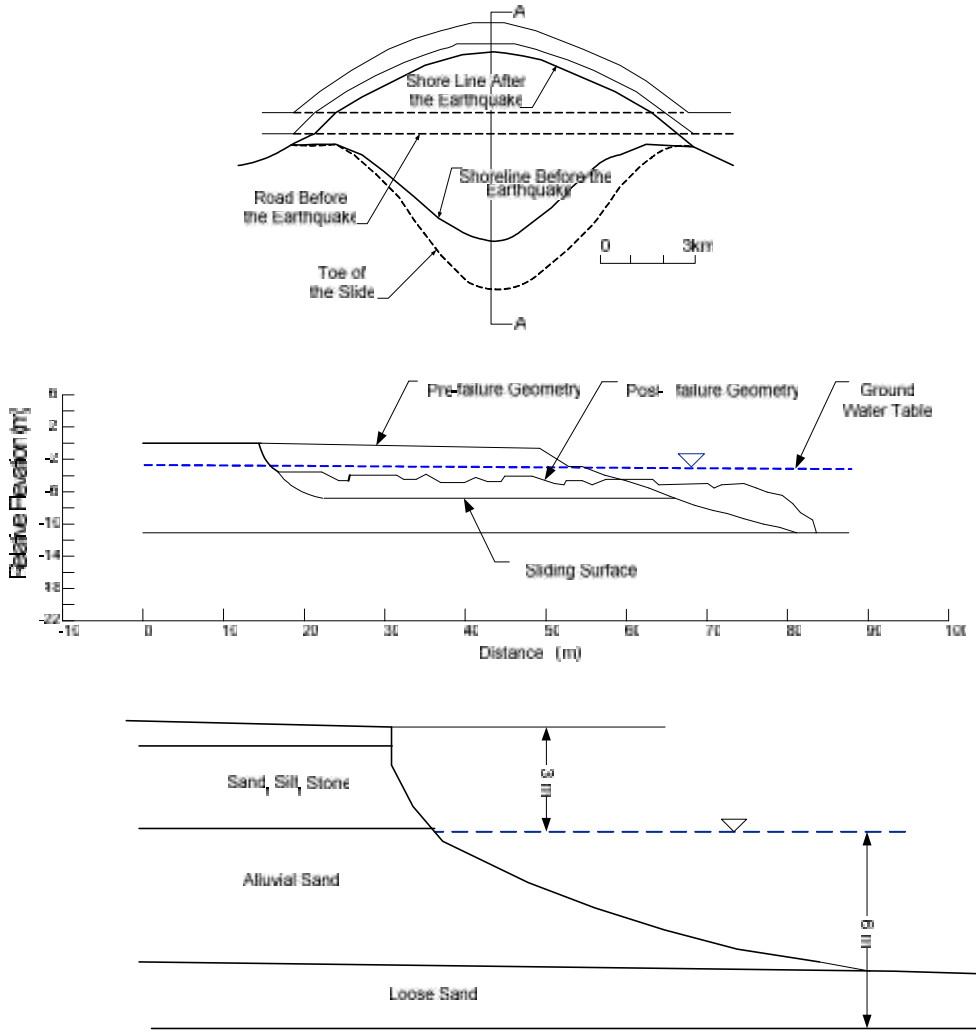

Figure A.17 Coastal slide at Kamenari showing plan view, the cross-section at A-A, and a more detailed soil profile at the failure site (reproduced from Ishihara 2005)

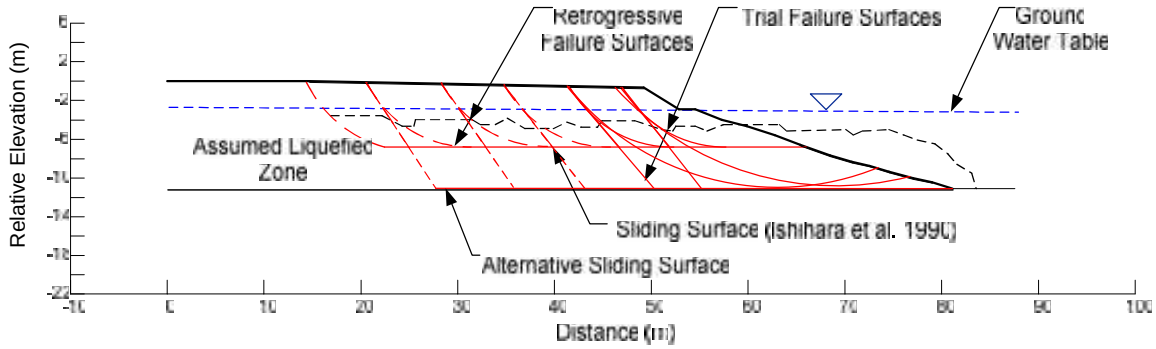

Figure A.18 Pre-and post-failure geometries of Kamenari landslide with failure and trial failure surfaces

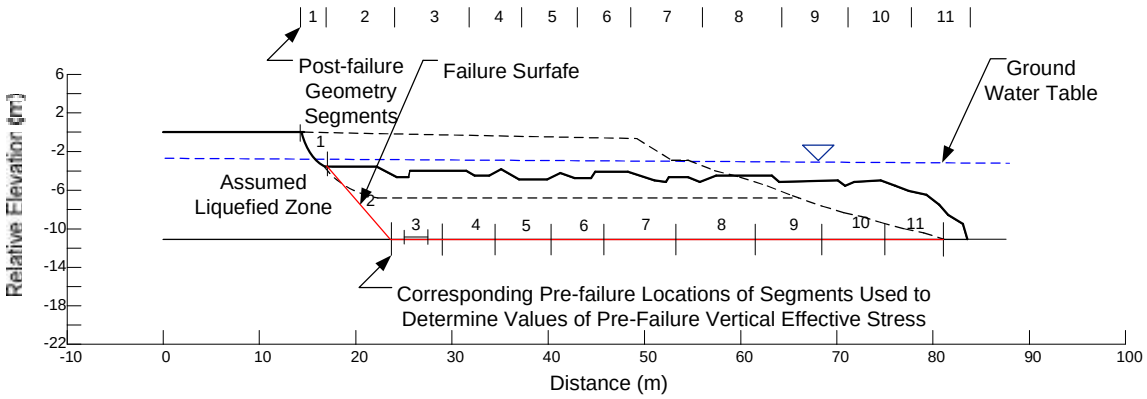

Figure A.19 Pre-and post-failure geometries of Kamenari landslide with final failure surface

(a)

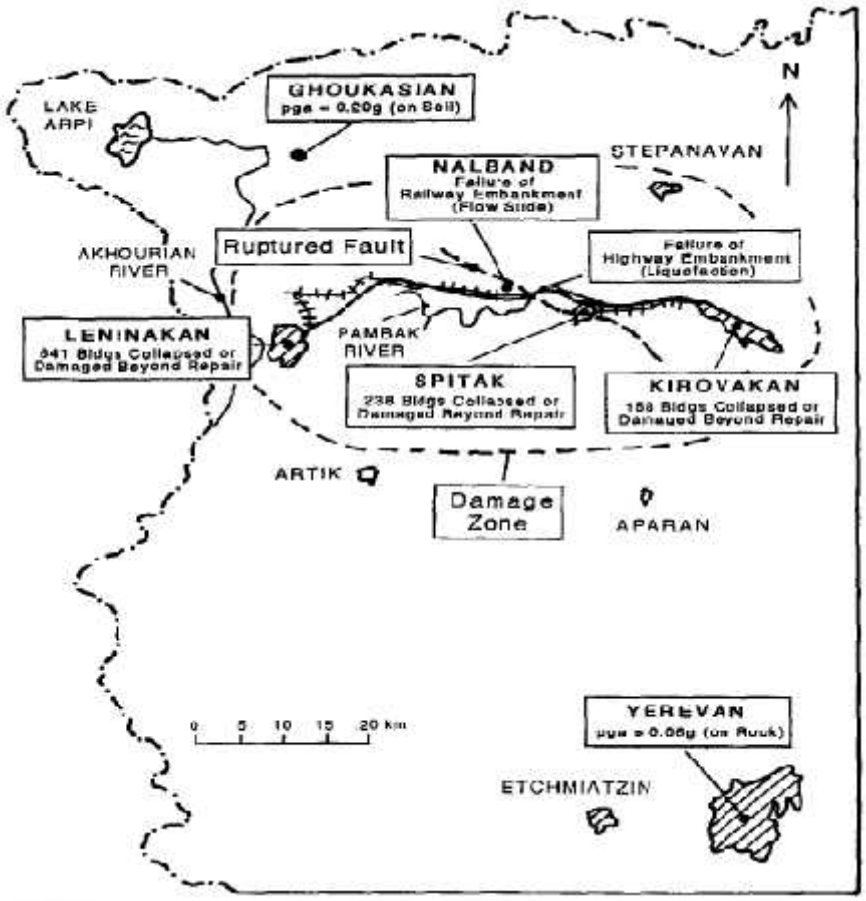

(b)

Figure A.20 (a) Map of damaged region with sites analyzed by Yegian et al. (1994); and (b) photo of damaged embankment (from Yegian et al. 1994e)

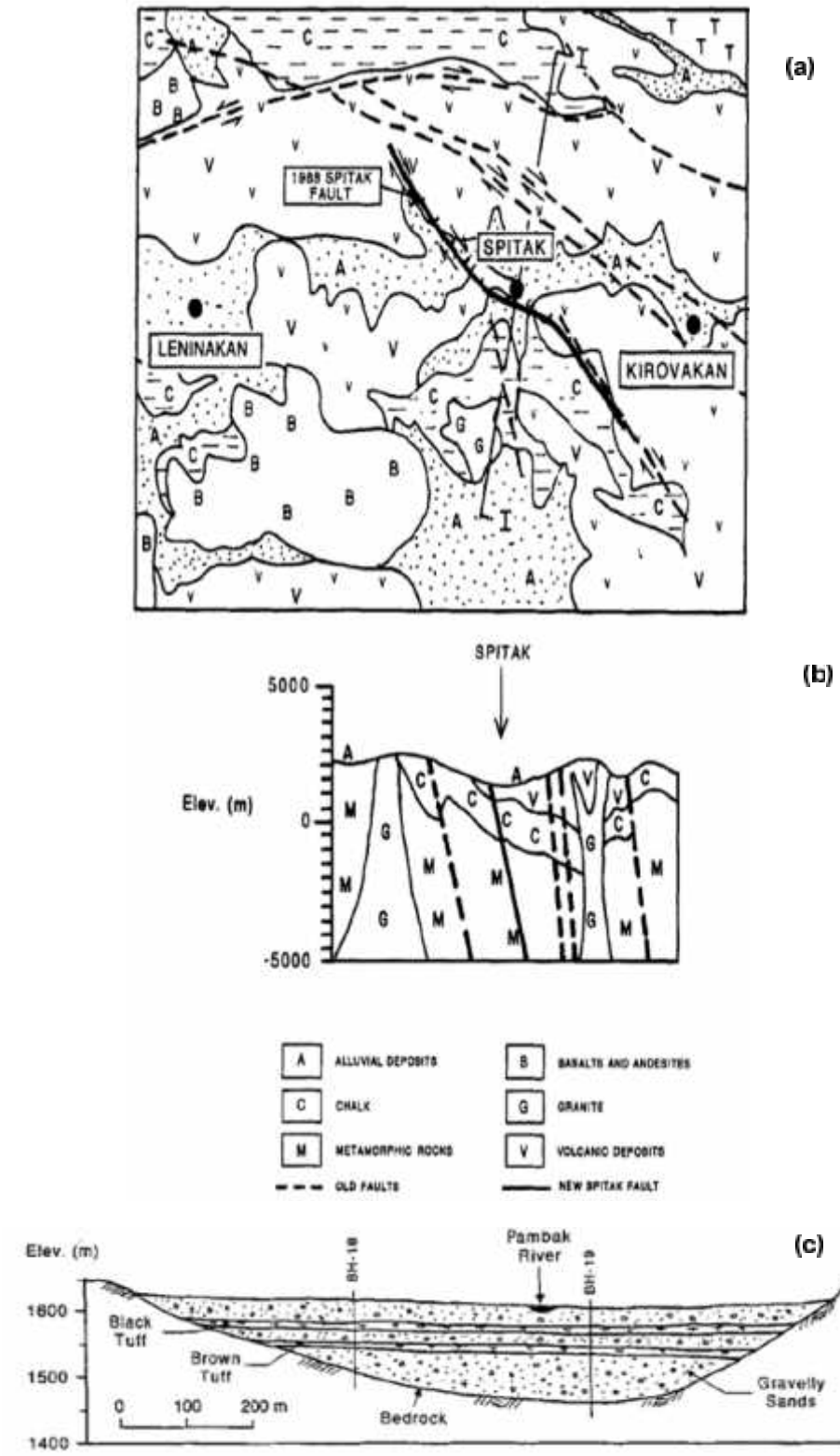

Figure A.21(a) Geological map of affected region; (b) geological cross-section of Spitak; and (c) cross-section of Pambak River Valley near the failed Spitak embankment (from Yegian et al. 1994e)

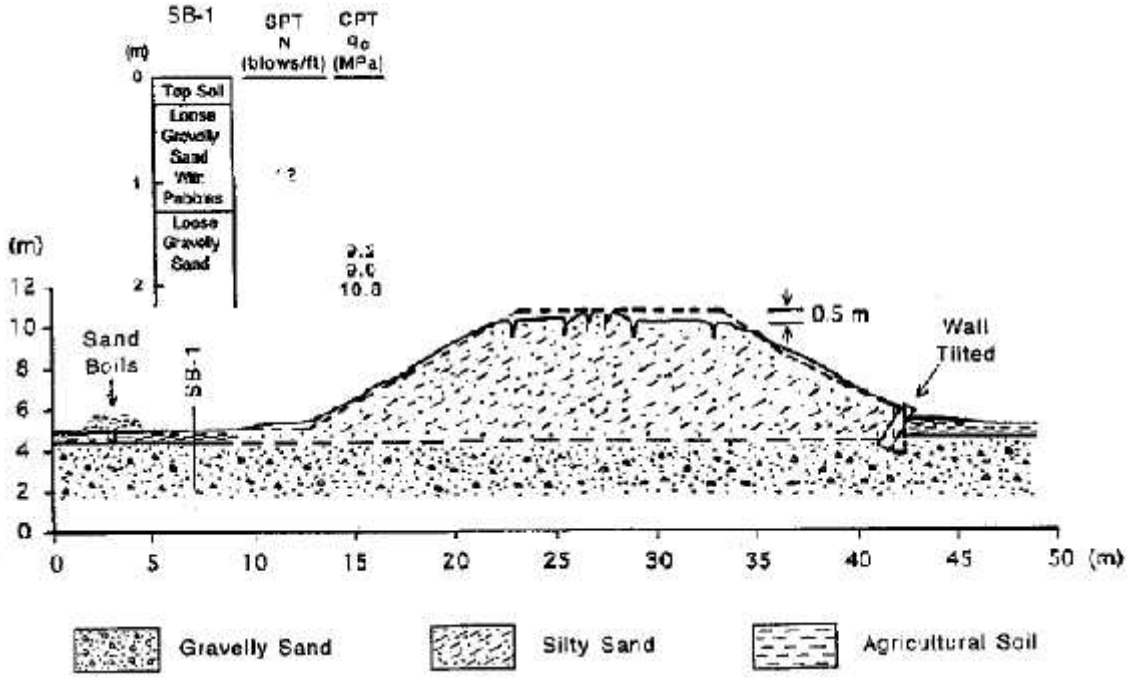

Figure A.22 Spitak highway embankment cross-section before and after failure (from Yegian et al. 1994e)

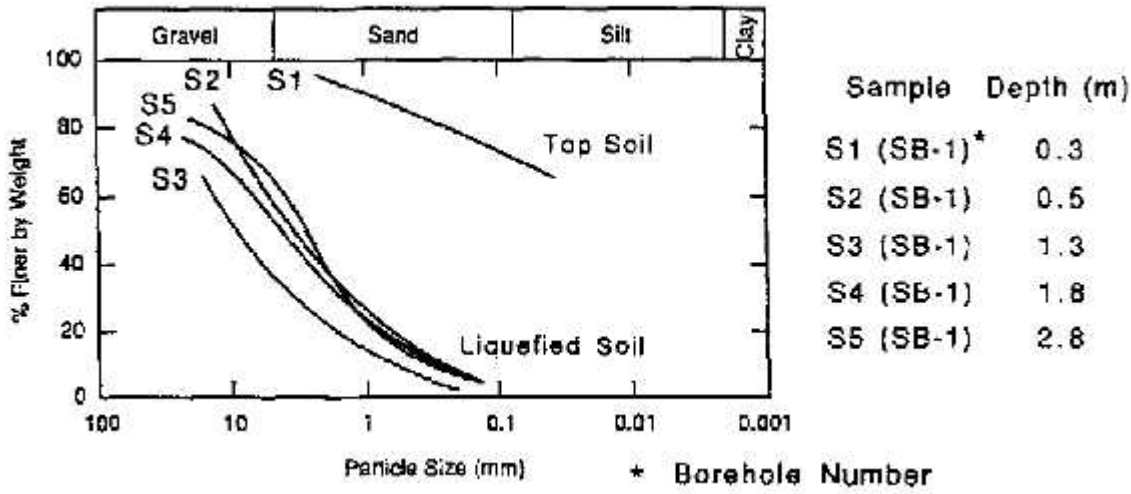

Figure A.23 Grain-size distribution curves of soil samples from the Spitak embankment (from Yegian et al. 1994e)

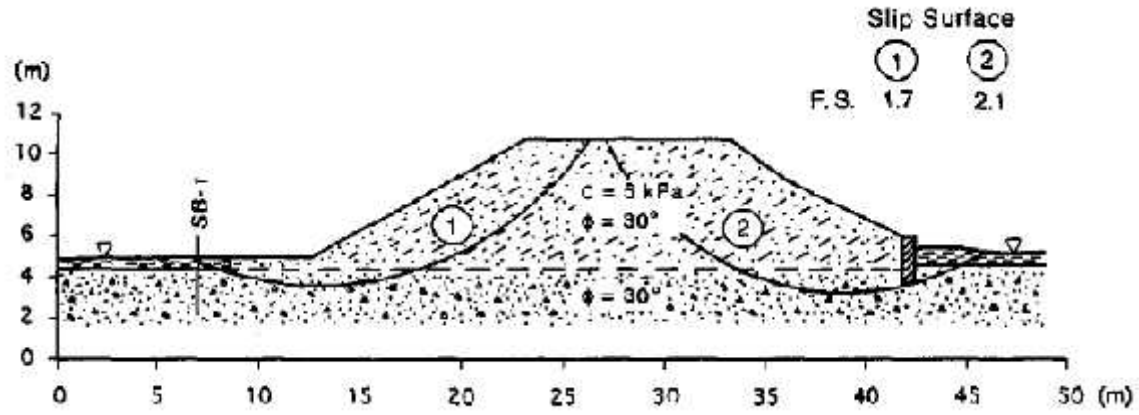

Figure A.24 Pre-failure geometry of Spitak highway embankment with trial failure surfaces by Yegian (1994e) (from Yegian 1994e)

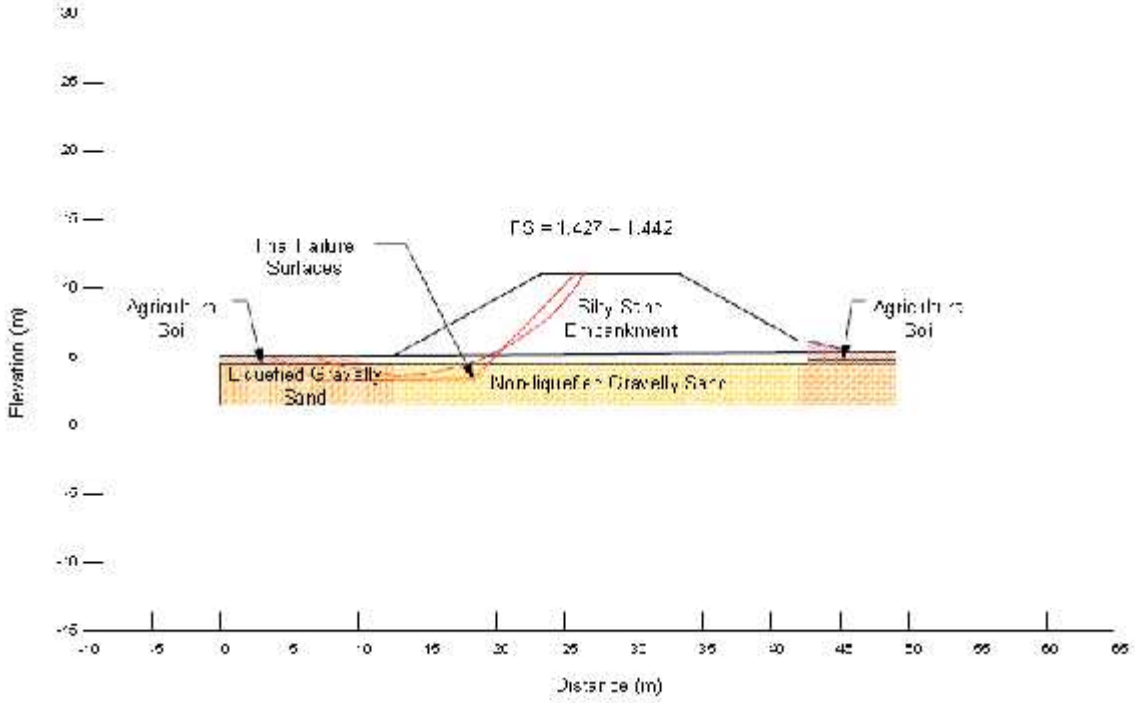

Figure A.25 Static slope stability analysis of slide 1 to check FS considering liquefaction of the toe only

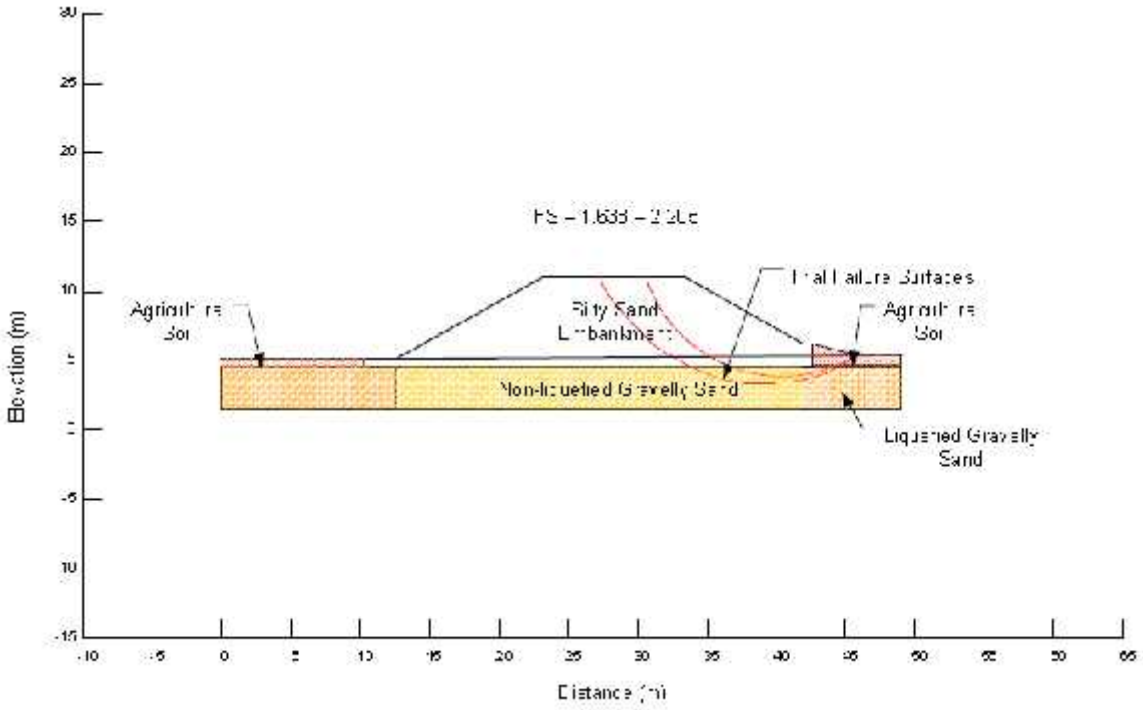

Figure A.26 Static slope stability analysis of slide 2 to check FS considering liquefaction of the toe only

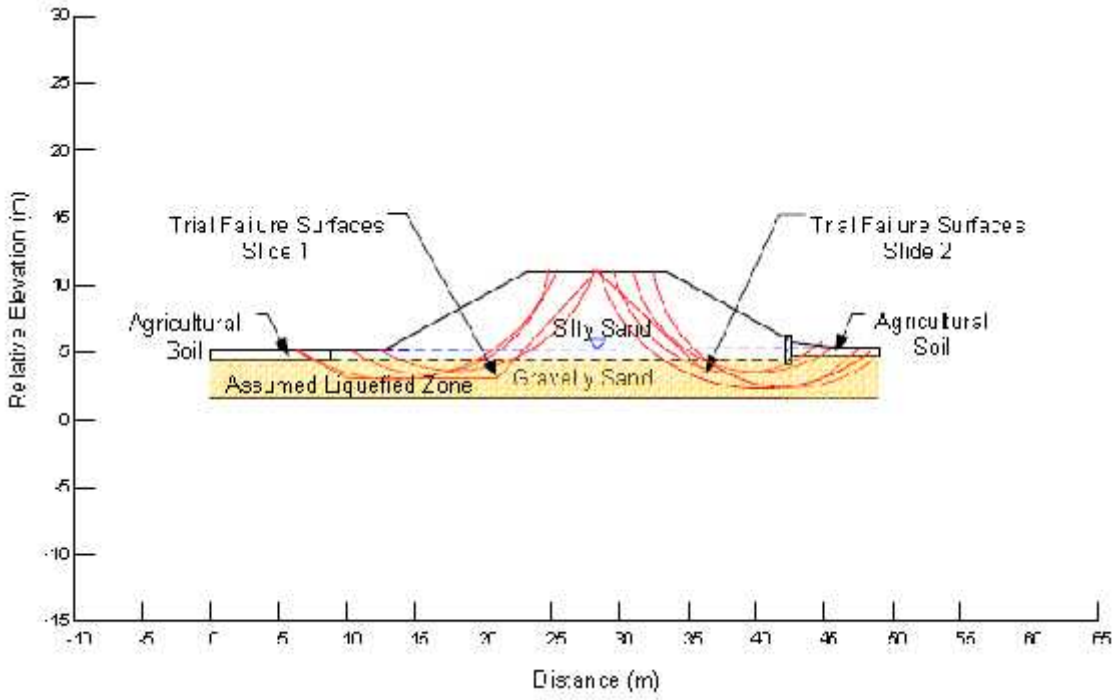

Figure A.27 Pre-failure geometry of Spitak highway embankment reproduced with trial failure surfaces for Slide 1 and Slide 2

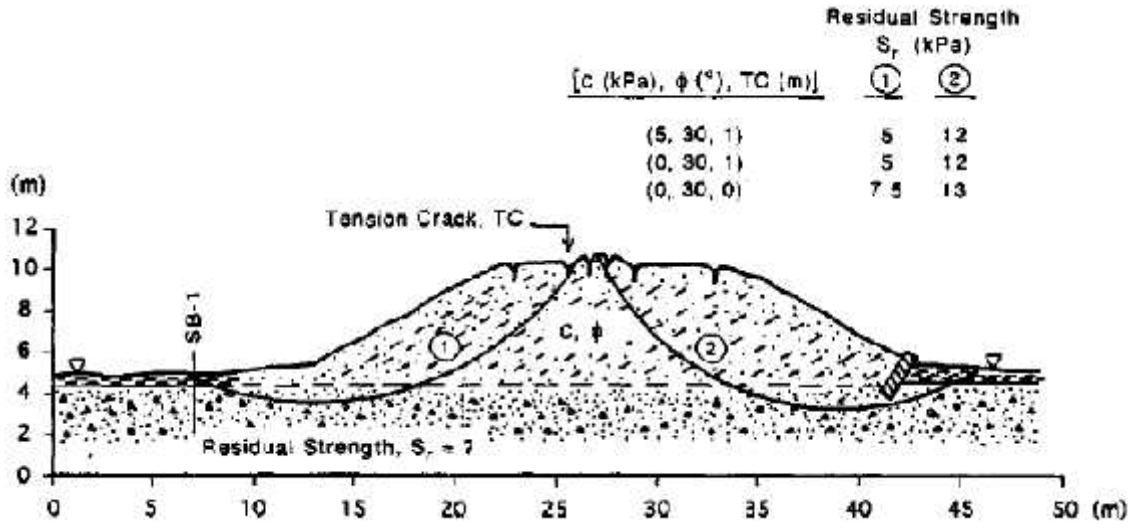

Figure A.28 Post-failure geometry of Spitak highway embankment with trial failure surfaces by Yegian (1994e) (from Yegian 1994e)

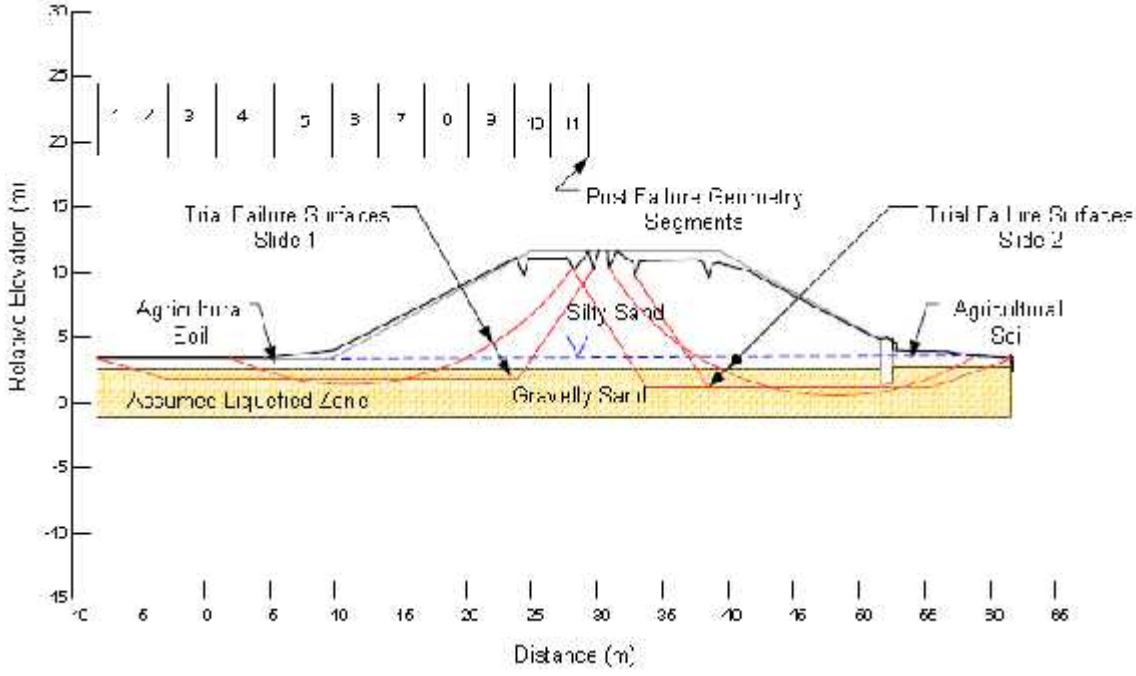

Figure A.29 Post-failure geometry of Spitak highway embankment reproduced with trial failure surfaces and liquefied shear strength ratio analysis for Slide 1

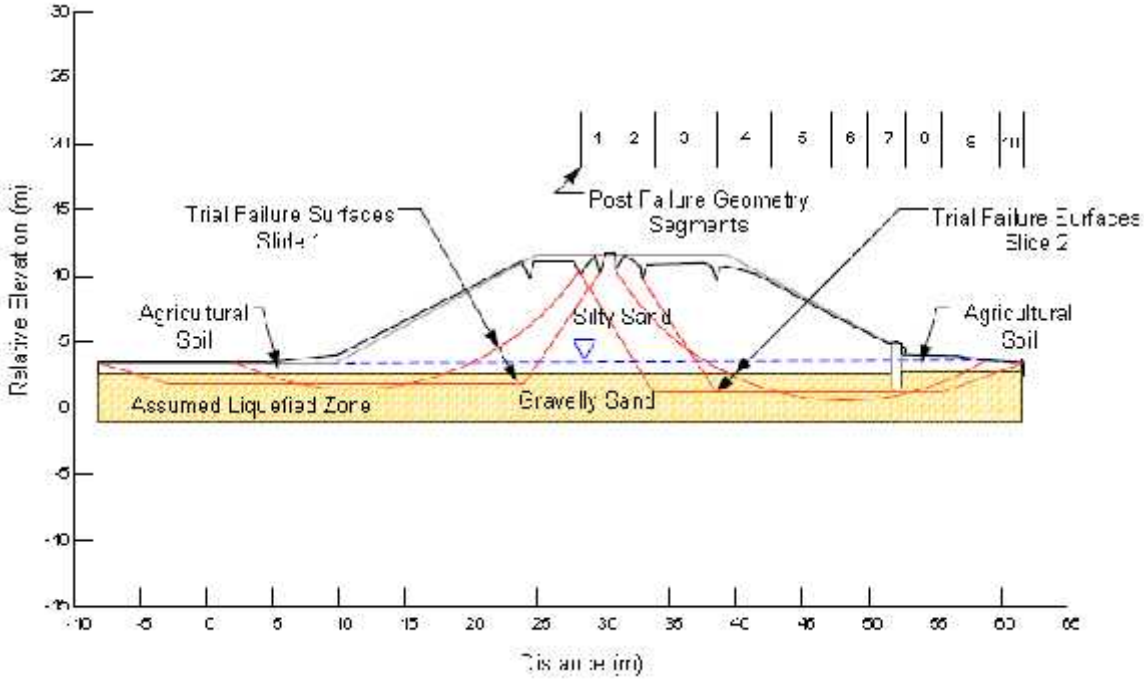

Figure A.30 Post-failure geometry of Spitak highway embankment reproduced with trial failure surfaces and liquefied shear strength ratio analysis for Slide 2

Figure A.31 Location of the epicenter of January 23, 1989 Tajik earthquake (from Ishihara et al. 1989)

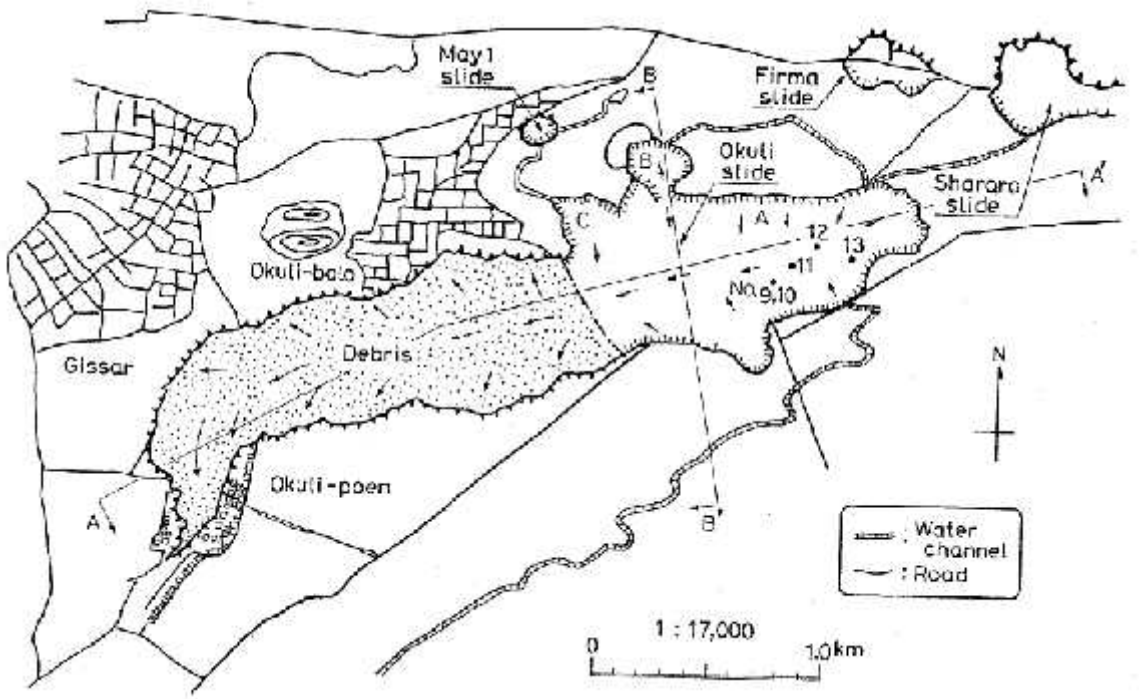

Figure A.32 Plan view of the area in Gissar affected by landslides (from Ishihara et al. 1990)

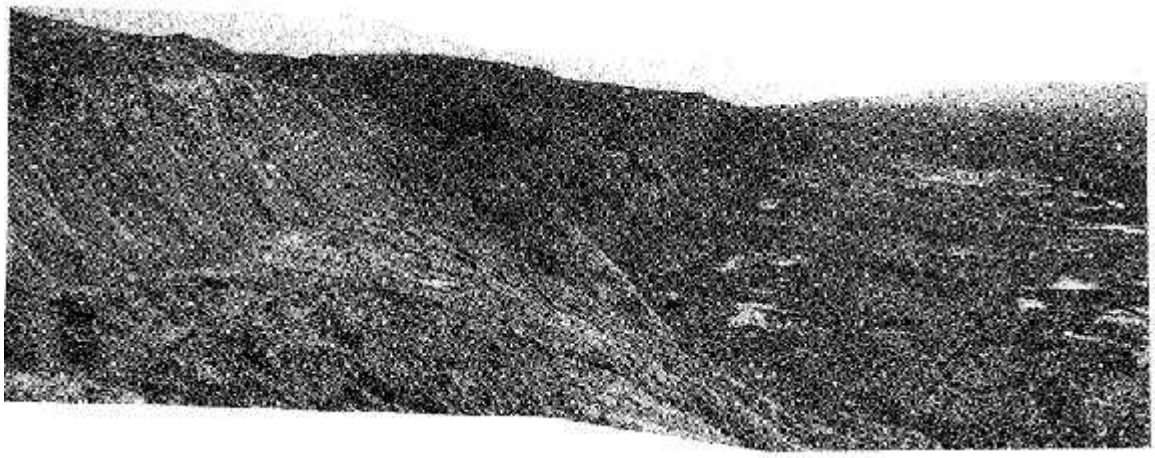

Figure A.33 A view looking eastward from the northern hill at the mud flow resulting from the Okuli landslide (from Ishihara et al. 1990)

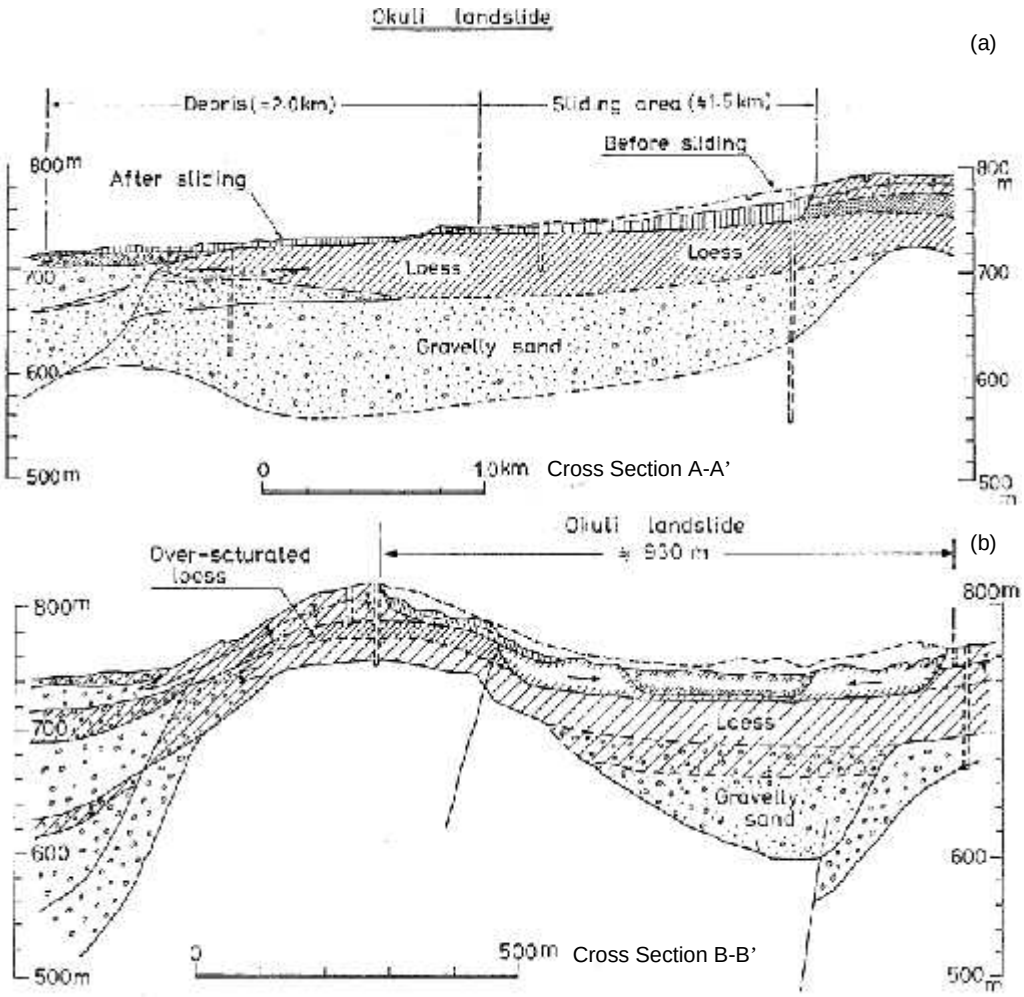

Figure A.34 Geological section of Okuli landslide (from Ishihara et al. 1990). Locations of cross-sections are shown in Figure 2.

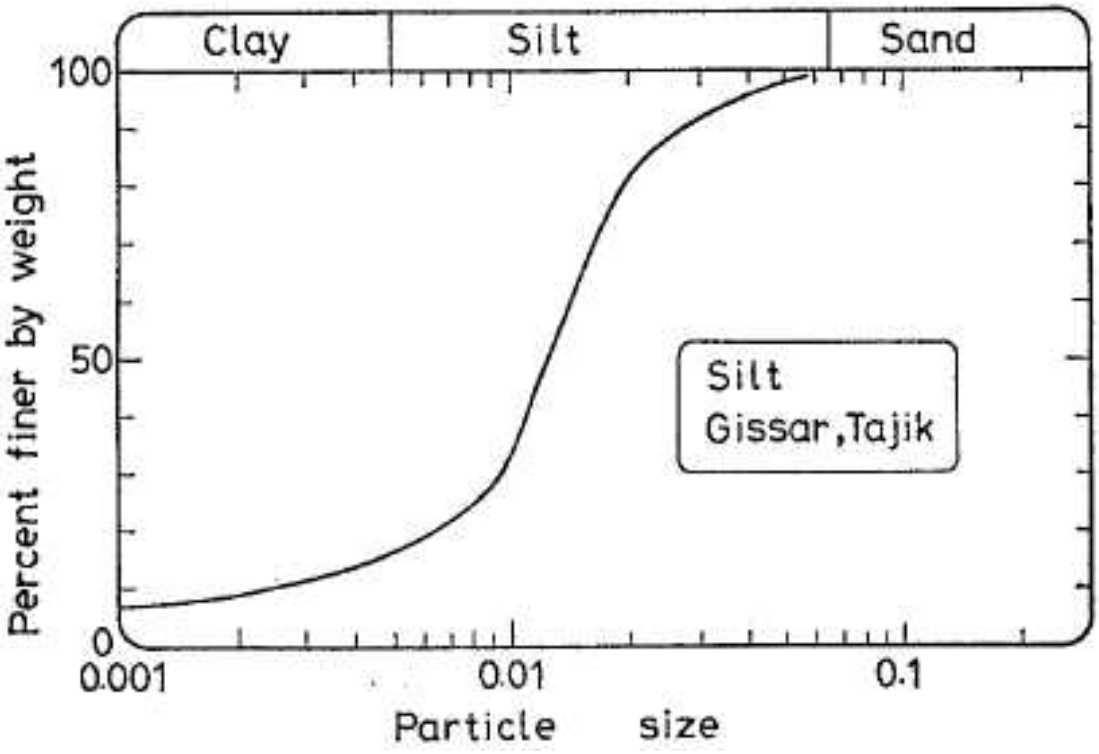

Figure A.35 Grain size distribution of the loess soil involved in Okuli and other landslides (from Ishihara et al. 1990)

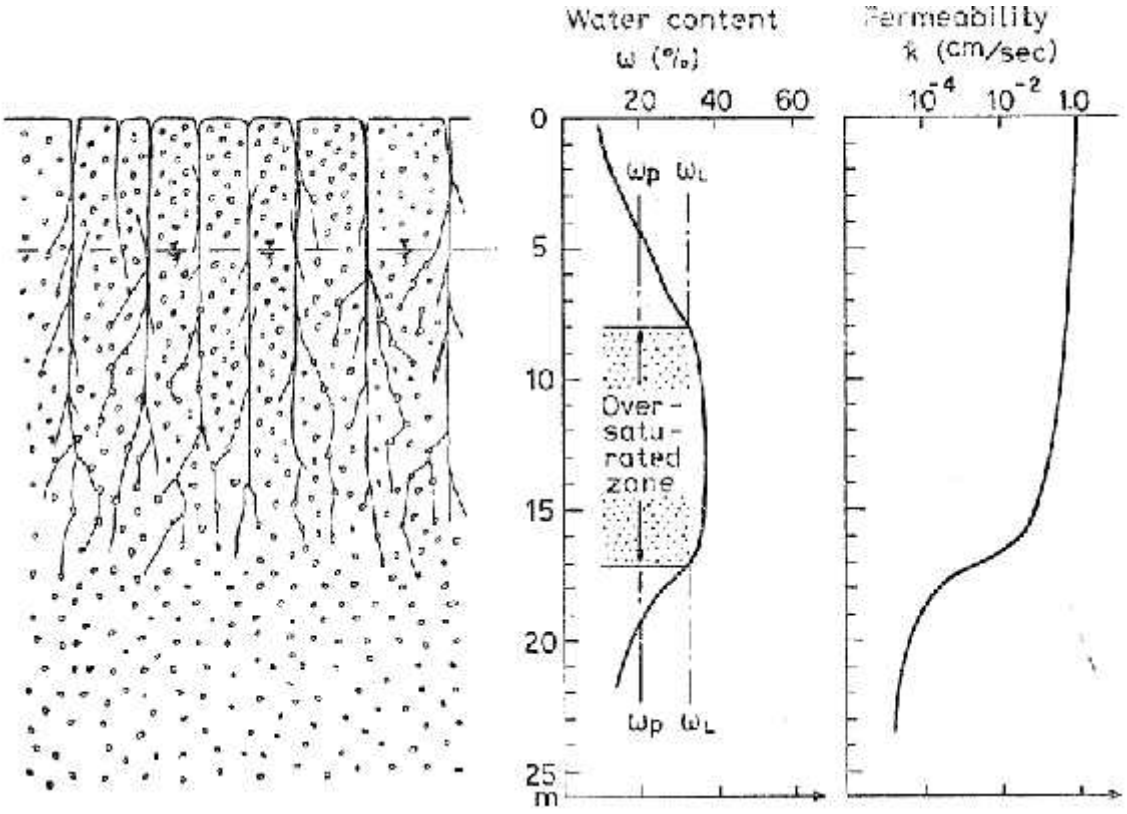

Figure A.36 Schematic diagram illustrating mechanism of saturation of loess from 7 m to 17 m below grade (from Ishihara et al. 1990)

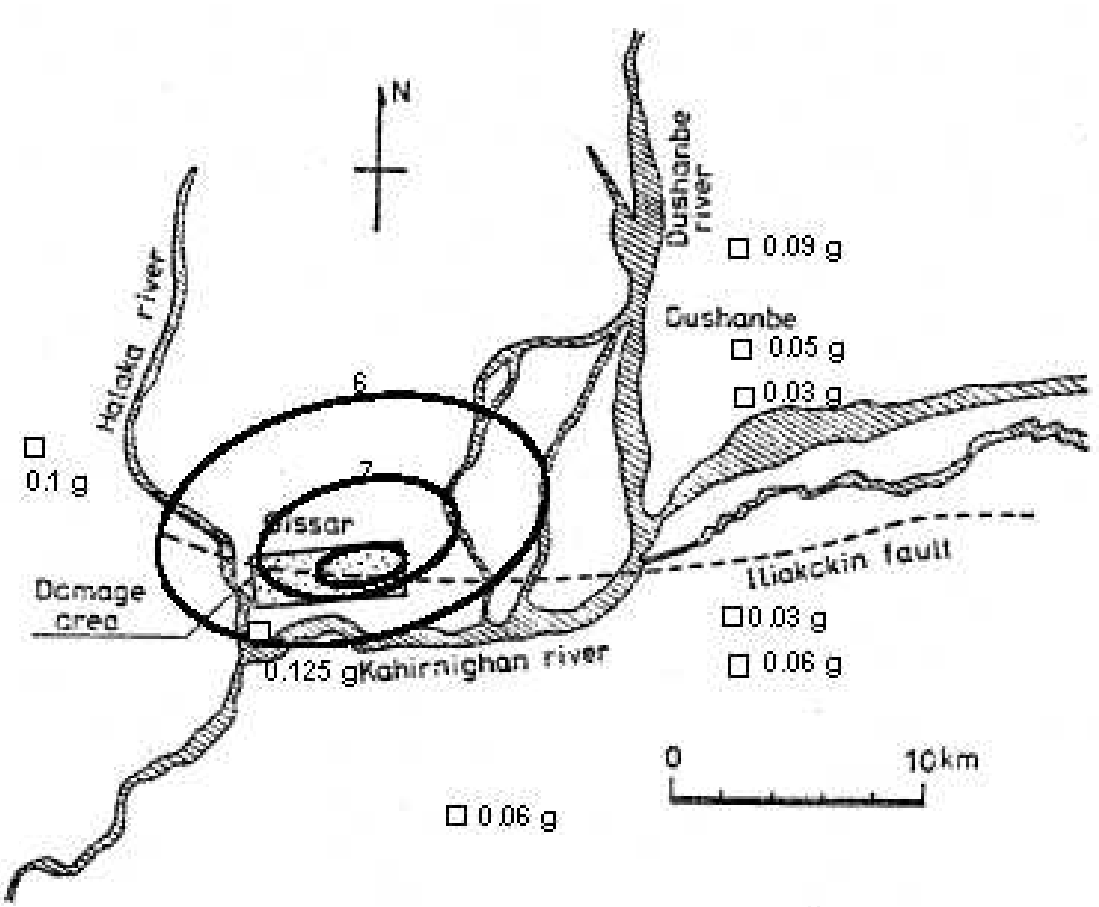

Figure A.37 Map of the Dushanbe, Tajikistan vicinity and modified Mercalli intensity contours for 1989 Tajik earthquake (from Olson 2001, modified from Ishihara et al. 1990)

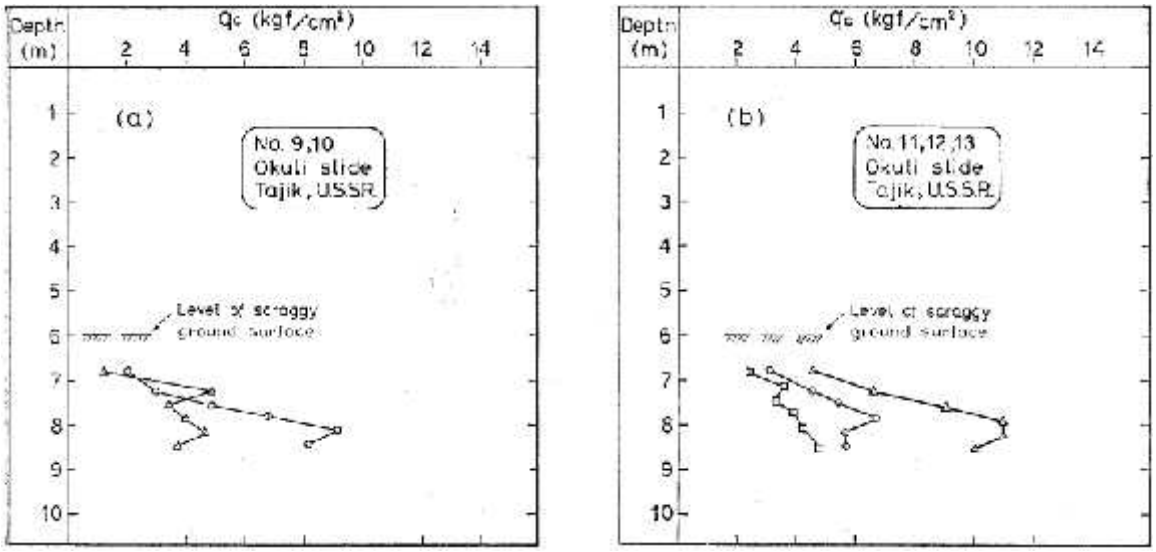

Figure A.38 Cone penetration test results at the Okuli slide area (from Ishihara et al. 1990)

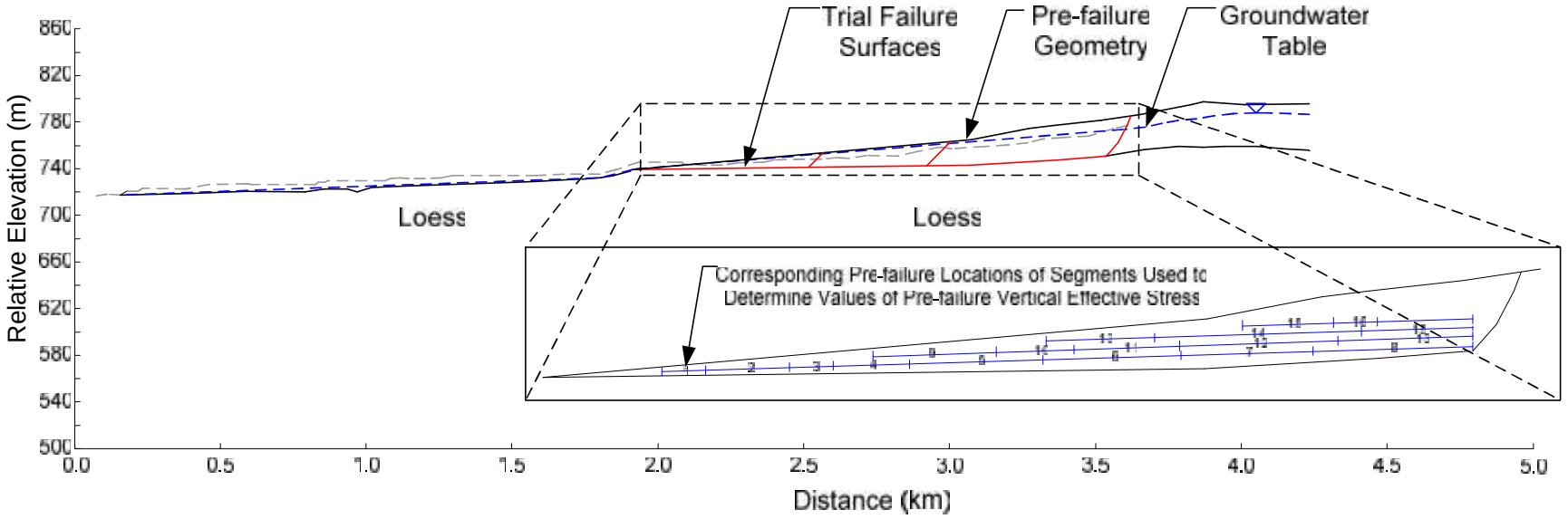

Figure A.39 Pre-failure geometry of Okuli landslide with trial failure surfaces and post-failure segments arranged in the liquefied zone

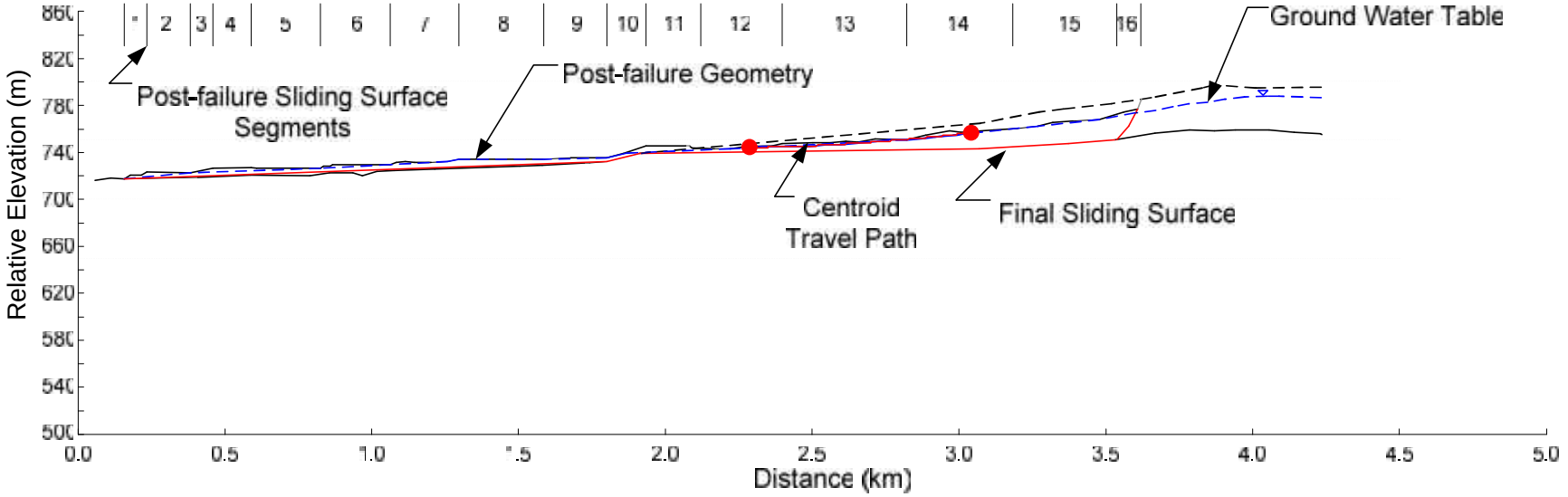

Figure A.40 Post-failure geometry of the Okuli landslide with final failure surface, post-failure segments, and pre- and post-failure centroid positions

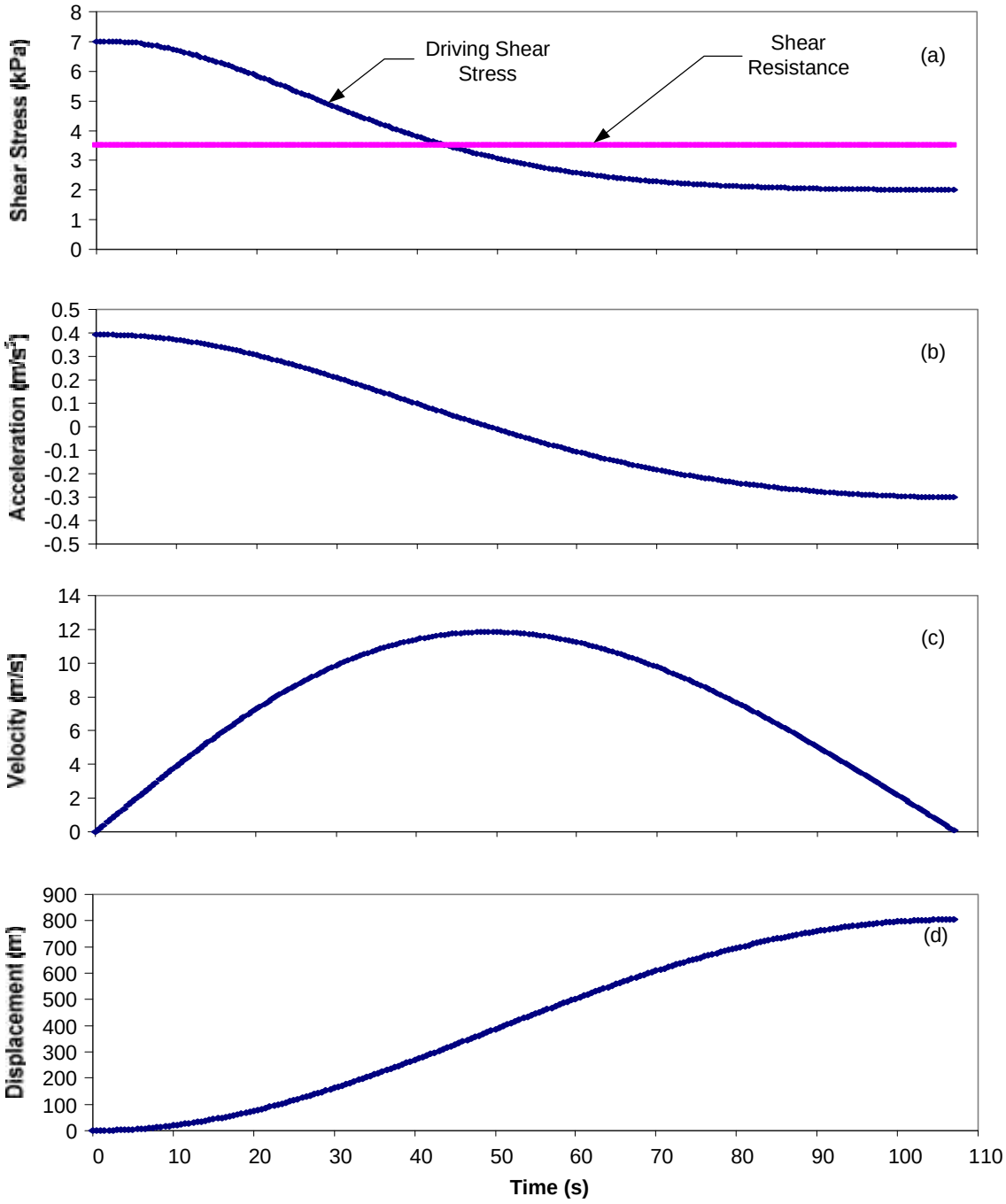

Figure A.41 Kinetics analysis for Okuli landslide

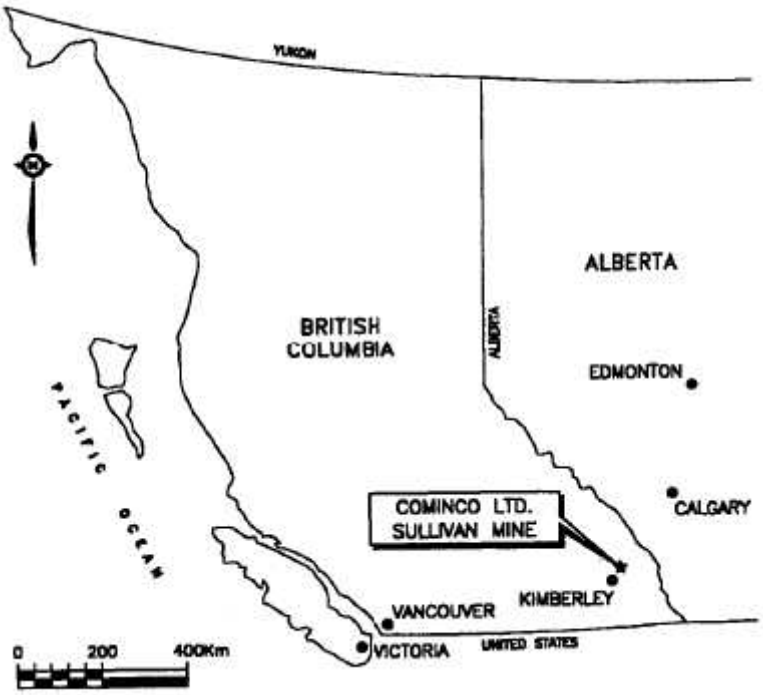

Figure A.42 Location map of Sullivan Tailings Dam (from Davies et al. 1998)

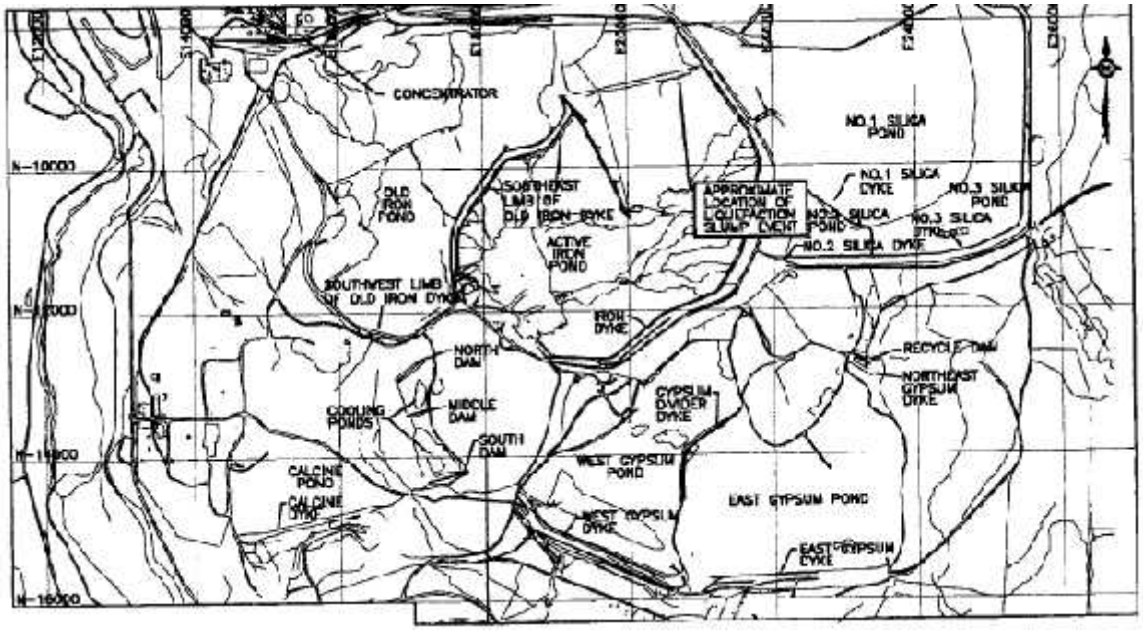

Figure A.43 General site layout with approximate location of liquefaction failure (from Davies et al. 1998)

Figure A.44 Aerial photograph of Sullivan dam failed section (from McLeod et al. 2003)

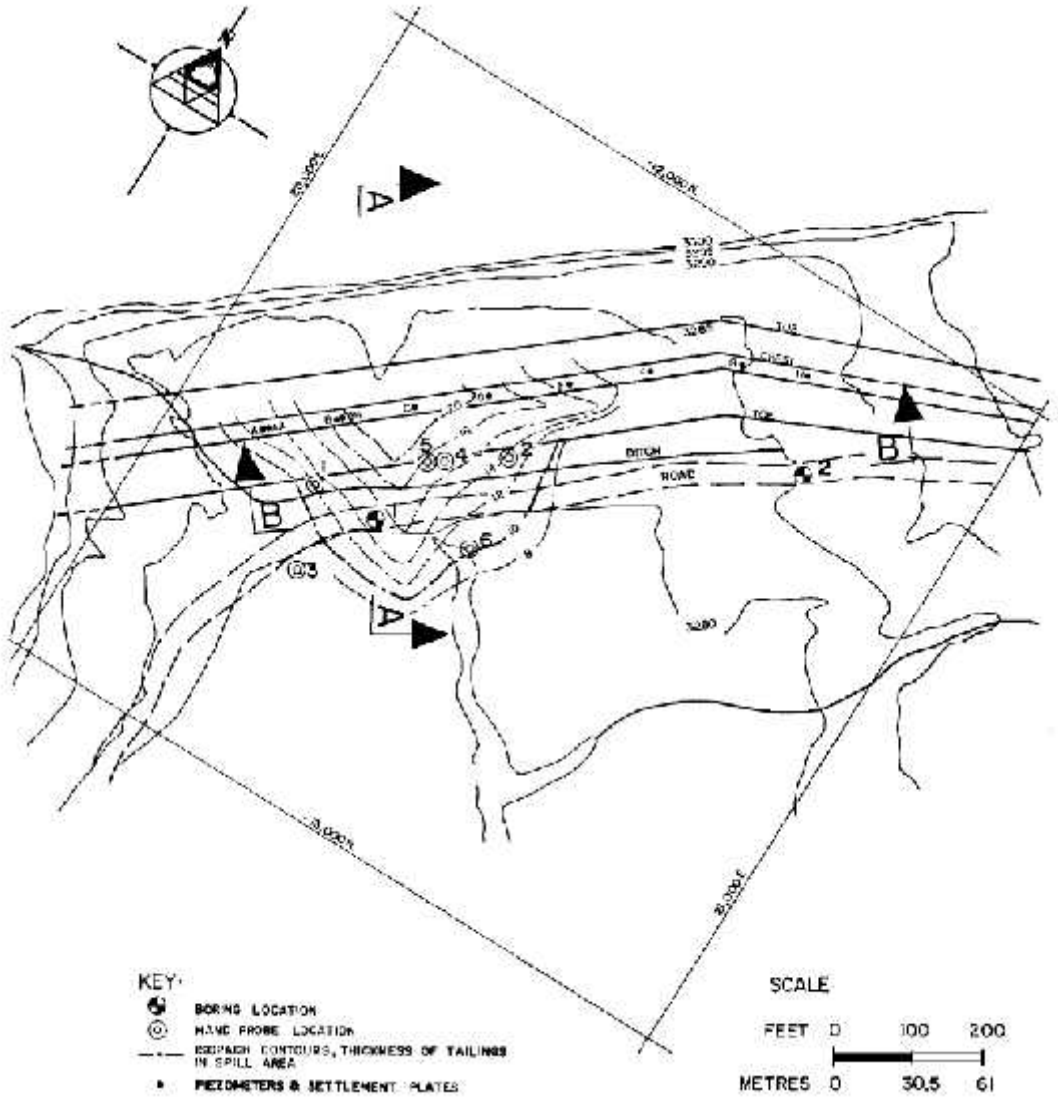

Figure A.45 Elevation contours of the failed tailings dam section, including thickness of the tailings in the failure zone (from Robinson 1977)

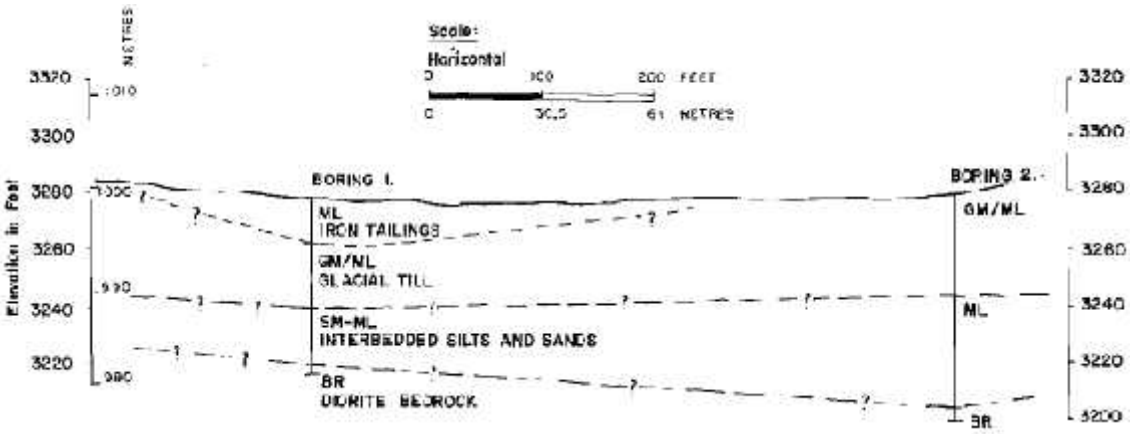

Figure A.46 Profile section B - B (from Robinson 1977)

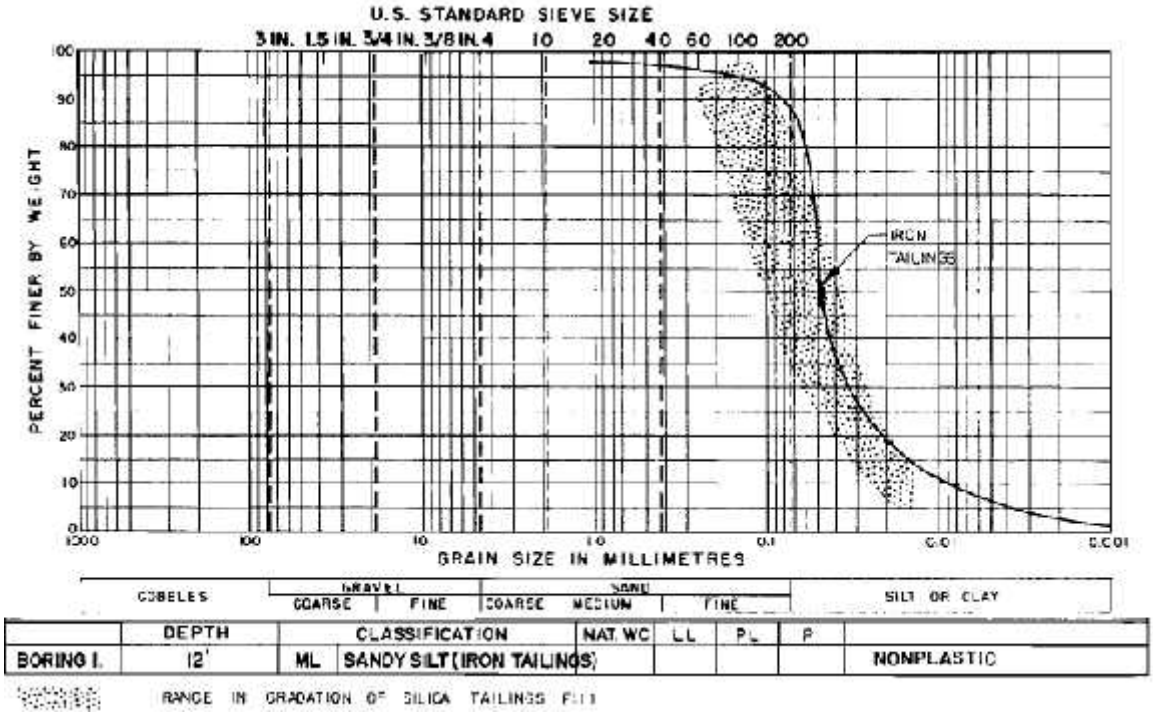

Figure A.47 Gradation curve of iron tailings (from Robinson 1977)

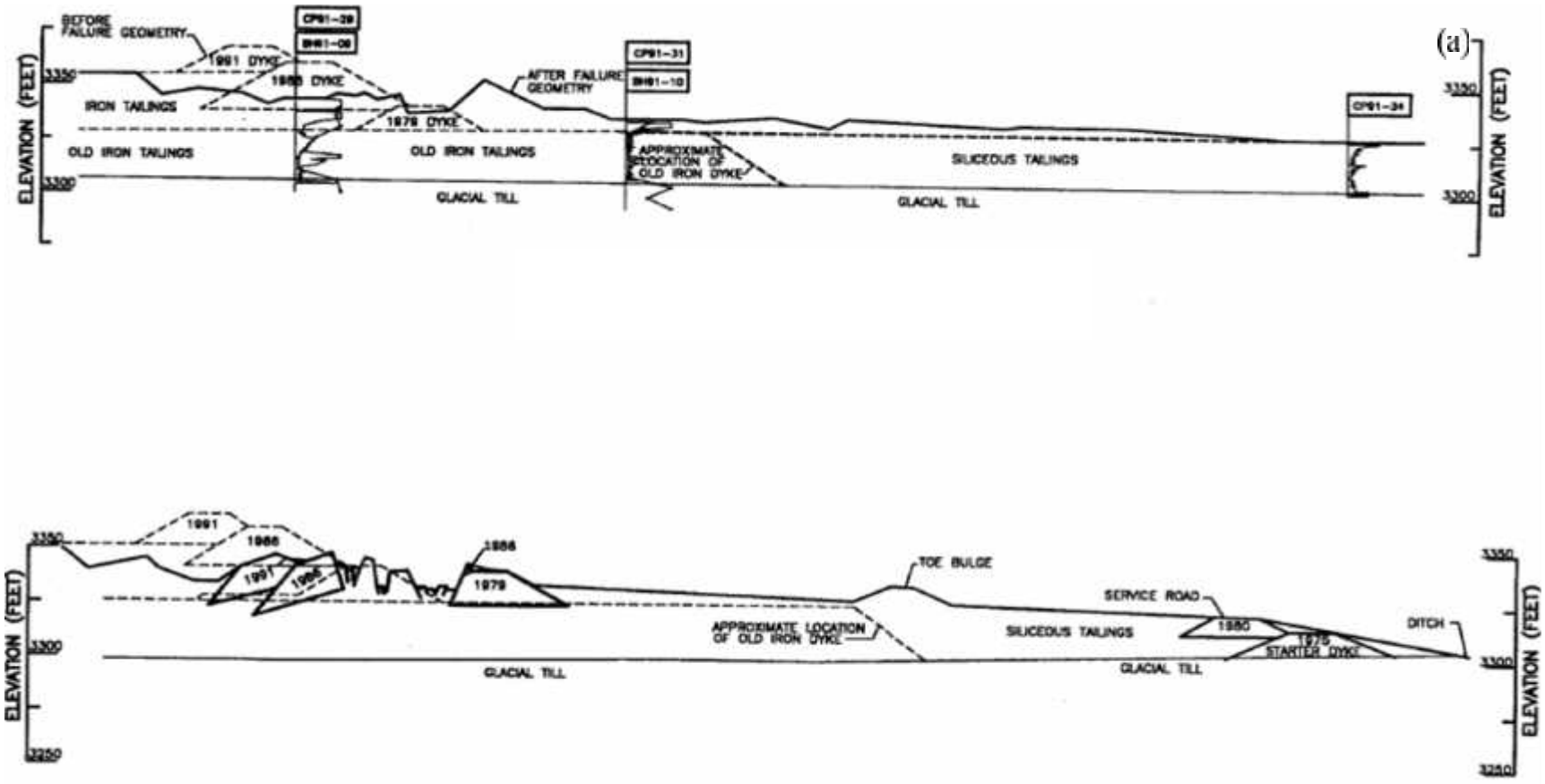

Figure A.48 Cross section through the failure zone and respective location of dykes in post-failure geometry interpreted by (a) Davies et al. (1998), and (b) Jefferies and Been (2006)

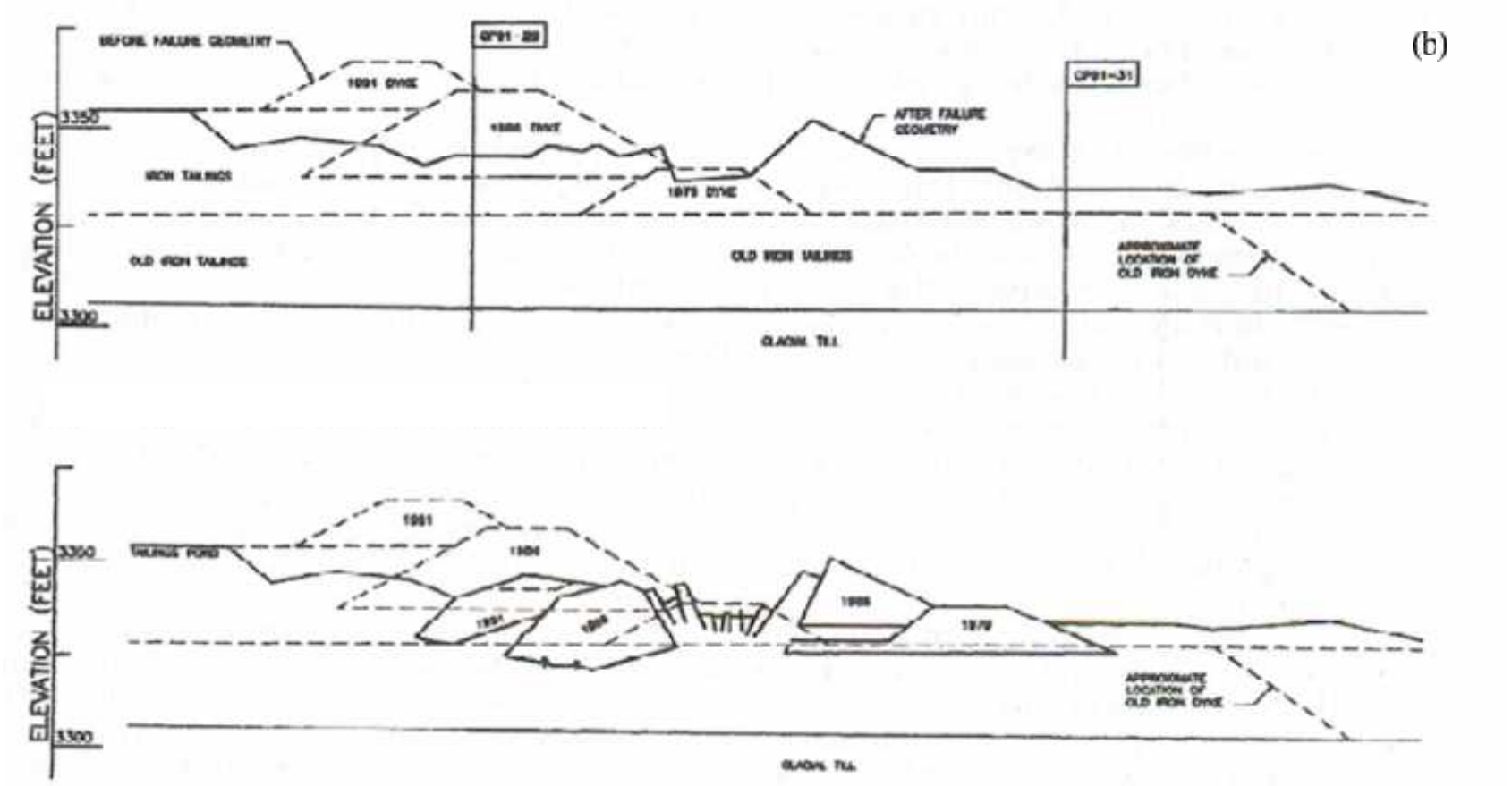

Figure A.48 Continued

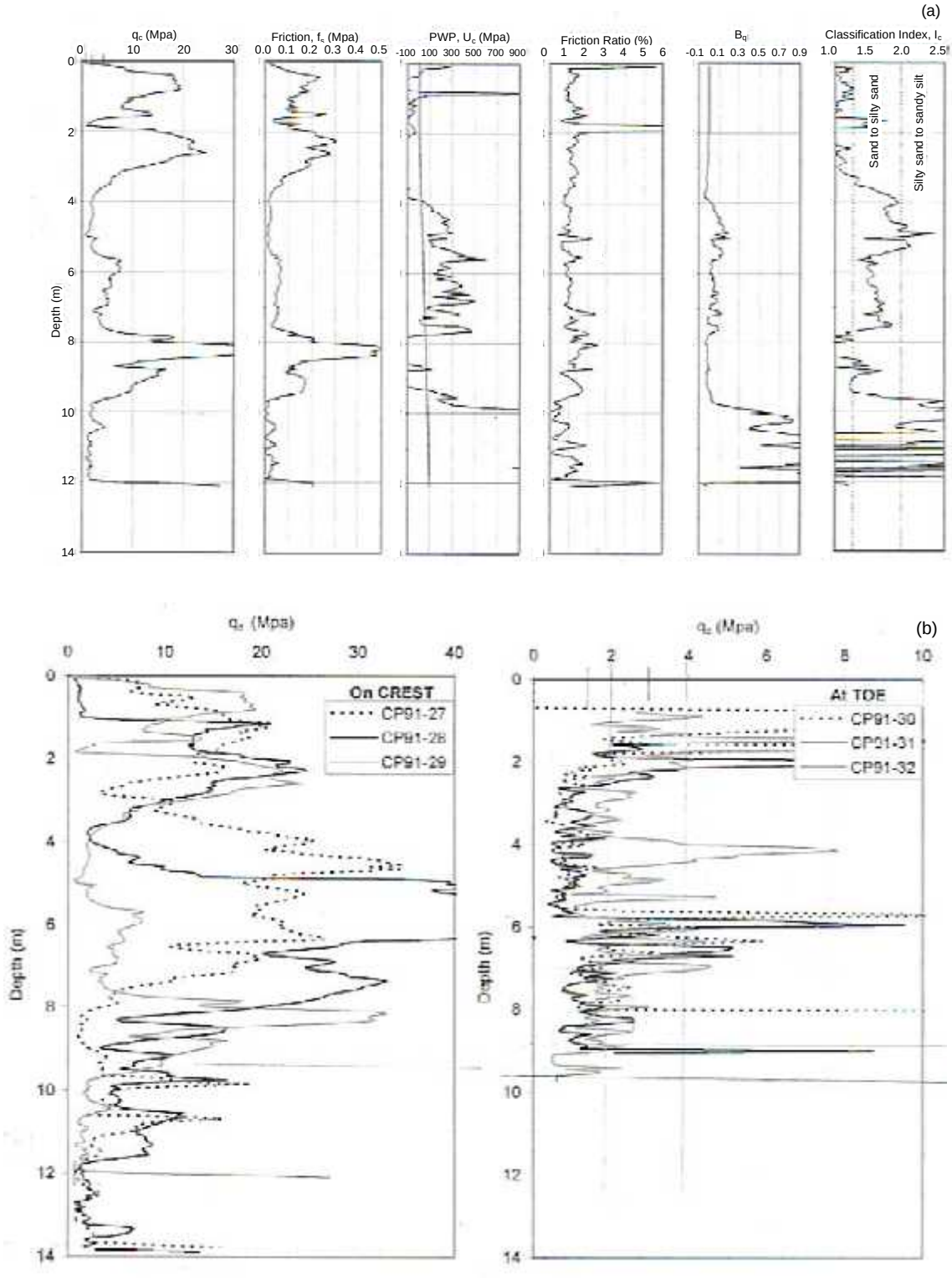

Figure A.49 CPT soundings through Sullivan Dyke failure. (a) Example of measured CPT data (CP91-29, through centerline of failed mass); (b) comparison of six CPT soundings from failure area (from Jefferies and Been 2006)

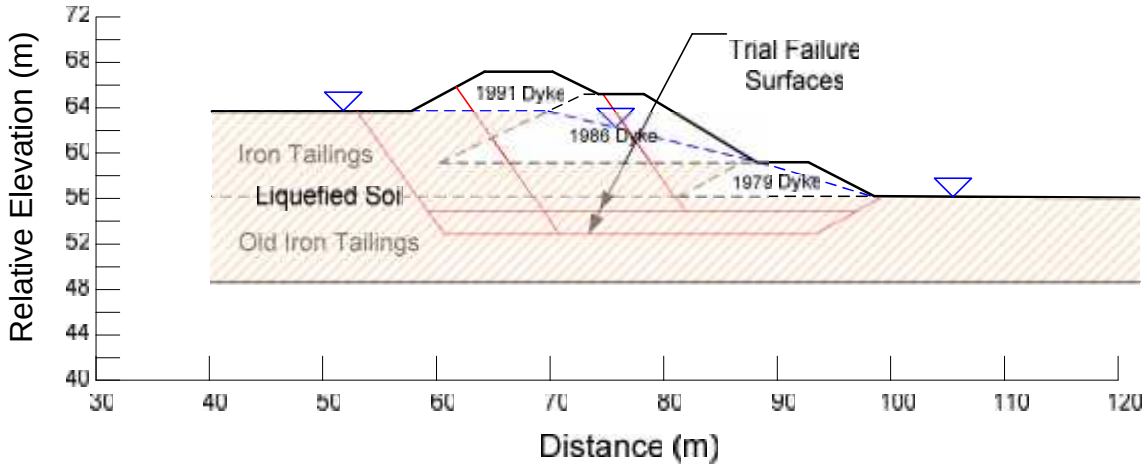

Figure A.50 Pre-failure geometry reproduced with trial failure surfaces and an assumed phreatic surface

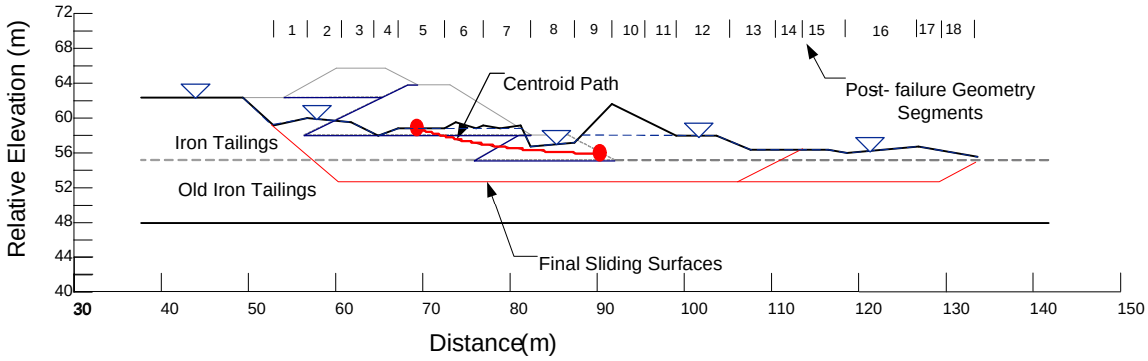

Figure A.51 Post-failure geometry reproduced with trial failure surface and an assumed phreatic surface

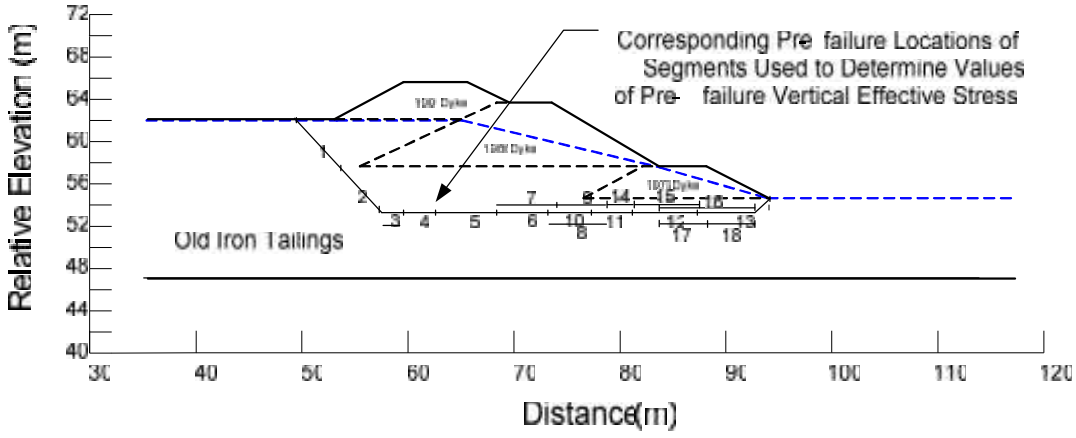

Figure A.52 Segments from post-failure geometry are adjusted in pre-failure geometry to determine values of pre-failure vertical effective stress

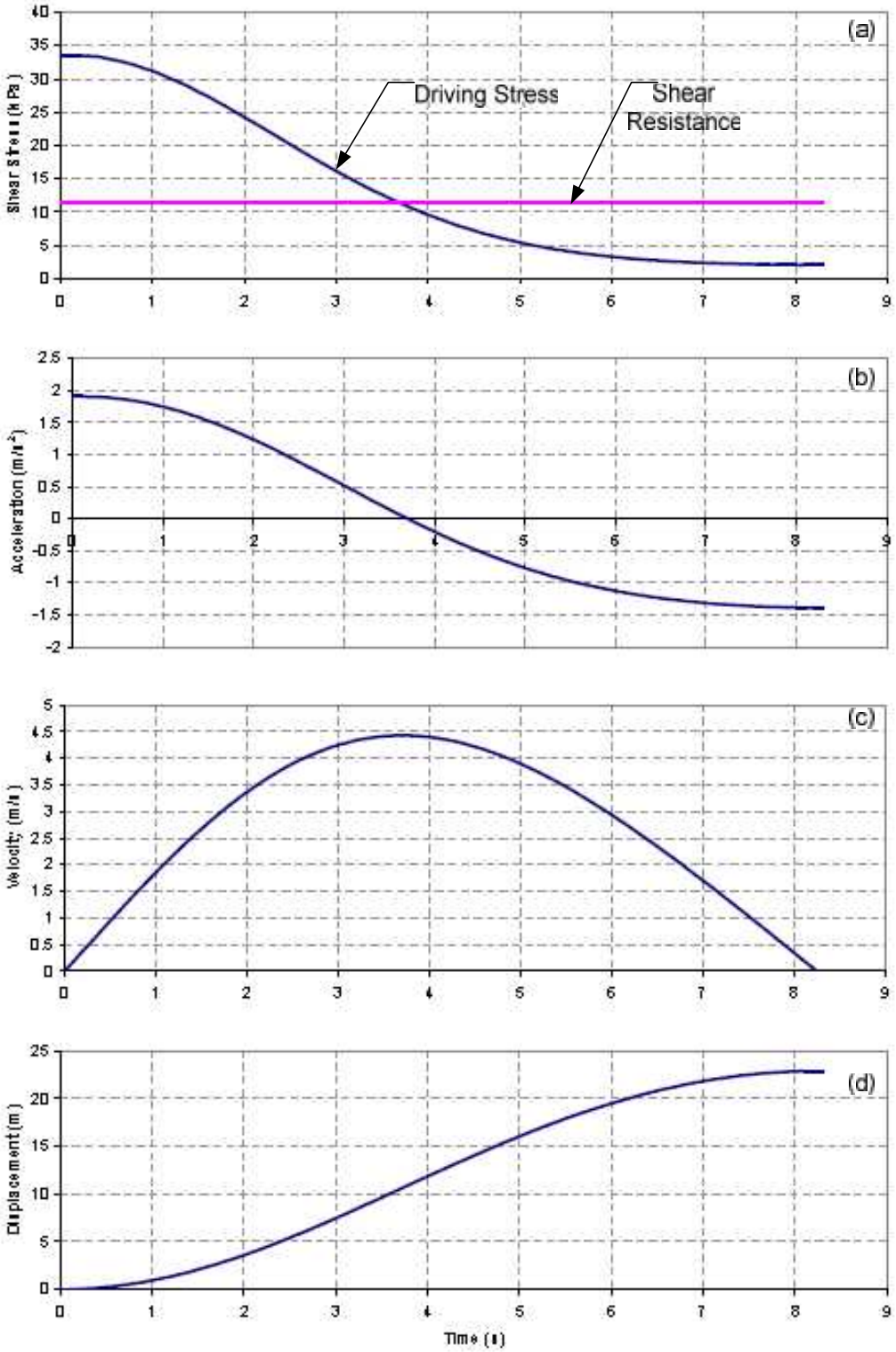

Figure A.53 Kinetics analysis results for Sullivan Tailings Dam

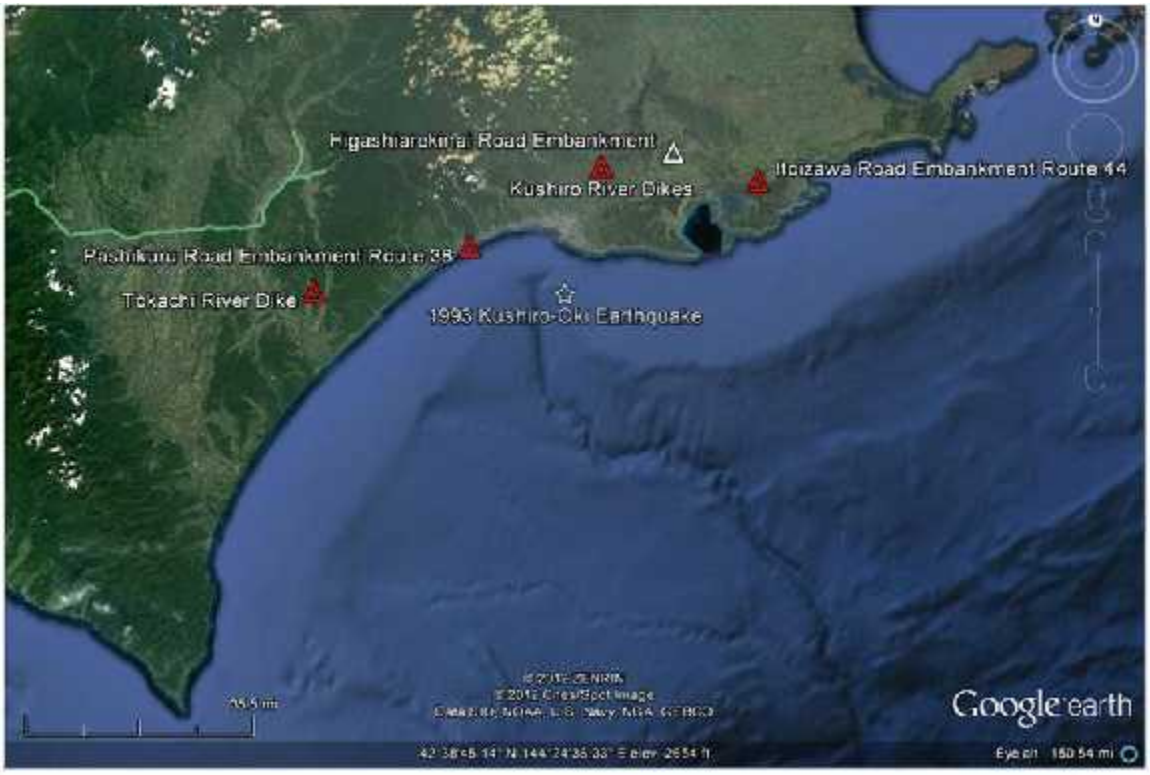

Figure A.54 Location map of river dikes and highway embankments that failed during the 1993 Kushiro-Oki earthquake analyzed in this study

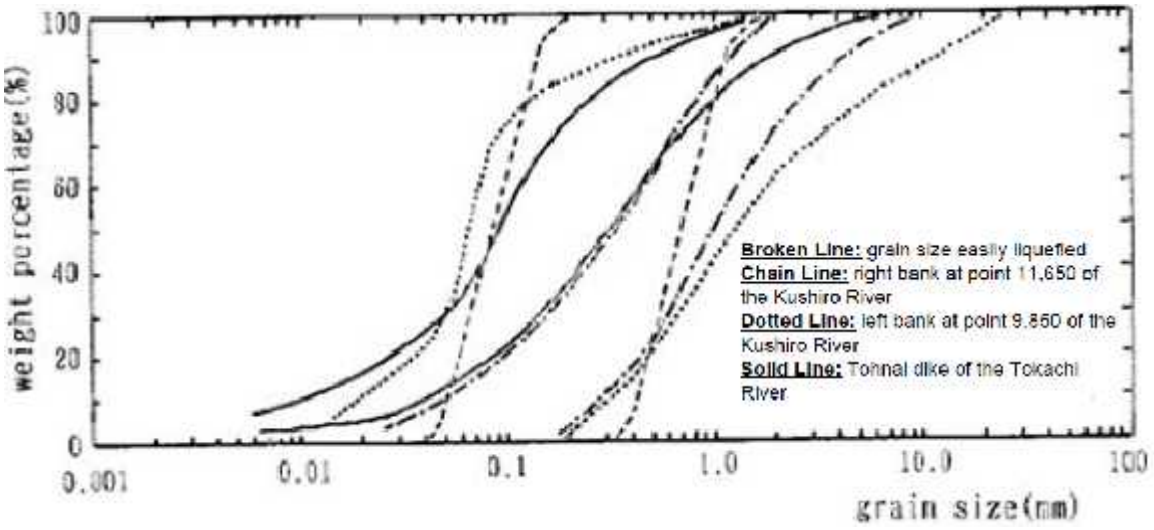

Figure A.55 Grain size distributions of fill materials used for river dikes constructed along the Kushiro and Tohnai Rivers (from Sasaki et al. 1993)

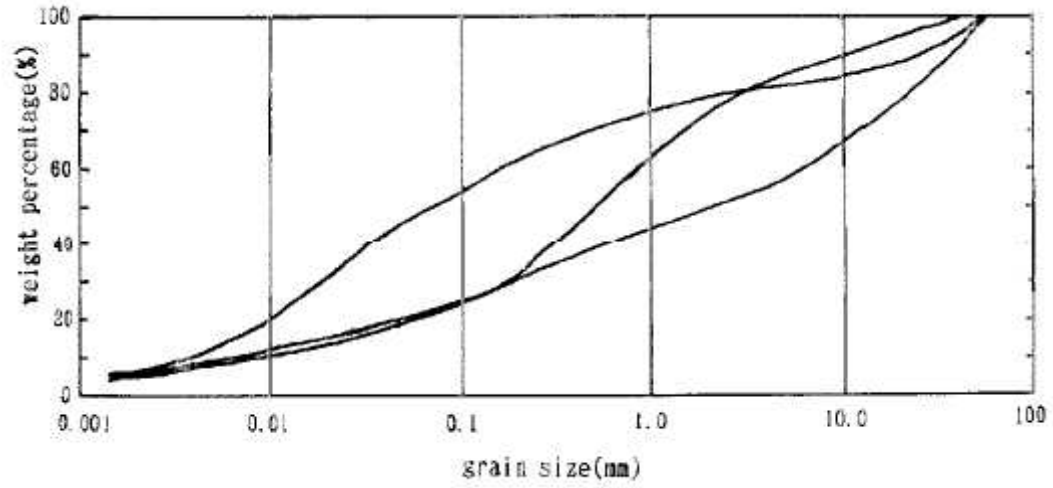

Figure A. 56 Grain size distribution curves for the fill materials used for the embankment at Route 38, Pashikuru (from Sasaki et al. 1993)

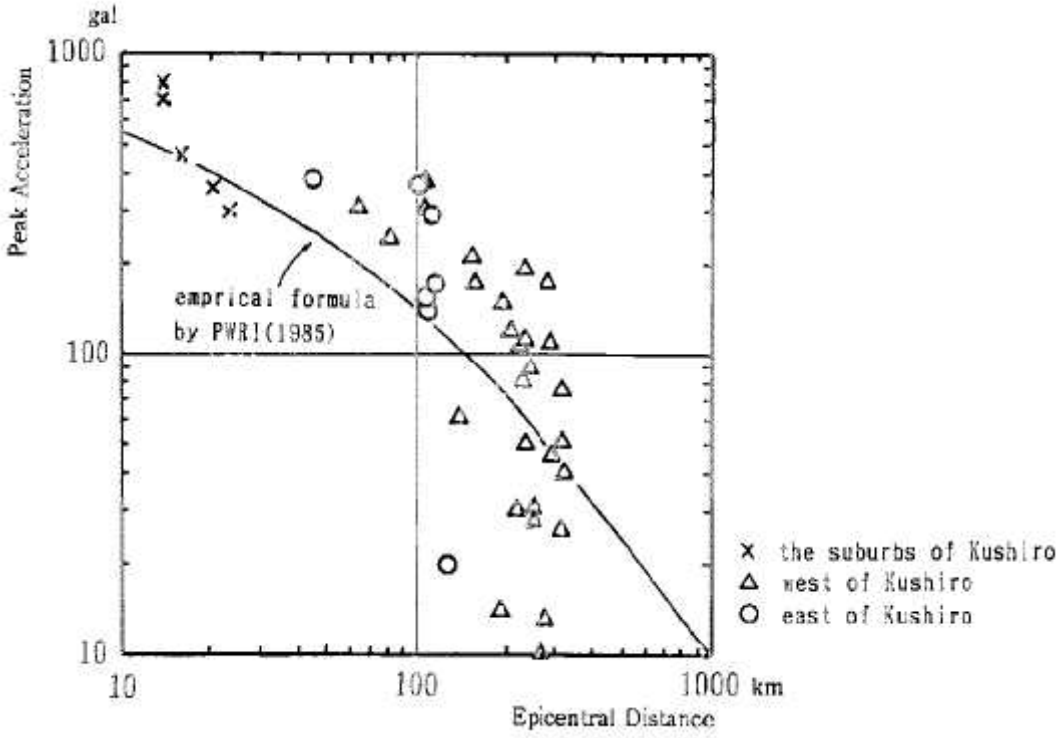

Figure A.57 Comparison of ground motions measured during 1993 Kushiro-Oki earthquake with attenuation relationship developed by Japanese Public Works Research Institute (PWRI 1985) (from Sasaki et al. 1993)

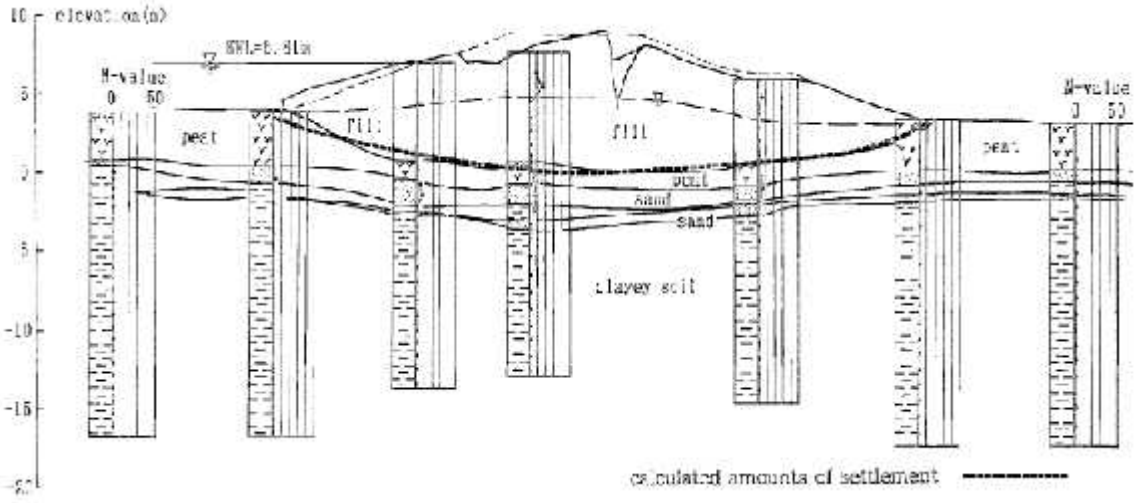

Figure A.58 Failure of dike along right bank of Kushiro River at station 11,650 (from Sasaki et al. 1993)

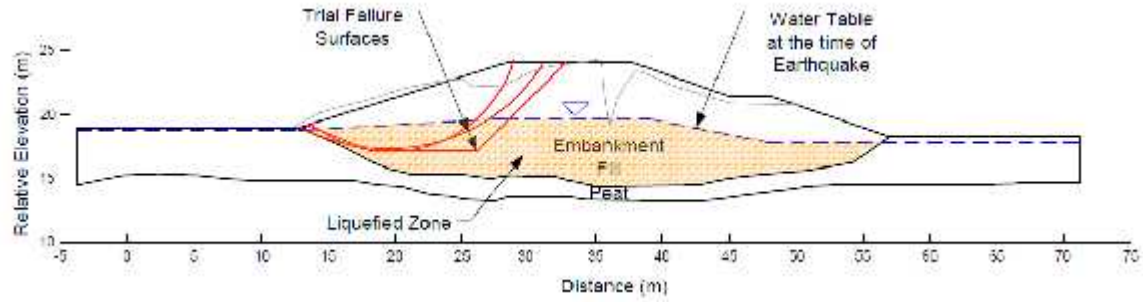

Figure A.59 Pre-failure geometry of dike along the right bank of the Kushiro River with trial failure surfaces

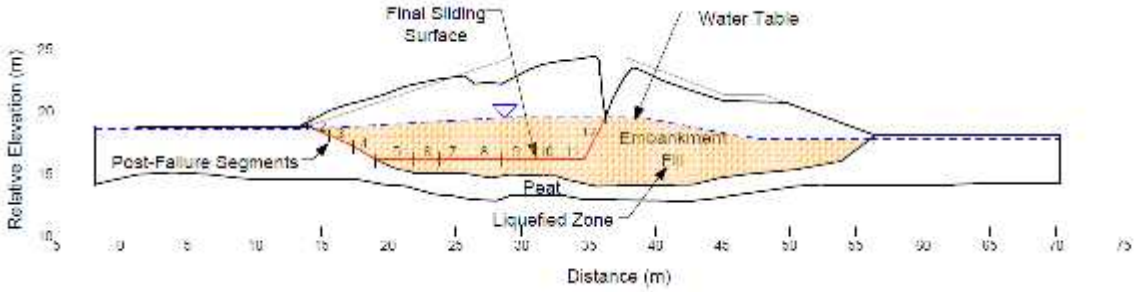

Figure A.60 Post-failure geometry of the dike along the right bank of the Kushiro River illustrating with final sliding surface and post-failure segments

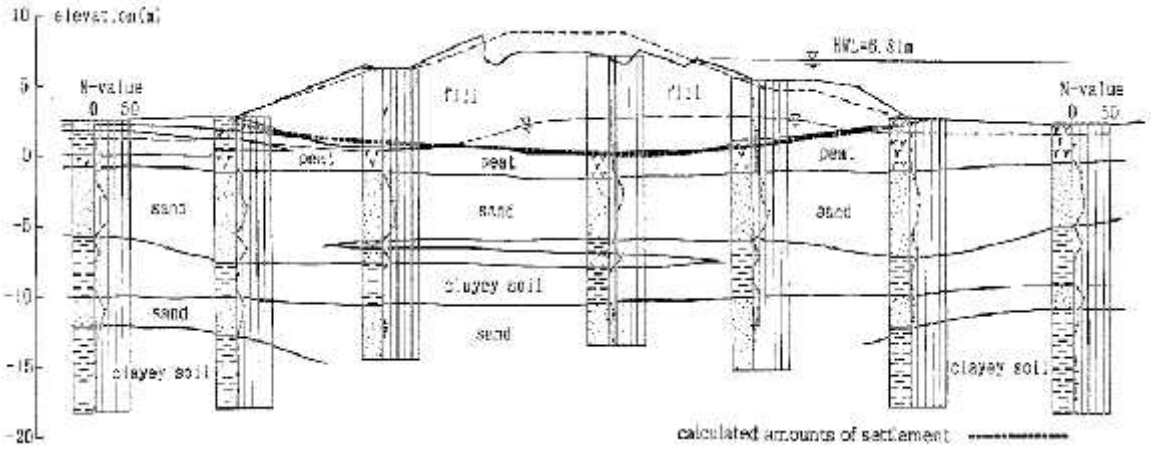

Figure A.61 Failure of dike along left bank of Kushiro River at station 9,850 (from Sasaki et al. 1993)

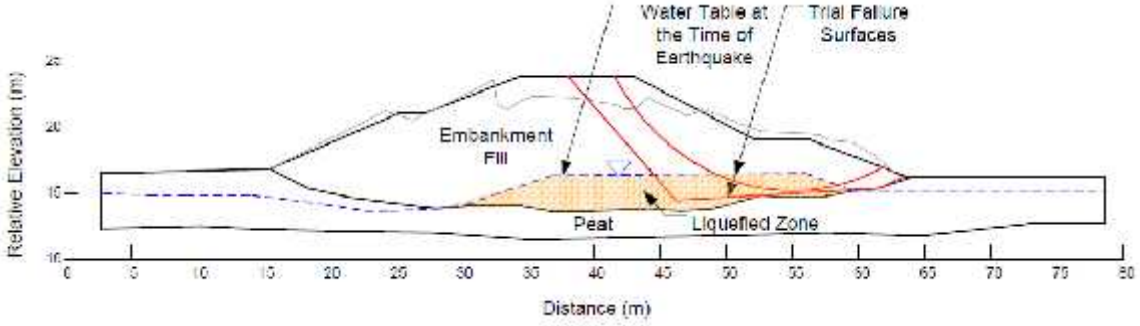

Figure A.62 Pre-failure geometry of dike along the left bank of the Kushiro River with trial failure surfaces

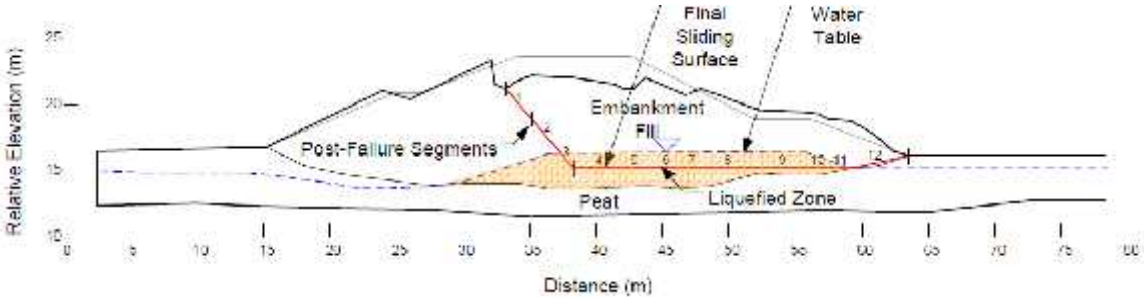

Figure A.63 Post-failure geometry of the dike along the left bank of the Kushiro River illustrating with final sliding surface and post-failure segments

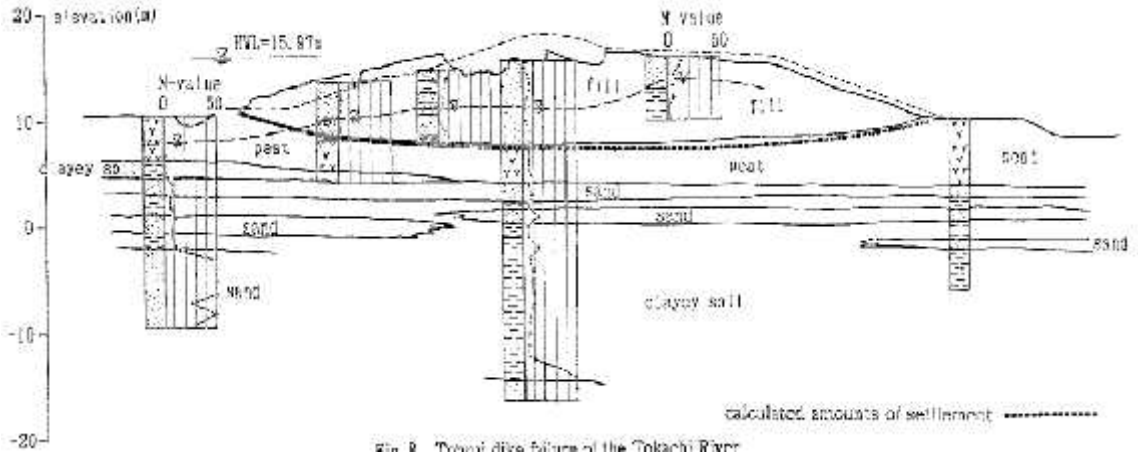

Figure A.64 Pre- and post-failure geometries of the Tohnai dike failure along the right bank of the Tokachi River (from Sasaki et al. 1993)

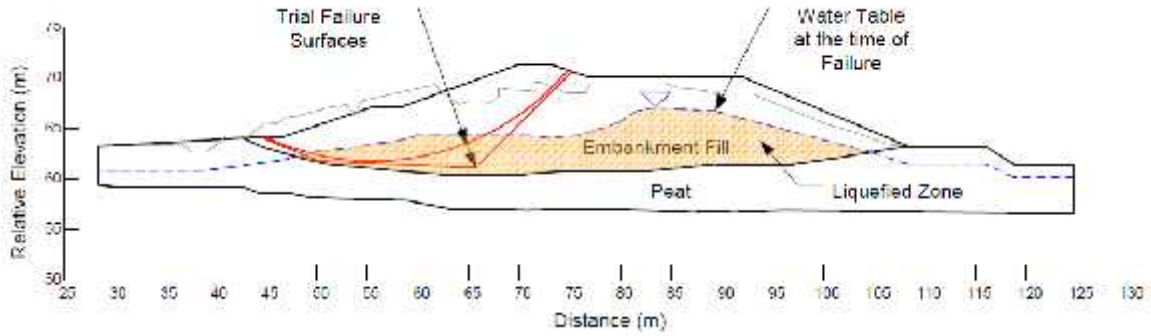

Figure A. 65 Pre-failure geometry and trial failure surfaces for the Tohnai Dike along the right bank of the Tokachi River

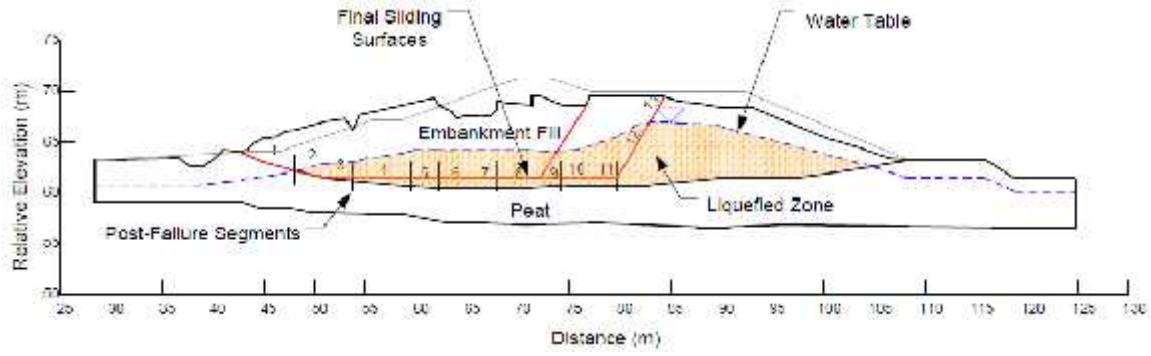

Figure A.66 Post-failure geometry and critical failure surface for the Tohnai Dike along the right bank of the Tokachi River

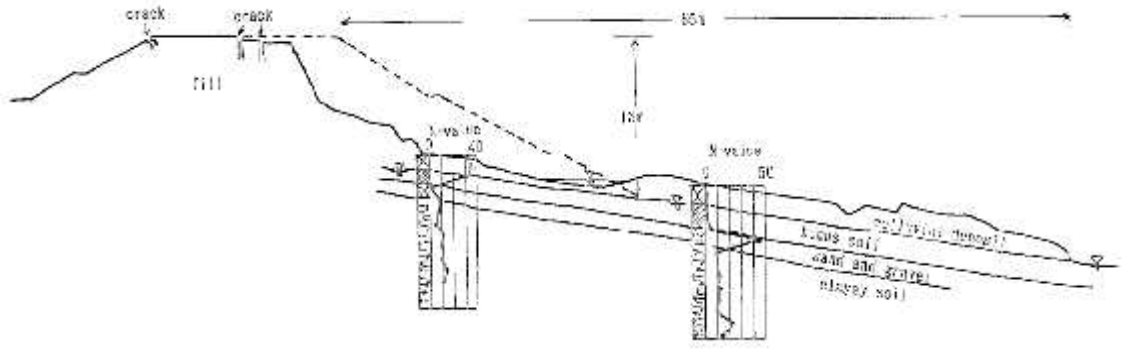

Figure A.67 Route 38 embankment, Pashikuru failure (from Sasaki et al. 1993)

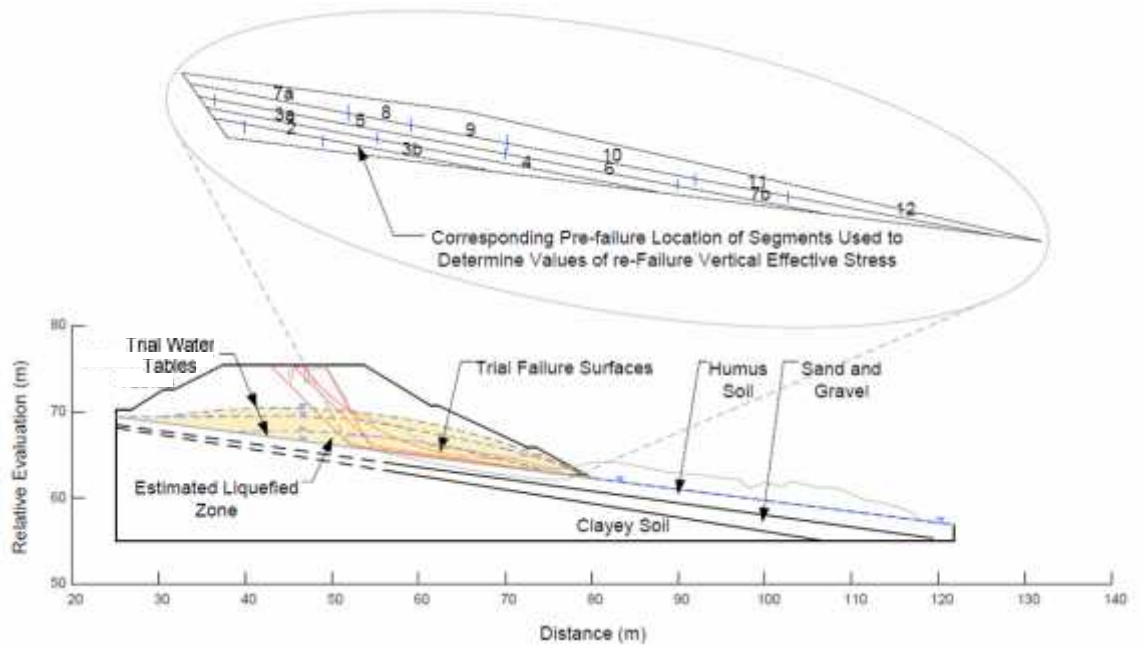

Figure A.68 Pre-failure geometry of Route 38 Pashikuru embankment with trial failure surfaces

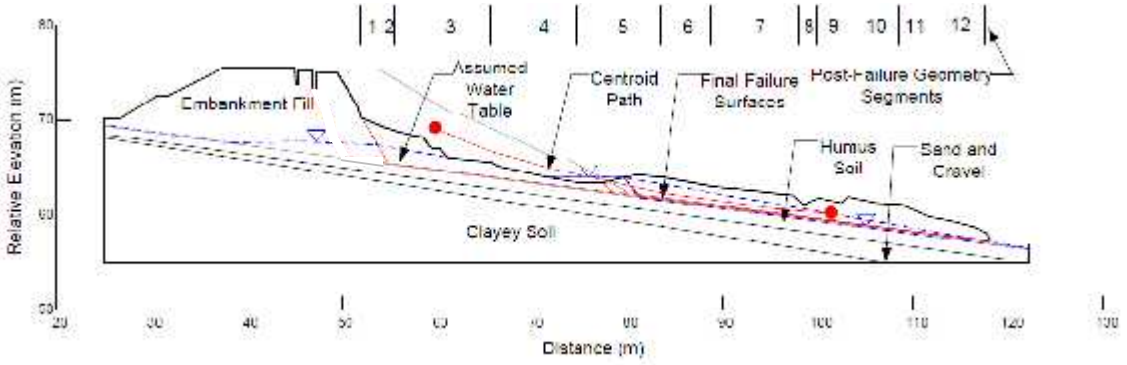

Figure A.69 Post-failure geometry and critical failure surface for Route 38 Pashikuru embankment

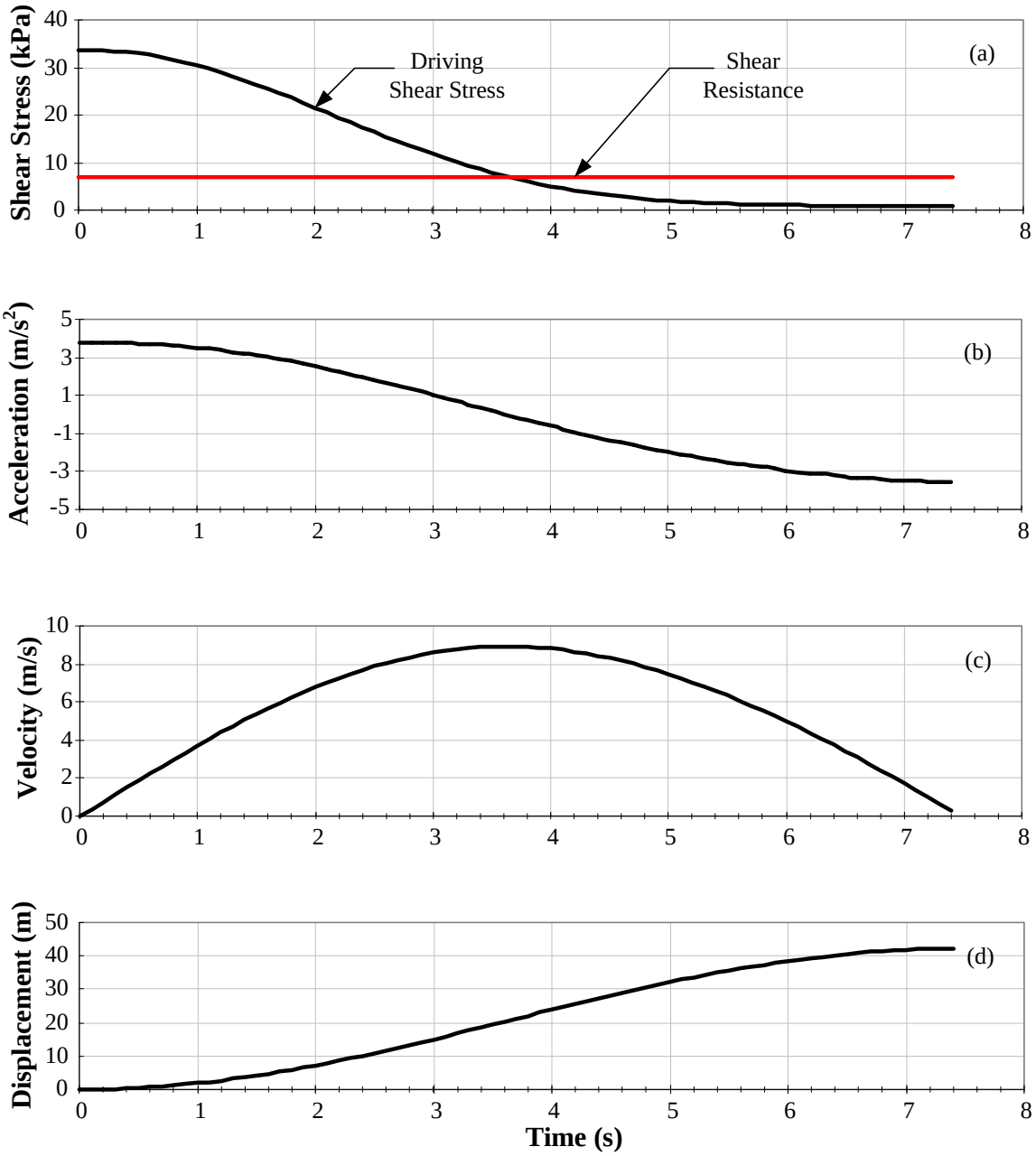

Figure A.70 Kinetics analysis of Route 38 Pashikururoad embankment

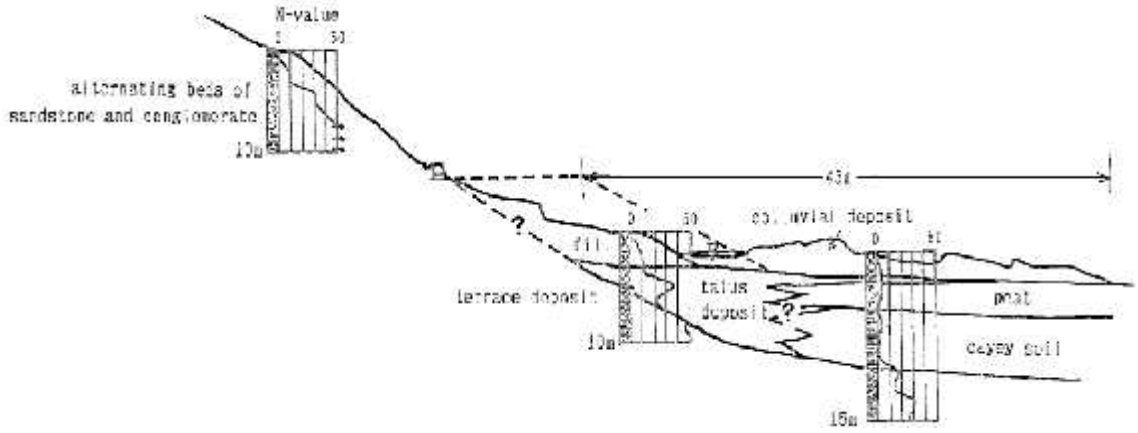

Figure A.71 Route 44 Itoizawa road embankment failure (from Sasaki et al. 1993)

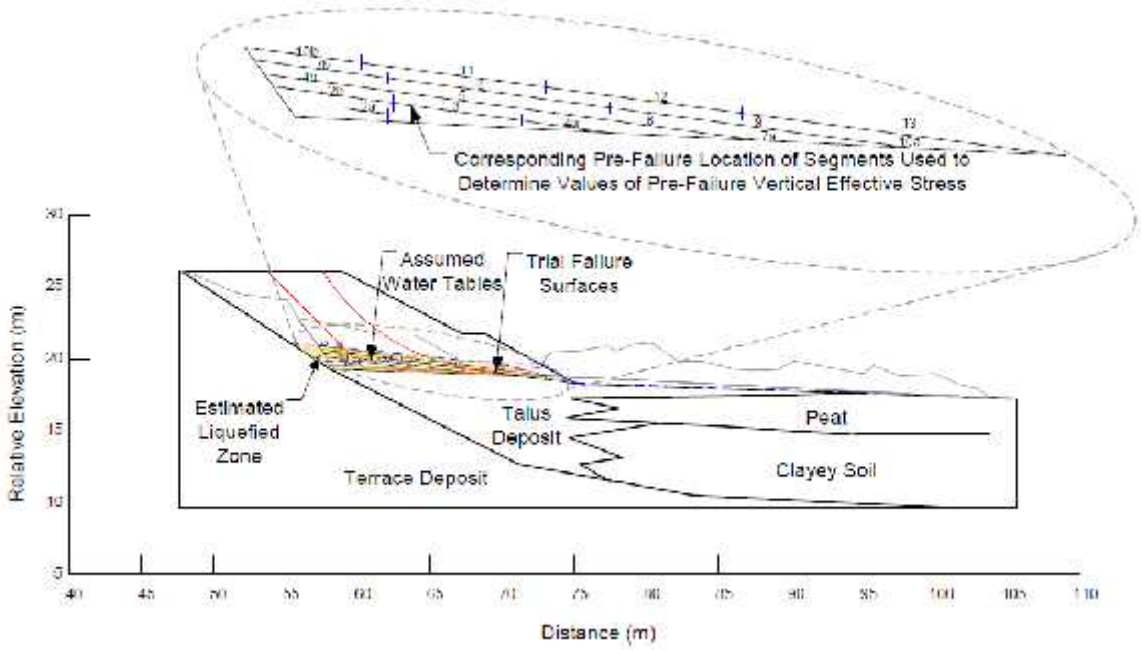

Figure A.72 Pre-failure geometry of the Route 44 Itoizawa embankment with trial failure surfaces

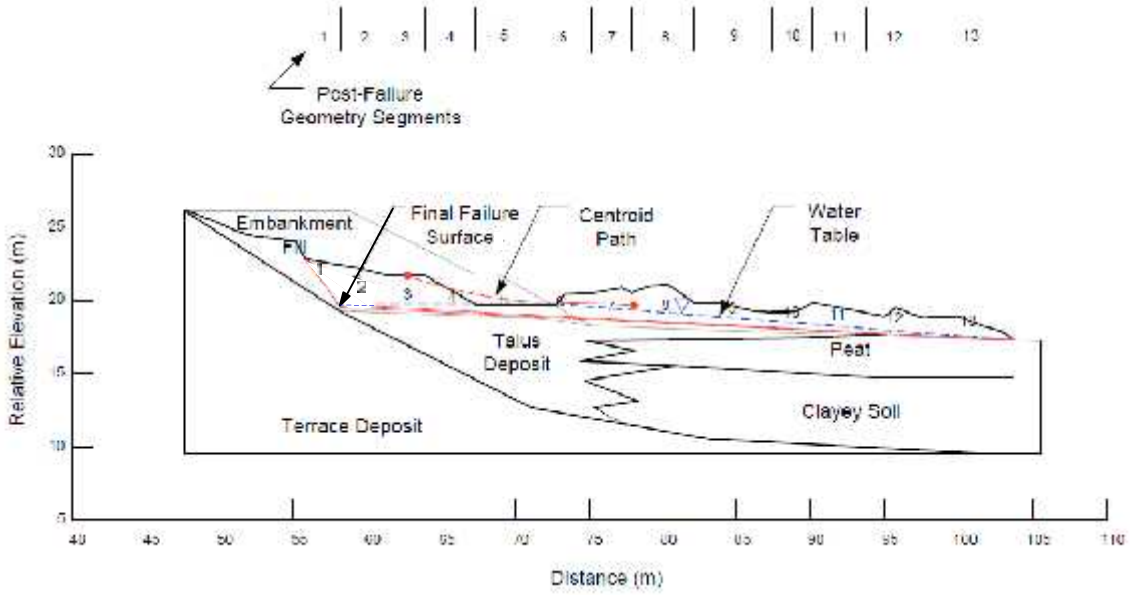

Figure A.73 Post-failure geometry of Route 44 Itoizawa embankment, with final sliding surface and approximate centroid path

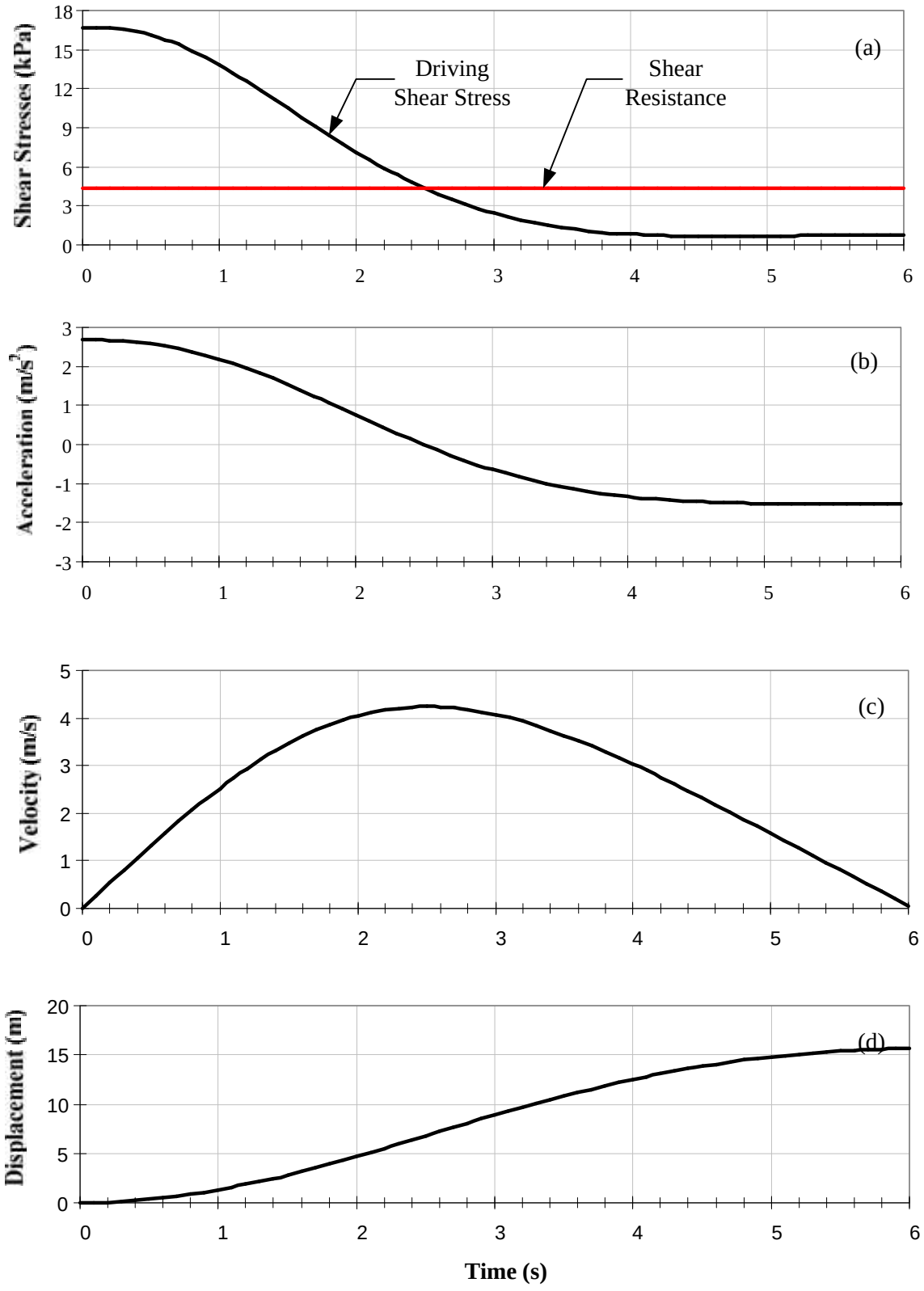

Figure A.74 Kinetics analysis of Route 44 Itoizawa road embankment

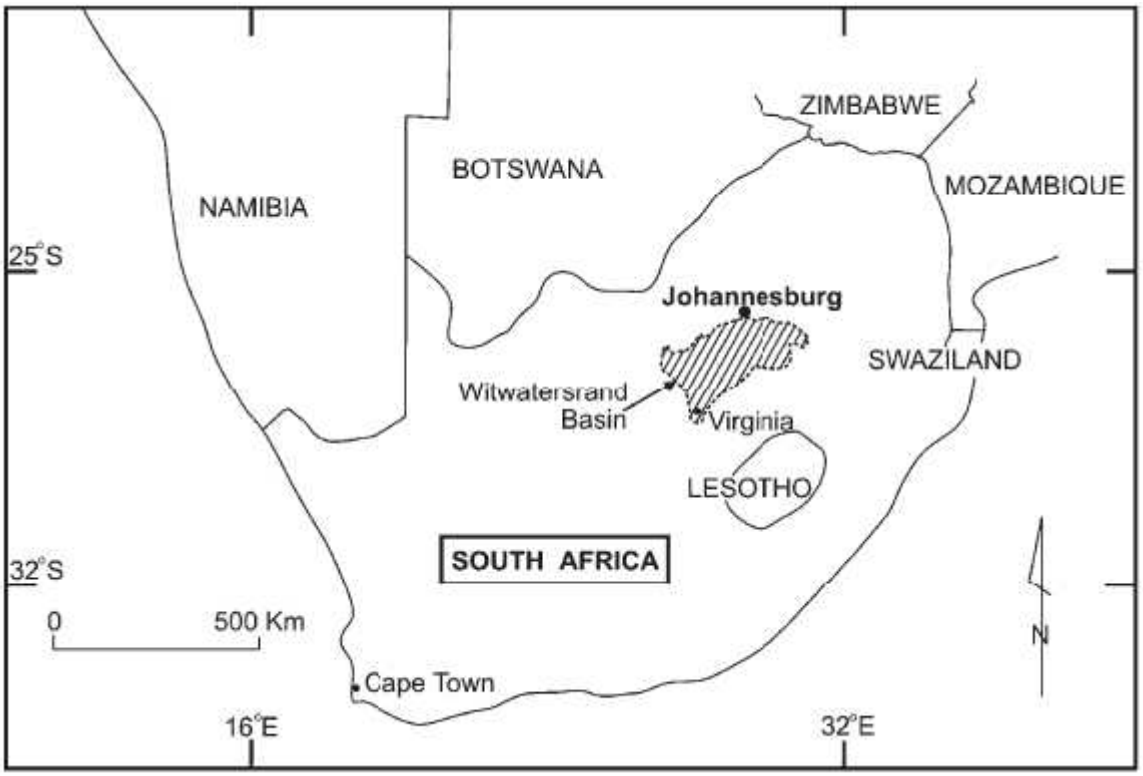

Figure A.75 Location of the city of Virginia, South Africa and the Witwatersrand Basin (from Niekerk and Viljoen 2005)

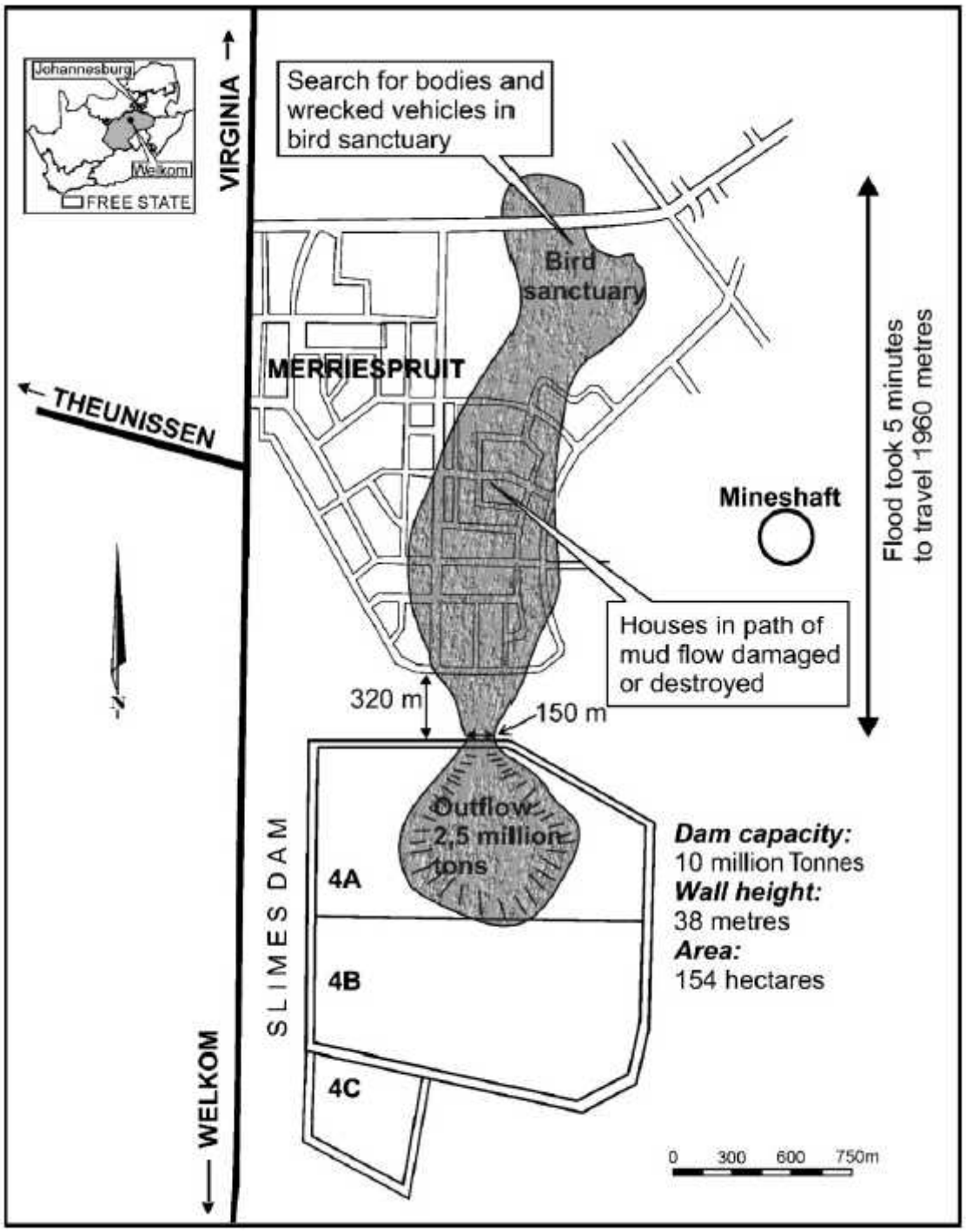

Figure A.76 Plan view of Merriespruit Dam and Merriespruit Village with the flow path and damage caused by the liquefied tailings (from Niekerk and Viljoen 2005)

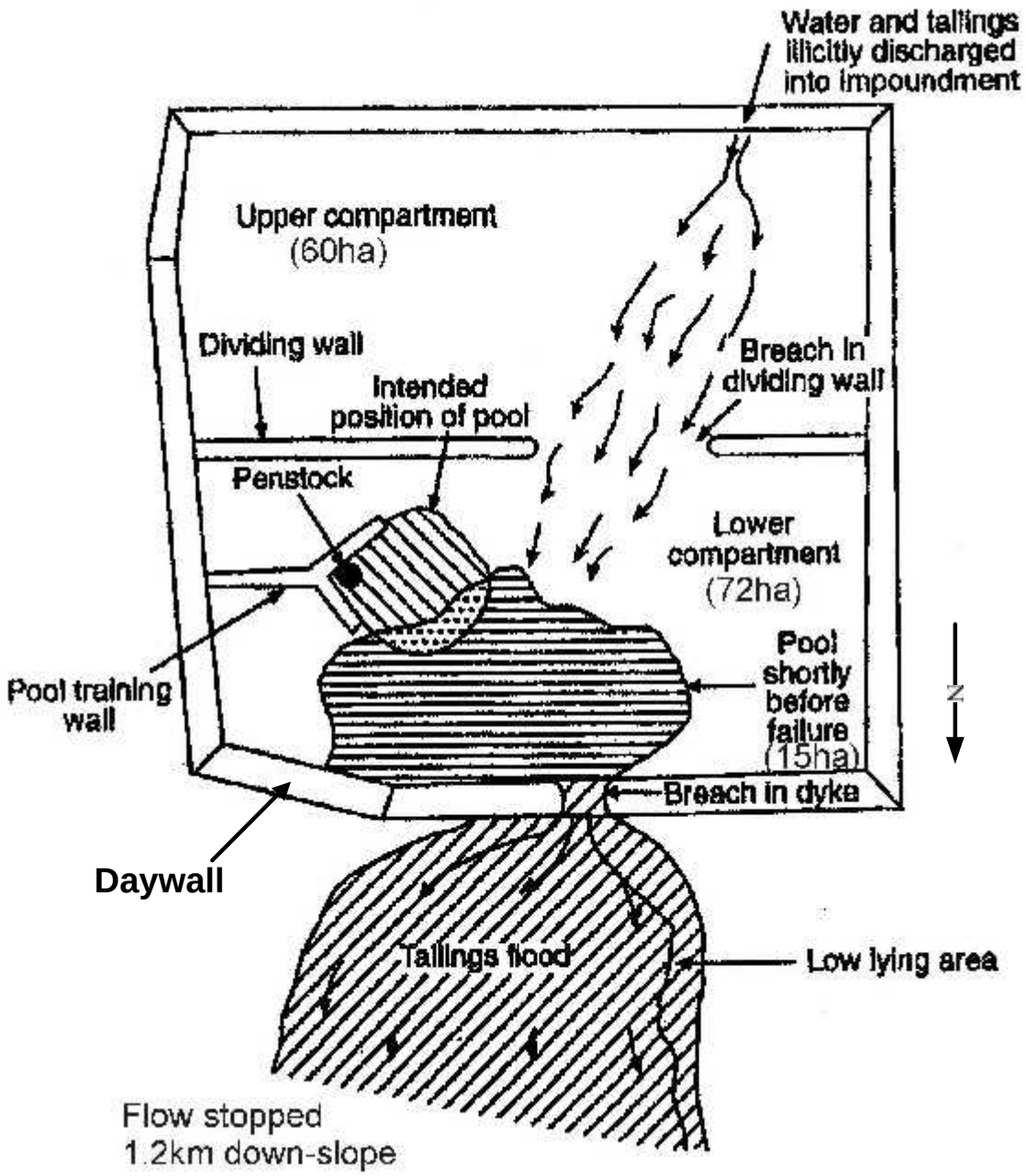

Figure A.77 Plan view of Merriespruit dam showing the position of the pool at the time of failure, the intended location of the pool, the breach in the perimeter dyke, and the initial flow path of the failed tailings (from Blight and Fourie 2005)

Figure A.78 Aerial photographs of Merriespruit Dam failure (from www.tailings.info; reproduced with permission from Jon Engels)

Figure A.79 Photograph of Merriespruit dam showing the failure of the perimeter embankment (from www.tailings.info; reproduced with permission from Jon Engels)

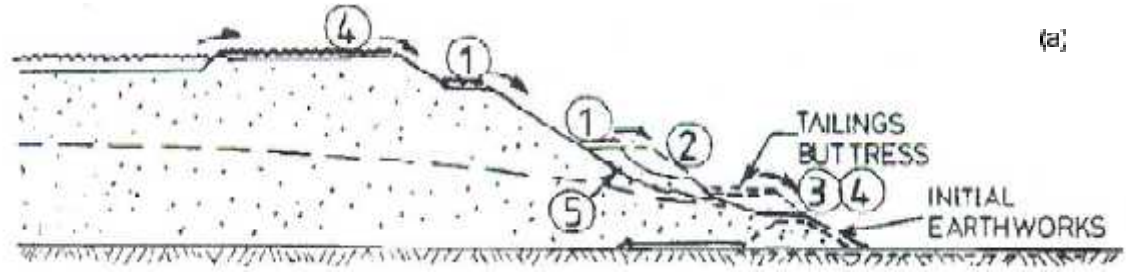

Critical section of north wall during early stages of failure

1. Berms overtop after thunderstorm.
2. Loose tailings infill to earlier failures on lower slope erodes.
3. Tailings buttress starts to fail.
4. Pool commences overtopping and erodes slopes and tailings buttress.
5. Unstable lower slope fails and failed material is washed away.

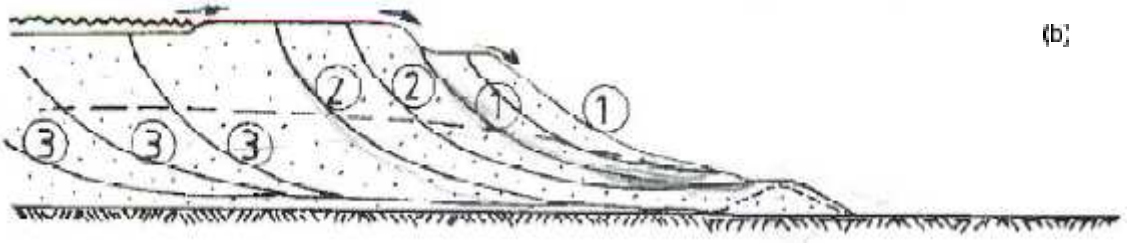

Critical section of north wall during failure

1. Lower slopes fail and are washed away.
2. Domino effect of local slope failures which are washed or flow away.
3. Major slope failures with massive flow of liquid tailings engulfing town.

Figure A.80 (a) Section of north wall illustrating potential early stages of failure; (b) retrogressive failure of slope and tailings (from Wagener et al. 1997, 1998)

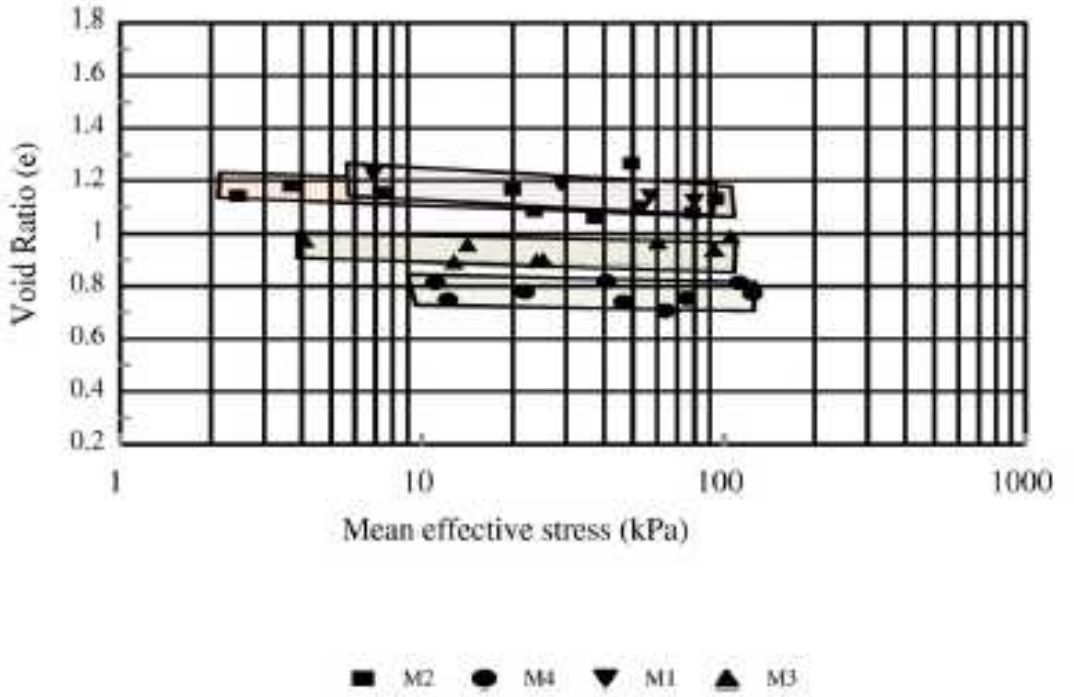

Figure A.81 Critical state lines for M1, M2, M3, and M4 tailings (from Fourie and Papageorgiou 2001)

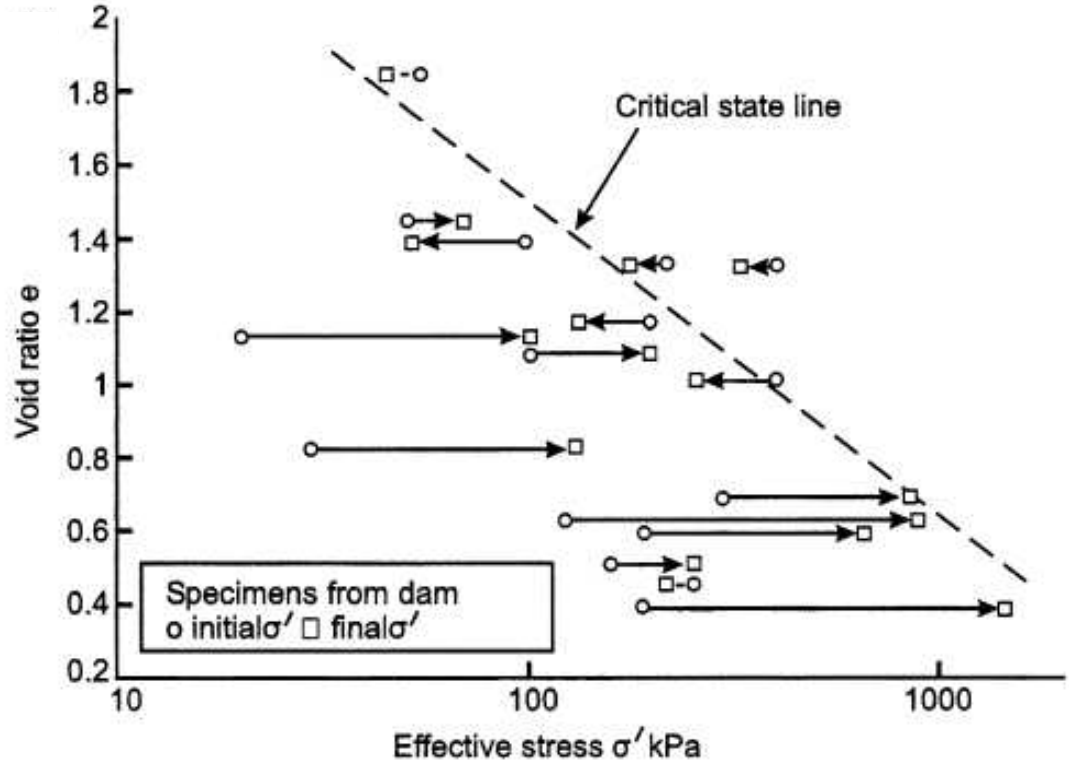

Figure A.82 Unconsolidated-undrained triaxial compression test results of undisturbed tailings samples showing contractive and dilative behavior (from Blight and Fourie 2005)

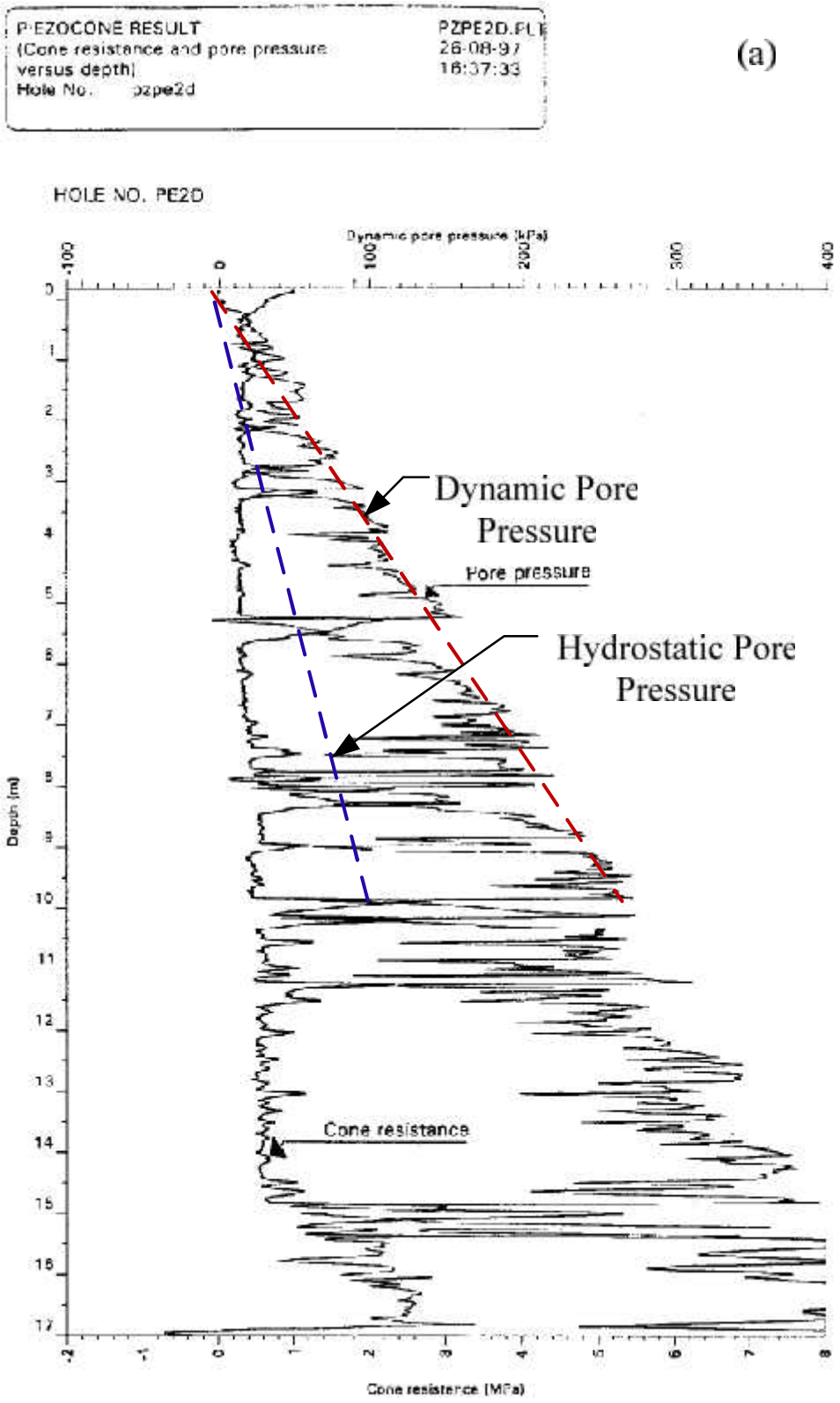

Figure A.83 Results of five piezocone soundings (a through e) conducted along perimeter slope and within impoundment of Merriespruit tailings dam after failure (from Wagener et al. 1998)

(b)

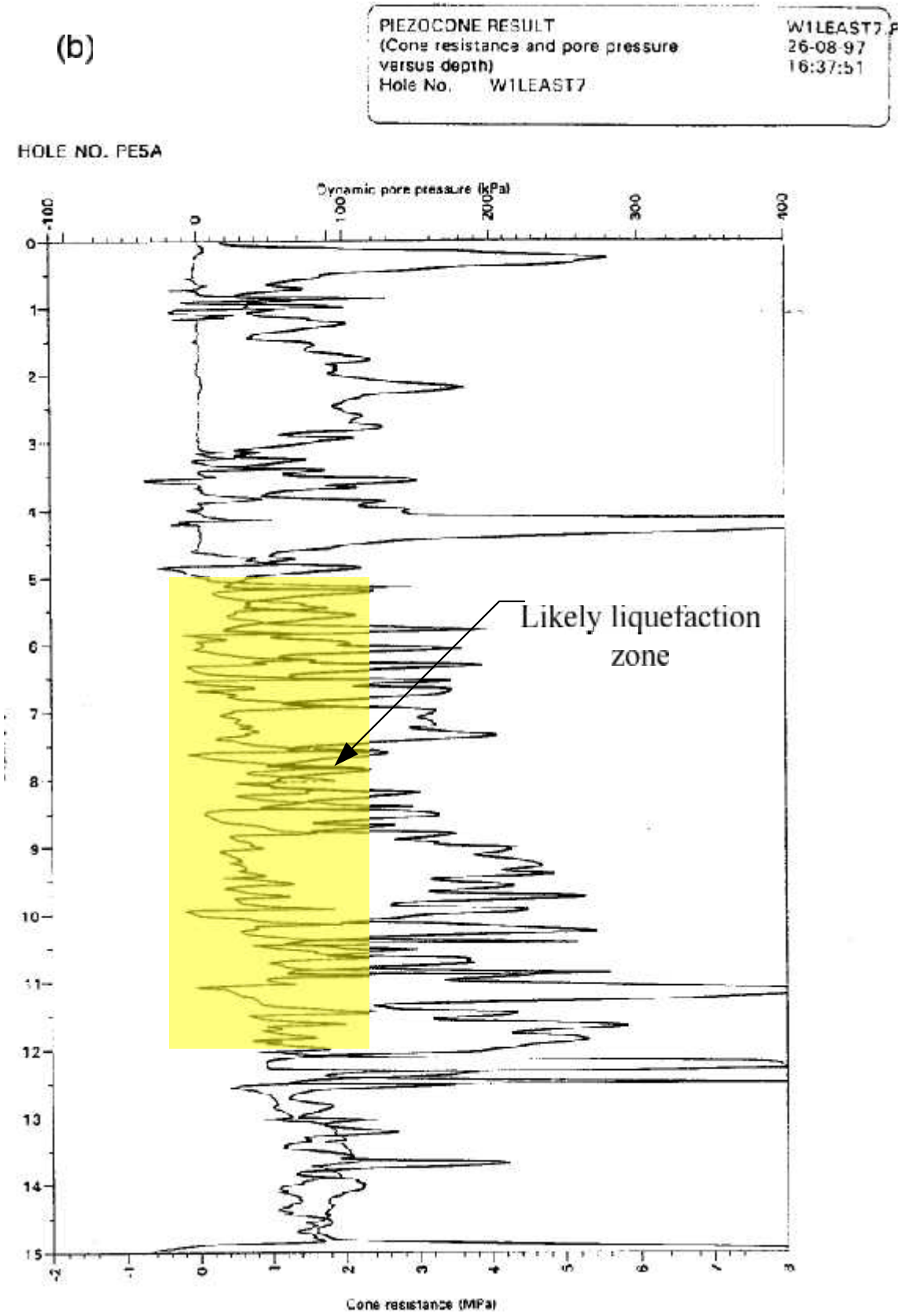

Figure A.83 Continued

(c)

PIEZOCONE RESULT
(Cone resistance and pore pressure versus depth)
Hole No. W1LWEST1

W1LWEST1
26-08-97
16:38:09

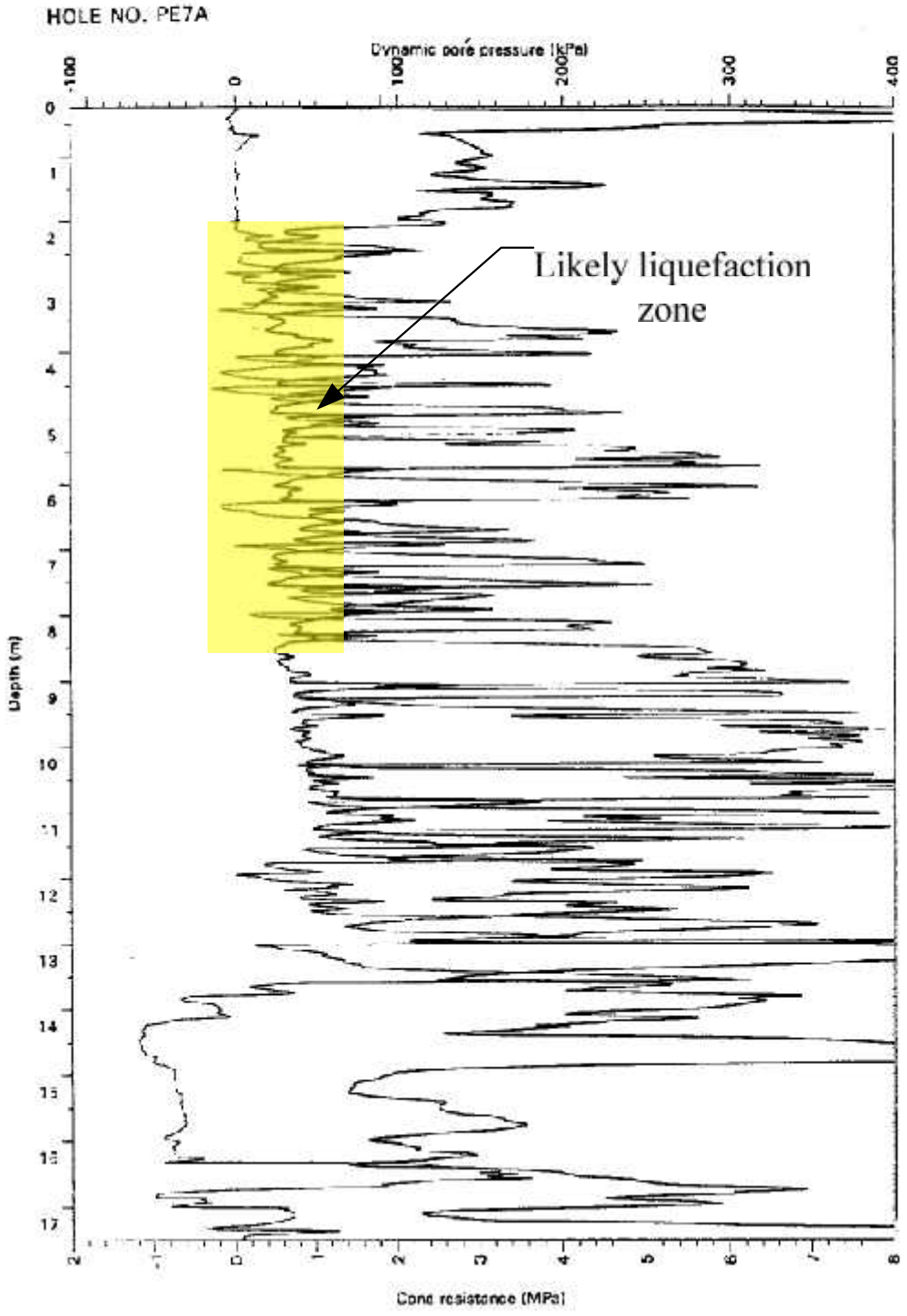

Figure A.83 Continued

(d)

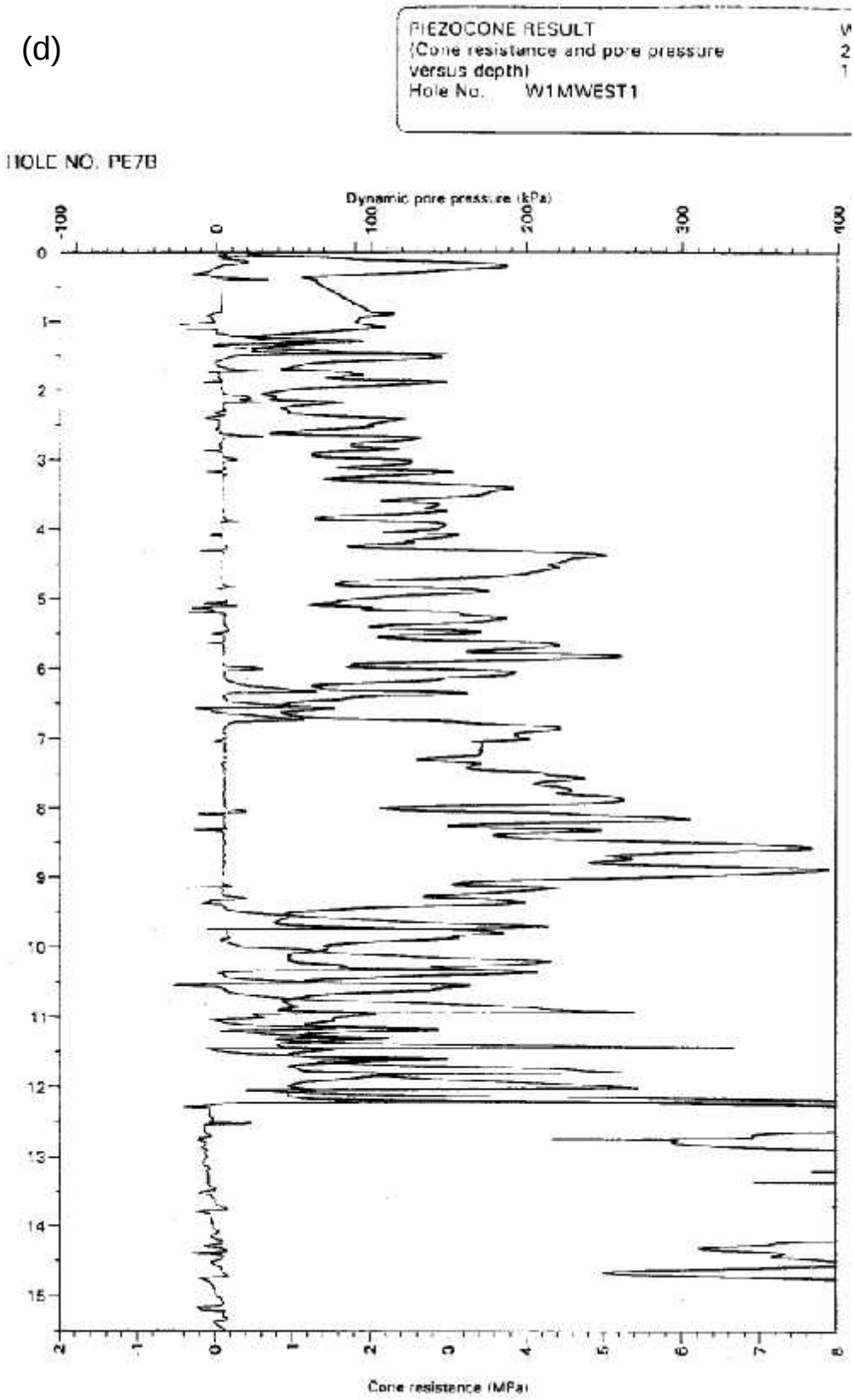

Figure A.83Continued

(e)

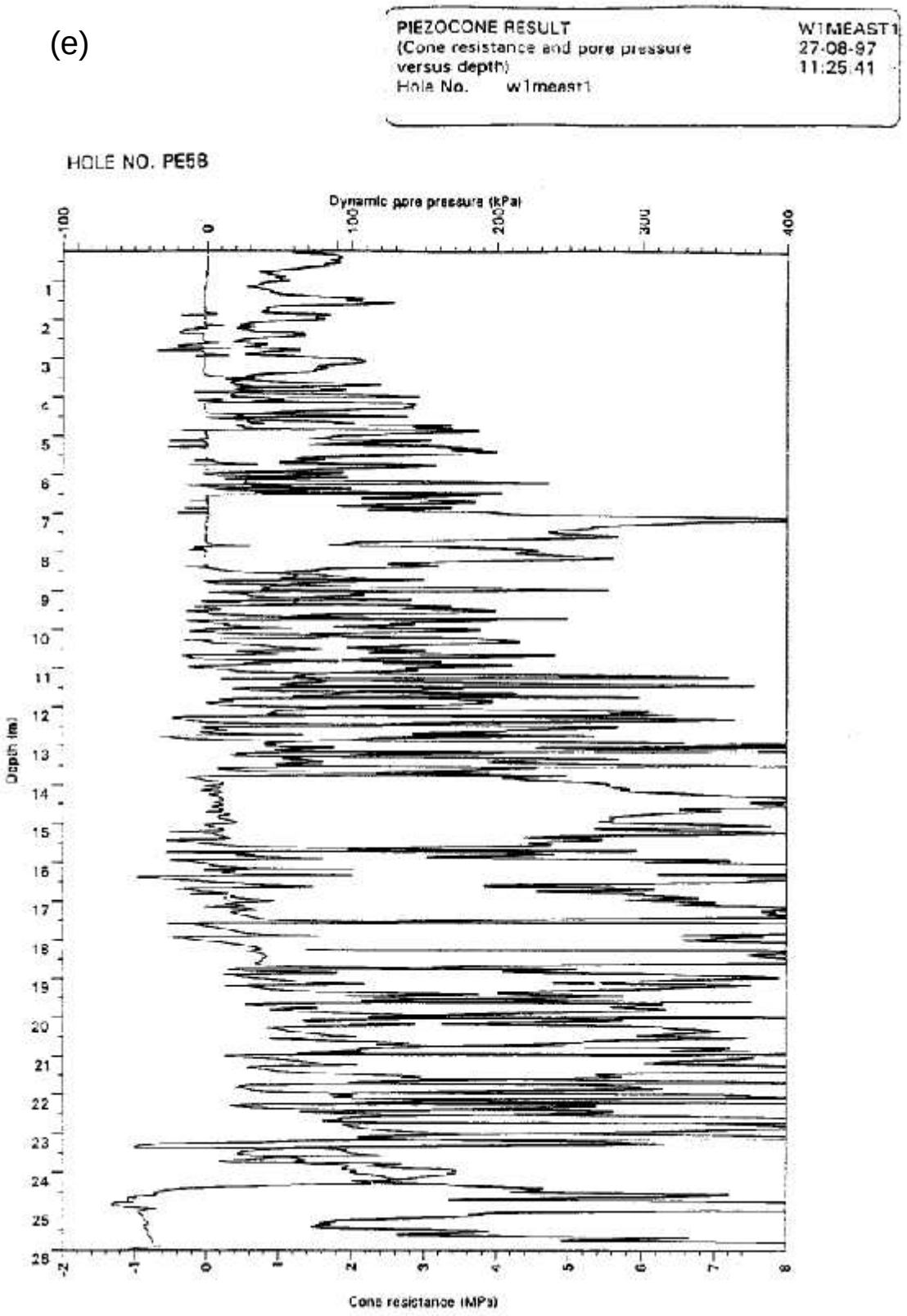

Figure A.83 Continued

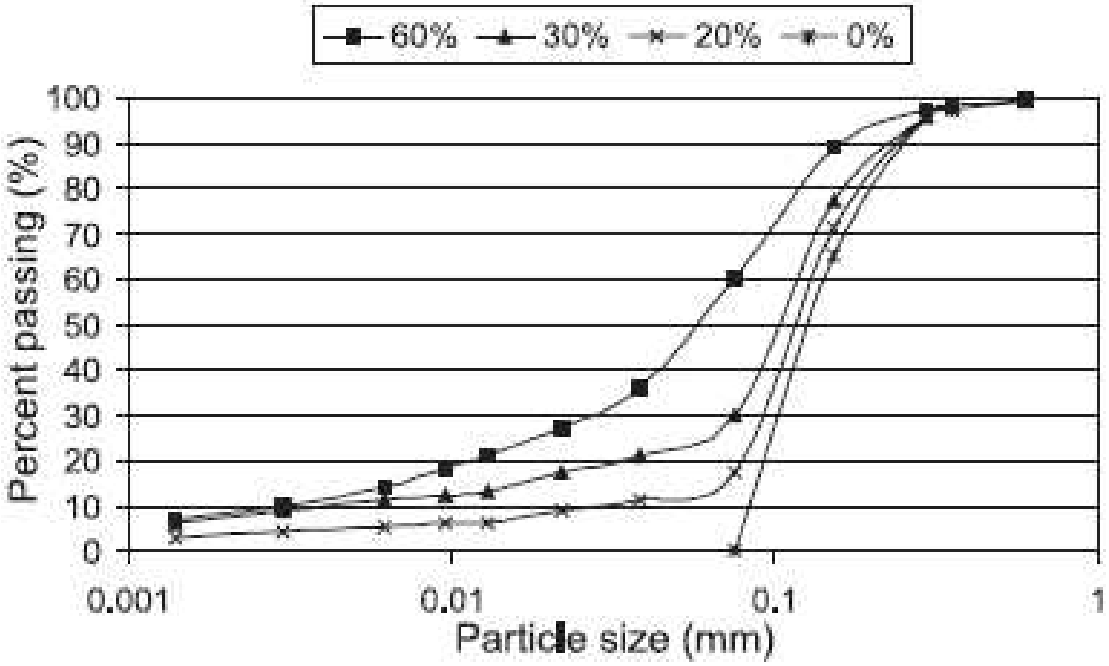

Figure A.84 Grain size distribution curves for the original tailings material (FC ~ 60%) and the three sieved tailings materials (FC ~ 0%, 20%, and 30%) (Fourie et al. 2001)

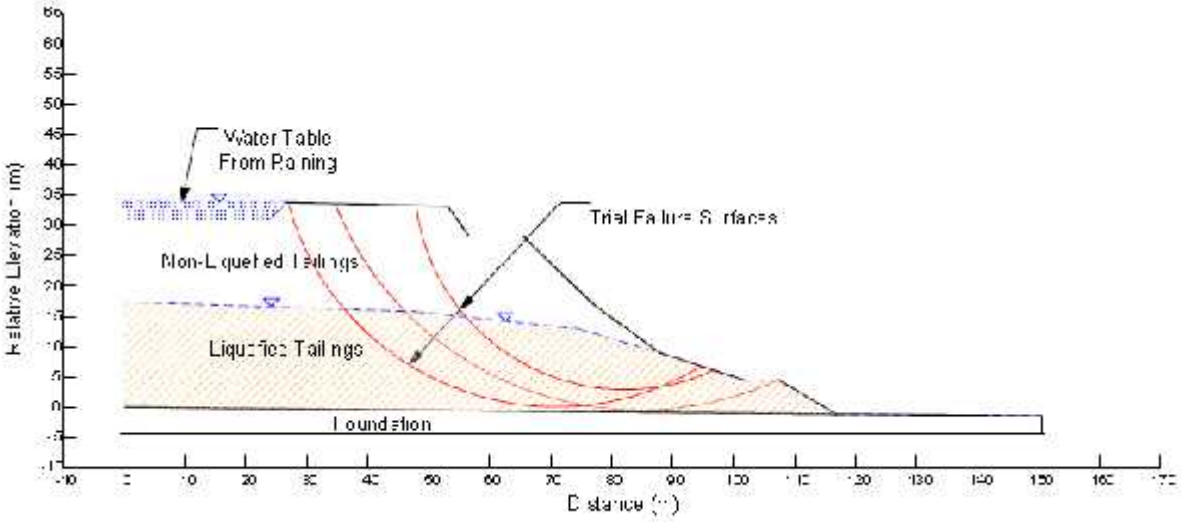

Figure A.85 Pre-failure geometry of Merriespruit tailings dam and trial initial failure surfaces

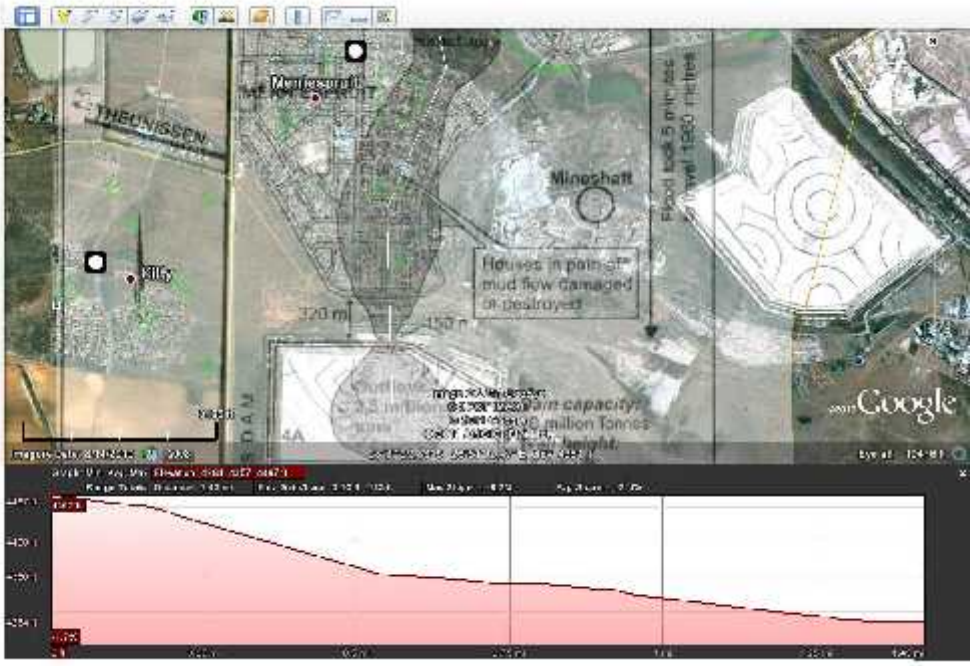

Figure A.86 Estimation of ground slope from elevation profile defined by Google Earth Inc. © 2011 by overlapping the plan view given by Niekerk and Viljoen (2005) on the background Google Earth image.

Figure A.87 Location map of King Harbor Mole B (image courtesy of Google Earth © 2011)

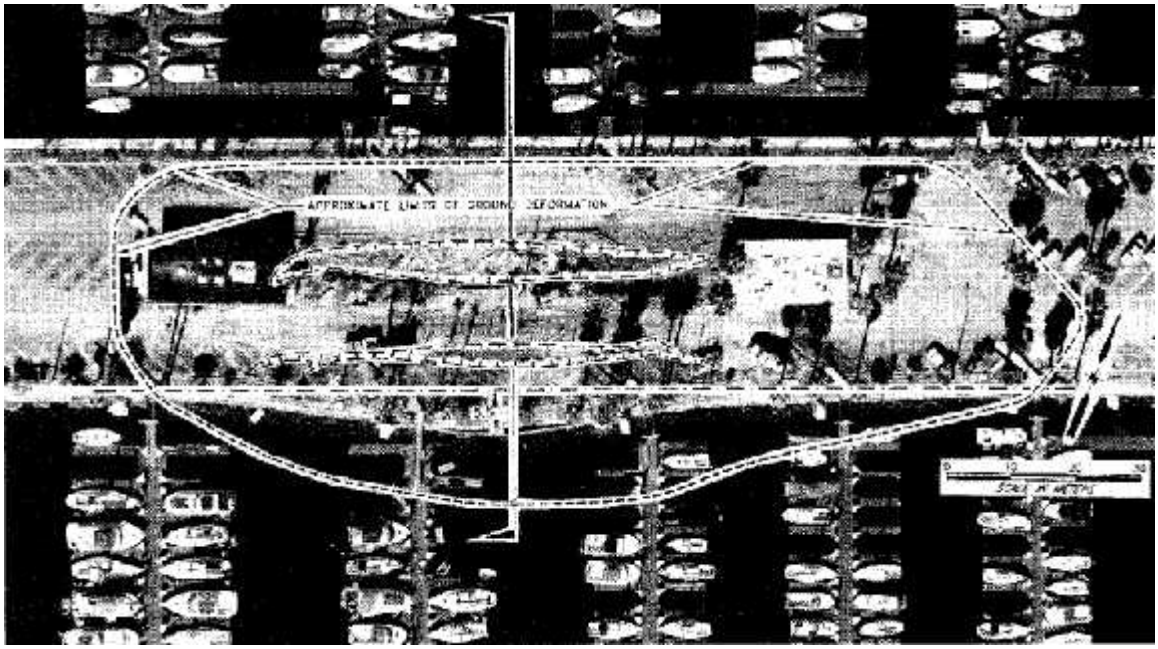

Figure A.88 Aerial view of Mole B nine days after the Northridge earthquake (from Kerwin and Stone 1997)

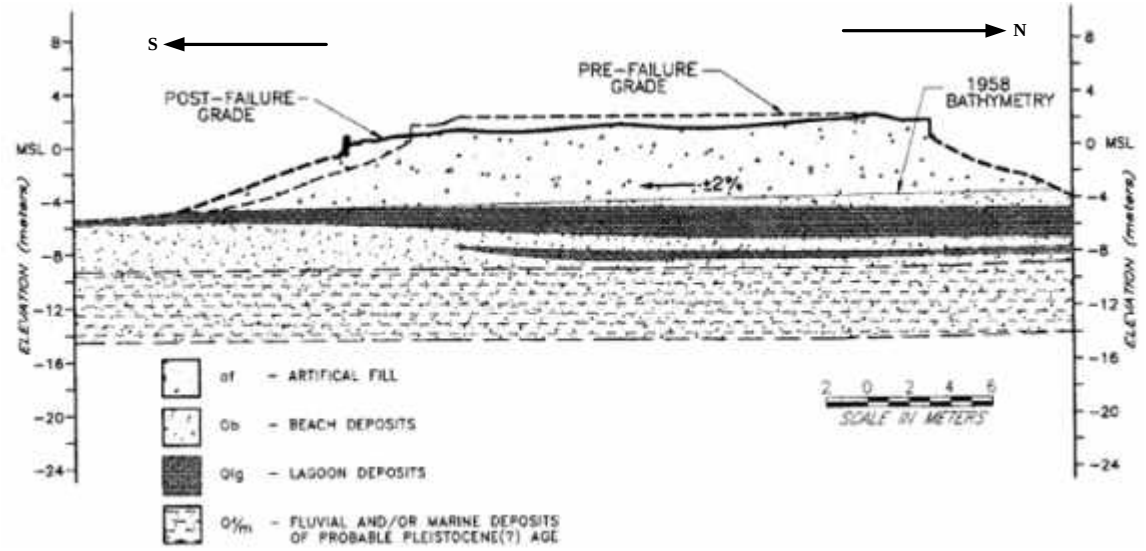

Figure A.89 Cross-section through the failed portion of Mole B showing soil stratigraphy (view toward the west) (from Kerwin and Stone 1997)

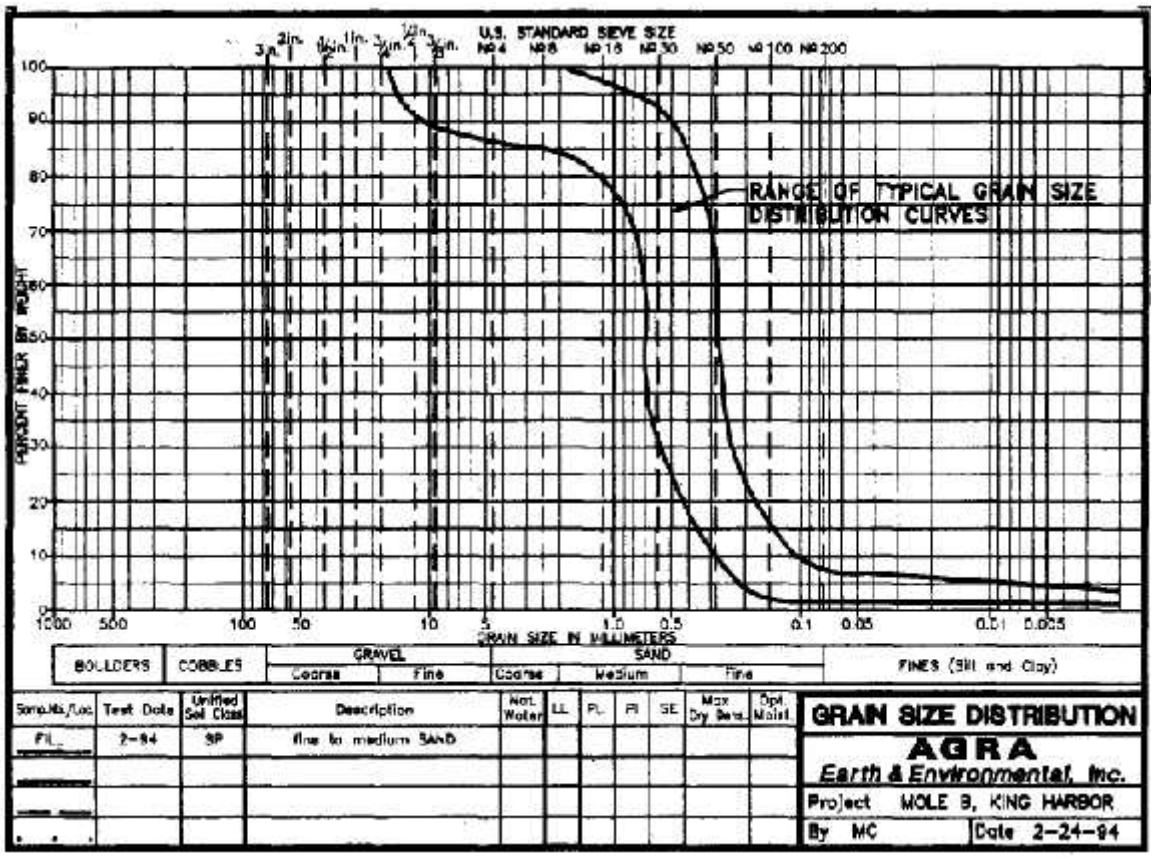

Figure A.90 Typical range of grain size distributions for fill materials at Mole B (from Kerwin and Stone 1997)

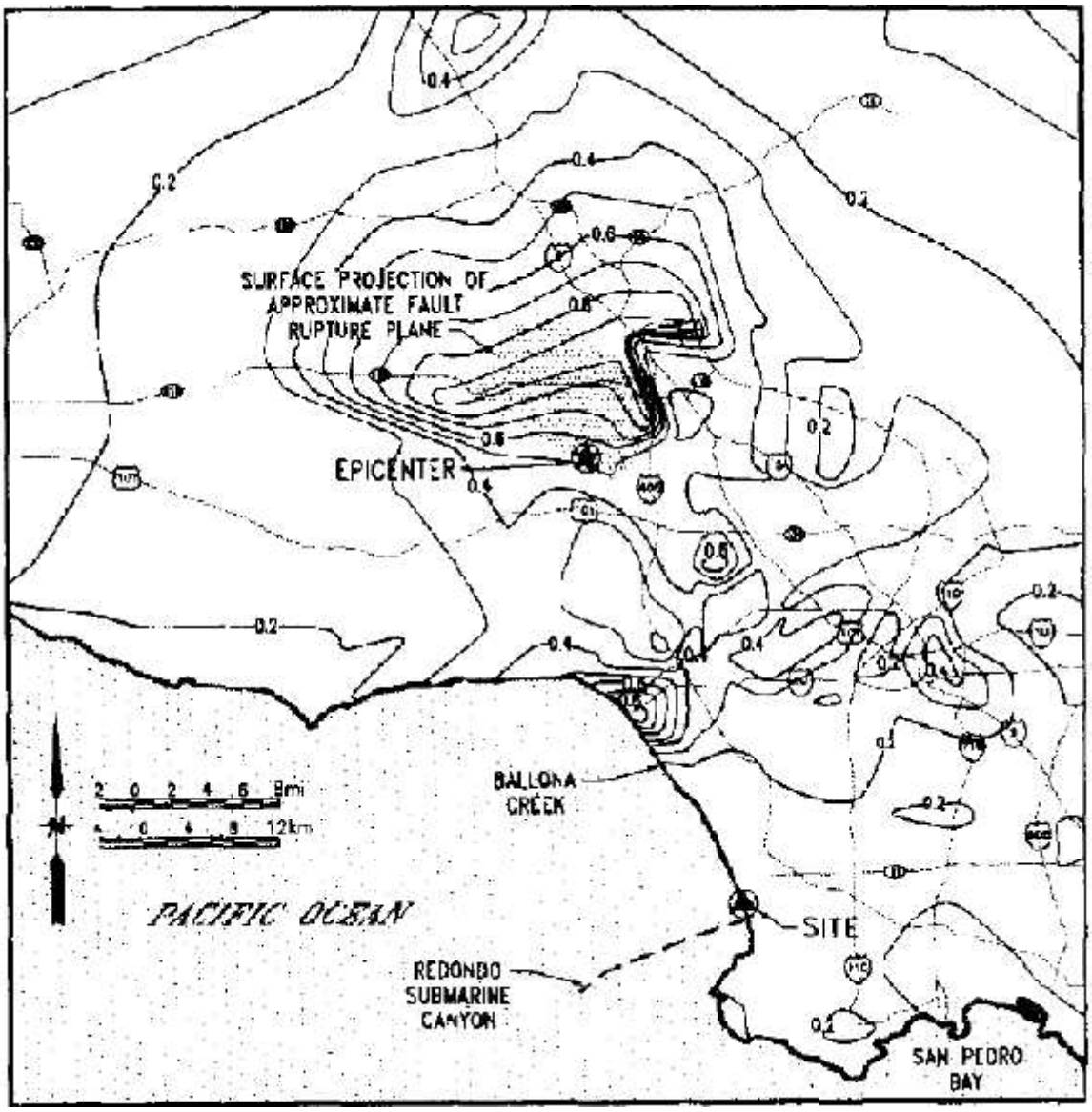

Figure A.91 Contours of maximum horizontal acceleration produced by Northridge earthquake based on recordings at rock and soil sites (from Stewart et al. 1994)

Figure A.92 Looking west along southern graben or fissure zone on the morning of the earthquake (from Kerwin and Stone 1997)

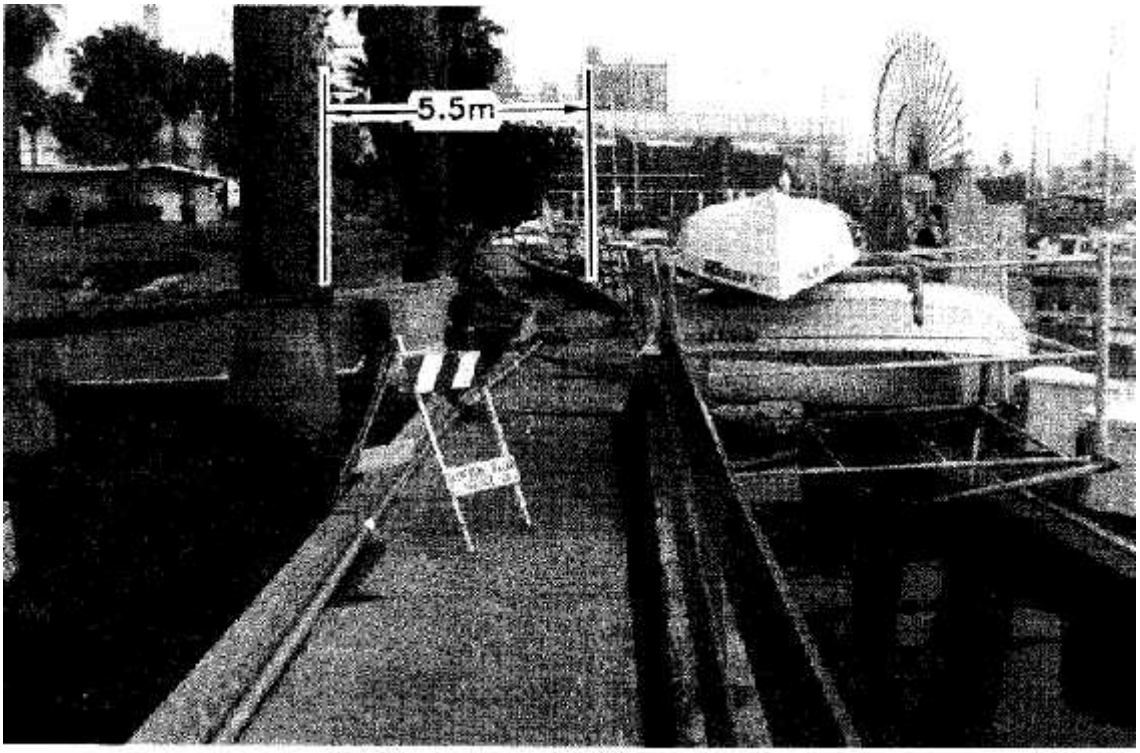

Figure A.93 Looking east at area of maximum horizontal seawall displacement. In the foreground near the barricade, the wall face has been displaced from a location at left edge of photo (from Kerwin and Stone 1997)

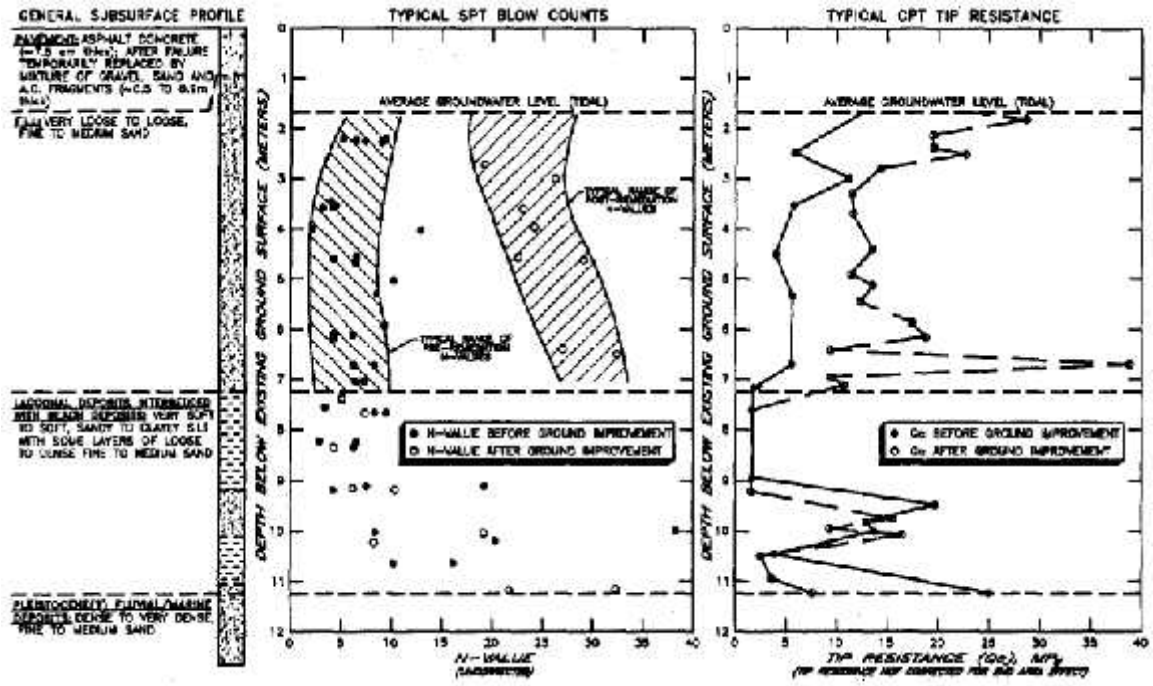

Figure A.94 Typical profile of SPT blow counts and CPT tip resistance comparing the pre-and post-remediation values versus depth (from Kerwin and Stone 1997)

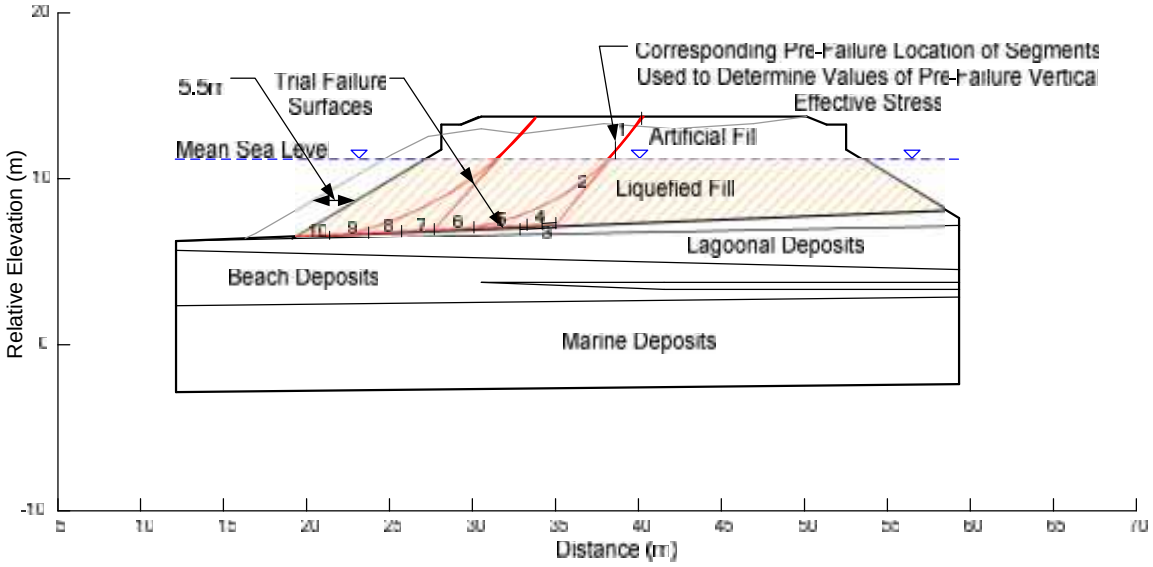

Figure A.95 Pre-failure geometry of King Harbor Mole B with trial failure surfaces

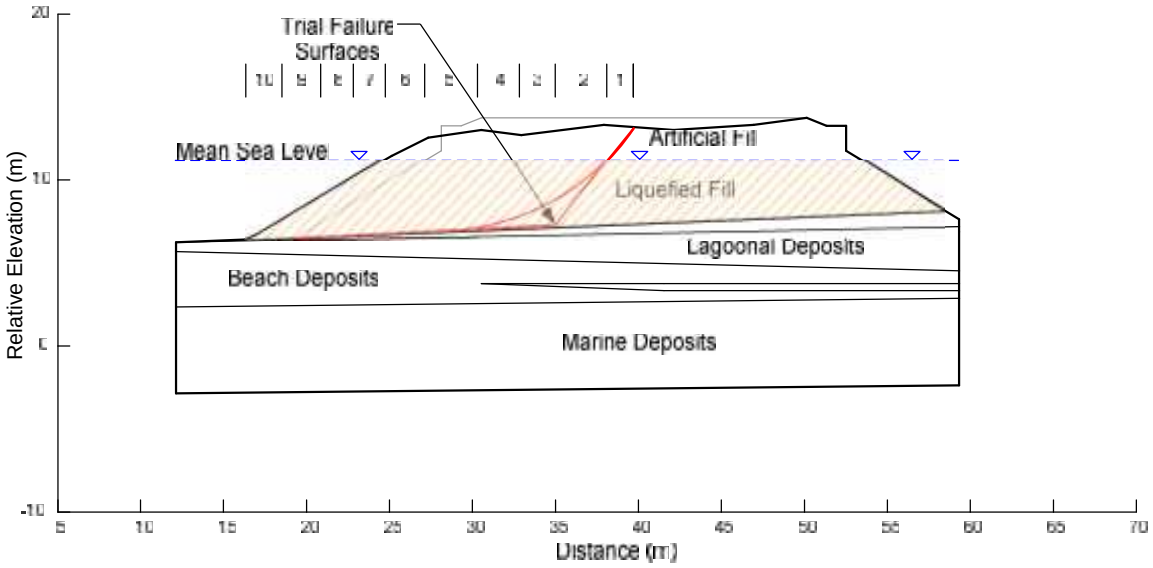

Figure A.96 Post-failure geometry of King Harbor Mole B with critical circular and noncircular sliding surfaces

Figure A.97 Locations of Kobe earthquake epicenter, surface fault rupture, nearby characterized faults, recording stations, and approximate locations of dikes, dams and landslides analyzed in this study

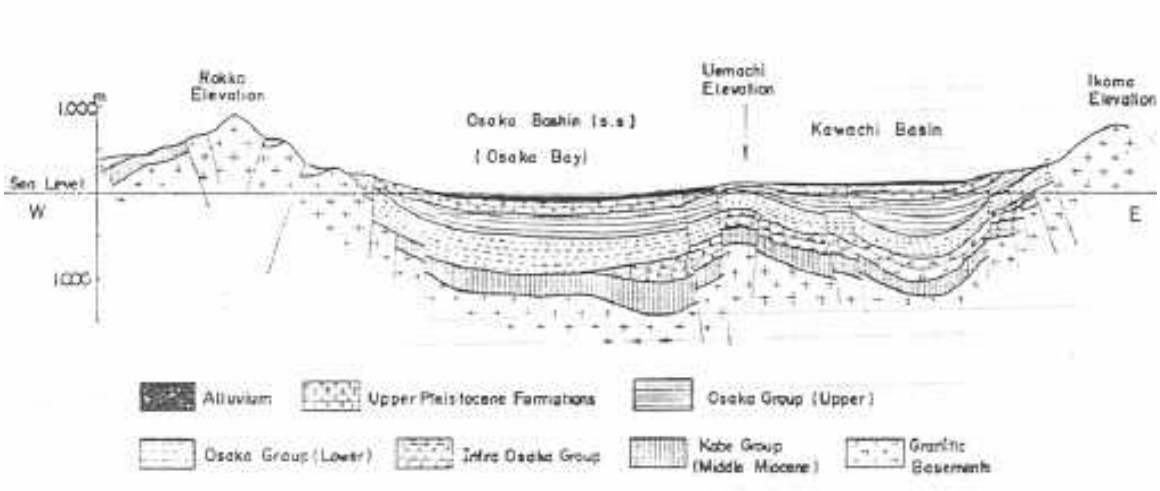

Figure A.98 Geological cross-section of Osaka Basin (from Rasheed and Nakagawa 2004)

Geologic Time			Absolute Age (Ka)	Formation		Geological Feature
Quaternary	Holocene		0 10	Alluvium		Composed of soft cohesive soil, loose sand and sandy gravel wide distribution over the alluvial plain (fan, natural levee sand bank, bar); landfill; man-made island.
	Pleistocene	Late PLS	20	Upper Pleistocene		Alternating beds of marine clay with sand and non-marine sandy gravel, sand and clay; adequate bearing strength in sand of gravel bed as the foundation; development of terrace in uplift region.
			130			
		Middle PLS	200			
			600	Osaka Group	Upper Subgroup	Alternating beds of marine clay with sand and non-marine sandy gravel, sand and clay; sand with gravel rich facies in general at marginal area of the basin.
			700		Middle Subgroup	Alternating beds of marine clay with sand and non-marine sandy gravel, sand and clay.
		Early PLS	1200			
			1700		Lower Subgroup	Non-marine alternating beds composed of clay, sand and gravel (marine facies is not found). Osaka Group forms hilly land at uplifting area.
N	PLO		3000			
N: Neogene, PLO: Pliocene, PLS: Pleistocene						
Basement rocks						
Neogene			15(Ma) 32	Nijo Group		Andesitic Volcanic rocks, pyroclastic rocks and sedimentary rocks.
Paleogene			65	Kobe Group		Mainly lacustrine sedimentary layers with intercalations of thick tuffacious beds.
Cretaceous			70	Izumi Group		Alternating beds of mudstone and sandstone (marine)
			90	Granitic rocks		Ryoke or Sanyo type granitic rocks (granite~ granodiorite)
			143	Acidic Pyroclastics		Rhyolitic pyroclastic rocks
Pre-Cretaceous				Tanba Group Ultra-Tanba Group		Pre-Cretaceous accretional prism composed of shale, sandstone, chert, green rocks, etc.
Ka; 10^3 years, BP, Ma: 10^6 years, BP						

Figure A.99 Stratigraphy of the Osaka Basin (Nakagawa et al. 1996)

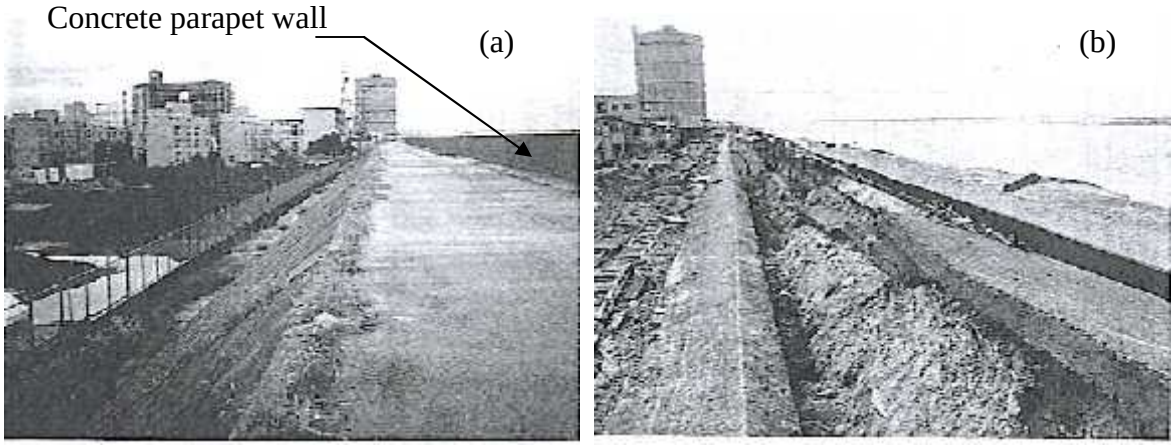

Figure A.100 Damage to the Torishima dike; (a) photograph before the earthquake; and (b) photograph after the earthquake, looking downstream (from Matsuo 1996)

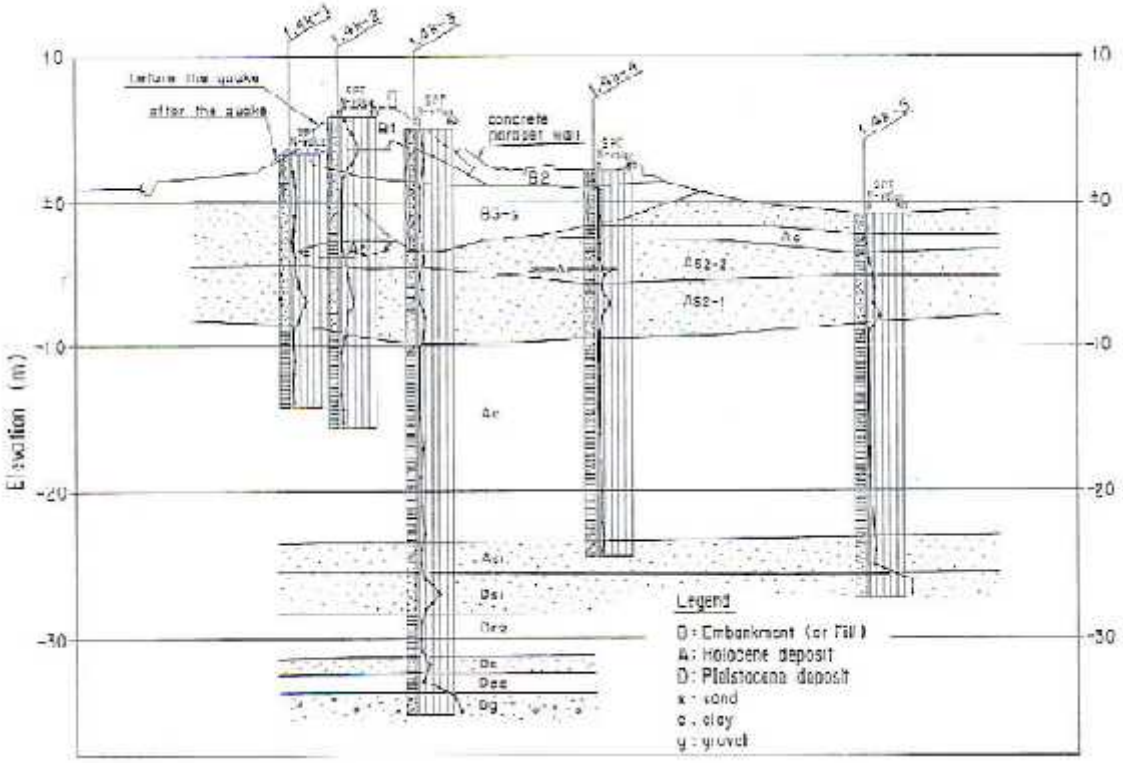

Figure A.101 Pre- and post-failure geometries of Torishima dike (from Matsuo 1996)

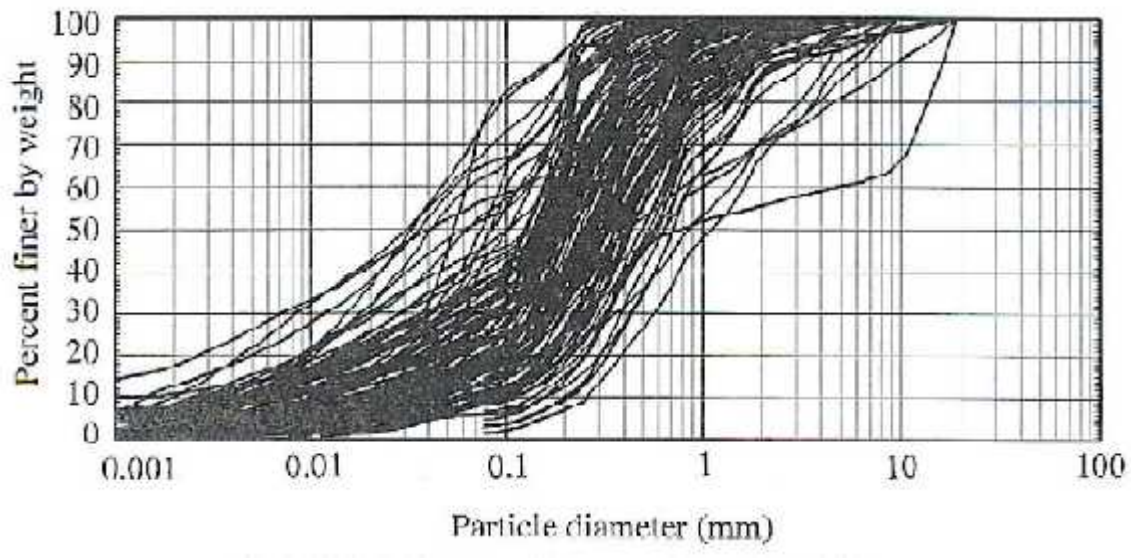

Figure A.102 Grain size distributions of Yodo-gawa River dike soils (from Matsuo 1996)

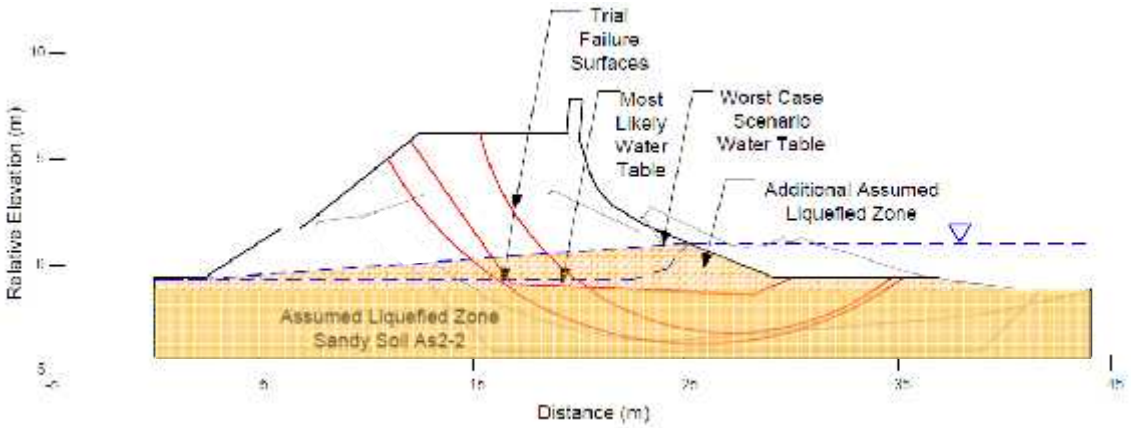

Figure A.103 Pre-failure cross-section of Torishima dike with trial failure surfaces

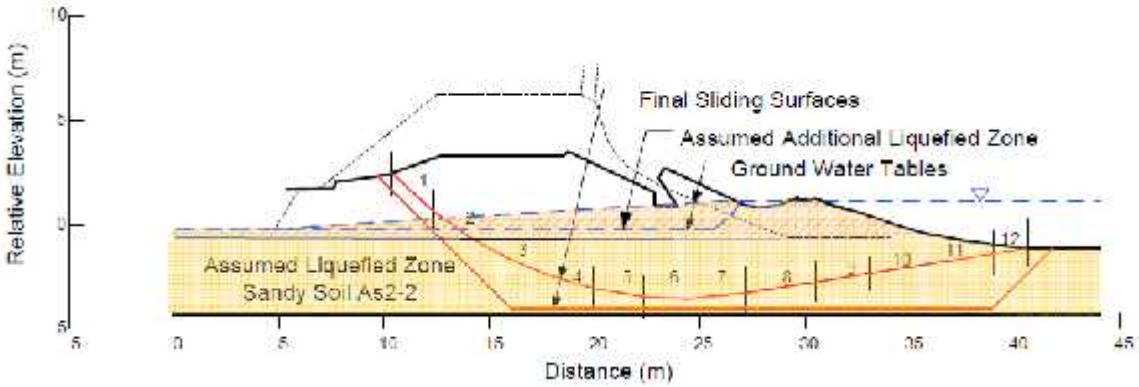

Figure A.104 Post-failure geometry of Torishima dike with analyzed critical circular and noncircular sliding surfaces and post-failure geometry segments

Figure A.105 Damage to the Nishijima dike (looking downstream). The Yodo-gawa River is seen on the left hand side of the photograph. The water seen in the right hand side is a tributary river (from Matsuo 1996).

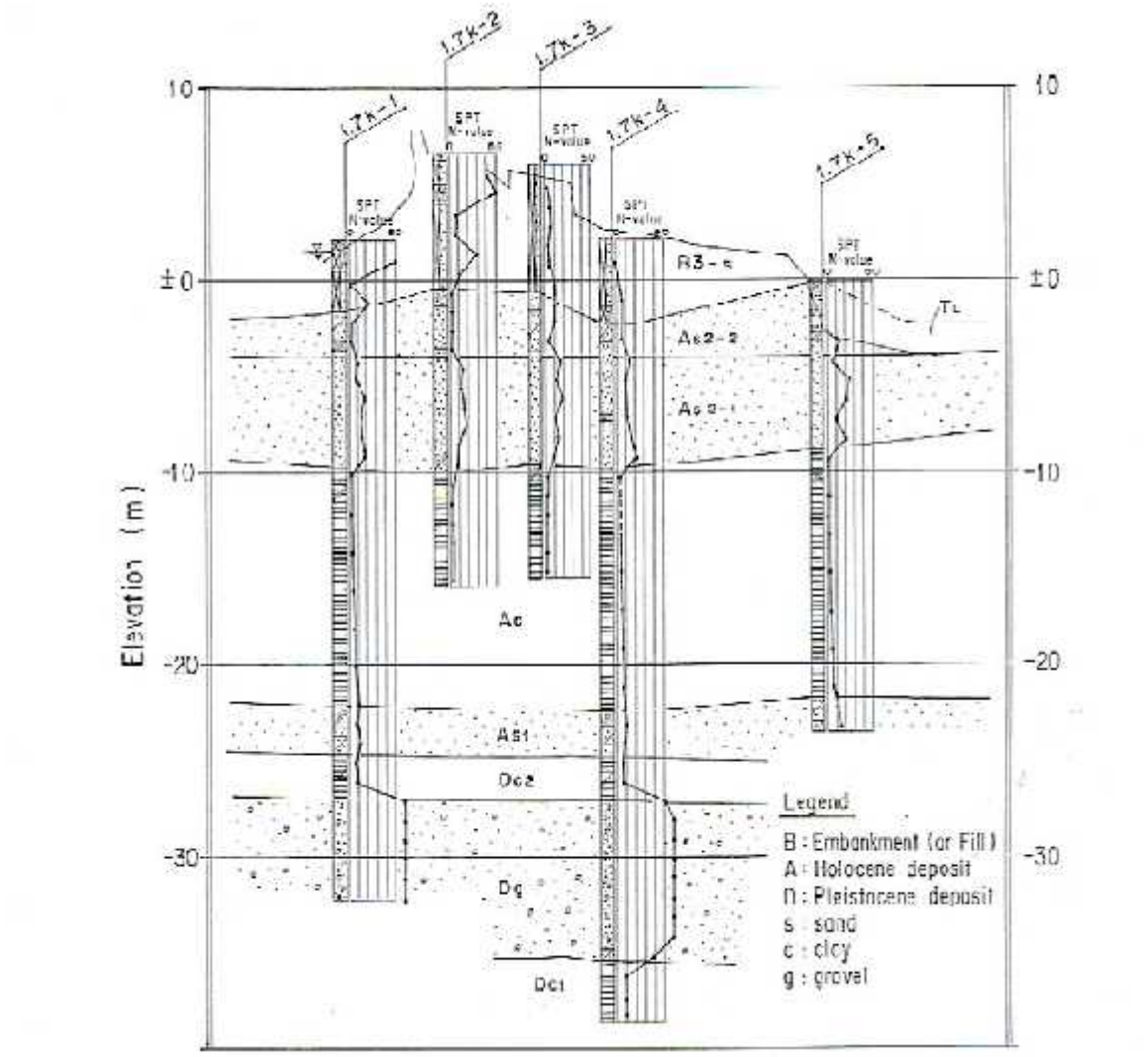

Figure A.106 Pre- and post-failure geometries of Nishijima dike with SPT bore logs and soil layers

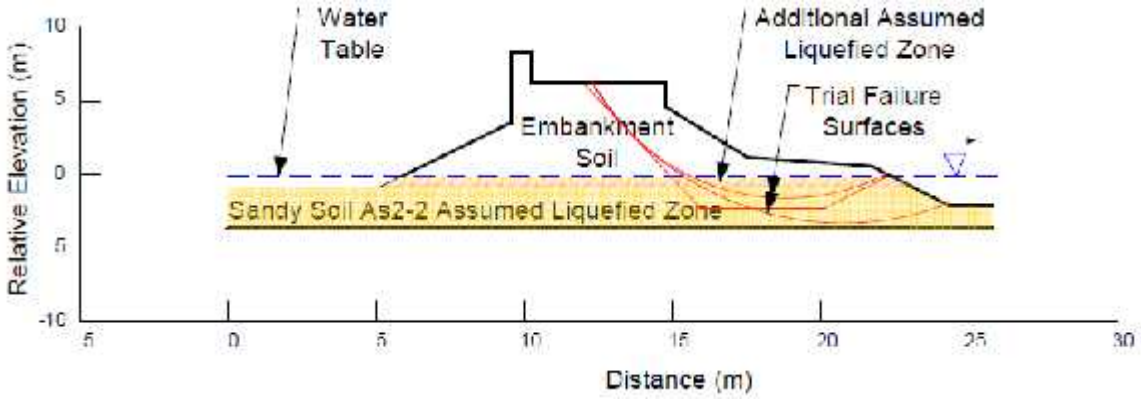

Figure A.107 Pre- failure geometry of Nishijima dike with trial initial failure surfaces

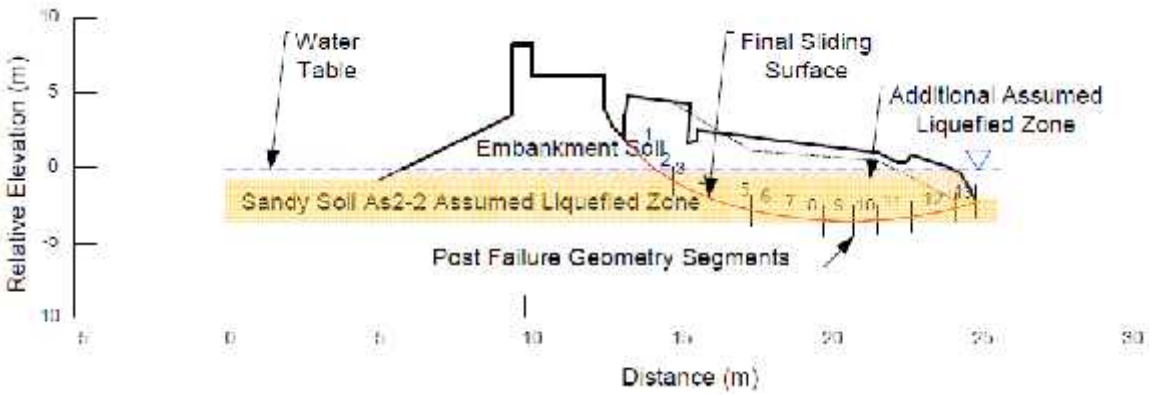

Figure A.108 Post-failure geometry of Nishijima dike with critical circular sliding surface

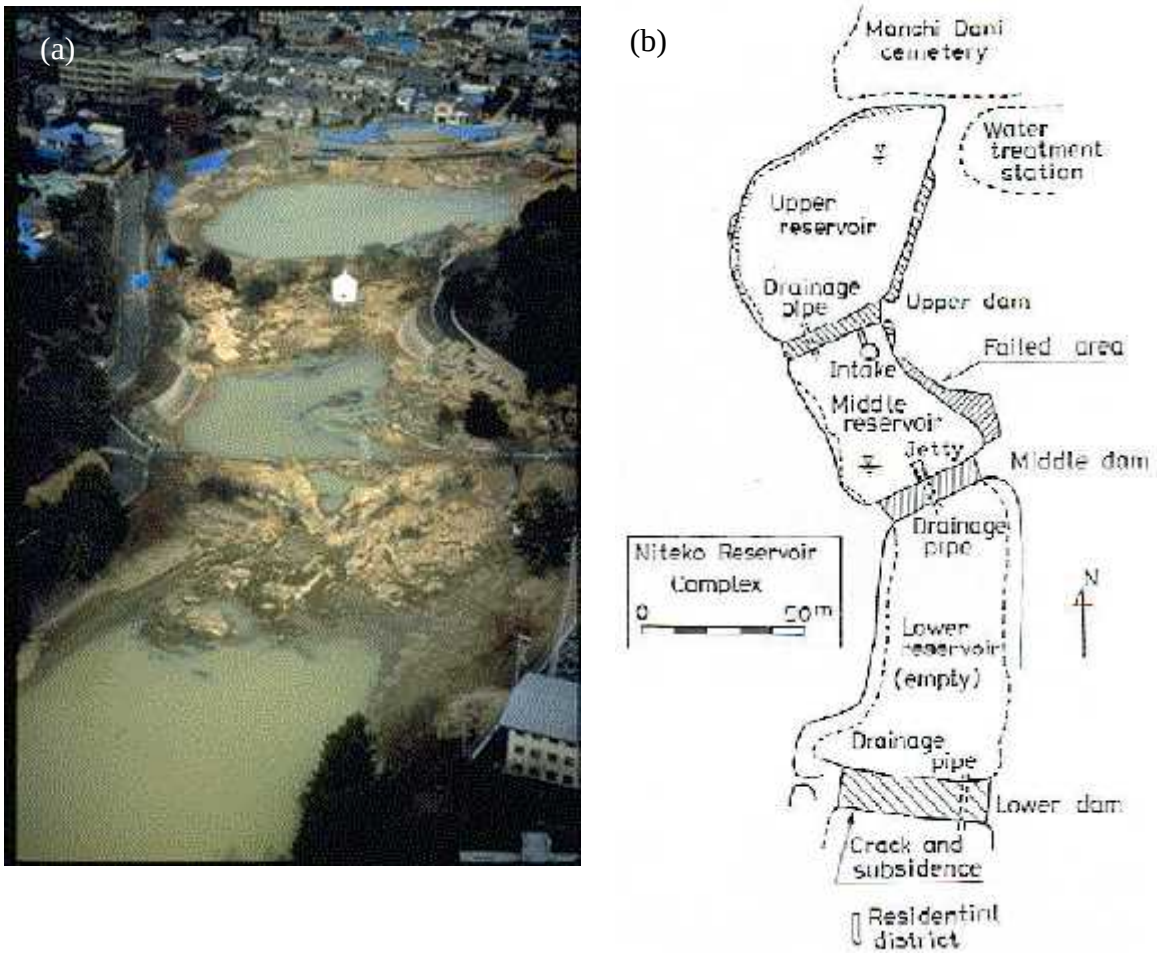

Figure A.109 (a) Aerial photograph of the flow failures at the Upper and Middle Niteko dams (from Akai et al. 1995); (b) Plan view of Niteko reservoir complex (from Towhata et al. 1996)

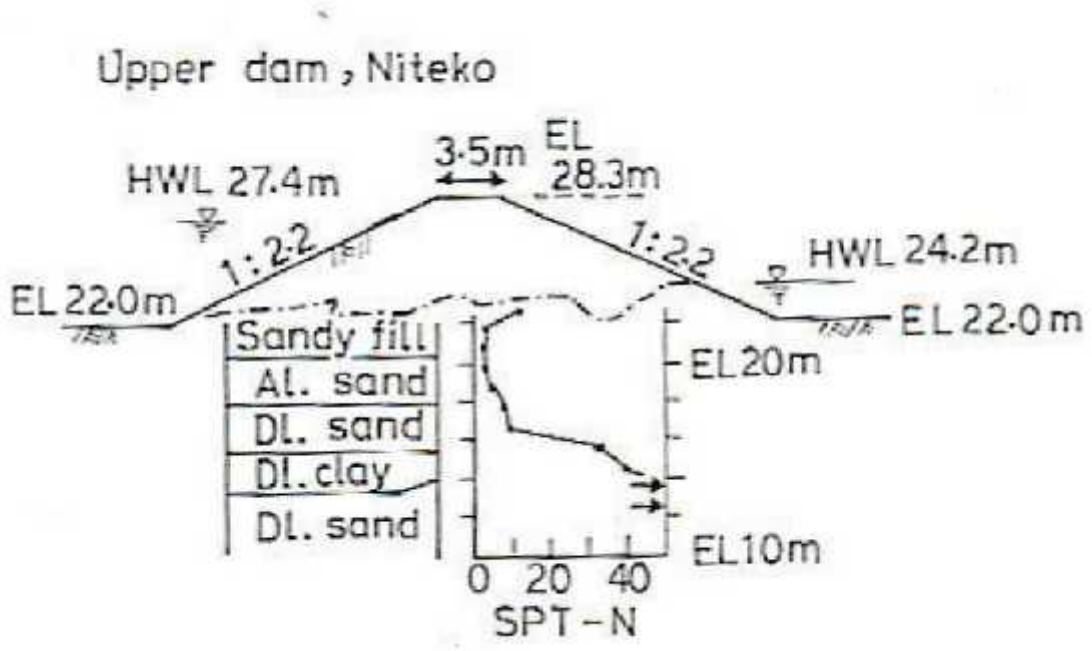

Figure A.110 Pre- and post-failure geometries of Upper Niteko dam with SPT bore log and soil layers (from Towhata et al. 1996)

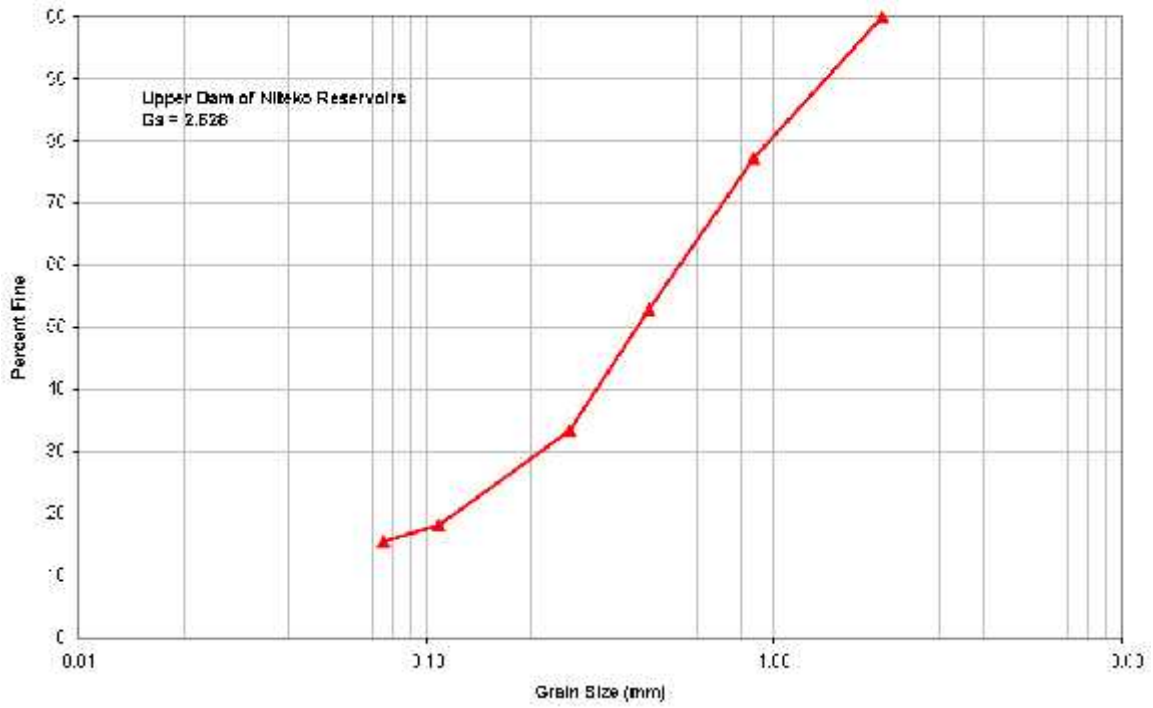

Figure A.111 Grain size distribution for fill soil at Niteko reservoir (reproduced from Towhata et al. 1996)

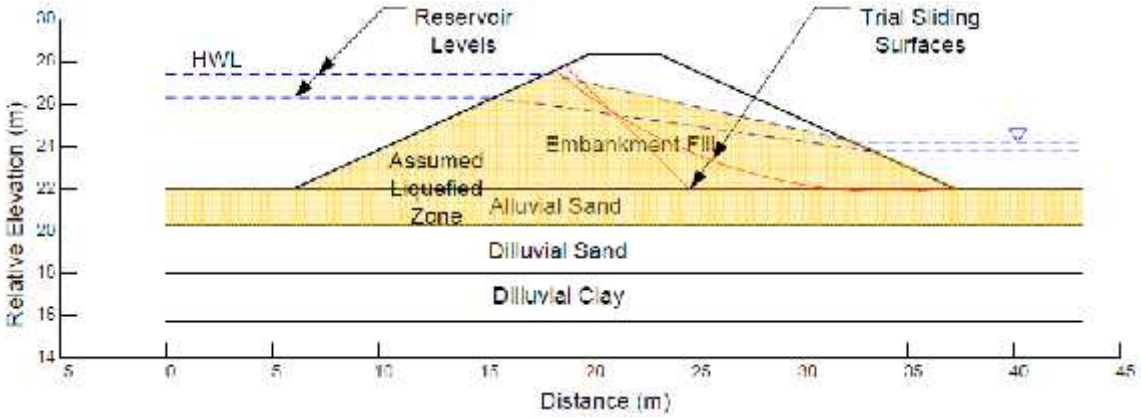

Figure A.112 Pre-failure geometry of Upper Niteko dam with trial circular and noncircular surfaces analyzed in this study

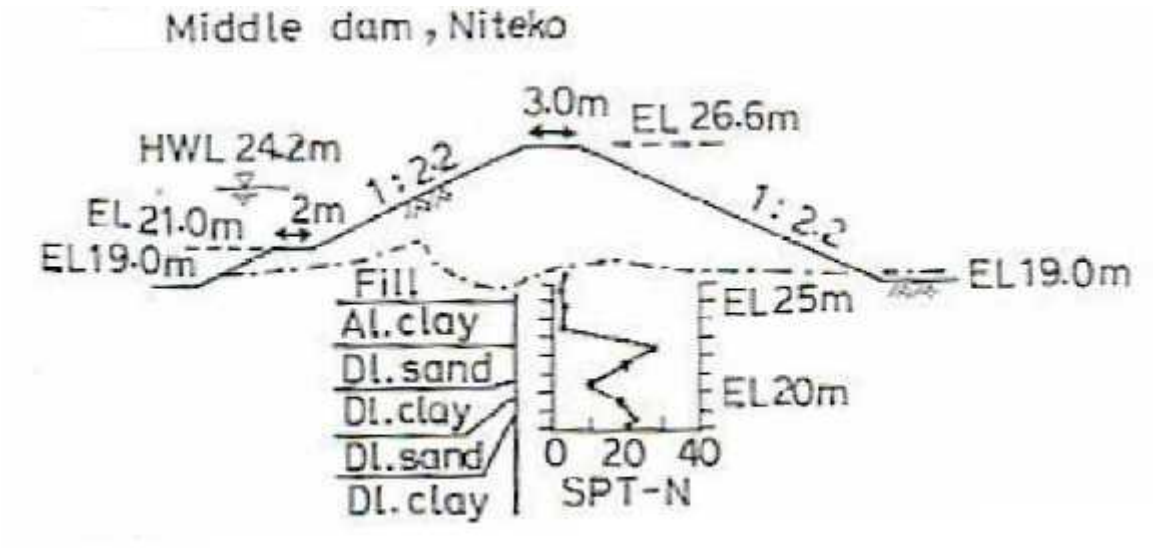

Figure A.113 Pre- and post-failure geometries of Middle Niteko dam with SPT bore log and soil layers (from Towhata et al. 1996)

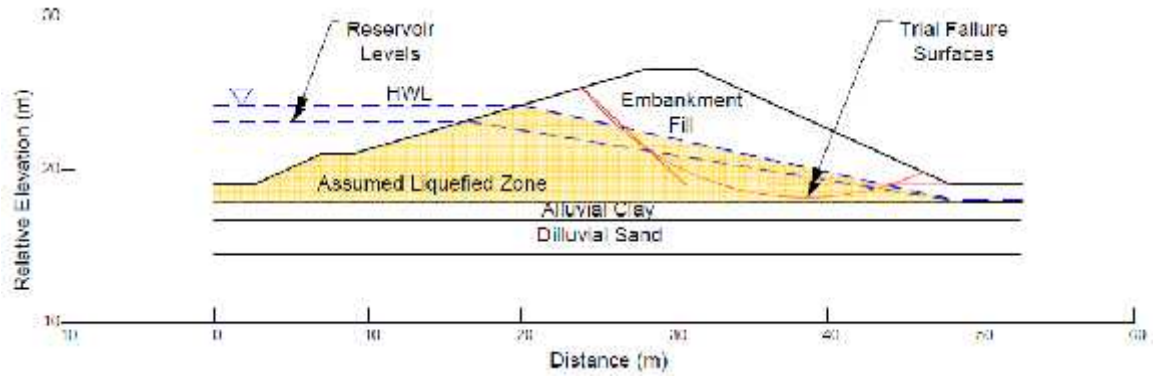

Figure A.114 Pre-failure geometry of Middle Niteko dam with critical circular and noncircular surfaces analyzed in this study

Figure A.115 (a) Aerial photograph of Nikawa landslide; (b) plan view of Nikawa landslide (Sassa et al. 2004, Sassa et al. 1995 [http://www.landslide-soc.org/publications/l-news/09/0906.htm])

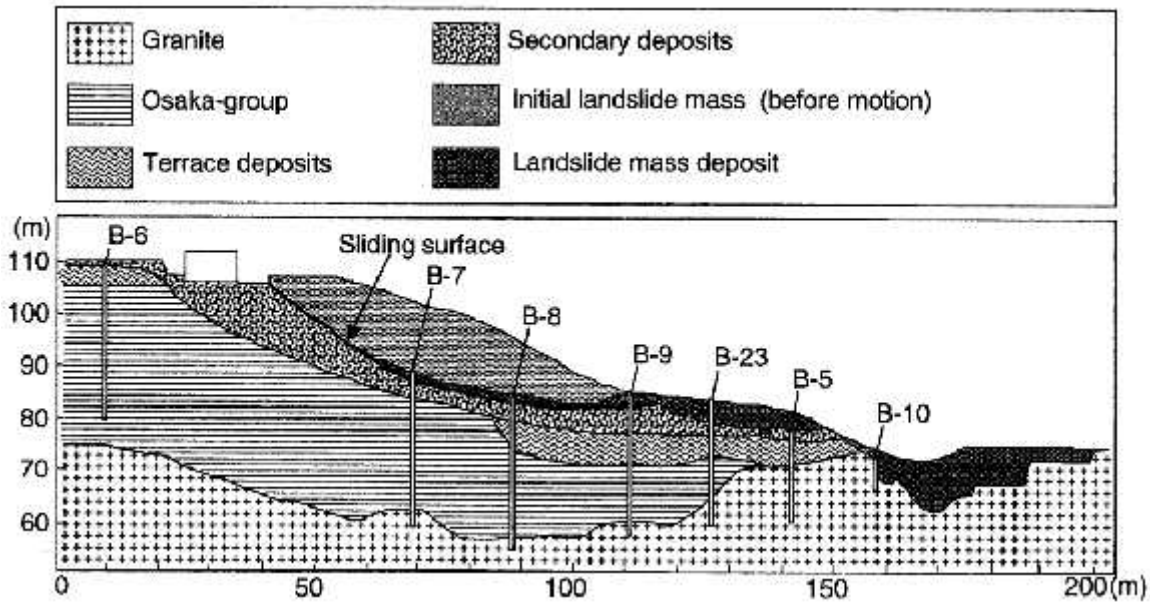

Figure A.116 Longitudinal cross-section of the Nikawa landslide (from Sassa et al. 1995, 1996)

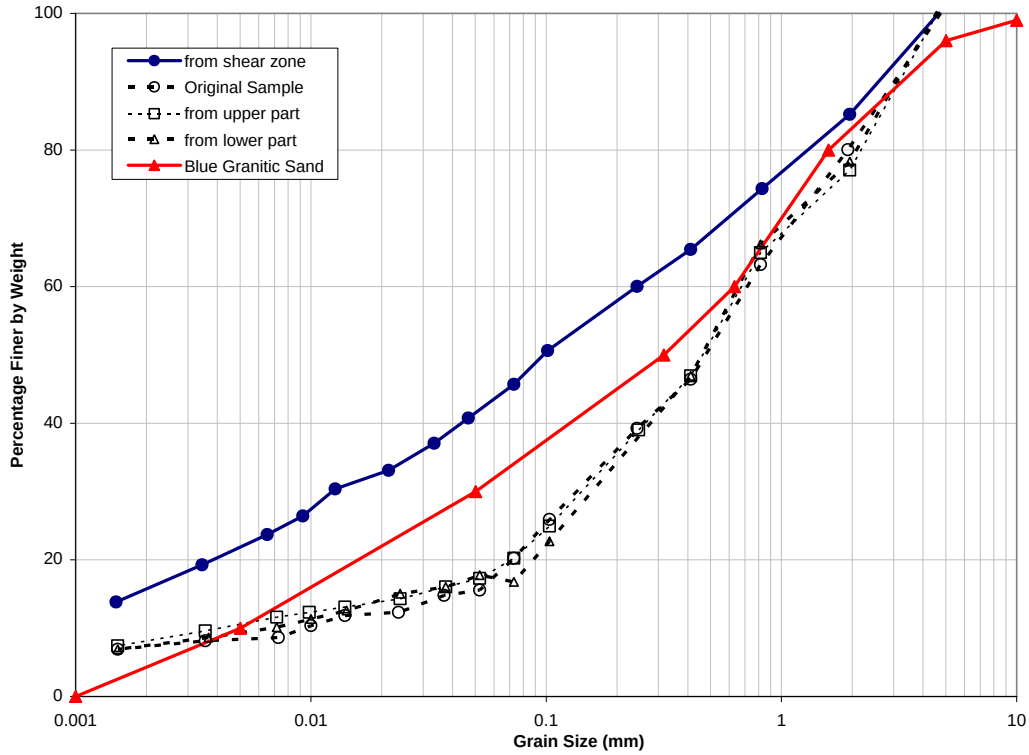

Figure A.117 Grain size distributions for a blue granitic sand found at the landslide site, an original sample (retrieved from outside of the shear zone), a sample taken from the shear zone, and specimens taken from ring shear tests performed by Sassa et al. (1995). One specimen was taken from the upper portion of the split ring and one specimen from the lower portion of the split ring. The sample was sheared to a displacement of 42 m at a normal shear stress of 196 kPa and a shear speed of 3 mm/sec.

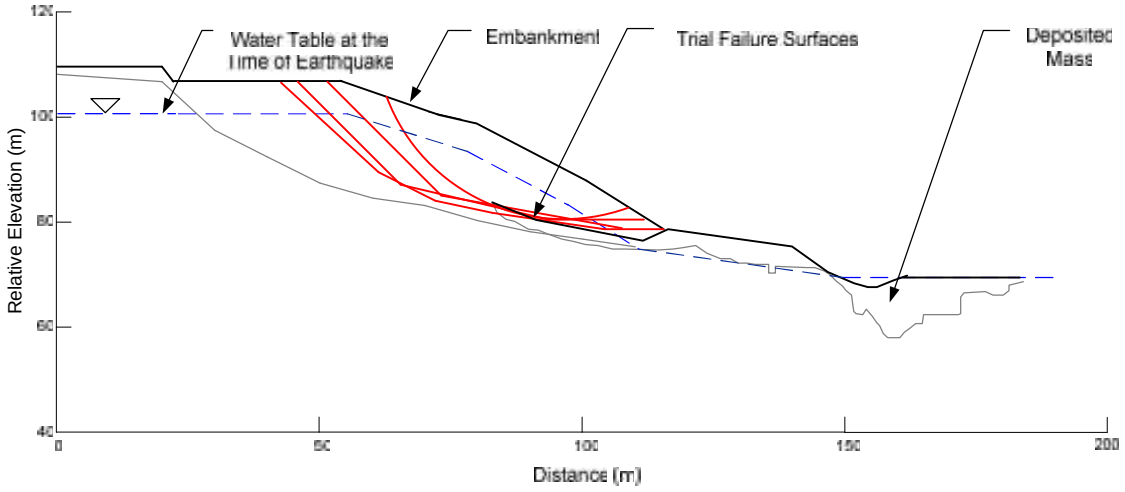

Figure A.118 Pre-failure cross-section of the Nikawa landslide with trial failure surfaces

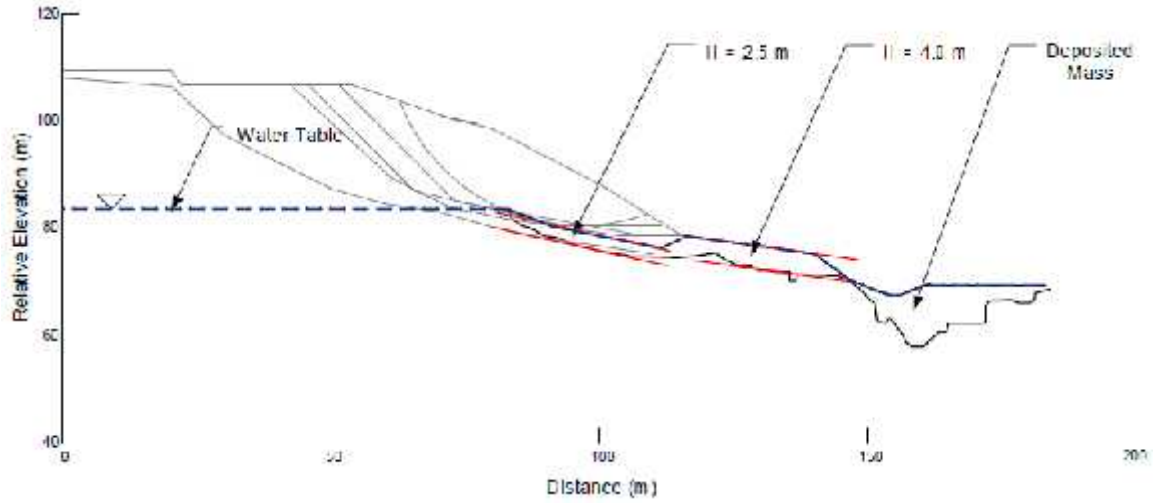

Figure A.119 Post-failure cross-section of the Nikawa landslide with infinite slope analysis sections

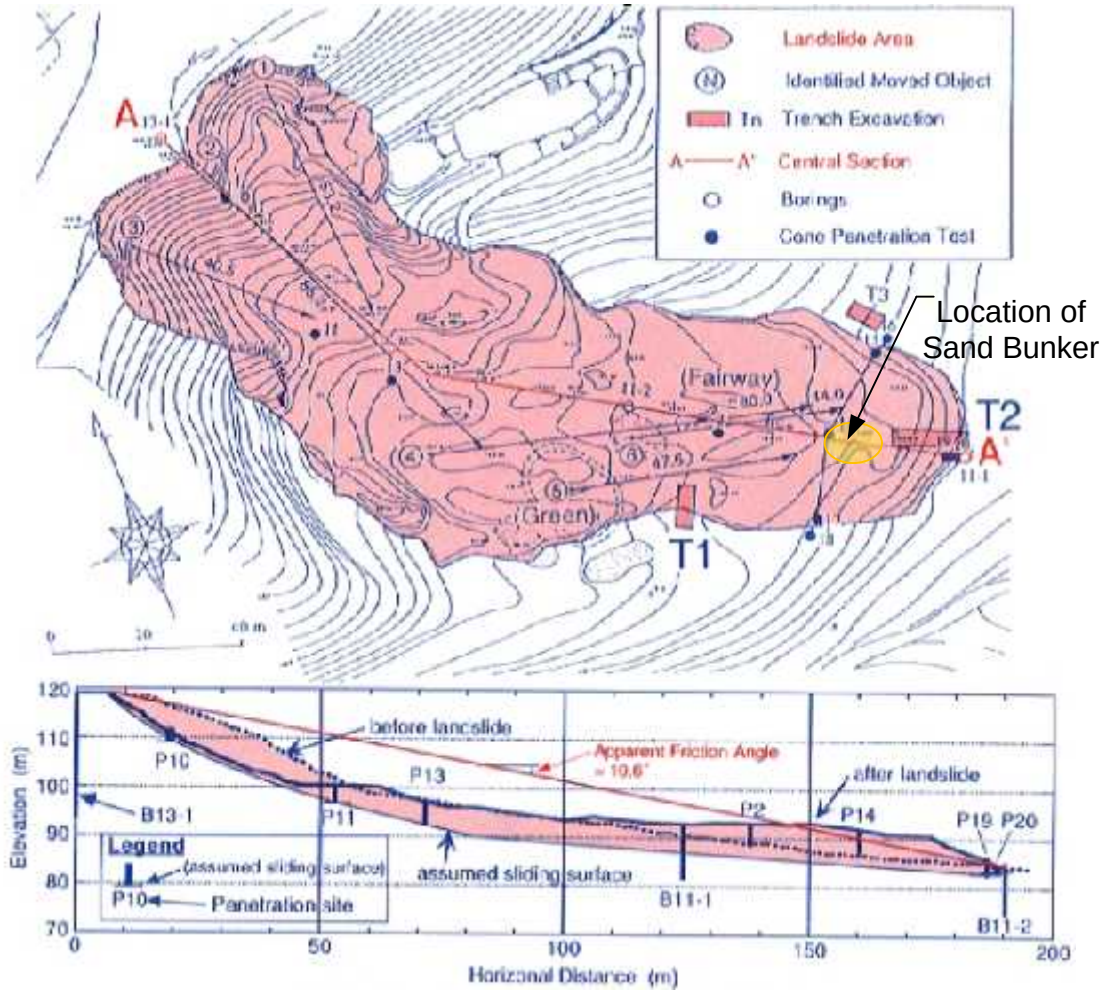

Figure A.120 Takarazuka landslide. (a) Plan view; (b) cross-section illustrating pre- and post-failure geometries and locations of boring logs and penetration tests (Sassa et al. 1995 [http://www.landslide-soc.org/publications/l-news/09/0909.htm])

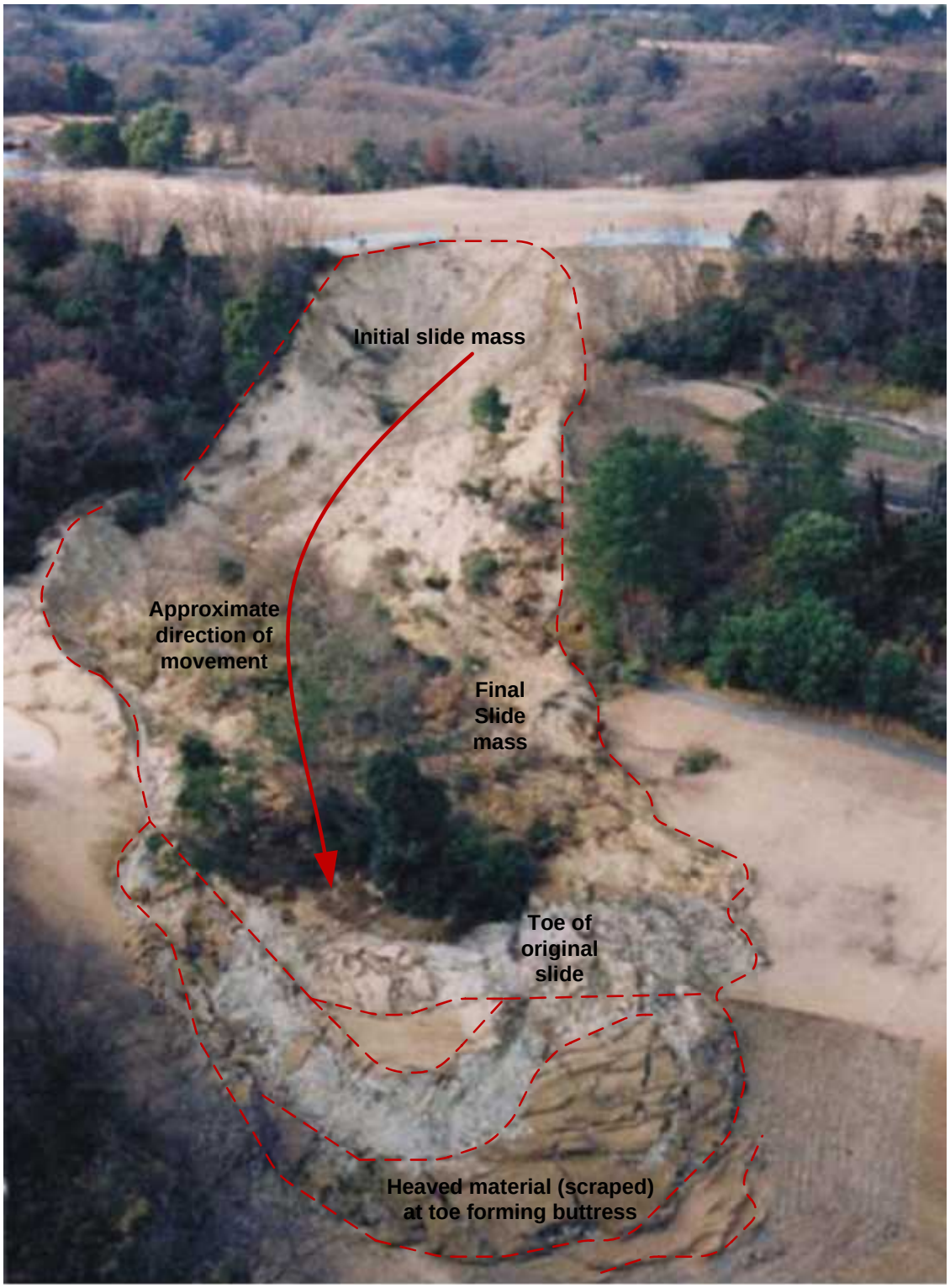

Figure A.121 Aerial view of the Takarazuka landslide illustrating location of initial and final sliding masses (modified from Sassa et al. 1996)

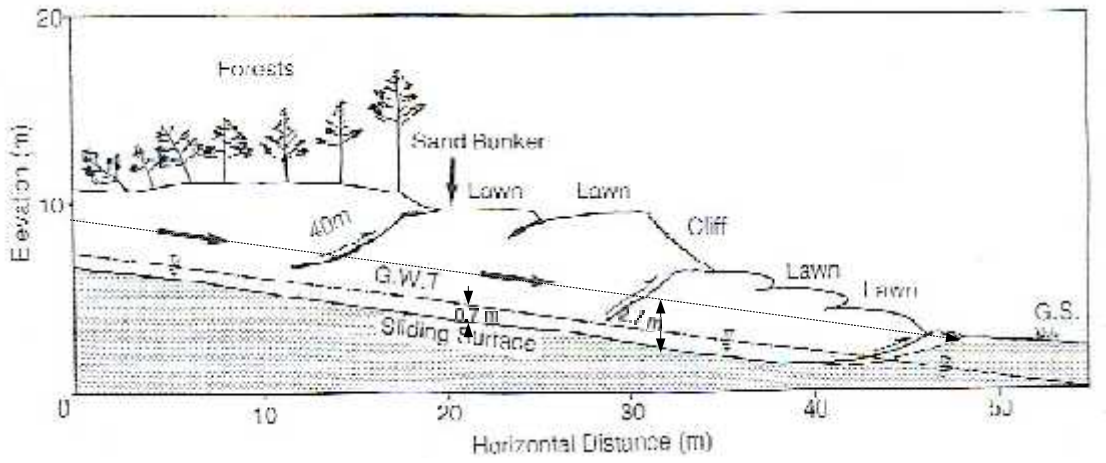

Figure A.122 Illustration of the longitudinal central section of the toe of the Takarazuka landslide estimated from trenches T1 and T2, as well as surface surveying (from Sassa et al. 1996)

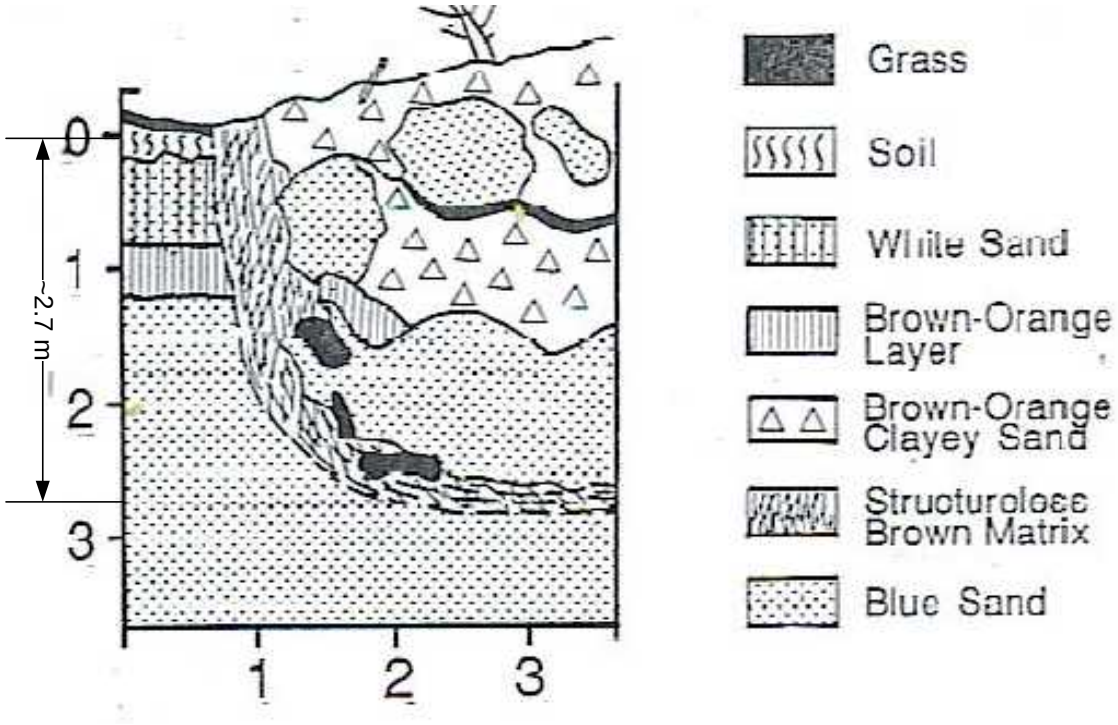

Figure A.123 Sketch of trench T1. The location of trench T1 is illustrated in Figure A.120 (from Sassa et al. 1996).

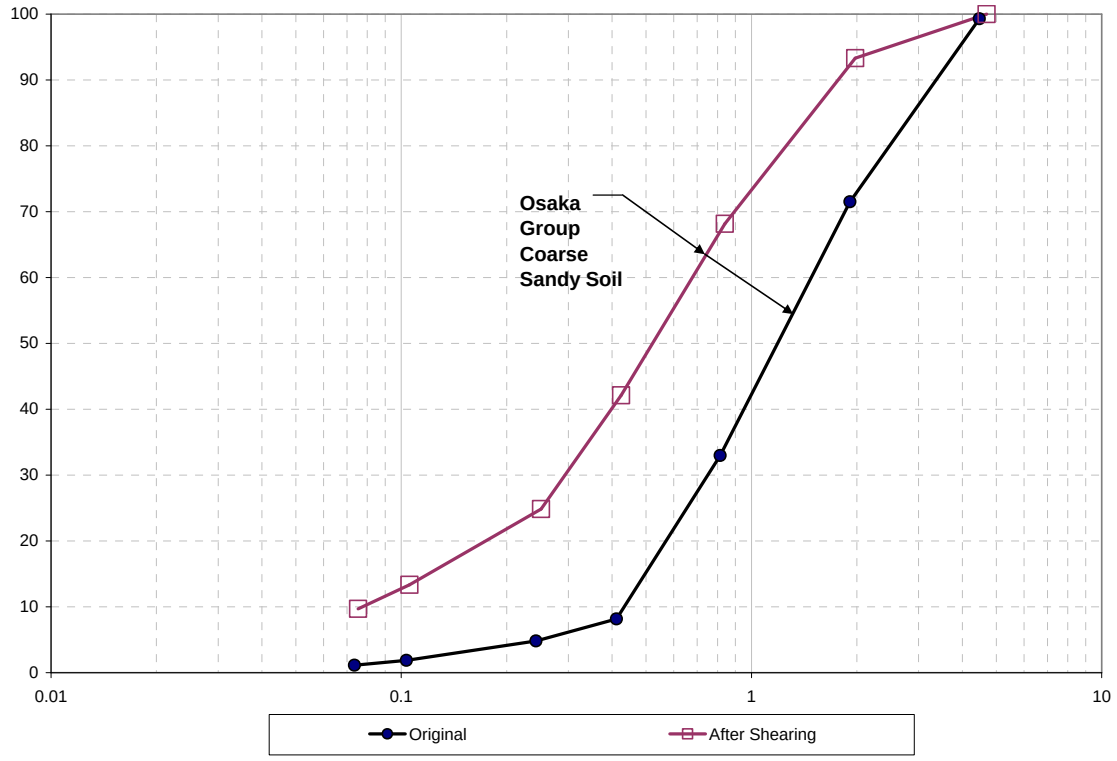

Figure A.124 Grain size distributions of specimens taken from the Takarazuka landslide site (data from Okada et al. 2004 and 2005).

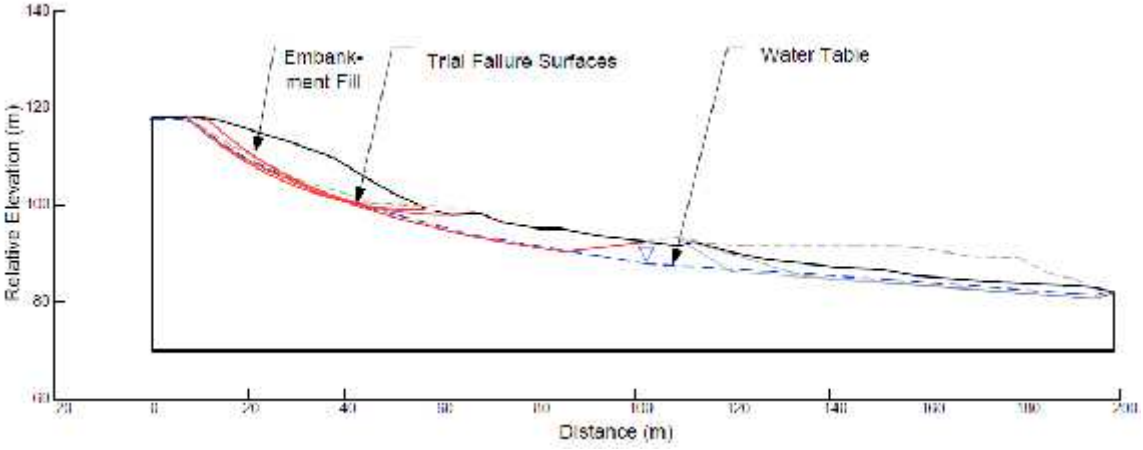

Figure A.125 Pre-failure geometry of the Takarazuka landslide with trial initial failure surfaces analyzed in this study

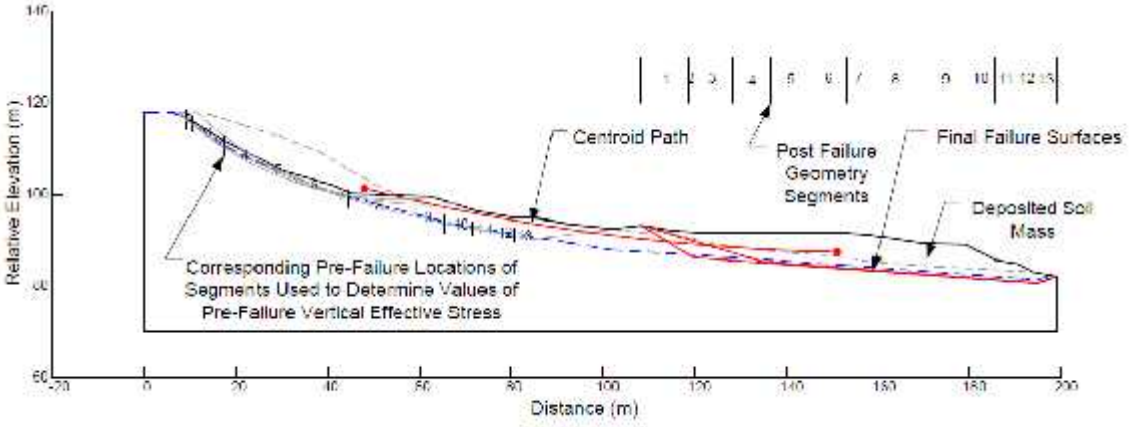

Figure A.126 Post-failure geometry of the Takarazuka landslide with trial failure surfaces analyzed in this study, and potential movement of the sliding mass center of gravity.

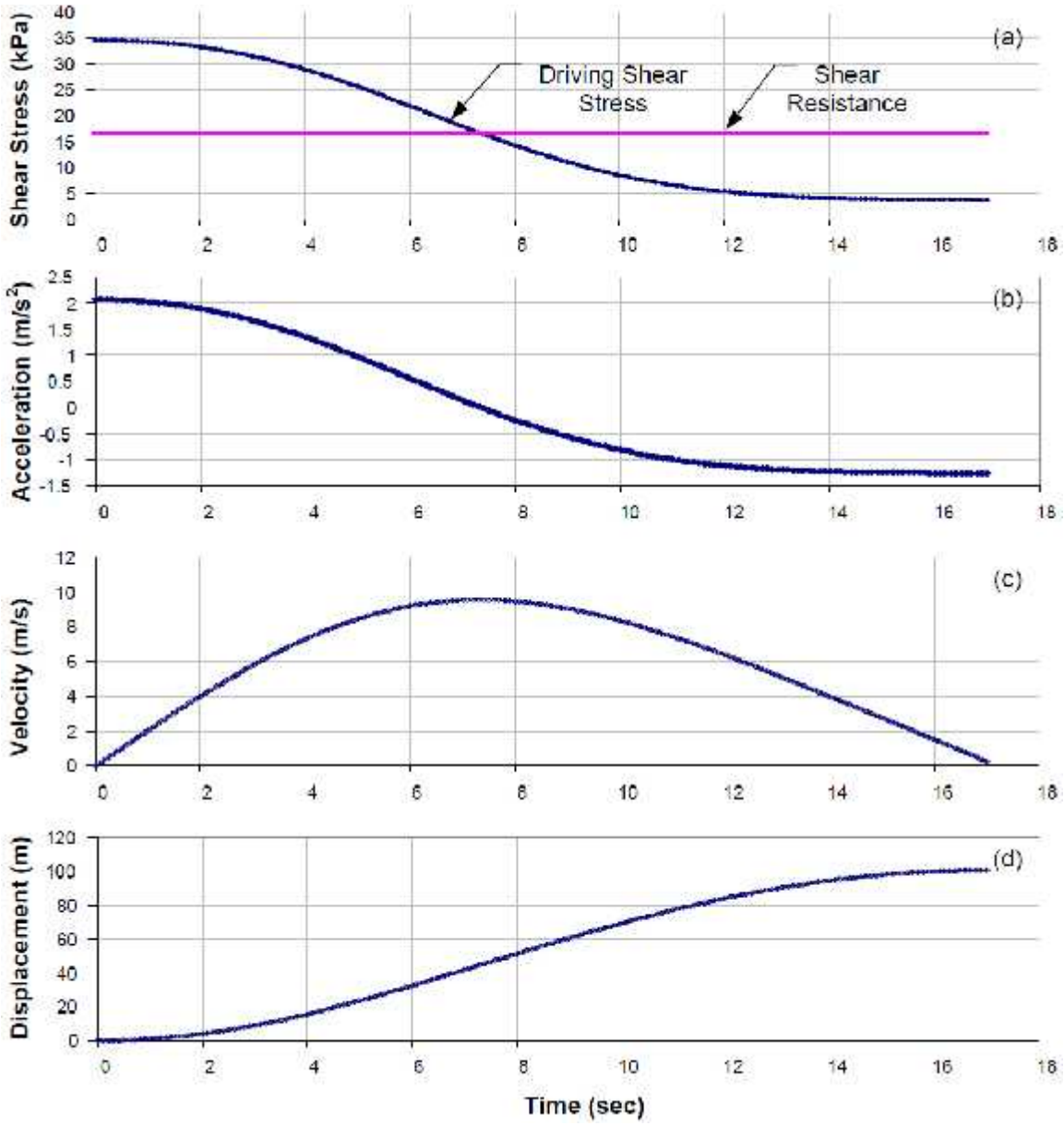

Figure A. 127 Kinetics analysis results of Takarazuka landslide

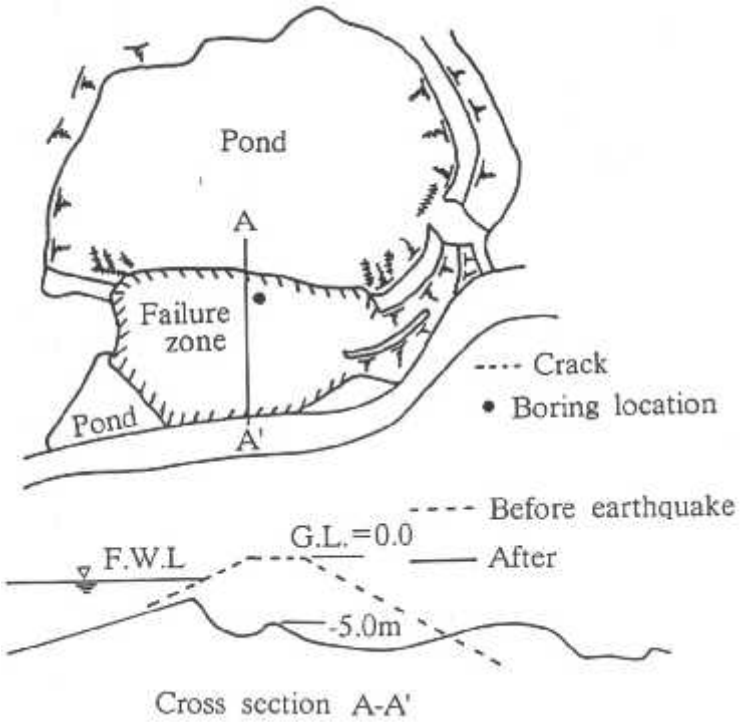

Figure A.128 General plan view of and cross-section through Idenoshiri Dam after the earthquake (from Tani 1996)

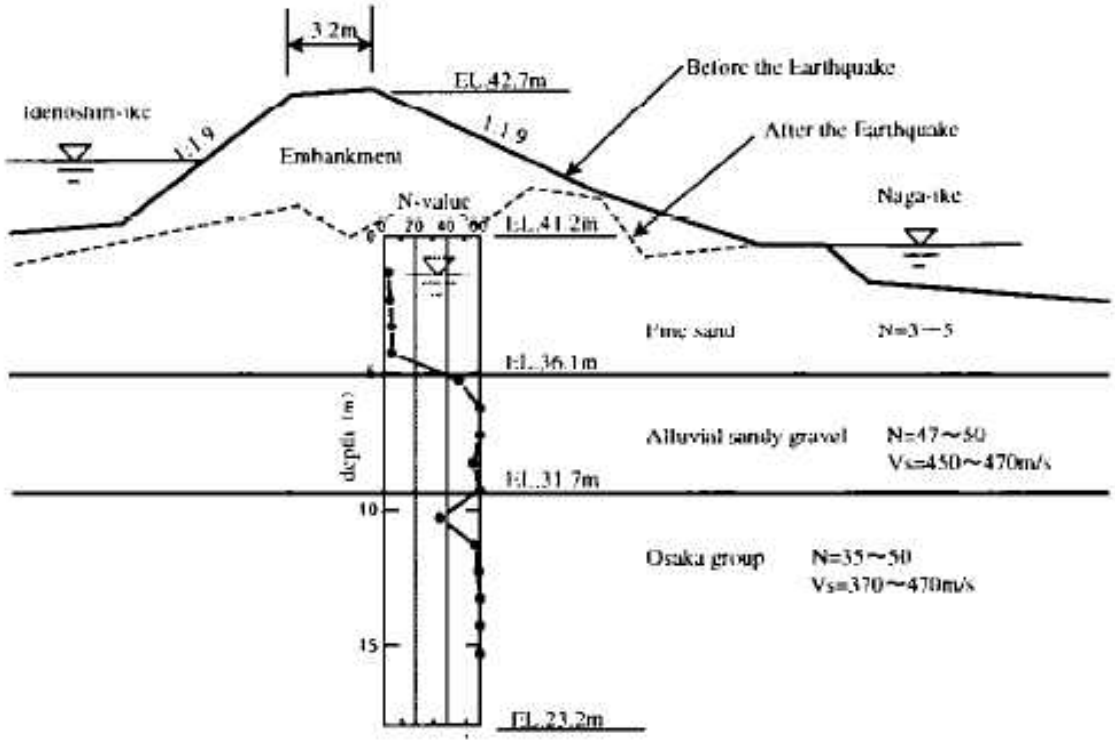

Figure A.129 Cross-section of Idenoshiri Dam with SPT borehole data and soil layers (from Uchida et al. 2001)

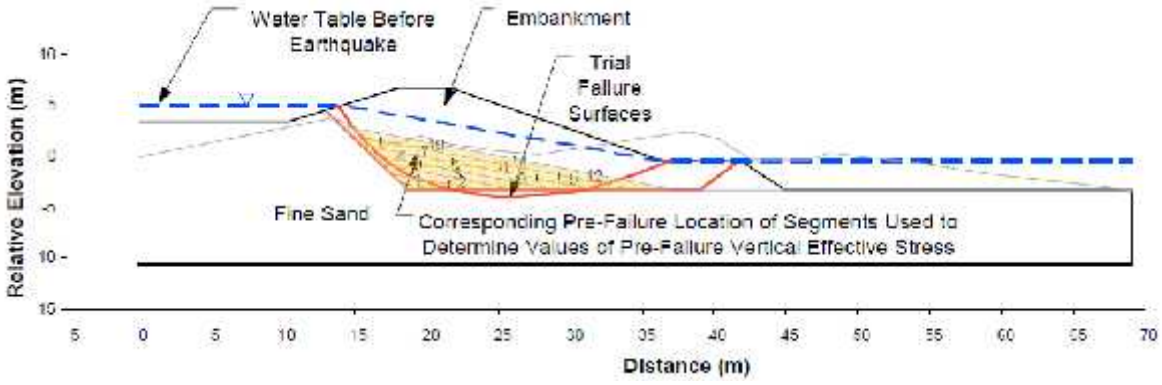

Figure A.130 Pre-failure geometry of Idenoshiri Dam with trial initial failure surfaces. Prefailure geometry is bold, and the post-failure geometry is grey.

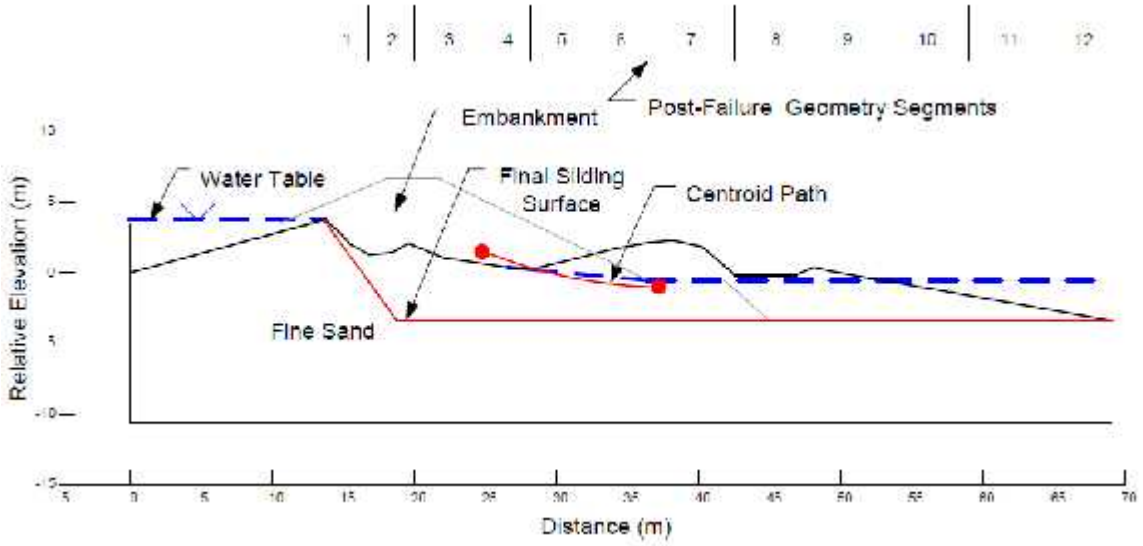

Figure A. 131 Post-failure geometry Idenoshiri Dam with final failure surface and possible center of gravity path

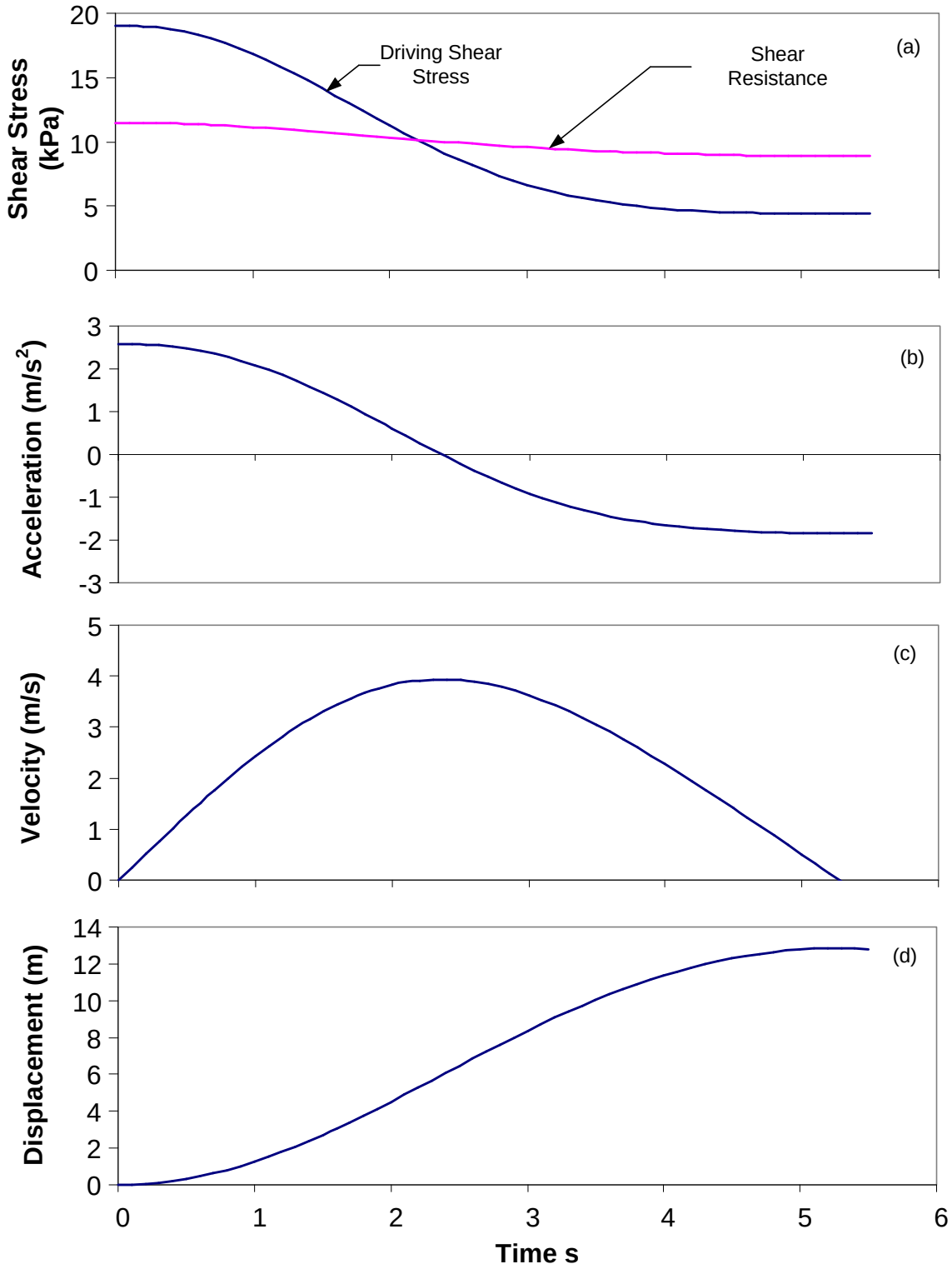

Figure A.132 Kinetics analysis results for Idenoshiri Dam

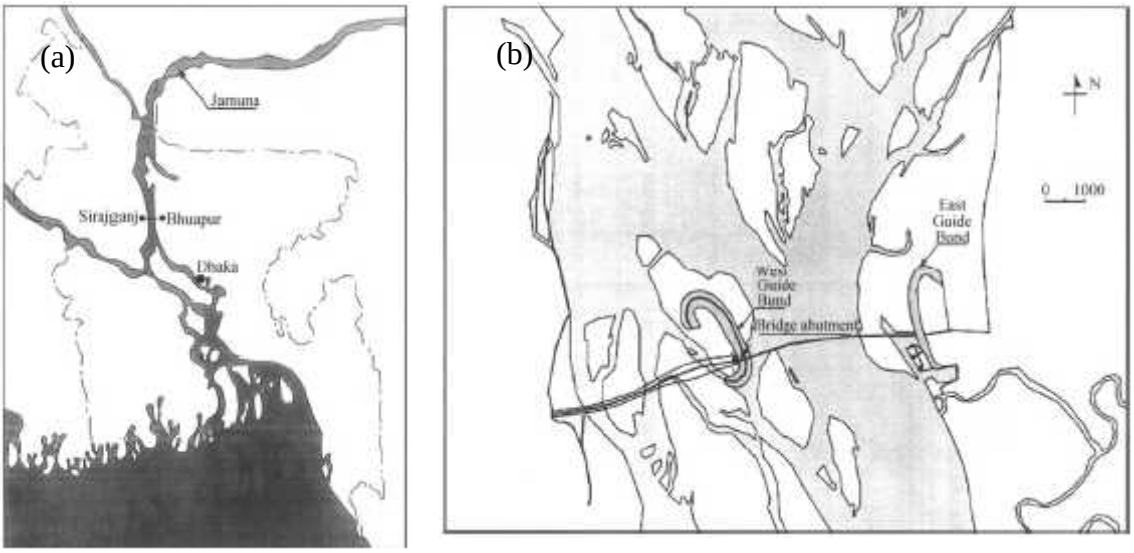

Figure A.133 Location maps of Jamuna Bangabandhu Bridge. (a) General location of Jamuna Bridge; and (b) locations of the east and west guide bunds (from Ishihara 2008)

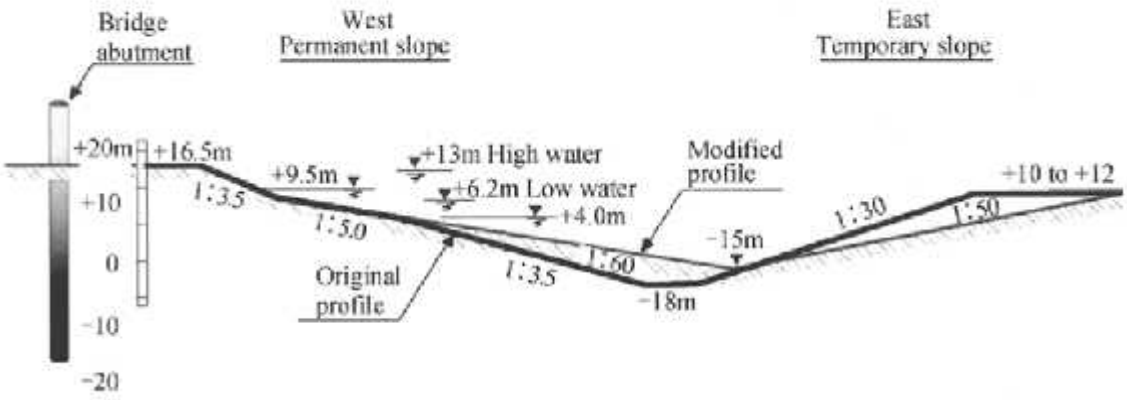

Figure A.134 East-west section through West Guide Bund Channel (from Hight et al. 1999)

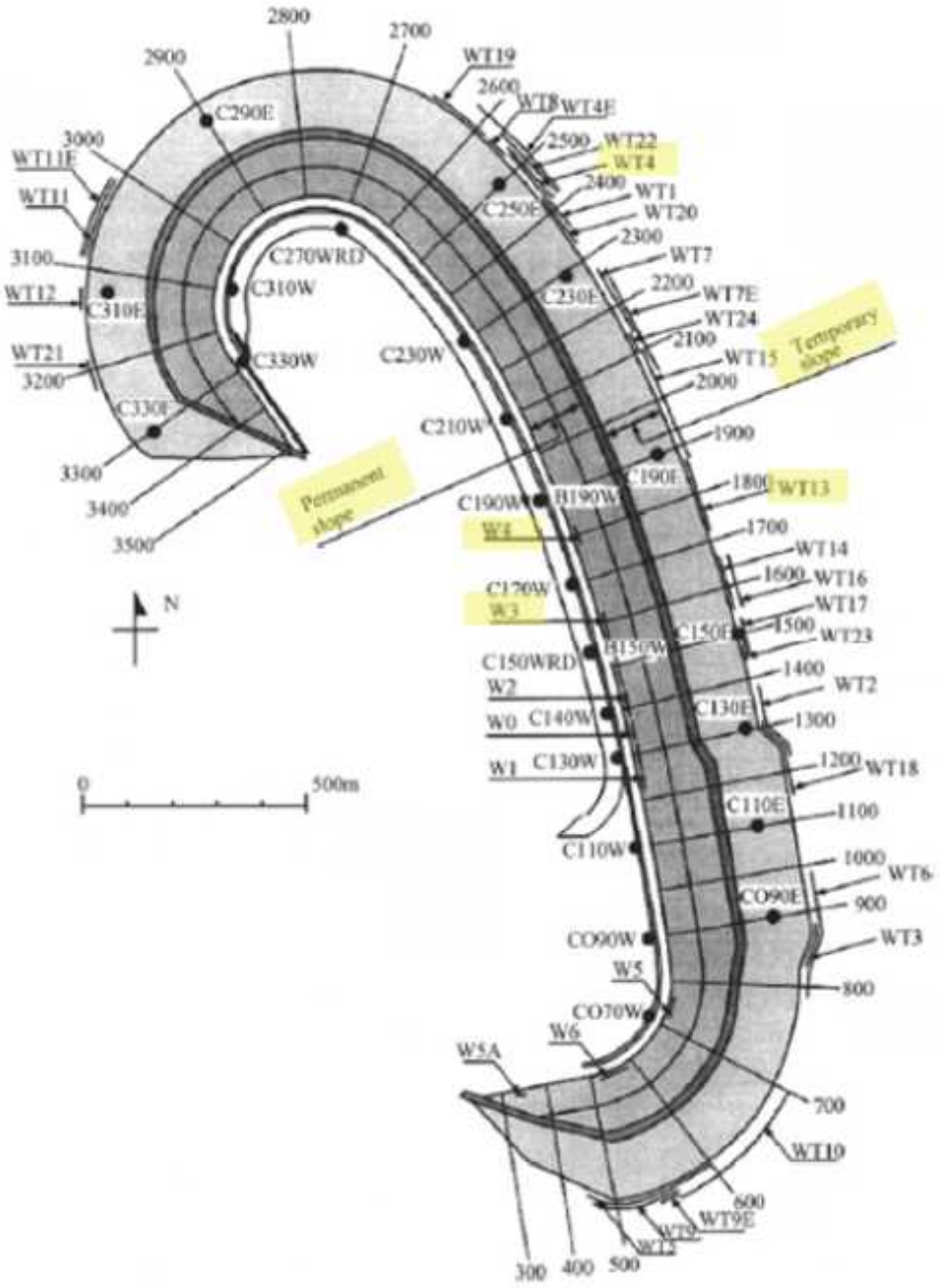

Figure A.135 Locations of slides in West Guide Bund of Jamuna River Bridge on temporary and permanent slopes. The slides analyzed in this study are highlighted. Black dots show the location of CPT performed after failure (from Ishihara 2008)

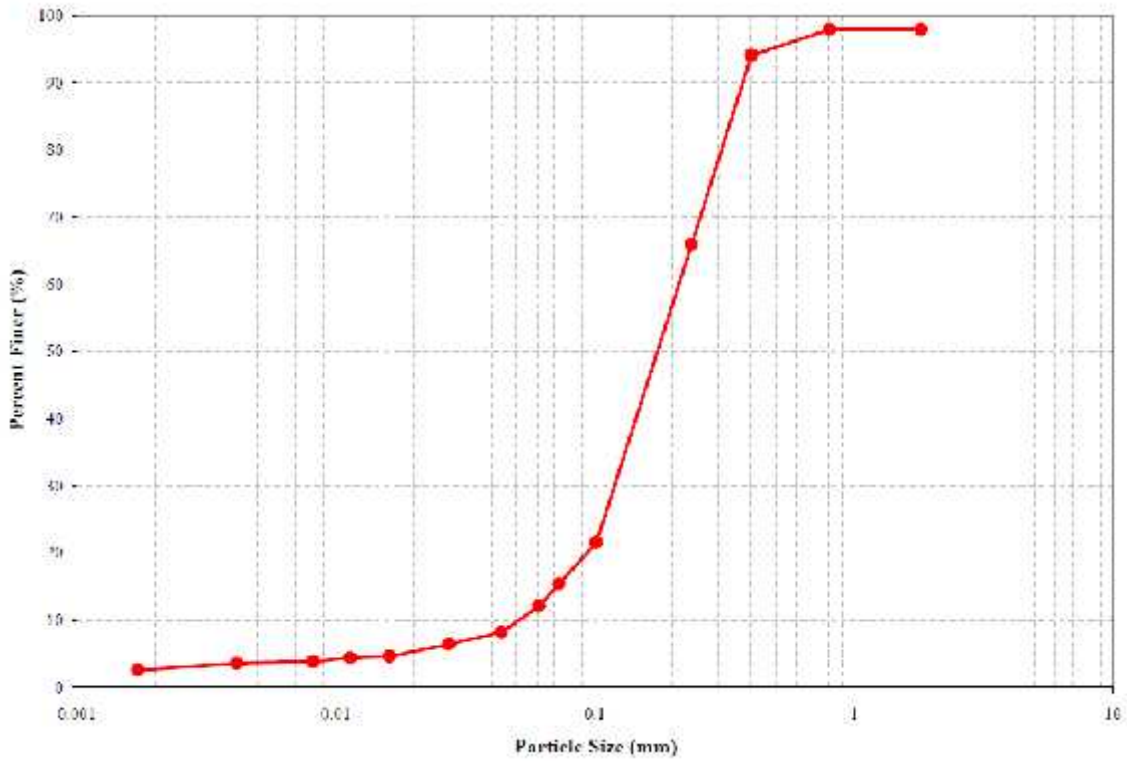

Figure A.136 Grain size distribution of the Jamuna River sand (from Ishihara 2008)

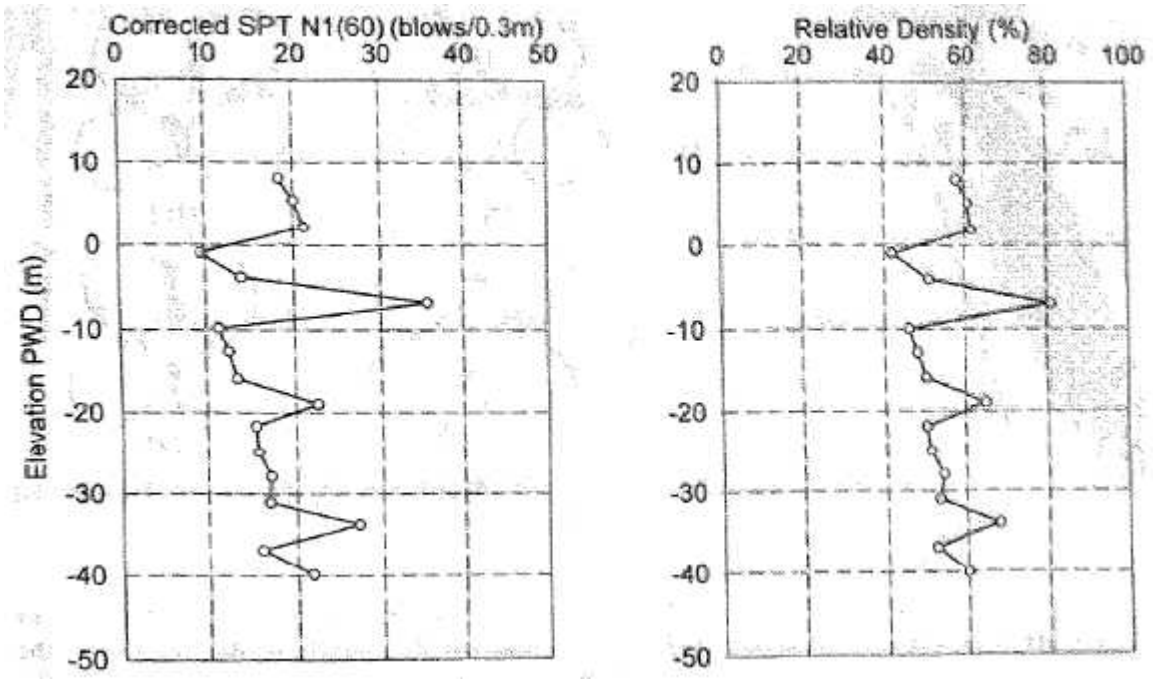

Figure A.137 Profiles of (a) SPT blow count; and (b) estimated relative density (from Hight et al. 1999)

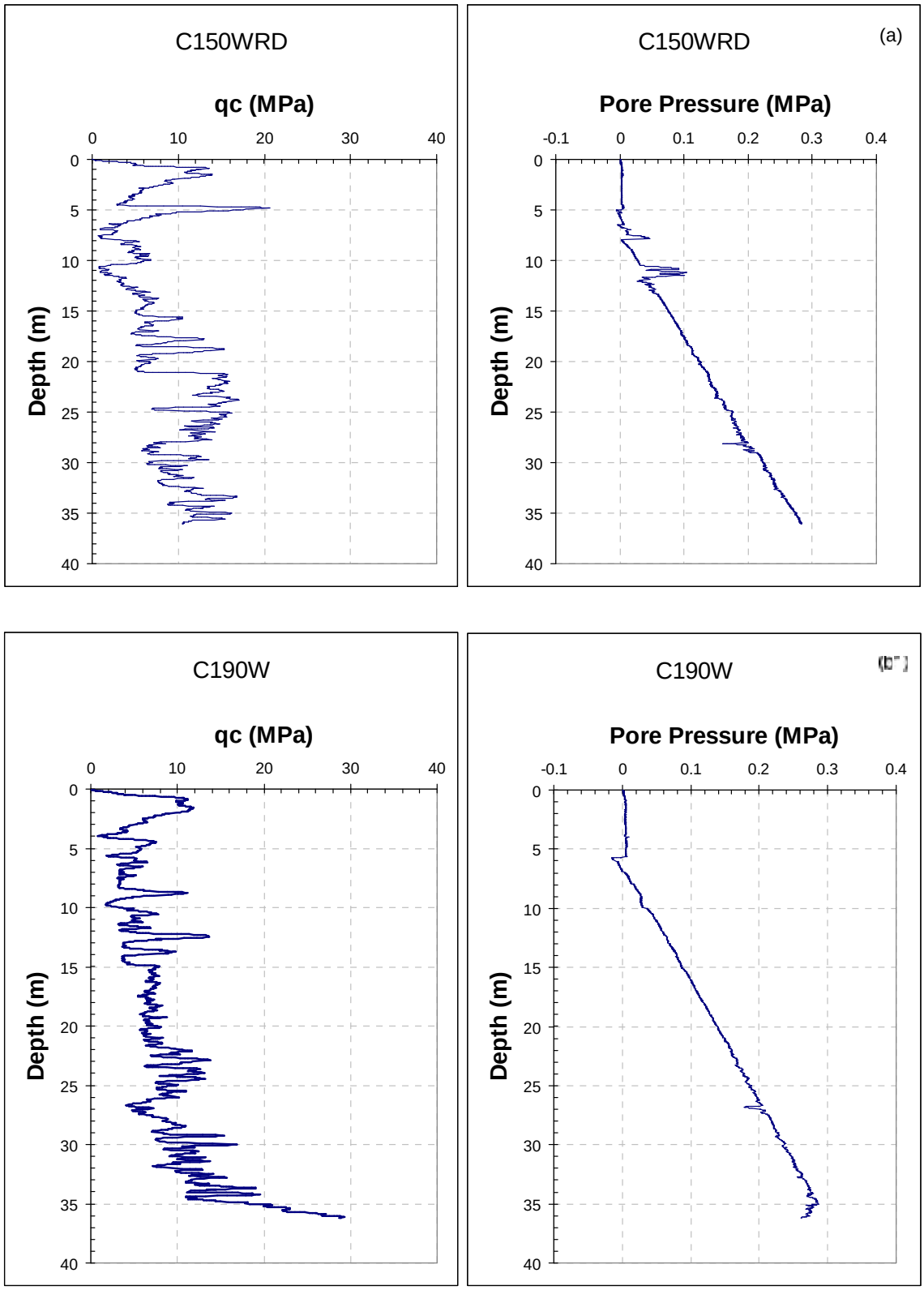

Figure A.138 CPTs conducted after the failures on the east and west banks of the West Guide Bund close to: (a) section 1500W3; (b1 and b2) section 1800W4; (c) section 1800WT13; and (d) section 2500WT4 that failed during dredging (data provided by Prof. Yoshimine)

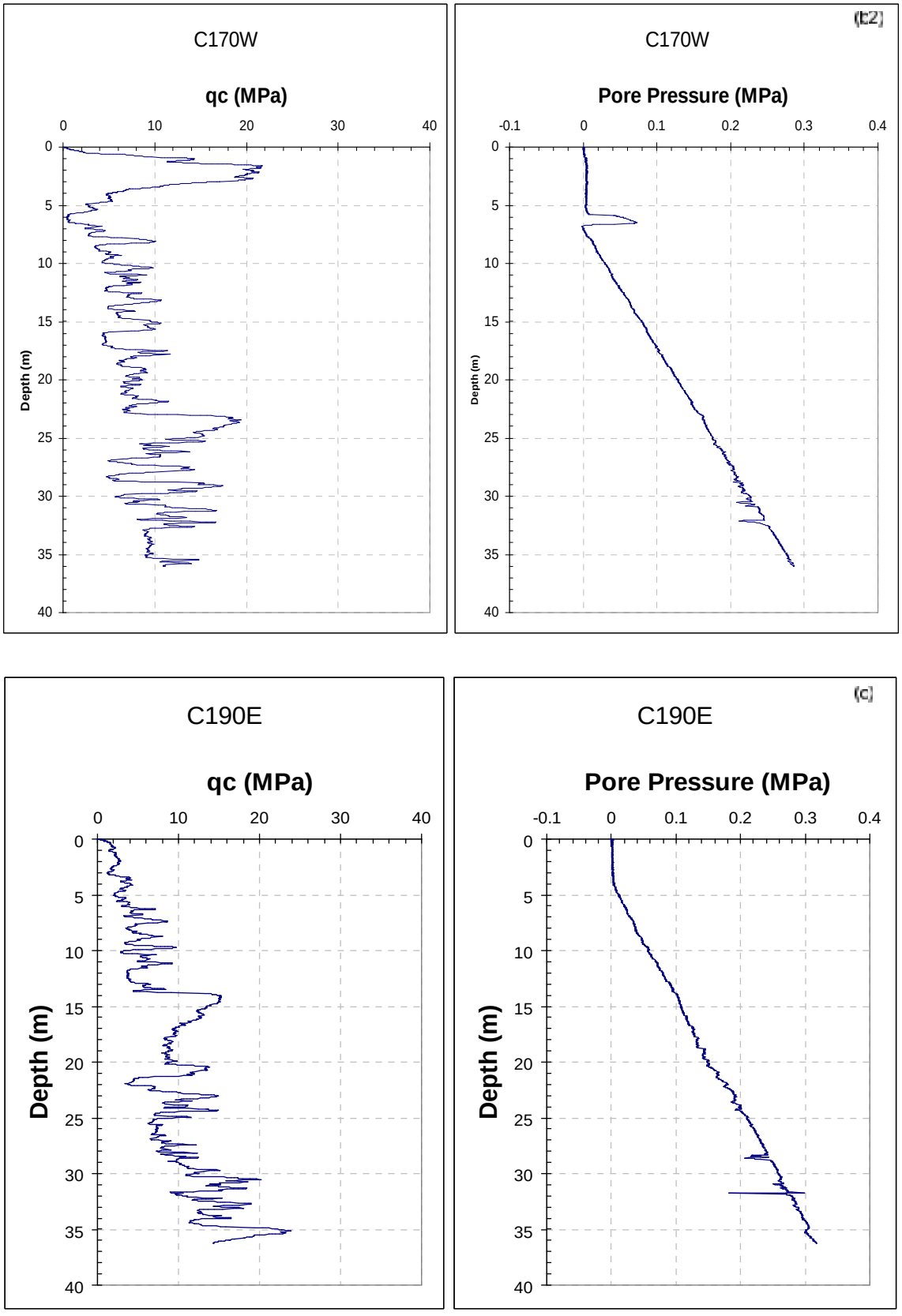

Figure A.138 Continued

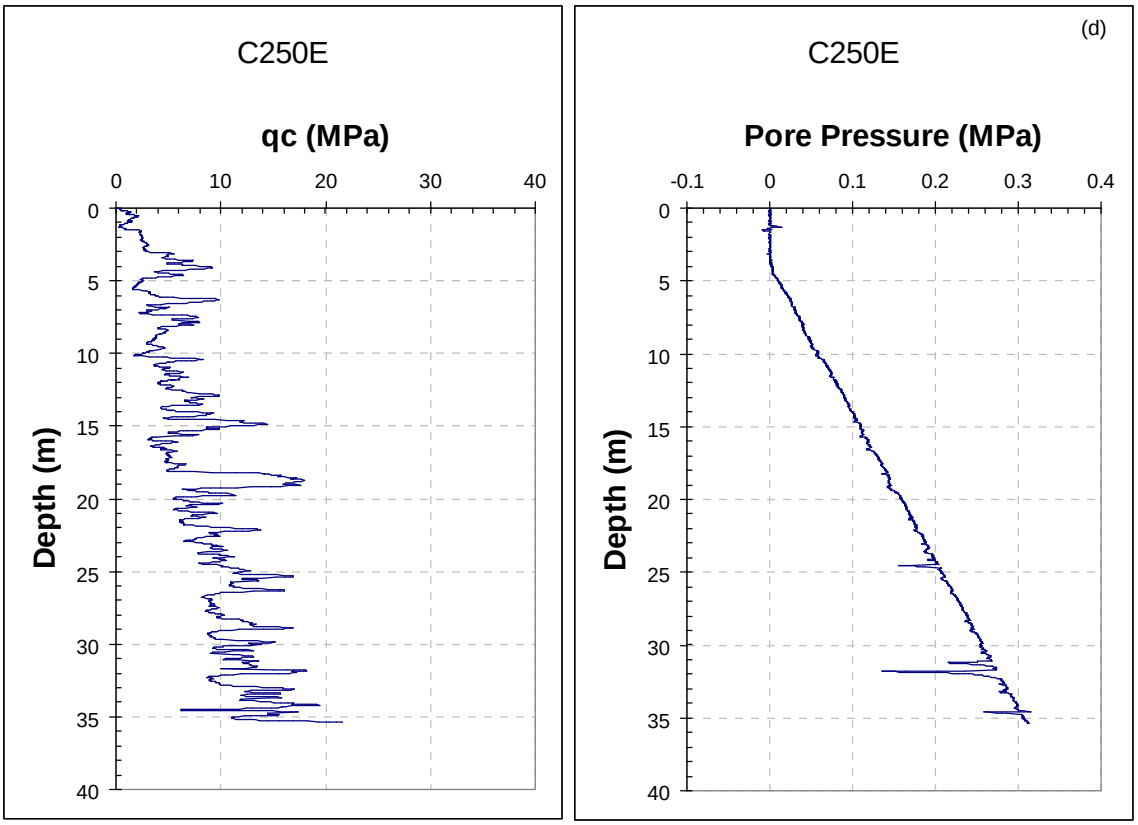

Figure A.138 Continued

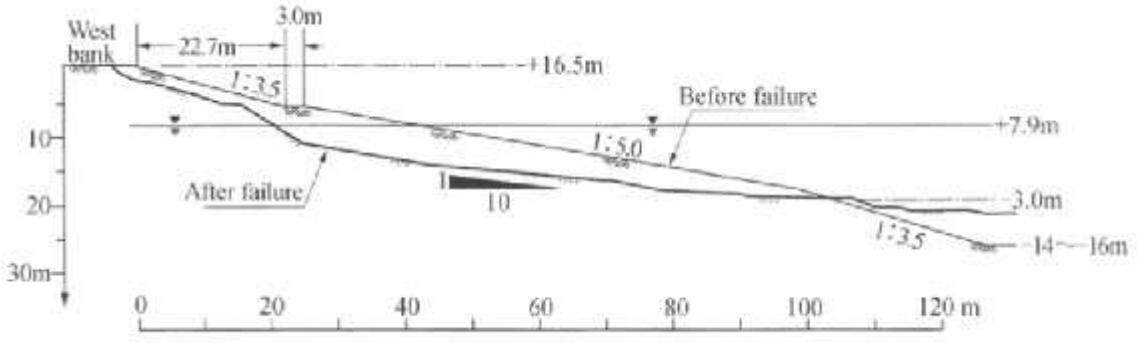

Figure A.139 Pre-and post-failure geometries of 1500 W3, which failed on Dec. 3, 1995 (from Ishihara 2008)

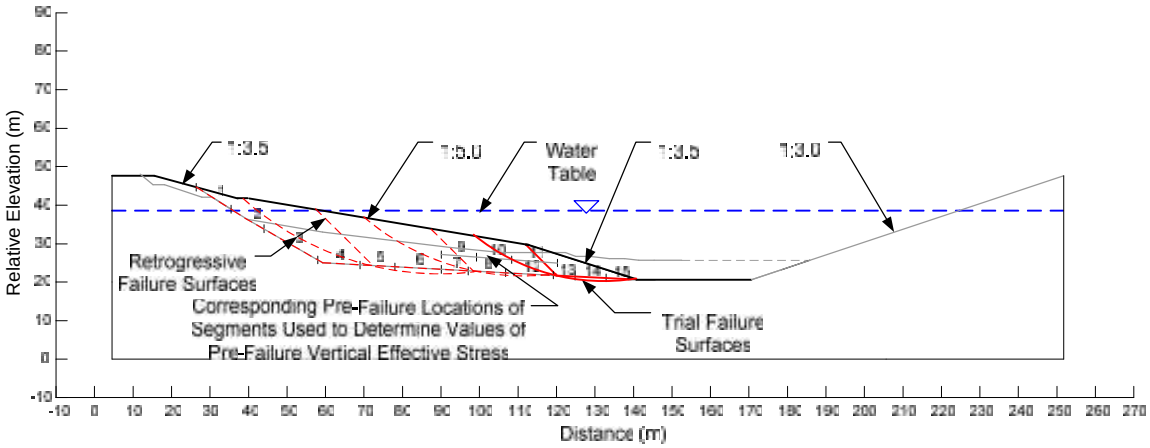

Figure A.140 Pre-failure cross section of the 1500 W3 slide, with the critical initial failure surface and inferred retrogressive failure surfaces

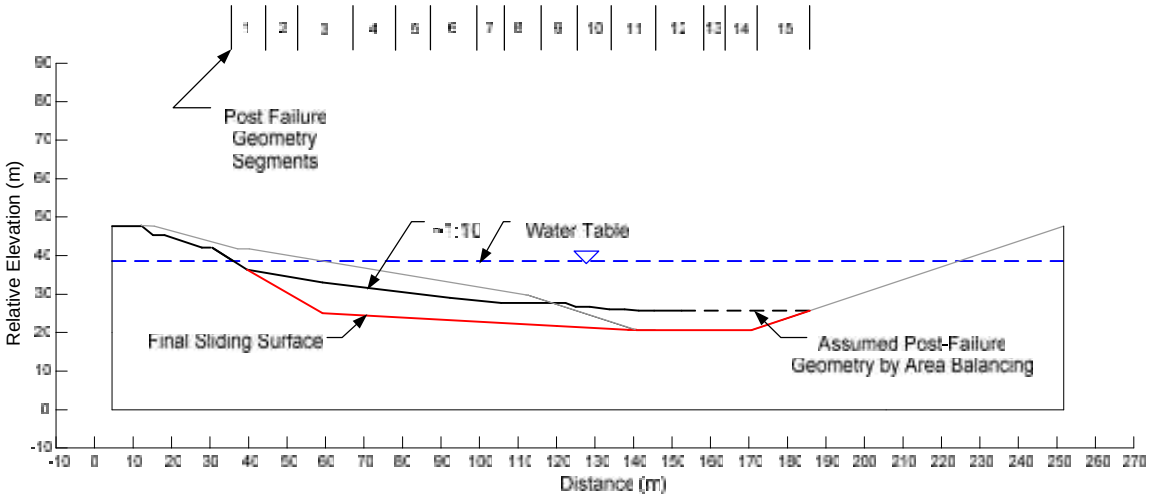

Figure A.141 Post-failure cross section of the 1500 W3 slide with the critical final sliding surface

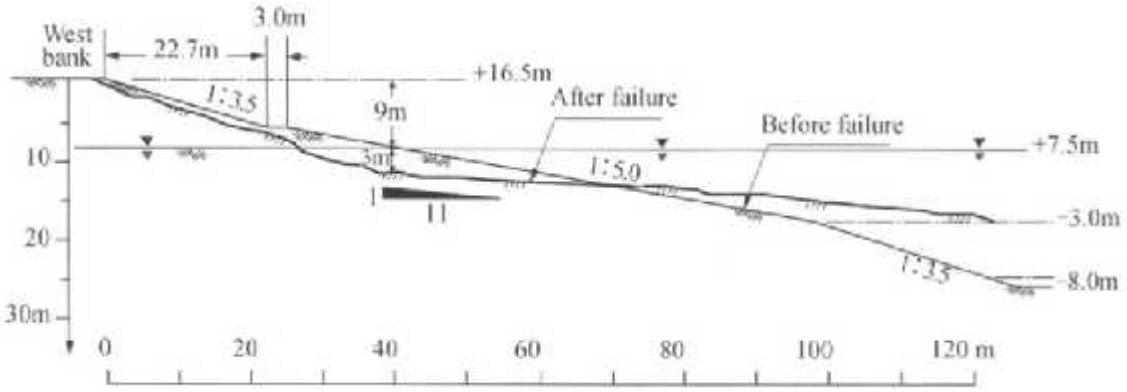

Figure A.142 Pre-and post-failure geometries of 1800 W4, which failed on Dec. 15, 1995 (from Ishihara 2008)

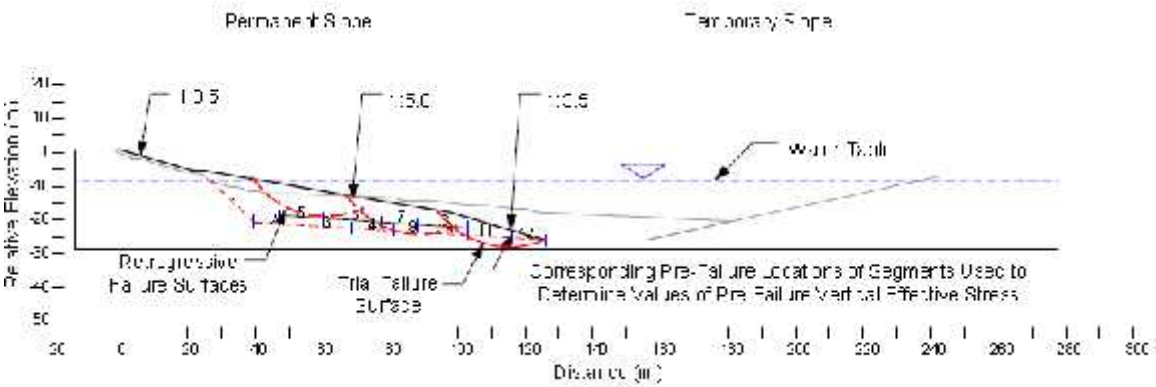

Figure A.143 Pre-failure cross section of the 1800 W4 slide, with the critical initial failure surface and inferred retrogressive failure surfaces

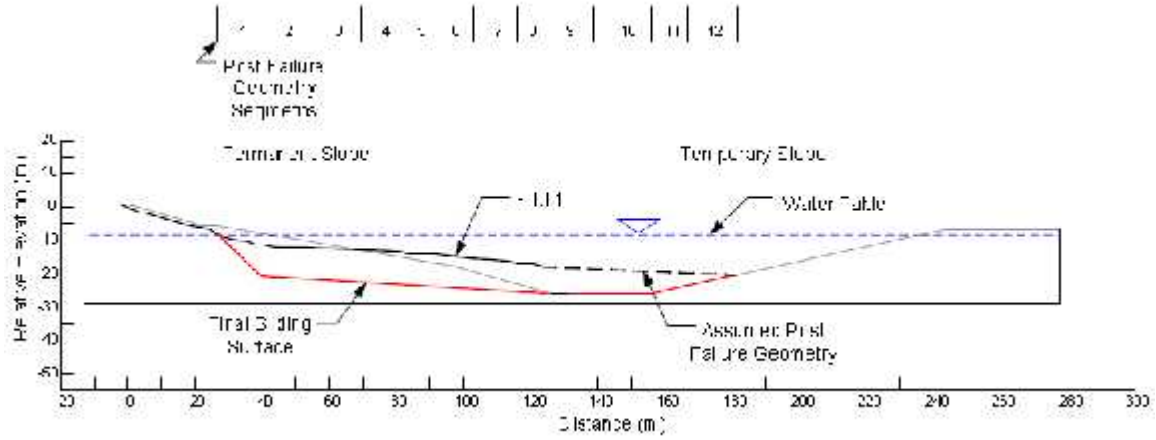

Figure A.144 Post-failure cross-section of the 1800 W4 slide with the critical final sliding surface

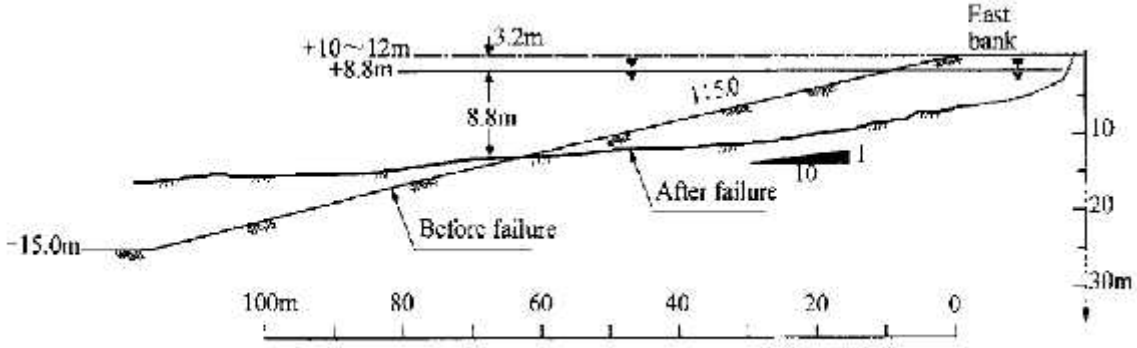

Figure A.145 Pre-and post-failure geometries of 1800 WT13, which failed on May 6, 1996 (from Ishihara 2008)

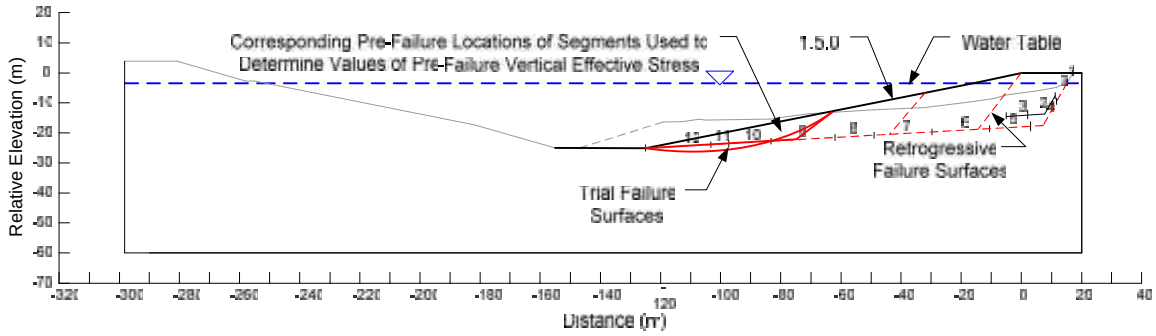

Figure A.146 Pre-failure cross section of the 1800 WT13 slide, with the critical initial failure surface and inferred retrogressive failure surfaces

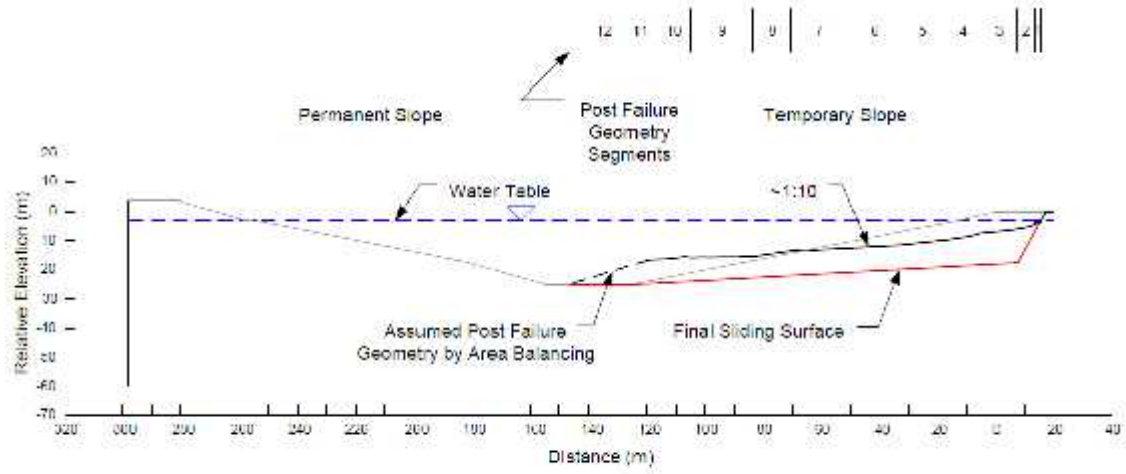

Figure A.147 Post-failure cross-section of the 1800 WT13 slide with the critical final sliding surface

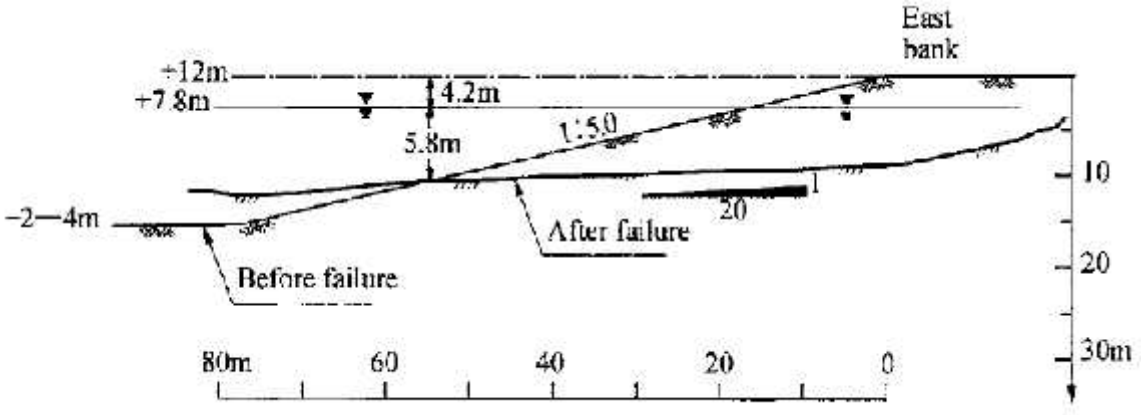

Figure A.148 Pre-and post-failure geometries of 2500 WT4, which failed on April 20, 1996 (from Ishihara 2008)

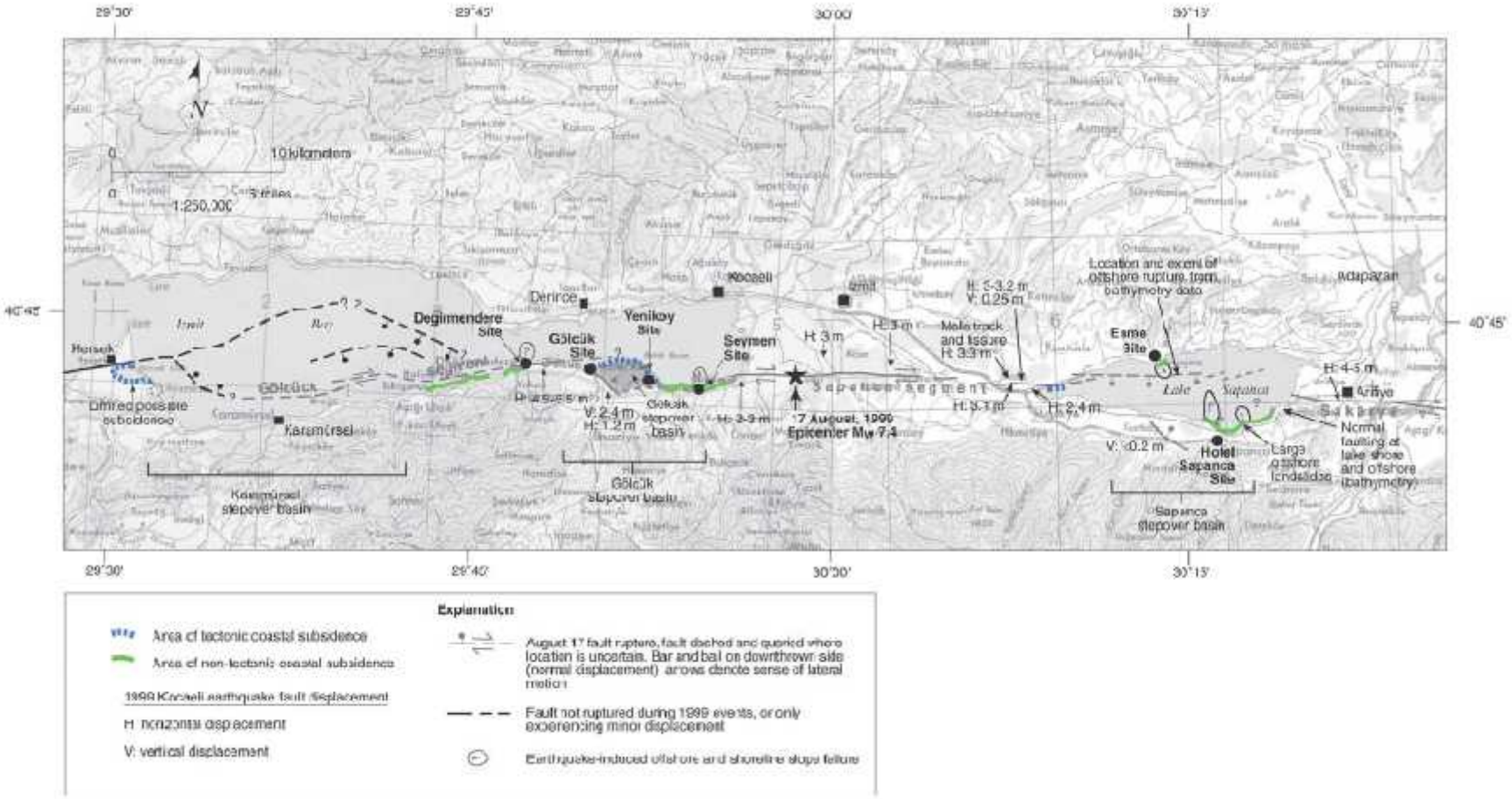

Figure A.149 Location of Kocaeli earthquake epicenter, pull-apart basin, and Degirmendere study site (from Rathje et al. 2004)

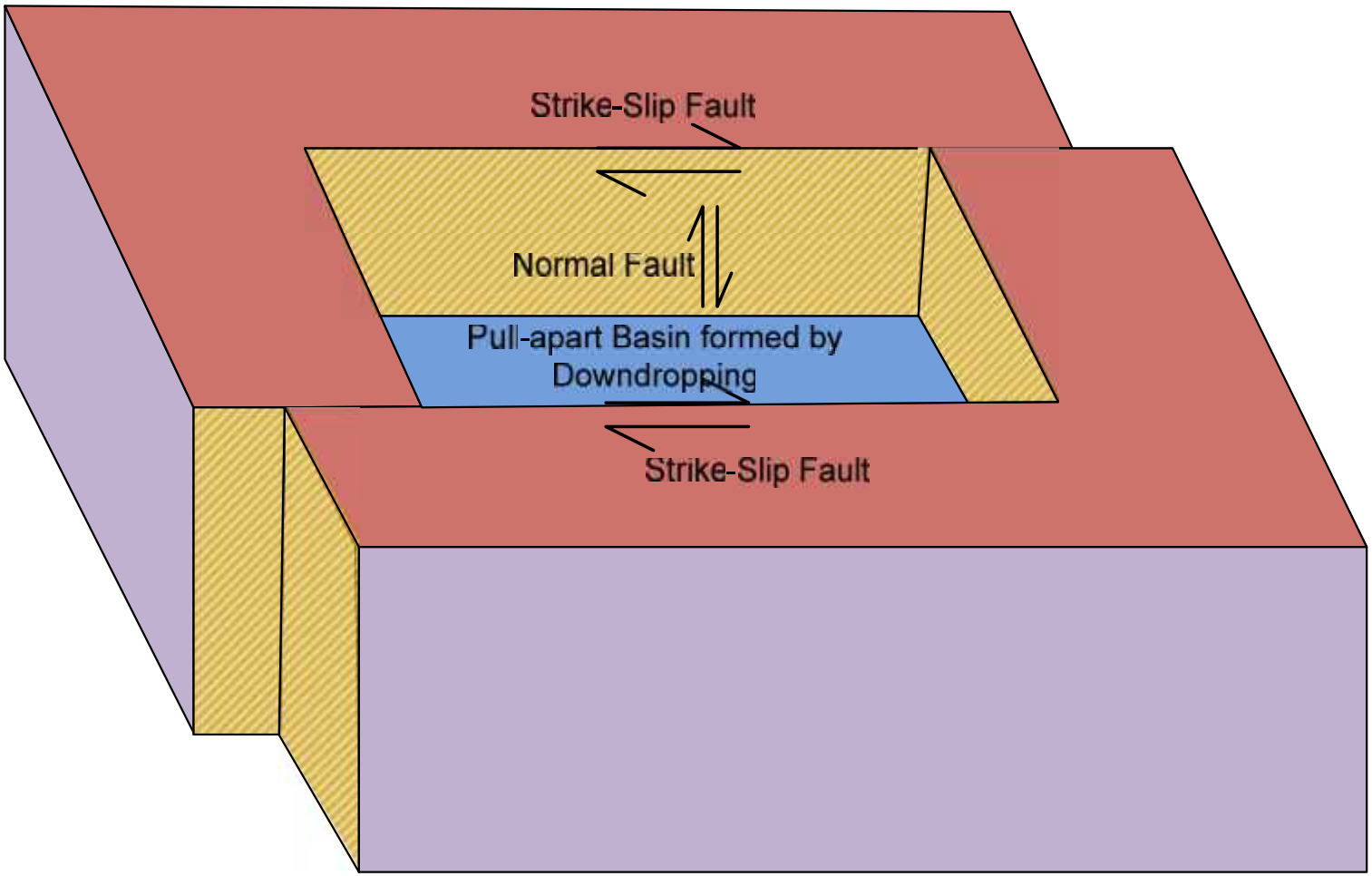

Figure A.150 Schematic diagram showing formation of pull-apart basin at a stepover of strike-slip fault. Normal faults are also shown (from USGS http://woodshole.er.usgs.gov/project-pages/dead_sea/tectonic.html)

Figure A.151 Aerial photographs showing pre- and post-failure coastline at Degirmendere (from Cetin et al. 2004)

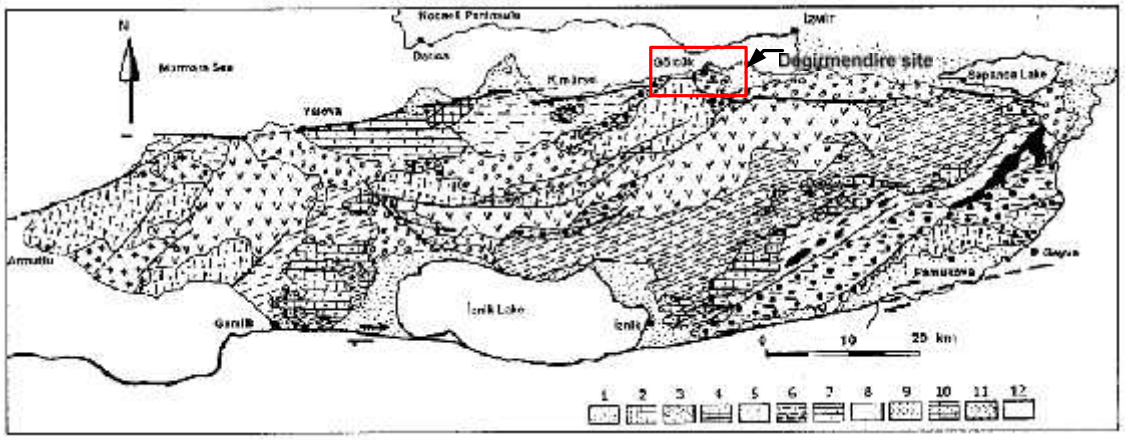

1. Pamukova metamorphics
2. Sedimentary cover of Pamukova metamorphics (Triassic) (Ballikaya formation)
3. Lower part of the Iznik Metamorphics (Triassic)
4. Alicyayla limestone (Upper Triassic – Middle Jurassic)
5. upper part of the Iznik Metamorphics, ophiolitic metaolistostrome; black shading shows ophiolitic rocks (Upper Jurassic – Lower Creataceous)
6. Bakacak formation (Campanian – Maastrichtian)
7. Incebel formation (Paleocene-Lutetian)
8. Sarisu volcanics (Lutetian)
9. Fistikli granitoid (Eocene)
10. Kilinc formation (Sarmasiyan/Ponsian)
11. Pliocene detritals
12. recent deposits

Figure A.152 Geological map of Armutlu peninsula (from Aydan et al. 2008)

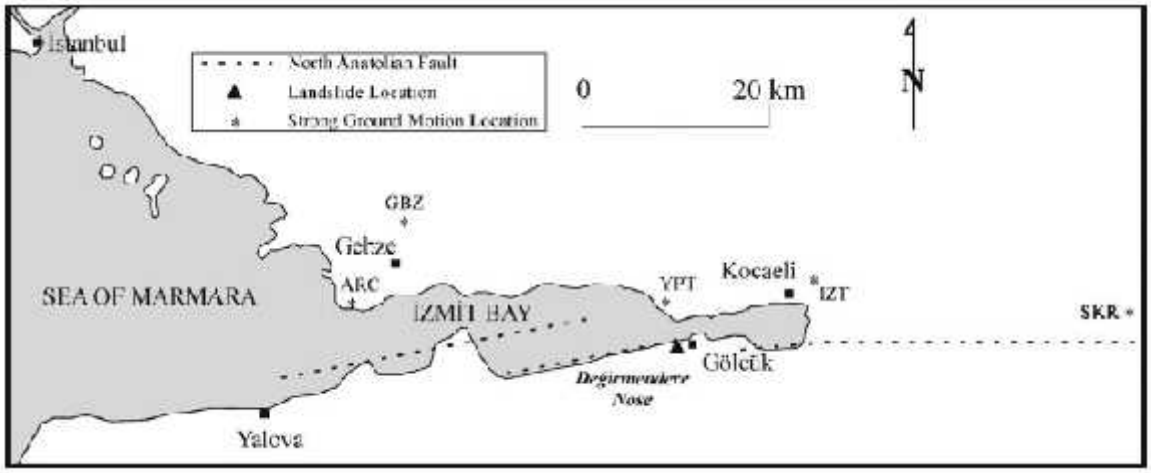

Figure A.153 Locations of strong motion recording stations (Cetin et al. 2004a)

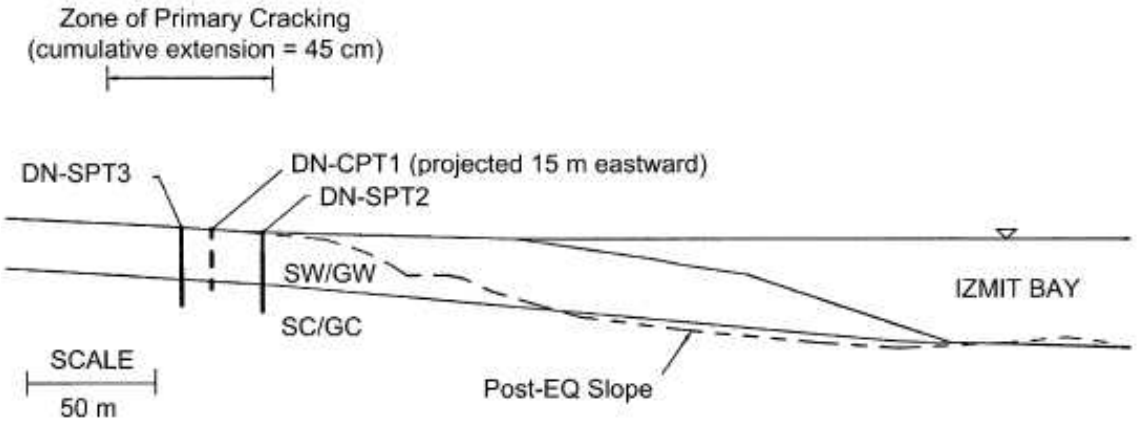

Figure A.154 Pre- and post-failure geometries of the Degirmendere site (Rathje et al. 2004)

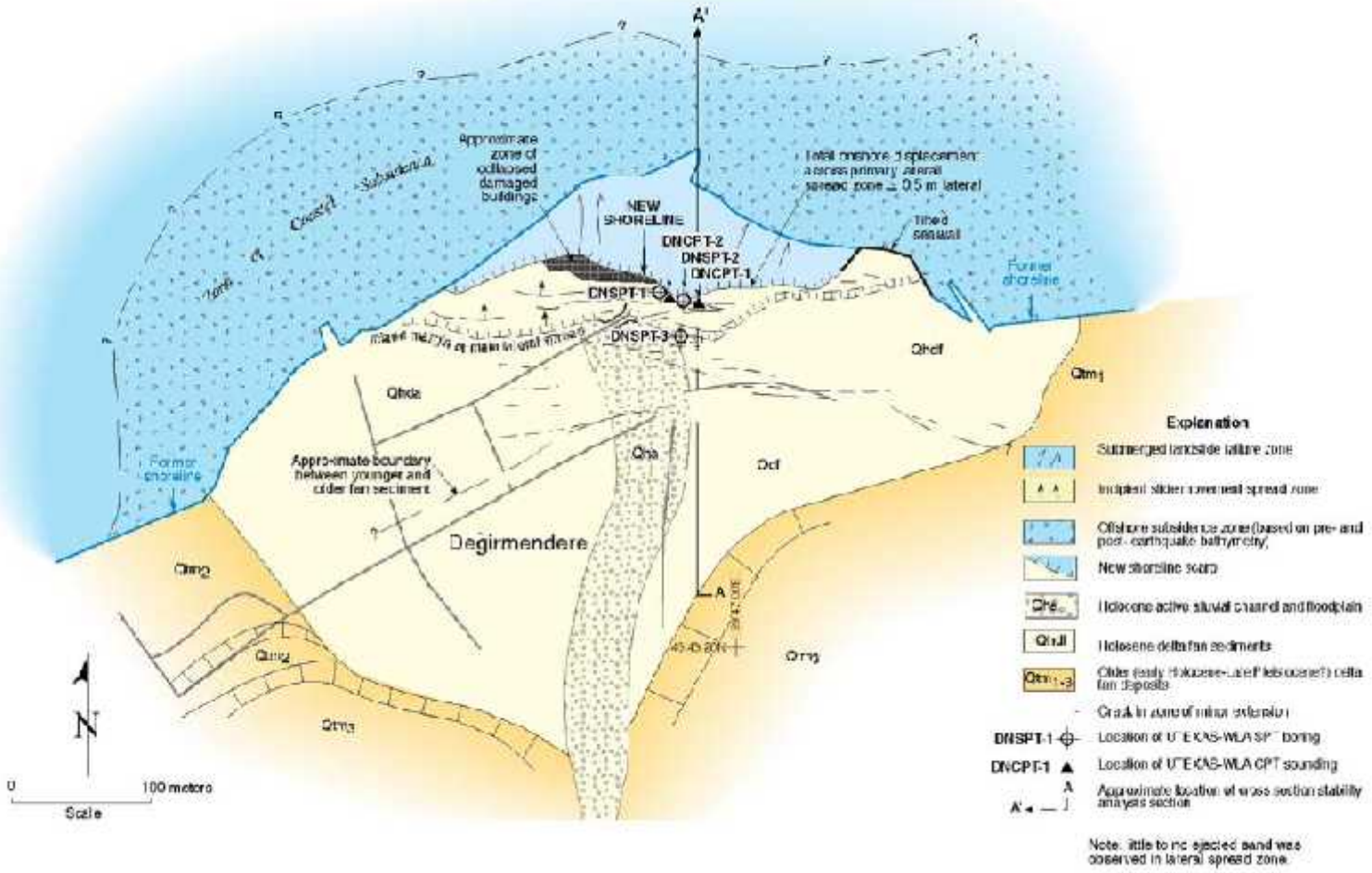

Figure A.155 Plan view of Degirmendere flow slide site showing the locations of tests performed at the site (from Rathje et al. 2004)

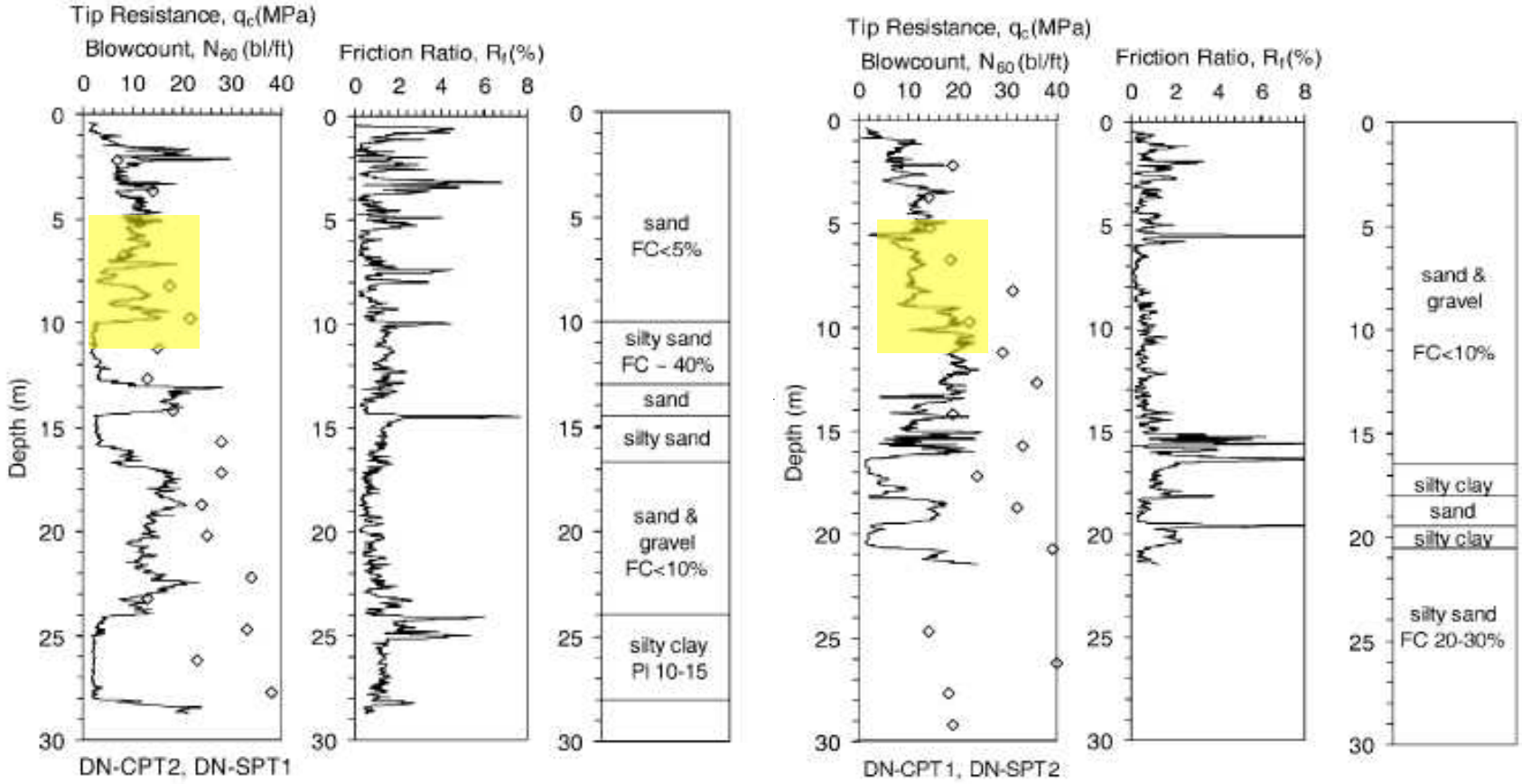

Figure A.156 SPT and CPT results from Degirmendere site. Likely liquefied zones are highlighted (Rathje et al. 2004)

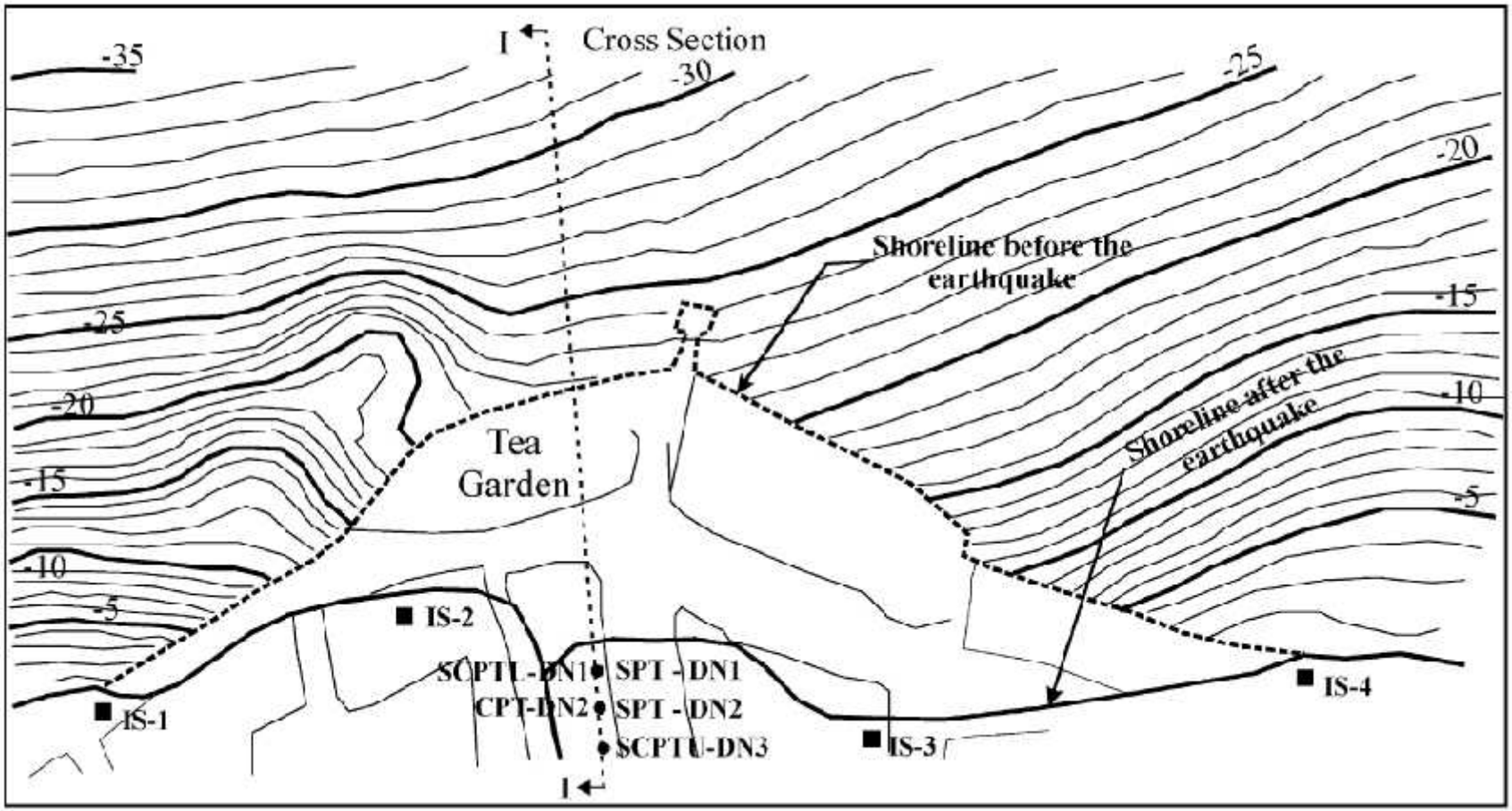

Figure A.157 Locations of penetration tests and cross-section location at Degirmendere site studied by Cetin et al. (2004a)

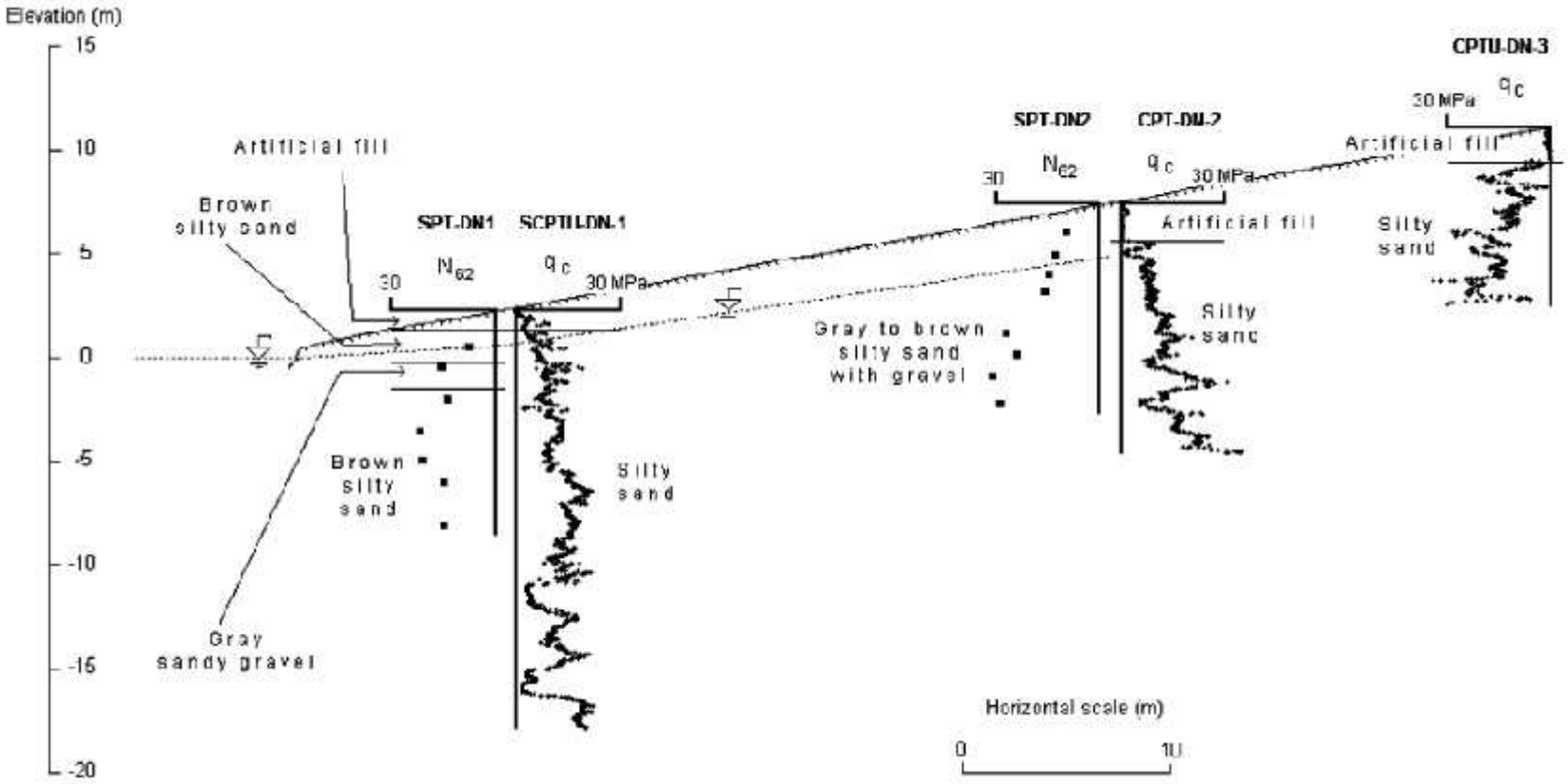

Figure A.158 Cross-section I-I (Figure A.157) through Degirmendere slope (Cetin et al. 2004)

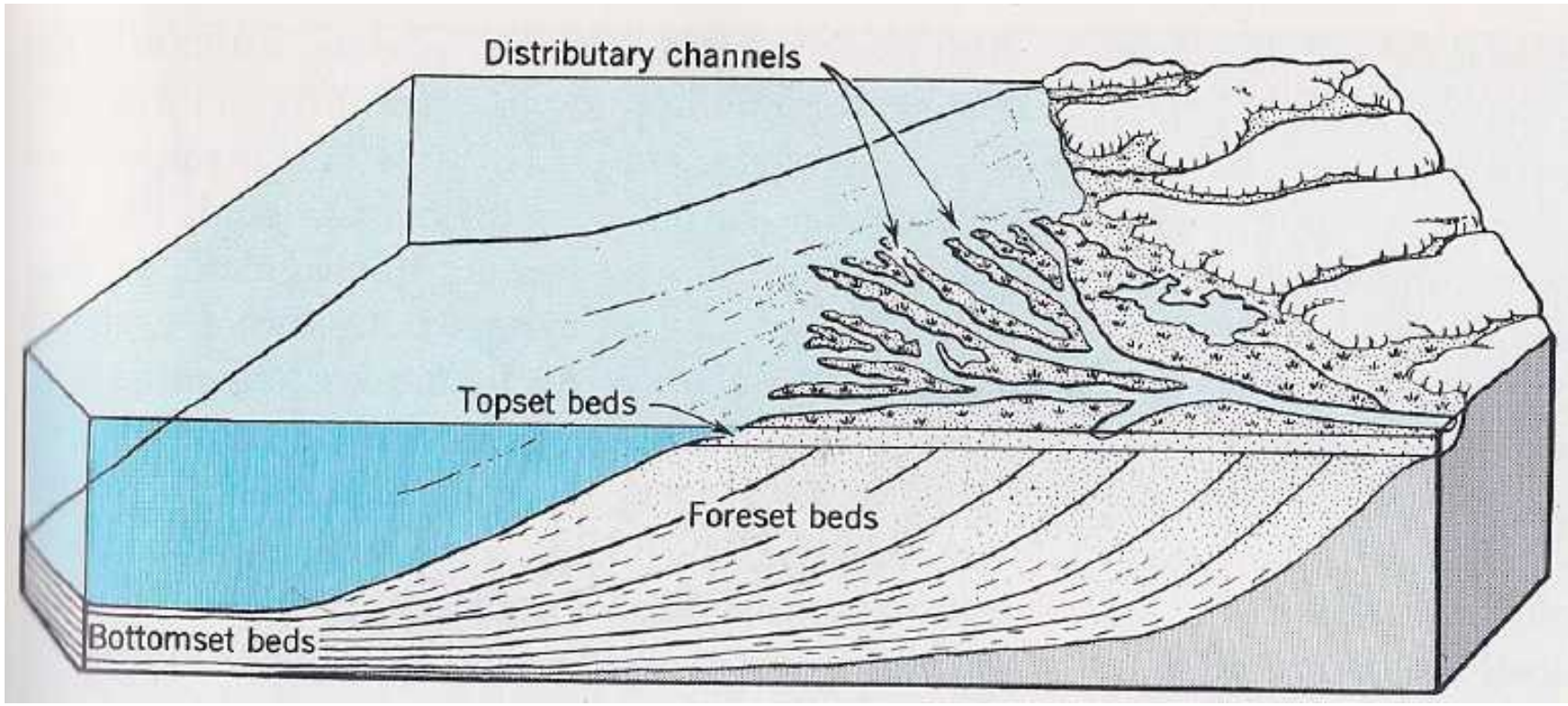

Figure A.159 Schematic delta depositional environment showing downstream sediment accretion

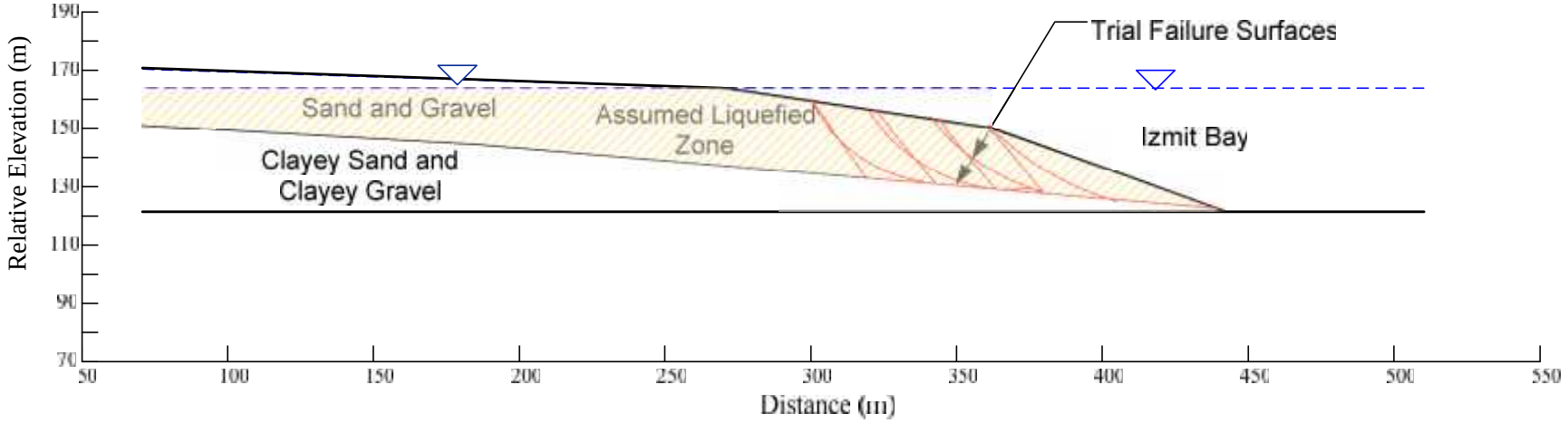

Figure A.160 Pre-failure geometry of Degirmendere slope with trial failure surfaces. All of the sandy soils within the delta were considered to be potentially liquefiable because the exact locations of the looser sand and silty sand beds are not known.

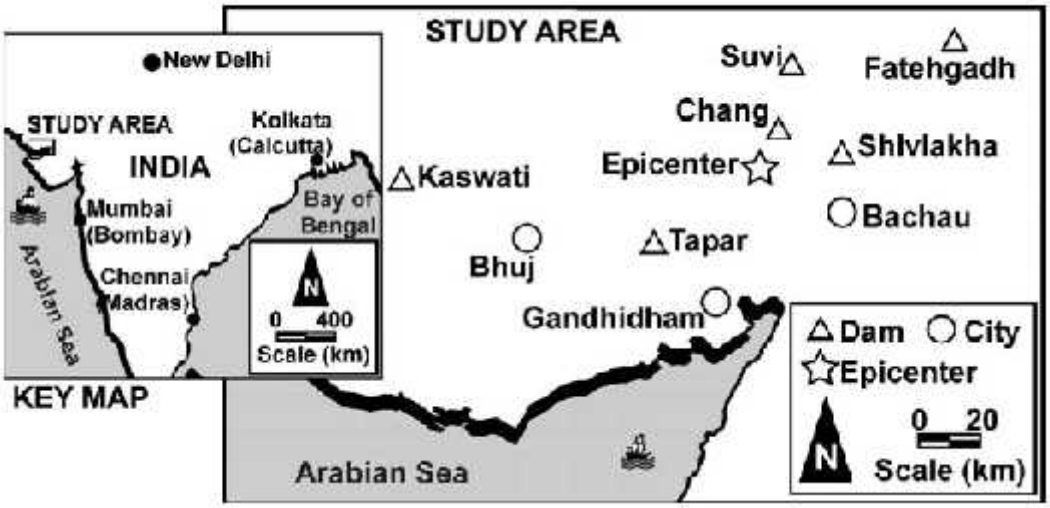

Figure A.161 General and regional location map showing earthquake epicenter and locations of dams damaged during the earthquake (from Singh et al. 2005a)

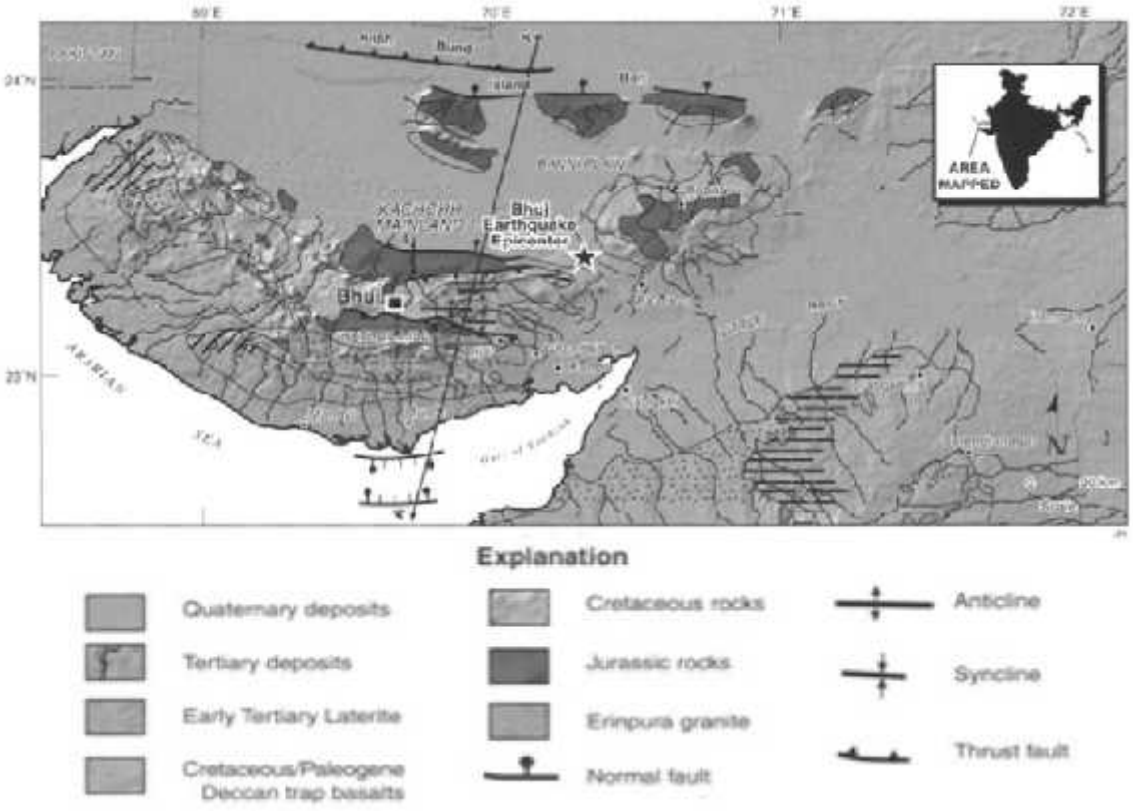

Figure A.162 Map showing general distribution of sediments deposits and rocks of region impacted by Bhuj earthquake (from Merh 1995 and EERI 2001)

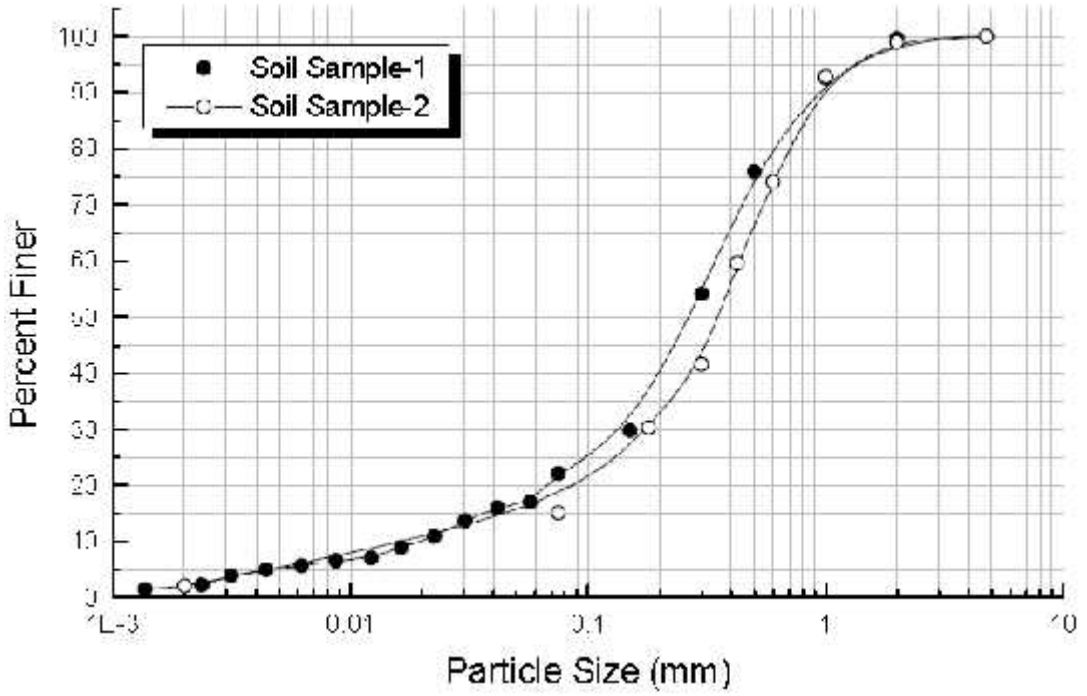

Figure A.163 Grain size distributions of of two samples from the Bhuj region (from Sitharam et al. 2004)

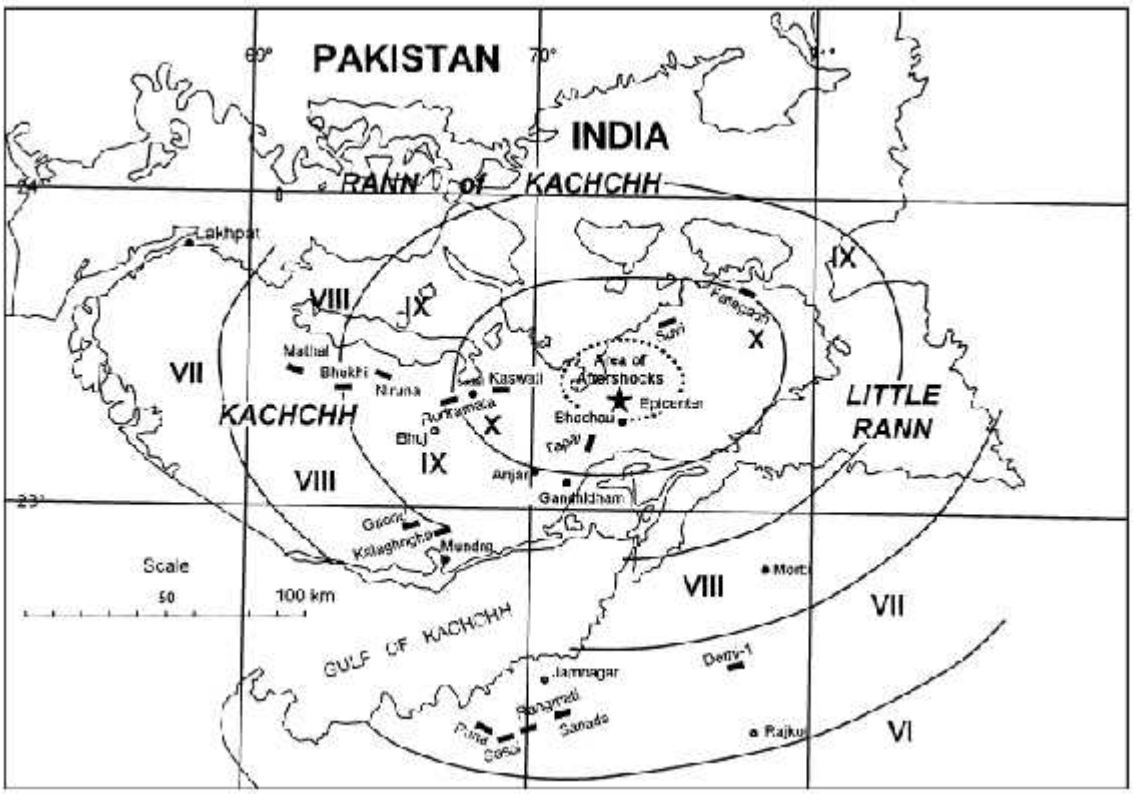

Figure A.164 Map of Kachchh region with location of dams, earthquake epicenter, and Modified Mercalli intensities (from Krinitzsky and Hynes 2002)

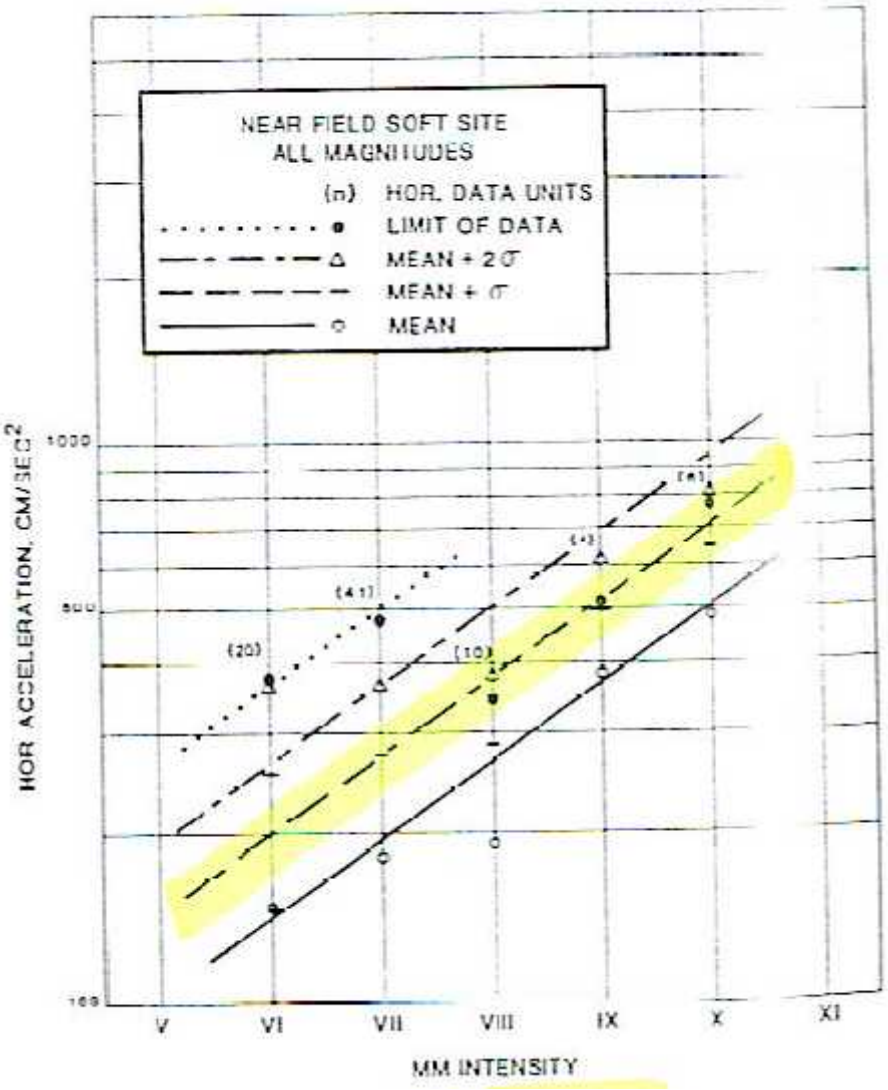

Figure A.165 Horizontal acceleration prediction from MMI (from Krinitzsky and Chang 1988)

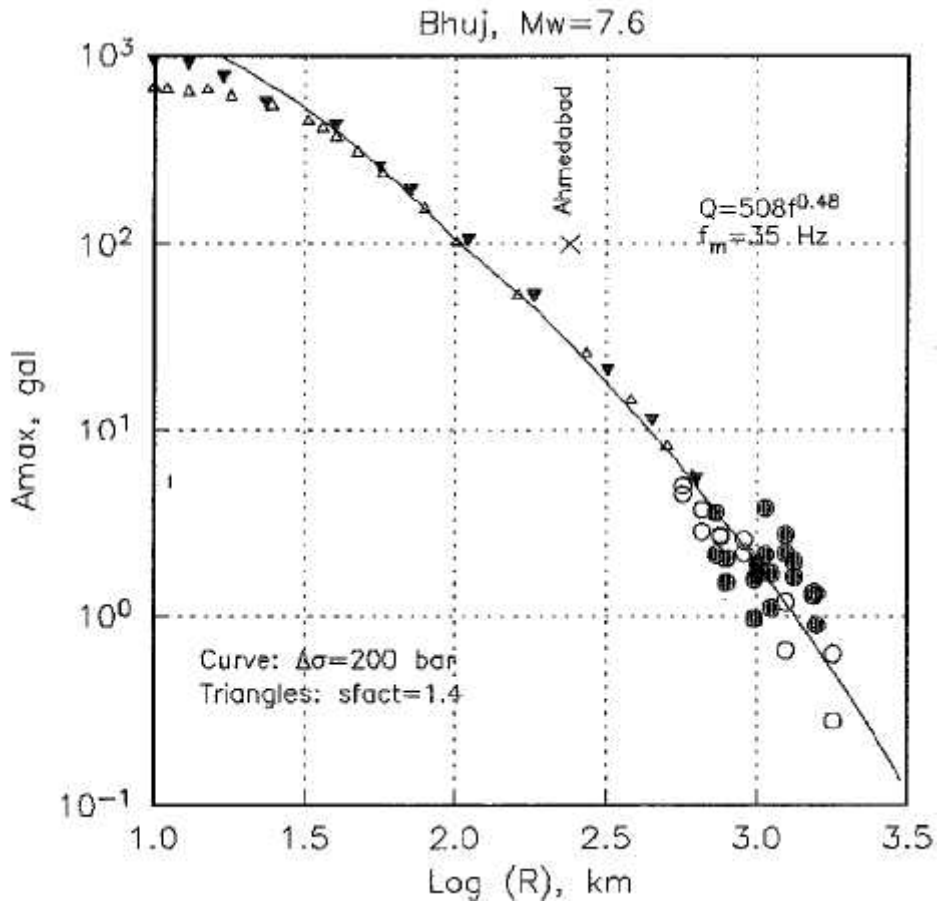

Figure A.166 Attenuation relationship proposed by Singh et al. (2003) for Bhuj main shock [see Singh et al. (2003) for description of symbols]

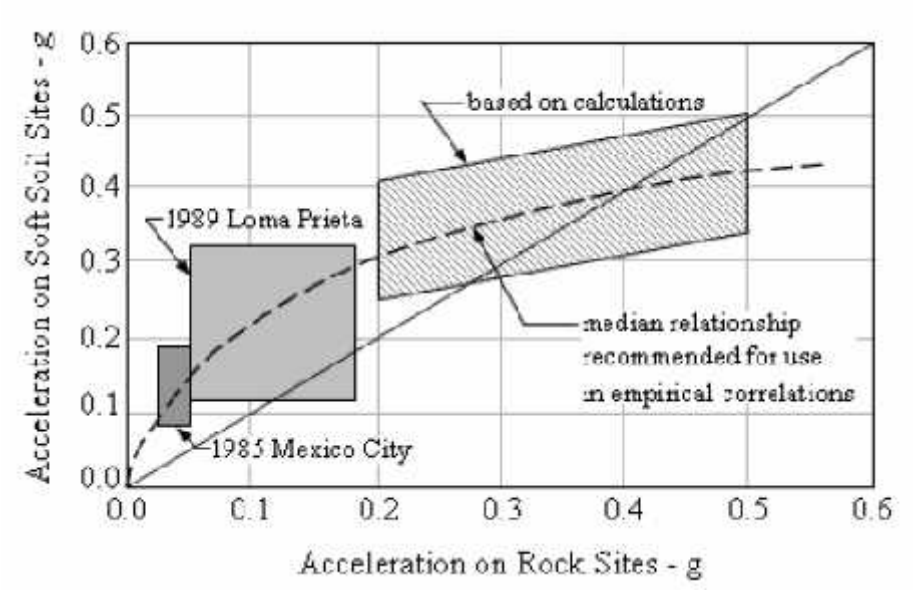

Figure A.167 Amplification factors for soft soil sites proposed by Idriss (1990)

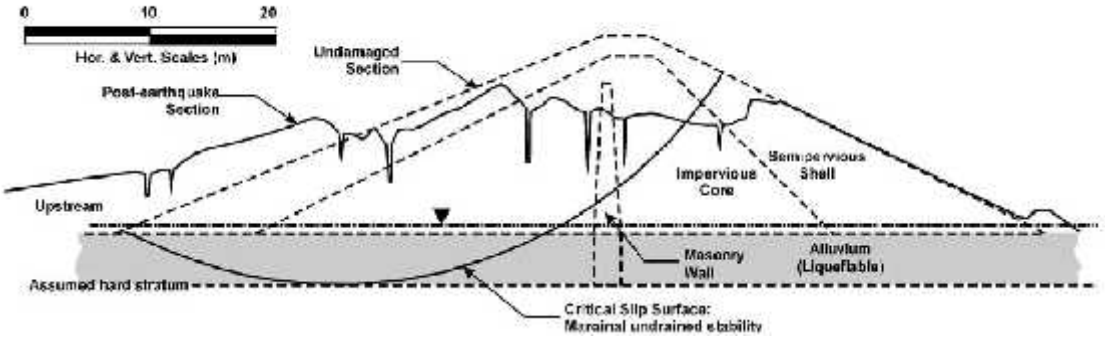

Figure A.168 Pre- and post-failure geometries of Chang Dam (Singh et al. 2005a)

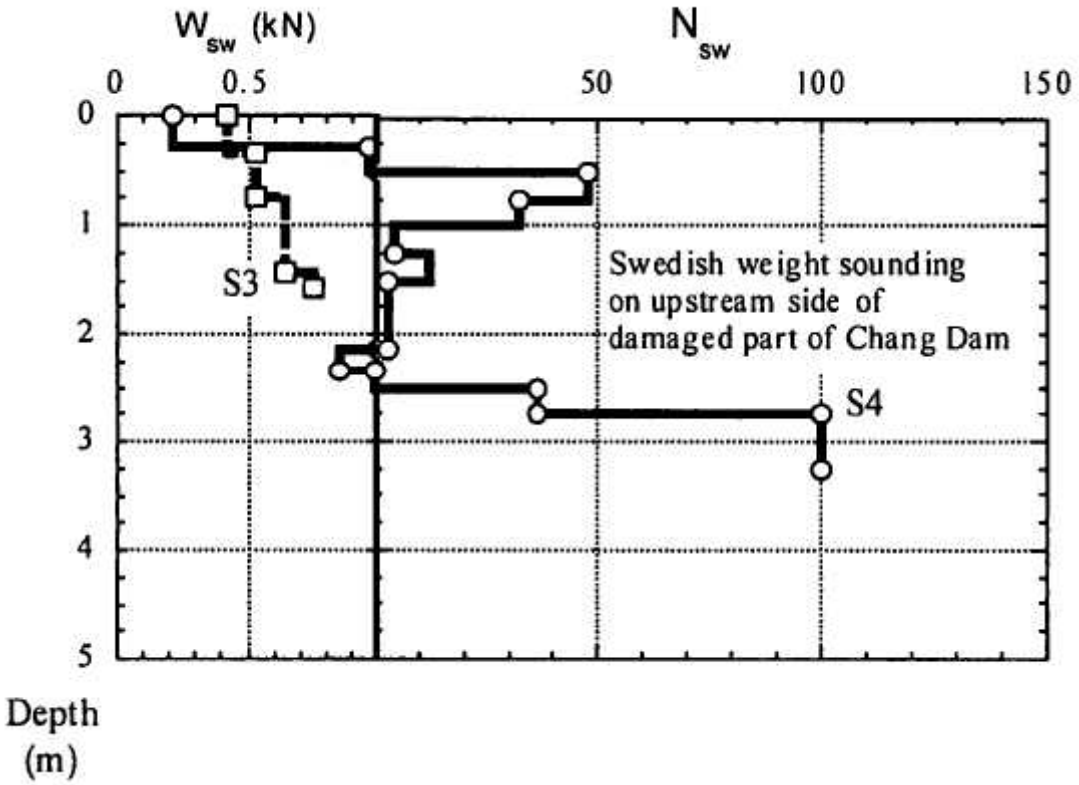

Figure A.169 Swedish weight soundings performed on upstream side of Chang Dam (from Towhata et al. 2002)

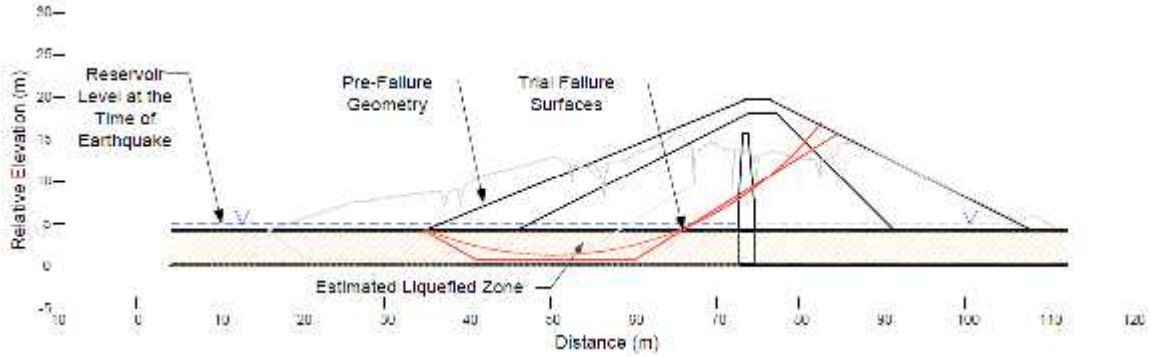

Figure A.170 Pre-failure cross section of Chang Dam with critical circular and noncircular failure surfaces

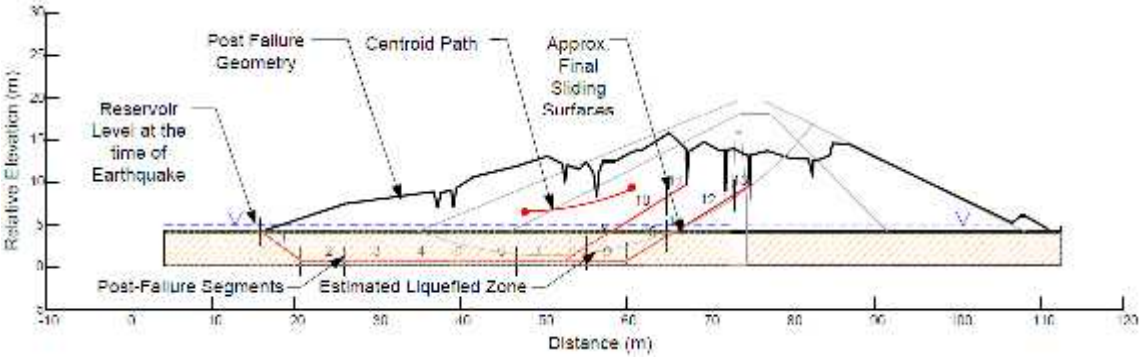

Figure A.171 Post-failure geometry of Chang Dam with two potential critical final sliding surfaces and corresponding post-failure geometry segments

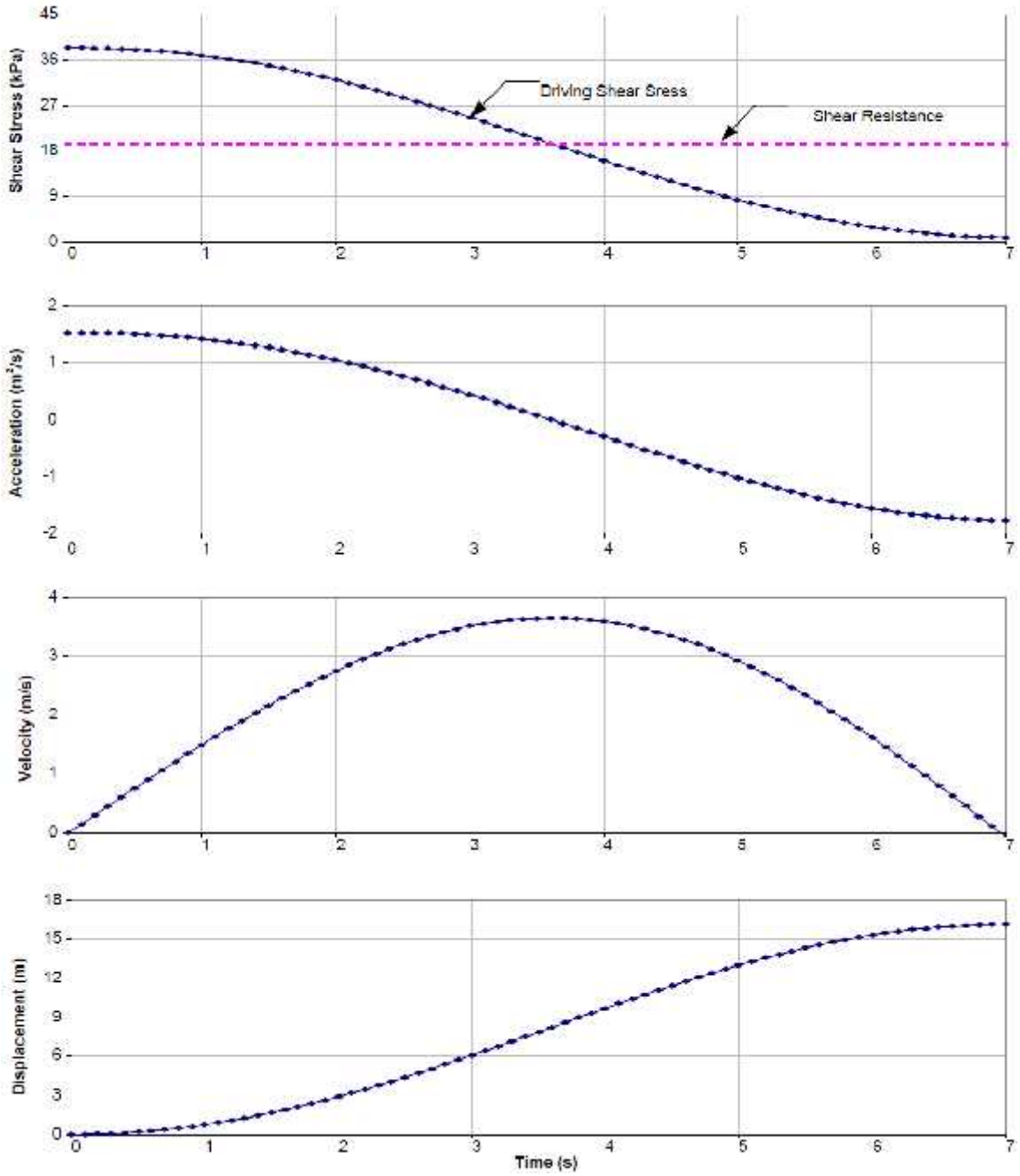

Figure A.172 Kinetics analysis results for Chang Dam

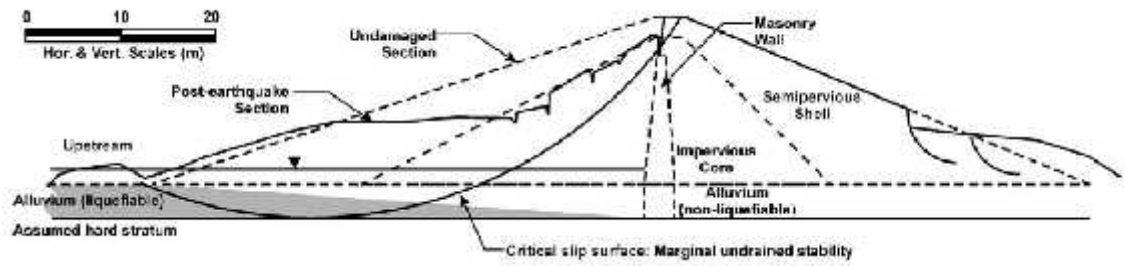

Figure A.173 Pre-and post-failure geometry of Shivlakha Dam (from Singh et al. 2005a)

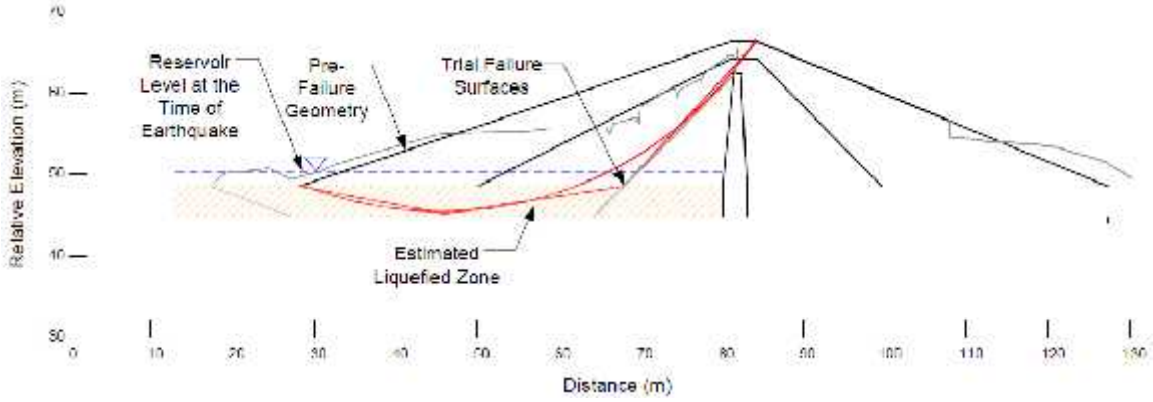

Figure A.174 Pre-failure cross section of Shivlakha Dam with critical circular and noncircular failure surfaces

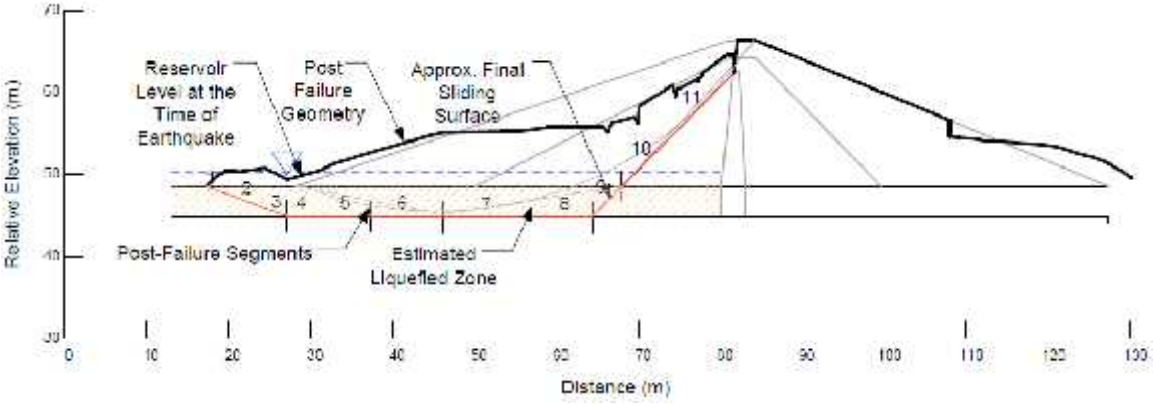

Figure A.175 Post-failure geometry of Shivlakha Dam with critical final sliding surfaces and locations of post-failure geometry segments

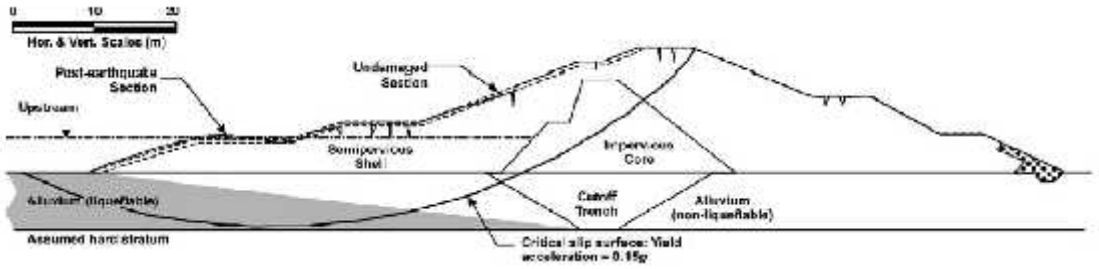

Figure A.176 Pre-and post-failure geometries of Tapar Dam (from Singh et al. 2005a)

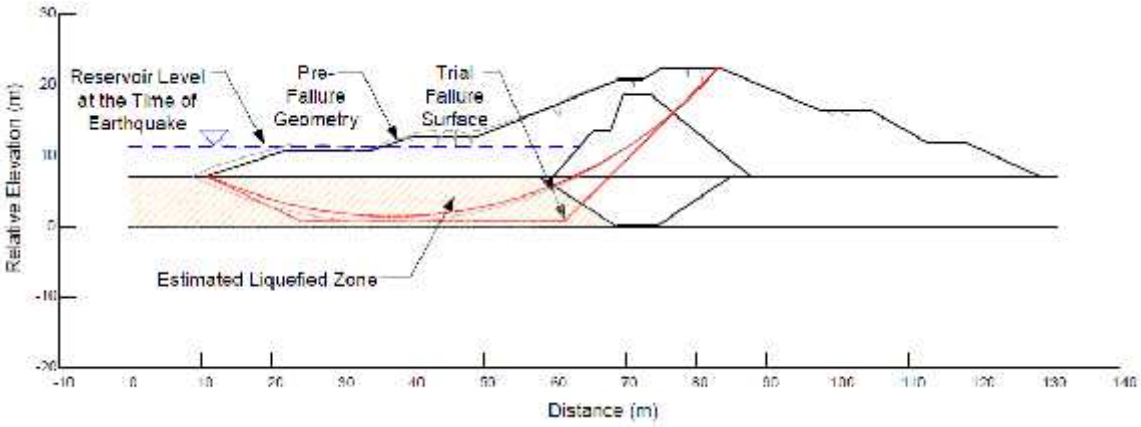

Figure A.177 Pre-failure cross section of Tapar Dam with critical circular and noncircular failure surfaces

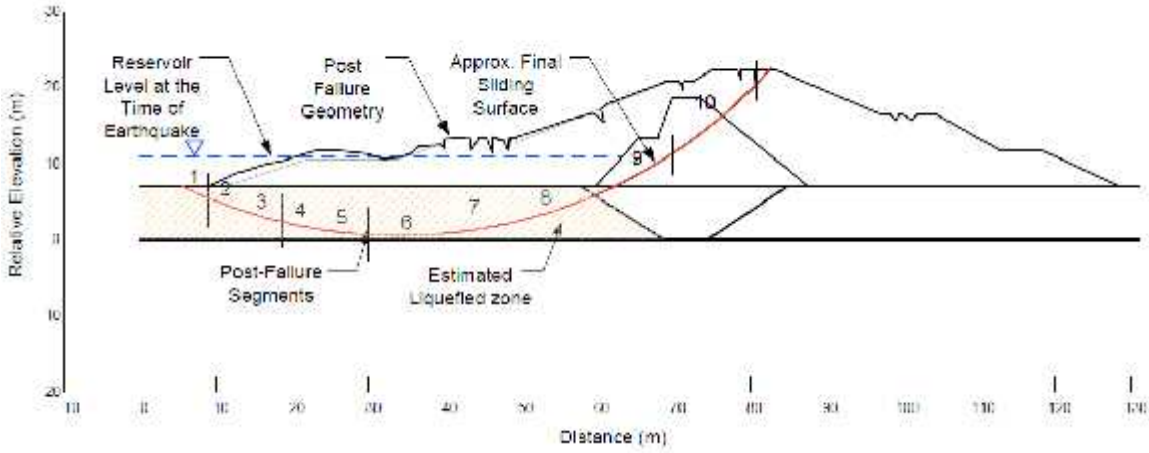

Figure A.178 Post-failure geometry of Tapar Dam with critical final sliding surfaces and locations of post-failure geometry segments

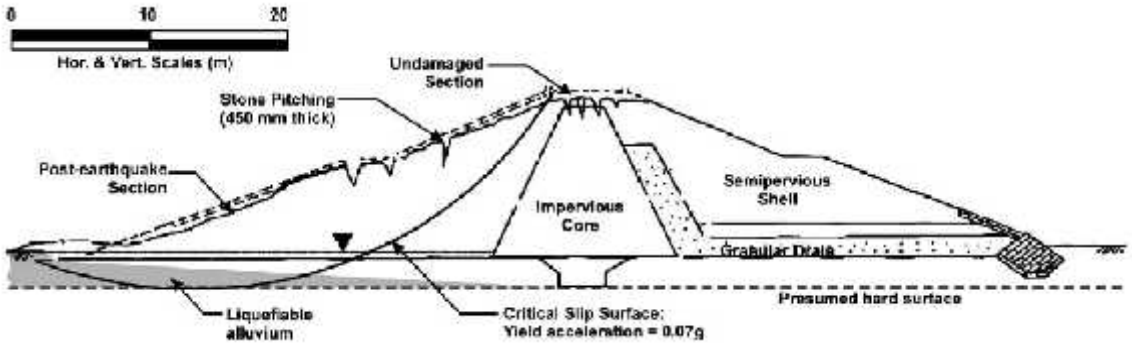

Figure A.179 Pre-and post-failure geometries of Fatehgadh Dam (from Singh et al. 2005a)

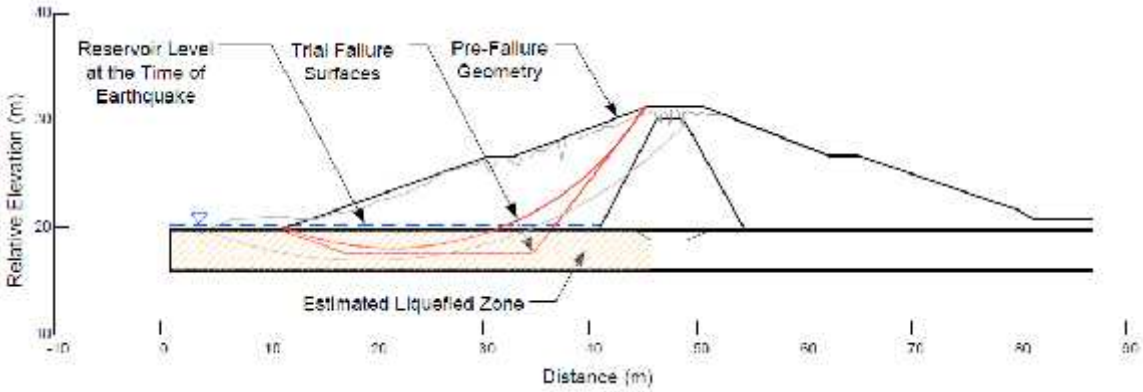

Figure A.180 Pre-failure cross section of Fatehgadh Dam with critical circular and noncircular failure surfaces

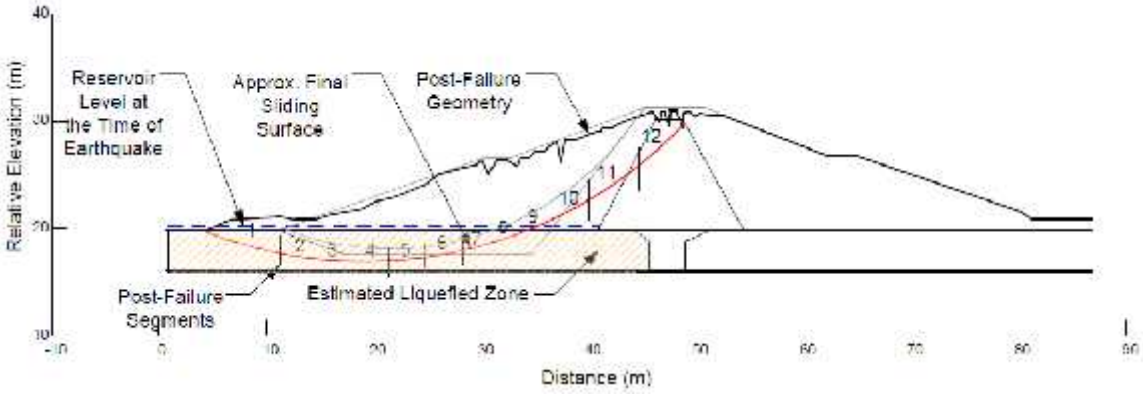

Figure A.181 Post-failure geometry of Fatehgadh Dam with critical final sliding surfaces and locations of post-failure geometry segments

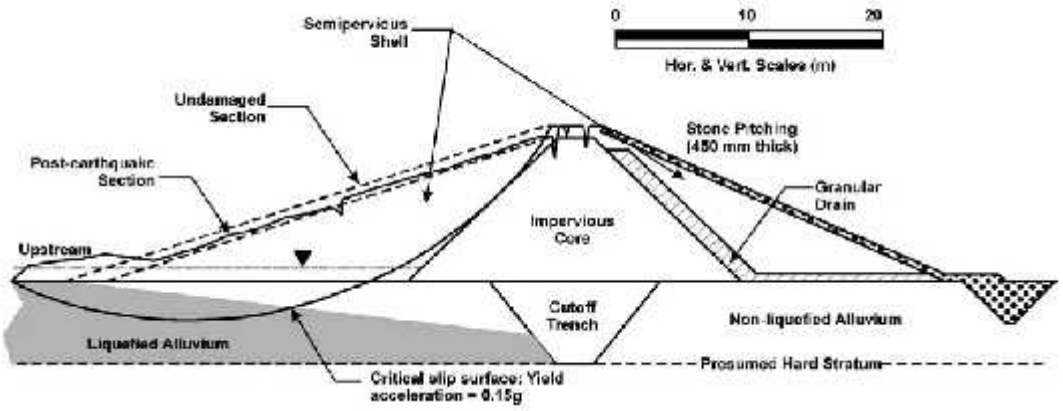

Figure A.182 Pre-and post-failure geometries of Kaswati Dam (from Singh et al. 2005a)

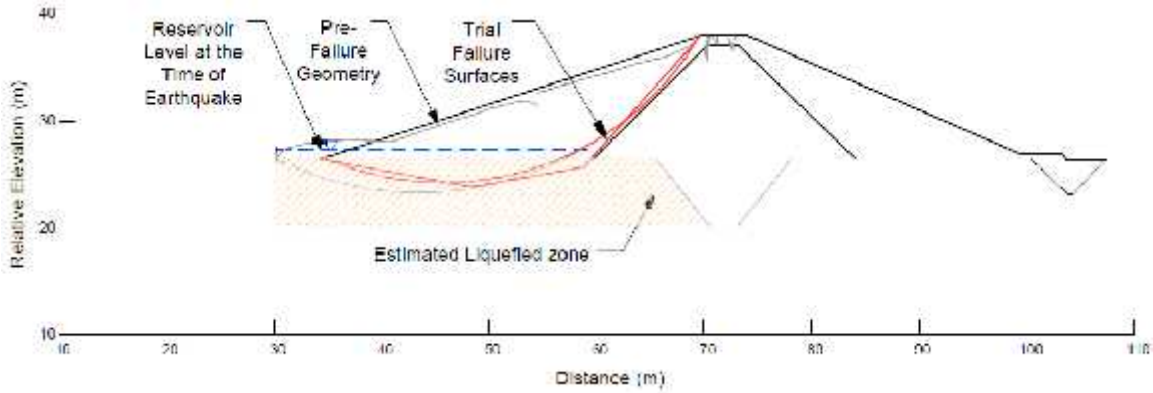

Figure A.183 Pre-failure cross section of Kaswati Dam with critical circular and noncircular failure surfaces

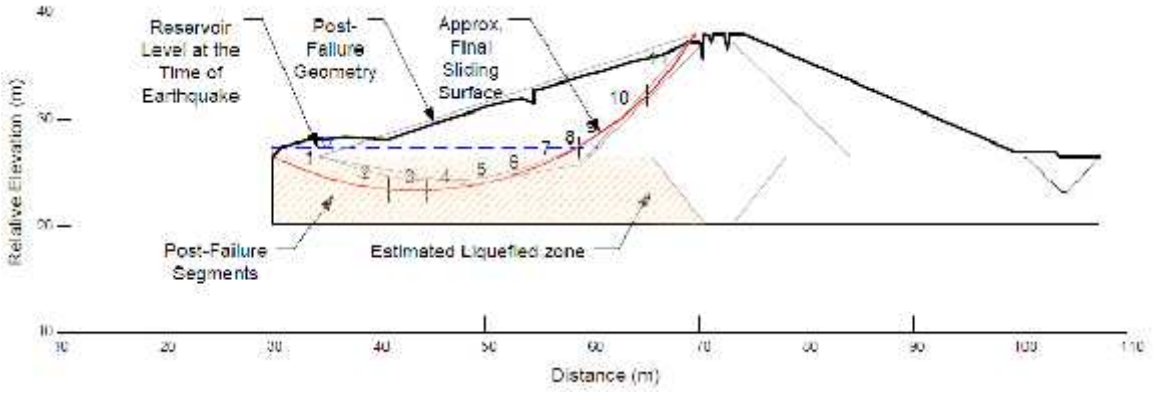

Figure A.184 Post-failure geometry of Kaswati Dam with critical final sliding surfaces and locations of post-failure geometry segments

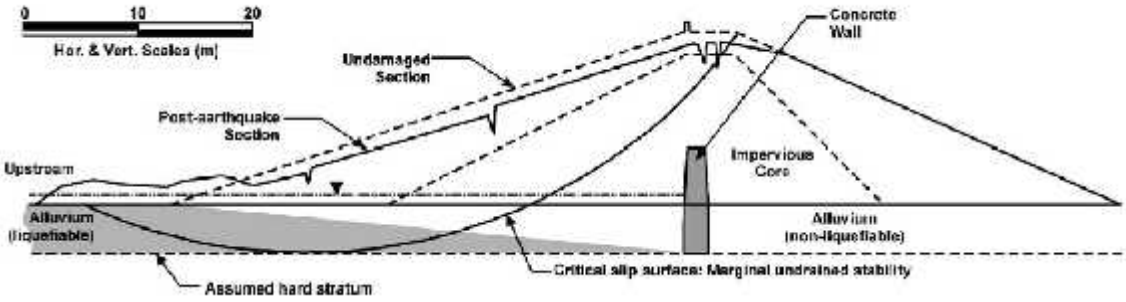

Figure A.185 Pre-and post-failure geometries of Suvi Dam (from Singh et al. 2005a)

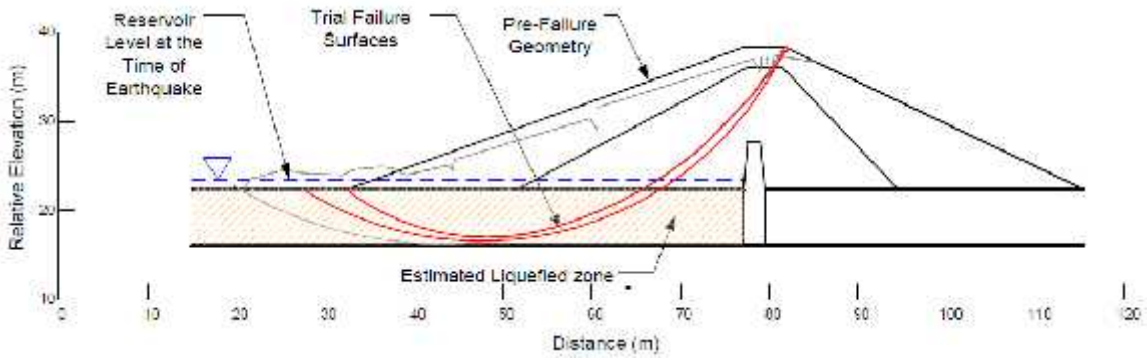

Figure A.186 Pre-failure cross section of Suvi Dam with trial circular failure surfaces

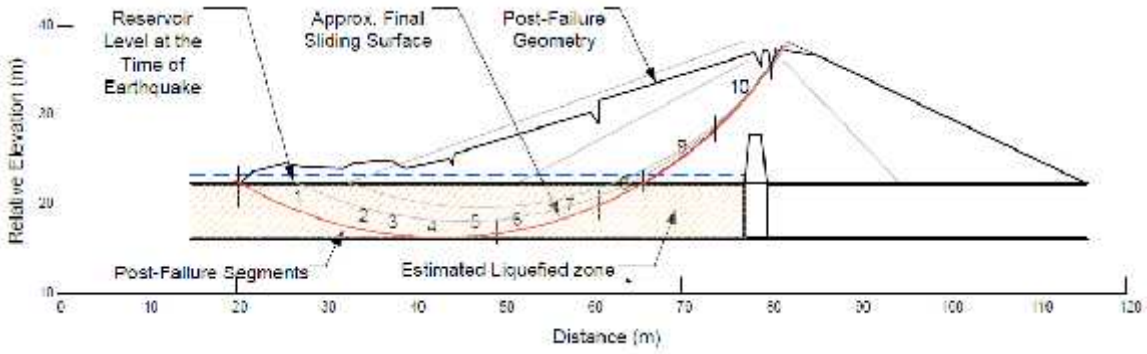

Figure A.187 Post-failure geometry of Suvi Dam with critical final sliding surface and locations of post-failure geometry segments

Table A.1 Estimation of PGA for seismic case histories analyzed in this study

Case History No.	Structure Name	R km	R_{rup} km	R_{jb} km	Z_{tor} km	W km	$Z_{1.0}$ m	$Z_{2.5}$ m	Dip Angle deg
1	Barahona Tailings Dam	180	101	152	0 to 25	32	330 to 830 (260 to 340)	1700 to 3500	20 to 30
2	Kamenari Landslide	50 to 60	18.3	21.6	7	23	33 to 850 (23 to 337)	637 to 3575	14
3 and 4	Spitak Embankment 1 and 2	-	1.5	0	16	16	360 (285)	1813	50 to 70
5	Okuli Landslide	14	-	-	-	-	-	-	-
7	Right Bank	25	-	-	-	-	-	-	-
8	Left Bank	25	-	-	-	-	-	-	-
9	Tohnai Dike	70	-	-	-	-	-	-	-
10	Route 38 Road Embankment	40	-	-	-	-	-	-	-
11	Route 44 Road Embankment	50	-	-	-	-	-	-	-
14	Torishima Dike	40	17.26	14	13.3	12.68	849.8 (337.1)	3570	85
15	Nishijima Dike	40	17.26	14	13.3	12.68	849.8 (337.1)	3570	85
16	Upper Niteko Dam	36	3.18	1.6	13.3	12.68	849.8 (337.1)	3570	85
17	Middle Niteko Dam	36	3.18	1.6	13.3	12.68	849.8 (337.1)	3570	85
18	Takarazuka Landslide	50	3.83	2.85	13.3	12.68	849.8 (337.1)	3570	85
19	Nikawa Landslide	50	3.83	2.85	13.3	12.68	849.8 (337.1)	3570	85
20	Idenoshiri Dam	28.5	4.63	4.83	13.3	12.68	849.8 (337.1)	3570	75
25	Degimendere Slope	13	-	-	-	-	-	-	-
26	Chang Dam	13	12.8	12.8	10	30	850 (337)	3600	54
27	Shivlakha Dam	28	25.8	25.8	10	30	851 (337)	3600	54
28	Tapar Dam	43	14.5	0	10	30	852 (337)	3600	54
29	Fatehgadh Dam	80	66	66	10	30	853 (337)	3600	54
30	Kaswati Dam	110	13	0	10	30	854 (337)	3600	54
31	Suvi Dam	37	29.5	29.5	10	30	855 (337)	3600	54

Table A.1 Continued

Case History No.	a_{max} (g) Abraham Silva (2008)	Boore Atkinson (2008)	Campbell Bozorgnia (2008)	Chiou Youngs (2008)	Idriss (2008)	a_{max} (g) Others
1	0.089 to 0.185	0.034 to 0.057	0.053 to 0.069	0.054 to 0.145	-	0.122 to 0.193[1]
2	0.286 to 0.32	0.136 to 0.188	0.13 to 0.17	0.206 to 0.25	-	0.21 to 0.26[2]
3 and 4	0.95	0.59	0.48	1.14	0.65	0.5 to 0.1[3]
5	-	-	-	-	-	0.15[4]
7	-	-	-	-	-	0.36[5]
8	-	-	-	-	-	0.36[5]
9	-	-	-	-	-	0.19[5]
10	-	-	-	-	-	0.28[5]
11	-	-	-	-	-	0.23[5]
14	0.22	0.21	0.20	0.25	0.32	0.32[6]
15	0.22	0.21	0.20	0.25	0.32	0.32[6]
16	0.43	0.29	0.35	0.50	0.47	0.57[6]
17	0.43	0.29	0.35	0.50	0.47	0.57[6]
18	0.42	0.28	0.34	0.45	0.47	0.55[6]
19	0.42	0.28	0.34	0.45	0.47	0.55[6]
20	0.39	0.26	0.32	0.38	0.42	0.53[6]
25	-	-	-	-	-	0.3 to 0.4[7]
26	0.56 to 0.44	0.24 to 0.21	0.24 to 0.22	0.4 to 0.36	0.33 to 0.28	0.5[8];NA[9]
27	0.35 to 0.28	0.17 to 0.15	0.14 to 0.13	0.28 to 0.25	0.2 to 0.17	0.45[8];NA[9]
28	0.52 to 0.41	0.52 to 0.45	0.28 to 0.26	0.58 to 0.53	0.3 to 0.26	0.41[8];0.7[9]
29	0.18 to 0.14	0.08 to 0.07	0.07 to 0.06	0.12 to 0.11	0.08 to 0.07	0.3[8];0.7[9]
30	0.55 to 0.44	0.52 to 0.46	0.3 to 0.28	0.59 to 0.53	0.33 to 0.28	0.28[8];0.7[9]
31	0.32 to 0.25	0.16 to 0.14	0.13 to 0.12	0.25 to 0.23	0.17 to 0.15	0.42[8];0.7[9]

Notes: R = epicentral distance; R_{RUP} = closest distance to rupture plane; R_{JB} = horizontal distance to surface projection of rupture; Z_{TOR} = depth to top of rupture; W = down-dip rupture width; $Z_{1.0}$ = depth (in m) to the Vs = 1.0 km/s horizon (values in parentheses are for Chiou and Youngs (2008) model); $Z_{2.5}$ = depth (in m) to Vs = 2.5 km/s horizon.

References: Troncoso et al. (1993); Anicic et al. (1980) at Herceg-Novi about 12km from Kamenari site; Yegian et al. (1994b); Ishihara et al. (1990); Sasaki et al. (1993); Fukushima and Tanaka (1992); Cetin et al. (2004a); Singh et al. (2005); Krinitsky and Hynes (2002).

Table A.2 Soil parameters used for the analyses of the Torishima and Nishijima dikes (from Ozutsumi et al. 2002)

Soil	ρ_{sat} (t/m^3)	N (bpf)	Vs (m/s)	ϕ' (deg)	c' (kPa)
B (surface soil)	1.85	5	180	38.0	0.0
B (embankment)	1.85	5	180	25.0	20.0
As2-2	1.80	4	135	38.0	0.0
As2-1	1.85	12	165	40.0	0.0
Ac (upper)	1.65	-	145	34.1	0.0
Ac (lower)	1.75	-	180	39.8	0.0
As1	1.75	6.5	190	38.0	0.0
Ds1	1.85	13	225	39.0	0.0
Dc2	1.75	7.5	190	39.8	0.0

Notes: ρ_{sat} = saturate density; N = SPT blow count; Vs = shear wave velocity; ϕ' = effective-stress friction angle; c' = effective-stress cohesion intercept.
Legend: B = Recent sand fill; As = Holocene sand deposit; Ac = Holocene clay deposit; Ds = Pleistocene sand deposit; Dc = Pleistocene clay deposit.

Table A.3 Index properties of soil samples for samples obtained from Bhuj alluvium (Sitharam et al. 2004)

Index Properties	Soil Sample No. 1	Soil Sample No. 2
Specific Gravity	2.66	2.67
Coarse Sand (%)	-	1.00
Medium Sand (%)	35.00	39.42
Fine Sand (%)	43.00	44.44
Silt Content (%)	20.00	13.00
Clay Content (%)	2.00	2.14
Maximum Void Ratio (e_{max})	0.68	0.71
Minimum Void Ratio (e_{min})	0.42	0.37

Table A.4 Soil properties used in limit equilibrium slope stability analyses for Bhuj earthquake cases (from Singh et al. 2005)

Soil Unit	Unit Weight (kN/m^3)	c' (kPa)	ϕ' (deg)
Semi-pervious shell	18	9	30
Impervious core	20	65	0
Masonry wall	22	80	0
Non-Liquefied Alluvium	20	0	41

A.14 References

Abrahamson, N. A., and Silva, W. J., (2008). Summary of the Abrahamson and Silva NGA ground-motion relations: *Earthquake Spectra,* vol. 24, no. 1, p. 67 – 97.

Akai, K. Bray, J. D., Boulanger, R. W., Christian, J. T. 1995. Geotechnical reconnaissance of the effects of the January 17, 1995, Hyogoken-Nanbu earthquake, Japan. *Report No. UCB/EERC-95/01 August 1995.* p. 151.

Andrus, R. D., and Youd, T. L. (1989). Penetration tests in liquefiable gravels, *Proc., 12th Int. Conf. on soil Mech. And Found. Engrg.,* A. A. Balkema, Rotterdam, The Netherlands, 679-682.

Anicic, D., Berz, G., Boore, D., Bouwkamp, J., Hakenbeck, U., McGuire, R., Sims, J., and Wieczorek, G., (1980). Reconnaissance report Montenegro, Yugoslavia earthquake April 15, 1979, *EERI,* p. 102.

Asian Development Bank (2000). Project completion report on the Jamuna Bridge project in Bangladesh. *Jamuna Bridge Project,* Loan 1298-BAN[SF].

Aydan, O., Ulusay, R., Atak, V.O., (2008). Evaluation of ground deformation induced by the 1999 Kocaeli earthquake (Turkey) at selected sites on shorelines, *Environmental Geology,* vol. 54, p. 165-182.

Baker, C., Hatzfeld, D., Lyon-Caen, H., Papadimitriou, E., and Rigo, A., (1997). Earthquake mechanisms of the Adriatic Sea and Western Greece: implications for the oceanic subduction-continental collision transition, *International Journal of Geophysics,* vol. 131, p. 559-594.

Bardet, J. P., Deaton, S., Frost, D., Goel, P., Lettis, W., Moss, R., Patel, U., Rathje, E., Seed, R., Singh, J. P., Stewart, J., Vandhana, S. V., and Wright, R. H. 2001. Initial geotechnical observations of the Bhuj, India, earthquake of January 26, 2001. *Preliminary report of the India – US geotechnical earthquake engineering reconnaissance team,* Geo-earthquake Engineering Reconnaissance Report(GEER – 004).

Beck, S., Barrientos, S., Kausel, E., and Reyes, M., (1998). Source characteristics of historic earthquakes along the central Chile subduction zone, *Journal of South American Earth Sciences,* vol. 11, no. 2, p. 115-129.

Benetatos, C., and Kiratzi, A., (2006). Finite-fault slip models for the 15 April 1979 (Mw 7.1) Montenegro earthquake and its strongest aftershock of 24 May 1979 (Mw 6.2), *Science Direct Tectonophysics,* vol. 421, p. 129-143.

Bennett, R. A., Hreinsdottir, S., Buble, G., Basic, T., Bacic, Z., Marjanovic, M., Casale, G., Gendaszek, A., and Cowan, D., (2008). Eocene to present subduction of southern Adria mantle lithosphere beneath the Dinarides, *The Geological Socisety of America,* vol. 36, no. 1, p. 3-6.

Bishop, A.W. (1955). The use of the slip circle in the stability analysis of slopes, *Geotechnique,* vol. 5, issue 1, p. 7 to 17.

Blight, G.E. and Fourie, A.B. (2005). Catastrophe revisited – disastrous flow failures of mine and municipal solid waste, *Geotechnical and Geological Engineering*, Vol. 23, p. 219 to 248.

Boore, D. M., and Atkinson, G. M., (2008). Ground-motion prediction equations for the average horizontal component of PGA, PGV, and 5%-dumped PSA at spectral periods between 0.01s and 10.0s: *Earthquake Spectra,* vol. 24, no. 1, p. 99-138.

Boore, D. M., Sims, J. D., Kanamori, H., and Harding, S., (1981). The Montenegro, Yugoslavia, earthquake of April 15, 1979: source orientation and strength, *Physics of the Earth and Planetary Interiors,* vol. 7, p. 133-142.

Campbell, K. W., and Bozorgnia, Y., (2008). NGA ground motion model for the geometric mean horizontal component of PGA, PGV, PGD and 5% damped linear elastic response spectra for periods ranging from 0.01 to 10 s: *Earthquake Spectra,* vol. 24, no. 1, p. 139-171.

Cetin K. O., (2000). Reliability – based assessment of seismic soil liquefaction initiation hazard. Dissertation submitted in partial fulfillment of the requirement for the degree of *Doctor of Philosophy*, University of California at Berkeley; 2000.

Cetin K. O., Isik N., and Unutmaz B. (2004a). Seismically induced landslide at Degirmendere Nose, Izmit Bay during Kocaeli (Izmit) – Turkey earthquake, *Soil Dynamics and Earthquake Engineering,* Vol. 24, p. 189 – 197.

Cetin K. O., Seed R. B., Kiureghian A. D., Tokimatsu K., Harder L. F., Kayen R., and Moss R. E. S. (2004c). SPT – based probabilistic and deterministic evaluation of seismic soil liquefaction potential. *Journal of Geotechnical and Geoenvironmental Engineering ASCE,* Vol. 130, No. 12, p. 1314 – 1340.

Cetin K. O., Youd T. L., Seed R. B., Bray J. D., Stewart J. P., Durgunoglu H. T., Lettis W., and Yilmaz M. T. (2004b). Liquefaction – induced lateral spreading at Izmat Bay during the Kocaeli (Izmit) – Turkey earthquake, *Journal of Geotechnical and Geoenvironmental Engineering ASCE,* Vol. 130, No. 12, p. 1300 – 1313.

Chiou, B.S.-J., and Youngs, R. R., (2008). An NGA model for the average horizontal component of peak ground motion and response spectra: *Earthquake Spectra,* vol. 24, no. 1, p. 173-215.

Console, R., and Favali, P., (1981). Study of the Montenegro earthquake sequence (March-July 1979), *Bulletin of the Seismological Society of America*, vol. 71, no. 4, p. 1233-1248.

Davies, M.P., Dawson, B.D., and Chin, B.G. (1998). Strengths backfigured from liquefaction case histories. *Proceedings of the 2nd International Conference on Case Histories in Geotechnical Engineering,* St Louis, Mo, 1693-1701.
EERI, 1993. Report of the January 15, 1993 Kushiro-oki Earthquake. *EERI Newsletter,* June 1993, Vol. 27, No. 6.

Fiegel, G. F., and Kutter, B. L., 1994. Liquefaction induced lateral spreading of mildly sloping ground. *Journal of Geotechnical Engineering, ASCE,* 120(12): 2236 – 2243.

Fourie, A.B., and Papageorgiou, G. (2001). Defining an appropriate steady state line for Merriespruit gold tailings, *Canadian Geotechnical Journal,* Vol. 38, p. 695 to 706.

Fourie, A.B., and Tshabalala, L. (2005). Initiation of static liquefaction and the role of Ko consolidation, *Canadian Geotechnical Journal,* Vol. 42, p. 892 to 906.

Fourie, A.B., Blight, G.E., and Papageorgiou, G. (2001). Static liquefaction as a possible explanation for the Merriespruit tailings dam failure, *Canadian Geotechnical Journal,* Vol. 38, p. 707 to 719.

Fukuoka, H., Sassa, K., Scarascia-Mugnozza, G., 1997. Distribution of landslides triggered by the 1995 hyogo-ken nanbu earthquake and long runout mechanism of the Takarazuka golf course landslide. *Journal of Physics of the Earth* 45 (2): 83-90.

Fukushima, Y. and Tanaka, T. (1990): A new attenuation relation for peak horizontal acceleration of strong earthquake grond motion in Japan. *Bulletin of the Seismological Society of America,* 80(4), 757-783.

Fukushima, Y. and Tanaka, T. (1992). Revised attenuation relation for peak horizontal acceleration using a new data base. *Programme and abstracts of seismological society, Japan,* No. 2, pp. 116.

Gerolymos, Nikos, and George Gazetas. 2007. A model for grain-crushing-induced landslides-application to Nikawa, Kobe 1995. *Soil Dynamics and Earthquake Engineering* 27 (9): 803-17.

Gupta, S. K. 1972. Chronology of raised beaches and inland coral reefs of saurashtra coast. *Journal of Geology* 80 (3): 357.

Gupta, S. K., and B. S. Amin. 1974. Io/U ages of corals from saurashtra coast. *Marine Geology* 16 (5) (7): M79-83.

Hengesh, J., W. Lettis, C. Saikia, H. Thio, G. Ichinose, and P. Bodin. 2002. Bhuj, India earthquake of January 26, 2001 - reconnaissance report. *Earthquake Spectra* 18 : XVII.

Hight D.W., Georgiannou V. N., Matin P.L. and Nundegar A.K. (1999). Flow slides in micaceous sands. *Proc. International Symposium on Problematic Soils,* Sendai, Japan, 2: 945-260.

http://earthquake.usgs.gov/earthquakes/world/events/1988_12_07_ev.php

Inada 1982. Methods of in situ soil investigations. *Japanese Society of Soil Mechanics and Foundation Engineering*, 217 p.

Ishihara K. (2008). Flow slides of underwater sand deposits in Jamuna River bed. *Geotechnical Engineering for Disaster Mitigation and Rehabilitation,* Science Beijing and Springer-Verlag GmbH Berlin Heidelberg, p. 3-34.

Ishihara K., (2005). Characteristics of waterfront landslides induced by earthquakes, *Proceedings of the Fifteenth (2005) International Offshore and Polar Engineering Conference* Seoul, Korea, June 19-24.

Ishihara, K., Okusa, S., Oyagi, N., and Ischuk, A., (1990). Liquefaction-induced flow slide in the collapsible loess deposit in Soviet Tajik, *Soils and Foundation,* vol. 30, no. 4, p. 73-89.

Ishihara, K., Troncoso, J., Kawase, Y., and Takahashi, Y., (1980). Cyclic strength characteristics of tailings materials, *Soils and Foundations,* vol. 20, no. 4, p. 127-142.

Jefferies, M., and Been, K. (2006). Soil liquefaction. *Taylor and Francis,* p. 479.

Jibson, R.W. and Jibson, M.W. (2005). Slope performance during an earthquake – Java Programs for using Newmark's method and simplified decoupled analysis to model slope performance during earthquakes. *USGS Open-File Report 03-005.*

Karakaisis, G. F., Karacostas, B. G., Papadimitriou, E. E., and Papazachos, B. C., (1985). Properties of the 1979 Montenegro (Southwest Yugoslavia) seismic sequence, *PAGEOPH,* vol. 122, p. 26-35.

Kerwin, S.T., and Stone, J.J. (1997). Liquefaction failure and remediation: King Harbor Redondo Beach, California, *ASCE* vol. 123, no. 8, p. 760 to 769.

Kokusho, T. 2000. Mechanism for water film generation and lateral flow in liquefied sand layer. *Soils and Foundations,* 40(5): 99-111.

Krinitzsky, Ellis L., and Mary E. Hynes. 2002. The Bhuj, India, earthquake: Lessons learned for earthquake safety of dams on alluvium. *Engineering Geology* 66 (3-4) (11): 163-96.

Kulasingam, R., Malvick, E. J., Boulanger, R. W., and Kutter, B. L., 2004. Strength loss and localization at silt interlayers in slopes of liquefied sand. *Journal of Geotechnical and Geoenvironmental Engineering.* 130(11): 1192-1202.

Kulhawy, F. H., and Mayne, P. W. (1990). Manual on estimating soil properties for foundation design, *Electric Power Res. Inst. EL-6800; Prof. 1493-6*, Electric Power Res. Inst., Palo Alto, Calif., 2-38.

Liu, H., and Qiao, T. 1984. Liquefaction potential of saturated sand deposits underlying foundation of structure. *In* Proceedings of the 8th world conference on earthquake engineering, San Francisco, Calif., 21-28 July 1984. Prentice-Hall, Englewood Cliffs, N.J. Vol. 3, pp. 199-206.

Loukidis, D., Lee, S., Yi, Q., and Bourdeau, P. (2001). Analytical study of the Nikawa Landslide. *Proceedings of the 4th international conf. on recent advances in geotech. Engg. And soil dynamics San Diego, CA, March 26-31, 2001* paper no. 5.31.

Matsuo, Osamu. 1996. Damage to river dikes. *Soil and Foundation*: 235-40.

McLeod, H., Murray, L., and Crippen, K. (2003). Tailings dam versus a water dam, what is the design difference? *http://www.infomine.com/publications/docs/McLeod2003b.pdf* Merh, Sukumar S., Sukumar S. Merh, and Sukumar S. Merh. 1995. *Geology of Gujarat*. Bangalore: Geological Society of India.

Meyerhof, G. G., (1965). Bearing capacity and settlement of pile foundations, *ASCE Journal of Geotechnical engineering*, vol, 102, no. GT3, p. 197-228.

Nakagawa, Koichi. 1996. Geological characteristics and problems in and around osaka basin as a basis for assessment of seismic hazards. *Soil and Foundation*: 15-28.
O'Rourke, T. (1989). Armenia earthquake reconnaissance report, Chapter 5: Geotechnical Aspects, p. 54-69.

Olson, S. M. 2001. Liquefaction analysis of level and sloping ground using field case histories and penetration resistance. *PhD. Thesis, University of Illinois at Urbana-Champaign, Urbana, IL.*

Ozutsumi, O. 2002. Effective stress analyses of liquefaction-induced deformation in river dikes. *Soil Dynamics and Earthquake Engineering* 22 (9): 1075-82.

Pacheco, J. F., Estabrook, C. H., Simpson, D. W., and Nábělek, J. L. (1989). Teleseismic body wave analysis of the 1988 Armenian Earthquake. *Geophysical Research Letters*, Vol. 16, No. 12, p. 1425 – 1428.

Rathje E. M., Karatas I., Wright S. G., and Bachhuber J., (2004). Coastal failures during the 1999 Kocaeli earthquake in Turkey, *Soil Dynamics and Earthquake Engineering,* Vol. 24, p. 699 – 712.

Richard A. B., Sigrún Hreinsdóttir, Goran Buble, Tomislav Basic, Zeljko Bacic, Marijan Robertson, P. K., and Campanella, R. G. (1985). Liquefaction potential of sands using the CPT, *Journal of Geotechnical Engineering*, ASCE, 111(3), 384-403.

Robinson, K.E. (1977). Tailings dam constructed on very loose saturated sandy silt. *Canadian Geotechnical Journal,* Vol. 14, p. 399 – 407.

Sasaki, Y. and Shimada, K. 1997. Yodogawa dike damage by the Hyogoken-Nanbu earthquake. *Seismic Behavior of Ground and Geotechnical Structures, Seco Pinto (ed) 1997 Belkema, Rotterdam,* p. 307-316.

Sasaki, Y., Oshiki, H., and Nishikawa, J. (1993). Embankment failure caused by the Kushiro-Oki earthquake of January 15, 1993. *Proceedings of 13th International Conference on Soil Mechanics and Foundation Engineering,* New Delhi, India, Vol. 1, 61-68.

Sasaki, Y., Tamura, K., Yamamoto, M., and Ohbayashi, J. (1995). Soil improvement work for river embankment damaged by the 1993 Kushiro-oki earthquake. *Proceedings of Earthquake Geotechnical Engineering,* No. 14-16, Tokyo, Japan, Vol. 1, 43-48.

Sassa, K., Fukuoka, H., and Sakamoto, T. (1995). The rapid and disastrous Nikawa Landslide. *Landslide News,* No. 9, pp.6-9.

Sassa, K., Fukuoka, H., and Scarascia-Mugnozza, G. (1996). Earthquake-induced-landslides: Distribution, motion and mechanisms. *Soil and Foundation*: 53-64.

Sassa, K., Wang, F., and Fukuoka, H. (2000). Geotechnical simulation test for the Nikawa Landslide induced by January 17, 1995 Hyogoken – Nambu Earthquake. *Journal of the Japanese Geotechnical Society of Soils and Foundations,* Vol. 40, No. 1, p. 35 – 46.

Sassa, K., Wang, G., and Fukuoka, Hiroshi. (2004). Assessment of landslide risk during earthquake/rainfall on urban area. *Annuals of Disaster Prevention Research Institute, Kyoto University*, No. 47 C.

Seed H. B., and Idriss I. M. (1971). Simplified procedure for evaluating soil liquefaction potential, *Journal of Soil Mechanics and Foundation Division,* Vol. 97 (SM9), p. 1249 – 1273.

Seed, H. B., and De Alba (1986). Use of SPT and CPT tests for evaluating the liquefaction resistance of sands, *Proceedings, INSITU'86, ASCE Special Conference on*

Use of In Situ Testing in Geotechnical Engineering Special Publication No. 6, ASCE, New York, N. Y.

Singh, R., Roy, D. and Jain, S. K. 2005a. Analysis of earth dams affected by the 2001 Bhuj earthquake. *Engineering Geology* 80 (3): 282-91.

Singh, R., Roy, D. and Jain, S. K. 2005b. Investigation of liquefaction failure in earthen dams during Bhuj earthquake. *Indian Institute of Technology, Kharapur.*

Singh, Raghvendra, Debasis Roy, and Debatosh Das. 2007. A correlation for permanent earthquake-induced deformation of earth embankments. *Engineering Geology* 90 (3-4) (3/27): 174-85.

Singh, Raghvendra. 2005. Analysis of earth dams affected by the 2001 bhuj earthquake. *Engineering Geology* 80 (3): 282-91.

Sitharam, T. G., and Govendaraju, L. 2004. Geotechnical aspects and ground response studies in bhuj earthquake, India. *Geotechnical and Geological Engineering* 22 (3): 439-55.

Sitharam, T. G., Govinda Raju, L., and Srinivasa Murthy, B. R. 2004. Cyclic and monotonic undrained shear response of silty sand from Bhuj region in India. *ISET Journal of Earthquake Technology,* Paper No. 450, Vol. 41, No. 2-4, p. 249-260.

Sivakumar Babu, G. L. 2007. Analysis of stability of earthen dams in kachchh region, gujarat, india. *Engineering Geology* 94 (3): 123-36.

Skempton A. W. (1986). Standard penetration test procedures and the effects in sands of over burden pressure, relative density , psection size, ageing and overconsolidation. *Geotechnique*, 36, 3, 425-447.

Skempton, A. W. (1986). Standard penetration test procedures and the effects in sand of overburden pressure, relative density, particle size, ageing, and over consolidation. *Geotechnique*, 36, 425-447.

Stewart, J.P., Bray, J.D., Seed, R.B., and Sitar, N. (1994). Prelininary report on the principal geotechnical aspects of the January 17, 1994 Northridge earthquake, *Report No. UCB/EERC-94/08,* Earthquake Engineering Research Center, Univ. of California at Berkeley, Calif., p. 20 to 33.

Tani, Shigeru. 1996. Damage to earth dams. *Soils and Foundations*(Special): 263-72.
Terzaghi, K., Peck, R. B., and Mesri, G. (1996). *Soil Mechanics in Engineering Practice, Third Edition.* John Wiley & Sons, Inc., New York, 549 p.

Tokimatsu, K. (1988). Penetration tests for dynamic problems, *Proceedings of the 1st International Symposium on Penetration Testing,* Rotterdam, p. 117 – 136.

Tokimatsu, K. (1988). Penetration tests for dynamic problems. *Proceedings of 1st international symposium on penetration testing, Rotterdam,* pp. 117-136.

Towhata, I. 2002. Geotechnical reconnaissance study on damage caused by 2001 Gujarat earthquake, India. *Soil and Foundation* 42 (4): 77-88.

Towhata, I. 2002. Geotechnical reconnaissance study on damage caused by 2001 gujarat earthquake, india. *Soil and Foundation* 42 (4): 77-88.

Towhata, Ikuo. 1996. Dynamic failures of subsoils observed in waterfront areas. *Soil and Foundation*: 149-60.

Trifunac, M. D., and Brady, A. G., (1975). On the correlation of seismic intensity with peaks of recorded strong ground motion, *Bulletin of the Seismological Society of America*, vol. 65, p. 139-162.

Trifunac, M. D., and Ivanovic, S. S., (2003). Re-occurrence of site-specific response in former Yugoslavia-part 1: Montenegro, *Soil Dynamics and Earthquake Engineering,* vol. 23, p. 637-661.

Trifunac, M.D., Todorovska, M.I., and Ivanovic, S.S. (1994). A note on distribution of uncorrected peak ground accelerations during the Northridge, California earthquake of 17 January 1994, *Soil Dynamics and Earthquake Engineering,* Elsevier Science Publishing Co. Inc., London, England, vol. 13, p. 187 to 196.

Troncoso, J. H., Avendano, A., and Vergara, A., (1993). The seismic failure of Barahona tailings dam, *Proceedings of the 3rd International Conference on Case Histories in Geotechnical Engineering, St. Louis, Missouri,* June 1-4, paper no. 2.56.

Uchida, K., Torii, T., Tsujino, S., and Ando, S. (2001). A study on failure mechanism of embankment dams for irrigation damged by the 1995 Hyogoken-Nanbu earthquake. *Proceedings of the 4th international conf. on recent advances in geotech. Engg. And soil dynamics San Diego, CA, March 26-31, 2001* paper no. 5.27.

USGS (2010). Notes about the Armenia earthquake, 7 December 1988. *http://earthquake.usgs.gov/earthquakes/world/events/1988_12_07_ev.php*

USGS (2010). Preliminary earthquake report, http://neic.usgs.gov/neis/eq_depot/1999/eq_990817/

USGS (2011). Historic Earthquakes – Northridge, California, *http://earthquake.usgs.gov/earthquakes/states/events/1994_01_17.php*

Viti, M., D'Onza, F., Mantovani, E., Albarello, D., and Cenn, N., (2003). Post-seismic relaxation and earthquake triggering in the southern Adriatic region, *International Journal of Geophysics,* vol. 153, p. 645-657.

Wagener, F., Craig, H., and Blight, G., McPhail, G., Williams, A.A.B., and Strydom, J.H. (1998). The Merriespruit dam failure – A review, *Tailings and Mine Waste Conference 1998,* Belkem, Rotterdam

Wagener, F., Strydom, K., Craig, H., and Blight, G. (1997). The tailings dam flow failure at Merriespruit, South Africa: Causes and consequences, *Tailings and Mine Waste Conference 1997,* Belkem, Rotterdam.

Wang, F. -W. 2000. Geotechnical simulation test for the nikawa landslide induced by January 17, 1995 hyogoken-nambu earthquake. *Soil and Foundation* 40 (1): 35-46.

Yegian, M. K., Ghaharaman, V. G., and Gazetas, G. (1994a). 1988 Armenia earthquake. I: Seismological, geotechnical, and structural overview. *Journal of Geotechnical Engineering,* ASCE, vol. 120, issue 1.

Yegian, M. K., Ghahraman, V. G., and Gazetas, G. (1994b). 1988 Armenia earthquake – II: damage statistics versus geologic and soil profiles. *Journal of Geotechnical Engineering,* ASCE, vol. 120, issue 1, p. 21-45.

Yegian, M. K., Ghahraman, V. G., and Gazetas, G. (1994c). Ground-motion and soil-response analyses for Leninakan, 1988 Armenia, earthquake. *Journal of Geotechnical Engineering,* ASCE, vol. 120, issue 2.

Yegian, M. K., Ghahraman, V. G., and Gazetas, G. (1994e). Liquefaction and embankment failure case histories, 1988 Armenia earthquake. *Journal of Geotechnical Engineering,* ASCE, vol. 120, issue 3.

Yegian, M. K., Ghahraman, V. G., and Gazetas, G. (1994e). Seismological, soil and valley effects in Kirovakan, 1988 Armenia, earthquake. *Journal of Geotechnical Engineering,* ASCE, vol. 120, issue 2.

Yoshimine M., Robertson P.K. and Wride C.E. (1999). Undrained shear strength of clean sands to trigger flow liquefaction. *Canadian Geotechnical Journal,* 36: 891-906.